Remote Sensing Image Analysis

Including the Spatial Domain

Edited by
Steven M. de Jong and Freek D. van der Meer

Springer

CD-ROM INCLUDED

Remote Sensing Image Analysis: Including the Spatial Domain

Remote Sensing and Digital Image Processing

VOLUME 5

REMOTE SENSING IMAGE ANALYSIS: INCLUDING THE SPATIAL DOMAIN

edited by

STEVEN M. DE JONG

Department of Physical Geography,
Faculty of Geosciences, Utrecht University,
The Netherlands

and

FREEK D. VAN DER MEER

Department of Earth Systems Analysis,
International Institute for Geo-Information Science and Earth Observation (ITC),
Enschede, The Netherlands
&
Department of Geotechnology,
Faculty of Civil Engineering and Geosciences,
Technical University Delft, The Netherlands

Including a CD-ROM with colour images

Visit Springer's eBookstore at: http://ebooks.springerlink.com
and the Springer Global Website Online at: http://www.springeronline.com

Preface

Since the launch of the first earth observation satellite ERTS-1 in 1972 much effort has been made to develop suitable and scientifically sound methods of information extraction from digital images. Over the years, Remote Sensing has proven to be a valuable tool for identifying objects at the earth's surface and for measuring and monitoring important biophysical characteristics and human activities on the terrain. Since the early days of earth observation, numerical methods of spectral analysis have been used to extract information from these digital images. Because computer power was limited, few spectral bands were recorded at pre-selected frequencies and visualization methods were very basic, it was only possible to transform the raw pixel data into meaningful classes on a pixel-by-pixel basis; one simply did not have the tools to analyse large amounts of remotely sensed digital data over a wide range of frequencies of light.

The 1980s saw the development of spectral-based algorithms for image analysis and image classification which were included in various kinds of image processing software packages. During the 1990s, spectral image analysis flourished anew when hyperspectral sensors with hundreds of spectral bands became available. Computers were much more powerful than before and visualization techniques had matured. The high spectral resolution images permitted the recording of spectral data in many spectral bands, which allowed the use of absorption feature identification and the application of sub-pixel methods such as spectral mixture analysis.

Spectral image analysis methods produce for many cases satisfying results but sometimes they fail to produce good results because not all the objects at the earth surface have unique spectral signatures. As a result, objects with similar spectral signatures cannot be spectrally separated and additional information is required to distinguish them. Information captured in neighbouring cells or information about patterns surrounding the pixel of interest may provide useful supplementary information. This type of information is referred to as information from the spatial domain. In spite of the extra amount of information available, initially there were relatively few efforts to extract the spatial information captured in the new, detailed airborne and spaceborne images.

Initially, only a few pioneers explored the methods and techniques of spatial analysis for remote sensing, among them P.J. Curran, D.L.B. Jupp, S.W. Wharton and C.E. Woodcock. The fact that spatial analysis received so little attention is suprising because spatial patterns in images may contribute significantly to image analysis and image classification. It is also surprising that the spatial aspects of image analysis received so little attention during the seventies and eighties because many environmental disciplines such as geography, ecology, soil science and forestry have a long history of coping with spatial patterns. In the past these disciplines developed intelligent hierarchical mapping systems like the physiographic approach of the CSIRO, Australia, or the Agro-Ecological Zones mapping method of the

United Nations Food and Agricultural Organisation (FAO). Only recently, have a wide range of researchers from various disciplines paid attention to spatial patterns in remotely sensed images and have studied how they can aid information extraction.

The objective of this book is twofold: 1) to bring together several new methods and approaches for analyzing and quantifying spatial patterns present in earth observation images, and 2) to illustrate these methods and techniques for a wide range of applications under varying natural conditions. The methods and techniques brought together in the chapters in the beginning of the book comprise different types of variogram analysis, various methods for texture quantification, smart kernel operators, pattern recognition, image segmentation methods, sub-pixel methods, wavelets and advanced spectral mixture analysis techniques. The effectiveness and the innovative aspects of these methods and techniques are illustrated in chapters 5 to 13 by a wide range of applications ranging from natural vegetation surveys in different types of landscapes, through general land cover mapping, urban mapping and geological applications such as mineral abundance and seepage mapping.

The book brings together contributions written by renowned researchers from all over the world and from a wide range of disciplines. The book is meant for professionals and researchers who use remote sensing image analysis, image interpretation and image classification in their work. It is also intended as a textbook and reference for PhD students and graduates in disciplines such as geography, geology, botany, ecology, forestry, cartography, water resource management, soil science, engineering, urban and regional planning or other disciplines using geospatial data extracted from earth observation imagery.

This book on 'Remote Sensing Image Analysis: Including the Spatial Domain' is a follow-up to a previous publication (2001) entitled 'Imaging Spectrometry: Basic Principles and Prospective Applications' by the same editors. That book emphasized the need for improved identification of objects at the earth's surface, the improvement of sensors such as Landsat TM and SPOT and the improved quantification of object properties, using a wide range of spectrally based analytical image processing techniques. This, second book shifts the attention from spectrally based techniques to spatial-based approaches. The editors and authors sincerely hope that this volume will introduce the possibilities of spatially-based image analysis methods to the attention of a wide range of researchers and image users, that it will inspire them to apply these methods in their work and will stimulate them to develop new algorithms and applications in this field.

Peter A. Burrough
Utrecht University
The Netherlands

Contents

4   Resolution Manipulation and Sub-Pixel Mapping   51
Peter M. Atkinson

**5   Multiscale Object-Specific Analysis (MOSA): An Integrative Approach   71
         for Multiscale Landscape Analysis**
Geoffrey J. Hay & Danielle J. Marceau

Including a CD-Rom with colour images

Acknowledgements

of the Environment, Northern Ireland; the Department of the Environment, Food and Rural Affairs; the Environment Agency; the National Assembly for Wales; NERC; the Scottish Executive; Scottish Natural Heritage.

About the editors

CV Prof. Dr. S.M. de Jong
Professor Dr Steven M. de Jong (1962) is head of the Land Degradation & Remote Sensing Section of the Department of Physical Geography at Utrecht University since 2001. From 1998 to 2001 he was head of the Remote Sensing Laboratory of the Department of Environmental Sciences of Wageningen University. De Jong completed his PhD study on applications of 'GIS and Remote Sensing for Mediterranean Land Degradation Monitoring and Modelling' in 1994 at Utrecht University. In 1987 he received his MSc in Physical Geography on 'Rural Land Evaluation Procedures using Geographical Information Systems' from Utrecht University in the Netherlands. He holds minors in Soil Physics, Soil Chemistry and Remote Sensing from Wageningen University. In 1997, 1998 and 2003 he was principle investigator for the experimental airborne campaigns in the Peyne area in southern France. In 1998 he conducted a remote sensing research project for urban mapping in Ouagadougou, Burkina Faso. De Jong worked as a visiting scientist at NASA Jet Propulsion Laboratory (JPL) in Pasadena, California in 1995 and 1996. During his stay at JPL he contributed to the applied research initiatives of the AVIRIS group. AVIRIS is JPL's Airborne Visible Infra Red Imaging Spectrometer. De Jong is currently chairman of the Research School ICG: Netherlands Centre for Geo-ecological Research. He is also chairman of the National Workgroup for Agricultural and Environmental Applications in Remote Sensing (WRSLN). De Jong was or is member of the organising committees of a number of national and international conferences and is editor of the book 'Imaging Spectroscopy: Basic Principles and Prospective Applications' published by Kluwer in 2001. He is having major scientific experiences in the field of imaging spectrometry, image processing, GIS, geostatistics, soil science, soil erosion modelling and field surveys.

CV Prof. Dr. Freek D. van der Meer

Prof. Dr. Freek D. van der Meer (1966) has a M.Sc. in structural geology and tectonics of the Free University of Amsterdam (1989) and a Ph.D. in remote sensing from Wageningen Agricultural University (1995) both in the Netherlands. He started his career at Delft Geotechnics (now Geodelft) working on geophysical processing of ground penetrating radar data. In 1989 he was appointed lecturer in geology at the International Institute for Geoinformation Sciences and Earth observation (ITC in Enschede, the Netherlands) where he worked too date in various positions. At present he is the chairman of the Department of Earth System Analysis. His research is directed toward the use of hyperspectral remote sensing for geological applications with the specific aim of using geostatistical approaches to integrate airborne and field data into geologic models. He teaches at post graduate, M.Sc. and Ph.D. level on these topics. On 1 November 1999, Dr. van der Meer was appointed part-time full professor of imaging spectrometry at the Delft University of Technology (Faculty of Civil Engineering and Geosciences). In 1999 he delivered his first Ph.D. graduate working on remote sensing for hydrocarbon microseepage detection, at present six related Ph.D. projects are starting/running under his guidance at ITC and DUT. Prof. Van der Meer published over 75 papers in international journals and authored more than 100 conference papers and reports. Prof. Van der Meer is editor of the book Spatial Statistics for Remote Sensing published in 2000 by Kluwer and editor of the book Imaging Spectroscopy: Basic Principles and Prospective Applications published by Kluwer in 2001. He is chairman of the Netherlands Society for Earth Observation and Geoinformatics, chairman of the special interest group geological remote sensing and council member of EARSeL, associate editor of the Journal of Applied Geosciences, associate editor of Terra Nova and series editor of the remote sensing and digital image processing book series of Kluwer.

Chapter 1
Basics of Remote Sensing

Steven M. de Jong, Freek D. van der Meer & Jan G.P.W. Clevers

1.1   Introduction

In July 1972 the first earth observation satellite was launched by the United States. In 1972 this satellite was called Earth Resources Technology Satellite-1 (ERTS-1), a name that held until January 1975 when it was renamed into Landsat-1. This first earth observation satellite held a four waveband multi-spectral scanning system (MSS) aboard in two visible and two near-infrared spectral bands and three return beam vidicon (RBV) television cameras. This sensor wrote history as it proved to be of great importance to give remote sensing worldwide recognition as an important environmental technique (Harper, 1983).

Remote sensing refers to obtaining information about objects or areas by using electromagnetic radiation (light) without being in direct contact with the object or area. So, remote sensing is day-to-day business for people. Reading the newspaper, watching cars driving in front of you, looking at a lecturer during classes are all remote sensing activities of the human eye. The human eyes register the solar light reflected by these objects and your brains interpret the colours, the grey tones and intensity variations. Next, these data are translated into useful information. The human eye however is limited to a small part of the total electromagnetic spectrum i.e. approximately 400 to 700 nm. In remote sensing various kinds of tools and devices are used to make electromagnetic radiation outside this range visible to the human eye, especially the near infrared, middle infrared, thermal infrared and microwaves. Remote sensing now plays an important role in a wide range of environmental disciplines such as geography, geology, zoology, agriculture, forestry, botany, meteorology, oceanography and civil engineering.

Since that first launch of an earth observation satellite remote sensing is increasingly used to acquire information about environmental processes such as agricultural crops, land cover, vegetation dynamics, water quality, urban growth, seabed topography etc. Remote sensing helped us to increase our understanding of the ecological system of the earth. Remote sensing helped us to measure the size of the ozone hole in the atmosphere, to notice the differences of atmospheric ozone concentrations between the southern and northern hemisphere and to understand the dynamics of ozone concentration in the atmosphere. Remote sensing is playing a key role in our efforts to understand the complex dynamics of ocean circulation such as El Niño, El Niña and the NAO: the Northern Atlantic Oscillation and to assess their effects on global and regional climates and extreme events. Long-term remote sensing observations of the Sahel region made us at least partly understand the complex cyclic pattern

of the advancing and withdrawing Sahara desert. The European Union is successfully using Earth observation images collected throughout the growing season of crops to control their subsidies on agricultural crops. Remote sensing is used in precision agriculture practices to follow crop development and to detect water or nutrient deficits. Remote sensing is used to collect information necessary for the maintenance of forests and to monitor nature reserves. Next, there is of course the role of remote sensing in our society as an instrument enabling us to monitor the activities of neighbouring, and maybe hostile states as shown during the first and the second gulf wares in the middle east.

1.2   Historic overview

In 1859 Gaspard Tournachon took an oblique photograph of a small village near Paris from a balloon. With this picture the era of earth observation and remote sensing had started. Other people all over the world soon followed his example. During the Civil War in the United States aerial photography from balloons played an important role to reveal the defence positions in Virginia (Colwell, 1983). Likewise other scientific and technical developments this Civil War time in the United States speeded up the development of photography, lenses and applied airborne use of this technology. Although the space era of remote sensing was still far away after the Civil war, already in 1891 patents were granted in Germany to successful designs of rockets with imaging systems under the title: 'new or improved apparatus for obtaining bird's eye photographic views of the earth'. The design comprised a rocket propelled camera system that was recovered by a parachute. Table 1.1, modified from Campbell, 1996) shows a few important dates in the development of remote sensing.

The next period of fast developments in earth observation took place in Europe and not in the United States. It was during World War I that airplanes were used on a large scale for photoreconnaissance. Aircrafts proved to be more reliable and more stable platforms for earth observations than balloons. In the period between World War I and World War II a start was made with the civilian use of aerial photos. Application fields of airborne photos included at that time geology, forestry, agriculture and cartography. These developments lead to improved cameras, films and interpretation equipment. The most important developments of aerial photography and photo interpretation took place during World War II. During this time span the development of other imaging systems such as near-infrared photography, thermal sensing and radar took place. Near-infrared photography and thermal infrared proved very valuable to separate real vegetation from camouflage. The first successful airborne imaging radar was not used for civilian purposes but proved valuable for nighttime bombing. As such the system was called by the military: 'plan position indicator' and was developed in Great Britain in 1941.

After the wars in the 1950s remote sensing systems continued to evolve from the systems developed for war efforts (Lillesand & Kiefer, 2000; Colwell, 1983; Harper, 1983). Colour infrared photography (CIR) was found to be of great use for the plant sciences. In 1956 Colwell conducted experiments on the use of CIR for the classification and recognition of vegetation types and the detection of diseased and damaged or stressed vegetation. It was also in the 1950s that significant progress in radar technology was achieved. Two types of

radar were developed at that time: SLAR: side-looking airborne radar and SAR: Synthetic Aperture Radar. Either development aimed at the acquisition of images at the highest possible resolution. Crucial to the SAR development was the ability to finely resolve the Doppler frequencies using a frequency analyses algorithm on the returning radar signal by the US Air Force research centre.

In the early 1960s the US started placing remote sensors in space for weather observation and later for land observations. TIROS (Television Infrared Observation Satellite) was the first meteorological satellite. A long series of meteorological satellites followed this one. 1960 was also the beginning of a famous US military space imaging reconnaissance program called Corona (McDonald, 1995). Unfortunately, much of this programme remained classified until 1995. In 1970 the TIROS programme was renamed into NOAA (National Oceanic and Atmospheric Administration). Until today the NOAA Advanced Very High Resolution Radiometer (AVHRR) is orbiting the globe and collecting information on weather patterns in visible, near infrared and thermal wavelengths. NOAA-17 was launched on June 24, 2002. The 1950s and 1960s were also important for the organisational development of remote sensing. Various civil research organisations and universities became highly interested in these new technologies. This resulted in the start of various professional organisations and the publishing of remote sensing journals such as the IEEE Transactions on Geoscience and Remote Sensing, International Journal of Remote Sensing, Remote Sensing of Environment and Photogrammetric Engineering & Remote Sensing. Today remote sensing is not only taught at the university level but also at high schools.

In the early 70s the first satellite specifically designed to collect data of the earth's surface and its resources was developed and launched: ERTS-1 Earth Resources Technology Satellite. Later, in 1975, this programme was renamed into Landsat. This first earth resources satellite was in fact a modified Nimbus weather satellite carrying two types of sensors: a four waveband multi-spectral scanner (MSS) and three return beam vidicon television cameras (RBV). The sensors aboard this satellite proved to be able to collect high quality images at a reasonable spatial resolution. These images gave remote sensing a worldwide recognition as a valuable technology. The main advantages recognized at that time were (Curran, 1985): ready availability of images for most of the world, lack of political, security and copyright restrictions, low cost, repetitive multi-spectral coverage and minimal image distortion.
Landsat 2 and 3 were launched in 1975 and 1978, respectively, and carried the same payload as the first satellite of this series. The payload was changed in 1982 with Landsat 4. The technically more advanced Thematic Mapper (TM) sensor replaced the RBV. An improved design of the TM, the ETM+ (Enhanced Thematic Mapper) was mounted aboard Landsat 7 and launched in 1999. The Landsat series is a very successful programme, various MSS and TM sensors exceeded by far its design life time and its imagery is probably the most widely used data in the Earth sciences. One black spot on its history record is the 'failure upon launch' of Landsat 6 in 1993.

Various other successful earth observation missions carried out by other countries followed the Landsat programme. In 1978 the French government decided to develop their own earth observation programme. This programme resulted in the launch of the first SPOT satellite in 1986. To the original SPOT design of three spectral bands a new sensor called Vegetation

was added aboard SPOT-4 in 1998. Other earth observation missions are the Indian Remote Sensing Programme (IRS) started in 1988, the Russian Resurs series first launched in 1985 and the Japanese ADEOS (Advanced Earth Observing Satellite) put in orbit in 1996. The European Space Agency (ESA) launched its first remote sensing satellite, ERS-1, in the year 1991. ERS carries various types of sensors aboard among which the AMI, a C-band (5 cm radar) active microwave instrument. The main focus of the ERS programme is oceanographic applications although it is also widely used for monitoring tropical forests. In 1995 ERS-2 was successfully launched. In March 2002 ESA launched Envisat-1, an earth observation satellite with an impressive payload of 13 instruments such as a synthetic aperture radar (ASAR) and a Medium Resolution Imaging Spectrometer (MERIS). An important recent development is the launch of high-resolution earth observation systems such as IKONOS and QuickBird. These systems have multi-spectral systems collecting information in 4 bands (blue, green, red and near-infrared) at a spatial resolution of 4 meters or better. IKONOS has also a panchromatic mode (0.45-0.90 µm) with a spatial resolution of 1 m. With IKONOS, QuickBird and similar systems, space borne remote sensing approaches the quality of airborne photography.

Table 1.1 – Milestones in the history of remote sensing (modified from Campbell, 1996).

1800	Discovery of Infrared by Sir W. Herschel
1839	Beginning of Practice of Photography
1847	Infrared Spectrum Shown by J.B.L. Foucault
1859	Photography from balloons
1873	Theory of Electromagnetic Spectrum by J.C. Maxwell
1909	Photography from Airplanes
1916	World War I: Aerial Reconnaissance
1935	Development of Radar in Germany
1940	WW II: Applications of Non-Visible Part of EMS
1950-	Military Research and Development
1959	First Space Photograph of the Earth (Explorer-6)
1960	First TIROS Meteorological Satellite Launched
1970	Skylab Remote Sensing Observations from Space
1971	Launch of Landsat-1 (ERTS-1): MSS sensor
1972-	Rapid Advances in digital image processing
1978	Launch of Seasat (first spaceborne L-band radar)
1982	Launch of Landsat-4: new Generation of Landsat sensors TM
1986	French Commercial Earth Observation Satelliet SPOT
1986	Development Hyperspectral Sensors
1990-	Development High Resolution Spaceborne Systems
	First Commercial Developments in Remote Sensing
1991	Launch of the first European Remote Sensing Satellite ERS1 (active radar)
1998	Towards Cheap One-Goal Satellite Missions
1999	Launch of EOS-TERRA: NASA Earth Observing Mission
1999	Launch of IKONOS, very high spatial resolution sensor system
2001	Launch of Landsat-7 with new ETM+ sensor
2001	Launch of QuickBird, very high spatial resolution sensor system
2002	Launch of ESA's Envisat with 10 advanced instruments

1.3 Concepts of Remote Sensing

Remote sensing, also called earth observation, refers in a general sense to the instrumentation, techniques and methods used to observe, or sense, the surface of the earth, usually by the formation of an image in a position, stationary or mobile, at a certain distance remote from that surface (after Buiten & Clevers, 1993). In remote sensing electromagnetic radiation coming from an object, in case of earth observation this object is the earth's surface, is being measured and translated into information about the object or into processes related to the object. In the former measurement phase the following components are relevant:
• the source of the electromagnetic radiance
• the path through the atmosphere
• the interaction with the object
• the recording of the radiation by a sensor.
These comprise the remote sensing system as illustrated in figure 1.1. The second phase can be considered to cover the following components:
• transmission, reception and (pre)processing of the recorded radiance
• interpretation and analysis of the remote sensing data
• creation of the final product.
The individual components will be briefly described in the next sections.

1.3.1 Sources of electromagnetic radiation

In remote sensing we restrict ourselves to the use of electromagnetic radiation as a characteristic of numerous physical processes. All materials with a temperature above 0K have the power to emit electromagnetic energy. Objects on or near the earth's surface are able to reflect or scatter incident electromagnetic radiation emitted by a source, which may be artificial, e.g., flash light, laser or microwave radiation, or natural, such as the sun. In the visible, near-infrared (NIR) and middle-infrared (MIR) part of the electromagnetic spectrum, we are measuring solar radiation reflected by objects at the earth's surface. In the thermal-infrared (TIR) part, particularly in the atmospheric window at about 10 μm (see figure 1.2), we are measuring emitted radiation by objects at the earth's surface, be it that this radiation is originating from the sun. In the microwave part of the spectrum, both reflection of solar light and emission occur at very low energy rates. As a result, radiation mostly is transmitted to the earth's surface by an antenna on board the remote sensing system and, subsequently, we measure the amount of radiation that is reflected (backscattered) towards the same antenna. The latter type of system is generally referred to as an active remote sensing system.

1.3.2 The atmosphere

Before solar radiation reaches the earth's surface, the atmosphere will influence it. In addition, the atmosphere will influence reflected solar radiation or emitted radiation by an object at the earth's surface before an airborne or space borne sensor detects it (Van der Meer & De Jong, 2001). The atmosphere consists mainly of molecular nitrogen and oxygen (clean dry air). In addition, it contains water vapour and particles (aerosols) such as dust, soot, water droplets and ice crystals. The changes of the radiation can vary with wavelength, condition of the atmosphere and the solar zenith angle (Slater, 1980). The most important processes here are scattering (Herman et al., 1993) and absorption (LaRocca, 1993). Scattering effects
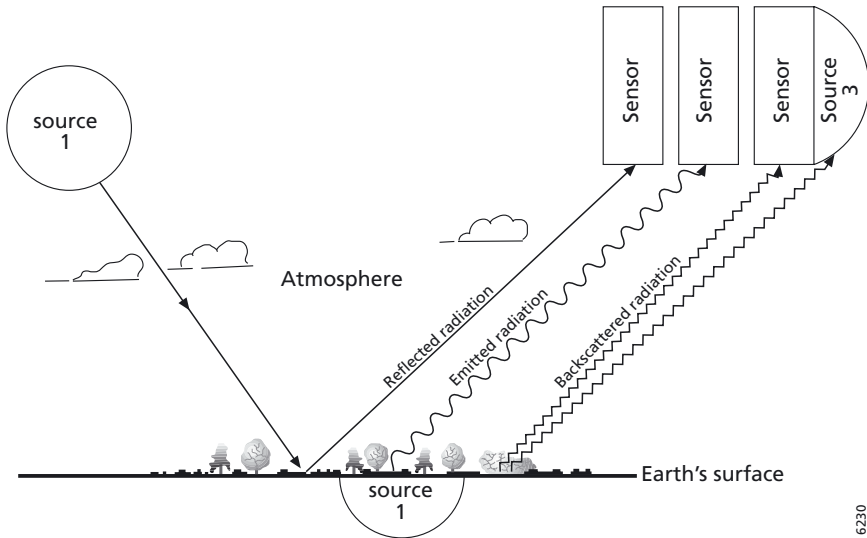
Figure 1.1 – The remote sensing system (modified from Curran, 1985).

can be divided into Rayleigh, Mie and non-selective scattering. These processes lead to the formation of diffuse radiation. A portion of the diffuse radiation goes back to space and a portion reaches the ground. The radiation, which has not been scattered, is called direct radiation. Absorption is caused, for example, by the presence of water vapour in the atmosphere. Scattering and absorption in the atmosphere cause an attenuation of the solar radiation before it reaches the earth's surface. This is illustrated in figure 1.2 for the entire electromagnetic spectrum used for Earth observation techniques. In parts of the electromagnetic spectrum the atmosphere is not or hardly transparent, these parts are not suitable for remote sensing. Those parts of the spectrum where the atmospheric transmittance is high are useful for remote sensing and they are called atmospheric windows. Figure 1.3 illustrates the effects of scattering and absorption in the optical part of the spectrum between 400 and 2500 nm as computed by the atmospheric transmission model Modtran (Wolfe and Zissis, 1993). Most of the absorptions are due to water in figure 1.3. Absorption due to oxygen occurs at 760 nm, carbon dioxide at 2005 and 2055 nm.

1.3.3 Object – radiation interaction

When electromagnetic radiation hits an object at the earth's surface, it can be transmitted, absorbed or reflected. The mutual magnitude of these processes is determined by the properties of the object. In remote sensing we can measure the amount of reflected solar radiation as a function of wavelength, called spectral reflectance. Figure 1.4 illustrates the spectral reflectance of some typical objects. Water absorbs most of the incoming radiation and reflects only a small amount of radiation particularly in the visible part of the spectrum, at longer wavelengths water does not reflect any significant amount of radiation. Soils exhibit quite a smooth spectral reflectance curve. Distinct spectral features are found in narrow spectral bands caused by absorption by minerals and iron oxide and can be detect by imaging spectrometers (Van der Meer and De Jong, 2001). Broader features occur at about 1400 nm
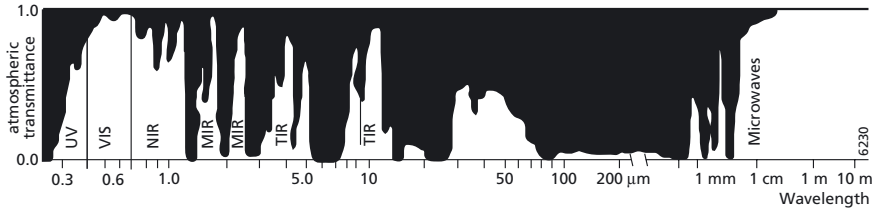
Figure 1.2 – Atmospheric transmittance for radiation as a function of the wavelength (modified from Lillesand and Kiefer, 2000).
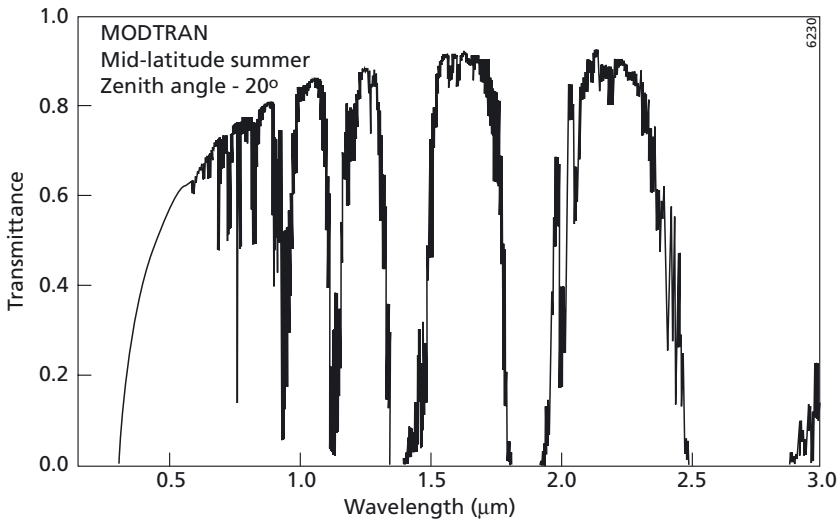
Figure 1.3 – Modtran modelled atmospheric transmittance, visible to near infrared. Most of the absorptions are due to water. Oxygen occurs at 0.76 μm, carbon dioxide at 2.0 and 2.06 μm. (source: http://speclab.cr.usgs.gov/index.html).

and at about 1900 nm, due to absorption by water. The absorption by water also causes the gradually decreasing reflectance with increasing wavelength in the mid-infrared region. The moisture content of the soil causes the spectral reflectance of a wet soil to be lower than that of a dry soil. Vegetation, on the other hand, shows a very characteristic reflectance curve. The reflectance in the visible part of the spectrum is low due to absorption of this radiation by the chlorophyll in the green plant parts. In the NIR region hardly any absorption occurs, and reflectance is determined by the amount of transitions between cell walls and air vacuoles in the leaf tissue. As a result, NIR reflectance of green vegetation is high, and a steep slope occurs in the curve at about 700 nm, the so-called red-edge region (Clevers and Jongschaap, 2001; Kumar et al., 2001). In the MIR region we observe a similar influence of water as observed for soils.
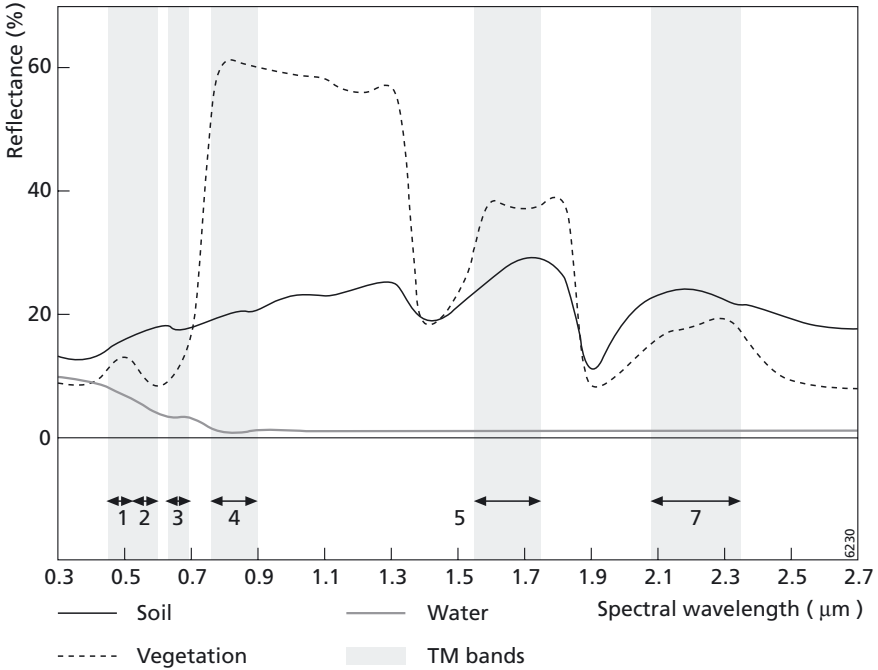
Figure 1.4 – Typical spectral reflectance curves for water, soil and vegetation.

In the thermal infrared part of the spectrum the amount of emitted radiation is measured. This amount can be related to the temperature of the feature observed. This provides information on, e.g., the (evapo)transpiration of the surface and thus gives relevant information for energy balance studies. An important property of the long wavelengths used in the microwave region is that they are not susceptible to atmospheric scattering. As a result they can penetrate through cloud cover, haze and all but the heaviest rainfall. A passive microwave sensor detects the naturally emitted microwave energy within its field of view. This emitted energy is related to the temperature and moisture properties of the emitting object. Since the amounts of emitted energy generally are very small, a passive microwave sensor is therefore characterised by a low spatial resolution.

Active microwave sensors provide their own source of illumination. They are called radars and measure the amount of energy scattered back towards the radar antenna. The radar echo is depending on the properties of the radar system like frequency, polarisation and the viewing geometry, and on the properties of the object like the roughness and electrical properties. So, with radar we get information on object properties like the geometry (terrain topography), roughness (height variations in relation to the applied wavelength) and moisture (determining the electrical properties of a soil or vegetation). An in-depth description of microwave remote sensing is given in volume 3 of this book series on 'Remote Sensing and Digital Image Processing' by Kozlov et al. (2001) or can be found in Henderson and Lewis (1998).

1.3.4 Sensors

Instruments capable of measuring electromagnetic radiation are called sensors. They can be classified as follows:

1. Passive sensors do not have their own source of radiation. They are sensitive only to radiation from a natural origin, usually reflected sunlight or the energy emitted by an earthly object. The classical example of a passive imaging sensor is the camera, which records the distribution of radiation from an object on a photosensitive emulsion spread out on a film. Other examples are the multi-spectral scanner, the thermal scanner and the microwave radiometer. Both sensor and object are passive.
2. Active sensors have a built-in source of radiation. The object is passive. Examples are radar (radio detection and ranging) and lidar (light detection and ranging).

Radiation can be recorded in an analogue form, the aerial photograph is a particular example, or radiation can be stored in a digital arrangement, a set of signal values on a magnetic device CD-rom or DVD, as in most remote sensing records at present. Visualized images (pictures) may be derived from digital data of imaging sensors. Before proceeding it is advisable to indicate which properties permit the observation and recognition of an object. 5 Main classes can summarize the many object characteristics:

1. Shape and size of the object; the spatial or geometric resolution is important for the sensor. In general, the size of the pixels (in terrain dimensions) is used as a measure.
2. Reflective and/or emissive properties of the object, the dynamic range and the radiometric resolution are important for the sensor. This dynamic range is defined as the number of digital levels in which the observed reflection or emission can be stored.
3. Spectral properties (wavelength, frequency, colour) of the object, the wavelength or frequency bands and the spectral resolution (i.e. the band width) are important for the sensor.
4. The effects of polarization of the object; the selection of polarization is important for the sensor, viz. (HH) horizontally polarized transmission and reception; (VV) vertical polarization and (HV) or (VH) cross polarization. This applies particularly to the microwave region.
5. Temporal effects (changes in time or location) of the object; the temporal resolution concerning a possible time interval between successive remote sensing surveys of the same region is important for remote sensing.

It is clear that the design and use of remote sensing systems should be preceded by many considerations depending on specific applications.

1.3.5 Transmission, reception and (pre-)processing

The energy recorded by the sensor has to be transmitted, in electronic form, to a receiving and processing station where the data are processed into an image (digital and/or hardcopy). Generally, the provider of the image data will already apply some pre-processing. Pre-processing operations are intended to correct for sensor- and platform-specific radiometric and geometric distortions of data. Radiometric corrections may be necessary due to variations in scene illumination and viewing geometry, atmospheric conditions, and sensor noise and response. Each of these will vary depending on the specific sensor and platform used to acquire the data and the conditions during data acquisition. Also, it may be desirable

to convert and/or calibrate the data to known (absolute) radiation or reflectance units to facilitate comparison between data.

1.3.6   Image analysis and interpretation

The outstanding advantage of digital recordings is that numerous manipulations can be applied to the observational data according to the methods of digital image processing and pattern recognition. A very extended set of algorithms can be applied in an automatic way by using one of the various software packages for image analysis that are on the market. In principle, three categories of information can be derived from remote sensing:

1 The assignment of class labels to the individual pixels or objects in an image, called classification creating, e.g., a thematic land cover map;
2 The estimation of object properties from remote sensing e.g. assessing the amount of biomass of agricultural crops or forest types;
3 The monitoring of the thematic class labels named under 1) or the object properties named under 2) over time.

Observing, for example, the properties of vegetation, one has to pay attention to numerous variables. Examples of these are the irradiance, the direction of the radiation source, the condition of the atmosphere and its influence on the detected radiation, the presence of surrounding objects, the viewing angle of the sensor and, last but not least, the variations pertinent to the vegetation such as growing stage, moisture content, leaf area index, number of leaf layers and soil background. In summary, information about the earth's surface and its features may be obtained from images by detection on the basis of:

• Spectral characteristics (wavelength or frequency, reflective or emissive properties);
• Spatial characteristics (viewing angle of the sensor, shape and size of the object, position, Site, distribution, texture);
• Temporal characteristics (changes in time and position);
• Polarization characteristics (object effects in relation to the polarization conditions of the transmitter and receiver).

These information-extraction algorithms can generally only be applied to earth observation images when the images are radiometrically processed i.e. converted from raw digital numbers into physical units such as radiance or reflectance. Such correction should account for sensor characteristics, terrain topography and atmospheric conditions. Details about radiometric processing can be found in Van der Meer et al. (2001). Furthermore, images must be geometrically corrected for the effects of scanner distortions of the image, orbital geometry and figure of the earth. Details on methods for geocoding and distortion correction are given in Schowengerdt (1997).

1.3.7   The final product

The output from remote sensing can be in various forms and often is information that is used as input for further analysis, e.g. in a geographical information system (GIS). On the one hand, information present in a GIS can help in the analysis and interpretation of remote sensing data. On the other hand, the results of a remote sensing analysis can be stored in a GIS. Subsequently, this information can be combined with other types of information for various types of studies or applications. As an example, a land cover map can be considered as an 'end product' of a remote sensing analysis. It can be used as input in a study towards groundwater pollution by combining it with various spatial and statistical data.

1.4   The chapters in this book

Conventionally used spectral classification methods of remote sensing images work on a pixel-by-pixel basis and ignore the useful spatial information surrounding the pixel. In this book we bring together a range of new and advanced image analysis methods aiming at quantitatively capturing that spatial information in earth observation images and use it effectively for applications such as land cover mapping, natural vegetation survey, soil mineral mapping, hydrocarbon seepage mapping and urban issues. In chapter 1 the basic concepts of remote sensing and the historic developments are briefly presented. The quintessence of the other chapters is briefly presented below. We are aware that there is some kind of overlap between a number of chapters, especially with respect to the basics of geostatistics and the basics of earth observation. We believe that this small degree of overlap is not harmful to the contents of the book but will allow the reader to consult the chapters individually.

Chapter 2 starts by presenting and discussing traditional approaches in geography, ecology, hydrology, geology and other disciplines of handling spatial variability in their mapping and surveying efforts of complex natural landscapes. Basic forms of earth observation such as black and white aerial photographs have played an important role in these mapping efforts since they were available. Next, we look at how sensors register reflected radiance from the earth surface and how the pixels, regularized or gridded sampling of the landscape, are imperfect capturings of the natural patterns that occur in the surrounding landscape. We then review a number of statistical and geostatistical models and how they can help us to quantitatively characterize spatial structures.

In chapter 3 Foody put emphasis on the fact that pure pixels in remote sensing images do not exist and hence, a pixel will never represent a single thematic class complicating the production of accurate land cover maps. Recognizing the fact that each remote sensing image has a certain degree of mixed pixels, methods are required to analyse images at the sub-pixel level. Foody reviews two methods to estimate sub-pixel composition, the linear mixture model and the soft or sub-pixel classification method. Next he identifies a number of current and future research topics such as the extraction of sub-pixel scale thematic information using support vector machines.

In chapter 4 Atkinson presents an overview of the meaning of terms such as spatial resolution, pixel size, up- and downscaling. Next the issue of scale, support and pixel size, spatial resolution and spatial extent is considered followed by an outline of geostatistics. Variograms, variogram models and kriging are summarized. Furthermore, Atkinson discusses a number of methods for downscaling i.e. increasing the spatial resolution of an already acquired data set and hence providing a representation of the data set at finer spatial resolution (super-resolution). Various methods for super-resolution mapping are presented such as sub-pixel classification, the Hopfield neural network approach and a pixel swapping method. The concepts and ideas presented in this chapter form a good basis for the later chapters in the book dealing with related techniques, methods and practical applications.

In chapter 5 Hay and Marceau presents a new and advanced multiscale approach for landscape analysis MOSA. MOSA stands for Multiscale Object-Specific Analysis. Hay and

Marceau claim that it is now widely recognized that landscapes are complex systems that are characterized by a large number of heterogeneous spatial components, non-linear interactions, emergence, self-organization, adaptation through time, and scale multiplicity. The later property refers to the fact that landscapes exhibit distinctive spatial patterns associated to different processes at different scales. Since there is no way of defining a priori what are the appropriate scales associated to specific patterns, and because there is a need to derive adequate rules for transferring information through multiple scales, it is imperative to develop a multiscale approach that allows dominant patterns to emerge at their characteristic scales of expression. In this chapter Multiscale Object-Specific Analysis (MOSA) is described as a multiscale approach for landscape analysis that has been developed for the particular spatial sampling context of remote sensing data where each pixel is considered as part of an image-object. This approach reduces the effect of the modifiable area unit problem (MAUP) and explicitly takes into account the hierarchical organization of the landscape. MOSA represents an integration of Object-Specific Analysis (OSA), Object-Specific Up scaling (OSU) and Marker-Controlled Segmentation (MCS) that allows for the generation of data at a range of scales from which objects can be detected, and for the delineation of individual objects as they emerge and evolve through scale. In chapter 5, a detailed description of MOSA is given, provide new information on the OSA kernel, and discuss improved methods for using MCS as a feature detector. This is followed by an application using an IKONOS-2 (Geo) dataset acquired over a highly fragmented agro-forested landscape in southwest Quebec, Canada.

In chapter 6 Chica-Olmo and Abarca-Hernández present texture-based and variogram-based methods to analyse and express quantitatively the spatial properties of remotely sensed imagery. Texture is a feature that has received great attention in image processing particularly in remote sensing applications. Valuable information can be extracted from textural analysis, about the spatial arrangement of the objects, thematic classes, in the image and their relationship with the environment. From a geostatistical point of view, diverse procedures can be developed for textural analysis of images. All of them use the variogram function as a powerful tool to analyse the spatial variability of digital values. This vector function locally represents the spatial variance of the data within a window and, consequently, can serve as an operator to create texture images calculated at a local level. The variogram offers wide possibilities to calculate textural operators or measures, on the basis of the different uni- or cross variant variogram estimators. In such cases, the measures are calculated for specific lag distances in a local neighbourhood, obtaining as the final result a set of geostatistical texture images. A second case analysed is the joint use of the variogram function with the well-known geostatistical estimation method of kriging through cross validation. The validation or experimental errors obtained in moving windows offer another interesting way to derive textural images. In an applied context, this textural information concerning the geostatistical analysis of the image, added to the spectral bands, plays an important role as contextual information for classifying remotely sensed images, in order to increase digital classification accuracy. A geological example to map important classes for mineral prospecting in South-east Spain is given.

In chapter 7 Berberoglu and Curran present the use of traditional land cover classifiers such as the maximum likelihood approach and the use of artificial neural networks to classify remotely sensed images. Next they provide a thorough overview of methods how to assess

texture from images by first and second order statistics, by geostatistics i.e. various types of variograms and by fractals and they discuss the pros and cons of a pixel-based classification versus a per-field approach. The previously discussed methods are applied to an IKONOS image of a study area located on the Cukurova plain in Turkey. This case study illustrates a method how to integrate spectral and spatial information captured by an image in two different classification methods: the widely used maximum likelihood approach and artificial neural networks. The increase of classification accuracy is presented and discussed together with the pros and cons of the various texture measures.

In chapter 8 Gong and Xu review the use of contextual information for urban areas and they stress the importance of contextual approaches to characterize spatial structural differences in high spatial resolution images of urban regions. Contextual spatial approaches are not only useful for panchromatic images but can also successfully be applied to multi-spectral data. Gong and Xu introduce the frequency-based contextual classifier (FBC). FBC creates frequency tables of pixel values in neighbouring cells within a kernel and assigns these values to the centre pixel. An important advantage is that frequency tables contain more spatial information than first-order statistical measures such as mean and standard deviation. The choice of the window size is crucial for the successful application of FBC. Example applications to a multi-spectral SPOT image, a CASI image and samples of an IKONOS image are presented and discussed.

In chapter 9 Van der Meer presents a geological application of a contextual image analysis method on hyperspectral HyMap imagery of the Cuprite dataset in Nevada by producing images of spectral absorption band parameters. Van der Meer describes that spectral reflectance in the visible and near infrared offers a rapid and inexpensive technique for determining the mineralogy of samples and obtaining information on chemical composition. Absorption-band parameters such as the position, depth, width, and asymmetry of the feature have been used to quantitatively estimate composition of samples from hyperspectral field and laboratory reflectance data. The parameters have also been used to develop mapping methods for the analysis of hyperspectral image data. This has resulted in techniques providing surface mineralogical information (e.g., classification) using absorption-band depth and position. However no attempt has been made to prepare images of the absorption-band parameters. A simple linear interpolation technique is proposed in order to derive absorption-band position, depth and asymmetry from hyperspectral image data. AVIRIS data acquired in 1995 over the Cuprite mining area (Nevada, US) are used to demonstrate the technique and to interpret the data in terms of the known alteration phases characterizing the area. Next we turn to look at stratified approaches. It is demonstrated that vegetation indices, red edge index and carter stress indices are highly correlated with lithology as shown in the analysis of Probe (HyMap) data from Santa Barbara (CA). This area is renown for oil and gas seeps. The analysis is a statistical data integration leading to mapping of oil and gas seeps from the relation between vegetation anomalies, soil mineralogical anomalies and the lithology. The last part of the chapter is devoted to contextual analysis. Here we introduce data inversion techniques that incorporate geologic prior knowledge. An example is shown on Hymap data from a sedimentary sequence. We exploit the systematic facies changes to outperform standard mapping approaches.

In chapter 10 Scholte, Gacía-Haro and Kemper presents a special case of spectral mixture analysis of imagery: the variable multiple endmember spectral mixture analysis for mapping heavy metal contamination of soils and for mapping mud volcanism. Spectral mixture analysis is a widely used method to determine the sub-pixel abundance of vegetation, soils and other spectrally distinct materials that fundamentally contribute to the spectral signal of mixed pixels. Spectral unmixing techniques strive at finding partial least squares solutions to the (linear) mixing of spectral components in order to derive fractional abundance estimates of selected endmembers. The Variable Multiple Endmember Spectral Mixture Analysis (VMESMA) is an integrated image analysis method that extends the possibilities of multiple endmember spectral unmixing allowing variable endmember sets for different parts of an image and standardization of the data prior to unmixing. VMESMA is based on a zonal partition of the area and a zone-dependent choice of multiple candidate submodels and unmixing algorithms, each valid within a scene sub-area. By formalising knowledge of the application domain into a simple scene model, the spatial relationships between the pixels can be used to meet the user requirements. In this chapter the current state of VMESMA is discussed in terms of geologic applications such as the mapping and monitoring of residual heavy metal contamination after the Aznalcóllar mining accident in Spain and mud volcanism associated with petroleum system properties in oil mud ejecta in Azerbaijan.

In chapter 11 Van der Werff and Lucieer presents the use of hyperspectral remote sensing to detect hydrocarbon seeps at the earth surface. These seeps or leakage areas of subsurface reservoirs manifest themselves by discoloured alterations zones or by harmful effects on vegetation. The spectral differences between the spectra of the seepages and the spectra of their background and surroundings are very small. As a result the seepage areas are difficult to identify. However, the seepage areas generally have specific spatial shapes such as a halo shape or an oval shape, either around a central vent. Van der Werff and Lucieer has developed an algorithm to detect specific halo-shape spatial patterns and to determine whether the spectra in these shapes are spectrally anomalous from other image parts. The algorithm is tested on simulated images produced by using spectra of oil seeps in California. Results are promising but future work is necessary to include more spatial shapes and spectra in the algorithm.

In chapter 12 Blaschke, Burnett and Pekkarinen introduce methods to work with image segmentation and objects in an image. Especially the new generation of sensors acquiring very high spatial resolution images provide new opportunities to identify objects, groups of pixels in an image that has a meaning in the real world or to apply image segmentation methods that match ecological mapping units used in the field. In this chapter the various types and methods of image segmentation are reviewed and the authors touch upon multi-scale approaches such as multi-fractal approach. In the second part of this chapter examples are given how image segmentation approaches and object-oriented classification can be used in forest stand mapping.

In chapter 13 Carvalho, Acerbi, Fonseca, Clevers and De Jong present the use of wavelets for multi-scale image analysis. Wavelets are tools that allow us to analyze datasets over various levels of scale and in different directions by de-composing the images into details at different resolutions. In this chapter the concept of the use of wavelets for remote sensing imagery is introduced and compared with other types of filtering and spatial analysis. The decomposed

images allow us to study the hierarchy of spatial information captured by a specific image or to study temporal variations at different levels of scale in time series of images. Next, the chapter provides a brief overview of applications of wavelets in remote sensing together with a reference overview. In the second part of the chapter various case studies are presented and discussed. The case studies comprise an example of the use of wavelets for image registration, a comparison of methods for feature extraction from images aiming at the fusion of images available at different spatial resolution and an application for change detection.

In chapter 14 Fuller, Smith and Thomson presents the operational use of contextual analyses of remotely sensed images for the production of land cover maps of the United Kingdom at a regular basis. This chapter examines the use of contextual procedures in pre-processing, classification and post-classification phases to produce national land cover maps from remotely sensed images. It looks first at the fairly simple contextual corrections by using kernels of variable size applied to the raster format Land Cover Map of Great Britain (LCMGB), made in 1990. It then examines the use of a geographical information system (GIS) in producing the Land Cover Map 2000 (LCM2000), an update and upgrade of the LCMGB. LCM2000 used image-segmentation and segment-based classification, wherein all pixels were classified in context. In addition around 12% of parcels required contextually based corrections to increase map accuracy. Finally, about 15% of parcels used external contextual data to extend the basic thematic classification to meet wider user needs. Contextual analyses were thus essential to the entire LCM2000 production process, controlling map structure, improving accuracy and adding thematic detail.

In chapter 15 Sluiter, De Jong, Van der Kwast and Walstra present a re-classification method called SPARK: spatial re-classification kernel. The conceptual idea behind SPARK is that the land use types of interest can be characterised by the spatial arrangement and the size of the objects in the image. These land cover types may include complex natural areas or irregular urban areas. In this chapter emphasis is put on Mediterranean types of shrub vegetation. The SPARK method starts by using a land cover map produced by any type of spectral classifier. Next spatial-based decision rules are defined using known local, spatial patterns of objects in heterogeneous and homogeneous land use types. These decision rules are then used to refine the initial classification. The SPARK concept is described in detail and a case study from an area in southern France is presented to illustrate the classification improvements and the effect of various kernel sizes. The results from SPARK differ from one vegetation type to another but most significant classification improvements are achieved for the open and complex shrub type of vegetation for kernel sizes of 3 by 3 and 5 by 5. One important conclusion is that SPARK successful identifies vegetation classes that are not distinguished at all by conventional classifiers.

The figures and graphs in this book were all reproduced in black and white to save costs. The CD-Rom enclosed in the book provides all the colour plates arranged by chapter.

Chapter 2
Spatial Variability, Mapping Methods, Image Analysis and Pixels

Steven M. de Jong, Edzer J. Pebesma & Freek D. van der Meer

2.1   Introduction

Remote sensing observations of the surface of the earth, collected by sensors mounted in an aircraft or on a spaceborne platform, provide valuable information that is not easily acquired by field surveying methods. While surveying in the field, it is difficult to obtain an overview of the landscape elements and their interrelations. The airborne and spaceborne images are helpful to locate objects in the terrain and to investigate their locations relative to each other. The imagery also helps us to study and monitor the continuous change of the earth surface resulting due to the seasonal cycle, due to geological and geomorphological forces or due to human activities. The images provide a synoptic view of the earth and are helpful to find answers to questions such as: where are objects of interest located, how are these objects arranged in relation to each other and how do these objects change over time. Having all these capabilities, remote sensing is a powerful tool for environmental studies. A problem is however, that we do not directly measure pertinent information about the objects of interest. When acquiring remote sensing images we basically measure reflected or emitted electromagnetic radiance while in fact we are interested in object identification, object properties and the spatial arrangement of these objects in the terrain. Before the image provide us with useful information, we have to translate the data of reflected or emitted electromagnetic radiance into, for us, useful information about the identity of an object or about certain object properties. Traditionally an image analyst carried out the extraction of information from imagery by visual interpretation. This visual interpretation is based on image properties like colour, pattern, shape, shadow, size, texture and tone of objects (USDA, 1993). Nowadays, this process of information extraction and translation of radiance into useful object identity or object properties is mainly computer-based.

This process of translating reflected or emitted electromagnetic radiation into useful information is normally referred to as image processing. Image processing comprises a number of preparatory steps i.e. geometric correction and radiometric processing of images, image enhancement or image improvement steps such as contrast stretch, image transformations and noise reduction. After these so-called pre-processing of the image, image analysis is normally continued by a number of information extraction steps. These information extraction steps refer to supervised or unsupervised image classification methods,

the use of spectral vegetation indices or other types of image ratioing, pattern recognition and/or visual interpretation.

Over the years considerable attention has been to paid to visual interpretation of images and automated image classification based on the spectral information captured by the pixels. Less attention is paid to the spatial patterns captured by images and how that type of information can play a role in information extraction from earth observation imagery. Over the last decennia a whole series of analysis and modelling techniques became available for the wider research community due to the increased power of the desktop computers. These methods include texture measures, aggregation methods, fractals and multi-fractals, geostatistics, wavelets and many others. The lack of attention in the past for spatial pattern information content of airborne and spaceborne images is surprising since many scientific disciplines concerned with the environment such as geography, geology, botany and forestry are traditionally working with spatial patterns of e.g. vegetation types, vegetation communities, soil types, soil catenas, geological structures and geomorphological patterns. In fact, surveying as practised by many disciplines comprise the recognition of spatial patterns and bringing order in complex spatial patterns by creating mapping units. The chapters in this book aim at bringing together a number of techniques and methods that were specifically developed and tested to extract and analyse spatial patterns and spatial information captured by remote sensing images. In this chapter we aim at presenting and discussing a number of general aspects and general techniques used in geography, geology, forestry, botany and other disciplines for investigating and quantifying spatial patterns.

2.2   Spatial variability in landscapes

2.2.1   Spatial variation

Today's landscapes are the result of various natural landscape forming processes in the past and present and sometimes by human interference. The variety of landscapes that we find on the earth surface is very high and the complexity of their development over time and space is equally high. This complex history and these complex interactions between the landscape forming processes make it difficult to comprehend the actual forms and the actual processes. Sometimes landscapes show abrupt, stepwise changes of e.g. natural vegetation, soil types or lithological formations but as often we see gradual changes of natural vegetation going from forest, to shrubs to grasslands, or gradual transition zones from soils rich in organic matter to soils poor in organic matter going hand in hand with a gradual change of soil colour. Awareness of this spatial variation of terrain properties is as old as man himself because this variation resulted in a spatial differentiation of the quality of the land to grow crops or to find resources (Hillel, 1992). The earliest farmers in history would select a piece of land showing the least constraints for growing their crops. Selection criteria would comprise factors such as: a flat area, sufficient soil depth, good water availability, well-coloured soil etc. By applying agriculture, man started to transform the land and terrain to his/her own purposes. Agricultural activities form a disruption of the natural environment as it replaces the natural ecosystem with an artificial one, established and maintained by man. The moment a farmer delineates a tract of land and separates it from the contiguous area by arbitrary boundaries

and establishing fields, he is changing the pre-existing environmental order. Man-influenced landscapes normally display more regular patterns than natural landscapes do.

It is also recognized for a long time that the spatial variation of land, terrain and vegetation properties plays at different levels of scales i.e. over various spatial dimensions. Landscape features vary in size by several orders of magnitude, from continents at one extreme to particles of sand or clay at the other. Already in the early sixties Tricart (1965) proposed an eight-level scalar hierarchy and Haggett et al. (1965) proposed a subdivision of the earth's total surface area by powers of 10, the so-called 'G$_a$ scale values'. Table 2.1 illustrates these two early landscape scales.

This hierarchy and 'natural scale' of a landscape is recognized and used by many surveying disciplines such as soil survey, vegetation mapping, geological mapping and hydrology. This awareness of scale, spatial extent and spatial variability has resulted in the development of various hierarchical mapping systems (Mitchell, 1991; Townshend, 1981; Dent and Young 1980). In the hydrology 'naturally homogeneous areas' were introduced as a necessary tool for hydrological modelling. These 'naturally homogeneous areas' in hydrology referred to as REA: Representative Elementary Area or HRU: Hydrological Response Unit, assume non-variability of the data and parameters within its delineation (De Wit, 2001; Blösch and Silvaplan, 1995). For modelling purposes not only the environmental variables such as hydraulic conductivity, evaporation, surface storage and surface runoff are presumed homogeneous in a REA or HRU but there is also non-heterogeneity of the processes assumed within the frontiers of these units. Imeson et al. (1995; 1996) introduced a similar concept and approach in land degradation research. The mapping units that Imeson distinguishes in the field are called 'Desertification Response Units' or DRU. The DRU concept was introduced aiming at linking hydrological and erosion processes from one temporal and spatial resolution to another. The size of a DRU typically covers a hill slope or a part of a hill slope and the DRU classification is based on spatial patterns of soil and vegetation because these patterns are thought to be the result of the movement of water, water availability and the redistribution of water in the landscape or the catchments.

When we are collecting information about landscape variables or terrain processes in our environment, we have to face the fact that we take only samples restricted to a certain points in time and that our sample has a certain, limited size. Either sampling effort (time and/or space) may have a good match with the temporal and spatial variation of the process involved

Table 2.1 – Landscape scales as proposed by Tricart (1965) and Haggett et al. (1965).

Order	Area (km²)	Ga scale	Example
I	10^7	1.71	Entire continent
II	10^6	2.71	Large plain or piedmont
III	10^4	4.71	Florida Peninsula, Lowland Britain
IV	10^2	6.71	Sicily, Sardinia
V	10	7.71	Forests, Provinces
VI	10^{-2}	9.71	River terrace, alluvial fan
VII	10^{-6}	13.71	Soil polygon, runnel
VIII	10^{-8}	15.71	Pebble

or may not. A nice illustration of this problem is given by Fonseca de Seixas (1998) in figure 2.1. The left part of figure 2.1 shows the temporal distribution of precipitation for a study area in Portugal over 100 years. When we measure precipitation, for this case at a time step t, we will obtain a fairly accurate view of the temporal distribution of rainfall in this area. When our measuring interval is reduced to thirty times the t-interval i.e. '30t', we will miss important information about the temporal distribution and variability of the precipitation in this area. The sampling interval, in this case t or 30t, will have a clear impact on our perception about the irregularity of rainfall in this area in Portugal.

A similar example can be given for spatial variation in the terrain and size of sampling (or support). The two graphs on the right hand side of figure 2.1 show, at two different sampling
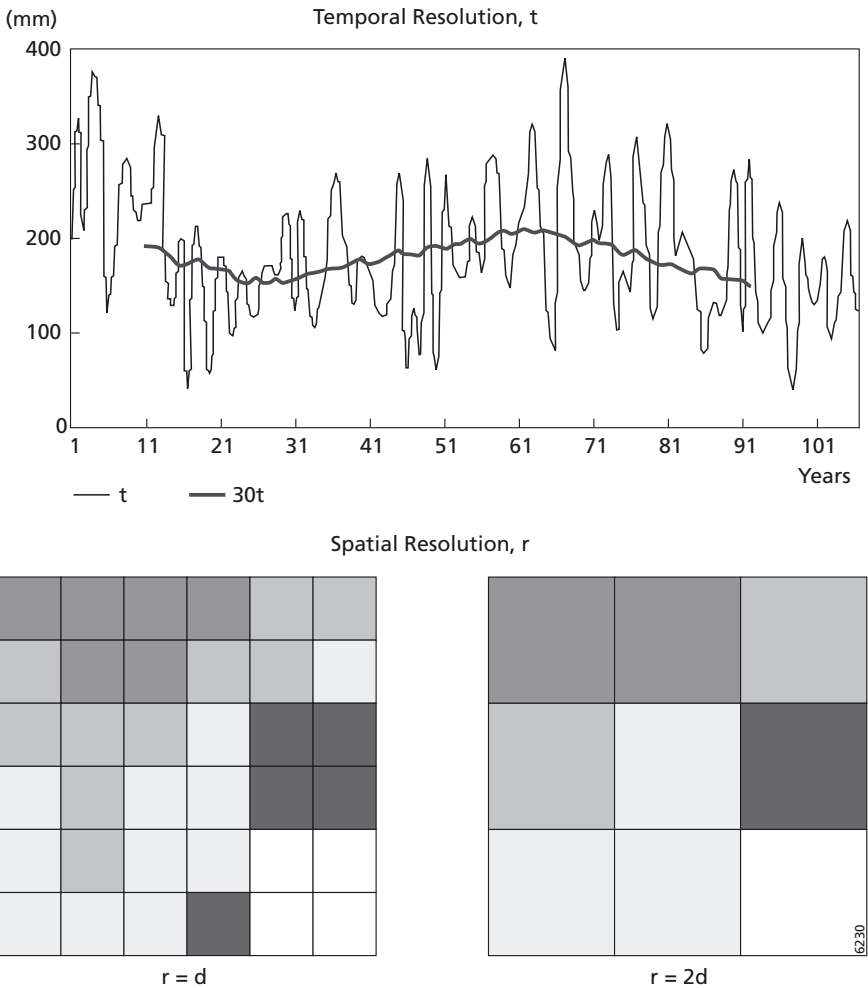
Figure 2.1 – The effect of data sampling resolution in variability patterns. Left for the temporal domain, right for the spatial domain (source: Fonseca de Seixas, 1998).

intervals, the amount of spatial variation that we will capture at sampling distance d or at sampling distance 2d. The two graphs illustrates that different sampling size will yield significant different patterns for this environmental variable. In conclusion, the spatial resolution of our sampling effort has an important impact on the accuracy of the collected information: when the monitoring resolution becomes coarser, the spatial pattern will change or will even get lost. In the same way the pixel size of a remote sensing sensor is an important system variable determining success or failure to capture certain patterns of vegetation, rocks or land use.

Spatial scales and temporal scales are already for a long time recognized as important issues to consider and to understand in surveying and modelling. Forms in some landscapes show scale invariance while others do not. Scale invariance is one of the earliest issues taught to Geography and Geology students by pointing out that it is important to include an object to a photograph that points out the scale of the photo. Such an object is normally a coin, a hammer or a person. Any object will do as long as it illustrates the size of the geomorphologic or geological feature on the photo. Mandelbrot described already in the eighties the issue and theory behind scale invariance as 'fractals' (Mandelbrot, 1982). Mandelbrot has trigged by his famous book 'The Fractal Geometry of Nature' a wide range of studies to quantify spatial patterns and to study and understand scale invariance. A fractal is an object whose shape is independent of the scale at which it is regarded. Scale invariance is also referred to as 'self-similarity' by other authors (Turcotte, 1992). Fractal dimensions, quantitative measures to describe complicated, irregular features of variation and 'roughness' of several types of objects, are useful tools to typify and differentiate landscapes (Klinkenberg and Goodchild, 1989; De Jong and Burrough, 1994; Quattrocchi et al., 1997). Fractal dimensions can be derived from variograms or from kernel algorithms and use the same theoretical basis as hierarchical mapping systems.

2.2.2 Hierarchical mapping approaches

Hierarchical mapping systems use terrain information such as geomorphology, geological structures, climate patterns and vegetation patterns as a basis for mapping. Depending on the spatial scale of the survey geomorphology, geology, climate, relief and vegetation patterns are important variables for distinguishing land units and for defining mapping units. Usually these mapping units are considered internally homogeneous, similar to the REA, the HRU and the DRU in hydrology and land degradation. Although this assumption of internal homogeneity will in practice never be completely true, these mapping unit approaches often form a useful approximation and conceptualisation of reality. The process of using various sources of information to divide the landscape or terrain in to mapping units is in literature often referred to as regionalisation of the terrain (Townshend, 1981).

The physiographic approach is one of the most widely applied methods for regionalisation (Mitchell, 1991; Townshend, 1981). Physiography is the comprehensive study of surface form, geology, climate, soils, water and vegetation and their inter-relationship. The physiographic approach to regionalisation is thus the subdivision and characterization of the Earth's surface in terms of a wide range of properties. The relative importance of the selected physiographic properties will vary from one survey to another. This importance depends on the type of area under investigation and on the final objectives and types of use of the final maps. The

role of vegetation type and vegetation cover in the physiographic approach has been under discussion over the years. Vegetation cover is usually an important guide in recognizing land units, particularly when the terrain is viewed from the air on aerial photographs or satellite imagery. Researchers opposed of using vegetation in the physiographic approach considered vegetation rather as an ephemeral than a permanent characteristic of the landscape. Furthermore, they considered vegetation as an organic substance of the landscape and as such vegetation is an intrinsically different phenomenon in the landscape than the physical terrain elements rocks, soil, water bodies and relief. The latter landscape elements are non-organic and considered to be less dynamic. Other researchers are in favour of using vegetation information in their land mapping efforts. These researchers often have a background in life sciences or are frequently using remote sensing imagery for their mapping work. Substantial reasons for using vegetation information in surveys are that vegetation is closely integrated with the land surface and influences its character.

Vegetation is omni-present at the Earth surface except for some permanent snow and ice fields and for the most extreme desert areas. In humid climates, the vegetation cover is generally thick enough to completely obscure the surface of the ground. Mitchell (1991) describes three ways in which vegetation is important for the evaluation of landscapes and terrains: 1) vegetation serves an index for the recognition of terrain types, 2) vegetation is an attribute in their definition and 3) vegetation is a natural resource physically attached to the terrain elements of interest and influenced by these terrain elements.

When landscape elements or terrain properties are studied from the air, vegetation cover is usually an important guide in recognizing them. This relation is true for undeveloped areas with low population density where the ecological vegetation status (climax) reflects site characteristics but is also true for developed areas such as western Europe where there is a close relationship between agricultural land use and site properties. The most important factor in this relationship is most probably the effect of ground and terrain configuration on soil moisture conditions. Therefore, vegetation is a valuable index of terrain in areas where soil levels falls below thresholds critical to plant growth. At a second level, other terrain factors such as slope, aspect, soil depth and nutrient status are important and determine to a certain degree the plant cover in particular localities. From the early days of the development of remote sensing, i.e. the aerial photography in the second half of the 19th century, landforms have been studied from the air (Verstappen, 1977) and as vegetation is such an important spatial component in airborne and spaceborne images, it is good to understand reflectance properties of vegetation and how they are visible in remote sensing scenes.

2.2.3   Spectral properties of vegetation

The optical properties of vegetation and individual leaves are described in detail by Kumar et al. (2001), Ustin et al. (1999) and Lambers et al. (1998). Significant knowledge about individual leaf reflectance is available in the literature, far less is known about the behaviour of an entire canopy with respect to reflectance, light absorbance and photosynthesis. In general the reflectance of vegetation in the visible wavelengths (0.43-0.66 μm) is small and reflection in near infrared (0.7-1.1 μm) is large (figure 2.2). Three features of leaves have an important effect on the reflectance properties of leaves: pigmentation, physiological structure and water content.

Pigments, such as chlorophyll a and b, absorb radiation of the visible wavelengths. The species-specific structure causes discontinuities in the refractive indices within a leaf, which determine its near infrared reflectance. The absorption of light and photosynthesis is important for the production of oxygen and foodstuff for men. For the plant this process
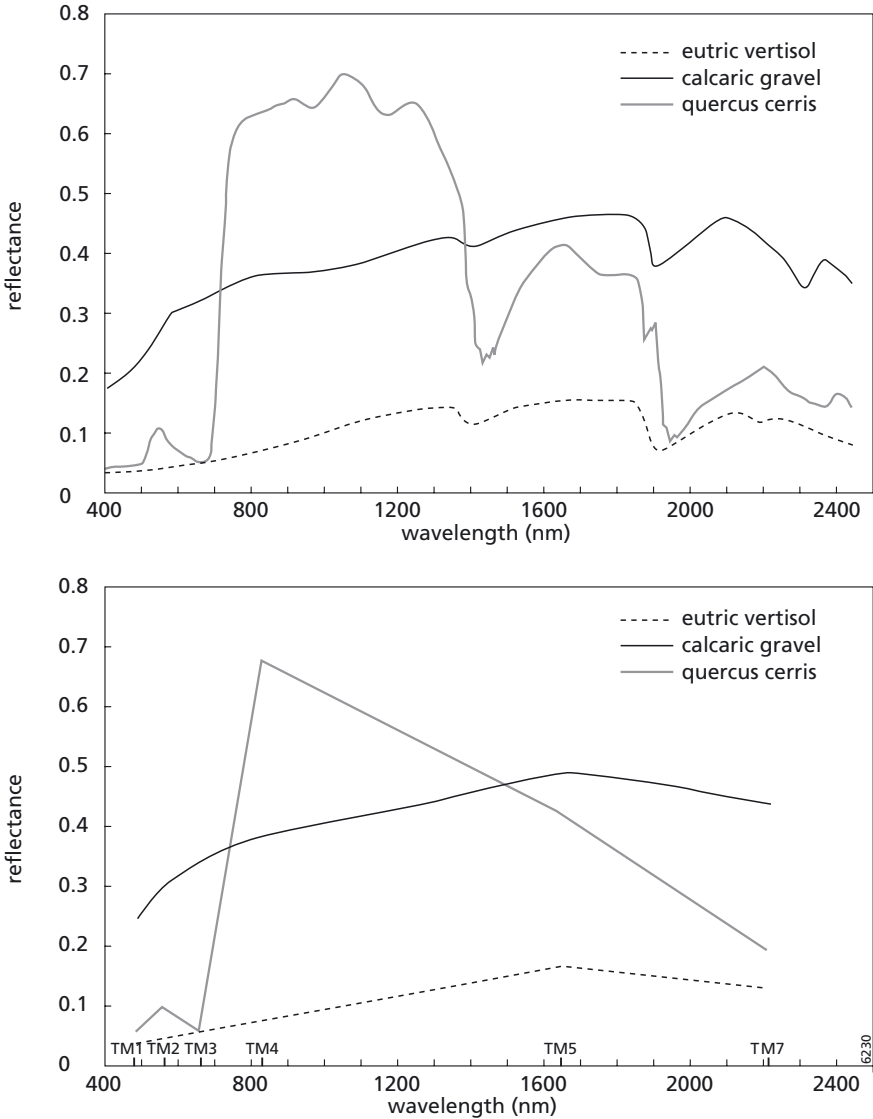
Figure 2.2 – Spectral signatures of vegetation, soil and parent material measured at high spectral resolution of 1.5 nm (upper graph) and at broadband resolution ranging from 60 to 270 nm corresponding to the Landsat TM sensor. The loss of information of this vegetation spectrum due to increasing spectral bandwidth is clearly visible.

is very important for trapping and transforming energy. The maxima of absorption of the pigments chlorophyll a are located at 430 nm and 480 nm and for chlorophyll b at 450 and 650 nm (Lambers et al., 1998; Bidwell, 1974). The reflectance properties of a vegetation canopy are affected by the spatial distribution of vegetated and non-vegetated areas, types of vegetation, leaf area index, leaf angle distribution and vegetation conditions. Some narrow absorption bands due to lignin, cellulose etc. are present in near and short-wave infrared wavelengths (Ourcival et al., 1999; Wessman et al., 1989; Vane and Goetz, 1988). However, the presence of water often masks their absorption features (Lacaze and Joffre, 1994). Furthermore, the bandwidth of the TM is too broad to detect these narrow absorption bands as shown in figure 2.2.

Water content of the leaves, and water in the atmosphere, reduce overall leaf reflectance and causes some narrow absorption features (water absorption bands). Three major water absorption bands are located near 1.4, 1.9 and 2.7 μm, two minor absorption bands occur near 0.96 and 1.1 μm (Irons et al., 1989). The presence of water reduces the overall reflectance in mid infrared of a leaf significantly making it more difficult to identify specific absorption features. The combined effect of pigments and physiological structure give healthy vegetation its typical reflectance properties. Combinations of the visible and near infrared spectral bands enables us to discriminate bare soil surfaces or water bodies from vegetation. These arithmetical band combinations can be referred to as 'spectral vegetation indices' (Huete and Jackson, 1987; Crist and Cicone, 1984) and provide us insight in the spatial patterns of vegetation cover or canopy structures. Spectral indices aim at enhancing the spectral contribution of green vegetation in images while minimizing contributions from soil background, sun angle and atmosphere by combining various spectral bands in visible and near infrared wavelengths.

These spectral vegetation indices comprise among others the Normalized Difference Vegetation Index or NDVI (Tucker and Sellers, 1986; Hurcom and Harrison, 1998), the Soil Adjusted Vegetation Index or SAVI (Huete, 1988) or the Tasselled Cap Greenness (Crist and Cicone, 1984; De Jong, 1994). Spectral Mixture Analysis or SMA is another sub-pixel method to reveal patterns of ecosystems in remotely sensed images (Foody, 2003; Scholte et al., 2003; Van der Meer and De Jong, 2001; Brown, 2001; Adams et al., 1993; 1985). The basic assumption of this spectral unmixing technique is that the signal recorded by the satellite sensor for each pixel is a linear combination of spectral signatures of pure components weighted by their abundance in that pixel. The components (or endmembers) are those elements that represent the spectral variability of the landscape e.g. for Mediterranean landscapes vegetation, soil and rock outcrops. The unmixing approach aims at unravelling the complex satellite spectrum by using the pure endmember spectra, it is useful for surveying as well as for collecting input for models and it does not suffer from the limitations of the spectral indices. The mathematical notation of the unmixing procedure is as follows (Adams et al., 1993; 1985; Van der Meer et al., 2001):

$$R_i = \sum_{n=1}^{n} (F_j \cdot RE_{ij}) + \varepsilon_i \qquad \sum_{n=1}^{n} F_j = 1 \qquad\qquad (2.1)$$

R_i: Reflectance value of a pixel in band i;

F_j: Fraction of endmember j (in terms of percentage of the pixel surface);

RE_{ij}: Reflectance value for band i of endmember j;

ε_i: Residual error in band i

n: Number of bands.

When using the unmixing approach for surveying, the equation is applied to spectral information contained in all pixels of a satellite image. The equation is then inverted and solved through a least squares regression, constraining the sum of fractions to one. Limitations of this method include: 1) the pixel composition is assumed to be made up by a limited number of elements (for mathematical reasons the number of elements cannot exceed the number of spectral bands plus one), 2) it is also assumed that the reflected light only interacted with one component on the ground while in practice multiple scattering often occurs (Adams et al., 1985).

Patterns of vegetation and patterns in landscapes at various level of scale are important to recognize and contribute significantly to our understanding of landscape formation and to our understanding of important landscape processes. Earth observation is an important tool to reveal these patterns and to study pattern size and pattern dynamics. Patterns are defined in the dictionary as 'an orderly sequence consisting of a number of repeated or complementary elements'. Patterns reveal a sort of 'organization' of variables in the space and/or time domain resulting from the system's structure and functioning. The 'organization' implies that the randomness is removed from the system and that patterns surfaces and can be discovered or identified. A wide range of examples of pattern formation in nature is given in Ball (1999). The reason why these patterns occur and the processes behind the various types of processes are still not fully understood. Studies are undertaken to simulate within the computer the development of patterns in a wide range of ecosystems (Rietkerk et al., 2002; Millington et al., 2001; Van de Koppel et al., 1997), remote sensing observations play or will play an important role in the validation of these computer simulation of natural patterns.

In ecology patterns have a specific position in the hierarchy. The ecological landscape approach suggested by Forman (1986) considers a three level data model. In this model he uses successively coarser description levels: particles, gradients and mosaics. Particles refer to the individual entities and variability is derived from the differences between these individuals. Gradients have a gradual variation over space with no explicit boundaries e.g. a trend. Mosaics are variables aggregated through similar values forming distinct spatial patches with distinct, crisp boundaries. Examples of this three level approach are: trees as particles, vegetation gradients and forest or shrub communities as mosaic. A more general example is houses as particles in the hierarchy, urban concentrations at the gradient level and a suburb or city at the third level. The bridge to remote sensing observation becomes immediately clear. The scales at which we monitor these kinds of ecosystems determine the level of detail that we will obtain. Earth observation images with a spatial resolution of 1 km (NOAA-AVHRR) will provide insight in patterns of cities and suburbs or forests, earth observation images with a resolution of 30 meters (Landsat TM) provide information on urban concentrations or vegetation patterns within a forest. High-resolution imagery (aerial photos, IKONOS)

or field observation provide information about the particles: the individual houses or the individual trees.

At this point we arrive at a very fundamental problem of the use of earth observation for mapping ecosystems or patterns at the earth surface. The traditional earth observation image analysis method is a classification of pixels based on the assumption that pixels capturing the same land cover class are close to each other in the feature space. The underlying assumption of this approach is that the patterns in an image relate to broad classes of land cover that are spectrally relatively separable. This assumption is not always valid e.g. in case of open shrub vegetation, fragmented landscapes, urban areas or at transition zones from one land cover type to another. The pixel is often larger than we would like it to be with respect to pattern variability in the landscape (Fisher 1997). The new modern remote sensing systems with pixel sizes of 1 meter have not really solved this problem because patterns occur at a variety of spatial scales and even often show a kind of scale invariance. The high-resolution images provide us only insight in an additional level of scale of the landscape pattern. In conclusion, image analysis methods are required that capture the spectral information in the image where appropriate, that capture spatial information from neighbouring pixels where appropriate and that uses either type of information, spatial and spectral, where appropriate. In later sections of this chapter we will discuss the spatial and spectral classifier that aims at implementing this approach. Figure 2.3 illustrates this problem. The figures show four different landscapes. Three complex Mediterranean areas in France and Spain:

a an open shrub area referred to as Garrigue with open and closed vegetation patterns,
b gullies and badlands with linear drainage patterns,
c an open grassland vegetation, referred to as Landes, and patterns are dominated by the underlying geology and
d a regular agricultural area in the polders in the Netherlands with well-defined field boundaries and mono-cultures within the parcels. Each landscape requires a different image classification approach.

We will now briefly look in the next section at how images are registered by sensors and the effect that this may have on image information and patterns. In the later section we present a number of statistical models useful for the analysis of remote sensing imagery.

2.3   Registration of spatial information by Remote Sensing sensors

In earlier sections we discussed that remote sensors register reflected or emitted electromagnetic radiance while image users are interested in object identification and object properties. Multispectral scanners are the most widely used instruments to register reflected sunlight in the optical domain. Multispectral scanners are mounted on airborne or spaceborne platforms. A scanner systematically scans the Earth's surface thereby measuring the electromagnetic energy reflected from the viewed area. These measurements are done simultaneously for several wavelength bands and this is the origin of the name multi-spectral scanner. A wavelength band is an interval of the electromagnetic spectrum for which the average reflectance is measured. Two types of multispectral scanners are most widely used
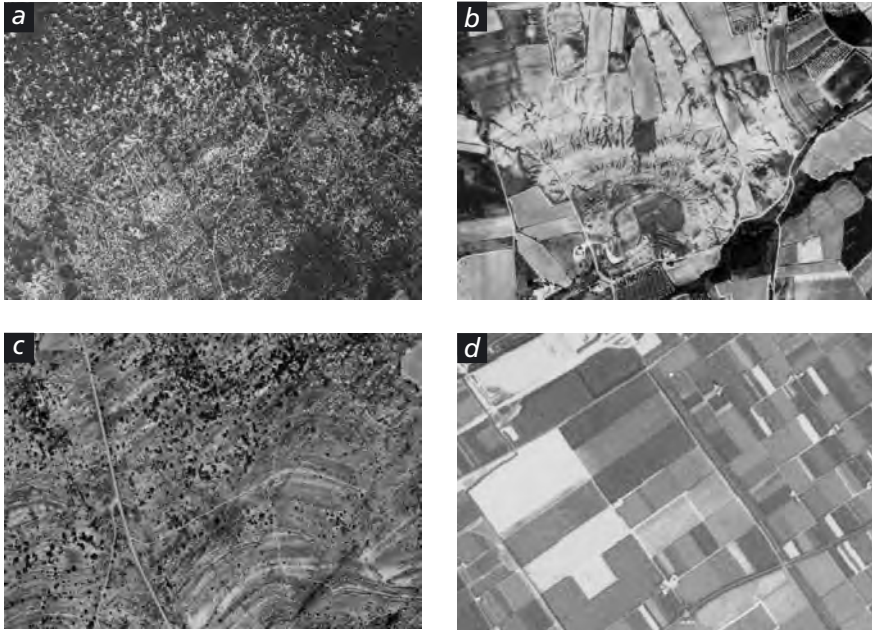
Figure 2.3 – An example of four different landscapes: a) an open shrub area (garrigue), b) a area with gullies and badlands, c) open natural grassland areas (landes) and d) an agricultural area with well-defined agricultural lots. Traditional pixel-based spectral image classification approaches will fail to produce reliable land cover maps for the first three examples but will produce excellent result for the agricultural area. Please consult the enclosed CDROM for a full colour version.

and distinguished here: the whiskbroom scanner and the pushbroom scanner (Janssen & Huurneman, 2001).

The sweeping motion of a rotating mirror scanning the Earth surface gives the name to the whiskbroom scanner. The whiskbroom scanner is a combination of a detector with a rotating mirror sweeping as a straight line over the Earth surface across the track of the satellite or aircraft. The Earth surface is scanned systematically, line by line as the platform moves forward. Whiskbroom scanners use solid-state detectors for measuring the electromagnetic energy transferred from the optical system to the sensor. The optical system focuses the incoming radiation at the surface of the detector. Techniques such as prisms or gratings are used to split the incoming radiation into spectral components and send that signal to separate detectors. These detectors transform the electromagnetic energy, or photons, into an electric current. This electric current, an analogue signal, is digitised into discrete levels of energy: the so-called Digital Numbers (DN). The range of the input radiance, between the minimum and the maximum level that the detector can handle is called the dynamic range. This range of incoming radiance is converted into specific data formats: 8-bit, 10-bit or 12-bit data formats. The Landsat Thematic Mapper used for example an 8-bit format, i.e. 256 levels of Digital Numbers while IKONOS uses a 12-bit format, 1024 levels of Digital Numbers. Each detector in the whiskbroom scanner has a specific spectral sensitivity. This is
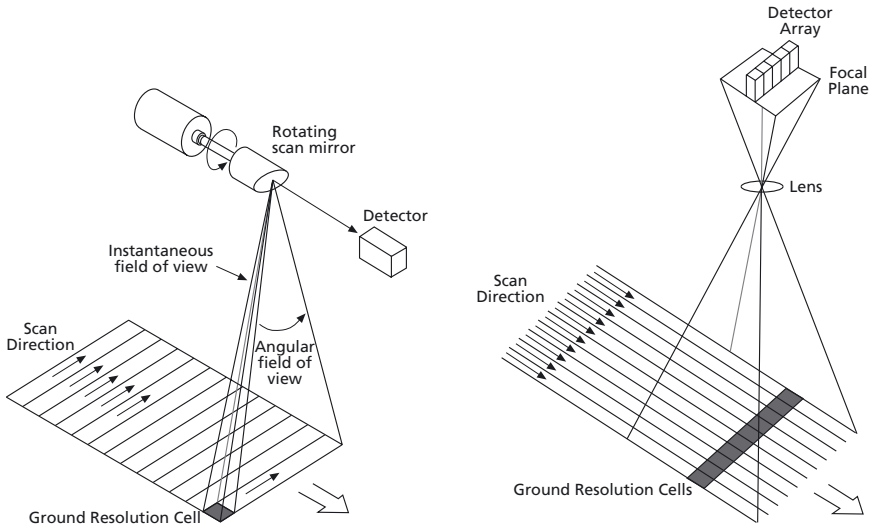
Figure 2.4 – Principle of the whiskbroom scanner (left) and the pushbroom scanner (right);
(modified from Janssen L.F.F. & G.C. Huurneman, 2001).

the spectral range in nm, or bandwidth, for which the sensor registers the incoming radiant energy. It is normally assumed that this spectral response curve has a normal distribution. The bandwidth of a sensor is usually determined by the difference between the two wavelengths where the spectral response curve is at 50% of its maximum and expressed as Full Width Half Max (FWHM) in nanometers.

The pushbroom scanner uses charge-coupled device (CCDs) to measure the electromagnetic energy. Lines of light-sensitive detectors (CCD-arrays) records one entire image line at a time. The main advantage of this type of scanner over the whiskbroom scanner is that each pixel in the line has its own detector allowing for a longer measurement time (integration time) resulting in an improved geometry and less noise. Furthermore, the pushbroom system has no moving parts that generate image noise. The pushbroom scanner measures continuously along the direction of the satellite or aircraft flight line and is therefore also referred to as an along-track scanner. Modern video recorders and digital cameras use CCD arrays for capturing images, the arrays used for Earth observation purposes are more sensitive.

The registered electromagnetic energy is stored or expressed in pixels. A pixel is the smallest element of an electronic image and can only be subdivided by creating repetitive information i.e. a finer resolution would mean that all new pixels would fit within old pixels and have the same values assigned (Fisher, 1997). The grid cell is a similar kind of object as the pixel in geographic information processing (Burrough and McDonell, 1998). The grid cell representation of space is known as the raster data model. When the grid cells represent the spatial variation of continuously varying attributes each grid cell will have a different value of the attribute (continuous data such as elevation). The grid cell may also represent thematic

data. The numerical label of the grid cell provides information about e.g. the type of land use or soil type present at this location.

The pixel in fact represents an average value in each of three dimensions: space, wavelength and time (Schowengerdt, 1997). The average value in the pixel over time is usually very small, the Landsat TM whiskbroom scanner only requires microseconds to register the information and this time step is insignificant for most applications. The averages over space and wavelength are important as they determine how well we can observe our objects and how well we can spot spectral differences required to identify object properties. So, the pixel size and the spectral resolution are important sensor system properties. Pixels are the result of the scanning system. Reflected light is scanned by means of a rapidly rotating scanning mirror (whiskbroom scanner) that deflects the incoming rays of light to form a set of lines across a detecting field. The varying intensities are stepwise stored, per pixel, per scanline and per spectral band. Later this information is used to create an image. While the information entering the sensor is registered several important transformations of the radiometric, spatial and geometric properties of the radiance occur (Schowengerdt, 1997). Generally, the sensor degrades the signal of interest. For proper image interpretation and analysis it is important to have some knowledge about the nature of the change of this signal. In summary the signal of interest in remote sensing observations is influenced by the sensor's spatial resolution (averaging out and/or mixing the reflected radiance over the pixel size), the sensor's spectral resolution (averaging out absorption bands and/or the overall reflectance curve), the spectral response function of the sensor (the range of reflectance values that can be captured), the imaging process in the optics and detector parts of the sensor and the geometric distortions arising from internal sensor or external platform factors. A detailed discussion about the effects of sensor characteristics on information content of a pixel is available in chapter 4 of Atkinson and in Schowengerdt (1997).

2.4   Statistical models for Remote Sensing data

In his book on statistics for spatial data, Cressie (1993) distinguishes three types of spatial data: point patterns, lattice data and geostatistical data. Point patterns consist of the spatial locations of events that take up very little space and can be considered points: the locations of lightning during a thunder storm, the locations of trees in a forest, etc. Lattice data are data with a finite, regular or irregular spatial index; these can be aggregated for larger, usually administrative regions, such as number of births or deaths per local community, or remote sensing images with a regular space index. Geostatistical data have a continuous spatial index; these are data that have some value at every location, and that could be measured everywhere, but that are usually measured on a limited number of locations, chosen during the research.

Statistical methods for regular lattice data, such as remote sensing images, have been applied for a long time in remote sensing research. These methods mainly aim at image restoration. They include discriminant analysis modified for spatial data (Switzer, 1980), smoothing techniques, contextual classification (Barnsley and Barr, 1996), edge detection, image partitioning, Min/Max autocorrelation factors or Maximum Noise Fraction transformations (Switzer and Green, 1984; Green et al., 1988), and Bayesian image restoration methods

Figure 2.5 – Part of the Peyne DAIS7915 image in false colour band combination. The location of the field samples for aboveground biomass estimates are indicated (+).

(Winkler, 2003). It should be noted that all these methods, do explicitly take the spatial (contextual) aspect of the problem into account. Some of them are multivariable and consider multiple bands simultaneously, and some of the methods use training data (e.g. discriminant analysis), while others do not (e.g. smoothing or Min/Max autocorrelation factors).

Application of geostatistical methods to remote sensing research is a little bit harder to imagine: the typical geostatistical problem where we have data at a finite amount of locations and want to predict (interpolate) or simulate values at unsampled locations does typically not hold when the primary variable of interest is a complete image. The image may however not be complete, and a notable exception is the replacement of clouded pixels with estimates based on surrounding, non-clouded pixels (Addink and Stein, 1999). De Jong et al. (2003) present another approach, where the primary variable of interest is aboveground biomass, measured for a limited number (120) of 30 m by 30 m plots in the field. From the 79 available DAIS7915 hyperspectral scanner images, five images, $R_1, \dots, R_5$, were selected to predict log-transformed aboveground biomass (AB) at each location s using a multiple linear regression model:

$$\log (AB(s)) = b_0 + b_1 R_1(s) + b_2 R_2(s) + \ldots + b_5 R_5(s) + e(s) \tag{2.2}$$

and assumed that the residual $e(s)$ is a spatially correlated, second order stationary variable. Prediction under this model is called universal kriging (or external drift kriging). Figure 2.5 shows an overview image (false colour composite) of the study area, and figure 2.6 shows the predicted values of biomass. The remote sensing images clearly have a large influence on the interpolated surface.

Biomass (kg/m²)

0.0-0.2	5.0-20
0.2-0.5	20-50
0.5-2.0	>50
2.0-5.0	
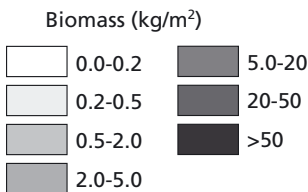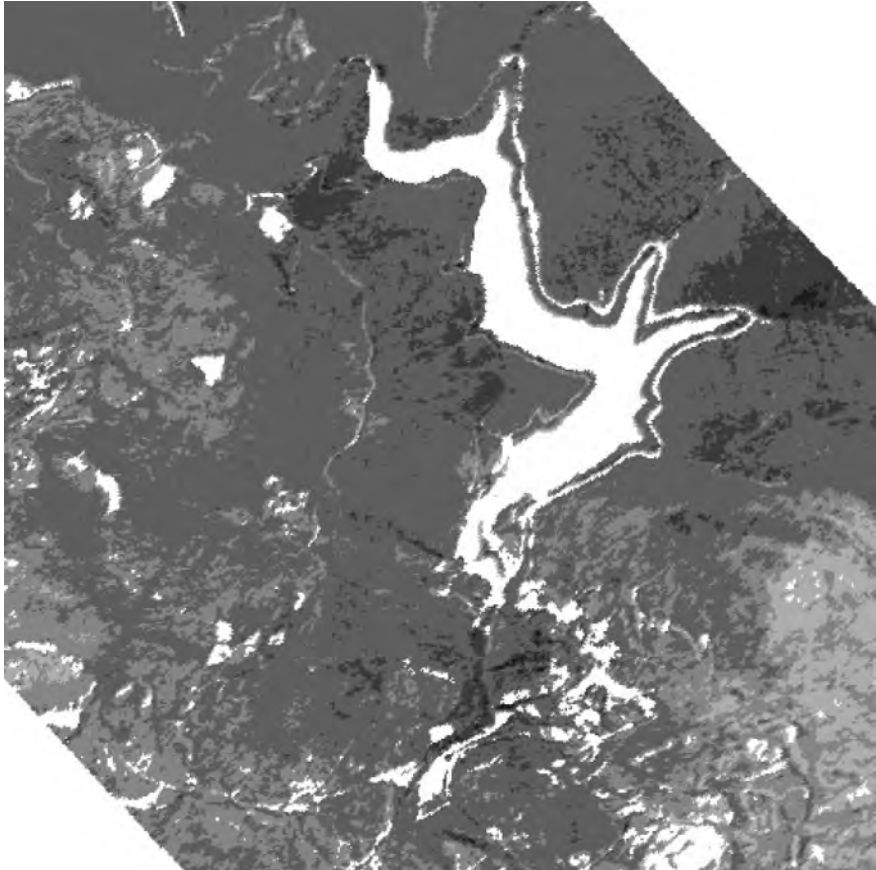
Figure 2.6 – Aboveground biomass predicted by universal kriging. Biomass values range from 0 (dark) to 50 kg/m² (bright).

In effect, hyperspectral remote sensing images are now used to globally predict biomass through a multiple regression relationship, and this component becomes dominant in areas with few spatially correlated measurements nearby; and spatial correlation in regression residuals helps interpolation nearby measurement locations.

Atkinson and Lewis (2000) review the various forms of using the variogram in classifying remote sensing images. This varies from using local sample variogram maps (Carr, 1996) to characterize spatial structure to parametric estimation of the variogram range parameter (Ramstein and Raffy, 1989); Herzfeld used detrended variogram coefficients to classify sea floor types, Wallace et al. (2000) used a similar analysis to classify desert vegetation communities. Bocher (2003) and Song and Woodcock (2003) investigate the use of the Average Local Variance function (ALV) respectively variograms to determine the optimal pixel size and the effect of scale in high resolution imagery for forest applications.

De Gruijter (1999) gives an overview of spatial sampling schemes for collecting ground truth data for remote sensing applications. Most of his review considers design-based approaches, where randomness comes from random sampling, i.e. random assignment of sample locations; model-based (geostatistical) approaches to choosing sampling schemes are reviewed only briefly. Model-based sampling schemes are often designed ad-hoc. Their design is less straightforward because the objectives are usually not simple: the sample data are needed both for inference of the spatial correlation structure, as well as for spatial prediction of the variable measured.

One important issue that is dealt with by geostatistics is change of support. Support is the physical size of a single measurement. When we increase the support of our measurements, the variability of the measurements decreases because the spatial variability of our subject inside the area on which we measure increases. Regularization is the measurement of averages over larger areas. The theory of regularization is briefly reviewed by Curran and
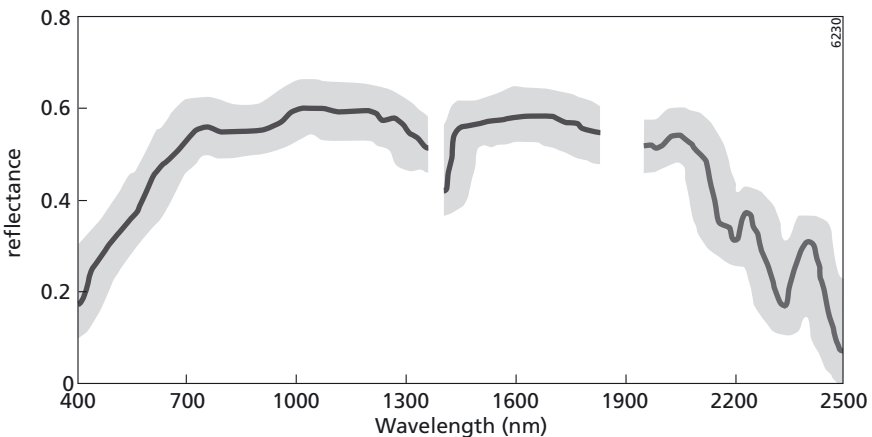
Figure 2.7 – A user-defined Epsilon band is drawn along the spectral signature and used to separate spectral homogeneous image sections from heterogeneous image parts.

Atkinson (1999), and dealt with extensively by Journel and Huijbregts (1983). The dependence of variability on measurement support is important for choosing pixel sizes and for collecting ground truth data. Pixel sizes can be chosen to some extent, as we can scale up (smooth) images to get data on a larger support than the support of pixels in the original image. Depending on the variable of interest, we can often choose a support for our measurements of ground truth data. If this support is e.g. smaller than that of the images, one should take into account the variability of measurement data within pixels of the image, when comparing pixel values with ground truth measurements at corresponding locations.

2.5   The spatial and spectral classifier

In the previous sections we introduced and discussed a number of topics: natural spatial variability that occur in landscapes, methods that were developed in various scientific disciplines to handle and quantify this spatial variability, the way pixels are used in remote sensing to capture information about objects at the earth surface, statistical models and geostatistical methods to capture spatial variability. Looking back at how remote sensing plays a role in our mapping efforts we may conclude that for quite a number of landscape conditions spectral pixel-by-pixel classification algorithms perform in a satisfactory way and provide useful products. In some situations where we have open type of vegetation such as in Mediterranean areas or Savannah type regions, contextual classification algorithms may yield better results. But also within one remote sensing scene we might want to use a combination of spatial and spectral analysis methods. For closed vegetation types within one scene we prefer to use spectral pixel-by-pixel classifiers while in that same scene we would like to use contextual approaches for shrub vegetations. A straightforward approach to achieve a separation of areas within one scene where per-pixel methods are more appropriate and where contextual methods will perform better was proposed for hyperspectral imagery by Hornstra et al. (2000) and De Jong et al. (2001) and is referred to as the spatial and spectral classifier (SSC).

The SSC method is applied to a hyperspectral image in three steps:
1 Stratification: extraction of homogeneous regions on the basis of spatial and spectral information;
2 Classification of the homogeneous regions;
3 Classification of the remaining (non-homogeneous) image parts.

In the stratification step a kernel is moved over the image. This kernel considers the spectral signature of four neighbours (left, right, above, under) with the spectral signature of the centre pixel. The similarity between the spectrum of the centre pixel and the spectra of its four neighbour is computed and a user-defined epsilon band along the spectrum as shown in figure 2.7. If the spectral signatures fall within the bandwidth of the epsilon line the centre pixel is labelled as a homogeneous area, otherwise it is labelled as a heterogeneous. A second criterion for a homogeneous area in the image is that it comprises at least 5 connected pixels.

In the second step of SSC the average spectral signature of each homogeneous area, i.e. a set of interconnected pixels, is computed and assigned to every pixel in this area. Next,

the homogeneous areas are classified following a supervised classification approach. Areas of known land cover are digitised on screen, their spectral properties are sampled and the conventional minimum distance to mean classifier is used to assign each pixel to thematic classes (Schowengerdt, 1997). As a result the classification of these homogeneous image parts is purely based on spectral information.

In the third step of SSC the heterogeneous areas are treated. These pixels are classified using spatial and spectral information. The minimum distance to mean classifier is adjusted in such a way that it accounts for the spectral signature of the pixel and for the spatial pattern of previously classified pixels in its neighbourhood. Class assignment of the conventional minimum distance to mean rule is based on the spectral, Euclidean distance between the pixel and the mean of every land cover class. In the SSC approach not only this spectral distance is considered but also the spatial distance between an unclassified pixel and a previous classified pixel in step 2 of SSC where the homogeneous-labelled pixels are thematically assigned. This spatial distance is computed using a growing ring (kernel) of pixels surrounding the unclassified pixel. The contribution of spatial versus spectral information to the classification rule can be adjusted using a factor α. The assignment of pixels to thematic land cover classes is based on the smallest value of the combined spatial distance and spectral distance using the following formula:

$$C = \min \left(\alpha \cdot d_{\text{spec}} + (1 - \alpha) \cdot d_{\text{spat}} \right) \tag{2.3}$$

Where C is the thematic land cover class, d_{spec}: the spectral distance between the unclassified pixel and the mean of the land cover class, d_{spat}: the spatial distance between the unclassified pixel and a previously classified pixel using the growing kernel and – is a factor to adjust the contribution of spectral versus spatial information in the classification procedure. In case of a chosen value of 0.5 for – the contribution of the spectral and spatial rule resembles. A value of 1.0 for – will result in a SSC classification that is purely based on spectral information.

The SSC method is tested and evaluated on a study area in southern France comprising an agricultural area of mainly vineyards and a natural vegetated area consisting of an open, complex Mediterranean shrub vegetation. Classification improvements for the agricultural area were modest but for the natural region the classification results improved significantly. More details about the SSC and these results are available in Hornstra et al. (2000) and De Jong et al. (2001). The SSC method is a nice example how we can combine the use of spectral and spatial pattern information in image classification procedures.

2.6   Conclusions

In this chapter we have discussed the problems of scale and temporal and spatial variability of landscapes and landscape processes. Over the years researchers have investigated in many different directions for methods to handle the problems of scale and the problems of spatial – temporal variability for surveying purposes and for process simulation studies. These methods include the development of hierarchical mapping methods such as the land system approach, various methods to define assumed homogeneous map units such as the REA: Representative

Elementary Area, HRU: Hydrological Response Unit and DRU: Desertification Response Unit. Later on, when computer power became widely available, also fractal and wavelets methods to quantitatively express scale invariance or 'landscape roughness' were and are investigated. In this chapter we also looked briefly at the development of statistical models to handle spatial variability and scale issues, and how variograms, interpolation methods and uncertainty assessments have grown out to common tools for geographers, geologists, ecologists and botanists. The role of earth observation for these disciplines, what type of information these sensors collect, how this information is technically collected and how useful information can be extracted from the images is also briefly touched upon. Remote sensing provides spatially distributed information of the landscapes or regions of interest and provides time series of images allowing us to detect changes over time. Remote sensing image analyses has focussed very much over the last decennia on the spectral analysis of images i.e. the spectral signature. Less attention is paid to the spatial patterns captured by these images while these spatial patterns have always yielded the basis for mapping and modelling efforts in environmental disciplines. The following chapters in this book will present a wide range of methods to analyse and quantify these spatial patterns captured in images acquired at different levels of scale and over various time steps and how these methods are useful to bridge the gap between surveying, geostatistical approaches and remote sensing.

Chapter 3
Sub-Pixel Methods in Remote Sensing

Giles M. Foody

3.1   Introduction

Theoretically, remote sensing is well-suited as a source of information on environmental features such as land cover. Remotely sensed imagery are available at a range of spatial and temporal scales, have a map-like format and, due to the nature of radiation interactions with the Earth's surface, depict variation in land surface properties that is linked to land cover. Indeed, as most general land cover classes (e.g. forest, grassland etc.) differ in their interaction with the radiations commonly used in remote sensing, it should be possible to accurately map and monitor land cover from remotely sensed data. Although the literature contains an enormous wealth of articles that demonstrate that it is possible to accurately map land cover from remotely sensed data it is often, in practice, an extremely difficult task (Townshend, 1992). Those studies that have succeeded in accurately mapping land cover have also commonly been based upon small test sites, often with ideal conditions (e.g. large relatively homogenous land cover parcels, insignificant topographic variability etc.) and used carefully selected and processed imagery. These successes do not mean it is generally easy to extract land cover information accurately from remotely sensed data. There are many instances in which an approach to land cover mapping developed successfully at one site fails to map land cover accurately when applied to another (Wilkinson, 1997; van Collie et al., 2001). Consequently, it is unsurprising that land cover maps often contain considerable error. For example, the IGBP global land cover map derived at the end of the last century provides a representation of the Earth's land cover that is estimated to have an area-weighted accuracy of ~67%, substantially below its target accuracy of 85% (Scepan, 1999). Thus despite a long history of research into the topic and a widely held view that land cover mapping is a basic and simple task it is apparent that the potential of remote sensing as a source of land cover data is unfulfilled (Townshend, 1992; Estes & Mooneyhan, 1994).

Many factors conspire to limit the ability to map land cover accurately from remotely sensed data. These range from issues associated with the sensor (e.g. the spectral wavebands in which it operates, its spatial resolution etc.), atmospheric attenuation (e.g. dynamic variation in haze and dust particles) and the methods used (e.g. the image analysis procedures used in mapping). In addition to these variables there are further, more subtle, complications. For example, the ground or reference data sets used in assessing the accuracy of a map derived from remote sensing often contain error and may lead to incorrect interpretation about the accuracy of the derived map (Foody, 2002a). The various factors that may act to limit map accuracy have been the focus of many investigations. In particular, since remotely sensed

imagery should be an excellent source of land cover information much attention has been directed at the image analysis procedures used, with the aim of finding tools that can extract more fully the land cover information contained in the imagery than the conventional techniques used widely in the past.

While many important and useful advances have been made by research into image analysis and classification techniques, a fundamental assumption that is commonly made in remote sensing is often unsatisfied. This assumption is that each pixel in the image represents an area on the Earth's surface that contains a single class. This is often not the case, with mixed pixels, containing areas of more than one class, present (Fisher, 1997; Cracknell, 1998). These mixed pixels cannot be allocated appropriately to a single class, irrespective of what method is used to derive that allocation. Without solving the problem of mixed pixels it is likely that the full potential of remote sensing as a source of land cover information will remain unrealised.
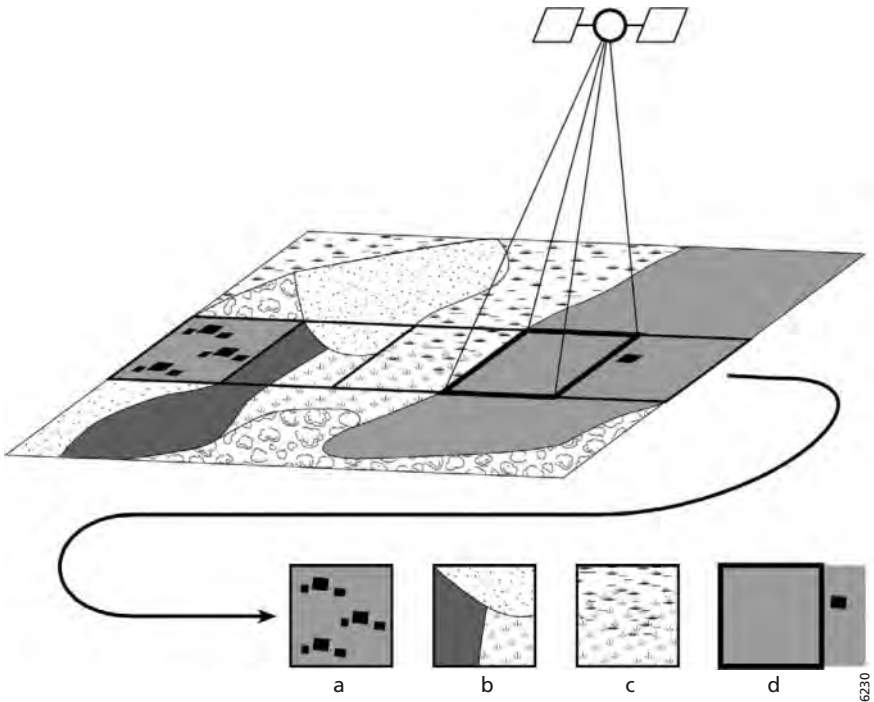
Figure 3.1 – Some common origins of mixed pixel problems. The diagram shows an extract of a satellite sensor image, perhaps part of a scan line of data, with four pixels highlighted. Each of the highlighted pixels represents a commonly observed mixing problem: (a) mixing caused by the presence of small, sub-pixel, targets within the area it represents, (b) mixing as a result of the pixel straddling the boundary of discrete thematic classes, (c) mixing due the gradual transition observed between continuous thematic classes and (d) a mixing problem due to the contribution of a target outside the area represented by a pixel but influenced by its point spread function (note that the pixel appears, superficially, to be pure but its spectral response is influenced by the small object that lies outside of the area represented).

There is, therefore, a need to derive thematic information at sub-pixel scales to reveal the nature of the class mixing. This chapter aims to discuss the mixed pixel problem and then outline some of the methods that may be used to determine sub-pixel scale thematic information. The ability to estimate sub-pixel scale information accurately would greatly facilitate the extraction of accurate and informative information from remotely sensed data and is the basis of contemporary super-resolution mapping approaches that are discussed in chapter 4 of this volume by Atkinson.

3.2   Mixed pixels

A remotely sensed image is simply a representation of the way radiation interacts with the Earth's surface. As a representation of the environment some degree of inconsistency with reality is to be expected. Various sources of inconsistency may be identified but of particular significance to the topic of this chapter is a basic property of the remotely sensed imagery. Typically the imagery comprise raster data and the fundamental spatial unit, the pixel, is defined primarily by sensor dependent variables. That is, the pixel is an arbitrary spatial unit. Its basic properties such as size, shape and location are determined mainly by the sensor (e.g. its altitude, look angle, field of view etc.) and not directly by the properties of the ground. Commonly, the area represented by a pixel will contain more than one thematic class. This situation may arise for many reasons (e.g. figure 3.1) and makes the data unsuitable for use with some conventional image analysis techniques. Consequently, the use of conventional 'hard' (one pixel one class) approaches to mapping from remotely sensed data will result in error if mixed pixels are present. The magnitude of the problem is also clearly a function of the proportion of mixed pixels within the remotely sensed data set.

The proportion of mixed pixels in an image is often large in remote sensing studies. The exact proportion of mixed pixels in an image is an interactive function of the properties of the sensor (e.g. spatial resolution) and land cover mosaic on the ground (e.g. the class composition, spatial arrangement etc.) and so the mixed pixel problem is a contextual issue. In general, the proportion of mixed pixels increases with a coarsening of the spatial resolution of the sensor and/or increasing fragmentation of the landscape represented by the image and there may be many more mixed than pure pixels within the image (Crapper, 1984; Campbell, 2002). Thus, coarse spatial resolution data sets such as those derived from the NOAA AVHRR (1.1 km spatial resolution) that are the foundation of many large area mapping investigations (Belward et al., 1999; Cihlar, 2000) are often dominated by mixed pixels (e.g. Foody et al., 1997).

As mixed pixels cannot be sensibly accommodated in a conventional hard image analysis, researchers have attempted to reduce the problem. Some have sought to use very fine spatial resolution imagery in the hope that this will reduce the proportion of mixed pixels. Unfortunately, the mixed pixel problem may not be removed by the use of fine spatial resolution data as mixing of a class's constituent parts (e.g. leaves, branches, trunks and soil surfaces of a forest class) often becomes increasingly important and over large areas the use of fine spatial resolution data may be impractical.

Multispectral image

Sub-pixel analysis

Fraction images

Asphalt

Grass

Trees

Water

'Target'

6230
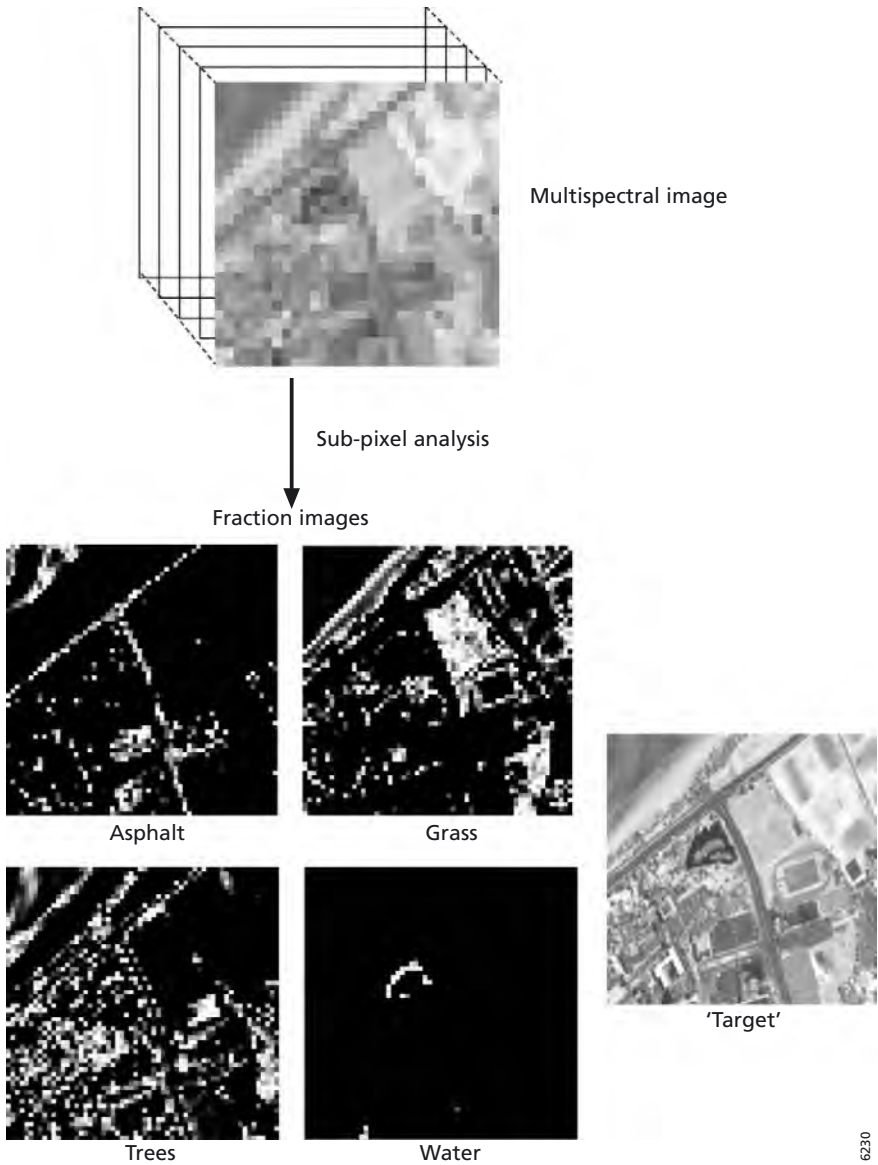
Figure 3.2 – An example of a typical sub-pixel analysis. Here a sub-pixel analysis (e.g. a linear mixture model or soft classification) is used to convert the multispectral image that depicts the spatial variation in surface radiance into fraction images that in turn depict the location of four land cover classes. In each fraction image the grey scale indicates the fractional cover of a class (100% cover – white; 0% cover – black). The 'target' image is a finer spatial resolution image of the input multispectral data set used to indicate the actual spatial distribution of thematic classes at the test site.

Since mixed pixels cannot be appropriately mapped by conventional methods alternative image analysis techniques have been evaluated. Often researchers have sought to derive sub-pixel scale information and some approaches for this are outlined below.

3.3   Estimating sub-pixel class composition

A variety of approaches may be used to derive sub-pixel scale information (Eastman & Laney, 2002). Here, two popular approaches to the derivation of sub-pixel scale information are briefly discussed. These are the use of additive, linear mixture, models and soft or sub-pixel classifications (Eastman & Laney, 2002). Each approach may be used to derive information on the sub-pixel scale thematic composition of image pixels. Commonly, these approaches are used to derive an estimate of the proportional coverage of each class in the area represented by a pixel but other information is sometimes derived. For example, sometimes the desired output may simply be a primary and secondary class label (Woodcock et al., 1996). The nature of the derived output impacts markedly on the means of its visual representation. Frequently, the derived sub-pixel information is mapped as fraction imagery or continuous fields (Shimabukuro et al., 1997; DeFries et al., 2000; Frizzelle & Moody, 2001), to represent the spatial distribution of the classes over the region imaged. As a simple example, figure 3.2 indicates the form output that is typically derived from a sub-pixel analysis.

3.3.1   Spectral unmixing

The basic and widely used linear mixture model is based on the assumption that the spectral response x_k of a pixel k is a linear weighted sum of spectral responses of its component classes (Settle & Drake, 1993), expressed by

$$x_k = Ef + e \tag{3.1}$$

in which E is a q by c matrix in which q represents the number of wavebands and c the number of classes, the term f represents a vector, of length c, that expresses the proportional coverage of the classes in the area represented by the pixel and e is a term that represents the residual error. The columns of the matrix E are end-member spectra, essentially the characteristic spectral responses of the classes. These can be difficult to define appropriately (Williamson, 1994; Atkinson et al., 1997; van der Meer & de Jong, 2000; Wu & Murray, 2003) and are commonly determined from 'pure' training areas. Once defined, the mixture model may be used to estimate the class composition of a pixel, represented by f, from its spectral response (Cross et al., 1991; Settle & Drake, 1993) subject to the constraints that

$$f_i \geq 0, i = 1,... c \quad \text{and} \tag{3.2}$$

$$\sum_{n=1}^{c} f_i = 1 \tag{3.3}$$

This simple approach to deriving sub-pixel information has been used widely in remote sensing (e.g. Cross et al., 1991, Drake & White, 1991; Quarmby et al., 1992; Cochrane & Souza, 1998; DeFries et al., 2000; Lucas et al., 2002). Commonly, the spatial distribution of the land cover classes is represented through fraction images. Typically there is one fraction

image for each class and in this representation the pixel's grey level scale is directly related to the proportional coverage of the class in the area represented by the pixel. Thus, a pixel representing an area that is comprised entirely of the class may be represented in white while one representing an area in which the class is absent would be black (figure 3.2).

Despite its simplicity and ability to derive accurate sub-pixel estimates under certain circumstances there are some concerns about the use of this approach to pixel unmixing. The use of the least squars error criterion, for example, makes the unmixing analysis prone to problems associated with outliers. A simple alternative that reduces this effect is to base the unmixing analysis on a least median square criterion (Rosin, 2001). Similarly, the assumption of linear mixing is often inappropriate in remote sensing, particularly of vegetated regions where the radiation interactions with the environment are known to be non-linear. In such circumstances non-linear mixing models may be more preferable than the basic linear model (Borel & Gerstl, 1994; Foody et al., 1997). Finally, the approach requires that the number of end-members is less than the number of spectral bands used in the analysis (Mather, 1999).

3.3.2   Soft classification

Hard supervised image classification techniques have been widely used for mapping land cover from remotely sensed data. These techniques operate by allocating each pixel in the image to one of the classes in the set defined by the analyst. For example, with the maximum likelihood classification, one of the most widely used hard classifiers in remote sensing, each pixel is allocated to the class with which it has the highest posterior probability of membership (Tso & Mather, 2001). Irrespective of the specific classifier used to derive the class allocations, a number of important assumptions are made in hard classification. In particular, it is typically assumed that the pixels are pure and that the classes are discrete, mutually exclusive and have been defined exhaustively. Since some or all of these assumptions are often untenable in remote sensing applications alternative approaches to mapping have been the topic of considerable recent research. Of relevance here is the development of soft or fuzzy classifications which can provide thematic information at sub-pixel scales.

In soft thematic mapping, each pixel is not forced or constrained to show membership to a single class. Consequently, each pixel may display multiple and partial class membership; since a single class label is no longer forced upon pixels the output is fuzzy but to avoid confusion with fuzzy sets and logic the term soft rather than fuzzy classification may be more appropriate. Since multiple and partial class membership is accommodated in a soft classification these techniques may sometimes be a useful means of reducing the mixed pixel problem and acquiring sub-pixel scale thematic information (Fisher & Pathirana, 1990; Foody, 1996).

Sub-pixel scale information is typically represented in the output of a soft classification by some measure of the way class membership is partitioned amongst the classes. The membership properties of pixels can be represented in a variety of ways in the output of a soft classification which influences the detail and accuracy of sub-pixel scale information conveyed by the analysis. Frequently, the grade or strength of membership a pixel displays to each class is derived and with many of the popular approaches to soft classification the measure(s) of the strength of class membership derived for a pixel are taken to reflect the

relative proportion of the classes in the area represented by the pixel. This type of approach allows a representation similar to the fraction images derived from linear unmixing methods to be generated (figure 3.2).

One problem with both the standard approach to unmixing and soft classification is the requirement to have defined all the classes (or end-members). Some soft classification approaches may, however, be useful if the set of classes has not been defined exhaustively. Thus for example, a soft classification depicting the spatial variation in the absolute strength of class membership may sometimes provide a more appropriate basis for thematic mapping than conventional approaches based on relative measures of class membership (Foody, 2000b; 2002b). Various measures of class membership have been used in soft classifications and some are are outlined below.

Many methods may be used to derive a measure of the strength of class membership that can be used to form a soft thematic map. The following sections briefly outline a selection of techniques that have been used recently in remote sensing applications; other approaches may, of course, be used. The approaches that have been commonly used in remote sensing studies range from those based upon the popular and established conventional statistical classifiers such as the maximum likelihood classifier through techniques based on evidential reasoning to neural network based approaches that have recently become a popular tool for the analysis of remotely sensed data (Tso & Mather, 2001). Some of the approaches are normally used in remote sensing for the production of hard classifications while others are fuzzy classifiers, the output of which may, of course, be hardened to give a conventional crisp class allocation. The salient features of some of the widely used approaches, including the measures of the strength of class membership derived, are briefly outlined in the remainder of this section.

3.3.2.1 Maximum likelihood classification

The standard maximum likelihood classification, one of the most widely used hard classification techniques in remote sensing, has often been adapted for the derivation of sub-pixel scale information. Although the maximum likelihood classifier is a conventional statistical classification technique that allocates each pixel to the class with which it has the highest likelihood or *a posterior* probability of membership (Schowengerdt, 1997; Mather, 1999b) it can be softened (Foody et al., 1992).

The basis of the maximum likelihood classification, and other related probabilistic classifiers which may be used in the same way, is the probability density function, which may be derived from,

$$p\,(x_k|i) = \frac{1}{\sqrt{2\pi}\,\sqrt{|M_i|}}\,\exp\left(-\frac{1}{2}\,D^2\right) \tag{3.4}$$

where $p(x_k|i)$ represents the probability density function for the pixel k with the data vector x_k as a member of class i, M_i is the variance – covariance matrix for class i and D^2 is the Mahalanobis distance between the pixel k and the centroid of class i. The Mahalanobis distance may be calculated from,

$$D^2 = (x_k - v_i)^{\mathrm{T}} M_i^{-1} (x_k - v_i) \tag{3.5}$$

where v_i is the mean vector for class i. The calculated Mahalanobis distance may be converted to a typicality probability by reference to a chi-squared distribution (McKay & Campbell, 1982). These probabilities lie on a 0-1 scale and represent the probability of observing a Mahalanobis distance as extreme as that observed for a particular pixel with respect to the specified class. Thus, the typicality probability provides an indication of the closeness of the pixel to a single specified class centroid. That is, the typicality provides a measure of the absolute strength of membership a pixel has to an individual class, irrespective of its membership to any other class. Note that the sum of the typicalities to all specified classes needs not sum to 1.0 for any one pixel. These properties of the typicality make it a very different measure of class membership to the posterior probability.

In a standard maximum likelihood classification, each pixel is allocated to the class with which it has the highest posterior probability of class membership, which is calculated from,

$$L(i|x_k) = \frac{P_i p\,(x_k|i)}{\sum\limits_{j=1}^{c} P_j p\,(x_k|j)} \tag{3.6}$$

where $L(i|x_k)$ represents the posterior probability of pixel with the data vector x_k belonging to class i, P_i the *a priori* probability for class i, and c the total number of classes. Posterior probabilities of class membership lie on a 0-1 scale but they are also constrained to sum to 1.0 for each pixel and are derived with respect to all defined classes (Campbell, 1984; Foody et al., 1992; Mather, 1999b). Thus, the posterior probability provides a relative measure of class membership. This situation makes the posterior probability attractive as an indicator of sub-pixel proportions. Indeed, posterior probabilities derived effectively as a by-product of a conventional maximum likelihood classification have been commonly used to estimate the composition of pixels. Although there is not a direct link between the proportional coverage of a class and its posterior probability (strictly an indicator of the uncertainty in making a particular hard class allocation), leading to its use a source of sub-pixel information being questioned (Lewis et al., 1999; De Bruin, 2000) many studies have found that, in practice, useful sub-pixel thematic information may be derived by this approach (e.g. Foody, 1996, Bastin, 1997).

3.3.2.2 Fuzzy c-means (FCM)

The FCM is a fuzzy classifier that has been widely used for the derivation of sub-pixel scale thematic information (Fisher & Pathirana, 1991; Foody, 1996; Atkinson et al., 1997; Bastin, 1997). The FCM is, essentially, a non-hierarchical clustering algorithm that may be used to sub-divide a data set into c classes. Pixels are initially assigned randomly to classes before being moved iteratively to other classes with the aim of minimizing the generalised least-squared error,

$$J_m(U, v) = \sum\limits_{k=1}^{n} \sum\limits_{i=1}^{c} (u_{ik})^m (d_{ik})^2 \tag{3.7}$$

where U is a fuzzy c-partition of the data set containing n pixels ($x_1, x_2, ..., x_n$), v_i is the centre of cluster i, d_{ik} is the distance between x_k and v_i measured using an appropriate

weight matrix and m is a user defined weighting component that lies within the range $1 \leq m \leq \infty$ which determines the degree of fuzziness of an analysis. When $m=1$ a conventional hard classification is obtained in which each pixel is associated unequivocally with just one class. For the derivation of sub-pixel scale information, it is, therefore, important that $m>1$, ensuring that multiple and partial class membership is allowed in the output. There is no optimal value of m and most studies have used a value in the range $1.5<m<3.0$ (Bezdek et al., 1984; McBratney & Moore, 1985; Foody, 1996). In a soft classification, attention is focussed on the elements of U, u_{ik}, that represent the grade of membership of a case to a class. These membership values are constrained to satisfy,

$$u_{ik} \in [0, 1] \tag{3.8}$$

$$\sum_{k=1}^{n} u_{ik} > 0, \, i = 1, \ldots, c \tag{3.9}$$

$$\sum_{i=1}^{c} u_{ik} = 1, \, k = 1, \ldots, n \tag{3.10}$$

In a fuzzy c-partition of a data set, the membership functions characterise the membership of each case in all classes. Memberships close to unity indicate a high degree of similarity between a case and a class whereas memberships close to zero indicate little similarity between a case and a class. It is apparent from the constraints defined above that the memberships lie on a 0-1 scale and sum to unity for each pixel. These constraints make the fuzzy memberships appear similar in general terms to posterior probabilities, although they are in reality quite different. The memberships are calculated from,

$$u_{ik} = \frac{1}{\sum_{j=1}^{c} \left(\dfrac{d_{ik}}{d_{jk}} \right)^{\frac{2}{m-1}}} \tag{3.11}$$

(Bezdek et al., 1984; Schowengerdt, 1997).

Although the FCM was originally proposed as a clustering (unsupervised) technique, the algorithm may be modified so that the classification is based on class centres provided by the analyst from training samples and so for use as a supervised classifier (Key et al., 1989; Foody, 1996). Indeed, the FCM has been commonly used in a supervised mode to derive sub-pixel scale thematic information from remotely sensed data (e.g. Foody, 1996; Atkinson et al. 1997; Bastin, 1997; Lucas et al., 2002). Although accurate estimates of sub-pixel class composition have been derived with the FCM it is apparent that accuracy is a function of the value of m used in the analysis (Foody, 1996) and thus this value should be carefully selected for the application in-hand.

3.3.2.3 Possibilistic c-Means (PCM)

The PCM is the possibilistic counterpart of the FCM. The main difference between the PCM and the more widely used FCM is the removal of the constraint for the memberships to sum to one for each pixel in the PCM (Krishnapuram & Keller, 1993; Foody, 2000b). With the PCM the strength of membership is derived from,

$$u_{ik} = \cfrac{1}{1 + \left(\cfrac{d_{ik}^2}{\eta_i} \right)} \qquad (3.12)$$

where η_i is a parameter that specifies the distance at which the membership to a class equals 0.5. As with the FCM, the parameter *m* controls the fuzziness of the analysis but its optimal value and interpretation differs between the two algorithms (Krishnapuram & Keller, 1996). The main attraction of the PCM for the derivation of sub-pixel scale thematic information is that, like the typicality probability, the membership values derived are measures of the absolute strength of class membership. Consequently, the memberships derived from the PCM are not affected by the presence of untrained classes. Although more accurate predictions of sub-pixel class composition may be derived from the FCM than PCM, the presence of untrained classes can markedly degrade the accuracy of sub-pixel estimates from the FCM while not affecting those from the PCM. Thus, in situations when the analyst may believe that the set of classes contained within the imaged area has not been defined exhaustively it may be preferable to use the PCM rather than FCM for the derivation of sub-pixel scale thematic information (Foody, 2000b).

3.3.2.4 Neural networks

Neural networks have recently become a very popular tool for the derivation of sub-pixel scale thematic information from remotely sensed data (Tso & Mather, 2001). A variety of types of network have been used for the derivation of sub-pixel scale thematic information, notably feedforward networks.

Feedforward networks have been widely used for the classification of remotely sensed data. A variety of feedforward networks have been used for estimating sub-pixel scale thematic information, including the multi-layer perceptron, radial basis function and probabilistic neural networks (Foody, 2001). While there are marked differences between these networks, each is constructed from a set of simple processing units that are arranged in a layered architecture with each unit in a layer linked to every unit in the adjacent layer(s) by a weighted connection. The architecture is determined, in part, by the data to be used and nature of the desired classification. For example, there is usually an input unit for each discriminating variable used (e.g. each spectral channel in the remotely sensed data set) and an output unit for each class to be mapped, although different architectures may be used (e.g. if the input data are thermometer encoded more input units may be required). The specification of network architecture is a subjective process, with no universally accepted rules, and the set of parameters to define differs between the various types of network available, although some contentious heuristics exist that may be used guide the construction of the network (e.g. Wang, 1994; Kanellopoulos & Wilkinson, 1997; Kavzoglu and Mather, 2001).

One attractive feature of feedforward networks for soft classification is the ability to directly include mixed pixels in the training stage, as the desired output vector for each training case can be specified (Foody et al., 1997); training may, however, be based upon pure pixels only. Once trained a feedforward neural network may be used to predict the class membership properties for other pixels in the data set. In a conventional hard classification, each pixel is typically allocated to the class associated with the most highly activated unit in the output

layer of the network. However, the magnitude of the outputs units may also be used to indicate the strength of class membership, which may be used to indicate sub-pixel class proportional cover. The outputs of the different types of network should, however, be treated differently. While the activation level of output units from each type of network can be expressed on a 0-1 scale such outputs should not necessarily be viewed as proportions or probabilities. For example, the sum of the activation level of all output units for a multi-layer perceptron may differ markedly from 1.0 (Foody, 2000a) and of the networks identified above only the probabilistic neural network outputs values that are essentially posterior probabilities (Foody, 2001). However, in many studies the magnitude of the activation level of output units has been found to be strongly related to the class composition (Foody, 1996; Atkinson et al., 1997; Moody et al., 1996; Frizelle & Moody, 2001).

In addition to the feedforward networks, other types of neural network have been used in sub-pixel scale studies. In particular, neural networks, based upon adaptive resonance theory (ART) and especially the ARTMAP type of network have been used to derive sub-pixel scale thematic information, Further information on the use of this type of neural network for the derivation of a soft classification is given by Carpenter et al. (1999) and Gopal et al. (1999).

3.4   Current research topics

Although there has been considerable research directed at sub-pixel scale issues in recent years there is considerable scope for further development. Presently, research is addressing a series of issues, including further development of the methods to extract sub-pixel scale thematic information, the evaluation of the accuracy of the calculated sub-pixel estimates and the design of refined means of representing the derived information.

Many other approaches in addition to those outlined above may be used for the derivation of a soft classification from which information on sub-pixel information can be derived. For example, evidential reasoning, based on Dempster-Shafer theory, may be used to indicate sub-pixel scale thematic information. To-date, evidential reasoning has been used mostly for the conventional hard classification of remotely sensed data (Lee et al., 1987; Wilkinson & Megier, 1990; Srinivasan & Richards, 1990; Peddle, 1993) as an alternative to standard statistical classifiers as it may accommodate uncertainty and ignorance that is often inherent in data sets. This is particularly useful when a diverse range of data sets of varying quality have been brought together for a classification (Richards et al., 1982). Evidential reasoning based approaches can, like the classifiers discussed above, be adapted for the production of a soft classification that conveys sub-pixel scale class composition information. For example, it is possible to map for each class the belief and plausibility measures, upon which the analysis is based. Although these may be difficult to interpret, particularly if precise information on the pixel composition is desired, the approach is worthy of further investigation. Another method that has considerable potential and which has recently been used for the derivation of sub-pixel information is based on support vector machines (SVM). SVMs can, under some circumstances, be equivalent to linear mixture models but may also be used for non-linear mixing (Brown et al., 1999; 2000).

Accuracy assessment is now widely accepted as a fundamental requirement for thematic classifications derived from remotely sensed data (Tso & Mather, 2001). This is true whether the information was derived from hard or soft classifications. The assessment of accuracy, particularly for soft classifications, is however, extremely difficult (Foody, 2002). Commonly, the accuracy of sub-pixel estimates is assessed by correlation of the derived estimates against those observed on the ground for a testing set or through the calculated root mean square error of the estimates. Although these measures provide a guide to accuracy of sub-pixel estimates they are far from complete measures of accuracy and further development on this topic is required.

The representation of sub-pixel thematic information is a difficult but important task. Map users typically want an easy to use map product, like a standard hard classification, but the output of a soft classification may be larger and more difficult to interpret. The output of a soft classification could for example, comprise a fraction image for each class which is difficult to compress into a readily interpretable map product. If the imagery contain few mixed pixels, it may be more appropriate in some circumstances, to use conventional hard techniques. Similarly the nature of the mixing can be important in selecting an appropriate form of visual representation. Since the number of classes mixed can sometimes be a problem some indication of the degree of mixing may be helpful. This is a difficult task but entropy may sometimes be used to describe partitioning of membership. Entropy, H, may be derived for a pixel from,

$$H = -\Sigma \, p \, (i) \log p \, (i) \tag{3.13}$$

where $p(i)$ is the proportional coverage of class i. Entropy is minimised when the pixel is associated with a single class and maximised when membership is partitioned evenly between all of the defined classes. An image depicting the entropy calculated for each pixel could be used to indicate the spatial distribution of class mixing. It may also help guide the selection of an appropriate means of representation. Fortunately, in most cases a mixed pixel comprises only a small number of classes, usually just two or perhaps three. Thus, it may not be necessary to derive a means of representing and storing the membership to all defined classes and it may be possible to generalise the data for mapping purposes by showing, for instance, the primary and secondary classes present. To obtain a guide to the number of classes that are present in a pixel, it is possible to quantify the diversity of classes and indicate the presence of common and rare classes (Ricotta & Avena, 2002). Drawing on the ecological literature, Hill's diversity numbers may be calculated from,

$$N\,(\#) = \sum_{i=1}^{c} p \, (i)^{\frac{1}{(1-\#)}} \tag{3.14}$$

where # specified the order of the diversity number. When #=0, 1 and 2 equation 3.16 returns the total number of classes contained, the number of abundant classes and the number of very abundant classes respectively (Ludwig & Reynolds, 1988).

A further issue related to the representation of the sub-pixel thematic information is that the estimates derived do not indicate the spatial distribution of the component classes within the area represented by a pixel. Thus, for example, a linear mixture model or soft classification

may be used to derive information on the proportional coverage of the classes in a pixel but they do not indicate where those fractional components lie. In the fraction image used to represent the output, the grey level for a pixel is simply proportional to the estimated coverage of the class. Ideally, the results of a sub-pixel analysis would be one in which not only is the class-composition of the pixel accurately estimated but that the factions are located correctly in space. This would provide substantially more information that many users would require, indicating greater spatial detail on the landscape mosaic and its fragmentation. Various studies have sought to try and locate the class fractions estimated from a soft classification (e.g. Foody, 1998, 2002c; Tatem et al., 2001, 2002). These studies typically have an ultimate aim of deriving a super-resolution map, one that depicts the thematic classes at a spatial resolution finer than the imagery from which the map was derived. Super-resolution mapping is a topic discussed in greater detail in the chapter by Atkinson (2003, this volume).

Finally, but of fundamental importance, there are concerns over the accuracy of sub-pixel composition predictions derived using methods such as those outlined above. Manslow & Nixon (2002) identify one major cause of uncertainty in sub-pixel composition estimates, that associated with the sensor's point spread function (PSF), that has important implications. They show that because of the PSF all information extracted from the remotely image is ambiguous and, with a hypothetical example, that the range of possible estimated compositional values for a mixed pixel is very broad. This limits not only the accuracy of sub-pixel estimation but also studies that attempt to study change in sub-pixel proportions. Issues such as this require considerable further investigation before the full potential of studying subtle changes in class composition associated with, for example, land cover modifications is realized.

3.5   Conclusions

The derivation of thematic information at sub-pixel scales has become an important topic in environmental remote sensing. This has typically arisen due to recognition that the commonly implicit assumption of pure pixels made in many image analyses is invalid, especially as a result of mixed pixels. This chapter has discussed the background to techniques that have commonly been used for the derivation of sub-pixel scale information. In particular, it has covered popular approaches such as linear unmixing and soft classification based approaches to the estimation of sub-pixel class composition. These estimates provide only a guide to the composition of the area represented by a pixel and are subject to significant uncertainties (e.g. due to the PSF). Nonetheless, sub-pixel scale thematic information is often useful and its accurate extraction represents a major advance in terms of information extraction from remotely sensed data over that derived with conventional hard image processing techniques. The topic is rapidly developing and one current focus of research is refining the representation of the derived sub-pixel information. This work is mainly addressing issues connected with locating the estimated sub-pixel class fractions geographically over the area represent by a pixel, which is a topic with discussed further in the chapter 4 on super-resolution mapping by Atkinson (this volume).

Chapter 4
Resolution Manipulation and Sub-Pixel Mapping

Peter M. Atkinson

4.1   Introduction

Although the most obvious source of information in a remotely sensed image lies, pixel-by-pixel, in its spectral values a second less obvious source of information exists in the spatial relations between the pixels. This source of information is frequently used implicitly (e.g. our brains make use of such information when we interpret a pictorial representation of a remotely sensed image) but is increasingly being used *explicitly* in a range of spatial models for the analysis of remotely sensed imagery (e.g., see Atkinson and Lewis, 2000, for a review of spatial classification methods). Such spatial models make use of the fact that the set of spectral values in an image are augmented by a set of (x, y) pixel locations in a given co-ordinate system. These pixel locations need not be stored individually: the x and y extremes, together with the number of pixels in each co-ordinate direction are sufficient, given that the spectral values are recorded in a known, ordered sequence (e.g., left-to-right, top-to-bottom). Knowing the (x, y) pixel locations enriches the spectral information available to the investigator, and allows much more than a pixel-by-pixel analysis of a remotely sensed image to be conducted. This *spatial* information is fundamental to the geostatistical and spatial analyses discussed in this chapter.

It is well known from everyday experience that 'zooming in' on a given scene or spatial representation will reveal increasing levels of detail. For example, as you move closer to this page you may be able to pick out or resolve spatial variation (on the page) or features (e.g., individual letters) that would not be resolvable if you were standing several metres away. If you were 100 metres away, the text may not be resolvable with the unaided eye, while some kilometres away the book itself may disappear completely. The same is true when a remotely sensed image is acquired of a given ground scene. For a particular sensor, the detail depicted in the image depends on the height of the sensor above the ground. At low altitudes the image will cover a small area, but resolve much detail, whereas at high altitudes the image will cover a larger area, but resolve less detail (per unit area on the ground).

The size of the pixels in an image is often referred to in remote sensing as the spatial resolution (although it will be explained below that the pixel size and spatial resolution do not have the same meaning). For satellite sensor imagery, the spatial resolution is fixed. When the sensor is mounted on an airborne platform the investigator may determine the
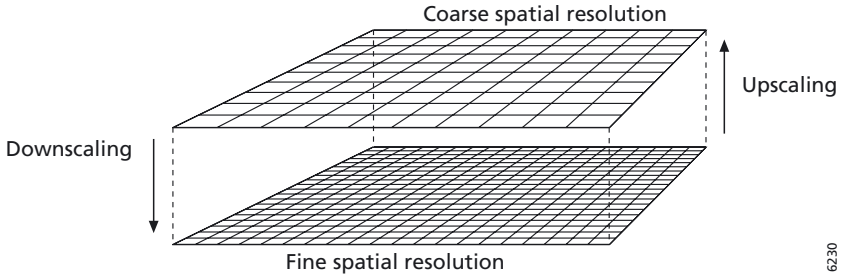
Figure 4.1 – Two remotely sensed images defined with different spatial resolutions illustrating the meaning of upscaling (reducing detail) and downscaling (increasing detail).

spatial resolution prior to data acquisition. However, even in these circumstances the spatial resolution is fixed once the image is acquired and so too is the level of detail in the image (see Fisher, 1997).

The focus of this chapter is on attempting the seemingly impossible: changing the spatial resolution (and, thus, the level of detail) *after* the image has been acquired. Increasing the area that a measurement represents is referred to as upscaling, whereas decreasing the area is referred to as downscaling (figure 4.1). While the former may be achieved through averaging of some form, the latter objective is less easily met and has led to some interesting solutions in recent years (e.g., Bierkens et al., 2000; Verhoeye and DeWulf, 2002; Zhan et al., 2002; Tatem et al., 2003). This chapter focuses primarily on downscaling in remote sensing.

Several different motivations exist for changing the spatial resolution. In a remote sensing context, it is frequently the case that imagery needs to be compared to ground data acquired *in situ* at the time of the sensor overpass. For example, the importance of calibrating remotely sensed images to absolute reflectance units, particularly for multi-temporal analysis, is widely acknowledged. Image calibration can be achieved using physical (radiative transfer) modelling, but is more commonly achieved using methods such as vicarious calibration and empirical (regression-based) calibration (e.g., Karpouzli and Malthus, 2003). Such methods depend on *in situ* measurements of reflectance of several homogeneous sites (targets) within the scene made using a field spectroradiometer. The problem is that often the pixels of the image are much larger than the area sensed by the spectroradiometer. Thus, either the area of the ground measurements should be increased, or that of the pixels decreased, so that comparison can be made on areas that match.

A similar requirement for a change of spatial resolution arises in remote sensing when the objective is to predict some property of interest at the ground (e.g., land cover, biomass) from a remotely sensed image using empirical or semi-empirical methods (Justice and Townshend, 1981). For example, where some ground property (e.g., biomass) has been measured over a small finite area (e.g. 1 m by 1 m), and these measurements are to be regressed on co-located pixels of a remotely sensed image (e.g., with pixels of 30 m by 30 m) some kind of upscaling or downscaling should be attempted to allow sensible combination. The objective in these

circumstances (once a sensible regression model has been fitted) is to apply the model to the whole image to allow prediction of the ground property spatially.

In a more general context, it is often necessary to change the spatial resolution of one image to allow comparison with another (Atkinson and Tate, 2000). For example, in a geographical information system (GIS) several useful operations require that different data layers (variables) are represented on the same grid at the same spatial resolution (such that pixels from different layers match perfectly). An obvious example is GIS overlay where several different input data layers are combined via particular arithmetic or Boolean operations to produce an output data layer. Overlay is commonly used as the basis for site suitability analysis (e.g., Carver, 1991), landslide hazard zonation (e.g., Atkinson and Massari, 1998) and a variety of other common applications. In all of these, some method of changing the spatial resolution is commonly required.

Although beyond the present scope, an important additional class of problem arises in the handling of census data, known as the modifiable unit area problem or MAUP (Openshaw, 1984). Changing the spatial resolution of census data is complicated by the fact that the areal units (e.g., enumeration areas) vary from place to place in their size, shape and orientation. The consequence is that statistical and geostatistical models should not be applied directly to such data without modification (Atkinson and Martin, 1999).

Accepting that upscaling and downscaling are important requirements in modern remote sensing analysis, the question is 'how can upscaling and downscaling be achieved?'. The answer lies in finding suitable models of (i) spatial variation (to allow use of the available spatial information (see first paragraph)) and (ii) the relation between spatial variation and spatial resolution (see section 4.3). This chapter explores such models and how they can be used to inform upscaling and downscaling in remote sensing.

4.2   Scale in Remote Sensing

Much has been written about scale in a remote sensing context (Curran and Atkinson, 1998; Atkinson and Tate, 2000; Atkinson, 2001; Tate and Atkinson, 2001) and such detail will not be repeated here. However, a brief review is presented for the benefit of the reader new to this field and to establish a common language for subsequent reference.

4.2.1   Defining scale

Scale is strictly the ratio between two sizes; usually the size of a representation (e.g., a map) and the actual size in reality (e.g., actual distance on the ground). However, for the purposes of this chapter, scale will be used simply to mean size (e.g., large scale investigation means a large investigation). This is the meaning used in everyday language. Having defined scale, it is most useful to distinguish between two kinds of scale: (i) scales of measurement and (ii) scales of variation. We shall now consider these in turn.

Weight, λ

The area on the ground that
a pixel represents
The area on the ground that actually contributes
to the observed signal, that is, the support

6230
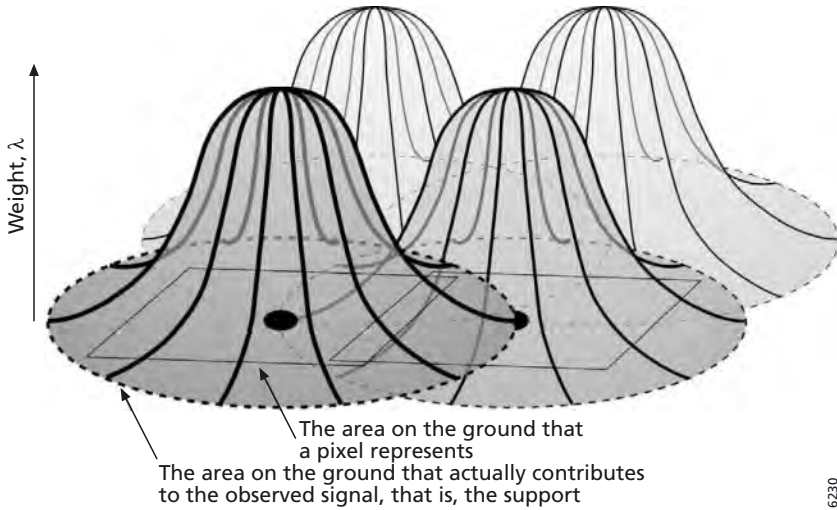
Figure 4.2 – Four pixels arranged as part of an image shown with the support of each individual observation. The supports, which overlap in this case, are different to the pixels.

4.2.2   Scales of measurement

Scales of measurement are implicit in the parameters of any spatial sampling strategy. Here, first-order (e.g., support) and second-order (e.g., spatial resolution) scales of measurement are distinguished.

4.2.2.1 Support and pixel size

The support is the size, geometry and orientation of the space on which an observation or datum is defined. In a remotely sensed image, each observation is made on a support that is actually centre-weighted (figure 4.2). This centre-weighting is referred to as the point-spread function of the sensor (see Manslow and Nixon, 2002, for a detailed analysis). It means that variation at the centre of an observation contributes more to the recorded value than the perimeter. It also means that some variation from outside the pixel boundaries contributes such that the supports constituting an image actually overlap (figure 4.2).

The pixel, by contrast, is the area on the ground (usually square or rectangular) that an image observation is taken to represent (figure 4.2). Thus, when a remotely sensed data set is displayed on a computer the set of recorded values are attributed to a set of pixels to form an image. The pixel, defined in this sense, does not usually match the actual support.

4.2.2.2 Spatial resolution and spatial extent

The support is one of several parameters of the overall sampling framework. Other parameters of interest are the sample size, n, the sampling scheme (e.g., random, systematic) and the sampling density. These additional parameters determine two further scales of measurement of interest: the spatial resolution and spatial extent. Together, the spatial resolution and extent determine the upper and lower bounds on the frequencies of spatial variation that are detectable in data.

The spatial resolution depends on the interaction between two or more observations. Thus, it can be considered as a second-order parameter of the sampling framework. Importantly, the spatial resolution is a function of both the sampling interval (or sample spacing) between any two observations in a sample and the support. In turn, the spacing between a data pair is a function of the sampling scheme, and sampling density. Thus, for example, in a random sampling scheme, the spatial resolution varies locally. In a remotely sensed image, the support (approximated by the pixel) and the sample spacing are fixed and approximately equal and, in any case, in constant proportion. Thus, the spatial resolution can be seen as a function of the support only. For this reason, the spatial resolution and the pixel size are used interchangeably in much of the remote sensing literature. However, it is important to be aware that in the general case, this is not so: for example, gridded point data have a spatial resolution, even though the support is zero.

In this chapter, in the context of change of scale in remote sensing, the support or pixel size is the primary interest because the sample spacing and the spatial resolution change as a function of it.

4.2.3   Scales of spatial variation

Spatial data are a function of both 'reality' and the sampling framework (figure 4.3). Measurement always occurs over some positive finite space (the support) and never at a point: all measurements are essentially integrals of the underlying variation over the support. As a consequence, spatial variation exists in, and is detectable in, spatial data only. Spatial variation cannot be detected in 'reality' independent of measurement (figure 4.3). Thus, our interest is in spatial variation in spatial data that are a function of both some underlying variation (not known) and the sampling framework (known). This fundamental dependence of spatial variation on the sampling framework underpins our ability to change the scale of measurement (upscale and downscale) as described later in this chapter.

Woodcock and Stahler (1987) distinguish, for convenience, between the H-resolution and L-resolution cases. H-resolution occurs when the spatial resolution is fine relative to either (i)
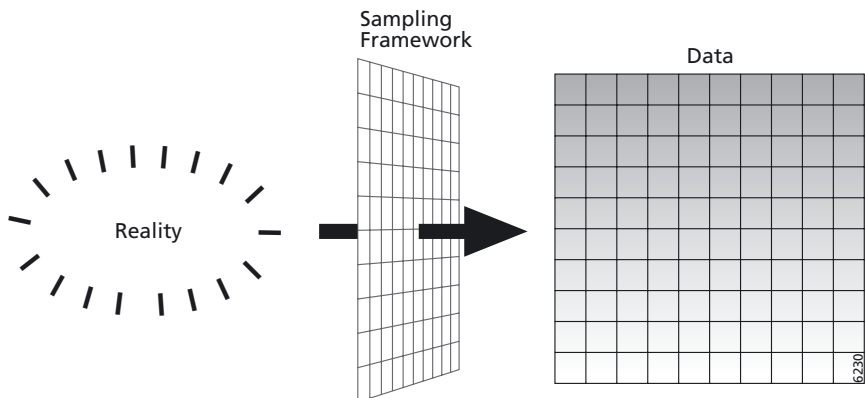
Figure 4.3 – Data are a function of reality and the sampling framework.

the frequency of continuous spatial variation or (ii) the size distribution of land cover objects in a remotely sensed scene. L-resolution refers to the inverse case where the spatial resolution is coarse relative to the frequency of variation or size of objects. In the H-resolution case, continuous spatial variation (e.g., in woodland biomass) and objects (e.g. land cover features) are sufficiently resolved. In the L-resolution case, variation and objects are not sufficiently resolved leading to a loss of detail in the resulting image. Woodcock and Strahler's system is useful because it highlights the dependence of scales of spatial variation on the sampling framework. However, to achieve a deeper understanding it is necessary to develop an appropriate model, and currently, that model is provided by geostatistics.

In the next section, some of the basic models of geostatistics are introduced. The concepts described underpin several of the methods for upscaling and downscaling in remote sensing discussed in later sections.

4.3   Geostatistics

Introductions to geostatistics are provided by many texts (e.g., Isaaks and Srivastava, 1989; Goovaerts, 1997; Armstrong, 1998; Chiles and Delfiner, 1999). A brief summary is provided here.

4.3.1   The RF model

A Random Function (RF) is the spatial equivalent of a Random Variable (RV), where the inter-dependence between any two point locations is expressed as a function of lag (separating distance and direction) (Matheron, 1965, 1971; Journel and Huijbregts, 1978; Goovaerts, 1997; Chilès and Delfiner, 1999). A realization of a RF is termed a Regionalized Variable (ReV). In geostatistics, spatial data (e.g., a remotely sensed image) are modelled as a realization of a RF (Goovaerts, 1997).

In geostatistics, the analysis is usually restricted to cumulative distribution functions (cdfs) involving at most two locations at a time. Thus, the one- and two-point cdfs, the covariance function, autocorrelation function and variogram describe RFs adequately for most applications (Goovaerts, 1997). Generally, only one realization (e.g., remotely sensed pixel) is available for a given location x_0. Thus, to allow statistical inference, a *stationary* RF model is chosen. That is, the various two-point functions (e.g., variogram) are made invariant with x. In these circumstances, the variogram can be defined as depending only on the lag h:

$$\gamma(h) = \frac{1}{2} E\left[\{Z(x) - Z(x+h)\}^2\right] \tag{4.1}$$

When the expected value $m=E\{Z(x)\}$ exists and is independent of x (is invariant within a region V) and the variogram exists and depends only on h, the RF is said to be intrinsically stationary (Myers, 1989).

4.3.2 Variogram estimation and modelling

For continuous variables, such as biomass and leaf area index, the sample semivariance is defined as half the average squared difference between values separated by a given lag intervals $\mathbf{h}_k$:

$$\hat{\gamma}\,(\mathbf{h}_k) = \frac{1}{2P(\mathbf{h}_k)} \sum_{\alpha=1}^{P(\mathbf{h})} [z\,(\mathbf{x}_\alpha) - z\,(\mathbf{x}_\alpha + \mathbf{h})]^2, \qquad h \in h_k \tag{4.2}$$

with $P(h_k)$ the number of value pairs separated by h. The variogram may be estimated for several different orientations to describe variation that may be anisotropic.

The sample variogram obtained from Equation 4.2 relates information at a set of discrete lags only. To use the variogram in geostatistics it is necessary to fit a continuous mathematical model to the sample variogram. The model fitted must be such as to ensure that all linear combinations of the RF result in non-negative variances. For the variogram, this property is referred to as conditional negative semi-definiteness (CNSD). It is customary to select a model as a linear combination of base models that are known to be CNSD (McBratney and Webster, 1986; Webster and Oliver, 1990). Three such base models are given below:

(i) the nugget effect model:

$$g\,(h) = \begin{cases} 0 & \text{if } h = 0 \\ 1 & \text{otherwise} \end{cases} \tag{4.3}$$

(ii) the spherical model:

$$g\,(h) = \begin{cases} 1.5\,\dfrac{h}{a} - 0.5\left(\dfrac{h}{a}\right)^3 & \text{if } h = 0 \\ 1 & \text{otherwise} \end{cases} \tag{4.4}$$

(iii) the exponential model:

$$g\,(h) = 1 - \exp\left(\frac{-h}{a}\right) \tag{4.5}$$

where a or r are the non-linear parameters (see figure 4.4). A model may be fitted to the sample variogram either visually or by some automatic process such as weighted least squares (Cressie, 1991), that is, by minimizing:

$$WSS = \sum_{k=1}^{K} \omega\,(\mathbf{h}_k)\,[\hat{\gamma}\,(\mathbf{h}_k) - \gamma(\mathbf{h}_k)]^2 \tag{4.6}$$

with weights $\omega(h_k)$ inverse proportional to the estimation error of $\hat{\gamma}(h_k)$. Sample variogram estimation and model fitting is described in a remote sensing context by Curran (1988).
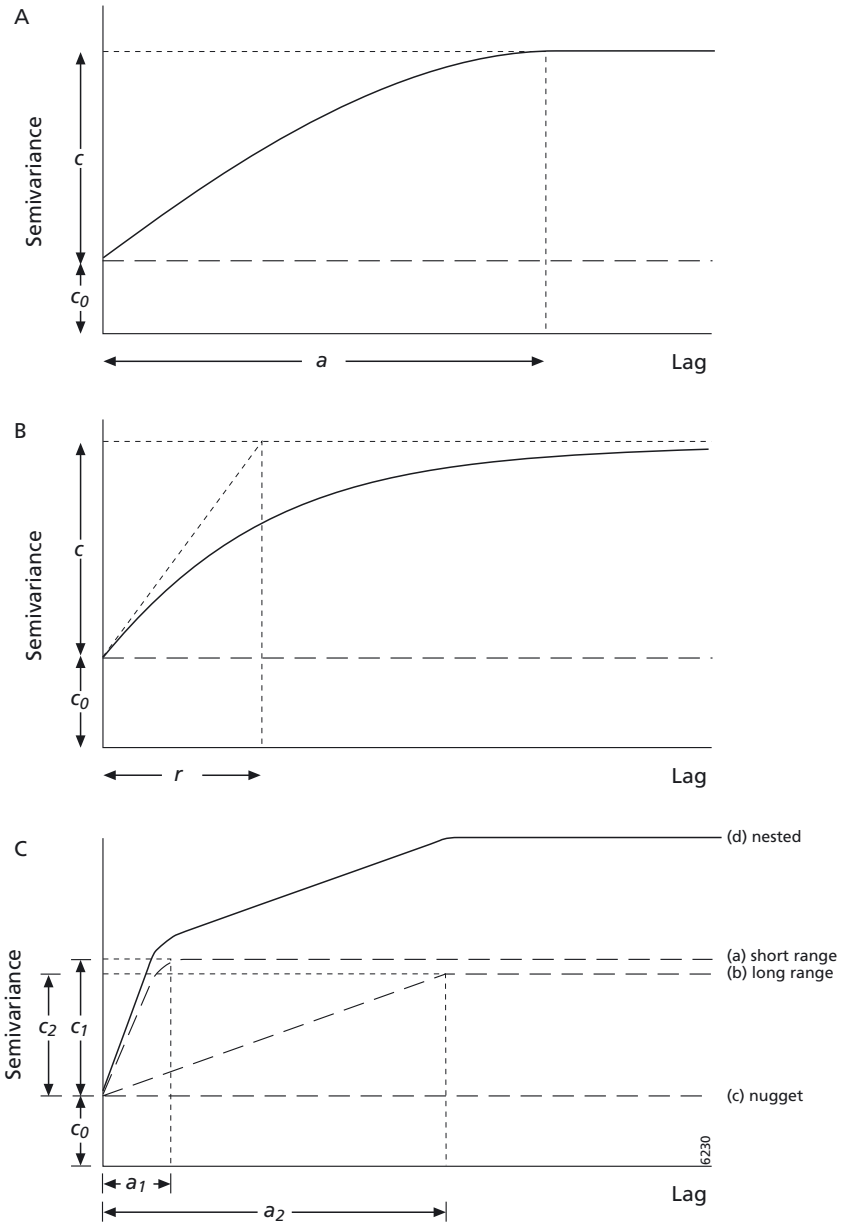
Figure 4.4 – Examples of variogram models: (a) the spherical (plus nugget) model showing the structured (or sill) variance, c, the nugget variance, c₀, and the range, a, (b) the exponential (plus nugget) model showing the sill variance, nugget variance and non-linear parameter, r (which is approximately one third of the effective range, a) and (c) a hypothetical nested model in which short-range and long-range components are combined with a nugget component.

4.3.3 Interpreting the modelled variogram

It is useful to consider what information the modelled variogram conveys about the spatial variation that it represents. Consider, for example, the parameters of an exponential model, without a nugget, fitted to a sample variogram. The sill c of the exponential model relates information on the *amount* of variation present in region V. In fact, the sill estimates the *a priori* variance $D^2(v, \infty)$ of Z (that is the variance obtained on a support v within an infinitely sized region). The non-linear parameter a or r of the model relates information on the *scale* of spatial variation (figure 4.4).

The variogram models described may be used singly or in positive linear combination. In particular, the nugget model is often fitted together with a structured component (such as an exponential or spherical model) to represent a discontinuity at the origin. The nugget variance (the sill of the nugget component) represents unresolved variation that exists at a micro-scale and measurement error, but it can also arise from uncertainty both in estimating the variogram and in fitting the model at short lags (Atkinson, 1997a). When muliple structured components are fitted the variation is said to be 'nested' (see Oliver, 2001 and figure 4.4).

4.3.4 Regularizing the variogram model

As implied in the introduction, observations are always obtained over a positive finite support v. As a consequence, the sample variogram is itself defined for a support or pixel of positive size. Further, the form of the spatial variation and the variogram depend on the support (figure 4.3). In the remainder of this section a *model* of regularization is described that allows one to change the support size and observe its effect on the variogram.

Let us define a RV $Z_v(\mathbf{x}_0)$ as a function of (i) some underlying RF $Z(\mathbf{y})$ defined on a *punctual* (or point) support $\mathbf{y}$ and (ii) a support of size v:

$$Z_v(\mathbf{x}_0) = \frac{1}{|\mathbf{v}|} \int_{v(\mathbf{x}_0)} Z(\mathbf{y})d\mathbf{y} \tag{4.7}$$

with $|\mathbf{v}|$ the area of integration. The relation between the punctual and regularized variograms at lag $\mathbf{h}$ is given by (Clark, 1977; Journel and Huijbregts, 1978; Jupp et al., 1988, 1989):

$$\gamma_v(\mathbf{h}) = \bar{\gamma}(v, v_\mathrm{h}) - \bar{\gamma}(v, v) \tag{4.8}$$

where $\bar{\gamma}(v, v_\mathrm{h})$ is the integral of $\gamma(h)$ between two cells of size v whose centroids are separated by $\mathbf{h}$:

$$\bar{\gamma}(v, v_\mathrm{h}) = \frac{1}{|\mathbf{v}|^2} \int_v \int_{v_\mathrm{h}} \gamma(\mathbf{y}, \mathbf{y}') \, d\mathbf{y}d\mathbf{y}' \tag{4.9}$$

where $\mathbf{y}$ covers a cell of size v and $\mathbf{y}'$ covers independently an equivalent cell at lag $\mathbf{h}$ away. The quantity $\bar{\gamma}(v, v)$ is the integral of $\gamma(h)$ within a cell of size v, written formally as:

$$\bar{\gamma}(v, v) = \frac{1}{|\mathbf{v}|^2} \int_v \int_v \gamma(\mathbf{y}, \mathbf{y}') \, d\mathbf{y}d\mathbf{y}' \tag{4.10}$$

where **y** and **y'** now cover the same cell independently.

Given Equation 4.8 and a model for the punctual variogram it is possible to estimate the regularized variogram for any new support of size *v*. The regularized function is estimated through numerical approximation, by discretizing the new larger support into several points arranged on a regular grid.

Equation 4.8 provides the investigator with a useful tool for exploring the relation between the observed variation and the support. For example, it provides information on which to base a choice of pixel size for a given remote sensing investigation (Woodcock and Strahler, 1987; Atkinson and Curran, 1997; Curran and Atkinson, 1999). Since no measurement is required except on the original support it amounts to *scaling the model* rather than the data. Equation 4.8 is important to understanding the effect of the support on the character of observed spatial variation and on the regularised variogram (Zhang et al., 1990).

4.3.5 Kriging

Ordinary kriging (OK) is an extension of simple kriging (SK) (see Goovaerts, 1997) to the case of an unknown mean. Since OK is usually performed within a local moving window or neighbourhood $W(\mathbf{V})$ centred on the block or cell $\mathbf{V}$ to be predicted at location $\mathbf{x}_0$, OK involves a locally varying unknown mean $m(\mathbf{x})$. The linear predictor $\hat{Z}(V(\mathbf{x}_0))$ (abbreviated to $\hat{Z}(V)$), for a support $\mathbf{V}$ that is larger than the quasi-point support of the data, is a linear combination of the $\alpha=1, 2, ..., n(\mathbf{x}_0)$ RVs $Z(\mathbf{x}_\alpha)$ plus the constant and unknown local mean $m(\mathbf{V})$ (Goovaerts, 1997):

$$\hat{Z}(\mathbf{V}) = \sum_{\alpha=1}^{n(\mathbf{x}_0)} \lambda_\alpha(\mathbf{V}) Z(\mathbf{x}_\alpha) + \left[1 - \sum_{\alpha=1}^{n(\mathbf{x}_0)} \lambda_\alpha(\mathbf{V}) \right] m(\mathbf{V}). \tag{4.11}$$

The unknown local mean drops out of Equation 4.11 when the weights sum to unity:

$$\hat{Z}_{OK}(\mathbf{V}) = \sum_{\alpha=1}^{n(\mathbf{x}_0)} \lambda_\alpha^{OK}(\mathbf{V}) Z(\mathbf{x}_\alpha) \quad \text{with} \quad \sum_{\alpha=1}^{n(\mathbf{x}_0)} \lambda_\alpha^{OK}(\mathbf{V}) = 1. \tag{4.12}$$

Since the weights sum to unity the linear predictor is unbiased. The prediction variance is the expected value of the squared difference between $\hat{Z}_{OK}(V)$ and $Z(V)$:

$$\sigma_E^2 = E\{[\hat{Z}_{OK}(\mathbf{V}) - Z(\mathbf{V})]^2\}. \tag{4.13}$$

This can be expressed as the minimum prediction variance or OK variance by

$$\sigma_{OK} = 2 \sum_{\alpha=1}^{n(\mathbf{x}_0)} \lambda_\alpha^{OK} \, \bar{\gamma}(\mathbf{V}, \mathbf{x}_\alpha) - \sum_{\alpha=1}^{n(\mathbf{x}_0)} \sum_{\beta=1}^{n(\mathbf{x}_0)} \lambda_\alpha^{OK} \lambda_\beta^{OK} \gamma(\mathbf{x}_\alpha, \mathbf{x}_\beta) - \bar{\gamma}(\mathbf{V}, \mathbf{V}) \tag{4.14}$$

where $\bar{\gamma}(V, x_\alpha)$ is the integral semivariance between the block to be predicted and the sample point α, $\beta(\mathbf{x}_\alpha, \mathbf{x}_\beta)$ is the semivariance between the sample points α and β (that is, all pairs of data locations) and $\bar{\gamma}(V, V)$ is the average within-block semivariance obtained from equation 4.10.

For OK, where the mean is unknown, a Lagrange parameter $\psi_{OK}(V)$ is required. For an intrinsically stationary RF model, the OK system is then given as:

$$\sum_{\alpha=1}^{n(\mathbf{x}_0)} \lambda_\alpha^{OK} \, \bar{\gamma} \, (\mathbf{x}_\alpha, V) + \psi_{OK} \, (V) = \bar{\gamma} \, (V, V) \tag{4.15}$$

$$\sum_{\alpha=1}^{n(\mathbf{x}_0)} \lambda_\alpha^{OK} \, (V) = 1 \tag{4.16}$$

The kriging prediction variance $\hat{\sigma}_{OK}^2$ of equation 4.14 can also be expressed by:

$$\hat{\sigma}_{OK}^2 = \sum_{\alpha=1}^{n(\mathbf{x}_0)} \lambda_\alpha^{OK} \, \bar{\gamma} \, (\mathbf{x}_\alpha, V) + \psi_{OK} \, (V) = \bar{\gamma} \, (V, V). \tag{4.17}$$

Given this brief introduction to geostatistics, it is now possible to turn our attention to the actual process of changing the scale of measurement.

4.4   Changing the scale of measurement

Many circumstances arise, both in remote sensing and GIS, where it is necessary to change the scale of measurement. Some examples were given in the introduction. Recent attempts to develop methods suitable for changing the scale of measurement are explored in this section.

4.4.1   Upscaling

Upscaling is an increase in the size of support (or corresponding decrease in the spatial resolution) (Bierkens et al., 2000). It is often required in remote sensing to relate quasi-point ground data (e.g., 1 m by 1 m support) to remotely sensed image pixels (e.g., 30 m by 30 m). Upscaling in these circumstances would be applied to the ground data, changing their support from 1 m by 1 m to 30 m by 30 m to facilitate comparison with the image.

The method used to upscale depends on the spatial arrangement of the ground data; in particular, whether the data are arranged such as to allow natural averaging within the larger supports. If averaging is possible, then a value can be predicted for the larger support by either simple or weighted averaging of the 1 m by 1 m data (figure 4.5).

If the ground data do not allow averaging then one has several options. First, the value of a 1 m by 1 m datum predicts the value for the 30 m by 30 m pixel that it falls within. The value is seen simply as an unbiased sample of the population (for the pixel or support to which it is to be compared). Interestingly, in this case where a single observation predicts a single pixel value, the prediction is unbiased. The problem in this case is the large uncertainty involved in prediction.

If the geostatistical technique of block kriging is used to make the prediction the actual value will not change, but the block kriging variance (Equation 4.17) will relate useful information on prediction uncertainty that accounts for the spatial position of the 1 m by 1 m value within the pixel. In practice, the kriging variance will be larger where ground observations are located towards the edge of the pixel.
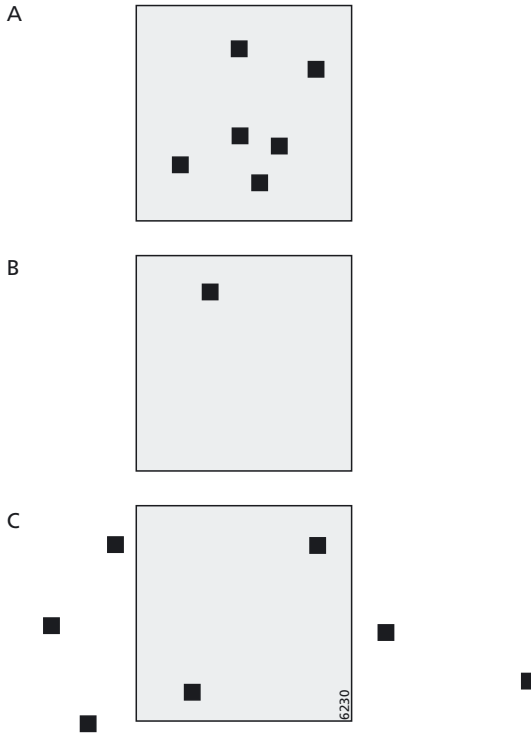
Figure 4.5 – Three hypothetical situations in which a value for the larger support (grey) may be predicted by smaller supports (black): (a) linear averaging, (b) a single ground observation (if block kriging is used to predict, the block kriging variance will impart useful information on uncertainty), and (c) block kriging (where multiple ground data are available proximate to the predicted block).

Block kriging provides a method for upscaling in the more likely circumstances where a spatial sample of ground data exists and the investigator wishes to use all the data to predict at several pixels (i.e., using data from both within and outside each larger pixel). In these circumstances, block kriging is the interpolation method of choice: (i) kriging is optimal in the sense of minimum prediction variance (depending on the appropriateness of the model), (ii) kriging is unbiased and (iii) block kriging allows prediction over the larger supports automatically (Equation 4.12).

While block kriging should be chosen above non-statistical interpolation methods such as inverse-distance weighting, there are some problems, the most important and relevant of which is 'smoothing'. Because data from outside the pixel are used to predict, the new support is artificially extended beyond the pixel leading to 'over-regularization' referred to as smoothing.

Smoothing is a problem because, as suggested above, upscaling is usually performed to allow comparison with a second variable. Smoothing alters the univariate character of the upscaled variable (in particular, a reduction in variance beyond that which occurs due to natural

averaging over the support). As a consequence, the bivariate relation between the upscaled ground variable and remotely sensed image is also altered. This could mean, for example, that the parameters of a fitted regression model might be biased. Affine corrections for adjusting such parameters to account for smoothing have been proposed (Atkinson and Kelly, 1997: Atkinson and Tate, 2000).

4.4.2   Downscaling

Downscaling is interesting because it attempts the seemingly impossible: increasing the spatial resolution of an already acquired data set. It is well known that one cannot increase the information content of a data set by manipulation alone. Thus, downscaling techniques make use of the available information (e.g., multispectral data) to provide a representation at a finer spatial resolution that is acceptable in terms of several criteria.

Super-resolution is a term that has commonly previously been used for methods that attempt to increase the spatial resolution of imagery by combining several alternative images of the same scene (e.g., images acquired at different dates). The spatial resolution is increased by taking advantage of the exclusive information provided by successive images (e.g., Pastina et al., 2003). Here, the term is used for methods that increase the spatial resolution of a classified remotely sensed image above that of the input imagery given only a single image (in several wavebands).

Methods for super-resolution mapping can be divided into two classes each with different objectives. In the first class, the objective is to *maximise* the spatial correlation between sub-pixels. This amounts to spatial clustering of the classes to which sub-pixels are assigned, and is applicable in the H-resolution case. In the second class, the objective is to *match* the spatial correlation between sub-pixels with some prior model (e.g., spatial covariance or variogram model). This objective is applicable in the L-resolution case.

Several methods of super-resolution classification have been developed over the last few years, including some by researchers at the University of Southampton. In the following sections, a broad overview of these techniques is given.

4.4.2.1 Sub-pixel classification

Foody (1998) used an interpolation-based technique to map the boundary of a lake with sub-pixel geometric precision. While visually appealing results were produced, the approach was under-constrained. Specifically, the predicted boundary between lake and not lake need not honour any prior model (e.g., pixel-level soft land cover proportions, if these are known). Further, the algorithm may be subject to effects such as smoothing which may affect the precision of the final vector boundary.

Flack et al. (1994) developed a technique based on the Hough transform for, first, detecting linear features in remotely sensed images of agricultural scenes and, second, unmixing the signal on either side of the boundary. The technique is suitable for application to linear features in unprocessed remotely sensed images. More recently, Aplin et al., (2001) developed a similar technique for converting the output from a per-pixel soft-classification of land

cover into a per-parcel hard classification. Ordnance Survey Land-line vector data were used to constrain the sub-pixel map.

Several authors have attempted super-resolution mapping directly from multispectral remotely sensed imagery. For example, in a series of papers, Schneider (1993, 1999) and Steinwendner et al. (1998) document a technique for sub-pixel mapping of linear features based on a 3 by 3 pixel kernel or moving window. The approach was extended to include neural network prediction of vector boundaries, but is restricted to remotely sensed images and the detection of linear features.

4.4.2.2 Super-resolving a soft classification

Soft classification predicts the land cover class proportions within a pixel (where a hard classifier would assign the whole pixel to a single class). However, the soft classifier does not predict where within a given pixel the proportions occur. Atkinson (1997b) suggested super-resolving the output from the soft classifier.

Land cover classification from remotely sensed imagery was originally performed using hard classification in which a pixel is allocated to one class only (Thomas et al., 1987). However, many pixels in remotely sensed images represent more than one land cover class. Such 'mixed pixels' occur where the frequency of spatial variation in land cover is greater than the spatial resolution (Woodcock and Strahler's (1987) L-resolution case). However, some pixels will be mixed even in the H-resolution case because they lie across the boundaries between scene 'objects'.

Mixed pixels led to the development of several approaches for soft classification in which a pixel is allocated to all classes in varying proportions (Bezdek et al., 1984; Adams et al., 1985). Examples of techniques for soft classification applied to remotely sensed imagery include the linear mixture model, (e.g., Foody and Cox, 1994; Garcia-Haro et al., 1996), fuzzy *c*-means classification, (e.g, Bezdek et al., 1984), feed-forward, back-propagation (FFBP) neural networks (Paola and Schowengerdt, 1995; Atkinson et al., 1997) and support vector machines (e.g., Brown et al., 1999).

All of the above techniques may be used to provide a soft classification of land cover that is both more informative and potentially more accurate than the equivalent hard classification. However, while the land cover proportions within each pixel may be predicted, the spatial location of each land cover class within each pixel is not. It would be useful to know *where*, within the pixel, each class is located spatially. That goal is the goal of super-resolution classification.

Atkinson (1997b) applied some of the fundamental concepts underpinning geostatistics (e.g., spatial dependence, spatial correlation) to allow prediction at the sub-pixel scale. In particular, it was suggested that as a first approximation, and with no prior knowledge, proximate sub-pixels should have a higher probability of being allocated to pixels of the same class than sub-pixels further apart. The method of super-resolution classification proposed adjusted sub-pixel class allocations based on the proportions of each class found in pixels neighbouring the 'current' sub-pixel. The basic idea was to maximize the spatial correlation

between neighbouring sub-pixels under the constraint that the original pixel proportions were maintained (Atkinson, 1997b). This objective is reasonable where the land cover target of interest is larger than the pixels in the imagery (H-resolution).

Verhoeye and De Wulf (2002) attempted to allocate sub-pixel hard classes using a technique similar to the spectral mixture model. The pixel proportion constraints were built into the mixture model and a solution was achieved by least squares approximation. The linear solution allowed each sub-pixel class to be predicted based on pixel-level neighbouring information. However, this 'mixing of scales' led to linear artefacts in the final map.

Zhan et al. (2002) implemented an inverse distance weighting algorithm to interpolate unknown sub-pixel classes from neighbouring pixel-level land cover proportions. Alternative schemes were proposed for locating the 'point' meant to represent the location of the neighbouring pixel. Specifically, the corners and the centres of the neighbouring pixels were used. However, scales were once again mixed.

4.4.2.3 Hopfield neural network solution

Tatem et al. (2001a) developed a Hopfield neural network (HNN) technique for super-resolution classification. A HNN is a fully connected recurrent network, and is used essentially as an optimization tool (Hopfield and Tank, 1985). It attempts to minimize an Energy function $E_{ij}(t)$, defined for pixel (i, j) at time (iteration) t, which is defined in terms of a goal G_{ij} and constraint C_{ij}, as follows:

$$E_{ij}(t) = k_1 G_{ij} + k_2 C_{ij} + b \tag{4.18}$$

where, k_1 and k_2 and are weights and b is a bias. The HNN has been applied previously in remote sensing for feature tracking (e.g., Coté and Tatnall, 1997).

The goal was used to maximise the spatial correlation between sub-pixels whereas the constraint was used to maintain the original predicted class proportions at the pixel level. The HNN approached a solution iteratively by adjusting the actual values of the soft class proportions per-sub-pixel. The method is ideally suited to the H-resolution case where the objects of interest are much larger then the pixels. Initially, the HNN was designed to deal with the binary case (i.e., target on a background) (Tatem et al., 2001). However, the HNN was later extended to the multivariate case (i.e., land cover classification) (Tatem et al., 2001b).

In later research, the HNN technique was developed to match the spatial correlation between sub-pixels to some prior (variogram) model (Tatem et al., 2002). Specifically, the clustering goal was replaced by a seven-part goal (to match the variogram over the first seven lags to those of a variogram obtained from training data). The objective was to reduce the overall error between the predicted and observed variograms obtained at the sub-pixel scale. The method is ideally suited to the L-resolution case where the objects to be resolved are smaller than or equal to the original pixels. The method was able to reproduce accurately the spatial character of the target image, and in many cases led to an increase in per-sub-pixel accuracy
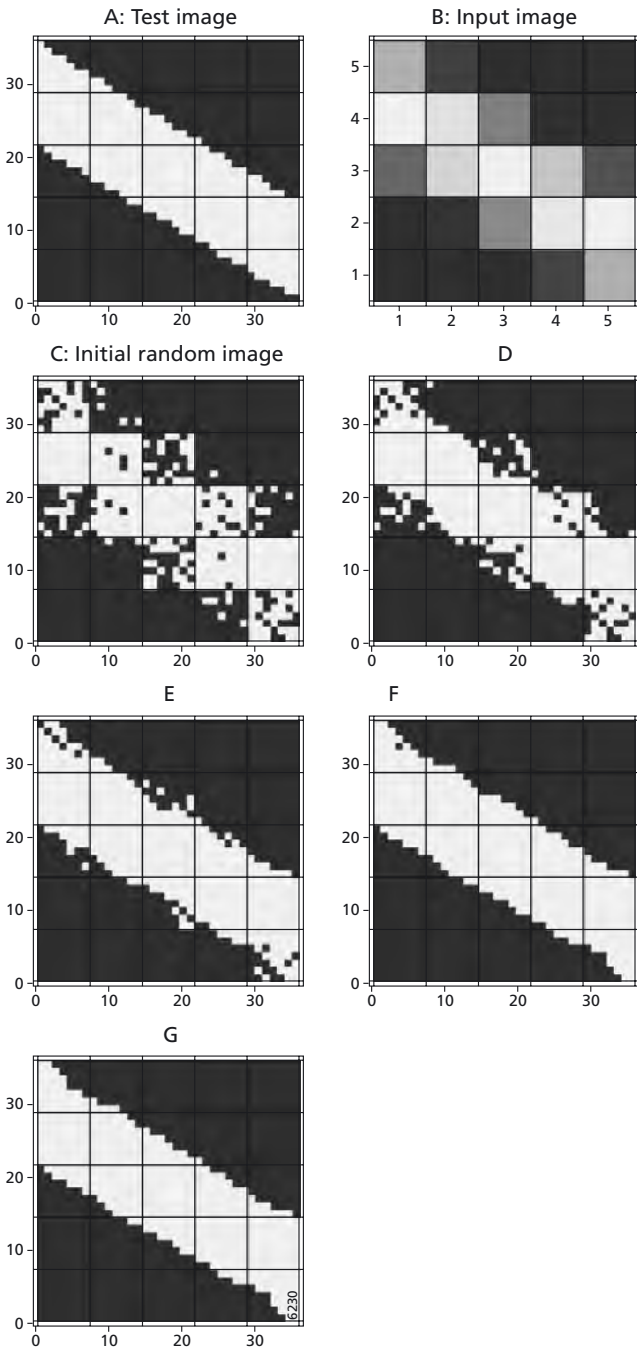
Figure 4.6 – Super-resolution mapping of a linear feature: (a) test image, (b) image of proportions input to the optimization algorithm, (c) random initial allocation to sub-pixels, (d) solution after 3 iterations, (e) solution after 6 iterations, (f) solution after 9 iterations and (g) solution after 12 iterations.

compared to the soft classification. Further, both the 'clustering' goal and the 'matching' goal can be run on different classes simultaneously within the same image.

4.4.2.4 Pixel-swapping solution

More recently, attention has been turned back to pixel-swapping type algorithms because they are conceptually and computationally simpler than their HNN counterpart. Two main algorithms have been developed. First, a simple pixel-swapping approach was used to achieve super-resolution classification in the H-resolution case. The algorithm was first developed for the binary case (Atkinson, 2004a). The technique allows sub-pixel classes to be swapped within the same pixel only, thus, ensuring that the original soft class proportions are maintained exactly at the pixel level. Swaps are made between the most and least 'attractive' locations if they result in an increase in spatial correlation between sub-pixels. Some results for a simple linear feature are reproduced in figure 4.6. The method was extended to the multivariate case simply by running the basic binary algorithm once for each class for each pixel and iteration. In both cases, the algorithm is applicable only in the H-resolution case.

To deal with the L-resolution case a new method based on the two-point histogram was developed (Atkinson, 2004b). The two-point histogram is the full set of transition probabilities between a selected pixel and its neighbours at given lag vectors away. In remote sensing, it is equivalent to the grey-level co-occurrence matrix (Haralick et al., 1973). The variogram (or covariance function) was not used because it conveys only one half of the available information (i.e., the difference, but not direction), such that

A-to-B = B-to-A = *different*
A-to-A = B-to-B = *same*

Given a random variable Z that can take one of k=1, ..., K outcomes (i.e., a categorical variable) the two-point histogram for a particular lag (distance and direction of separation) $\mathbf{h}$ is the set of all bivariate transition probabilities (Deutsch and Journel, 1998):

$$p_{k,k'}(\mathbf{h}) = \Pr \left\{ \begin{array}{l} Z(\mathbf{x}) \in \text{category } k, \\ Z(\mathbf{x} + \mathbf{h}) \in \text{category } k' \end{array} \right\} \tag{4.19}$$

independent of $\mathbf{x}$, for all k, k' = 1, ..., K. The objective function corresponding to the two-point histogram control statistic is as follows:

$$O = \sum_{\mathbf{h}}^{K} \left(\sum_{k=1}^{K} \sum_{k'=1}^{K} \left[p_{k,k'}^{training}(\mathbf{h}) - p_{k,k'}^{realization}(\mathbf{h}) \right]^2 \right) \tag{4.20}$$

where $p_{k,k'}^{training}$ (h) are the target transition probabilities, for example, calculated from a training image and $p_{k,k'}^{training}$ (h) are the corresponding transition probabilities of the realization image (i.e., the current image being altered).

A pixel-swapping algorithm was developed in which pixel swaps are retained if the objective function is approached and rejected otherwise. The method depends on obtaining the target two-point histogram from a training image. This is reasonable where, for example, a small

area is covered by a fine spatial resolution image (classified) and the larger area of interest is covered by an image with a coarser spatial resolution.

4.4.2.5 Continuous variables

The super-resolution methods described above are not applicable to the continuous case (e.g., prediction of biomass). However, recent research has shown that it is actually possible to use geostatistical kriging to downscale from block data (areal averages) to point data (Kyriakidis, 2004). Such a development is novel (previously only punctual and block kriging were demonstrated). Block-to-point prediction provides a linear solution to downscaling, meaning that a single unique solution is achieved in any given scenario and iteration is not required. Further, since the solution is general and can be applied to blocks of any size, shape and orientation, the method provides a potential solution to at least part of the MAUP. The problem is that the method depends on estimation of the point-to-point spatial covariance and this is, in practice, not possible (Atkinson, 1997a) not least because measured variables are ill-defined for a point support as discussed above.

4.5 Discussion

Given the nature of this chapter (a review), this discussion section is brief, focusing mainly on current research issues.

4.5.1 Applications

It should be obvious that downscaling is a valid objective in its own right: increasing the spatial resolution of any image may provide valuable information to the user. This is true in a broad variety of fields in which image analysis is important (e.g. medical imaging).

Downscaling also has potential *application* where (as with upscaling) the objective is to compare one variable (e.g. remotely sensed image) with another (e.g. ground data). Importantly, downscaling may allow comparison (e.g., calibration) to occur at the measurement scale that is most relevant to the investigator (i.e., the support of the ground measurement of the actual property of interest). Such calibration has not been conceivable previously. As an example, consider the problems inherent in calibrating MODIS imagery (spatial resolution of 250 m or 500 m) (e.g., Cohen et al., 2003). It is time consuming (and in some cases prohibitively difficult) to measure ground properties over entire pixels. Downscaling might allow an informed comparison at the quasi-point scale (e.g., with point measurements of soil moisture, air temperature etc.).

4.5.2 Issues of generalization and accuracy

Most investigators feel instinctively that a fine spatial resolution is somehow 'better' than a coarse spatial resolution. Thus, investigators often expect prediction accuracy (e.g., classification accuracy) to increase with spatial resolution. However, it has been known for over twenty years that, paradoxically, the inverse is often true (Justice and Townshend, 1981). Classification accuracy often decreases because smaller pixels may resolve within-class variation that leads to confusion between classes (e.g., revealing soil patches within a field of cereals, where the investigator wishes the whole field to be classified as cereals).

The question is 'if more data lead to lower accuracy, what is the point of investing the extra effort?'. The answer is that while accuracy per-pixel may decrease, an increase in spatial resolution will, except in a few extreme cases, lead to an increase in spatial *information* (where 'spatial information' is interchangeable with 'spatial variation', see Atkinson, 1995). Thus, the investigator has the opportunity to aggregate the data in knowledge-driven ways (e.g., per-field amalgamation), leading to a potential increase in accuracy (per-field) (Aplin et al., 1999; Berberoglu et al., 2000).

Super-resolution techniques for processing the output from a soft classifier, as described above, produce a hard classification at the sub-pixel scale. For the H-resolution case, the accuracy of interest to their investigator is the geometric accuracy of the representation of the boundary between land cover objects. This accuracy can be assessed on a per-sub-pixel basis (e.g., root mean square error), but might be more appropriately measured in terms of the geometric displacement of the predicted vector boundary from the true boundary using GIS-based techniques. Implicit in such an approach is the need to convert the data provided by the super-resolution technique to the object-based model. The per-sub-pixel accuracy of the super-resolution classification should be greater than that achieved using the output of the soft classifier alone (i.e., by subtracting the predicted land cover proportions per-sub-pixel from the known hard classes).

In the L-resolution case, per-sub-pixel and geometric measures of accuracy become less relevant because it is clear that with little or no pixel-to-pixel correlation there is little hope of increasing the per-sub-pixel accuracy above that achievable with a soft classifier. The sub-pixel map achieved using spatial covariance 'matching' type algorithms is similar to geostatistical simulation in that reproducing the character of spatial variation takes precedence over per-sub-pixel prediction accuracy (Tatem et al., 2002). Such maps may have utility in a broad range of application that require realistic maps as input (e.g., dynamic simulation models). More research is required to investigate the range of possible realizations that can be achieved, for example, by selecting alternative random starting positions for algorithms such as the HNN.

4.5.3   Error and the PSF

The constraint of the HNN algorithm maintains as far as possible the original pixel-level land cover proportions predicted by a soft classifier. Similarly, the pixel swapping algorithms described in section 4.2.4 currently do not allow swapping between pixels, thus, guaranteeing that the original proportions are maintained. These strategies are sensible where the predictions made by the soft classifier are perfect. However, in the presence of measurement error this strategy may be sub-optimal (Atkinson, 1997b). In particular, we know that soft classification is rarely perfect (Congalton, 1991; Foody, 2002). To deal with this uncertainty, Tatem et al. (2003) modified the HNN weights (k_1 and k_2), to effectively relax the proportion constraint.

Since the point-spread function implies that some variation from neighbouring pixels contaminates the signal for the current pixel it may be desirable to allow some mixing or swapping of land cover between neighbouring pixels. Further research is required to model

the relation between the parameters of the PSF model and the amount of mixing (swapping) that is required.

4.5.4 Future research

Perhaps more fundamental than the above points is the requirement for a non-stationary approach to super-resolution mapping, both in relation to the HNN and the pixel-swapping algorithms. Currently, the variogram or two-point histogram used as the objective function is stationary (i.e., the same across the entire image). However, it is clear that within an image the sub-pixel pattern of texture and context will vary locally from place to place. The problem is that the sub-pixel variogram (two-point histogram) is estimated from training data that do not share the same spatial reference system as the target image (if they did, the super-resolution mapping would be redundant). Thus, there exists no sub-pixel information on which to base a local modification of the objective function. However, pixel-level data do exist in the soft classified input to the super-resolution technique. To make use of that local information it is necessary to downscale the information using the inverse of the regularization Equation (4.8) or its equivalent. It should be possible to convolve the objective function locally and alter it iteratively such as to match the observed equivalent at the pixel-scale. This is the subject of current research.

4.6 Conclusion

It is often necessary to change the spatial resolution of remotely sensed imagery or of ground data acquired in support of a remote sensing investigation as a precursor to further remote sensing analysis. For example, it is often necessary to fit a remote sensing model (e.g., regression) to image pixels and ground data that are defined on quite different supports. Upscaling and downscaling techniques provide a reasonable basis for making the comparison on the same support given original data defined on different supports.

This chapter has focused on

1   The variogram regularization model
2   Techniques for upscaling and downscaling
3   Techniques for increasing the spatial resolution of a classification

It is hoped that this chapter will act as a spur to other researchers to take this growing field forward.

Chapter 5

Multiscale Object-Specific Analysis (MOSA): An Integrative Approach for Multiscale Landscape Analysis

Geoffrey J. Hay & Danielle J. Marceau

5.1   Introduction

Landscapes are increasingly regarded as complex systems composed of a large number of spatially heterogeneous components that interact in a non-linear way and exhibit emergence, self-organization and adaptive properties through time (Waldrop, 1992; Prigogine, 1997; Kay and Regier, 2000; Wu and Marceau, 2002). An important characteristic of complex systems is that their hierarchical structure is defined at different critical levels of organization where interactions are stronger within levels than among levels, and where each level operates at relatively distinct temporal and spatial scales (Simon, 1962; Allen and Starr, 1982). Therefore, scale is central to the realization of hierarchy and the organization of landscapes (Levin, 1992).

In general terms, scale refers to the spatial dimensions at which entities, patterns and processes can be observed and measured. From an absolute perspective, scale corresponds to a standard system, such as cartographic scales and census units, used to partition geographical space into operational spatial units. From a relative framework, scale is a variable intrinsically linked to the entities under observation, and corresponds to one's window of perception. Thus every scale reveals information specific to its level of observation (Marceau, 1999). As defined in landscape ecology, scale is composed of two fundamental parts: grain and extent. Grain refers to the smallest intervals in an observation set, while extent refers to the range over which observations at a particular grain are made (O'Neill and King, 1998). In remote sensing, scale corresponds to the spatial, spectral, temporal, and radiometric resolution of the sensor. Here the term spatial resolution is equivalent to grain, while extent represents the total area that an image covers. In this discussion, small scale refers to a small area, and large or coarse-scale represents a large area.

Scale has been recognized as a key component for understanding the structure and the spatio-temporal dynamics of landscapes for more than fifty years and has been the subject of an abundant literature (for a review, see Marceau, 1999). During this time, two principal challenges have been addressed, respectively known as the scale and scaling problem. The former refers to identifying the 'natural' or preferred scale(s) at which ecological patterns

and processes occur, while the later refers to deriving appropriate rules for transferring data or information across scales (Caldwell et al., 1993; Jarvis, 1995). Theoretical frameworks, such as Hierarchy theory (Allen and Star, 1982; O'Neill et al., 1986) and the Hierarchical patch dynamics paradigm (HPDP – Wu and Loucks, 1995) have been proposed to express the intricate relationship among pattern, process, and scale explicitly in the context of landscapes, and to provide an operational framework for scaling. Useful concepts such as scale domain and scale threshold have also been defined. A scale domain represents a segment of the scale spectrum where patterns do not change, or change monotonically with changes in scale, while a scale threshold defines the end or beginning of a scale domain (Meentemeyer, 1989).

More recently, another challenge that has been identified as a mandatory requirement for deciphering the complexity of landscapes is referred to as multiscale analysis. The rationale behind multiscale analysis is as follow. Since landscapes are known to exhibit distinctive spatial patterns associated to different processes at different scales, landscape analysis performed at a unique scale is doomed to be incomplete and misleading (Marceau et al., 1994a; Hay et al., 1997; Wu et al., 2000). Furthermore, there is no way of defining a priori what are the appropriate scales associated to specific patterns. In addition, scaling requires obtaining information about the patterns (and processes) occurring at a range of scales in order to detect scale thresholds and derive adequate rules for the transfer of information through multiple scales. Thus, it is imperative to develop a multiscale approach that allows dominant patterns to emerge at their characteristic scales, with no a priori user knowledge, in order to obtain adequate and complete information about the vertical structure of the landscape.

The idea of multiscale analysis is not new. Wu et al. (2000) distinguish between two general approaches for multiscale analysis that have been developed and applied over the last four decades: the direct and indirect approaches. An indirect approach refers to the use of a dataset acquired or resampled at a series of discrete scales. An example is provided by Marceau et al. (1994a,b) who resampled high-resolution airborne data at different resolutions to study the impact of scale and spatial aggregation on classification accuracy results. The principal limitations of the indirect approach are that scales are arbitrarily chosen and do not represent the full vertical continuum of landscapes. Consequently, significant patterns and processes can go undetected or erroneously identified.

In contrast, the direct multiscale approach attempts to capture the dominant patterns as they emerge at specific scales from a unique dataset. A number of computational techniques developed to generate multiscale representations (Starck et al., 1998) can be associated to this group. These include fractals (Mandelbrot, 1967), quadtrees (Klinger, 1971), spectral analysis (Platt and Denman, 1975), pyramids (Klinger and Dyer, 1976), wavelets (Daubechies, 1988), beamlets (Donoho and Huo, 2000), scale space (Lindeberg, 1994; Hay et al., 2002a), and multiscale object-specific analysis (MOSA) (Hay, 2002; Hay et al., 2003).

Among these, the last method exhibits novel characteristics that are of significant importance for multiscale landscape analysis:

- First, MOSA has been developed for the particular spatial sampling context provided by remote sensing imagery. Remote sensing represents an unprecedented means to gather data at a wide range of spectral, spatial and temporal resolutions and can be judiciously used to address a number of challenges related to the scale issue (Marceau and Hay, 1999).
- Second, this approach is based on an object-specific framework (Hay et al., 1997; 2001). This means that individual image-objects rather than arbitrary spatial units are the basis for analysis and scaling. Image-objects are considered as perceptual entities that visually represent objects in an image that are composed of similar digital numbers/grey-tones, and which model real-world entities. Such an object-based approach offers two main advantages. First, it reduces the effect of the modifiable areal unit problem (MAUP). The MAUP originates from the use of arbitrarily defined and modifiable spatial units used to acquire data over a geographical area (Openshaw, 1984). Examples are provided by remote sensing data (Marceau et al., 1994a; Marceau and Hay, 1999) and census data. Because these data do not explicitly correspond to geographical entities, but rather are an aggregation of the content of the spatial units, the value of the analysis results based upon them may not possess any validity independently of the units that are used. One way to overcome the MAUP is to focus the analysis on meaningful geographical entities (or objects) rather than arbitrary defined spatial units (Fotheringham and Wong, 1991). A second advantage of the object-specific approach is that it explicitly considers the hierarchical structure of the landscape by allowing the aggregation of smaller landscape components into the larger objects they are part of at their next scale of expression.
- Finally, this object-specific framework satisfies two major requirements for multiscale analysis (Hay et al., 2002a). First, the generation of datasets that represent a range of 'natural' scales from which objects can be detected. And second, the delineation and identification of individual objects as they evolve through scale.

In an effort to better understand complex landscape behavior through scale, we propose a multiscale approach that judiciously integrates ecological theory, remote sensing data, spatial modeling, and computer vision capabilities for the automatic delineation, evaluation, and visualization of dominant landscape objects through scale. Because there exists no single optimal scale for analyzing the myriad different spatial characteristics of landscape components (Marceau et al., 1994 a, b; Hay et al., 1997), we suggest that an effective multiscale approach should be guided by the intrinsic scale of the varying sized, shaped, and spatially distributed 'image-objects' that compose a remote sensing scene, rather than a static (and often arbitrary) user-defined scale of analysis (Hay et al., 2001).

The objective of this paper is to present a detailed description of Multiscale Object-Specific Analysis (MOSA) as a novel integrative approach that reduces the effects of MAUP, and automatically delineates multiscale landscape structure from remote sensing imagery. In particular, we report on the implementation of a new object-specific analysis kernel and new methodology that significantly improves the results of automatic object delineation using object-specific data and marker-controlled segmentation (MCS).

This chapter is organized in the following manner. First, a description of the remote sensing dataset used for analysis is presented. This is followed by a detailed description of the three components of MOSA. We then provide a brief interpretation of the results obtained from

applying MOSA to the dataset, and conclude by discussing the benefits and limitations of this technique.

5.2   Methodology

The methodological framework developed in this study represents an integration of techniques and concepts ranging from Landscape Ecology and Computer Vision, to Geographic Information Science. As a result, a number of different computer software programs were employed. Unless explicitly stated, all object-specific code was written by the first author in IDL 5.6 (http://www.rsinc.com/idl), and marker-controlled segmentation code was written in Matlab 5.1 (http://www.mathwork.com).

5.2.1   Remote Sensing dataset

The remote sensing image used in this study is a 500 by 500 pixel sub-image of a panchromatic IKONOS-2 (Geo) scene acquired in August 2001, over a highly fragmented agro-forested landscape in the Haut-St-Laurent region in south-west Quebec, in Canada (Figure 5.1). This site is composed of an agricultural matrix textured with forest patches of varying size and shape. Three land-use classes dominate the scene: Agriculture, Fallow land and Forest. In order to illustrate how image-objects evolve through scale over a relatively large extent (i.e., 2 km) while still maintaining a fine level of detail, the panchromatic image was resampled from its original 1 m spatial resolution to 4 m using the object-specific upscaling technique, which is considered a robust upscaling technique (Hay et al., 1997).

5.2.2   MOSA description

MOSA represents an integration of three principal methods: Object-Specific Analysis (OSA), Object-Specific Upscaling (OSU), and Marker Controlled Watershed Segmentation (MCS). In general terms, OSA is a multiscale approach that employs different sized adaptive kernels to automatically define unique spatial measures specific to the individual image-objects composing a remote sensing scene (Hay et al., 1997, 2001). These 'object-specific'
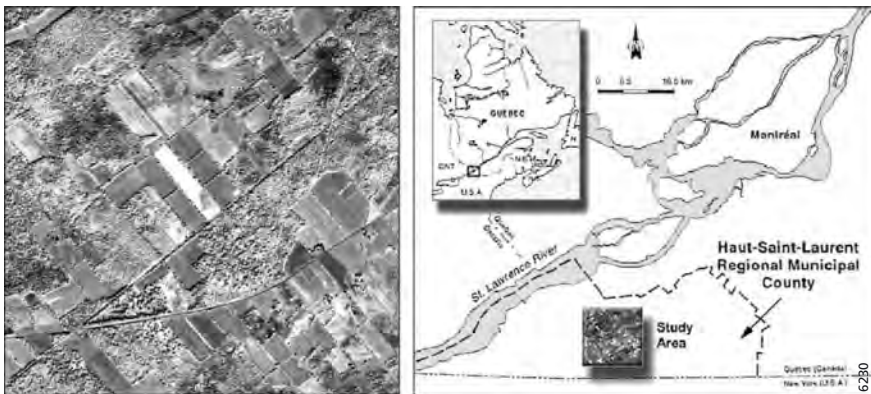
Figure 5.1 – Original panchromatic IKONOS dataset and location of the study area.

spatial measures are then used in a weighting function to automatically upscale (OSU) the image to a coarser resolution by taking into account the spatial influence (i.e., area) of the image-objects composing the scene at the finer resolution. Because image-objects, rather than arbitrary pixels, are the basis for upscaling, the effects of the modifiable areal unit problem (MAUP) are reduced in the upscaled image. MCS is then applied to the newly upscaled data to automatically segment them into topologically discrete image-objects that strongly correspond to visual interpretation. The elegance of utilizing MCS as a feature detector is that it requires inputs that are automatically and explicitly met by OSA/OSU outputs. Details regarding each component and their interaction are provided in the following sections.

5.2.2.1 Object-specific analysis (OSA)

Strahler et al. (1986) noted that in a remote sensing image, two fundamental resolution types exist:

1 Low-resolution (L-res): where pixels are larger than image-objects; thus, a single pixel represents an integration of many smaller image-objects;
2 High-resolution (H-res): where pixels are smaller than image-objects; consequently, a single image-object is composed of many individual pixels.2.

In object-specific analysis, we are interested in defining the detailed spatial characteristics of individual image-objects. Consequently, an underlying premise of OSA is that all pixels within an image are exclusively considered high-resolution samples of the image-objects they model, even though, both high- and low-resolution (L-res) samples exist in a single image. This is because pixels represent the fundamental primitive from which all image-objects are generated. Thus individual pixels are required to define the larger image-object(s) they are a part of.

OSA thresholds and heuristics

Hay et al. (1997) observed that when plotting the variance of grey-values generated by sampling image-objects within increasingly larger kernels, the resulting plots produced curves with distinct breaks, or 'thresholds' in variance as the analyzing kernel contacted the image-object's edges (for a more detailed discussion, see Hay et al., 2001). After many hundreds of experiments on different sized, shaped and spatially arranged image-objects ranging from text, human faces, unique sized and shaped geometric shapes, to trees, roads and fields in H-res airborne imagery, it became apparent that the kernel size defined at these thresholds strongly corresponded to the known size (i.e., area) of specific image-objects. As a result, the shape of these variance curves was used to create a set of robust heuristics that define the spatial extent (i.e., kernel area) where an individual pixel is spectrally related to the image-object it is a part of. Rather than a single threshold value being used for all sizes of analyzing kernels, we have defined three robust threshold values that are representative of the pixel/image-object relationship over of a specific range of scales. In fact, a single threshold value does not work for all scales, thus supporting the concept of scale domains.

The primary OSA heuristic is composed of three different percentage values, each of which represents the difference in variance defined between two concurrent kernels over a specific range of kernel sizes. If the difference in variance between the two kernels is less than or

equal to the heuristic threshold value, processing is stopped. When a 'threshold' is reached, the corresponding mean, variance and area values are also recorded for the pixel under analysis within the specified kernel. This object-specific process is then applied to all the remaining pixels within the original image (O_I), resulting in the generation of corresponding Variance (V_I), Area (A_I), and Mean (M_I) images. These three images are referred to as the first image-set (IS_I) (i.e., V_I, A_I, M_I), and this form of adaptive-kernel processing is referred to as object-specific analysis.

The variance image is essentially a gradient or edge image. Bright tones correspond to high variance values, thus the edge between two or more image-objects, while dark tones indicate low variance, or homogeneity, thus more 'object-like'. The area image defines the spatial influence, i.e., the kernel area or number of pixels 'spectrally related' to the pixel under analysis. Dark tones represent small area values, which correspond to object centers, while bright tones represent large area values. The mean image is composed of an average of the H-res pixels that constitute part of individual objects assessed at their respective scales; thus the mean image is a model of what the scene looks like at the next level of (non-linear) multiscale analysis.

The OSA kernel

For simplicity and convenience, object-specific analysis was initially conducted using odd sized square kernels i.e., 3 by 3, 5 by 5, etc. (Hay, 1997). However, based on the relationship between 2D Gaussian filters and mammalian vision (Hay et al., 2002a), and the diagonal bias inherent to square kernels, a square approximation of a round kernel was developed and used (Hay et al., 2001). To further improve the sensitivity of this kernel for defining complex edges, two different sized 'round' kernels are currently assessed within the same kernel diameter. For example, if the kernel size is 9 by 9, a square kernel consists of 81 pixels. In the current method, two 'round' kernels of different total area are defined within the same (9 by 9) window (Figure 5.2). The first kernel is based on the number of pixels less than the kernel radius. This results in 49 pixels. The second kernel represents the number of pixels less than or equal to the kernel radius, resulting in 69 pixels (table 5.1). In both cases, each round kernel is centred in the square window, and the pixel being assessed is the centre pixel. Thus, in a 9 by 9 window, the variance of the pixel grey-values is defined, then the threshold heuristic is evaluated based on the difference between the 49 pixel sample (in the first round kernel) and the 69 samples (in the second round kernel), instead of the 81 samples that constitute the
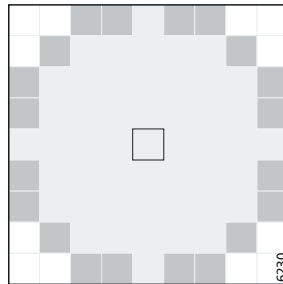
Figure 5.2 – Two round kernels defined within a square window.

Table 5.1 – The number of pixels taken into consideration within a square window and two round kernels.

Kernel diameter (D_{pixels})	3	5	7	9	11
Circle (LT D/2)	5	13	29	49	81
Circle (LE D/2)	9	21	37	69	97
Square (D x D)	9	25	49	81	121

entire square window. At the next scale of analysis (i.e., a kernel of 11 by 11 pixels) analysis is conducted on the difference between 81 and 97 pixels (table 5.1). This new filter set has resulted in improved sensitivity to object edges, faster processing as convolution is performed twice within a single window of the same size, and the minimization of the diagonal bias inherent to square kernels.

5.2.2.2 Object-specific upscaling (OSU)
The unique area values defined for each pixel by OSA are used as part of a weighting scheme to upscale an image to a coarser resolution. The resolution of the upscaled image can either be defined manually according to user requirements, or automatically by statistical properties of the objects composing the image. Because both of these upscaling forms take into account object-specific weights, they are referred to as object-specific upscaling. In the following section, we report on the automated method.

The OSU resampling heuristic
An important premise of OSA is that spatially dominant objects should have greater 'influence' in the upscaled image than smaller objects. We intuitively recognize this attribute when we move away from a local scene. Smaller objects seem to disappear while larger objects persist. An explanation for this is partly found in Slater (1980). If an object is less than ¼ the size of the instantaneous field of view (IFOV) of the sensor, its influence in the corresponding pixel is equal to the point spread function (PSF) of the sensor – which in modern sensors is typically very small. In simple terms, IFOV represents the ground area visible by a sensor at a specific time, and the PSF defines the spatial influence of a point of light resulting primarily from imperfections in the lens of the sensor (Duggin and Robinove, 1990). Consequently, if the object of interest is less than ¼ the size of the smallest resolvable component in the scene, the sensor is unable to visually detect it. From an object-specific perspective, this translates as: if an image-object is composed of fewer pixels than the smallest kernel can discern, its spatial characteristics cannot be defined.

Since the ¼ resampling heuristic describes how the signal of real-world components are modelled by a sensor, we adopt it for automatically defining appropriate minimum upscale resolutions in the following manner:

$$upscale\_res = pixel\_size + (pixel\_size \cdot min\_win \cdot res\_heur) \quad (5.1)$$

where:
- *upscale_res* represents the length (i.e., diameter) of the square upscale kernel defined in pixel units that are equivalent to those of the original image;

- *pixel_size* initially is the value 1, where it represents a single pixel in the original image (regardless of its spatial resolution);
- *min_window* represents the smallest sized kernel. In the case of a square 3 by 3 kernel, this value is 3 (i.e., the square root of the total number of pixels in the kernel). However, in the new 'round' kernel, the smallest analyzing kernel is composed of five pixels (that make a cross in a 3 by 3 window), consequently the min-window value equals the square root of 5 (i.e., $5^{0.5}$);
- *res_heur* equals 0.25 (i.e., ¼) as previously discussed.

Based on Equation 5.1, the first upscale_res equals 1.559 [i.e., $1 + (1 \times 5^{0.5} \times 0.25)$]. That is, each pixel in the first upscale image has a grain equal to 1.559 pixels in the panchromatic image. This represents a spatial resolution of 6.24 m (i.e., 4 m x 1.559 pixels). The extent of the new upscale image is obtained by dividing the length of the original image (i.e., 500 pixels) by 1.559, resulting in 321 pixels. Essentially, the upscale kernel is used as a mask to generate a weighted area value for each pixel in the following manner. Beginning at the origin, the upscale kernel is overlaid on the corresponding A_I, and each area pixel (within the mask) is divided by the sum of all area pixels in the mask. This generates a fractional area weight that sums to one. Each area weight (in the mask) is multiplied by its corresponding original grey value, and then summed. This summed value represents the new area weighted upscale value that corresponds to the original pixels in the upscale mask. The non-overlapping upscale kernel is then applied to the remaining data resulting in a new upscale image. The placement of the upscale mask (i.e., beginning at the origin) is completely arbitrary and thus subject to the aggregation problem, however incorporating object-weighted values reduces this problem. Due to the discrete nature of pixels, it is not possible to create a kernel with 1.559 by 1.559 pixels. In all cases window sizes are rounded up, thus 1.559 pixels becomes 2 pixels.

During heuristic development, it became apparent that over 90% of the image-objects within each image were assessed within relatively small kernels; however, the remaining 10% requires 3-4 times the processing of the smaller kernels. In addition, the locations that required the most processing seldom, if ever, corresponded to recognizable image-objects. Since the upscaling algorithm is designed to be area weighted (based on kernel size), large area values, which corresponded to non-recognizable image-objects, would have more influence in the upscaled image. To remedy this, the upscaling weight is calculated (as defined above) but using an inverse area value i.e., $(1.0/Area_I)$. Thus each upscale increment spatially biases recognizable image-objects.

To determine the upscale resolution for coarser scales, this process is iterated using upscale_res as the new pixel_size. Consequently, the next upscale_res equals 2.43 [i.e., $1.559+(1.559 \cdot 3 \cdot 0.25)$]. That is, at the second upscale iteration, a single upscale pixel is now equivalent to 2.43 pixels – with a spatial resolution of 9.72 m (i.e., 4 m 2.43 pixels), and an image extent of 206 pixels. When applied for two more iterations, the resulting upscale resolution, and grain and extent of the upscaled images are defined in table 5.2.

Iterative OSA and OSU
Based on promising results from early research, Hay et al. (1997) recognized that the application of OSA/OSU rules revealed patterns that accurately correspond to the spatial
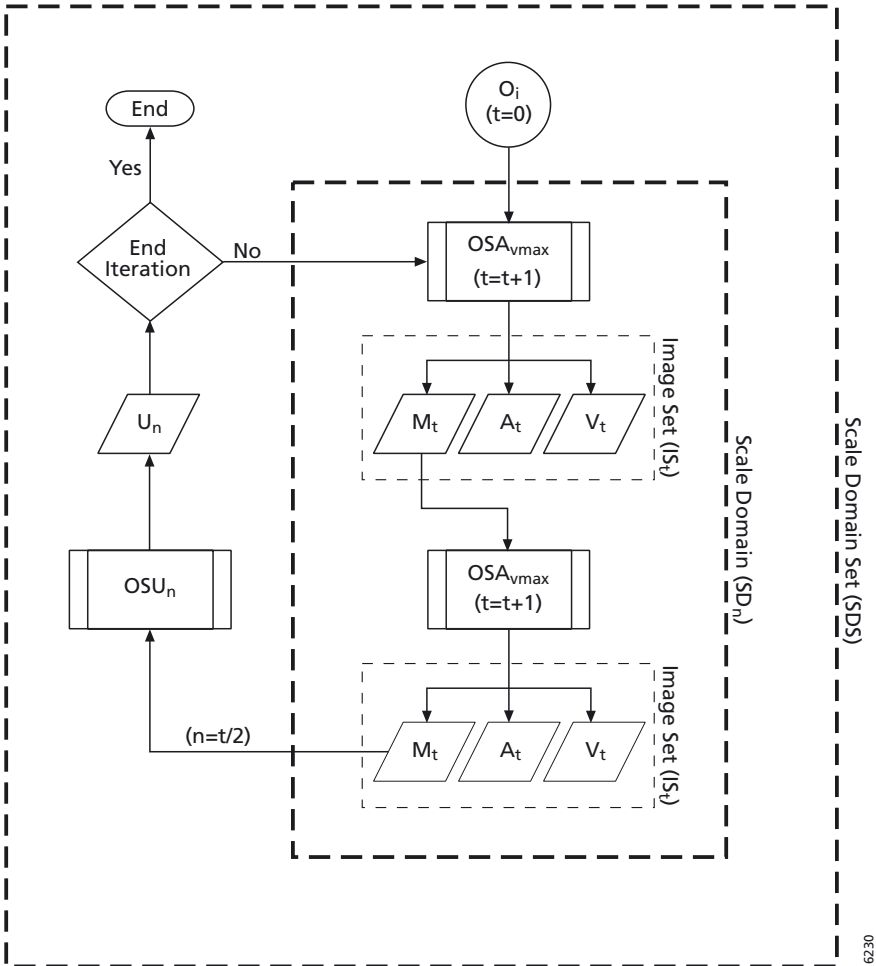
Figure 5.3 – A flowchart summary of iterative OSA/OSU processing.

extent of objects at their next (coarser) scale. This led to the hypothesis that by continuously applying object-specific rules to the M_I generated at each OSA iteration, new spatial patterns will emerge that represent dominant landscape objects, and that these patterns will correspond to real-world objects through a wide range of scales (Hay and Marceau, 1998).

To test this hypothesis, Hay et al. (2001) developed an iterative multiscale framework that represents a nested hierarchy of two image-sets (IS_t), each of which possesses membership in a unique scale domain (SD_n). They recognized that there is often a range of scales between the end point of identifiable scale domains where certain image-objects exist and the point where new image-objects emerge at their next scale of expression (see Hay et al., 2001 for an in-depth discussion). To exploit this information, the initial framework was modified as follows (see Figure 5.3 for an overview): at the first OSA iteration, every pixel is locally assessed

U₄
Grain: 23.88 m²
Extent: 85 pixels²

U₃
Grain: 15.16 m²
Extent: 132 pixels²

U₂
Grain: 9.72 m²
Extent: 206 pixels²

U₁
Grain: 6.24 m²
Extent: 321 pixels²

O₁
Grain: 4.0 m²
Extent: 500 pixels²
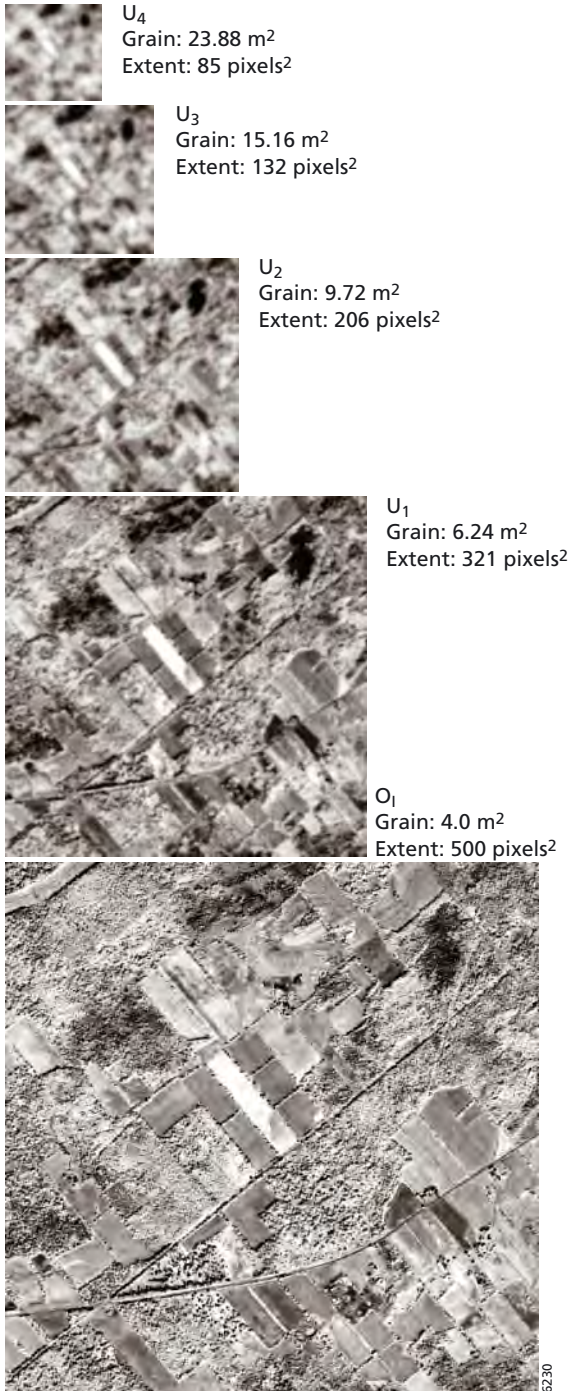
Figure 5.4 – A comparison of the original image (O₁) and Upscale images (U₁₋₄) through scale.

within progressively larger kernels until a local maximum variance (OSA_{vmax}) threshold is reached. When applied to the entire image, this process generates the first image-set (i.e., V_1, A_1, M_1) – as previously described. In the second iteration, each pixel in the newly generated M_1 is locally assessed until a minimum variance (OSA_{vmin}) threshold is reached (Figure 5.3). The resulting images become the second image-set (i.e., V_2, A_2, M_2) where they represent the beginning scale of all newly emergent image-objects.

Recall that minimum variance indicates that pixels are very similar, thus the corresponding image structures are most 'object-like'. As a result, odd-numbered OSA iterations define scales that represent the spatial extent or 'end' of objects, while even-numbered OSA iterations define the beginning scale of all newly emergent image-objects. Consequently, data within the even-numbered OSA iterations (i.e., $IS_{2, 4, 6...}$) are selected for upscaling (OSU) as they contain the new image-objects we are interested in. For example, within IS_2, OSU is applied to the newly generated Mean image (M_2), resulting in a new Upscale image (U_1) (Figure 5.3). U_1 is then considered the new base image, and the entire OSA/OSU process is repeated on the new images, until the number of pixels composing them is too small for further processing (Figure 5.4). If upscaling were applied to the original IKONOS image several iterations further, we would eventually end up with the Upscale data set being represented by a single pixel with a 2000 m spatial resolution.

The result of this iterative object-specific analysis and upscaling approach is a nested hierarchy of image-sets (IS_t), each composed of two V_I, A_I and M_I that have membership in a unique scale domain (SD_n), where n indicates the location of each scale domain within the nested hierarchy (Figure 5.5). Within each SD_n, all images share the same grain and extent, and represent the result of multiscale analysis specific to the image-objects composing them. However, all images in a SD_n have a coarser grain than those of the previous SD_{n-1} (due to

Table 5.2 – Information for generating a scale domain set.

SD_n	IS_t Components	OSA_t	OSU_n	Upscale Resolution (OI pixels)	Grain (m^2)	Extent ($pixels^2$)	# Pixels
	OI			1.0	4.0	500	250000
SD_1	$IS_1 = V_1, A_1, M_1$	1			4.0	500	250000
	$IS_2 = V_2, A_2, M_2$	2			4.0	500	250000
	U_1	1		1.559	6.24	321	103041
SD_2	$IS_3 = V_3, A_3, M_3$	3			6.24	321	103041
	$IS_4 = V_4, A_4, M_4$	4			6.24	321	103041
	U_2		2	2.430	9.72	206	42436
SD_3	$IS_5 = V_5, A_5, M_5$	5			9.72	206	42436
	$IS_6 = V_6, A_6, M_6$	6			9.72	206	42436
	U_3		3	3.789	15.16	132	17424
SD_4	$IS_7 = V_7, A_7, M_7$	7			15.16	132	17424
	$IS_8 = V_8, A_8, M_8$	8			15.16	132	17424
	U_4	4		5.907	23.88	85	7225
SD_5	$IS_9 = V_9, A_9, M_9$	9			23.88	85	7225
	$IS_{10} = V_{10}, A_{10}, M_{10}$	10			23.88	85	7225

	Variance	Area	Mean
SD$_1$ Grain: 4.0 m^2	V$_2$	A$_2$	M$_2$
SD$_2$ Grain: 6.24 m^2	V$_4$	A$_4$	M$_4$
SD$_3$ Grain: 9.72 m^2	V$_6$	A$_6$	M$_6$
SD$_4$ Grain: 15.16 m^2	V$_8$	A$_8$	M$_8$
SD$_5$ Grain: 23.88 m^2	V$_{10}$	A$_{10}$	M$_{10}$
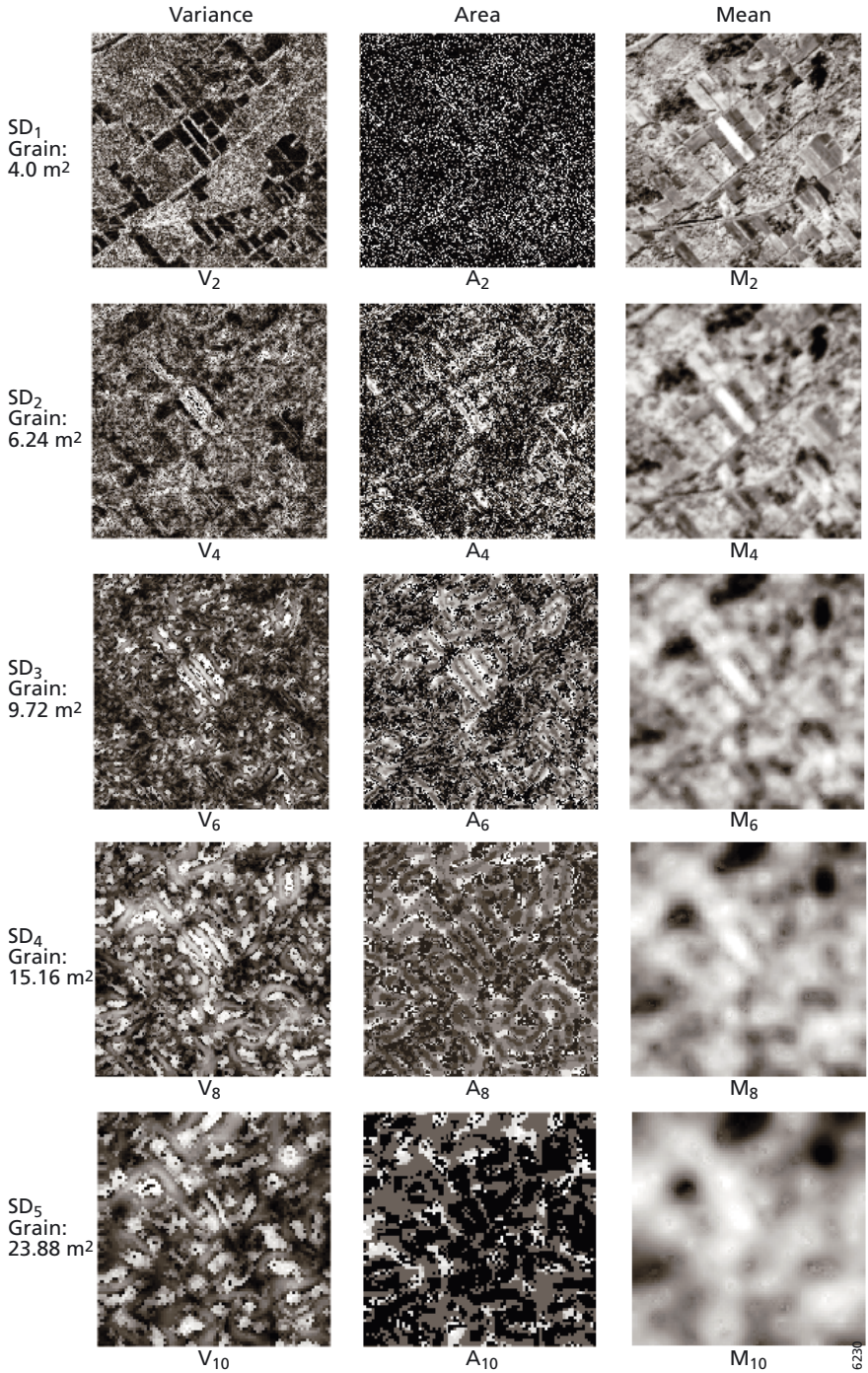
Figure 5.5 – Variance (V$_I$), Area (A$_I$) and Mean (M$_I$) images generated at each scale domain.

upscaling), though they share the same extent (i.e., the same ground area) through all image-sets. This effect is illustrated by the Upscale images in Figure 5.4.

We note that instead of continuing to apply OSA_{vmax} to the M_I generated from each OSA_{vmin} iteration (Figure 5.3), object-specific upscaling is first applied to ensure that the initial image-object heuristics maintain the same conditions for which they were originally designed, and to reduce unnecessary computation and data generation/storage. The combination of all SD_n generated from a single image is referred to as a scale domain set (table 5.2).

5.2.2.3 Marker-controlled segmentation (MCS)

Once OSA/OSU processing has been completed, and a multiscale dataset has been generated, MCS is used as a feature detector to automatically delineate and label individual image-objects as they evolve through scale. MCS is a watershed transformation technique that detects regional similarities as opposed to an edge-based technique that detects local changes (Beucher and Lantuéjoul, 1979; Meyer and Beucher, 1990). The key characteristics of this technique are the ability to reduce over-segmentation due to noise by placing markers or 'seeds' in user-specified areas, and to define regions (i.e., image-objects) as closed contours.

The watershed transformation

The intuitive idea behind the watershed transformation is borrowed from geography. Essentially a topographic surface is flooded with water and the resulting watersheds divide the surface by representing domains of attraction of rain falling over the region (Roerdink and Meijster, 2000). When applied to an image, bright pixels correspond to peaks, dark pixels correspond to valleys, and watersheds are defined as closed contours surrounding local minima (i.e., a local catchment basin). However, the standard watershed transformation is known to produce over-segmentation due to noise and not to real objects. Filtering could be applied to reduce over-segmentation but is often based on subjective decisions (i.e., filter type and size).

In an effort to resolve this over-segmentation problem, Meyer and Beucher (1990) introduced the concept of marker-controlled segmentation (MCS). In MCS, markers are intelligently used as spatial identifiers (or 'seed') for unique regions/objects in the image. Thus, rather than defining watersheds at the location of noise, watersheds are only defined around specific markers. Typically, markers are individually defined and placed in the image by the user, or regional minima are automatically generated and used as markers. However, we note that (image) regional minima do not – by default – represent special object-like characteristics except in object-specific datasets.

The MCS procedure

The general procedure associated with MCS involves three steps. First, an edge detector is used to enhance intensity variations in an image. This type of detector is typically referred to as a 'gradient operator', and the resulting image is the 'gradient image' (G_I). Second, a relevant marker set is obtained and applied to this gradient image. Third, watersheds are delineated from this combination of markers and edges.

An integration of new object-specific and MCS methods
In recent studies that integrated OSA, OSU and MCS (Hall et al., 2003; Hall and Hay, 2003), Variance images were used as gradient images, rather than haphazardly choosing a gradient operator and (static) kernel size from which to generate gradient images. Then unique markers were generated for each scale domain by automatically defining regional minima in the corresponding Area images, as these datasets explicitly represent object-specific information. The resulting markers where then 'imbedded' in the gradient image using a simple operator, and the Matlab watershed algorithm was applied. Each polygon in the resulting watershed images (W_I) was then labeled with a value equal to the average of the corresponding M_I pixels located within its perimeter.

While these recent results were significantly better than haphazardly generating a gradient image and using the regional image minima as markers, we recognized that their was still a problem – at least visually – with over-segmentation, even if it was all object related. In a new effort to reduce over-segmentation, while producing watersheds that visually correspond well to image-objects, we have incorporated pre-processing of the object-specific data with a median filter, generated new gradient images instead of using the Variance images, and developed a more object-specific approach to automatically define markers. In all cases, the new methods can be automatically implemented using data inputs that continue to be met by the Variance, Area and Mean images. These methods are described in detail in the following sections.

Pre-processing with a median filter
A detailed visual inspection of each V_I, A_I, M_I reveals that a significant amount of salt and pepper (isolated high or low) pixel values exist in each image. As previously noted, these signals will lead to over-segmentation when the watershed transform is applied. Thus, a 3 by 3 median filter is applied to each of the V_I, A_I, and M_I, as well as the O_I. All subsequent feature detection will be applied to these images (unless otherwise stated). Median filtering is a nonlinear operation that replaces each point with the median of the one- or two-dimensional neighborhood of a given width. It is similar to smoothing with a boxcar or average filter but preserves edges larger than the neighborhood, while simultaneously effectively reducing salt and pepper noise (Lim, 1990).

Recall that in OSA, we are interested in the spatial/spectral relationship between pixels and the image-objects they are a part of, thus no pre-processing or smoothing of the original image is performed. Consequently, the maximum H-res content is maintained in the O_I. However, in the object delineation portion of MOSA, we are no longer interested in individual pixels, but rather unique pixel groups that represent specific image-objects. When we take this into consideration, along with the fact that the smallest object-specific kernel resides within a 3 by 3 pixel window, and that edges larger than this are preserved, median filtering is an excellent and effective approach for defining the spatially dominant pixel groups that make up the image-objects within each scale domain image.

Generating new gradient images
While a significant amount of edge information visually exists in each Variance image (figure 5.5), discretizing these edges for use as gradient images is not trivial due to their

representation by a wide range of grey-tones. Therefore, rather than using the variance images as gradient images (G_I), new gradient images are generated for each scale domain by subtracting the Mean image from the corresponding resolution Upscale image (U_I) and defining the absolute value of the result. For the gradient images displayed in Figure 5.6, the following equations were used:

$$G_2 = \text{abs}\,(O_1 - M_2) \tag{5.2}$$

$$G_4 = \text{abs}\,(U_1 - M_4) \tag{5.3}$$

$$G_6 = \text{abs}\,(U_2 - M_6) \tag{5.4}$$

$$G_8 = \text{abs}\,(U_3 - M_8) \tag{5.5}$$

$$G_{10} = \text{abs}\,(U_4 - M_{10}) \tag{5.6}$$

Where $G_{2,4,6,8,10}$ represent the newly generated Gradient images, abs represents the absolute value, O_I represents the original IKONOS panchromatic image, $M_{2,4,6,8,10}$ represent the newly generated Mean images, and U_{1-4} represent the newly generated Upscale images. All MCS processing is applied to the (new median filtered) datasets originally generated by OSA/OSU at their native grains and extents as defined in table 5.2.

This method for generating new gradient images is similar to the technique in mathematical morphology where external contours (i.e., object edges) can be created by defining the difference between the original and the dilated image. Other contours can also be created by the difference between the original and the eroded image, and the dilated and the eroded image (Haralick and Shapiro, 1992). However, in each of these cases, a fixed sized structuring element must be defined for erosion and or dilation, which directly influences the shape of the resulting contours. In the case of OSA, each M_I represents the result of a dynamically sized and shaped structuring element (i.e., the object-specific kernel) that is specific to the different sized, shaped and spatially arranged image-objects within each scene. By using the absolute value, all difference, or changed values are represented by relatively large (i.e., bright) grey tones that exist within the tails of each GI histogram.

Image-object markers
Object markers are generated by combining regional minima from the corresponding variance and area images using a logical AND operation. More specifically, the regional minima algorithm (imregionalmin available in Matlab) is first applied separately to the V_I and A_I of each SD_n. In this algorithm, regional minima are connected components of pixels (i.e., 8-connected neighbors) with the same intensity value, whose external boundary pixels all have a value greater than this intensity value. The resulting dataset is a binary image, where values equal to one represent regional minima. Variance minima values represent areas of low heterogeneity that conceptually correspond to object centers. Area minima indicate that the object-heuristics for the pixel being assessed were met within a small analyzing kernel and also correspond to object centers. Based on an extensive visual analysis of the images in each SD_n, it became evident that the local Area minima represent both image-object centers and
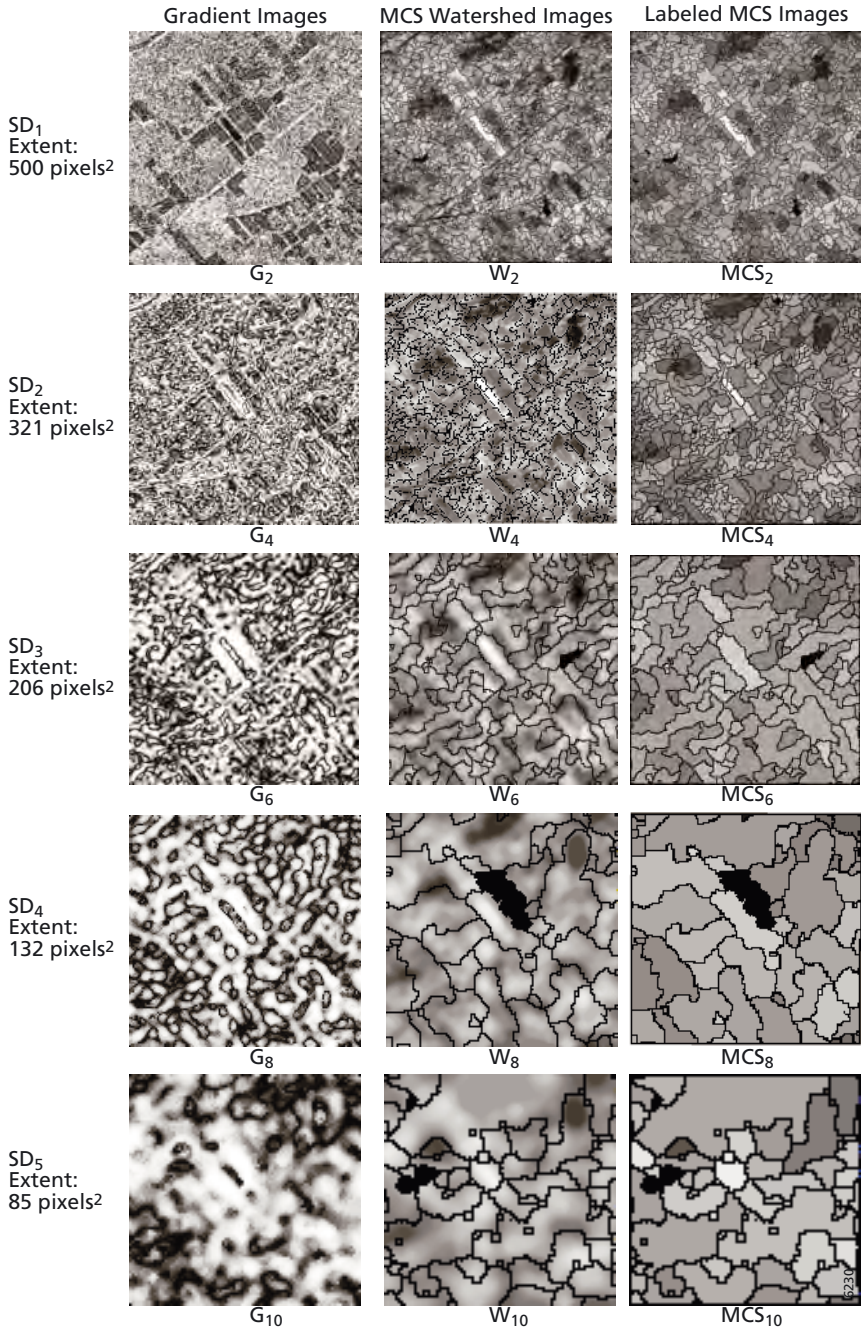
Figure 5.6 – Gradient (G_I), Watershed (W_I), and labeled Marker Controlled Segmentation (MCS_I) images generated at each scale domain. The MCS_I are overlaid on their corresponding Mean images to illustrate how well MCS works as a feature detector.

the edges between two or more image-objects. Hay et al. (2001) refer to these edge locations as edge-objects. That is, both image-objects and edge-objects are typically composed of (relatively) small area values. Thus, exclusively using markers derived from Area minima – as done in earlier studies (Hall et al., 2003; Hall and Hay, 2003) – does not provide optimal results. Fortunately however, only image-objects are composed of both (relatively) small area, and (relatively) small variance values. Thus to ensure that image-objects, rather than edge-objects are defined as markers, the AND logical operator is applied to the regional Area minima and the regional Variance minima datasets. This produces a combined binary marker dataset, where only identical values (i.e., ones) are defined.

In the case where a large (homogeneous) image-object exists within the image, OSA defines this object as being composed of relatively small area values. This is because even though the extent of the object is large, it is composed of pixels that are very similar (i.e., low internal variance), thus the object-specific heuristics are met within a relatively small kernel size. This is done so that computing time is not wasted trying to define very large kernels composed of many small grain pixels. Instead the data are upscaled using an inverse area value (thus smaller areas i.e., objects are more heavily weighted as described in the OSU resampling heuristic section) and a more appropriate kernel grain is used to evaluate the persistent object(s) at the next scale.

Imbedded markers and watershed analysis
To define individual image-objects, the new (combined) marker sets were 'imbedded' within the corresponding gradient image. More explicitly, the location of each marker set was defined within the appropriate gradient image using the Matlab imimposemin function. This function modifies the intensity image using morphological reconstruction so the intensity image only has regional minima wherever the binary (marker) image is nonzero. The Matlab watershed algorithm (Vincent and Soille, 1991) was then applied to each 'imbedded' image. This resulted in the generation of 10 watershed images (W_I), each containing 'empty' polygons (five of which ($W_{2, 4, 6, 8, 10}$) are overlaid on their corresponding scale domain M_I and illustrated in Figure 5.6). Only the watershed boundaries (i.e., 'catchment basins') separating image-objects are generated by this algorithm.

Object labeling
Each pixel in the Mean images represents a member of a newly detected image-object. Since these images are generated from average values calculated within unique threshold kernels, they represent the dominant image structure defined at a specific spatial resolution within a unique scale domain (Hay et al., 2001). Therefore, each newly defined – though empty – watershed polygon is used as a mask to generate a value equal to the average of the corresponding MI pixels located within its perimeter. In essence, each watershed polygon now spatially represents the average grey-tone, and areal extent of a unique image-object. This step is referred to as object labeling and represents the automatic delineation of discrete multiscale objects in each of the five scale domains. This procedure was also applied by Hall et al., (2003) and Hall and Hay (2003).

5.3 Results

In this section, we briefly describe a number of the images resulting from OSA, OSU, and MCS that are illustrated in Figures 5.4, 5.5 and 5.6. To make visual analysis possible, these images have been resampled to a common size, and where necessary, contrast stretched.

Figure 5.4 provides an overview of how the visual information and digital size of all images in the corresponding scale domains change with upscaling. Multiscale images are often illustrated in an oblique plan view, with the smallest image on the top, and the largest on the bottom where they form a pyramidal structure. In Figure 5.4, they are presented linearly scaled in a stair case pattern, so that their spatial dimensions provide a relative comparison of their changing size through scale. As the number of pixels composing the image at each new scale domain decreases, the grain of each pixel increases, while the extent remains constant (see table 5.2). Through scale, small features including roads, hedgerows, and farmhouses disappear while larger features persist, such as extensive forested areas and agricultural fields. This occurs irrespective of whether the features are represented by bright or dark tones. The spatial extent of each image-object is its key to persistence in MOSA. However, if different neighboring image-objects are composed of similar grey-values, then through scale, these individuals merge. This is particularly evident in the dark-grey toned agricultural fields that surround the bright central (corn) field. Through scale, the smaller hedgerows that separate the individual fields 'disappear' and the fields appear to merge together (see OSU_{2-3}). Finally in U_4, they become indistinguishable from the matrix.

In Figure 5.5 in each Variance image, bright areas (i.e., high variance) define edges that represent the meeting of two or more image-objects, while dark areas (i.e., low variance) correspond to image-object interiors. In the Area images, bright values indicate that the pixel under analysis belongs to an object that is composed of many different parts over a relatively large area – thus the large analyzing kernel. This typically occurs at an edge between two or more different image-objects, while dark values represent a relatively small, more homogeneous area – thus more object like. In the Mean images, each pixel is a member of (thus an averaged value of) a new image-object that exists over a wider extent than the individual pixel. Thus, each Mean image appears blurred or more diffuse through scale.

In V_2, fields are dark, which indicates that they are composed of similar (i.e., low variance) parts, while the bright linear features (edges) that surround them correspond to hedgerows, and roads. The spatially dominant forest is represented as a (light and dark) textured structure that visually corresponds to differences in stand density (including canopy gaps and large crown structures), species and age classes.

As we move through scale, fields that exhibited similar grey-tones in Figure 5.4, and that appeared homogeneous (i.e., dark) in V_2 on Figure 5.5, become merged with their similar toned neighbors in $V_{4, 6, 8, 10}$. This characteristic is apparent in M_2, where the bright toned (corn) field is also composed of a darker lower portion. Even though this field appears relatively bright at a fine scale, through scale its darker lower section appears to merge with the darker neighboring fields (see the evolution in $M_{4, 6, 8, 10}$), while the bright upper portion

of the field appears through scale to merge with other bright fields that are located above and below it, even though they are some distance away (compare M_2 with $M_{8, 10}$).

In Figure 5.6, the gradient images have been histogram equalized to illustrate the changes resulting from subtracting each Mean image from its corresponding Upscaled image (refer to the Generating new gradient images section). Dark tones represent small differences between these two scenes, while bright tones represent large differences. By generating an absolute difference image, we are only able to detect whether or not change has occurred through scale, not the direction of change (i.e., if the change was in the M_I or the OSU_I).

The MCS Watershed Images illustrate how well the over-segmentation problem has been reduced by the new MCS methodology. Each image represents the polygonal results of MCS overlaid on their corresponding scale domain Mean image. Based on the complexity of these multiscale scenes, this methodology automatically delineates image-features that strongly correlate to image-objects as viewed by a human analyst. This visual correlation is stronger at finer scales (i.e., $W_{2, 4, 6}$) than at coarser scales (i.e., $W_{8, 10}$), due to the fact that at finer scales there are more markers. In addition, while the pre-processing of the data with a median filter removed many fine components from all the datasets, the generation of the marker sets for each scale domain (composed of AI and VI minima), represents an additional level of filtering that was not applied to the mean image nor the gradient images. Since the mean images are partially responsible for the generation of the gradient images, and the gradient images are an important component in the delineation of MCS watershed, there visually appears to be more image-objects, particularly in the coarser scale mean images than the overlaid watersheds delineate.

In each labeled MCS image, all image-objects are labeled with unique grey tone values derived from their corresponding M_I within explicit boundaries (refer to the Object labeling section). Consequently, fewer and larger, more homogeneous polygons appear as scale increases. The polygon boundary that corresponds to the large bright corn field in M_2 appears to persist in scale through the full range of watershed and MCS images; however its tonal value changes through scale as it incorporates components from its neighbors. In the top left corner of $MCS_{2, 4, 6, 8}$, the power-line right of way (displayed in G_2 as a thick dark diagonal line) appears to persist from SD_{1-4}, then merges with its surroundings at SD_5. In MCS_{10} the large dominant grey polygon in the upper portion of the image visually corresponds to the forest that dominates the upper section of the scene.

In the MCS Watershed images and labeled MCS images, the polygon lines appear to increase in thickness through scale. This is because a single pixel at a coarser scale represents a larger grain than at a finer scale. Thus when resampled (for visual analysis) to a smaller common grain size, it will be composed of more, finer resolution pixels. In these images, the dominant (wedge shaped) road structure is visible as a dividing line between different scene components in W_2 and W_4, but begins to disappear in the coarser scales. This is because the grain in SD_3 (9.72 m^2) is actually larger than the width of the individual gravel roads in the scene.

It can also be observed that several watershed polygons are not empty, but instead are filled completely in black. This is because the markers and the watershed represent the exact same size. A workaround could be to invert the watershed image, and use erosion to remove all single pixel watershed boundaries leaving only the filled watersheds (which now equal one and are slightly smaller than the original watershed), then subtract this new image from the inverted pre-erosion image, resulting only in the contours of the (previously) filled watersheds. This new contour image would then be inverted (thus the center pixels of each 'filled' watershed now equals one), and added back to the original watershed image. Thus, watersheds filled with black (zero) values would now be equal to one, and the visual impression would be that all watershed polygons were now 'empty'.

5.4   Discussion

Bottom-up and top-down scaling
Although OSA/OSU is designed as a bottom up approach to scaling, the way in which the datasets are generated, represents a fully decomposable scaling framework, similar (in principal) to the wavelet decomposition tree with its high and low resolution components (Starck et al., 1998). Therefore, not only is it possible to create coarse scale representations from fine scale components, as illustrated herein, but conceptually it should be possible to take the final M_I (which in this case is generated at SD_5) and in combination with the appropriate A_I deconvolve the preceding MI (i.e., M_{10-1}) back to the original IKONOS panchromatic input image (while allowing for minimal rounding error).

Therefore, we suggest that OSA/OSU provides not only a sound methodology for upscaling but that it also provides a pathway for downscaling (i.e., integrating image information from coarse scales to finer scales). Thus, it may be possible to take coarse scale data generated at regional scales i.e., the spatial pattern of trace gas fluxes, or the spatial pattern of net primary productivity (NPP), that geographically correspond to an area over which OSA/OSU images have been generated, and to use the A_I at each SD_n to determine the location, and weight/ percentage of the coarse scale data to be down sampled. This assumes that the OSA/OSU images generated are based on suitable data from which the surrogate measure (i.e., NPP) can be generated at from finer scales.

Scale manifolds
OSA/OSU allows for discrete levels or SD_n to been generated where each image in these sets has the same grain and extent; however, the size of the window used to determine the spatial characteristics of individual image-object in each image are of varying size. Thus, while it is simple to imagine how the images in Figures 5.4, 5.5 and 5.6 may be hierarchically layered upon each other in a manner similar to the 'scaling ladder' conceptualized in the HPDP (Wu, 1999), the reality is that in object-specific analysis the 'spaces' between the rungs of the ladder – which represent the 'optimum' scale of analysis – are not equal. Instead, they are of varying size, dependent upon the spatial characteristics of the object under analysis. Consequently, there should be a separate ladder for each image-object through scale. If this were the case, then it would be more plausible to visualize the hierarchical levels as stacked 2.5 dimensional layers or manifolds as modelled by Hay et al., (2002b). In relation to the previous discussion

on scaling, these object-specific manifolds represent a spatial scaffold between image-objects at different scales showing how components spatially evolve through scale.

5.5   Conclusion

MOSA is an integration of Object-Specific Analysis (OSA), Object-Specific Upscaling (OSU), and Marker Controlled Watershed Segmentation (MCS). This non-linear framework for automatic multiscale scene generation and feature extraction allows dominant image-objects to emerge at their respective scales, and requires no a priori scene information. In this paper, we have presented a detailed description of MOSA, provided new information on the OSA kernel, and discussed improved methods for using MCS as a feature detector. In summary, this framework also exhibits the following characteristics.

- Object-specific analysis can be applied to any digital data regardless of whether it is considered high resolution (i.e., sub-meter <5 m), medium resolution (5-30 m) or low resolution (greater than 30 m). The ability to define image-objects is dependent upon the relationship between the size of the image-objects composing a scene, the spatial resolution of the pixels that compose the image-objects, and the size/shape of the analyzing kernel. Thus, if coarse grain data are used (i.e., TM, MODIS, AVHRR), then the spatial characteristics of relatively coarse grain image-objects will be defined.
- The underlying ideas and heuristics are conceptually simple, are based upon strong empirical evidence, and follow many concepts of Complex Systems and Hierarchy theory.
- The OSA kernel represents a close approximation of an isotropic filter (i.e., a square approximation of a round kernel with no preferential orientation), thus reducing the diagonal bias common in square kernels. In addition, we have defined and incorporated three robust empirical scale-dependent threshold conditions that are representative of the pixel/image-object relationship over an explicit range of scales, thus supporting the concept of scale domains.
- OSA/OSU allows for upscaling between objects and within an image hierarchy, where it incorporates a 'generic' point spread function in relation to object size for determining an appropriate upscale resolution for the next iteration of processing (Hay et al., 2001).
- OSU takes into account the relationship between the pixel size and the image-objects from which the original OSA heuristics were developed. Thus at fine scales, results visually model known image-objects very well. Therefore, a precedent exists on which to base results at coarser unverifiable image-scales.
- OSU incorporates object-specific weights, thus minimizing the effects of the modifiable areal unit problem (MAUP).
- Land-cover classifications have been shown to improve with the addition of object-specific datasets as additional logic channels (Hall et al., 2003).
- OSA/OSU has been statistically proven to produce better-upscaling results than cubic convolution, bilinear interpolation, nearest neighbour and non-overlapping averaging (Hay et al., 1997).
- MCS is well documented in the literature, and watershed segmentation algorithms are commonly available in popular image processing packages.

- Decomposability is possible by mapping each OSA/OSU image to corresponding Mean and Area dataset; thus the ability exists for explicitly tracking information over scales in a bottom up, and top down approach.
- One of the greatest limitations of the MOSA is that it has not yet been tested over a large number of different landscapes, or by a significant number of researchers. However, further testing and validation are underway. In addition, no commercial software is available and its object modeling is done empirically. Thus, the results of multiscale analysis require validation against field data, which becomes difficult if not impossible as scales become coarser.
- While the incorporation of MCS into MOSA represents an elegant feature detection solution that capitalizes on the explicit object information inherent to the Variance, Area and Mean datasets, further refinement of automatically defined marker sets is required – particularly for coarser scale delineation.

Currently there is no integrated topological solution in MOSA for hierarchically linking and querying delineated image-objects through scale; however, an extended goal of MOSA includes not only automated object-specific feature detection, but also the classification (Hall et al., 2003) and linking of image-objects through scale (Hay et al., 2003). At present, we are developing a topological mechanism similar to that described by Hay et al., (2002b) for the linking and querying of dominant blobs (i.e., image-objects) though scale space. Once completed and implemented in MOSA, the spatial characteristics of individual image-objects can be assessed using spatial statistics and landscape metrics to evaluate how landscape components (i.e., image-objects) become fragmented and/or connected to each other through scale.

Chapter 6

Variogram Derived Image Texture for Classifying Remotely Sensed Images

Mario Chica-Olmo & Francisco Abarca-Hernández

6.1   Introduction

Geostatistical methodology has evolved considerably during the last few decades, since its beginning in the early 1970s, in which theory and practice have achieved a parallel and harmonious development. The main scientific advances made during this relatively short period have enabled a proliferation of geostatistical methods that have become more and more sophisticated and better suited to respond to new practical situations. From this viewpoint, it is striking how many, and how varied, are the scientific and technical fields in which these theoretical principles are being used to resolve complex problems related to estimation and/or simulation of spatial variables. Such problems arise from a wide spectrum of disciplines and fields of application such as geology, edaphology, forest management, environmental studies, oil and water resources, spatial economy, etc. Remote sensing also plays an important role in this activity, and since the pioneering studies that sought a link between geostatistical methods and satellite imagery (e.g. Curran, 1988) more and more research has been carried out to show the wide methodological variety of geostatistical applications in this field of remotely sensed data analysis. These applications form part of the digital processing of satellite image data, with a noticeable number of them applying variographic analysis to characterise the spatial variability of digital values. Another group of applications, no less important, are based on estimation methods for image integration and improvement of digital classification results. The common start point for all these approaches is the assumption that the digital number registered in the image is a regionalised variable in the sense proposed by Matheron (1971), i.e. it is a variable that presents a spatial distribution and a spatial variability function defined by the variogram. Today, this hypothesis is widely accepted for the spatial study of the spectral response of land cover classes, as represented in digital values of the image. Such broad-based acceptance has been gained on the basis of the satisfactory results obtained from numerous practical applications.

Texture is a visual feature of the image that is of great interest in the field of digital image processing, including satellite images. It represents tonal variations in the spatial domain and determines the overall visual smoothness and coarseness of image features (Lillesand & Kiefer, 1994). Texture provides important information about the arrangement of the objects and their spatial relationships within the image, which is a factor of great interest for photointerpretation and land cover classification. A wide variety of methodologies have been

proposed for texture analysis; among them, perhaps, one of the best known is the study of the local variation of the image brightness, such as the variance operator described by Russ (1999). This idea of creating local texture variance operators can be exploited by studying the variogram function. In such a case, we would not be just considering a single statistical parameter, as is the local variance of data within a window, but the overall information that can be derived from this geostatistical function of spatial variability. This can be achieved because the variogram is a powerful tool to analyse the spatial variability of digital values at both global (whole image) and local (window) scales. Consequently, it seems logical to consider the variogram function as the starting point from which various geostatistical texture operators calculated in a local neighbourhood could be obtained, using different types of variogram estimators.

The objectives of this work are to show the relation between the variogram function and the textural aspect of remotely-sensed images, to quantify this relationship by means of different variogram estimators and thus obtain texture images and, finally, to use this contextual information to improve the results of the remotely-sensed data classification. The main problems encountered are described and aspects for further development are suggested.

6.2 Texture and variogram

Satellite images are a particular case especially well suited for visual characterization by means of texture operators. Some well-known examples such as categorization of crops, urban regions and other land uses show distinctive textures that the interpreter can easily recognize. It is widely accepted that texture is a descriptor of the visual characteristics of an image, such as the smoothness, roughness, symmetry, regularity, etc. That is why authors have always attempted to use the results of their practical work to arrive at a qualitative definition of the textural aspect of images. For example, Picket (1970) remarked that texture could be used to describe the variations in bidimensional matrices, while Dury (1987) defined it as the frequency of tone change and the ordering within an image. Hawkins (1970) argued that the textural aspect of an image depends on three fundamental aspects:

a A local pattern that is repeated over a region (image), of sufficient size in relation to the size of the pattern;

b This pattern corresponds to a non-random arrangement of elemental constituents (pixels) and

c These constituents are uniform entities with approximately the same dimensions throughout the region. We find that although the above qualitative descriptions of texture seem reasonable, they do not, in fact, enable us to determine a simple, universal measure of texture.

Grey value variations occur at a greater or lesser frequency and intensity within the image, depending on the nature of the land cover studied. For example, in a landscape modelled by the action of runoff water, most of the high-frequency variations of digital values arise from a pattern of linear shapes caused by the effect of the fluvial network. On the other hand, the variations in digital values due to changes in reflectivity at the contact between different types of land uses are characterised as being low-frequency features. Figures 6.1$_{a-d}$

show some examples of the textural aspects provided by satellite images. Specifically, Figures 6.1$_{a,b}$ represent two subscenes of the panchromatic band of a SPOT image with a spatial resolution of 10 m. The two regions present notably different organisational aspects (texture) of grey values: the first basically shows crop distributions, while the second reveals a region with smooth changes of relief and scant vegetation. Another example is that of the Synthetic Aperture Radar images in Figures 6.1$_{c,d}$ (with a spatial resolution of 6 m), which represents a hilly area with smooth relief, and a modern urban zone, respectively. The two images are readily photointerpreted because of the marked differences in their textural aspects. These examples provide a good description of what is frequently found in satellite images, which contain regions characterised not so much by a unique value of brightness, but by a variation in brightness from one pixel to the next or within a small region. This is particularly important in satellite image photointerpretation, when visual examination of an image suggests that the basis for discriminating various structural regions (e.g. land uses) is a texture rather than the degree of brightness or even a particular colour.

It seems evident that all these descriptive features of texture have a strong loading of subjectivity and do not always have a precise physical meaning, which clearly complicates the
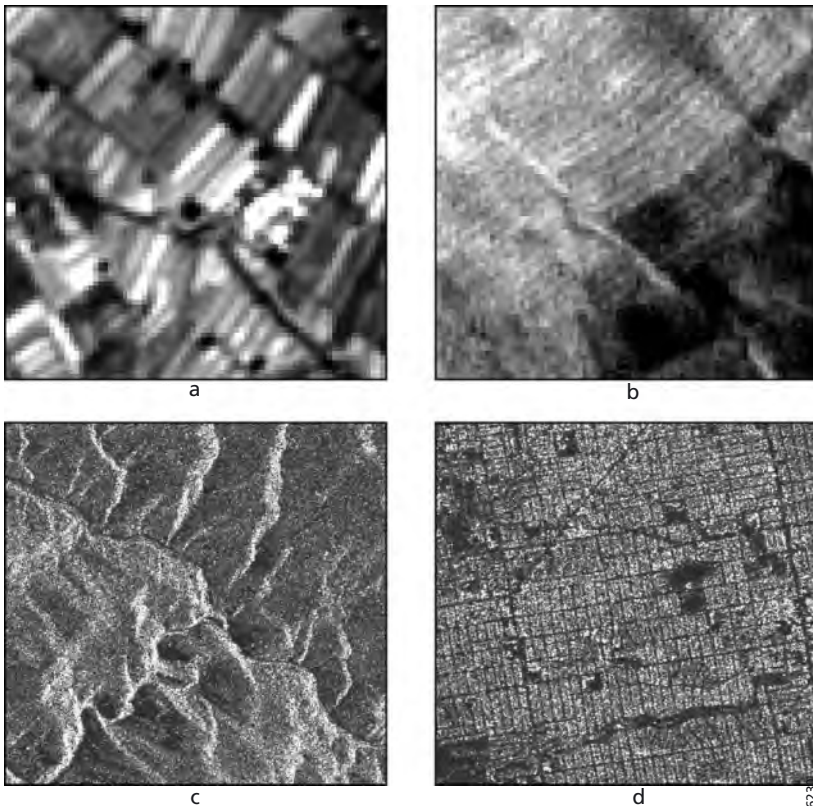
Figure 6.1 Some examples of digital images showing different textural aspects, corresponding to SPOT panchromatic (a, b) and Synthetic Aperture Radar (SAR) subscenes (c, d).

analyst's task of establishing a universal quantitative significance for this term. However, it is also correct to consider that texture of an image is related to measures of the rate of local and/ or global spatial variation of grey values. In fact, in our case, a satellite image can be viewed, in terms of relief, as a terrain model where digital numbers represent elevations in each pixel of the image. In such a situation, it would be easy to consider a quantitative concept of texture as a measure of the roughness of the relief. Thus, it would be possible to define diverse texture operators in order to obtain texture images, in which brightness represents the texture and where main regions may be distinguished and extracted according to their range of degrees of brightness. Many authors have established diverse operators in order to quantify the textural characteristics of images (Pratt, 1991; Russ, 1999). Basically, in image processing, three main groups of textural analysis methods can be distinguished: statistical, structural and spectral. The first of these characterises texture by means of global or local statistical operators depending on the grey levels of the image. It is a broad field, providing measures such as smoothness, roughness, regularity, symmetry, uniformity, etc. (e.g. histogram measures, run-lengths and co-occurrences of grey levels). Structural techniques deal with the spatial arrangement of the constituent parts within the image, and are based on measures of regularity of the spacing of parallel lines. Finally, spectral techniques are based on the Fourier transform and detect global periodicities by identifying characteristic spikes (frequencies).

Our interest lies in the group of statistical methods, particularly those that take into account the spatial relationships between pixels. Spatial statistical operators calculate the textural index over the whole image or in a local neighbourhood by means of moving windows that are displaced pixel by pixel. The value thus calculated in the window is assigned to the central pixel, using different approaches such as local statistical parameters (Sun & Qin, 1993), entropy (Haralick & Shanmugham, 1974), measures on the matrix of co-occurrence (Marceau et al., 1990; Carlson & Ebel, 1995; Molina & Chuvieco, 1996), and more recently by using geostatistical parameters based on the variogram function (St-Onge and Cavayas, 1995; Lark, 1996; Carr, 1996; Chica-Olmo & Abarca, 2000). The present work is centred on the latter methodology, in which the variogram function is used as a textural descriptor of satellite images.

6.2.1   The variogram function as a textural descriptor

Texture, in a statistical sense, may be analysed in terms of the two essential characteristics of digital values: local or global variability and spatial correlation. The first characteristic is closely related to the statistical dispersion, which is frequently analysed by calculating the variance (i.e. variance operator), a statistical measure of the dispersion of digital values with respect to the mean value, or the central pixel value, within a moving window (Woodcock & Harward, 1992). The second characteristic, spatial correlation, assumes that digital values are not completely randomly distributed within an image and, consequently, that there exists a spatial variability (or dependence) structure associated with each landcover class. In this sense, an important result was reached by Lark (1996), who showed that the amount of variability between pairs of pixels depends on their spatial relations and it can be used as a texture descriptor of each landcover class. This result leads directly to the use of the geostatistical approach for texture analysis, because it offers the advantage that both aspects are jointly analysed, as discussed below.

As remarked in the introduction, the basic hypothesis of the digital number of a remotely sensed image as a regionalized variable is now widely accepted in practice (Curran, 1988; Atkinson, 1993; Chica-Olmo & Abarca, 1998, etc.). This variable interpreted as a function $DN(x)$ provides the radiometric digital number DN of a pixel x spatially referenced by a geographic coordinate system or, simply, by raster coordinates of the image. Thus, the whole image is viewed as a particular regionalisation of the $DN(x)$ function, characterized by both random and spatial correlation aspects related to the above mentioned texture components. Under the intrinsic geostatistical hypothesis, both aspects are studied through the variogram function expressed by the classical equation (Matheron, 1971):

$$\gamma(h) = \frac{1}{2} E \{DN(x) - DN(x + h)\}^2 \tag{6.1}$$
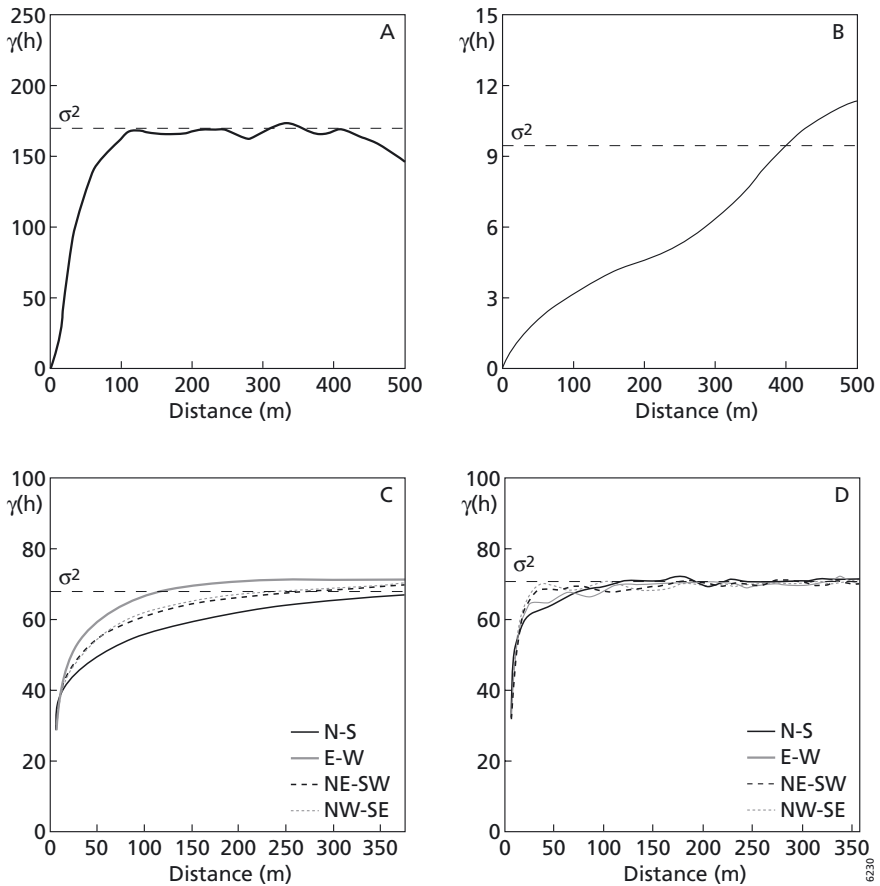
Figure 6.2 – Variograms of digital number values of SPOT (a,b) and SAR (c,d) subscenes shown in figure 6.1.

where $\gamma(h)$ represents half of the mathematical expectation of the squared differences of pixel pair values at a distance h, i.e. semivariance; $\gamma(h)$ is a vectorial function depending on the modulus and the angle of the distance vector h between the pixels $(x+h)$ and x.

The use of this function in image processing has been widely accepted because it is a powerful tool for the analysis of the spatial autocorrelation of radiometric data and, more specifically, of the spatial variability structure (Ramstein and Raffy, 1989). Variogram applications are based on the classical steps of the calculation, modelling and interpretation of the experimental variogram. Computing the variogram function does not present any difficulty, given the raster structure of a satellite image, except that computing time may be lengthy, depending on the size of the image. Variogram modelling is a step required for most geostatistical applications, i.e. spatial estimation and simulation (Atkinson et al., 1994; Dungan et al., 1994). Finally, variogram interpretation is usually focussed on relating range and sill parameters (see also chapter 4 of Atkinson), the behaviour at the origin of the variogram (nugget effect) and spatial anisotropy to the spatial distribution of the radiometric values. As noted above, texture is closely related to the spatial variability of grey values and consequently to the variogram. This relationship has been studied by different authors (Lacaze et al., 1994; Lark, 1996; Carr, 1996, etc), who consider the variogram a potentially useful descriptor of image texture and demonstrate its possibilities to identify multiscale spatial patterns. Miranda et al. (1998) found that each landcover class in an image presents a different spatial variability pattern, i.e., a different variogram. Consequently, this spatial pattern could be considered contextual information of interest for the digital classification of landcover classes.

In order to facilitate comprehension of how the variogram function characterises the textural aspect of an image, a variographic analysis was carried out on the images shown in Figures 6.1a-d. In the case of the SPOT subscenes, the omnidirectional variograms present very different aspects (Figures 6.2a, b). The variogram for the area in which crops are cultivated presents rapid growth from the origin, which indicates a strong loss of correlation at short distances (approximately 100 m, the average size of the plots). On the contrary, the variogram for the area with a flat relief presents a high degree of spatial continuity, characterised by the slow, gradual growth of the function, and by its much greater range. Obviously, this different behaviour of variograms reflects the textural differences clearly visible between the two images. In the example of the radar subscenes, the variograms were directionally calculated in the four principal directions (Figures 6.2c, d). In this case, we observe a notable geometric anisotropy of the variograms for the first sector, due to the predominantly N-S orientation of the drainage network. On the contrary, the variograms for the urban area show no significant anisotropy. The spatial correlation synthesized in the range of the variogram is greater for the first sector than for the second. This fact may be explained by the smooth variation in the brightness of the first image, in contrast to the strong local variation in the brightness of the urban texture. In both cases, the experimental variograms were fitted as the sum of two structures plus a nugget effect, the parameters of which are shown in Table 6.1. The first structure is spherical and the second is exponential. The two spatial structures are associated with different 'frequencies' of the regionalisation of the digital values. If these results are interpreted in the sense of the Fourier analysis, the nugget effect is associated with image noise, i.e. high-frequency component; the short-range spherical structure is associated with local variations, and the exponential structure with global-scale variations, i.e. low-frequency

Table 6.1 – Fitted variogram model coefficients of the Synthetic Aperture Radar (SAR) subscenes (nugget and sill values x 10^6).

SAR subscene	Nugget (C_0)	1st Structure			2nd Structure			Dispersion (%)		
		Mod.	Range (C_1)	Sill (A_1)	Mod.	Range (C_2)	Sill (A_2)	C_0/σ^2	C_1/σ^2	C_2/σ^2
1	17.0	Sph.	18.8	19.8	Exp.	351.5	33.2	24.3	28.3	47.4
2	24.0	Sph.	13.0	74.0	Exp.	138.7	30.0	18.8	57.8	23.4

component. Table 6.1 shows the important value of the nugget effect, representing intra-pixel variability, with weights in terms of global variance of almost 25% and 19% for the first and second sectors, respectively. Due to the strong degree of spatial anisotropy in the first sector, a geometric anisotropy factor of 0.4 was assumed for the second structure; in consequence, the range of the N-S direction is 2.5 times greater than that for the E-W direction. No anisotropy was detected in the first structure. An isotropic variogram model was fitted for the second sector, as there was no evidence of directional anisotropy in the experimental variograms. With respect to the analysis of the textural aspect, we should note the importance of the first spherical structure, for which the ranges in the two sectors are similar, 19 m and 13 m respectively; nevertheless, in terms of the local variation of image brightness, the percentages of variance of this first structure are very different, with the second doubling the values of the first, 28% and 58% respectively. This means that the textural aspects of the first image are determined mainly by the long-range structure, while in the case of the second image, urban area, the texture is defined by the short-range structure. This experimental finding coincides with simple visual observation of the images.

The above examples show that the variogram is a highly useful function as a textural descriptor of satellite images. This tool enables us to characterise the textural aspect of an image, both in global terms and locally, using a set of geostatistical texture operators capable of quantifying the ordering and change frequency of the digital values within a neighbourhood.

6.2.2 Geostatistical texture operators based on the variogram

One of the more commonly used texture operators in image processing is the variance in neighbourhood regions (Russ, 1999). Its calculation is simple using statistical procedures based on moving windows, from the sum of the squares of the differences between the grey value for each pixel belonging to the neighbourhood with respect to the mean value or the central pixel value. The end value can become quite large, and so the result is sometimes displayed as the mean value of the square root of this difference. For this purpose, the sum of squares is normalized by dividing by the number of pixels in the neighbourhood and then calculating the root-mean-square difference of the values. Like other texture operators, e.g. the range operator, the variance also responds to the variation of pixels in the region. It is less sensitive to the individual extreme pixel values and produces an image with less noise than does the range operator. Moreover, the variance responds to the boundaries between regions of different brightnesses and is sometime used as an edge detector (Russ, op cit.).

The variogram can be considered a generalisation of the variance operator discussed above, as it is essentially a spatial function and not a simple statistical parameter. As a vector function it depends on the distance between the central pixel and the neighbourhood pixels of first order, second order, etc.; moreover, it takes directional anisotropies into account. A further advantage of the variogram is that it can be calculated between pairs of radiometric bands, to describe the covariance between two bands of an image (cross-texture) and even between two bands of different sensors (pseudo cross-texture).

The variogram provides a great many ways of characterising the textural aspect of an image. Thus, Chica-Olmo & Abarca (2000) proposed a set of geostatistical texture operators (GTO) based on the variogram, some of which consider the cross relations between pairs of bands. Specifically, the following functions may be used as simple and cross operators: simple variogram, madogram, rodogram, cross and pseudo-cross variogram (Chica-Olmo & Abarca, 2000, Deutsch & Journel, 1992; Myers, 1991 and Wackernagel 1995).

i) Simple variogram (SV)
The statistical inference of the direct variogram is obtained from the estimator of equation (1):

$$\gamma_k(h) = \frac{1}{2n(h)} \sum_{i=1}^{n(h)} \{DN_k(x_i) - DN_k(x_i + h)\}^2 \qquad (6.2)$$

where $n(h)$ is the number of distant pairs h, $DN(.)$ are the digital values of pixels x_i and x_i+h, and k is the sensor band.

ii) Madogram (MA)
This is similar to the direct variogram but instead of square differences the absolute difference is taken (Deutsch & Journel, 1992). This function is equivalent to the first-order variogram (Matheron, 1982):

$$\gamma_k(h) = \frac{1}{2n(h)} \sum_{i=1}^{n(h)} |DN_k(x_i) - DN_k(x_i + h)| \qquad (6.3)$$

iii) Rodogram (RO)
This is also similar to the direct variogram, but considers the square root of the absolute difference instead of squared differences:

$$\gamma_k(h) = \frac{1}{2n(h)} \sum_{i=1}^{n(h)} \sqrt{|DN_k(x_i) - DN_k(x_i + h)|} \qquad (6.4)$$

iv) Cross variogram (CV)
This is a bivariate function that quantifies the joint spatial variability (cross correlation) between two bands. It is defined as half of the average product of the h-increments relative to the radiometric bands *j, k:*

$$\gamma_{jk}(h) = \frac{1}{2n(h)} \sum_{i=1}^{n(h)} \{DN_j(x_i) - DN_j(x_i + h)\} \cdot \{DN_k(x_i) - DN_k(x_i + h)\} \qquad (6.5)$$

v) Pseudo-cross variogram (PV)
This considers the variance of the cross increments instead of the covariance of the direct increments as above:

$$\gamma_{jk}(h) = \frac{1}{2n(h)} \sum_{i=1}^{n(h)} \{DN_j(x_i) - DN_k(x_i + h)\} \cdot \{DN_j(x_i) - DN_k(x_i + h)\} \qquad (6.6)$$

The specific contribution of each type of variogram regarding the spatial pattern recognition in an image depends on each land cover studied, but is basically related to the meaning given by the above equations. Although all types of variogram are fairly similar, because all of them quantify the spatial variability of the digital values, nevertheless, there are some differences between them. Three are univariate functions and the other two are bivariate functions. In the univariate case, two functions use absolute differences (madogram and rodogram) and another is based on quadratic differences to highlight the texture contrast (simple variogram); they all provide an adequate representation of the observed spatial variability according to Carr (1996) and Miranda et al. (1998). The cross functions measure the variance of the differences between two radiometric bands (cross-variogram) and the variance of the cross differences of two radiometric bands (pseudo cross-variogram). Deutsch & Journel (1992) provide a more detailed description of measures of spatial variability based on the variogram of interest for elaborating new geostatistical operators for textural analysis.

These texture operators are of considerable interest for applications of supervised digital classification of images. This is illustrated by a geological example in which these spatial variability operators are used to construct synthetic images that represent the textural character of various lithologies outcropping in the study area.

6.3   Calculating geostatistical texture images

6.3.1   Using variogram-based texture operators
In a practical sense, any algorithm of texture operators must be easy to implement in the computer. In the case of variogram-based texture operators this is easily achieved, by means of simple algorithms designed to operate in moving windows, which assign the value derived to the central pixel. The process should consider aspects such as the number of sensor bands selected, the window size, the overlap between adjacent windows, the lag distance and direction(s) of the calculation, as is shown in Figure 6.3. Thus, a set of geostatistical texture images (GTI) is obtained by computing geostatistical texture operators (GTO) within a neighbourhood using moving windows. Selection of the window size is a practical problem that must be resolved by empirical criteria. Previous experience has shown the convenience of obtaining a window size that is not too large (to limit computing time and to avoid the influence of the texture features of adjacent landcover classes) but not too small (otherwise a robust variogram estimator would not be obtained). Several trials with different window sizes (e.g. 3 by 3, 5 by 5, 7 by 7 and 9 by 9 pixels) must be made for each particular case. The
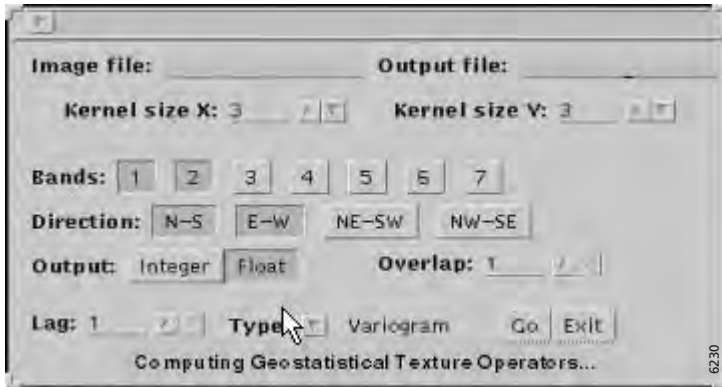
Figure 6.3 – Graphic interface of the computer program used for calculating geostatistical texture images based on the variogram function.

variogram functions are calculated for each of these windows and for each one a single value is selected and assigned to the central pixel of the window. Concerning the specific lag *h* that should be used in calculating geostatistical texture images, there is no simple, general principle that can be applied. Assigning the values of these functions to the central pixel for only one lag distance might mean the application is not making maximum use of the available information, but it would be impractical to use all the possible values of the semivariances calculated in the moving window, due to factors such as the computing time and the similarity of values for closed semivariance lags. For instance, for a 7 by 7 window size, only 3 lags are available and probably lag h=1 is the most important because it is the one that best describes the radiometric differences in the immediate neighbourhood of the central pixel. Clearly, this aspect needs to be taken into account in order to optimise the information provided by the variogram estimators. Another interesting possibility is to use the variogram slope calculated from lags h = 1 and 2.

Another topic that must be considered is the use or otherwise of directional variograms. This option is significant when the spatial distribution of DNs reveals anisotropy in the main directions (N-S, E-W, N45E, N45W) as shown in Figure 6.2. Nevertheless, the use of directional variograms would require a greater effort, given the number of possible directions and the number of types of variograms. For example, with the four main directions and the five types of variogram, a set of 20 GTI would be obtained. In practice, the omnidirectional variogram could be applied, in particular when lag h=1 is used, because anisotropy is usually imperceptible for this lag.

Figures 6.4$_{a-c}$ show a set of geostatistical texture images corresponding to three different estimators: simple variogram, cross-variogram and pseudo cross-variogram, calculated on the principal components PC1 and PC3 of a Landsat TM image. It is noticeable that each texture image shows a different aspect related to the specific local spatial variability of the single or cross variables used.

a) Simple variogram

b) Cross variogram

c) Pseudo-cross variogram
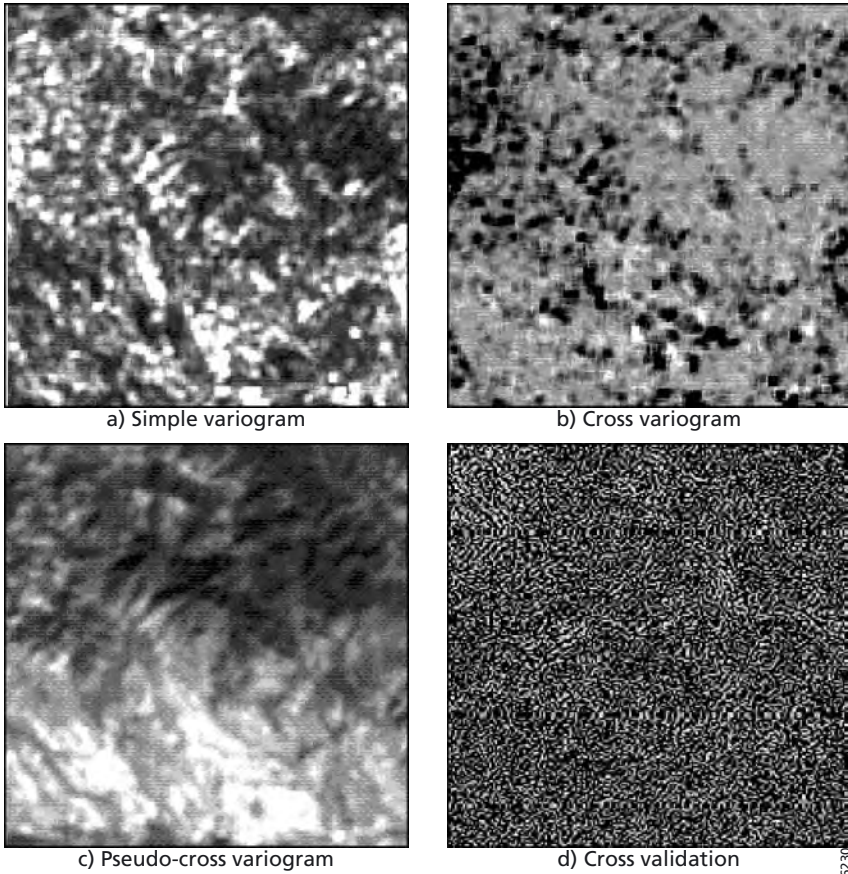
d) Cross validation

Figure 6.4 – Some examples of geostatistical texture images (GTI) calculated from PC2 and PC3 principal components of a Landsat TM image: a) simple variogram, b) cross variogram, c) pseudo-cross variogram and d) cross validation method.

6.3.2   Using the cross validation method

Another way to use the variogram function to produce texture images is by using the geostatistical technique of cross validation, based on the well-known method of ordinary kriging (Matheron, 1971). The procedure is simple and consists of estimating the central pixel value in a window, $DN(x_o)$, from its neighbours $DN(x_i)$, with the peculiarity that the central pixel does not intervene in the estimation process. The procedure, based on a moving window, is repeated for all the pixels of the image producing as a result an image of the experimental or validation errors (as well as the theoretical errors). The main hypothesis is that the experimental error calculated $\varepsilon(x)=[DN*(x)-DN(x)]$ is a textural measure of the image. This assumption seems justifiable, because an image with a homogeneous degree of brightness is better restored, that is, smaller experimental errors are produced and these have a lower degree of dispersion, than an image with marked local grey-level variations. The validation error reflects the contrast between the experimental value of the central pixel and the most

probable value deduced from its neighbourhood (kriging estimator). The experimental error image (i.e. texture image) thus constructed depends on the spatial variability characteristics of the pixels (i.e. variogram function) and the estimation neighbourhood. The main statistical characteristic of the resulting image is a normal distribution with mean $E[\varepsilon(x)]=0$ and variance $E[\varepsilon(x)]^2=\sigma_k^2$ (kriging error).

As stated above, the method uses the kriging estimator of the digital number in the pixel x, $DN^*(x)$, calculated as a linear combination of the n experimental values of the neighbourhood, $DN^*(x_o)=\Sigma\lambda_i DN_i(x)$. The weights λ_i assigned to the neighbourhood values are optimally obtained by minimising the error variance. This aspect leads us to the kriging system as it is described by Atkinson in section 4.3.5 of chapter 4 (equation 4.15 and 4.16). As can be seen, an optimal joint use of the experimental information represented by the image $DN(x)$ and the structural information provided by the variogram $\gamma(h)$ is applied in the method. Figure 6.4$_d$ shows an example of texture image obtained by cross validation, corresponding to the principal component PC2 of a TM Landsat image obtained from a neighbourhood of 3 by 3 pixels.
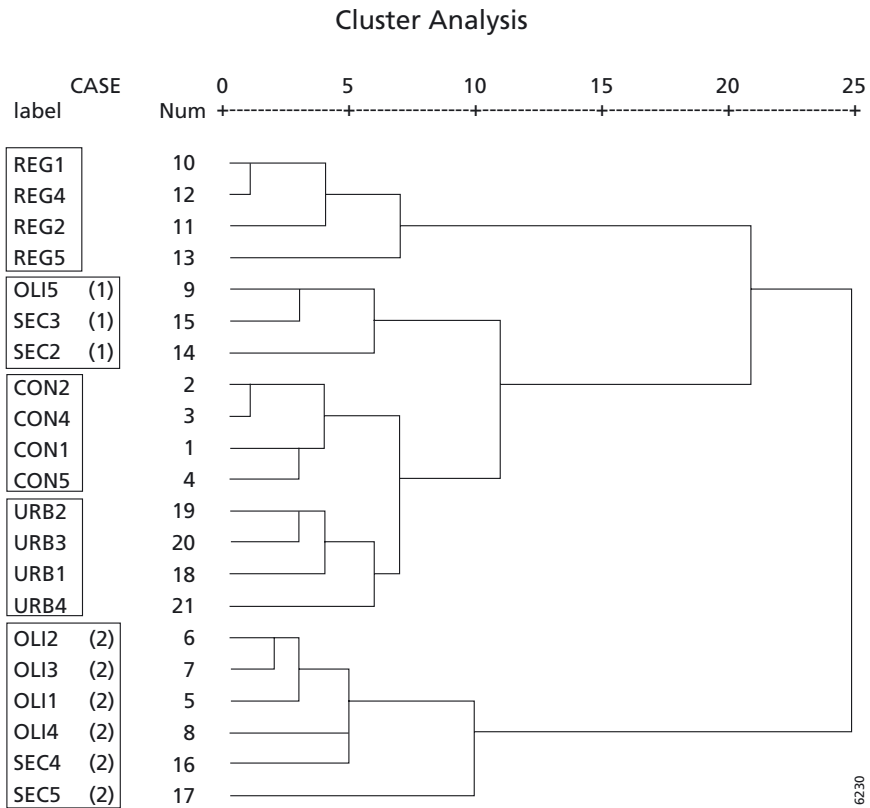
Figure 6.5 – Cluster analysis of a set of training areas based on geostatistical parameters deduced from variogram modelling of the radiometric bands of a Landsat TM image. The clustering shows an arrangement of the training sites in the main thematic classes.

6.4   Using the variogram function in Remotely Sensed image classification

We have seen how the variogram function is a powerful tool to analyse the local spatial variability of digital values in remotely sensed images. This function is used directly or indirectly (cross validation) to obtain texture images, which are of interest as contextual information to improve the results in supervised digital classification. In this respect, it is interesting to note that the information contained in the variogram, can assist in the prior task of training area characterisation, helping to separate thematic classes before the digital classification algorithm (e.g. the maximum-likelihood rule) is applied. Figure 6.5 illustrates this aspect with reference to a land cover classification study. The results are derived from a cluster analysis of a set of training areas corresponding to five thematic classes. The variables used for the clustering are the parameters obtained exclusively from the variogram modelling step, i.e. nugget effect, slope at the origin and sill, corresponding to the radiometric bands of the Landsat TM sensor and to those transformed by principal component analysis (PCA) of each training site. Looking these results we can conclude that thematic classes present differentiated spatial variability structures, which leads us to admit the possibility of a variographic characterisation of the training areas; indeed, this variability facilitates the identification of some mixed classes. Consequently, it seems reasonable that this interesting information concerning the spatial variability, expressed in terms of texture images, in addition to the radiometric data, should improve the classification results obtained.

6.4.1   An example of using geostatistical texture images in supervised digital classification

Geological setting
The use of geostatistical texture images in supervised digital classification is illustrated by the results of an application in a pilot area in the province of Almería (SE Spain). This is an area often used for mineral prospecting related to gold and lead-copper-zinc polymetallic sulphur deposits. In geomorphologic terms, the relief shape is conditioned by the structure and nature of the outcropping volcanic materials (domes, calderas and volcanic flow). Also characteristic are the flatlands of Quaternary deposits, resulting from the erosion of these volcanic rocks in a Mediterranean, semi-arid climate. The volcanic outcrops in the area are mainly Neogene of a calco-alkaline nature, varying between andesites and rhyolites. The materials are affected, to a greater or lesser extent, by hydrothermal alteration processes, favoured by the presence of fractures and fissures, associated with significant mineralisations of gold and polymetallic sulphurs. The predominant volcanic rocks in this sector sometimes present similar mineral compositions, although the structural and textural aspect derived from the formation process is well differentiated; subvolcanic intrusions, ignimbrites, coladas and flows of volcanic material, domes, etc. Moreover, there are important outcrops of Tertiary materials, mainly comprising reef limestones and Quaternary deposits. In total, six lithologic classes were studied and are represented in the geologic map in Figure 6.6.

Radiometric information
A Landsat TM subscene obtained on 7 July 1991 was selected for the study, in which a target area sized 230 by 260 pixels (around 55 km²) was selected. Radiometric information
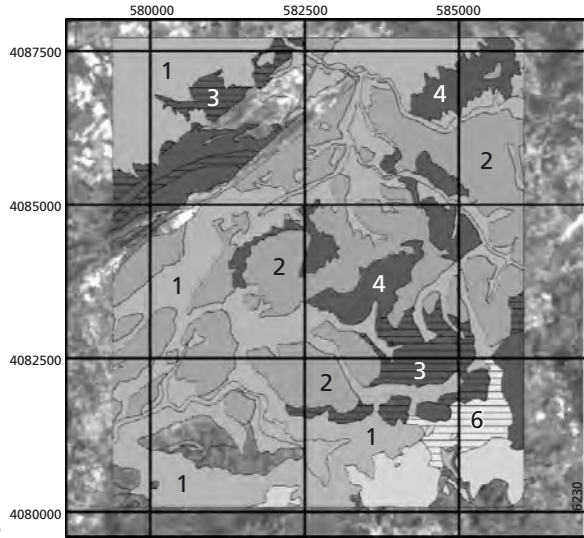
Figure 6.6 – Lithologic map of the study area. Please consult the enclosed CDROM for a full colour version.

is constituted, basically, of the set of TM bands (the TM6 thermal band was discarded); in addition to these spectral data, a principal components analysis (PCA) was performed, in order to characterise and highlight the main spectral properties of the lithologic classes being studied. The new bands were obtained using the Feature Oriented Principal Components Selection (FPCS) method proposed by Crosta & McMoore (1989). By this technique, the weights of the eigenvectors are examined to determine the principal components that are best related to the theoretical spectral data of the thematic classes studied, which in the present case are the lithologies.

The results of the principal component transformation of the TM bands did not unequivocally separate the geologic aspects of interest related to iron oxides and hydrothermal alteration (hydroxyl) and so, two groups of bands representative of the spectral information of the geologic aspects above referred were chosen. The TM1, TM3, TM4 and TM5 bands were used to analyse iron oxides and the TM3, TM4, TM5 and TM7 bands were used for the analysis of hydrothermal alteration minerals. Interpretation of the two groups of eigenvectors obtained from the calculation of the principal components was carried out separately (Table 6.2). In each case, the first component was interpreted as the albedo image, in which all the bands had a positive weight. In the first group of bands, PC2 contrasted the ferrous minerals with a high weight of TM5 and the low one of TM4. PC3 contrasted the iron oxides with a high weight of TM1 and the low one of TM3. The second group of bands revealed spectral data on the alteration minerals. PC2 showed the contrast between the visible red and the near infrared, on the one hand, and the mid infrared on the other; it also highlighted the ferrous minerals with a high weight of TM5 and a low weight of TM4. In particular, PC3 with a high weight of TM7 and a low weight of TM5 contrasted the alteration minerals. In order to simplify the study, a representative component of each group, PC2 and PC3, respectively,

Table 6.2 – Principal Component Analysis of the two groups of TM bands used for mineral characterisation: a) iron oxide and b) hydroxyl. The eigenvector loading of the first three components is shown.

(a)	PC₁	PC₂	PC₃	(b)	PC₁	PC₂	PC₃
TM1	0.404	-0.617	0.655	TM3	0.402	-0.681	0.277
TM3	0.438	-0.349	-0.416	TM4	0.369	-0.482	-0.493
TM4	0.394	-0.188	-0.592	TM5	0.731	0.527	-0.327
TM5	0.700	0.680	0.217	TM7	0.409	0.163	0.757

was selected to highlight the properties of interest of the geologic materials in the study area. Thus, in addition to the TM radiometric data, we had these two extra synthetic bands from which geostatistical texture images will be obtained.

Acquiring the texture images and performing discriminant analysis
The texture information deduced from the variogram was obtained following the above criteria described for TGO and the cross validation method for the PC2 and PC3 components. In the first case, a moving window of 7 by 7 pixels was used; this size produced the best results in the different tests carried out. As a result, a set of texture images was obtained by assigning the following function values to the central pixel of the window: simple variogram (SV), madogram (MA), rodogram (RO), cross variogram (CV) and pseudo-cross variogram (PV). Because vector functions were used in every case, a lag of h=1 pixel (30 m) was arbitrarily selected as representative of the inter-pixel variation within the window, calculated as the mean value of the four principal directions (NS, EW, N45W and N45E).

For the two principal components, PC2 and PC3, a total of 8 texture images (6 simple variograms and 2 cross variograms) were obtained for each of the six lithologies. This number of complementary synthetic bands seems high, and they probably contain redundant information, especially in the univariate operators. The multivariate statistical technique of discriminant analysis is appropriate for analysing the most relevant texture images, with respect to the goal of digital classification. For this purpose, discriminant analysis is applied to a group of randomly selected pixels in the training areas corresponding to the outcropping lithologic classes. In the present case, each pixel selected has a total of 14 variables: 6 TM bands and 8 textural measures of spatial variability. The results of the discriminant analysis shown in Table 6.3 reveal various interesting features. As expected, there is a marked increase in the percentage of accuracy classification with the joint use of spectral information (TM bands) and texture information (GTI). The contribution of texture information in relative mean terms is around 33%, but on occasion it reached 60%. A surprising factor is the significant weight of the cross variograms in the improvements observed, equivalent to the sum of the weights of the univariate functions (SV, MA and RO). This could be interpreted in the sense that these univariate functions transmit texture information that is similar, and therefore partially redundant. On the other hand, the use of combinations of texture operators was seen to double the precision of using just a single operator, with mean values of 45.7% and 20.8%, respectively. This seems to indicate the existence of a certain synergy between texture images.

Supervised classification

The above results were applied to perform a supervised classification of the image, following the maximum-likelihood decision rule, expressed in the following equation (Erdas, 1997):

$$D = \ln(a_c) - [0.5 \ln (|Cov_c|)] - [0.5 (X - M_c)^{\mathrm{T}} (Cov_c^{-1}) (X - M_c)] \tag{6.7}$$

where D is the weighted distance of a class, c is a particular class, X is the vector of measures of the candidate pixel, M_c is the mean of samples of class c, a_c is the a priori probability that a pixel candidate will belong to class c, Cov_c is the matrix of covariance of the pixels in the sample from class c, $|Cov_c|$ is the determinant of Cov_c, Cov_c^{-1} is the inverse of Cov_c, ln is the natural logarithm, and T is the transposition function.

The aim of this classification is to compare the results of standard classification methods, using only the TM bands, with those in which texture information from GTI images is added. Two different situations were considered: firstly, using a combination of the best texture operators, i.e. simple variogram (SV) and the madogram (MA) of the two principal components, and the cross variogram (CV) and the pseudo cross variogram (PV) between

Table 6.3 – Results of discriminant analysis of the lithologic classification adding variogram–based textural information (GTO) to the radiometric TM bands (SV, simple variogram; MA, madogram; RO, rodogram; CV, cross variogram and PV, pseudo-cross variogram).

Bands combination	Number of bands	accuracy (%) Overall	accuracy (%) Relative	Bands combination	Number of bands	accuracy (%) Overall	accuracy (%) Relative
TM	6	41.0	–	TM+SV+MA+RO	12	53.6	30.7
TM+SV	8	42.8	4.4	TM+ CV+PV	8	54.2	32.2
TM+MA	8	52.4	27.8	TM+CV+PV+MA	10	62.6	52.7
TM+RO	8	52.4	27.8	TM+CV+PV+RO	10	62.6	52.7
TM+CV	7	48.8	19.0	TM+CV+PV+SV+MA	12	65.7	60.3
TM+PV	7	51.2	25.0				

Table 6.4 – Results of supervised classification in the training areas using: a) TM bands, b) TM bands and the best combination of geostatistical texture operators (GTO) and c) TM bands and cross validation method. Data show the percentage of pixels correctly classified and the relative accuracy for each lithologic class.

Lithology	TM (%)	TM+GTO (%)	Relative accuracy (%)	TM+C_V (%)	Relative Accuracy (%)
Anphibole dacite	72.2	94.8	31.3	89.2	23.5
Anphibole andesite	56.3	85.3	51.5	67.0	19.0
Rhyolite	87.1	90.5	3.9	95.5	9.6
Altered volcanic rocks (rhyolite and andesite)	87.3	99.3	14.0	96.3	10.3
Reef limestone	77.1	90.7	17.6	91.7	18.9
Quaternary deposits	77.4	91.9	18.7	87.1	12.5
Average	75.6	91.9	22.8	87.8	15.6

these principal components. In the second situation, the texture image obtained from the cross validation was used.

The supervision step was performed for 41 similarly-sized training areas for which ground-truth data was recorded for the set of lithologic classes classified. These training areas were established in a field reconnaissance campaign in which radiometric data (GER 2100 spectroradiometer) and petrologic samples were gathered and analysed. The training areas, in total, represented 3% of the surface area studied.

a) TM data classification   b) TM + GTO data classification
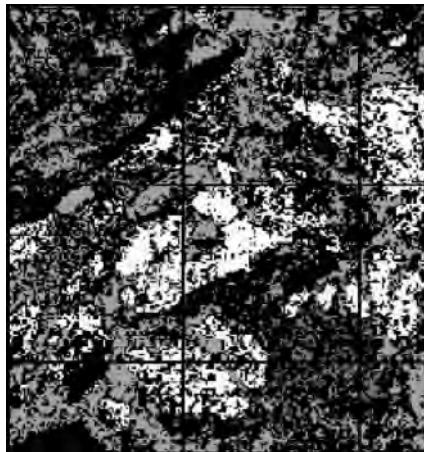
c) TM + cross validation data classification

Figure 6.7 – Classified images of the study area: a) TM bands, b) TM bands and geostatistical texture operators and c) TM bands and cross validation method. Please consult the enclosed CDROM for a full colour version.

The main results are shown in Figure 6.7a-c as classified images and synthesised in Table 6.4, which shows the percentages of pixels correctly classified in the training areas. A simple analysis of these results enables us to compare the standard classification using the TM bands with that obtained by adding texture images, derived from the variogram and the cross validation. These data show that the increase in the accuracy rate is very acceptable, as was foreseeable from the results of discriminant analysis. In the case of using variogram-based operators, GTO, the improvements in the classification results varied depending on the lithologic type. The values ranged from an improvement of 51% for the amphibolic andesites to one of only 4% for the rhyolites, with a mean value of the improvement of about 23%. Moreover, the textural information derived from cross validation improved the results of TM classification, with a mean value for the whole group of lithologies of 16%. In this case, also, the results depend on the lithologic classes.

6.5   Conclusions

The texture information obtained from satellite image processing is not only useful for interpreting the main features of the image, but also as contextual information for digital classification purposes. The present contribution shows that geostatistical analysis of the spatial variability of satellite images provides significant textural information that markedly improves the results of supervised digital classification obtained by classical methods.

Geostatistical methods, by means of the variogram function, offer a wide range of possibilities to analyse the textural aspect of an image from the general viewpoint of the spatial variability of the digital values in moving windows. Both the variogram-based operators, TGO, and the cross validation method allow us to create texture images that, added to the data from radiometric bands, improve the results of supervised classification. In this sense, the results clearly show the advantages of using texture images as contextual information to improve the results of supervised classification. The average improvements are around 23% using TGO and 16% for the cross validation method. The difference between the two values may be due to the fact that, in the case of TGO, a group of 4 texture images were used, while only one was used in the cross validation case. The extreme values observed are surprising, and we assume they are due to the physical and textural characteristics of these outcropping rocks. The present results were found to be dependent on the image characteristics and, particularly, on the thematic classes studied. As for any experimental work, it would be advisable to test the validity of the present results by studying other areas with different thematic and textural characteristics from those used in the present study. This aspect of thematic class dependence makes it difficult to generalise on the extent to which the improvement in the results could be achieved in other studies. Nevertheless, what is predictable is that the results would be improved in those cases in which the thematic classes present differences in their spatial variability structures (variograms). Moreover, the applications must always be oriented, that is, the texture images should be obtained from the bands that are of greatest interest; alternatively, as in the example discussed, principal components should be used to obtain a better spectral characterisation of the thematic classes. In an operational context, during definition of the training areas, variographic analysis offers excellent information

on the separability of the thematic classes and provides an initial evaluation of the spatial information that can be obtained from calculating the TGO operators.

Due to the quantity of texture images that can be obtained from the TGO, it is important to apply a prior discriminant analysis in order to evaluate the contribution of each of the TGO to class separability. Thus, it is a simple matter to select the operator or combination of operators of greatest interest for the supervised classification phase.

Another aspect is evident in the results obtained: the supervised classification shows that the incorporation of TGO into the classification produces more homogeneous results than those obtained only from the radiometric values of the TM bands. Furthermore, cross validation, a method that is straightforward to apply, produces very interesting results; indeed, for some thematic classes, it improves on those obtained with TGO, although in general terms of the treated image, the results are inferior to those obtained with the TGO combination applied.

Finally, perhaps, one of the most rewarding features arising from this study is the usefulness of the cross textural operators, i.e. cross variogram and pseudo-cross variogram, based on using two different types of information (bands). This aspect could open a new dimension in the texture analysis of multispectral satellite images, one of great interest that has yet to be investigated in depth.

Chapter 7

Merging Spectral and Textural Information for Classifying Remotely Sensed Images

Süha Berberoglu & Paul J. Curran

7.1 Introduction

Remotely sensed land cover information is used among other things to help

i   Understand relations between land cover and key environmental variables (Townshend, 1992; Curran et al., 1997);

ii To enable modelling and prediction of environmental changes at the landscape scale (Anderson et al., 1976; Singh, 1989; Yuan et al., 1998); and

iii To devise and monitor policies for sustainable use of the environment (Running et al., 1995; Verstraete et al., 1996).

However, the production and updating of land cover maps with remotely sensed data becomes problematic if the environment varies over a wide range of spatial frequencies (m to km) (De Jong & Burrough, 1995). A landscape with a variety of spatial frequencies results in a complex remotely sensed scene that an image at one spatial resolution is unable to capture. Fortunately, when using the more common types of satellite sensor imagery some of the unresolved spatial frequencies are coarser than those of the spatial resolution. Therefore, where different land cover classes are not spectrally separable in the remotely sensed data the accuracy of a land cover classification may be increased through the use of spatial (i.e., textural) information (Berberoglu et al., 2000; De Jong et al., 2001).

The finer the spatial resolution of a remotely sensed image the greater the potential number of spatial frequencies within that image. Not surprisingly, therefore, the new sources of fine spatial resolution imagery have increased the amount of information attainable for the classification of land cover at local and regional scales (Aplin et al., 1997). Satellite sensor imagery with spatial resolutions of around 1 m in panchromatic mode and around 4 m in multispectral mode are now available widely. Associated with this increase in available spatial resolution is, commonly, an increase in the internal variability that can be recorded within remotely sensed land cover parcels. This internal variability can lead to decrease in per-pixel classification accuracy for spectral based classification methods (Cushnie, 1987; Townshend, 1992). As a result of this, traditional image classification techniques will need modification if they are to fully exploit the benefits of fine spatial resolution remotely sensed data.

Synergy between spatial variability (e.g., texture) and spectral brightness (e.g., tone) has great potential to overcome the problem of misclassification of land cover in fine spatial resolution

imagery (Stein et al., 1998). Image texture can be derived using first order measures (such as standard deviation, variance, mean), second and third order measures (such as the co-occurrence matrix) and geostatistical measures (variogram) (table 7.1). In addition, it may be preferable to classify the spatial units comprising the scene (land cover parcels or fields) rather than the arbitrary spatial unit of a pixel.

The aim of this chapter is to investigate the utility of two groups of changes to traditional land cover classifiers (Maximum Likelihood (ML) and Artificial Neural Networks (ANN)). First, the use (along with tone) of texture derived from both a co-occurrence matrix and geostatistics (such as the variogram and variance) and second, their application in both a per-pixel and per-field format.

7.2   Background

Haralick (1979) gives the following definition of texture '*Image texture is described by the number and types of its primitives and the spatial organisation or layout of its primitives. The spatial organisation may be random, may have a pairwise dependence of one primitive on a neighbouring primitive, or may have a dependence of a primitive at a time. The dependence may be structural, probabilistic or functional*'. For our purposes, texture is a measure of the spatial variation of digital image spectral brightness or digital number (DN). There are many fields of image processing in which texture plays an important role, such as medical diagnostics (Gibson & Gaydeck, 1995), food science (Basset et al., 2000) and industrial pattern recognition (James, 1987).

Textures can be divided into two types: deterministic and stochastic. Deterministic texture is regular, (e.g., a mosaic) and the displacement of primitives can be described by rules. Stochastic texture is characterised by statistical measures or by texture models (Haralick, 1979). The estimated coefficients of these models are used as texture features as they give indication of roughness, smoothness or regularity of objects. Stochastic texture has long been used for the visual identification of land cover types on aerial photographs (Kaiser, 1955; Lark, 1996) and radar imagery (Kurvonen et al., 1992). However, stochastic texture with spectral brightness (tone) is used increasingly in the analysis of satellite sensor imagery (Shih & Schowengerdt, 1983; Lee & Philpot, 1991; Palubinskas et al., 1995; Ryherd & Woodcock, 1996). To do this the output image generated by a texture measure (e.g., standard deviation of a pixel matrix) is incorporated as an additional band together with multispectral bands. Such an approach utilises only one of Rubin (1990) refer to as the three basic components of texture. The first component is local contrast, the difference in brightness between adjacent light and dark areas: high local contrast has a rough texture and low local contrast has a smooth texture. The second component is size of the light and dark areas: coarse and fine are used to describe the size of these areas. The last component is the preferred orientation of the light and dark areas. If there is no preferred orientation and the light and dark areas are equidimensional, then the texture is isotropic but, if the areas are consistently longer in one direction than in another then the texture is anisotropic. Algorithms are available that can capture one, two or all components of image texture. When quantifying texture in remotely sensed imagery decisions are needed not only in relation to the algorithm, but

also the remotely sensed imagery, classifier and quantisation level. In the following sections we will review traditional and more recent texture measures (variance, co-occurrence matrix, variogram) and combine these texture data with radiance data prior to classifying with ML and ANN in both per-pixel and per-field formats.

7.3   Texture measures

Four groups of techniques have been used to extract textural information from remotely sensed images (table 7.1). We will use three in this chapter variance (first order), co-occurrence matrix (second order) and the variogram.

Variance
Variance, the average squared deviation of a set of values around a mean, is an important descriptive statistic with many applications in inferential procedures. The formula for sample variance (s^2) is as follows:

$$s^2 = \frac{\sum (X_i - \bar{X})^2}{n-1} \tag{7.1}$$

This is simple to calculate, does not require a large window but is sensitive to noise (e.g., erratic values).

Grey level co-occurrence matrix
This group of texture measures does not use a window of pixels rather, it uses on the co-occurrence matrix (Haralick, 1979) to quantify textural variation (Sonka et al., 1993). It has been applied in several remote sensing applications (Connors et al., 1984; Argenti et al., 1990; Dreyer, 1993; Augusteijn et al., 1995; Dikshit, 1996; Bruzzone et al., 1997). The matrix records the number of pixels with a grey scale i which are separated from pixels with a grey scale j by a particular distance and direction. For an image I(x, y) (i.e., the grey-level set) and a transition vector $\delta=(a, b)$:

$$P_\delta (i, j) = P (I (x, y) = i, I (x + a, y + b) = j) \tag{7.2}$$

The estimation is made by counting all occurrences of such transitions in the image, and dividing it by the number of pixels in the image. Thus, it can provide a statistical description of the relation between neighbouring pixels, which is an advantage over first order statistics (Sali & Wolfson, 1992). From these matrices fourteen features have been used for the quantification of texture (Haralick et al., 1973). Six of the more commonly used texture measures derived from co-occurrence matrix were used here and these were selected on the basis of recommendations in the literature (Irons & Petersen, 1981; Dawson & Parsons, 1990; Dikshit, 1996; Wood, 1996; Kaminsky et al., 1997; Narasimha Rao et al., 2002) (table 7.2).

Where i, j are the grey levels of paired pixels and $P(i, j)$ are the probabilities of co-occurrence. This (and the variance approach to texture quantification) presents texture as a single value, so

Table 7.1 – Major texture analysis techniques used in remote sensing.

Texture measures in remote sensing	Advantages	Disadvantages	References
First order statistics Standard deviation, Variance.	• Simple to calculate • Indicates local variance	• No directionality (isotropy, anisotropy) • No distance function (relation between different pixels) • Sensitive to noise	Forest mapping (Arai, 1993) Local variance at different spatial resolutions (Woodcock & Strahler, 1987)
Second order statistics Co-occurrence matrix Contrast, Angular second moment, Correlation, Entropy, Dissimilarity, Homogeneity, Sum average, Sum variance, Sum entropy, Difference variance, Difference entropy, Information measures of correlation, Maximum correlation coefficient.	• Describe relation between different pixels (regionalised variables) • Sensitive to directionality • Insensitive to noise • Does not over-emphasise field boundaries	• Computationally intensive • Similarity among the statistics derived from co-occurrence matrix	Introduction (Haralick et al., 1973) Vegetation classification (Dikshit, 1996) Land cover mapping (Marceau et al., 1990) Forest regeneration (Luckman et al., 1997)
Geostatistics Variogram, Correlogram, Covariance function, General relative variogram, Rodogram, Madogram, Pairwise relative variogram.	• Provides different scene measures (sill, range, nugget) • Sensitive to directionality • Insensitive to noise • Robust • Mathematically simple • Underlying assumptions not rigid • Requires mean be weakly stationary • Easy to interpret	• Computationally intensive • Large data set required to fit a variogram model • One 'unusual' DN value causes misquantification of all surrounding pixels	Radar image texture (Carr, 1996; Miranda et al., 1996, Rubin, 1990) Optical image texture (De Jong & Burrough, 1995; Hay et al., 1995) Spectral/spatial combination (Van der Meer, 1994; 1996) Biomass (Atkinson & Curran, 1995; Dungan, 1995) Optimum sampling in image data (Atkinson & Curran, 1997; Ramstein & Raffy, 1989; Van der Meer, 1997) Optimum sampling in ground data (Webster et al., 1989; Atkinson, 1995; Hedger et al., 1996; Cetin & Kirda, 2003)
Fractals	• Utilises multi-spatial resolution data • Can quantify roughness • Computationally not intensive • Uses spatial units larger than pixels	• Some methods for assessing fractal dimension result lumped values for entire image rather than spatial pattern. • Noise has severe effect on this assessment.	Introduction (Burrough, 1981) Vegetation and topography (Bian & Walsh, 1993) Land degradation (De Jong & Burrough, 1995)

Table 7.2 – Six texture measures derived from grey level co–occurrence matrix.

Texture measures derived from Co-occurrence Matrix	Formula
Contrast	$\sum_{i,j} \|i - j\|^2 P(i,j)$
Angular second moment	$\sum_{i,j} P^2(i,j)$
Correlation	$\sum_{i,j} [ijp(i,j) - \mu_x\mu_y] / \sigma_x\sigma_y$
Entropy	$-\sum_{i,j} P(i,j) \log p(i,j)$
Dissimilarity	$\sum_{i,j} [p(i,j) \cdot \|i - j\|]$
Homogeneity	$\sum_{i,j} [p(i,j) / 1 + (i - j)^2]$

ignoring important information contained in the spatial distribution of this texture. Another way of measuring texture that captures such spatial variation is geostatistics.

Variogram
Geostatistics (Journel & Huijbregts, 1978; Goovaerts, 1997) provides a set of statistical tools for handling the spatial (and temporal) data. A key function of geostatistics is variogram which relates variance to spatial separation and provides a concise description of the scale and pattern of spatial variability.
In the Earth sciences many properties exhibit spatial dependence; the tendency for observations closes together in space to be more alike than those further apart (Curran & Atkinson, 1998). The variogram is computed by starting with a small value of distance (which is always equal to one pixel) that is increased incrementally in order to quantify the differences between data values as a function of separation distance. This separation distance, *h*, is called lag.

$$\gamma(h) = \frac{1}{2} E[\{Z(x) - Z(x + h)\}^2] \tag{7.3}$$

The experimental (or sample) variogram is computed for the $p(h)$ paired observations, $z(x_i)$, $z(x_i + h)$, $i = 1, 2, ..., p(h)$:

$$\hat{\gamma}(h) = \frac{1}{2p(h)} \sum_{i=1}^{p(h)} \{z_v(x_i) - z_v(x_i + h)\}^2 \tag{7.4}$$

where, v is the support (the size, geometry, orientation) of the area over which measurements are made. The variogram is now familiar in remote sensing (Curran, 1988, Woodcock et al., 1988a; Woodcock et al., 1988b; Curran & Atkinson, 1998; Herzfeld, 1999; Collins & Woodcock, 1999) and many detailed introductions to the variogram and associated geostatistical techniques are available (Isaaks & Srivastava, 1989). Typically, the shape of the variogram resembles one of three basic models (exponential, linear and spherical) and the coefficients of these models may be used, for instance, in classification or to inform sampling or mapping. The three important coefficients to consider when interpreting the variogram (Curran, 1988; Woodcock et al., 1988a, b; Cohen et al., 1990) are given in figure 7.1.
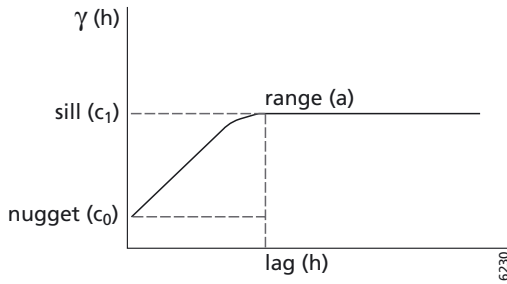
Figure 7.1 – Spherical model fitted to a typical variogram (with three of the more important coefficients).

The nugget variance, c_o, is the point at which the model crosses the ordinate or y-axis and is a measure of spatially-independent variation. The n structured components $c_1, ..., c_n$ represent the spatially-dependant variation accounted for by each component of the model. The range, a, represents the limit of spatial dependence, the lag h at which semi-variance reaches its limit. The range can be used as a measure of spatial dependency, or homogeneity and it is related to the size of the objects in the scene and so is a textural measure of coarseness. The height of the variogram, the sill, is a measure of spatially-independent and spatially dependant variation for a given size of support and is related to the proportion of the area covered by objects, which is a function of their number, density and characteristic contrast between light and dark areas. Variograms for rough textures, have a higher sill than smooth textures and the average value of the semi-variance will deviate from the sill value when a new texture is encountered. The shape of a variogram is related to variability in the size of objects in the terrain. A more rounded or gradually sloping shape is characteristic of higher variance in the size of objects. Regularization (coarsening the spatial resolution) reduces the overall variance of the data, blurs fine scale variation (Atkinson, 1995), decreases sill height and increases the range and nugget variance.

The variogram within a moving window has been used to quantify texture in remotely sensed imagery (Miranda et al., 1992; Miranda & Carr, 1994; Miranda et al., 1996; Carr, 1996). For example, Miranda et al. (1992) used variograms to distinguish between different land cover classes and increase the accuracy of land cover classifications and Carr (1996) used semi-variance and spectral information (separately and in combination) within a supervised classification to distinguish between land cover. Carr (1996), like other authors, observed that classification accuracy was greater when semi-variance was used in combination with spectral information than when the latter was used alone. Another approach has been to use the square root of the difference between paired observations rather than the semi-variance (half the squared difference) for discriminating between land cover classes (Lark, 1996). Coefficients of models fitted to variograms have also been shown to be effective in identifying different land cover classes (Cohen et al., 1990; Rubin, 1990). For example, Ramstein and Raffy (1989) found that range, a, was a useful land cover class descriptor. Using a similar approach Herzfeld & Higginson (1996) extracted several features from the variogram which related to seafloor topographic form. Variograms can give complete mathematical

descriptions of image texture. However, calculating numerous variograms for an entire image is computationally intensive and the variogram is a rather complex function which does not lend itself to simple, automated textural classification of images.

7.4 Per-pixel vs per-field approach to image classification
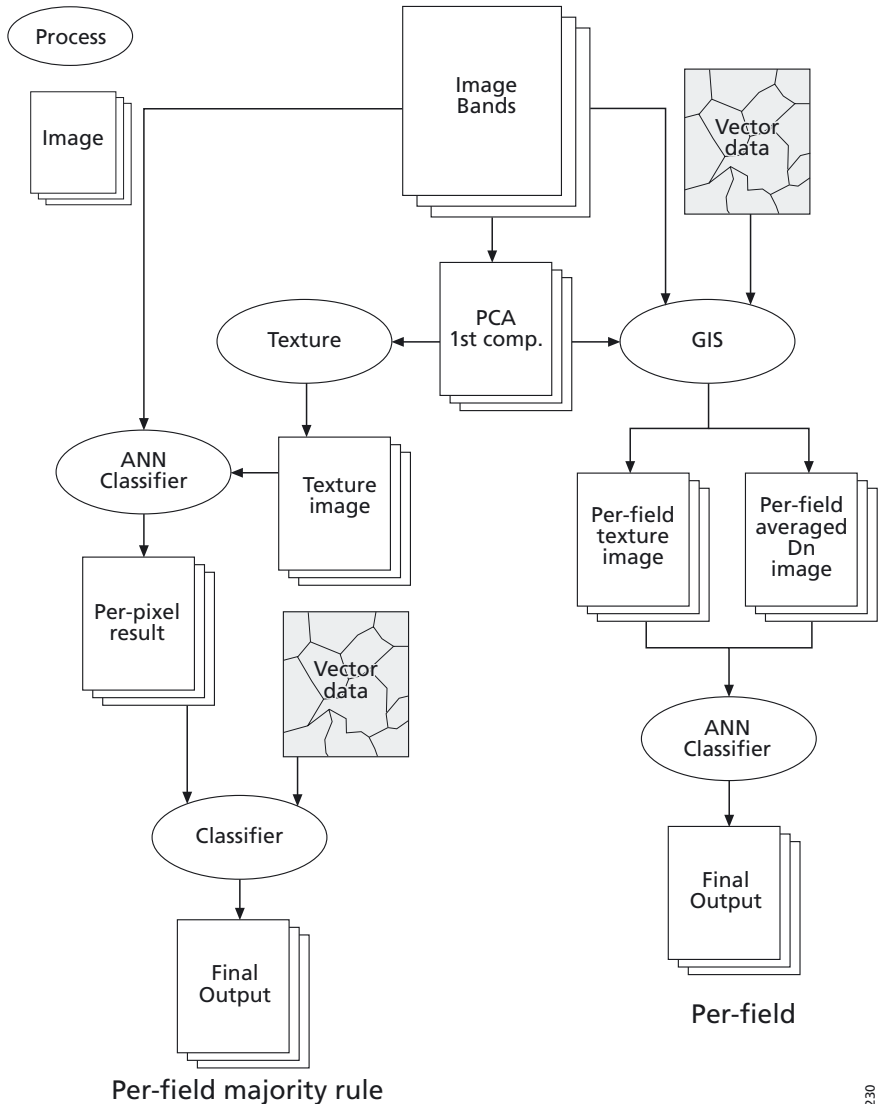
Figure 7.2 – Flowchart of per-field majority rule and per-field approaches (Berberoglu et al., *2000).*

Pixels, the basic spatial units within a remotely sensed data are as a consequence the basic spatial units for image classification. However, extracting useful information from individual pixels can be inhibited by the contribution of signals from surrounded pixels (Townshend, 1981) and within land cover variability (the result of soil background, vegetation phenology, atmospheric effects, sun and sensor geometry). As a result of this, the most representative spatial unit in the terrain is not a pixel but the land cover parcel, in this case a field. The radiance of a field is spatially variable and for reasons given above the radiance of individual pixels within the field has little meaning. However, per-field approaches utilise the average radiance and variability of that radiance, so providing a representative description of this primary unit in the terrain. The value of a per-field approach in increasing classification accuracy has been shown in several studies (Pedley & Curran, 1991; Lobo et al., 1996; Aplin et al., 1997). However, this accuracy can be increased even further by including a measure of spatial variability (e.g., texture) to the per-field classification (Curran & Ojedele 1988).

Agricultural land cover is spatially very varied, particularly so in the summer months. This wide range in spatial frequencies, from variability within fields to variability in field size, can be utilised by land cover classifiers. There are two groups of per-field approaches (figure 7.2):

1 The spatial variability can be quantified using a textural measure and then combined with spectral data in a classifier or
2 The spatial variability of the scene can be reduced by smoothing or removing within-field variability (due to stoniness, drainage, etc.), through low-pass filtering or the use of a per-field classifier.

The per-field classification approach typically involves the integration of vector data and raster images within a geographical information system (GIS). The benefits of integrated approach are an increase in accuracy, a decrease in classification time (because classifiers are dealing with fields rather than many pixels) and a reduction in within-field spectral mixing. However, the requirement for field boundary information in the form of vector data has often restricted the use of a per-field approach.

In this study the second approach was utilised as field boundary information were available and as has been noted by Berberoglu et al. (2000) this second approach is likely to be the more accurate of the two.

7.5   Classification algorithms

Of the many algorithms available for image classification only two will be explored here: maximum likelihood (ML) and artificial neural network (ANN). An ML classifier uses training data as a means of estimating means, variance, covariance and probabilities of classes. It assumes that the distribution of the data is Gaussian. Under this assumption, the distribution of the pattern can be described by the mean vector and the covariance matrix and used to compute the statistics of probability (Lillesand and Kiefer, 1994). However, the training data and the classes themselves may not display Gaussian frequency distribution. In such situations ANN is one of several artificial intelligence techniques that have been used for automatic image classification as an alternative to conventional statistical technique. There
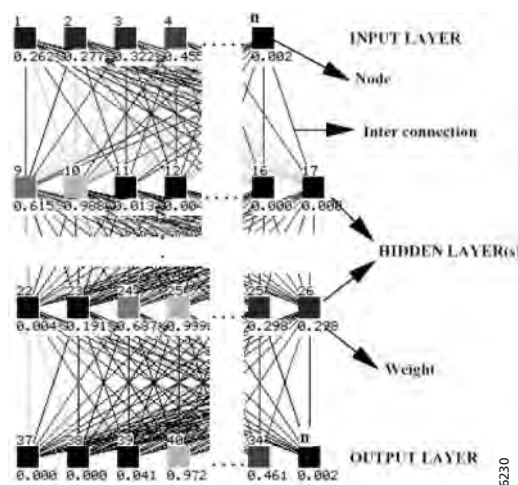
Figure 7.3 – Artificial Neural Network architecture (numbers below the nodes indicate weight and are unitless).

are six ANN models; Hopfield networks, Hamming networks, Carpenter/Grossberg classifier, Kohonen's self-organising feature maps, single layer perceptron and multi-layer perceptron.
The multi-layer perceptron (Rumelhart et al., 1986) is the most commonly encountered ANN model in remote sensing (because of its successful generalisation capability) and is the model used in this study.
This type of ANN model consists of three or more layers which are generally interconnected to the previous and next layers, but there are no interconnections within a layer and each layer consists of processing elements called units or nodes (figure 7.3).

The first layer is called the input layer and serves as a distribution structure for the data being presented to the network. It holds input values and distributes these values to all units in the next layer and so no processing is done in this layer. The input values can be spectral bands or additional information such as texture. The final processing layer is called the output layer and in this case is land cover class. Layers in-between input and output layers are hidden layers and their number within the network is defined by user.
Supervised ANN classification consists of two stages; training and testing. In supervised training values for pixels, are presented to the neural network, together with a known land cover class. The aim of network training is to build a model of the data generating process so that the network in the testing stage can generalise and predict outputs from inputs it has not seen before. There are different types of learning algorithms for training the network. The commonly used algorithm in remote sensing is the 'back-propagation' or 'generalised delta rule' (Rumelhart et al., 1986). Network weights are adjusted to minimise an error based on a measure of the difference between desired and actual feed-forward network output. The interconnections between each unit have an associated weight. Each processing unit sums the values of its inputs. This sum is then passed through an arbitrary activation function to produce the unit's output value. Formally, the input that a single unit receives is weighted according to

$$net_j = \Sigma\ \omega_{ji}o_i \qquad\qquad (7.5)$$

where, ω_{ji} represent the weights between unit i and unit j and i, o_i is the output from unit i. The output from a given unit j is then computed from:

$$o_i = f\ (net_j). \qquad\qquad (7.6)$$

The function f is usually a non-linear sigmoid function that is applied to the weighted sum of inputs before the signal passes to the next layer (Beale & Jackson, 1990).

The actual output of the network is compared with a target and an error measure is calculated. In the backward phase this error is fed backward through the network towards the input layer to modify the weights of the connections in the previous layer in proportion to the error. This process is repeated iteratively until the total error in the system decreases to a pre-specified level or the rate of decrease in the total system error becomes asymptotic.

Alteration of the connection weights is done according to a generalised delta rule.

$$\Delta\omega_{ji}\ (n + 1) = \eta\ (\delta_j o_i = \alpha\Delta\omega_{ji}\ (n)) \qquad\qquad (7.7)$$

where, η is the learning rate parameter, δ_j is an index of the rate of the change of the error and α is the momentum parameter (Atkinson & Tatnall, 1997). One of the major features of ANNs is their ability to generalise, that is, to successfully classify patterns that have not been presented previously (Kanellopoulos et al., 1992; Foody & Arora, 1997). Five variables, in
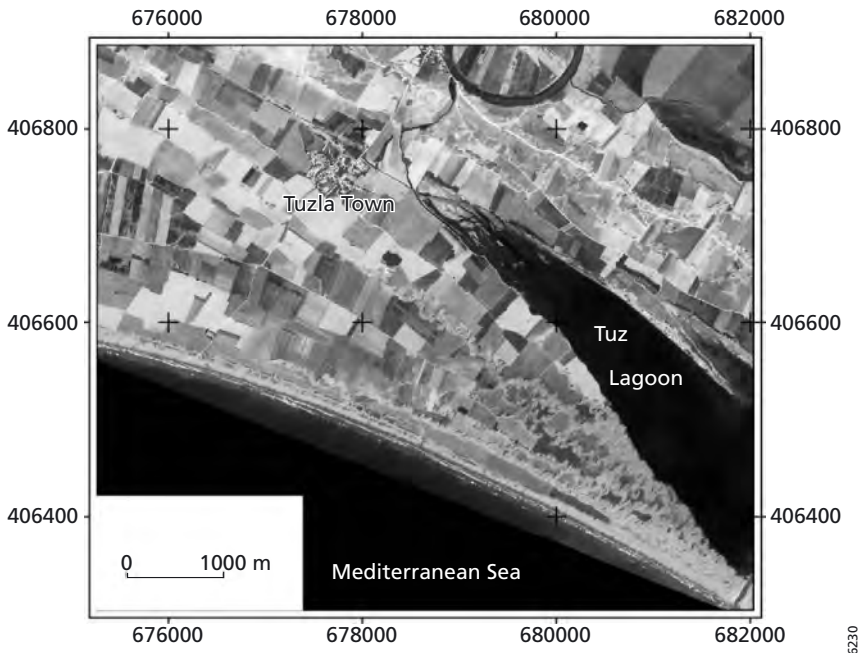
Figure 7.4 – Gray scale of June 2002 IKONOS sensor image of the study area. Units are in meters.

particular, affect the accuracy with which an ANN can classify: size of training set, network architecture, learning rate, learning momentum and training cycle. These variables which must be determined experimentally control the generalisation capability and total training time.

7.6   Study area

Study area is situated at the coastal edge of Cukurova Plain at the Eastern Mediterranean coast of Turkey. The study area covers approximately 5 by 10 km of agricultural land (comprising wheat, tomato, peanut, water melon, soil, fallow fields, burnt stubble) and coastal wetland ecosystems (comprising bulrush, coastal vegetation, sand dunes and lagoon) as shown in figure 7.4. An IKONOS sensor image with a spatial resolution of 4 m in four visible and near infrared wavebands was acquired on 14 June 2002 (figure 7.4). Additionally, land cover data were recorded one week either side of image acquisition and located using a GPS. The IKONOS sensor image was geometrically corrected using nearest neighbour and geocoded to the Universal Transverse Mercator (UTM) co-ordinate system. Fifteen approximately evenly distributed ground control points (GCPs) were selected from the image.

7.7   Image classification

IKONOS sensor image was classified using ML and ANN classifiers and both spectral and textural information (from the variance, co-occurrence matrix and variogram) in per-pixel and per-field formats.

Per-pixel approach
The ANN classification was performed using MATLAB software. This software simulated a feed-forward multi-layer perceptron model (MLP). The network architectures ranged from 4 to 10 input units (4 IKONOS sensor bands and, where relevant, textural measures). The first hidden layer included three times the number of input layer units. The network was trained with a learning rate of 0.01 and learning momentum of 0.5 as back-propagation requires small learning rates for stable learning. The network was trained until the root mean square error was minimised (gradient of the error at the outputs was less than 0.05), after 4000-8000 cycles. A sigmoid transfer function was utilised within the layers. The output was a hard classification, with only the code of the predicted class of membership indicated for each pixel.

Texture measures
All texture measures were extracted from the first principal component (Benediktsson & Sveinsson, 1997) of the four wavebands and these were used to create 'texture waveband(s)'. Then, per-pixel ML and ANN classifications were applied. Evaluation of the utility of these two classifiers and associated texture measures was based on classification accuracy.

Table 7.3 – Error matrix for the classification of IKONOS sensor imagery using ML and ANN and variance as a measure of texture (PA: Producer's accuracy (%); UA: Users Accuracy (%)).

| Land covers | Variance (Var) | | | |
| | ML | | ANN | |
	PA	UA	PA	UA
Wheat	88.9	66.0	81.6	73.2
Tomato	12.9	22.2	14.7	25.0
Peanut	94.4	47.9	77.2	62.0
Water melon	25.2	39.1	36.9	44.9
Soil	92.1	68.3	63.3	85.0
Fallow field	100	22.4	56.5	53.1
Burnt stubble	66.7	27.8	45.4	55.5
Bulrush	89.4	51.8	86.4	63.0
Coastal veg.	32.9	45.3	46.1	55.7
Dune	92.7	45.8	86.1	67.5
Lagoon	89.9	81.7	91.7	82.5
Settlement	23.3	89.8	78.0	54.2
Overall accuracy	54.9		64.4	

Table 7.4 – Error matrix for the classification of IKONOS sensor imagery using ML and ANN incorporating statistics derived from the co-occurrence matrix (PA: Producer's accuracy (%); UA: Users Accuracy (%)).

| Land covers | Spectral bands only | | | | CM (3 statistics) | | | | CM (6 statistics) | | | |
| | ML | | ANN | | ML | | ANN | | ML | | ANN | |
	PA	UA	PA	UA	PA	UA	PA	UA	PA	UA	PA	UA
Wheat	84.2	66.0	77.5	71.1	50.4	66.0	76.9	72.2	48.3	73.2	84.7	62.9
Tomato	14.9	30.0	14.1	30.5	18.4	25.0	15.8	25.0	25.0	27.8	19.3	30.5
Peanut	75.0	54.9	65.6	69.7	59.0	57.7	72.7	67.6	77.5	43.7	87.6	54.9
Water melon	26.4	33.3	61.7	42.0	28.1	13.0	40.0	55.1	42.8	34.8	38.8	58.0
Soil	73.7	81.7	60.4	82.5	66.7	53.3	65.8	85.0	62.9	46.7	70.6	80.0
Fallow field	77.8	28.6	61.1	44.9	60.0	42.8	74.2	46.9	100.0	20.4	65.5	38.8
Burnt stubble	73.9	47.2	45.6	72.2	37.1	72.2	44.8	72.2	32.6	80.5	41.0	69.4
Bulrush	93.0	49.4	83.9	64.2	89.8	54.3	87.5	43.2	84.8	69.1	78.8	82.7
Coastal veg.	34.3	56.6	44.2	53.8	37.8	55.7	43.9	54.7	33.3	59.4	39.5	60.4
Dune	92.6	60.2	77.1	65.1	51.2	79.5	86.4	68.7	42.5	57.8	91.8	67.5
Lagoon	89.4	91.7	97.2	88.3	97.1	83.3	97.1	85.0	95.8	76.7	95.2	82.5
Settlement	27.3	40.7	100.0	10.2	100.0	22.0	77.8	47.4	95.6	37.3	76.9	50.8
Overall accuracy	58.9		63.0		55.7		64.4		54.3		64.6	

Variance

Variance was simple and speedy to calculate. Variance provided largest accuracies only when incorporated within the ANN classifier (table 7.3). Variance over-emphasised the field boundaries and linear features such as roads, this problem was even more severe with the ML classifier.

A classification incorporating co-occurence matrix (3 statistics) texture for part of the study area
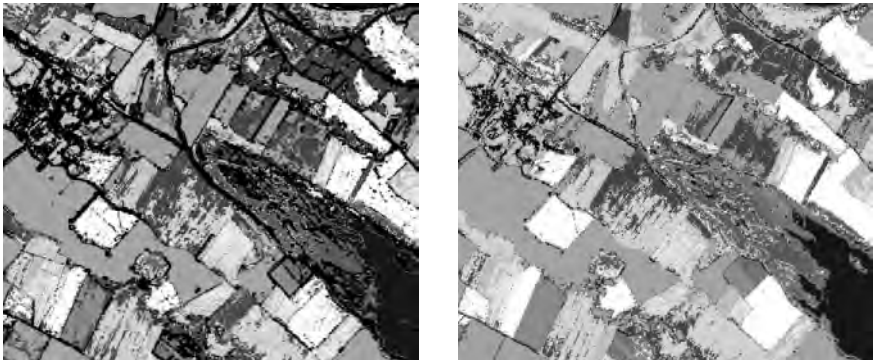
A classification incorporating semi variance lag of 1,2 and 3 pixels texture for part of the study area

☐	Wheat	☐	Soil	☐	Coastal veg
☐	Tomato	☐	Fallow field	☐	Dune
☐	Peanut	☐	Burnt stubble	☐	Lagoon
☐	Water melon	☐	Bulrush	☐	Settlement
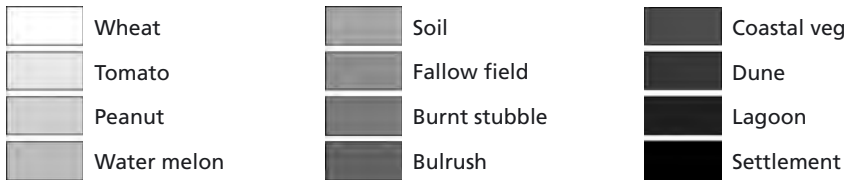
Figure 7.5 – Classifications incorporating various texture measures. First column is ML, second column is ANN classifications.

Co-occurrence matrix

Six textural measures were calculated from four directions (0°, 45°, 90°, 135°) of a co-occurrence matrix (table 7.2) and a mean value of all of these directions is presented (table 7.4). Land cover classification with ML and ANN classifiers utilised first, all co-occurrence matrix statistics (table 7.2) and second, three co-occurrence matrix statistics: contrast, angular second moment and correlation. The addition of co-occurrence matrix texture information increased by 1.4% and 1.6% respectively the overall classification accuracy of the ANN classifier but did not increase the accuracy of the ML classifier (figure 7.5). The majority
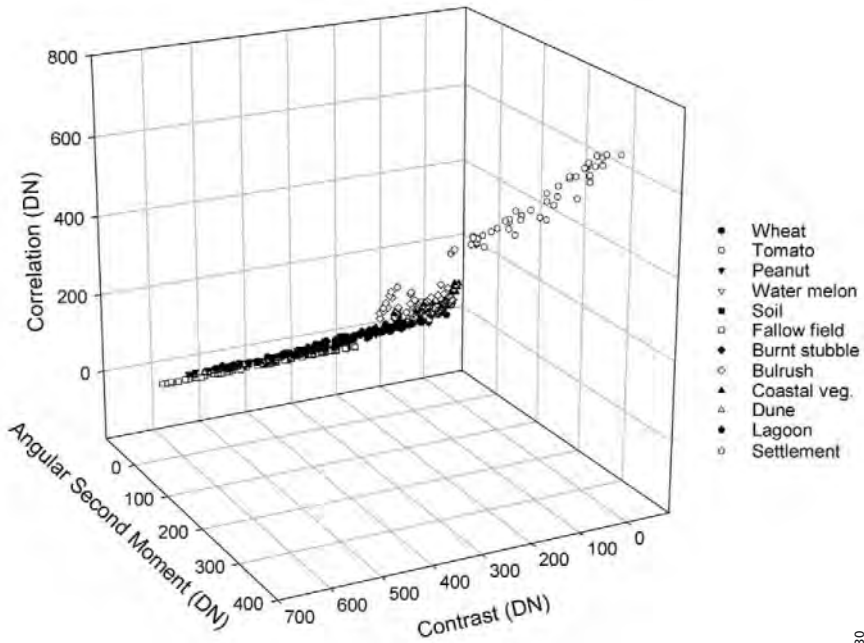
Figure 7.6 – Distribution of co-occurrence matrix statistics in 3D feature space.

of the textural measures (variance, variogram etc.) emphasised class boundaries where the spatial variation is high however, statistics derived from co-occurrence matrix also provided information about within-class variation.

For example, correlation and angular second moment were able to measure high spatial variation for land covers with a relatively smooth texture (e.g., water), contrast measured texture independently of within class spectral variation. However, co-occurrence statistics did not provide a 'signature' for individual classes, as it is shown in figure 7.6.

Variogram
An algorithm based on the variogram computer code in the geostatistical software library GSLIB (Deutsch & Journel, 1992) was used in this chapter to compute the variogram and variance. Variogram coefficients used calculated as texture measures included (i) an approximation of variogram range, (ii) the semi-variance at various lags and (iii) variance. The variogram range was computed using two approximations; (i) the method of Ramstein & Raffy (1989) and (ii) the roots of the first derivative of a third-order polynomial fitted to the variogram; both were unstable in the first approach this was because the semi-variance at large lags was computed from too few data and in the second approach this was because the small number of pixels in each window restricted the number of lags for which semi-variance could be computed. In many instances, very large ranges were estimated if the variograms did not reach a limit. Therefore, range was not employed in the analysis that follows.
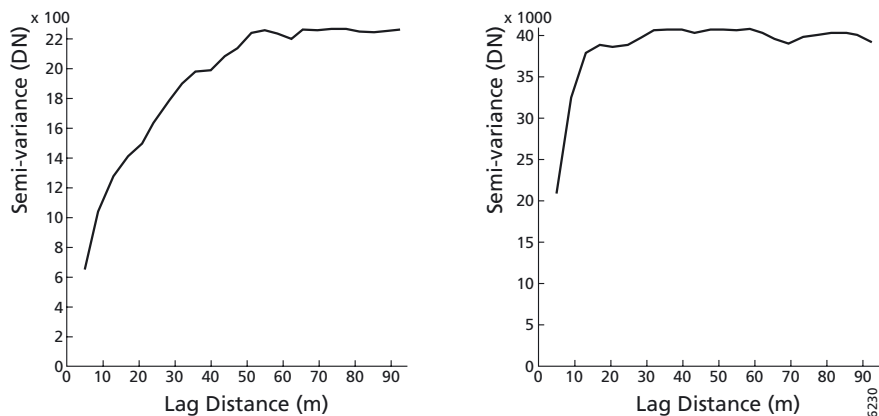
Figure 7.7 – Variograms from IKONOS sensor imagery.

Table 7.5 – Error matrix for the classification of IKONOS sensor imagery using ML and ANN incorporating variogram texture (PA: Producer's accuracy (%); UA: Users Accuracy (%)).
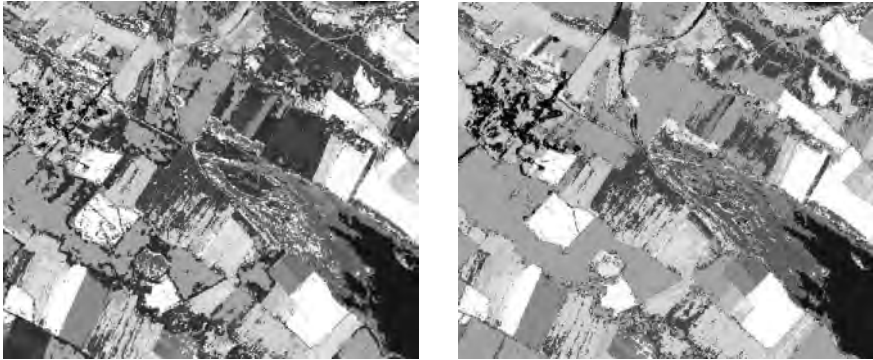
| | Semi-variance lag of 1 | | | | Semi-variance lag of 2 | | | | Semi-variance lag of 3 | | | |
| | ML | | ANN | | ML | | ANN | | ML | | ANN | |
Land cover	PA	UA	PA	UA	PA	UA	PA	UA	PA	UA	PA	UA
Wheat	87.8	67.0	82.1	80.4	88.7	64.9	75.8	74.2	87.3	63.9	80.9	70.1
Tomato	14.0	22.2	19.4	19.4	15.0	25.0	13.6	38.9	14.5	25.0	10.8	25.0
Peanut	92.0	48.6	75.6	65.5	93.3	49.3	89.2	58.4	93.3	49.3	81.0	69.0
Water melon	23.5	40.6	29.0	55.1	24.6	40.6	40.5	43.5	22.8	37.7	40.0	43.5
Soil	88.9	73.3	63.3	83.3	88.9	73.3	65.1	80.8	89.0	74.2	68.6	80.0
Fallow field	100.0	22.4	54.5	36.7	100.0	20.4	70.0	42.8	100.0	20.4	82.6	38.8
Burnt stubble	61.5	22.2	50.0	63.9	66.7	27.8	48.1	72.2	66.7	27.8	41.3	72.2
Bulrush	92.3	44.4	83.0	54.3	83.8	38.3	97.4	46.9	79.4	33.3	83.3	61.7
Coastal veg.	34.0	48.1	43.9	50.9	33.5	49.0	45.2	57.5	33.5	50.0	49.6	59.4
Dune	92.1	42.2	85.7	65.1	97.4	44.6	78.1	68.7	97.3	43.4	85.3	69.9
Lagoon	89.7	80.0	97.0	81.7	89.7	80.0	93.3	81.7	88.9	80.0	97.0	80.0
Settlement	25.0	91.5	69.4	42.4	25.3	93.2	72.9	59.3	25.7	93.2	72.7	67.8
Overall accuracy (%)	54.9		63.2		54.9		63.2		54.3		65.3	

Lags

The effects on classification accuracy was determined for texture measures derived from the average values of semi-variance at lags of 1, 2 and 3 pixels over a moving window (figure 7.7).

The size of this window should be related to the size of objects in the scene. For example, when classifying large continuous area of Brazilian rain forest Miranda and Carr calculated variogram textural measures over very large windows (e.g., 22 by 22 pixels for training) (Miranda & Carr, 1994; Miranda et al., 1998). However, Miranda et al. (1996) suggested that smaller window sizes were preferable for the calculation of variogram texture where land covers were smaller in area and large windows would increase the risk of contamination by class mixing. For this reason in this study window size of 7 by 7 was used. It is possible

Table 7.6 – Error matrix for the classification of IKONOS sensor imagery using ML and ANN incorporating variance and variogram texture (PA: Producer's accuracy (%); UA: Users Accuracy (%)).

| | Var+ Semi-variance lag of 3 | | | |
| | ML | | ANN | |
Land covers	PA	UA	PA	UA
Wheat	86.9	61.8	73.7	75.2
Tomato	13.3	22.2	11.1	16.7
Peanut	89.7	49.3	80.3	66.2
Water melon	21.7	33.3	28.8	43.5
Soil	91.4	70.8	72.0	81.7
Fallow field	100.0	18.4	86.4	38.8
Burnt stubble	64.3	25.0	41.8	77.8
Bulrush	78.6	40.7	92.5	45.7
Coastal veg.	32.2	47.2	44.5	53.8
Dune	96.9	37.3	81.4	68.7
Lagoon	88.9	80.0	94.2	80.8
Settlement	24.1	94.9	69.0	67.8
Overall accuracy	53.0		63.6	
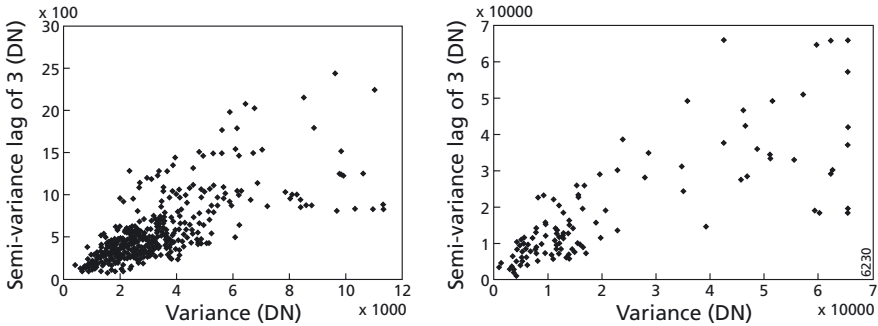
Figure 7.8 – Relationship between semi-variance and variance for two land cover classes.

to calculate lag of 1 pixel by using smaller window sizes such as 3 by 3 or 5 by 5, however computing semi-variance at a lag of 1 pixel over a larger window provides more robust measures over a wide range of lags. For each pixel, average values of semi-variance for a lag of 1, 2 and 3 pixels were computed and used in the classification along with spectral data (table 7.5). This measure of texture, at a semi-variance lag of 3 pixels with ANN classifier, provided in the most accurate classification of land cover.

Variance
Semi-variance at a lag of 3 plus variance over the entire image were measured for each pixel of a first principal component image within a moving 7 by 7 window. These texture measures were used in the same way as a band within ML and ANN classifiers with accuracy results given in table 7.6.

The use of the variance in addition to semi-variance at a lag of 3 did not increase the accuracy of classification. However, there is a strong linear correlation between semi-variance at a lag of 3 pixel and variance and pixels diverting from this linear trend tended to be edge pixels or pixels with extreme values as a result of class mixing (figure 7.8).

7.8 Per-field approach

To utilise texture more effectively a per-field rather than a per-pixel approach was applied. A per-field approach involved integration of spectral and vector (digitised field boundary) data. The field boundaries were digitised from an agricultural map. The resulting vectors were rasterised and used to ascertain which pixels were members of each field. Textural measures: variance, six statistics derived from the co-occurrence matrix and variogram were computed on a field-by-field basis and used in addition to spectral information. These texture measures were computed from the first principal component of the four wavebands. The inputs to the classifier were average values of texture within each field. An algorithm based on the gamv2.f variogram computer code in the geostatistical software library GSLIB (Deutsch & Journel, 1992) was modified and used to compute the variogram and variance texture measures on per-field basis. Co-occurrence matrix code written in FORTRAN was used to compute the six statistics (contrast, angular second moment, correlation, entropy, dissimilarity, homogeneity). Mean DN and texture measures for each field were used for only the ANN classifier as previous sections demonstrated that ANN was always more accurate than a ML classifier when utilising texture. 25 fields were used in a training set to classify 686 agricultural fields comprising wheat, tomato, peanut, water melon, soil, fallow field and burnt stubble. The size of the training set was very small and one of the main limitations for the ANN classifier. However, the training data set was representative because, each value was an average of pixel values within a field. The accuracy results were derived using whole fields rather than points (table 7.7) as such the accuracy figures are for the population. Texture was utilised more effectively in the per-field approach pixels were taken as a block and so the measure of texture was unaffected by neighbouring parcels. In addition to the use of variance and semi-variance at a given lag as measures of texture an approximation of the variogram range for each field (using the roots of the first derivative of a third-order polynomial fitted to the variogram (Lloyd & Atkinson, 1998) was employed. The highest overall accuracy, 73.4%, was achieved using DN and semi-variance at lag of 3 pixels and range.

7.9 Comparing texture measures

The range and semi-variance at a lag of 3 are provided some of the highest per-pixel classification accuracies (table 7.6) as they have captured relevant within field variation (figure 7.9) and so are of particular interest for per-field analysis.

In most cases, semi-variance at a lag of 3 increases linearly with variance. Exceptions to the general pattern are of interest include field 148 which is long and thin and so contain a great proportion of mixed pixels and field 389 that contains two crops in one field. The aim here is to identify texture measures which vary between classes rather than within them. As variance

Table 7.7 –Error matrix (%) for the per-field approach. (DN: mean (per-field) DN values (4 bands); var: variance; ran: range; CM: Co-occurrence Matrix; PA: Producer's Accuracy; UA: User's Accuracy).

Land covers	DN		DN+var		DN+ran		DN+3 lags		DN+var+3 lags		DN+ran+3 lags		CM (3 statistics)		CM (6 statistics)	
	PA	UA	PA	UA	PA	UA	PA	UA	PA	UA	PA	UA	PA	UA	PA	UA
Wheat	56.4	89.1	67.3	83.9	67.3	80.0	60.4	81.3	49.5	92.6	65.3	89.2	62.4	64.9	54.4	80.9
Tomato	63.6	62.2	35.2	55.4	47.7	59.1	55.7	57.6	51.1	52.3	67.0	64.1	32.9	45.3	51.1	44.1
Peanut	80.8	65.9	70.9	83.6	82.1	67.4	71.5	76.6	80.1	83.4	86.7	66.2	75.5	73.1	78.1	63.1
Water melon	49.2	68.1	61.5	41.2	55.4	44.4	52.3	59.6	64.6	26.6	64.6	45.2	60.0	33.9	49.2	47.8
Soil	99.3	72.8	100.0	69.1	89.5	84.8	87.4	77.2	87.4	81.2	88.8	94.8	80.4	76.7	79.0	80.1
Fallow field	60.9	84.1	37.9	71.7	63.2	78.6	56.3	49.5	41.4	72.0	50.6	91.7	63.2	82.1	57.5	63.3
Burnt stubble	52.4	91.7	57.1	29.3	42.8	64.3	38.1	21.6	38.1	88.9	57.1	70.6	28.6	85.7	33.3	58.3
Overall accuracy (%)	72.1		66.1		70.5		66.2		65.1		73.4		64.2		64.1	

Figure 7.9 – The relationship between semi-variance lag of 3 and variance for wheat fields. The number refers to the field.

Table 7.8 – The number of mis-classified fields according to field size (DN: mean (per-field) DN values (4 bands); var: variance; ran: range; CM: Co-occurrence Matrix).

Number of pixels in fields	Mis-classified field numbers by spectral and textural measures							
	DN	DN+var	DN+ran	DN+3 lags	DN+var+3 lags	DN+ran+3 lags	DN+CM3	DN+CM6
1-100	3	3	5	4	3	4	4	4
101-200	23	30	25	27	23	16	22	22
201-300	25	30	23	23	28	21	28	27
301-400	16	20	19	24	20	16	18	19
401-500	14	16	16	21	20	19	18	21
>501	132	153	136	153	165	129	175	173
Total	213	252	224	252	259	205	265	266

is a measure of deviation from the mean it is affected by the magnitude of variability only (for example, it may be high where there are distinct, isolated, homogeneous areas and where variation is scattered spatially). The variogram, in contrast, is a local measure and is affected directly by the spatial configuration of pixels. The semi-variance at a lag of 3 is, therefore, high only where values are scattered spatially (that is, where the configuration is irregular). More work is required on assessing the benefits of using different texture measures for classifying different kinds of land cover. Another potential issue affecting the performance of the texture measures is the size of the fields (table 7.8).

There is no obvious relationship between the number of pixels in a field and the number of mis-classified fields. However, the variogram with larger lags of pixels would be most profitably employed where the number of pixels are constant and reasonably large within the field.

To explore further the relationship between classifications produced using the variogram and statistics derived from the co-occurrence matrix several correctly classified and mis-classified fields were extracted from the data set. In addition to summary statistics (table 7.8) the fields on the image were examined visually and the nature of the textural variability and form of contamination (that is, scattered and discontinuous or homogenous blocks of mixed pixels)

were related to the success or otherwise of measures used to inform the classification in each case (table 7.9).

The fields classified correctly and mis-classified using 5 statistics derived from the co-occurrence matrix may be placed into four groups:

i   Correctly classified by semi-variance at a lag of 3 and range only: 19, 202, 455.
ii Correctly classified by semi-variance at a lag of 3 and variance only: 84, 479.
iii Mis-classified by semi-variance at a lag of 3 (and range, variance): 76, 111, 666.

The three groups form distinct collections of fields. The spatial variability apparent in the fields found within these groups may be summarised as:

i   Spatial variability was high with patches of distinct DN however, fields were large;
ii A large proportion of the area of these fields was very mixed and variation was visually erratic.;
iii Fields were visually mixed and small, additionally in most cases there appear to be grounds for adding within-field boundaries. The semi-variance with range and variance appeared to be less affected by class mixing within the fields.

Table 7.9 – Selected fields and summary statistics contrasting the use of different measures of texture.

Field no	Number of pixels	Land cover	Mean (DN)	SD (DN)	Min. (DN)	Max. (DN)	Correct	Mis-classified
202	530	Wheat	911.08	91.56	581	1222	Vario&R	Others
19	4235	Tomato	1062.22	49.88	827	1237	Vario&R	Others
666	416	Tomato	953.49	89.43	581	1202	Others	Vario&R
76	165	Peanut	1075.85	42.30	991	1176	Others	Vario&Var
111	224	Peanut	1029.61	48.32	816	1124	Others	Variog
84	1394	W.melon	1032.09	107.47	639	1244	Vario&Var	Others
479	348	W.melon	914.08	73.43	718	1085	Vario&Var	Others
455	355	Burnt stabble	817.70	71.04	731	1100	Vario&R	Others

Table 7.10 – Error matrix of per-pixel classification of agricultural sub-scene using ANN incorporating semi-variance (lag of 3).

	Wheat	Tomato	Peanut	Water melon	Soil	Fallow field	Burnt	User's accuracy (%)
Wheat	120540	13132	12152	4900	2744	8036	5880	72.0
Tomato	17248	30772	6272	25284	1176	4312	2744	35.0
Peanut	11564	5292	221284	17444	3724	1960	1568	84.2
Water melon	12348	27440	24108	48804	13132	9996	3136	35.1
Soil	4508	3332	83104	3920	300076	30184	0	70.6
Fallow field	1960	1764	3920	588	4704	76636	3724	82.1
Burnt stubble	196	196	196	0	0	5292	17248	74.6
Producer's accuracy (%)	71.6	37.5	63.0	48.3	92.2	56.2	50.3	68.0*

* Overall accuracy

7.10   Comparing per-pixel and per-field approaches

In addition to per-field classification of agricultural land cover, a per-pixel approach was used to classify the same agricultural sub-scene to enable direct comparison between the two sets of results. Per-pixel classification was implemented using semi-variance (lag of 3) plus spectral data and compared with per-field classification with range and semi-variance (lag of 3) plus spectral data. The accuracy for the per-pixel approach was determined by comparing the classified image to the reference land cover image. Thus pixels were assessed and accuracy figures refer to the population (table 7.10).

In comparison with the per-pixel classification, the per-field classification increased the accuracy with which the spatially more variable land covers (wheat, peanut, soil) were classified. The overall per-pixel classification accuracy was 65.3% versus 73.4% for per-field classification accuracy. Considerable misclassification occurred in several classes, for example tomato and water melon were confused as they were spectrally similar. Additionally, the soil background effect was severe as it increased the internal variability within agricultural fields. However, this high spatial frequency was used to provide additional information to discriminate between land cover classes in per-field classification.
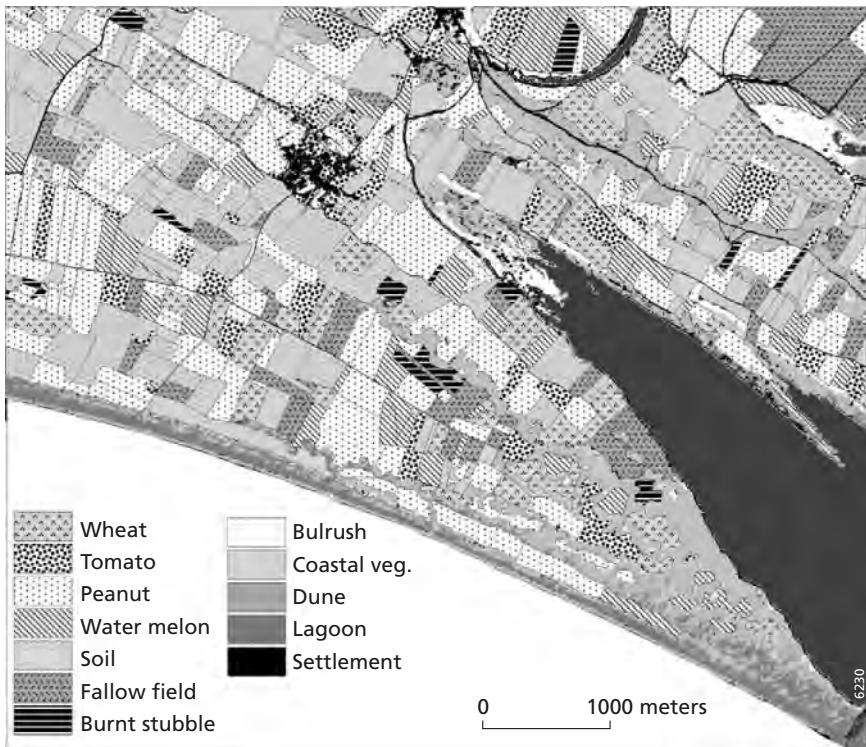
Figure 7.10 – Combination of classifications based on per-pixel and per-field approaches.

Table 7.11 – Error matrix of the combined per-pixel and per-field classification.

	Wheat	Tomato	Peanut	Water melon	Soil	Fallow field	Burnt stubble	Bulrush	Coastal veg.	Dune	Lagoon	Settlement	User's accuracy (%)
Wheat	77	6	11	3	0	0	0	0	0	0	0	0	79.4
Tomato	3	27	3	3	0	0	0	0	0	0	0	0	75.0
Peanut	0	0	129	6	6	0	0	0	0	0	0	0	90.8
Water melon	0	8	12	49	0	0	1	0	0	0	0	0	71.0
Soil	0	1	1	1	109	8	0	0	0	0	0	0	90.8
Fallow field	0	3	4	11	0	30	1	0	0	0	0	0	61.2
Burnt stubble	0	0	25	0	0	0	11	0	0	0	0	0	30.5
Bulrush	0	1	3	2	3	0	2	60	2	0	0	8	74.1
Coastal veg.	4	1	2	5	2	3	0	9	74	0	2	4	69.8
Dune	0	0	0	0	3	1	0	0	15	57	1	6	68.7
Lagoon	0	0	0	0	0	0	0	2	9	0	107	2	89.2
Settlement	0	11	5	2	1	1	1	0	1	0	0	37	62.7
Producer's accuracy (%)	91.7	46.5	66.1	59.7	87.9	69.8	68.7	84.5	73.3	100.0	97.3	64.9	76.7%*

* Overall accuracy

7.11   Combining per-pixel and per-field approaches

The effectiveness of a per-field approach was shown in previous section. However, field boundary data limits the use of a per-field approach for the classification of semi-natural vegetation. Fuzzy boundaries, sparse and scattered land cover types (particularly in the Mediterranean) make this approach less appropriate than the traditional per-pixel approach with texture data. Synergy of these approaches can be utilised to produce the most accurate classification. The agricultural land cover was masked out using field boundary data then per-pixel and per-field image classifications were performed for semi-natural and agricultural areas respectively. Outcomes of these classifications were mosaiced (figure 7.10). The accuracy of this classification was assessed by using the same ground control point as used in per-pixel approach section (table 7.11). The highest overall accuracy 76.7% was achieved using this combination technique.

7.12   Conclusions

This chapter has integrated spectral and spatial information in the form of various texture measures and digitised dominant spatial units (field boundary information) by using two classifiers (ML and ANN) with the aim of increasing the effectiveness of classification (by means of maximising the percentage accuracy) with which land cover can be classified. The spatial (textural) information was the variance, variogram and the co-occurrence matrix. Synergy of the techniques mentioned above enabled more accurate classifications than those obtained using standard techniques alone.

It is difficult to define suitable texture measure to incorporate into the classification of Mediterranean land cover, but the following findings are important for considering which texture measure, approach and classifier to use for successful classification:
- One of the principle findings of this study was that the ANN classifier utilised texture more effectively than ML, the increases in the accuracy were as great as 11%. The use of ANN alleviated the problems, in particular where the spectral properties of the land cover classes is complex and overlaps in the feature space. The success of the ANN classifier was mainly due to its generalisation capability.
- Utilising the vector-based boundary information as a means of delineating fields enabled the extraction of data on a field-by-field basis (per-field approach). This reduced the problem of the over-emphasis of boundaries in texture classification. This approach provided a larger number of pixels than a window to calculate texture and so, was not affected by localised deviations from the average spatial variability. Additionally, the classification on a per-field basis is advantageous as it (i) saves training time, (ii) reduces computational effort, (iii) increases accuracy and (iv) reduces the number of data to be classified. Furthermore, the final output from per-field approach was in an appropriate and comprehensive format for presenting the land cover information to planners and resource managers.
- For the classification of land cover types variogram measure of spatial variability provide more accurate classifications than do statistics extracted from the grey-level co-occurrence matrix commonly used in image processing. Variograms have been used extensively in

soil science and in geostatistics to describe patterns of spatial variation. However, in image analysis and particularly in remote sensing the application of variogram relatively new. Very few publications are available concerning variogram texture classification and optical image applications. The majority of published studies on the use of variograms for image classification relate to radar images and are without accuracy figures. In this study it was shown that variograms hold considerable potential for remotely sensed image classification. Furthermore, the variogram and the co-occurrence matrix are compared, in detail, for the first time within this study. This study was shown that the variogram is a promising tool and can be utilised for classifying appropriate data such as, high spatial resolution images, in such situations it can be an alternative to the traditional measure of texture. The primary advantage of the variogram measure appears to be that they are less adversely affected by high levels of contamination than are the statistics derived from the co-occurrence matrix. Another advantage of the variogram over other texture measures is the capability to compute the measure as a lag by lag basis. In this study only three and five lags could be analysed in per-pixel and per-field format respectively.

- Coefficients of variogram models, for example, the range could not be used in per-pixel format. This was due to the small number of pixels within the land cover parcels this is turn resulted in large ranges and as such the variograms did not reach a limit of semivariance which means texture was not quantified distinctively. However, range was employed in per-field classification as a result of taking blocks of pixels within the fields. Incorporating range together with variogram into the classification resulted highest classification accuracy.

- The use of the variance in conjunction with the variogram did not result in any increase in classification accuracy, however, plots of variogram vs variance revealed useful information for interpreting spatial variability.

This chapter proposed using three techniques to utilise spatial information more efficiently in land cover classification either singularly or in combination as alternatives to the traditional techniques.

Chapter 8
Contextual Image Analysis Methods for Urban Applications

Peng Gong & Bing Xu

8.1   Introduction

Per-pixel classification makes no use of spatial information in the image. It can be easily implemented in a computer system that can easily differentiate gray-level values. In contrast, visual interpretation always involves use of spatial features in the image such as texture, shape, shade, size, site, association etc. It usually requires a lot more computation to handle spatial information in a computer system. Compared with manual interpretation, computer techniques lag far behind. Algorithms using data from more than one image pixel in the classification of one pixel are referred to as contextual classification. A great deal of efforts has been made to develop contextual image analysis algorithms. In urban remote sensing, it is an important component to be able to characterize spatial structural differences in remotely sensed images. Contextual classification can be summarized in three types according to their use of spatial features at different stages: preprocessing, post-processing approach and use of contextual classifier (figure 8.1).

The indispensable part of a preprocessing classification method is the involvement of the spatial features. Once spatial features are extracted, any per-pixel classification algorithm can be used. Spatial features can be extracted using various spatial filters or more advanced texture analysis algorithms. For example, an edge-density image can be generated with a high-pass filter applied to an image followed by a thresholding and a smoothing filtering. Such an image can be used to separate the vegetation in the residential and industrial areas from that in the rural/agricultural areas. Use of this image with multispectral image has considerably reduced classification confusions between urban and rural areas (Gong & Howarth, 1990a). Because many spatial features can be extracted from one band of an original image, feature reduction methods can be applied to select and reduce the amount of redundancy. Gong et al., (1992) assessed a number of texture measures in urban land use classification, they found that the effect of most of spatial measures can be grouped into highlighting the low-frequency or the high-frequency component of the image. Therefore, most texture analysis performed to an image would achieve a smoothing or edge-enhancing effect. Another unique measure is entropy that measures the level of diversity in a pixel neighborhood.

The postprocessing method requires some spatial analysis based on the intermediate classification results obtainable from a multispectral classification of the original image. The
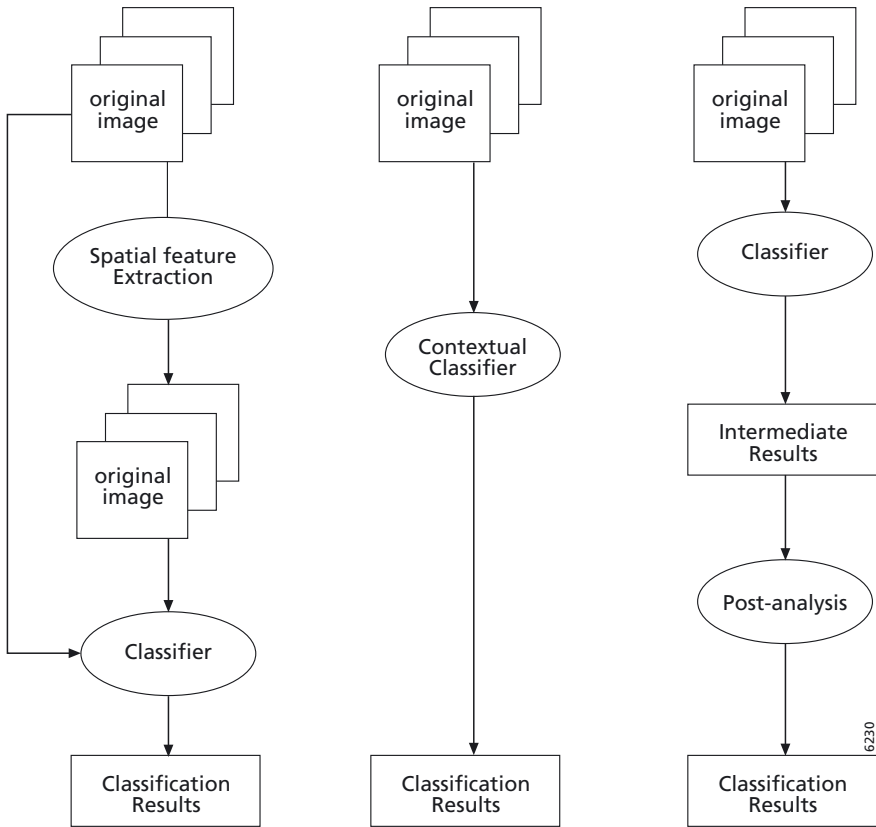
Figure 8.1 – Incorporation of spatial features into image classification through a preprocessing procedure (left), direct use of contextual classifier (middle) or a postprocessing procedure (right).

postprocessing analysis can be as simple as an application of a mode filter to the intermediate results or as complicated as a reclassification of the intermediate results into information classes. The mode filter modifies the classification results based on a majority role, thus it is also called a majority fiter. Simple postprocessing requires a careful initial classification. Some postprocessing algorithms are based on the modification of the probability values of each pixel based on the probability compatibility among pixels in a local neighborhood. This type of technique is known as probabilistic relaxation (Rosenfeld et al., 1976; Richard et al., 1982; Sun et al., 2003). Gong & Howarth (1989) applied probabilistic relaxation classification to urban land-cover classification and found that this algorithm can improve classification accuracy to a certain extent (5%) while the computation requirement was high. Some postprocessing can be done based on rough classification or clustering results leaving the postprocessing analysis to regroup the clusters into the final classes (Wharton, 1983; Zhang et al., 1988; Gong & Howarth, 1992a). Wharton used histogram based clustering to first transform an airborne multispectral image into clusters. Occurrence frequencies of the various clusters in a pixel neighborhood are used to classify land-use categories for the central pixel. Zhang et al. (1988) applied land cover classification to a selected section of Landsat

TM data and then used the occurrence frequencies to characterize land use types. Gong & Howarth (1992a) applied a similar approach to first classify SPOT multispectral image of an urban and rural-urban fringe area near Toronto, Canada, into 12 land-cover classes and then used the cover-frequency approach to re-map the land cover types into 14 land-use classes. In these post-processing algorithms, land-cover classification or clustering results become the intermediate results for further image classification. Compared to the direct use of maximum likelihood classification (MLC) for urban land-use classification, the indirect postprocessing techniques can improve the final land-use classification accuracy by 15-25%. This method outperforms such contextual image analysis algorithms as use of texture measures (Gong et al., 1992) and probabilistic relaxation (Gong & Howarth, 1989). This level of land use classification accuracy improvement over the MLC method is hardly matched by other contextual classification algorithms.

Instead of extracting contextual information and store them for subsequent classification as in the preprocessing and postprocessing contextual algorithms, a contextual classifier makes direct use of contextual information from a pixel window in pixel labeling. A frequency-based classifier can be considered as a contextual classifier as it can be directly applied to an image when the total number of gray-level values (or vectors in multi-dimensional space) in the image is not too big. Clearly, artificial neural network method can be applied to gray-level values (vectors) directly from pixel neighborhoods in an image. For instance, the gray-level vectors of multiple pixels of a pixel window can be organized in a composite gray-level vector and applied as input to a neural network (Hepner et al., 1990). As a natural extension to the Bayes rule, the *a posteriori* class probability calculation of a pixel can be characterized by the joint conditional probabilities of its neighborhood pixels. The decision of classification is governed by the compound information from a pixel neighborhood. This type of classification is known as compound decision method (Welch & Slater, 1971; Landgrebe, 1980; Swain et al., 1981). However, due to the computational complexity and unrealistic assumptions, this type of direct contextual classification has rarely been applied to land cover and land use classification.

While the minimum classification unit is usually a pixel in most of the classification algorithms, field-based (also known as region-based or object-based) classification methods have been developed since 1976 (Ketting & Landgrebe, 1976) for the classification of agricultural lands with remote sensing. In object based image classification, initially an image must be divided into homogeneous regions (objects). Classification decision is then made object-by-object. This can be considered as the preprocessing followed by per-object classification. Knowledge-based approaches have been developed to process aerial photograph based on homogeneous image segments (objects) using rules about neighborhood and shape and size features of individual segments (Mackeown, 1987). In computer vision, initial image segmentation is usually achieved by image thresholding, region-growing or clustering. The resultant segmented image can then be passed to region extraction procedure, where segments are treated as a whole object for successive processing. Gong & Howarth (1990b) employed a land cover classification to initially segment the original image and applied a knowledge-based algorithm to group land-cover polygons into land use types in the rural-urban fringe of Toronto using SPOT multispectral image. The classification decision is based on 'if – then' rules stored in a knowledge base whose rules are triggered by object properties

such as the texture, average gray-level vector, object shape and size and object neighborhoods. An approach based on image segmentation followed by knowledge based inferencing has been adopted by a new commercial package – eCognition.

In this chapter, we introduce the frequency-based contextual classifier (FBC). The simplicity and effectiveness of FBC are illustrated with multispectral images and a single panchromatic IKONOS image. The capability of FBC is further empowered by a preprocessing of the original image with a modified texture spectrum (TS) algorithm.

8.2   Frequency-based contextual classifier

Occurrence frequency, $f(i, j, v)$, is defined as the number of times that a pixel value v occur in a pixel window (also known as a kernel, a mask) centered at (i, j) with a lateral length of l. Because the information in a pixel window is used to classify a single pixel – the central pixel, we consider this type of classification a contextual classification. For a single band of image, v represents a gray level. For a multispectral image, v represents a gray-level vector. Within each pixel window, one can obtain an occurrence frequency table containing all possible vs.

When a pixel window at a given size is moved all over an image(s), one can generate a frequency table for each pixel in the image(s), except for those pixels close to the image boundary. Those pixels within a distance to the image boundaries of half the lateral length, l, of the pixel window used are called boundary pixels. To assure a small proportion of boundary pixels, the pixel window sizes used must be considerably smaller than the image size.

The number of occurrence frequencies in a frequency table increases linearly as the number of gray levels in an image increases, and exponentially as the number (or dimensionality) of spectral bands increases. For a single band of image quantized into n gray levels (e.g., for an 8 bit image n=256 gray levels while for a 16 bit image n=65536 gray levels), one can produce gray-level occurrence frequency tables with a maximum number of n frequencies in each table. The maximum number of frequencies in a frequency table will increase to nm when m spectral bands having the same number of gray levels are used. It requires a large amount of random access memory (RAM) in a computer to handle the nm frequencies. For this reason, efficient gray-level vector-reduction algorithms are needed. One such algorithm will be introduced in the following section. Frequency tables can be generated from gray-level vector-reduced images, clustered images, or land cover images as FBC is applicable to data of any scale of measurement.

There are several advantages of using frequency tables in comparison with the use of spatial statistical measures as in spatial feature methods. First, a frequency table contains more spatial information than many first-order statistical measures such as the mean, standard deviation, skewness, kurtosis, range, and entropy can all be derived from a gray-level frequency table (Gong & Howarth, 1992b). Second, more computation is required to obtain statistical parameters after frequency tables are produced. Therefore, it is unnecessary to use statistical measures because frequency tables can be quickly computed, directly compared and analyzed. The third advantage is that a feature selection procedure which is used to evaluate statistical

parameters is no longer needed because frequency tables contain more spatial information required for the classification than the most statistical parameters. Fourth, disk storage is not required by frequency tables due to the simplicity of their real-time creation.

The success of the frequency table method in land-use classifications depends largely on the appropriate pixel window size being selected for frequency table generation. If the window size is too small, sufficient spatial information cannot be extracted to a frequency table to characterize a land-use type. If the window size is too large, much spatial information from other land-use types could be included. There seems to be no effective criterion for selecting pixel window sizes. Parametric feature selection criteria do not work for frequency tables, simply because they are not parametric. Driscoll (1985) examined frequency means obtained from training samples using pixel windows with a range of successive sizes. The minimum window size was selected at which frequency means begin to stabilize in comparison to frequency means extracted from larger window sizes. Comparisons were made visually. This method is, however, based only on within-class variances. Thus, as in discriminant analysis, a separability measure was proposed by Gong & Howarth (1992b) to select optimal window sizes. However, they did not find it particularly useful. Other measures such as semi-variograms may also be applicable (Woodcock & Strahler, 1987), but our experience suggests that none of these methods are particularly effective. Therefore, optimal window sizes must be empirically determined at this point.

The minimum-distance classifier with the city-block metric (Gonzalez & Wintz, 1987) is used in the frequency-based classifier. A city-block distance between two vectors is calculated by first obtaining a difference between every two corresponding vector elements, and then summing all the absolutes of these differences.

For given mean histograms (frequency tables) of all c land-use classes, $h_u=(f_u(1), f_u(2), ..., f_u(N_v))$, $u=1, 2, ... c$, the city-block distance between a new histogram $h(i, j)$ and h_u is calculated from the following:

$$d_u = \sum_{v=0}^{N_v} \left| f_u(v) - f(i, j, v) \right| \tag{8.1}$$

The classifier compares all the c distances and assigns pixel (i,j) to the class which has a minimum distance d_u to $h(i, j)$.

To capture the spatial structure and brightness variation of a certain land-use type in hu, block-training strategy is applied. The shape and size of the training blocks contain clues for selecting the appropriate pixel window size to be used in generating frequency tables at the classification stage (Gong & Howarth, 1992b). A small training area may not reflect and capture the spatial pattern of the class while a relatively large and representative training area will only cause multiple counting of the pattern that can be eliminated by normalizing the frequency into percentage. A major barrier to improving classification accuracies in contextual image classification involving spatial features extracted from local neighborhoods (pixel windows) is the lack of methods in reducing the misclassification that occurs at boundaries of different classes. This type of misclassification is caused by the use of pixel neighborhoods
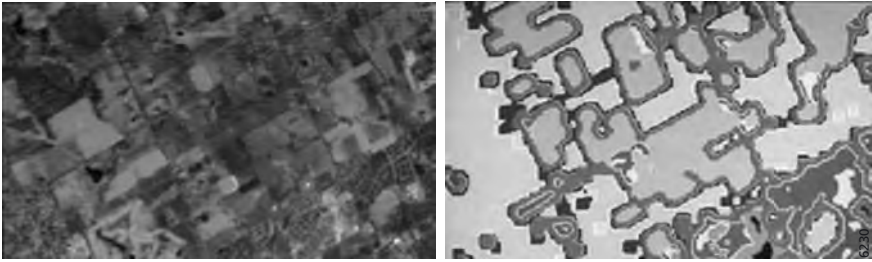
Figure 8.2 – A false color composite of a SPOT multispectral image of the northeast Toronto, Canada (left), and land-use classification results using the frequency-based contextual classifier (right) using a pixel window of 13 by 13. Most of the classification errors are at the borders between two land-use classes. Please consult the enclosed CDROM for a full colour version.
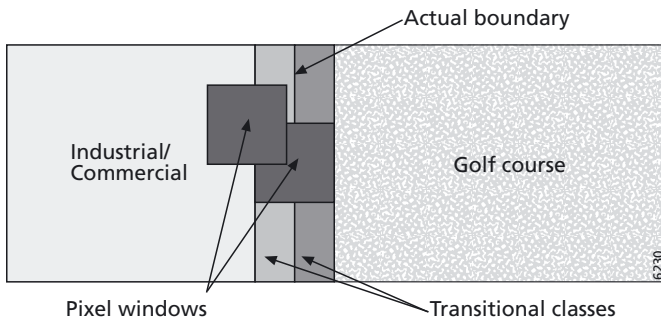
Figure 8.3 – An illustration of the pixel-window effect on the classification results at the boundary of two distinct land-use classes. The two patterns between A and B are the transitional classes which are misclassified by an frequency-based classifier (From Gong 1994).
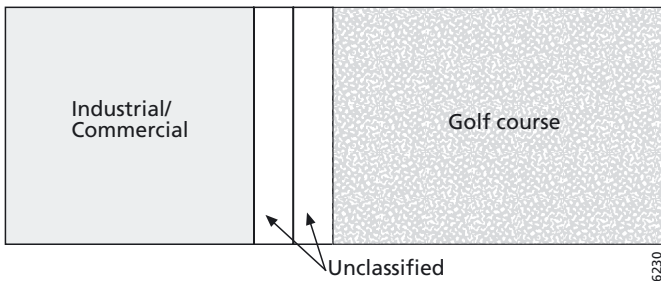
Figure 8.4 – An illustration of the thresholding and region-growing procedures. The thresholding prevents the area along the boundary of two classes from being classified. The region-growing algorithm will then be used to fill up the gap between classes A and B (From Gong, 1994).

(e.g., Gong & Howarth, 1992a;b; Eyton, 1993). An example illustrating this phenomenon can be found in figure 8.2.

The boundary effect can be illustrated using a simple example. In figure 8.3 there presumably exist only two land-use classes: Classes A and B. As a pixel window moves from the area of Class A across the boundary to the area of Class B, the occurrence frequencies extracted from each move of the pixel window change. Assume Class A is industrial/commercial with concrete surface dominant and Class B is golf course with grass dominant. If a pixel window moves from Class A to Class B, one will observe that frequencies extracted from this window change from concrete surface dominating, to similar proportions of concrete surface and grass, to high grass proportion and low concrete proportion, and finally to grass dominating the pixel window. The central two concrete and grass configurations are transitional from Class A to Class B, and depending on other classes included in the classification scheme their frequencies may be more similar to new residential or old residential classes. Thus, as a pixel window moves across the boundary between two classes, four or even more land-use classes would be obtained; those transitional classes are errors.

The level of boundary effects changes as the configuration of image resolution and class definition changes. For a given class, the size and shape of ground components affect the level of boundary effects. If those ground components are important features for discriminating the specific class from others. The image resolution needs to be sufficiently high to allow those components to be observable on the image. The pixel window needs to be large enough to allow those components to be covered in one pixel window in order to guarantee that frequencies extracted are representative to the class. Generally, boundary effects tend to be more serious as image spatial resolution improves because coarser resolution will smooth out the boundary effects. On the other hand, boundary effects will increase as the size of pixel window increases.

Since the boundary effect is a spatial problem, it should be corrected spatially. Gong (1994) proposed a two step correction. First, a threshold, $\beta \cdot l^2$ ($0 < \beta < 2$), is compared with the city-block distance d_u for class u. If $d_u(i, j) \leq \beta \cdot m^2$, pixel (i, j) is a candidate for land-use class u. Otherwise, pixel (i, j) is rejected from land-use class u. If more than one land use class is a candidate, pixel (i, j) belongs to the closest land-use class. $\beta=2$ is equivalent to applying no thresholding whereas $\beta=0$ implies that only those pixels whose calculated occurrence frequencies match exactly with those of a particular class will be classified. Therefore, by adjusting the threshold β between 0 and 2 some transitional classes between boundaries of two different classes may remain unclassified. Following the distance thresholding, some pixels will be left unclassified. Second, a simple region-growing procedure can be applied iteratively to fill up the gaps (unclassified pixels) between two classes (figure 8.3). In this procedure, only unclassified pixels may be affected. An unclassified pixel is first located. Its eight neighbors are then checked to see if any of these neighbors have been classified. If the answer is no, the algorithm searches for the next unclassified pixel and does the same neighborhood check. If the answer is yes, the majority rule is applied to label the unclassified pixel. The number of unclassified pixels is usually small (less than 10% in an image). In addition, the region-growing procedure is computationally simple. Therefore, it requires a very small amount of computation.
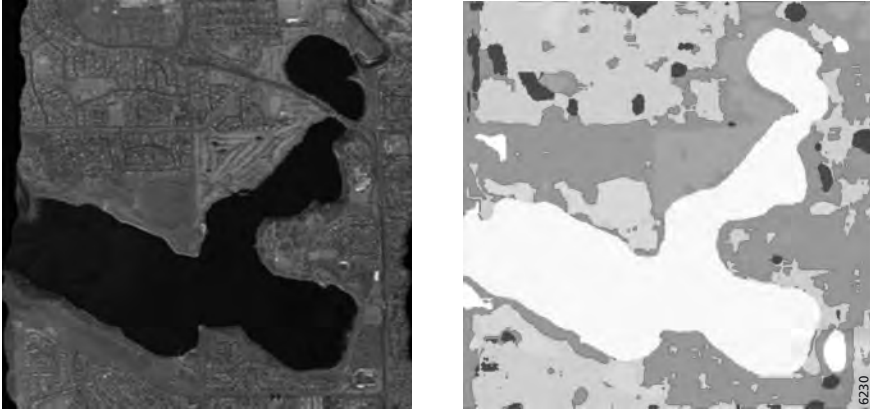
Figure 8.5 – An false color composite of CASI imagery obtained over the City of Calgary (left), and the frequency–based contextual classification result (right) with a thresholding and region growing adjustment to reduce the boundary effect. Please consult the enclosed CDROM for a full colour version.

The iterating region-growing procedure is terminated according to either (1) a user determined number of iteration or (2) when every unclassified pixel is assigned a class. If a classification scheme is not complete for an area, there should be pixels remaining unclassified at the end of a classification task. In this case, one should use the number of iterations as the criterion to control the region-growing procedure. A suggested number of iterations is $l/2 + 1$ (i.e., half of the lateral length of the pixel-window used plus one). This is because the maximum width of any unclassified gaps is l, and in each iteration the algorithm fills up a two-pixel wide gap. On the other hand, if the classification scheme is perfectly suitable for an area, the region growing could be terminated when all pixels are classified. The second criterion is selected to obtain an optimal land-use classification of a portion of the City of Calgary using an 8-band Compact Airborne Spectrographic Imager (CASI) image at a resolution of 7.5 m (figure 8.5). The 8-band image was first converted to a one-channel image with a gray-level vector reduction algorithm (Gong & Howarth, 1992b). The FBC was first applied to the gray-level vector reduced image without boundary effect reduction. The use of frequency distance thresholding and region growing has increased the overall classification accuracy from 85% to 89% for a total of 7 land use classes.

8.3   FBC applied to a modified form of texture spectrum

As explained earlier in the discussion of the properties of frequency tables, the size of frequency table increases linearly with the number of total possible gray-level values (vectors) and exponentially with the number of image bands. In order to make efficient use of the FBC technique, the number of gray-level vectors in multispectral space must be reduced. The simplest way of doing this is by compressing the number of gray levels in each band of the image. This gray-level vector reduction in multispectral space is less optimal than in eigenvector space. This was the reason for the development of the gray-level vector reduction

algorithm (Gong & Howarth, 1992b). In fact, frequency-based approaches can be applied not only to image gray levels, clusters or land cover classes but also to higher order statistics such as texture spectrum (TS) or gray-level coocurrence matrices (GLCM). In the following, we introduce how a modified version of TS can be constructed and applied with FBC to classify a panchromatic IKONOS image.

The original TS algorithm was to construct a texture unit (TU) histogram in a pixel window. TU is designed to consider the relationship of spectral properties of a pixel with its neighboring pixels within a 3 by 3 window. Each pixel has 8 neighbors along 8 directions (starting at the upper left: $135°$, $90°$, $45°$, $0°$, $315°$, $270°$, $225°$ and $180°$) coded from 1 to 8 (Wang & He, 1990). The order of direction can be arbitrary but need to be consistent throughout the entire classification process. The gray level value of the target pixel at the center is compared with that of each neighbor to produce U that takes one of three logical relationships 'smaller', 'equal', or 'greater' coded as '0', '1' or '2', respectively. A TU is calculated for the central pixel according to

$$TU = \sum_{i=1}^{8} U_i \cdot 3^{i-1} \tag{8.2}$$

Calculating TU for each pixel in an image will result in a TU image with a total possibility of 3^8 (6561) texture units. The TU histogram TS can then be built for a pixel window of a given size from the TU image.

Since TS is based on comparison of the gray-level value of the center pixel with those of its surrounding pixels, it is not as sensitive to noise as the GLCM that uses gray values directly. Wang & He (1990) did not apply the TS directly in image classification. They proposed three texture measures that can be calculated from a TS and tested the resultant texture images in classification. A comparison study conducted in a rural-urban fringe environment showed that the texture images extracted from TS performed poorer than the other texture extraction techniques such as GLCM and first-order statistical transformation (Gong et al., 1992). Here, we apply TS directly in the FBC. However, the high dimension of 6561 is a computational burden. One way to simplify this is to combine the logical comparisons of 'greater' and 'equal' into one 'greater and equal' (Gong et al., 1992). This will dramatically reduce the total number of texture units to 256. Because the 8 directions involve double comparison (e.g., a 'greater' at $45°$ from one pixel location is the 'smaller' at the other side of the pixel at $225°$) we can avoid the double comparison by using any 4 consecutive directions. We used the $135°$, $90°$, $45°$ and $0°$ to save some computation time (figure 8.6). This is achieved through the following:

$$\begin{cases} U_i = 0 \text{ if } v_0 < v_i \\ U_i = 1 \text{ otherwise} \end{cases} \quad i = 1, 2, 3, 4 \tag{8.3}$$

$$TU = \sum_{i=1}^{4} U_i \cdot 2^{i-1}$$

The 4-direction encoding would include almost all the information of an 8-direction encoding but all pixel pairs are compared only once instead of twice. The only difference is at the left column of each pixel window where the 0 degree comparison will be lost with the 4-direction method. The gain for the 4-direction comparison is the further reduction of the
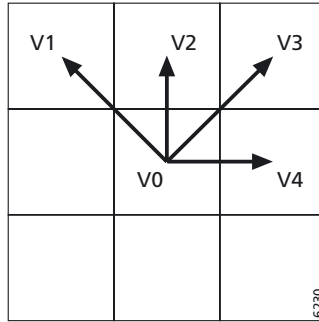
Figure 8.6 – The target pixel compared with its 4 neighbors with 16 texture units.
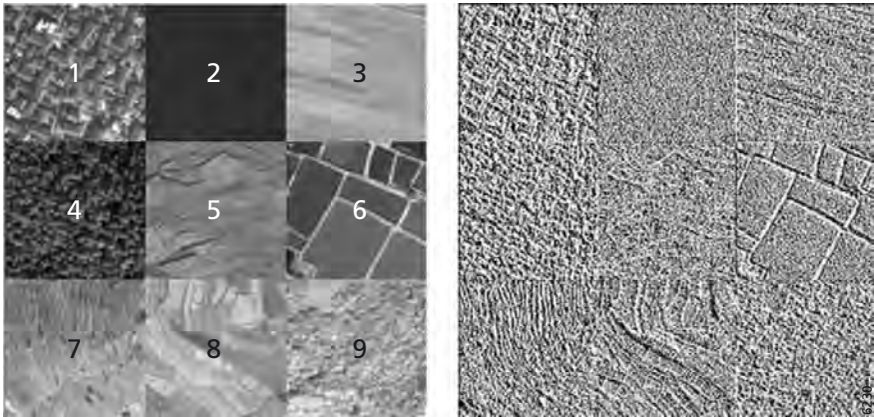
Figure 8.7 – Mosaic IKONOS panchromatic image (Left) with 9 sampled typical land-use classes in the suburban area of Xichang City, Sichuan, China. 1. Residential 2. Clear lake water 3. Lowland crop 4. Forest 5. Silt land 6. Fish pond 7. Terrace 8. Upland crop 9. Shrub. Right: the texture unit image.

total number of texture units from 3^8 to 3^4 (81) or 2^4 (16) depending on the number of logical comparisons between each pixel pair. Each value (TU) is a unique representation of spatial arrangement within one distance along 4 directions. The resulting 16 texture-unit image using the two logical comparison case is shown in figure 8.7. The sample image is a subset of IKONOS panchromatic image taken in December 2000 over the suburb of Xichang, Sichuan, China. A total of 9 subimages, each with a size of 128 by 128 representing a unique land use class, were selected from the IKONOS image and mosaiced for experiments.

Obviously the modified version of TS will significantly improve the computation efficiency when applied with the FBC algorithm in comparison to the original TS algorithm. The modified TS approach (N_{TU}=16) uses ⅕ of the computation time of that with 81 TUs; 1/16 of the computation time of that with 256 TUs; and only 1/410 of the computation time of the

original TS approach (N_{TU}=6561). In the meantime, we hope that the simplification of the TS will not lose much power in characterizing textures in a pixel neighborhood.

To evaluate the effectiveness of the modified TS algorithm, we tested some gray-level reduction algorithms that were applied to the raw IKONOS data. Although IKONOS images are encoded in 11 bits the actual effective data range for this area is only 371 (from 102 to 472). To allow for direct comparison, we used 4 methods to reduce the gray-level range of the mosaic image to 256 (equivalent to 8 bits), 81 and 16 (equivalent to 4 bits). Because image classification is a data generalization process, a preprocessing that reduces the data variability to some extent should not seriously influence the classification accuracy. According to Narayanan et al. (2000), reducing the data down to 4 bits would still reserve more than 90% of the information content. We applied 4 gray level reduction (GLR) schemes including the min-max linear compression (LC), gray level binning (BN), histogram equalization (HE) and piece-wise nonlinear compression (PC) (Jensen, 1996). LC reduces gray levels linearly within the specified minimum and maximum range. BN bins gray levels within every consecutive 2^7 of the original gray levels (2^{11}) into one gray level to achieve a 4 bit image. The resulting histogram is similar to that of LC. HE is designed in such a way that the histogram is theoretically adjusted to have the same frequency for each gray level. For the discrete case, this cannot be perfectly achieved but the histogram is flattened (Jensen, 1996, p. 150). Our HE algorithm first equalizes the original histogram and then reduces the total number of gray-level values from the original image to a specified smaller number such as 16, 81, and 256 to achieve the gray-level reduction effect.

The problem that might occur with HE is that it favors high-occurrence gray values while low-occurrence consecutive gray values are combined into one. However, relatively low-occurrence ones might contain useful information for classification. PC was purposely applied in this study to reserve relatively low-occurrence parts while equalizing high-occurrence parts of the original histogram. The original histogram was first segmented into 5 intervals according to its shape. The left tail and right tail having skewed distribution were empirically segmented into 2 individual intervals. LC was applied to each of the 2 tail segments while the remaining three middle intervals having relatively small-variance normal distributions were equalized. It was supposed to combine the strengths of both LC and HE, but decision on the cutting points for the two tail segments could be arbitrary. Experiments indicate that the effects of these GLR methods are not statistically different from each other. When the GLR images are applied with FBC to classify the 9 land use classes, they all resulted in substantially poorer classification accuracies than the use of TS algorithm with FBC (Xu et al., 2003).

In consideration of the subimage size used in the experiment, we chose one 64 by 64 pixel block as the training area for each land use class. Placing the training blocks was arbitrarily done as we consider each subimage a pure land-use class. To obtain a training histogram for each class with a specific window size, we compared the averaged histograms with frequencies in percentage generated from different window sizes ranging from 5 by 5 to 65 by 65 running through each particular training block. It was found that the average histogram of a specific land-use class does not vary with window size; in other words, the histogram running from varied window size was kept almost the same. This is logical since calculation

of frequency once from the whole training-block will be the same as generating frequency for each pixel once within a smaller window size and averaging them. This is however not quite intuitive. It suggests that we should choose a representative area for the particular class and generate a histogram from the whole training-block rather than calculating frequency tables of a specific window size and subsequently averaging them.
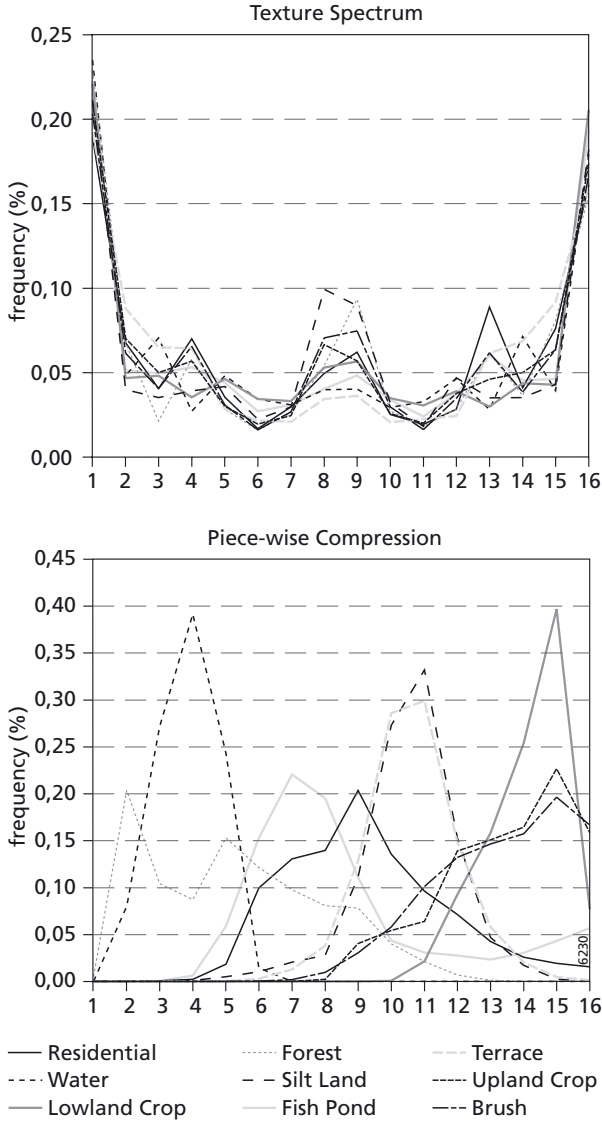

Figure 8.8 – TS obtained from training for each land use class (a) and histograms for each land use class obtained with piece-wise compression (b).

As for the TS approach, a histogram, i.e., the texture spectrum, was obtained for each class from the TU image (figure 8.8a). We notice the roughly symmetric behavior of the texture spectra. Our assumption was that the symmetric pattern was caused by the double counting in the use of 8 directions and it would disappear when only 4 directions were used. This was proven to be incorrect as the TS calculated from 4-direction texture unit images also shows symmetric patterns. We now suspect that it is due to the gray-level value comparison between the central pixel and its neighbors. The training histogram resulted from mosaiced image by using PC is shown in figure 8.8b.

For test sample selection, to avoid using the training pixels in accuracy assessment we chose a sample area of approximate 2000 pixels for each land-use subimage not overlapping with the training block. Test pixels were chosen at the center portion of each subimage to make sure that pixels subject to boundary effect are excluded from accuracy assessments. The same set of test pixels were used for all pixel window sizes tested in this study. Kappa coefficient and conditional kappa were used to assess the overall classification accuracy and per-class accuracy, respectively.

FBC was applied to the original image, gray-level reduced images created with different reduction methods and with different numbers of gray-level values, and texture-unit images created with the modified TS algorithm. To examine the overall classification results, we summarize the kappa coefficients obtained from each type of images with 11 pixel window sizes. The 4 gray-level reduction algorithms were applied to reduce the original image gray-level range from 371 to 256, 81 and 16, respectively. Shown in table 8.1 were only the accuracies obtained from the PC images with 16 gray levels. It is interesting to note that all the GLR methods produced similar results when compared among themselves and with those of the original image. The results seem to agree with the findings in Narayanan et al. (2000) that a 4 bit image does not lose much of the information for image classification. The highest accuracy level for the original image is 0.74 while the best accuracies for the PC images range between 0.71-0.73. For a total of nine land-use classes, we consider a kappa coefficient of over 0.7 quite satisfactory. This may represent the optimistic situation as no boundary effects have been considered in this experiment. When examining kappa coefficient against the window size, we see a similar pattern of better classification accuracy with increasing window size and then levels off at rather early stage for the PC image. We also compared the conditional kappa coefficients for each individual class produced from different gray-level images and found similar patterns for each class. In summary, GLR does not seem to affect the classification accuracy by much even if the gray levels of the original image are reduced down to only 16.

The best accuracies achieved by the modified TS methods were between 0.79 and 0.82. It is interesting to note here that the TS with only 16 texture units compared favorably to those TS with more TUs. Overall, they perform considerably better than the use of gray-level images. It seems clear that the inclusion of spatial arrangement information of gray-level values in a pixel neighborhood can considerably improve the performance of the FBC, as expected by Gong & Howarth (1992b). From table 8.1, we can also see that the gray-level images work better than the TS based methods at relatively smaller window sizes, but gradually reach their limits perhaps due to their inherent inability of considering spatial arrangement of pixels in a larger neighborhood.
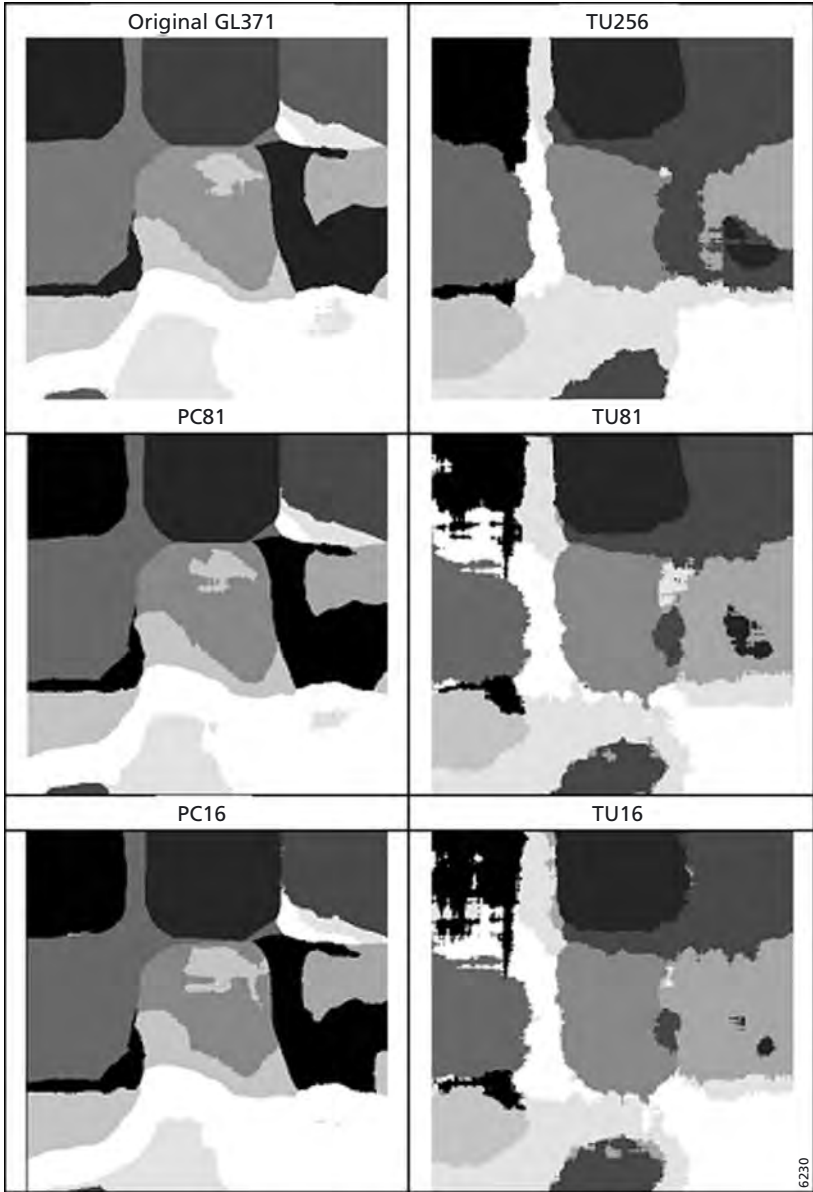
Figure 8.9 – The best classification results obtained with: the first column– the original image 371, the gray-level reduction (PC81, PC16); the second column– the modified TS methods (TU256, TU81, TU16) all at a pixel window size of 65.

Table 8.1 – Some of the classification results measured by kappa coefficients. Original image means all 371 gray-level values were used as entries in the frequency table; PC16 represents that the 371 gray-level values were reduced to 16 levels with a piece-wise compression; TU256 represents the simplification of the original logical comparison from 3 to 2 for all 8 directions in texture unit calculation; TU81 represents the use of only 4 directions for logical comparisons; TU16 represents the use of only 4 directions and reduction of the original 3 logical comparisons to 2.

Window Size	Original Image	PC16	TU256	TU81	TU16
5	0.33	0.46	0.21	0.13	0.13
11	0.55	0.60	0.47	0.33	0.31
17	0.63	0.65	0.62	0.49	0.47
23	0.68	0.69	0.70	0.59	0.58
29	0.68	0.68	0.73	0.65	0.65
35	0.68	0.69	0.77	0.69	0.70
41	0.69	0.70	0.78	0.72	0.73
47	0.70	0.71	0.79	0.76	0.77
53	0.71	0.71	0.79	0.77	0.79
59	0.72	0.70	0.80	0.78	0.81
65	0.74	0.72	0.81	0.79	0.82

Figure 8.9 shows the best classification results for some of the classification results with the FBC. It can be seen from all classification results that pixels at the edges of different land-use images are mostly misclassified. At the center of each land-use type, most classes are correctly classified. For the gray-level images, the confusion is primarily located among the last three classes. There is a tendency that large tracts of terrace and upland croplands are misclassified into shrubs. For the modified TS methods, the confusion seems to be caused by a misclassification of terraces into upland crop and upland crop into lowland crop. Therefore, the error patterns between the modified TS and the gray-level images are different.

It is interesting to note that the best accuracies are all associated with the largest window size. Because the subimage for each land-use type is 128 by 128 and the training block size was chosen to be 64 by 64, it is reasonable to expect that the best accuracies are obtained with the final window size of 65 by 65. Optimal window size is related to the actual size of various land-use patches and is often chosen based on a compromise between land-use patch and boundary effects.

8.4   Summary and conclusions

To make a better use of high spatial-resolution images, such as IKONOS, Quickbird, Landsat ETM+ and IRS panchromatic images, one cannot rely on information of a single pixel. Even with multispectral data, one should not only consider the spectral reflectance, but also explore and analyze the spatial relationship and context of neighboring pixels during the process of image classification. We introduced here the use of a frequency-based contextual classification (FBC) with example applications to multispectral SPOT image, CASI image and samples of the IKONOS image. Gray-level (vector) reduction has proven

to be an effective step in improving classification efficiency although this advantage may be small as the performance of computing hardware improves constantly. More importantly, we demonstrated in this chapter that the FBC is not limited to handling solely gray level, cluster, and land cover class data that are of different measurement scales. It can also be applied to texture statistics such as texture spectrum (TS) and gray-level co-occurrence matrix (GLCM) that are traditionally considered as intermediate results for texture feature extraction (Haralick, 1979; Wang & He, 1990). One of the advantages in working with such 'intermediate data' is to their capability of preserving more discriminating power as compared to the texture measure counterparts that are further derived from those 'intermediate results'. From our examples, we hope to conclude that

1 the FBC is a simple but powerful contextual image analysis tool for image classification. Its two primary disadvantages are the lack of efficiency in handling high dimensional data and the tendency of causing classification errors at borders of different land use classes in an urban area, a problem commonly found in a kernel-based operator. These have been overcome by the gray-level vector reduction algorithms proposed in Gong & Howarth (1992b), and by a simple thresholding during the classification stage and post-classification region growing (Gong, 1994).

2 For panchromatic high spatial resolution satellite images such as the IKONOS 1m data, FBC also demonstrated great potential. With 9 different types of land-use patterns in a suburban area of China, the FBC can reach a kappa coefficient of over 0.7.

3 A reduction in gray-level values to 16 from the original IKONOS image does not affect the accuracy of FBC. Not much difference in classification accuracy is observed between 4 different gray-level reduction schemes.

4 The direct use of the texture spectrum (TS) in the FBC can considerably improve the land-use classification accuracy over the use of gray-level images (Xu et al., 2003). The modified TS algorithm reported here substantialy cut down the size of the texture spectrum to 256, 81 and 16 possible values and therefore improve classification efficiency.

It is worthwhile to further test the modified TS methods in combination with the FBC contextual algorithm in classification of high resolution images. Expanding this strategy to the use of GLCM in place of the TS is also worthy of further study.

Chapter 9

Pixel-Based, Stratified and Contextual Analysis of Hyperspectral Imagery

Freek D. van der Meer

9.1   Introduction

Imaging spectrometers acquire imagery in many, narrow and contiguous spectral bands with the aim of collecting 'image radiance or reflectance spectra' that can be compared with field or laboratory spectra of known materials. Imaging spectrometry has been widely used in geologic mapping, specifically in so-called hydrothermal alteration systems. These are areas where the composition of host rocks is altered through the circulation of hot fluids giving rise to the formation of new mineral assemblages in a predefined order in (3D) space. Surface mineralogic information can be derived from imaging spectrometer data by comparing imaged reflectance spectra of unknown composition to data from spectral libraries. This comparison is mostly done on a pixel-by-pixel basis. In general, a matching is done to express the similarity between the unknown pixel spectrum and known spectra from spectral libraries. As a result, in geology, information on surface mineralogy can be derived from imaging spectrometry data, which in turn can be incorporated into geologic models.

When light interacts with a mineral or rock, light of certain wavelengths is preferentially absorbed while at other wavelengths it is transmitted in the substance. Reflectance, is defined as the ratio of the intensity of light reflected from a sample to the intensity of the light incident on it. Electronic transition and charge transfer processes (e.g., changes in energy states of electrons bound to atoms or molecules) associated with transition metal ions such as Fe, Ti, Cr, etc., determine largely the position of diagnostic absorption features in the visible- and near-infrared wavelength region of the spectra of minerals (Burns, 1993; Adams, 1974; 1975). In addition, vibrational processes in H_2O and OH^- (e.g., small displacements of the atoms about their resting positions) produce fundamental overtone absorptions in the mid- to shortwave infrared part of the spectrum (Hunt, 1977). The position, shape, depth, and width of these absorption features are controlled by the particular crystal structure in which the absorbing species is contained and by the chemical structure of the material. Thus, variables characterizing absorption features can be directly related to the chemistry and structure of the sample. The absorption depth is an indicator for the amount of the material causing the absorption present in a sample. Furthermore, the absorption-band depth is related to the grain or particle-size as the amount of light scattered and absorbed by a grain is dependent on grain size. A larger grain has a greater internal path where photons may be absorbed according to Beers Law. In smaller grains there are proportionally more surface

reflections compared to internal photon path lengths, if multiple scattering dominates, the reflectance decreases with increasing grain size.

Field and laboratory spectra have been used to relate absorption features to chemical composition of samples both the areas of soil science and mineralogy as well as in the area of vegetation science. For the analysis of hyperspectral image data there are several techniques available to surface composition (e.g., surface mineralogy) from a combination of absorption-band position and depth. However, no such technique provides spatial information on the variation of absorption-band depth, position and shape despite the fact that these parameters are of vital use in quantitative surface compositional mapping.

Reflectance spectra of minerals are dominated in the visible to near-infrared wavelength range by the presence or absence of transition metal ions (e.g., Fe, Cr, Co, Ni; Hunt, 1977; Burns, 1993). The presence or absence of water and hydroxyl, carbonate and sulphate determine the absorption features in the SWIR region. The hydroxyl is generally bound to Mg or Al. The water molecule (H_2O) gives rise to overtones as seen in reflectance spectra of H_2O-bearing minerals. The first overtones of the OH stretches occur at about 1.4 µm and the combinations of the H-O-H bend with the OH stretches are found near 1.9 µm. OH-groups commonly occurs in multiple crystallographic sites of a specific mineral and is typically attached to metal ions. Thus, there may be more than one OH feature. The combination metal-OH bend plus OH stretch occurs near 2.2 to 2.3 µm and is diagnostic of mineralogy. Carbonates also show diagnostic vibrational absorption bands due to the CO_3^{2-} ion at 2.50-2.55 µm, at 2.30-2.35 µm, and three weaker bands occur near 2.12-2.16 µm, 1.97-2.00 µm, and 1.85-1.87 µm.

Quantitative estimates of mineralogical composition and chemical analysis on the basis of spectroscopic data has been demonstrated by many authors (e.g., Adams, 1975; Swayze & Clark, 1990). Adams (1975) and Cloutis et al. (1986) showed that the iron absorption bands near 1 and 2 µm shift as a function of Fe to Fe+Mg ratio. Similarly, King & Ridley (1987) showed this effect for olivines. Mustard (1992) showed that the Fe:(Fe+Mg) ratio can be estimated from reflectance spectra. Duke (1994) found subtle shifts of the Al-OH absorption-band in muscovites with aluminium composition. As Al is substituted by Mg, the crystal becomes distorted causing slight changes in Al-OH bond lengths and thus shifts in the absorption-band position of the 2.2 µm absorption appear (Duke, 1994). Hence Duke (1994) found a way of quantifying the Al content of muscovites from the Al-OH absorption-band position. Van der Meer (1994, 1995) demonstrated that reflectance spectroscopy provides a measure for the ratio of calcite:dolomite in limestones. In soil science, reflectance spectroscopy has been used to quantify soil parameters such as organic matter, total iron, exchangeable Ca and Mg, and Ph (Ben-Dor et al. 1997; Shepherd & Walsh, 2002). Recently, Kariuki et al. (2003) show that cation exchange capacity (CEC) can be estimated from reflectance spectra. In vegetation sciences, reflectance spectra have been used for years to estimate foliar biochemistry. Since the pioneering work of Curran (1989) on leaf biochemistry and Wessman et al. (1988) on remote sensing of canopy biochemistry many authors have demonstrated that leaf constituents (notably leaf pigments) can be quantitatively assessed from spectral data (e.g., Curran et al. 1992; Fourty et al. 1996). Examples of biochemicals that are estimated include leaf water (Bowman, 1989), chlorophyll (Lichtenthaler et al. 1996)

and nitrogen (Yoder & Pettigrew-Crosby 1995). Recently, Kokaly & Clark (1999) presented a model for determining the concentration of foliar components from reflectance spectra using absorption band-depth analysis and multiple linear regression analysis to estimate a relation between reflectance and the concentration of several components (nitrogen and cellulose). Curran et al. (2001) show another example of biochemical analysis of leaf reflectance spectra using absorption-band position and depth analysis.

9.2 Pixel based analysis of hyperspectral imagery

9.2.1 Spectral matching techniques used for compositional mapping

There are various techniques to process hyperspectral imagery in order to obtain surface compositional information on a pixel-by-pixel basis for the entire image (see Van der Meer et al., 2001 for a review). Techniques that specifically use absorption band position and depth include (1) the Relative Absorption Band-Depth (RBD) approach of Crowley et al. (1989), (2) the Spectral Feature Fitting (SFF) technique of Clark et al. (1990a) and (3) the Tricorder (Crowley & Swayze 1995) and Tetracorder (Clark et al., 2003) algorithms developed at the USGS spectral laboratory. These techniques work on so-called continuum removed reflectance spectra (figure 9.1), thus acknowledging that the absorption in a spectrum has two components: a continuum and individual features. The continuum or background is the overall albedo of the reflectance curve. Removing this effectively scales the spectra to 100% when the spectral curve approaches the continuum. Mathematically this can be done as follows (Clark et al. 2003)

$$L_c(w) = L(w) / C_1(w) \text{ and } O_c(w) = O(w) / C_0(w) \tag{9.1}$$

where $L(w)$ is the library spectrum as a function of wavelength, w, O is the observed spectrum, C_l is the continuum for the library spectrum, C_o is the continuum for the observed spectrum, L_c is the continuum-removed library spectrum, and O_c is the continuum-removed observed spectrum.

Crowley et al. (1989) developed a method of mineral mapping from imaging spectrometer using Relative Absorption Band-Depth Images (RBD) generated directly from radiance data. In essence, RBD images provide a local continuum correction removing any small channel to channel radiometric offsets, as well as variable atmospheric absorption and solar irradiance drop off for each pixel in the data set. To produce a RBD image, several data channels from both absorption band shoulders are summed and then divided by the sum of several channels from the absorption band minimum. The resulting absorption band-depth image gives the depth of an absorption feature relative to the local continuum, which can be used to identify pixels having stronger absorption bands indicating that these may represent a certain mineral.

Spectral feature fitting (embedded in the ENVI software, Clark et al., 1990a) uses continuum removed pixel spectra, which are compared to continuum reference spectra of known mineralogy. A least-squares fit is calculated band by band between each reference end-member and the unknown (continuum removed) pixel spectra. A 'Scale' image is produced for each endmember selected for analysis by first subtracting the continuum-removed

spectra from one, thus inverting them and making the continuum zero. A large scale-factor is equivalent to a deep spectral feature, while a small scaling factor indicates a weak spectral feature. A least-squares-fit is then calculated band-by-band between each reference endmember and the unknown spectrum. The total root-mean-square (RMS) error is used to form an RMS error image for each endmember. The ratio of the scale image and the RMS image provides a 'Fit' image that is a measure of how well the unknown spectrum matches the reference spectrum on a pixel-by-pixel basis.

The (Tricorder and its successor) Tetracorder (Clark et al. 2003) uses spectral matching algorithms carried out in a two step process. First, the local spectral slope (the 'continuum') is estimated and removed both from reference and observed spectra. Next, the identification of materials from their spectra is constrained by (1) the goodness of fit of a spectral feature to a reference, (2) reflectance level, (3) continuum slope, and (4) presence or absence of key ancillary spectral features. The Tetracorder uses these reference continuum-removed-spectral features to compute a weighted *fit* between unknown spectra and known library spectra. By means of an expert system approach, surface compositional information is derived and results are validated.

These mapping methods described all produce validated surface compositional information (mostly mineralogical maps); however, they do not provide information on the absorption band position, depth and asymmetry on a pixel by pixel basis although these parameters are used in the matching performed. Since absorption band parameters are of importance to quantitative reflectance spectroscopy, there are attempts made to develop linear estimation methods to derive absorption-band parameters from hyperspectral image data.

Another spectral matching technique is the Cross correlogram spectral matching (CCSM; Van der Meer & Bakker 1997; 1998); an approach toward mineral mapping from imaging spectrometer data using the cross correlogram of pixel and reference spectra. A cross correlogram is constructed by calculating the cross correlation at different match positions, m, between a test spectrum (i.e., a pixel spectrum) and a reference spectrum (i.e., a laboratory mineral spectrum or a pixel spectrum known to represent a mineral of interest) by shifting the reference spectrum over subsequent channel positions by

$$R_m = \frac{n \sum \lambda_r \lambda_t - \sum \lambda_r \lambda_t}{\sqrt{[n \sum \lambda_r^2 - (\sum \lambda_r)^2]\,[n \sum \lambda_t^2 - (\sum \lambda_t)^2]}}$$ (9.2)

where R_m is the cross correlation at match position m, λ_t is the test spectrum, λ_r is the reference spectrum, n is the number of overlapping positions (spectral bands), and m the match position. The statistical significance of the cross correlation coefficient can be assessed by the a student's t-test and the skewness can be calculated as an estimator of the goodness-of-fit. The cross correlogram for a perfectly matching reference and test spectrum is a parabola around the central matching number (m=0) with a peak correlation of 1. Deviations from this shape indicate a different surface mineralogy. Mineral mapping on a pixel by pixel basis is achieved by extracting three parameters from the cross correlograms and combining these into a statistical estimate of the goodness of fit of the two spectra compared: the correlation coefficient at match position zero, the moment of skewness (based on the

correlation differences between match numbers of equal but reversed signs, e.g., $m=4$ and $m=-4$), and the significance (based on a student t-test testing the validity of the correlation coefficient at $m=0$). In order to evaluate the surface mineralogy maps a root mean square error assessment procedure is proposed in which the error is calculated from the difference between the calculated pixel cross correlogram and the ideal cross correlogram calculated for the reference as

$$RMS = \sqrt{\frac{\Sigma_O^M (R_M - R'_M)}{N}} \qquad (9.3)$$

where R_M is the pixel cross correlation at match position m, R'_M is the reference cross correlation at match position m, N is the number of match positions, M is the match number.

The most used mapping method in hyperspectral remote sensing is the spectral angle mapper. The Spectral Angle Mapper calculates the spectral similarity between a test reflectance spectrum and a reference reflectance spectrum assuming that the data is correctly calibrated to apparent reflectance with dark current and path radiance removed. The spectral similarity between the test (or pixel) spectrum, t, and the reference (or laboratory) spectrum, r, is expressed in terms of the average angle, Θ, between the two spectra as calculated for each channel, i, as

$$\Theta = \cos^{-1}\left(\frac{\sum_{i=1}^{n} t_i r_i}{\sqrt{\sum_{i=1}^{n} t_i^2 \sum_{i=1}^{n} r_i^2}}\right) \qquad (9.4)$$

In this approach, the spectra are treated as vectors in a space with dimensionality equal to the number of bands, n. The outcome of the spectra angle mapping for each pixel is an angular difference measured in radians ranging from zero to $\pi/2$ which gives a qualitative estimate of the presence of absorption features which can be related to mineralogy. The main problem using the spectral angle mapper is the appropriate selection of the threshold to classify the derived rule images. Since the angle is nor a physical nor a statistical measure, there is now statistically/physically sound approach to do so.

Table 9.1 – Hydrothermal alterations as they occur at Cuprite and associated main mineral phases (key minerals indicative for the phase are indicated in italics).

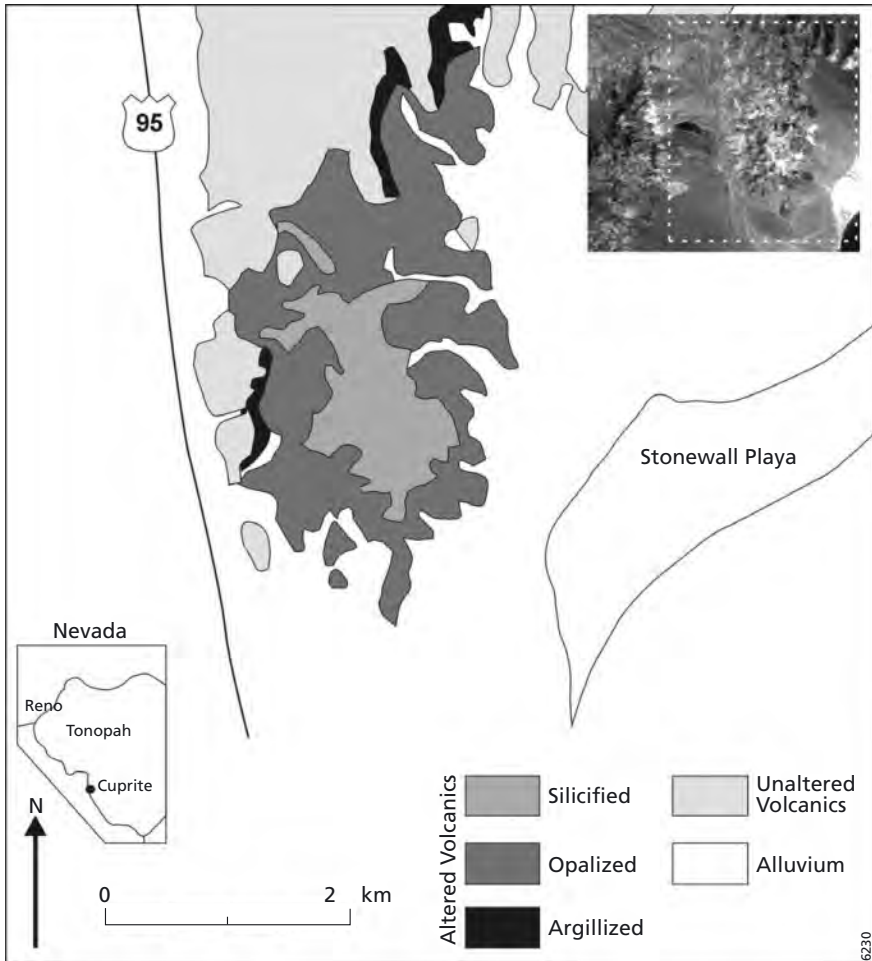| Phase 1 Propylitic	Phase 2 Potassic	Phase 3 Argillic	Phase 4 Sericitic	Phase 5 Advanced argillic	Phase 6 Low-temperature advanced
K-feldspar	K-feldspar	*Kaolinite ordered*	Kaolinite	Pyrophyllite	*Buddingtonite*
Chlorite	Sericite	Illite/smectite	Dickite	*Alunite*	Kaolinite
Carbonate	*Montmorillonite*	Gypsum	*Sericite*		Alunite
Montmorillonite					

Figure 9.1 – Location of the study area, hydrothermal alteration map (after Albers & Stewart 1972) and (inset) AVIRIS image with the mapped area outlined.

Here we demonstrate the use of this technique by applying this to AVIRIS data acquired at Cuprite (figure 9.1). The Cuprite mining site (Albers & Stewart, 1972; Abrams et al., 1977) is an area of extensive hydrothermal alteration related to early Miocene volcanism during which dacite and andesite flows were extruded and hot, acidic brines began circulating through the series of rhyolitic basalts, rhyolitic welded ash flows and air fall tuffs. Silicified rocks form a large irregular patch extending from the middle to the south end of the area. The silicified core represents the most intensely altered rocks at Cuprite containing quartz, calcite and minor alunite and kaolinite. Opalized rocks contain abundant opal and as much as 30% alunite and kaolinite. Locally, an interval of soft, poorly exposed material mapped as argillized rock separates fresh rock from opalized rock. In the argillized rocks, plagioclase is altered to kaolinite, and glass is altered to opal and varying amounts of montmorillonite and kaolinite.
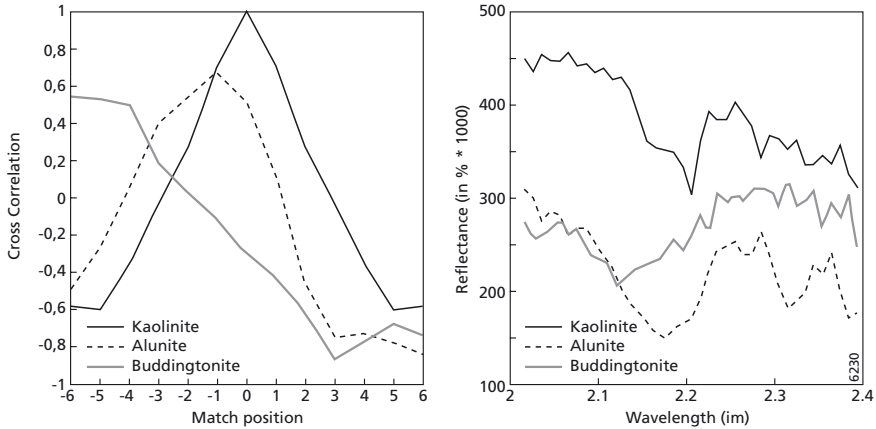
Figure 9.2 – AVIRIS spectra from target minerals (right) and correlograms for a kaolinite reference (left).

In figure 9.2 the target AVIRIS spectra are shown for the typical alteration mineral characterizing the system. Figure 9.3 shows the mineralogical assemblages whereas table 9.1 summarizes the key alteration zones and associated key minerals. For simplicity we use in our analysis the minerals kaolinite, alunite and the rare feldspar buddingtonite. Note that alunite is the pathfinder mineral for gold deposits associated with the high temperature alteration. We use the CCSM spectral matching algorithm. As an example, the skewness, significance and correlation image are shown for kaolinite as reference in figure 9.4. The final alteration maps are shown in figure 9.5. The distribution of the alteration assemblages as shown in figure 9.5 is characteristic for a fossilized hot-spring deposit, which are often mined for gold. The circular distribution of the mineral zones, demonstrates that alteration occurred along a central vent with the lateral mineral zoning controlled by a decrease of acidity and temperature.

Some problems related to spectral matching techniques are illustrated in figure 9.6. Here we calculated the correlation between a calcite laboratory spectrum (from the JPL 160 mineral library available in ENVI) and a dolomite spectrum and an iron rich dolomite spectrum. We calculate the correlation coefficient for parts of the spectrum starting with the first 800 (of a total of 826 channels of the Beckman spectrometer) channels and subsequently diminishing this number by steps of 50 channels such that at last we only calculate the correlation between the 50 channels in the long wavelength portion of the SWIR. For the calcite vs dolomite spectrum we can notice that the correlation is high (0.93) and diminishing to 0.84 when using only the last 50 channels of the spectrometer. This can be explained by the fact that calcite and dolomite have an absorption band around 2.3 micron which changes only from 2.35 to 2.3 micron for calcite versus dolomite. Hence the significant difference in the two spectra is in this part of the spectrum. In fact the graph tells us that including other wavelengths only adversely influences the matching result. The same can be observed when looking at the correlation graph of the calcite versus the iron-rich dolomite spectrum. However this graph shows various correlation maxima and minima because the shape of the graphs are similar

Alteration Zone

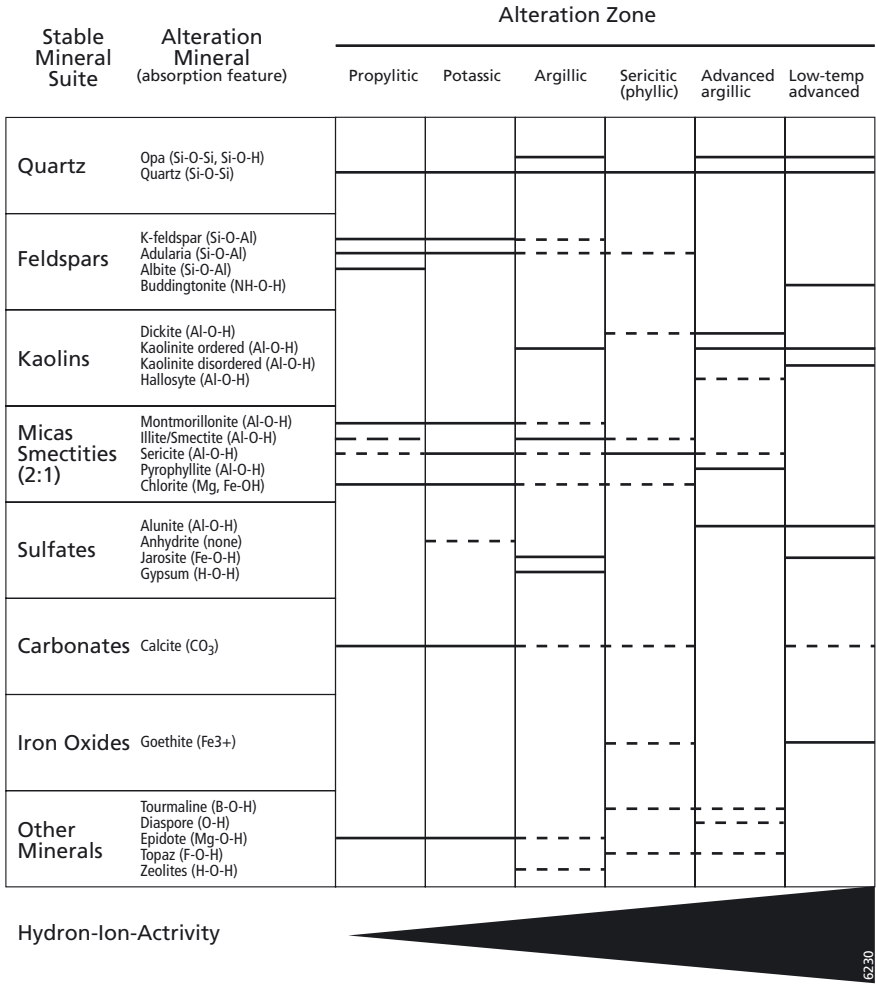| Stable Mineral Suite	Alteration Mineral (absorption feature)	Propylitic	Potassic	Argillic	Sericitic (phyllic)	Advanced argillic	Low-temp advanced
Quartz	Opa (Si-O-Si, Si-O-H) Quartz (Si-O-Si)						
Feldspars	K-feldspar (Si-O-Al) Adularia (Si-O-Al) Albite (Si-O-Al) Buddingtonite (NH-O-H)						
Kaolins	Dickite (Al-O-H) Kaolinite ordered (Al-O-H) Kaolinite disordered (Al-O-H) Hallosyte (Al-O-H)						
Micas Smectities (2:1)	Montmorillonite (Al-O-H) Illite/Smectite (Al-O-H) Sericite (Al-O-H) Pyrophyllite (Al-O-H) Chlorite (Mg, Fe-OH)						
Sulfates	Alunite (Al-O-H) Anhydrite (none) Jarosite (Fe-O-H) Gypsum (H-O-H)						
Carbonates	Calcite (CO$_3$)						
Iron Oxides	Goethite (Fe3+)						
Other Minerals	Tourmaline (B-O-H) Diaspore (O-H) Epidote (Mg-O-H) Topaz (F-O-H) Zeolites (H-O-H)						

Hydron-Ion-Actrivity

6230

Figure 9.3 – Major alteration zones characterizing the high sulfidation hydrothermal alteration system found at Cuprite and the mineral assemblages that are commonly found in these zones.

in parts of the spectrum but differ, particularly in the visible part of the spectrum. Hence including irrelevant information damages severely the matching result. Another point arises in thresholding the correlation to perform a classification. How to objectively determine a threshold? This is a particular problem when using the SAM technique because the angles will vary non-linearly with the percent spectrum mixed into a mixture.

9.2.2 Absorption band parameter estimates

Field or laboratory reflectance spectra have been used to derive compositional information on samples. Usually this involves a multiple-linear regression of absorption-band parameters and chemical composition. The following absorption-band parameters calculated from continuum removed spectra (figure 9.7) are often used: (1) the absorption-band position,
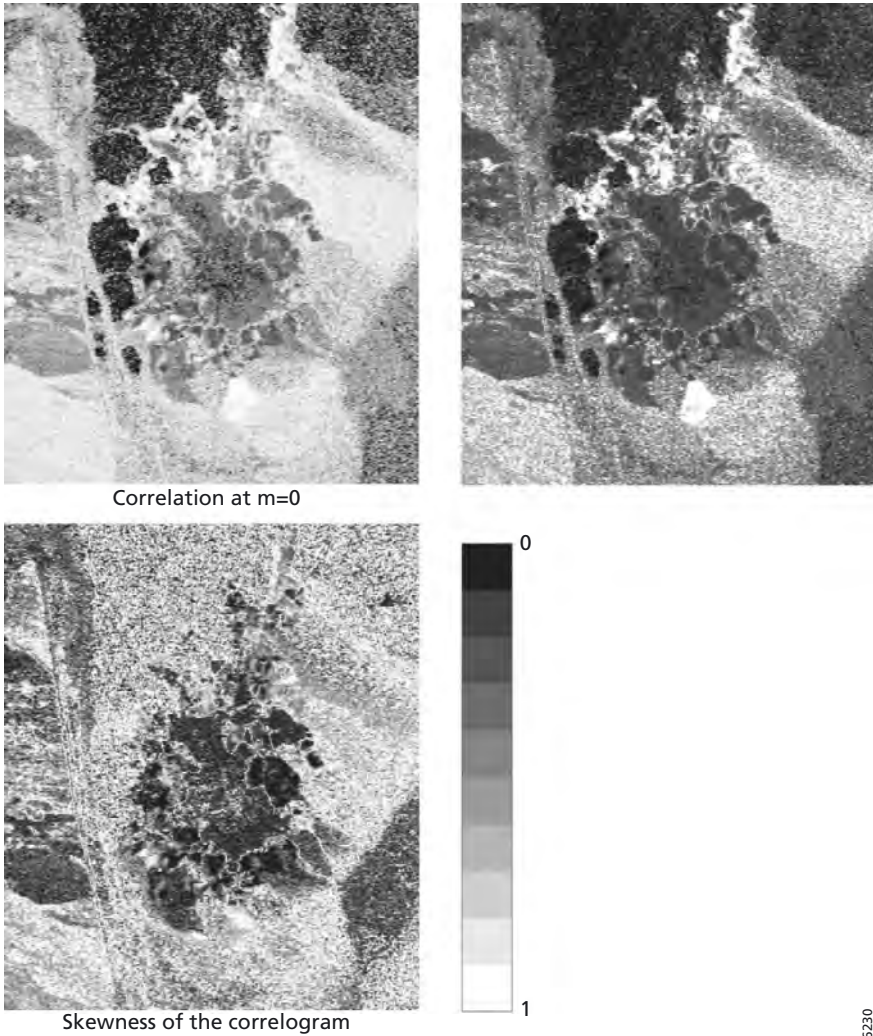
Figure 9.4 – Skewness, significance and correlation at match position 0 for kaolinite as reference.

(2) the absorption-band depth and (3) the absorption-band asymmetry. The depth of an absorption band, D, can be defined relative to the continuum, R_c, as

$$D = 1 - \frac{R_b}{R_c} \tag{9.5}$$

where R_b is the reflectance at the band bottom, and R_c is the reflectance of the continuum at the same wavelength as R_b (Green & Graig 1985). These Hull quotient spectra (also referred to as continuum removed spectra) are used to characterize absorption features, known to be attributed to a certain mineral of interest, in terms of their position, depth, width, and
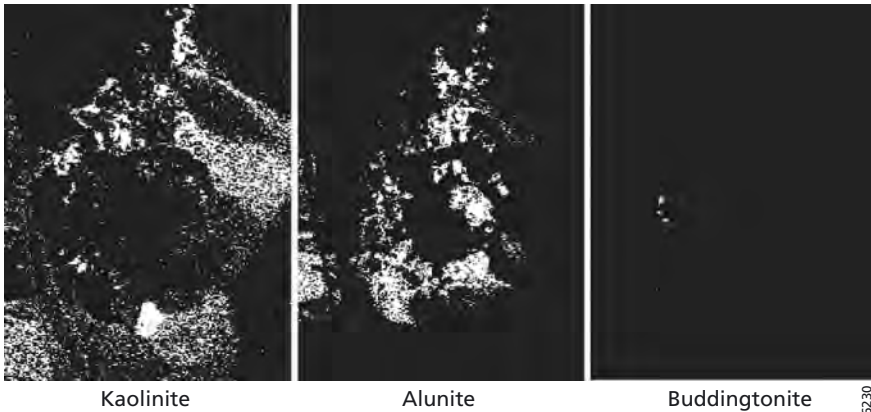
Kaolinite   Alunite   Buddingtonite

Figure 9.5 – Final alteration maps at Cuprite based on CCSM.

asymmetry. The absorption band position, λ, is defined as the band having the minimum reflectance value over the wavelength range of the absorption feature. The relative depth, D, of the absorption feature is defined as the reflectance value at the shoulders minus the reflectance value at the absorption band minimum. The asymmetry factor, S, of the absorption feature is defined as

$$S = A_{\text{left}} / A_{\text{right}} \tag{9.6}$$

where A_{left} is the area of the absorption from starting point to maximum point and the A_{right} is the area of the absorption from maximum absorption point to the end point (shoulder) of the absorption. Values for S range from -1.0 to infinity where S equals 0 for a symmetric absorption feature. Features in which the area on the left-hand side is greater than the area on the right-hand side (i.e., absorption features skewed to longer wavelength) will result in asymmetry values greater than 1. Features in which the area on the left-hand side is smaller than the area on the right-hand side (i.e., absorption features skewed to shorter wavelength) will result in asymmetry values between 0 and 1. Okada & Iwashita (1992) produced waveform characteristics on hyperspectral imagery, however the algorithms were not very well documented.

The absorption band parameter definition as discussed above assumes nearly continuous (contiguous) spectral data, whereas imaging spectrometers acquire data in a large number of discrete spectral bands. The band center wavelength position is usually used for further calculations, thus providing spectral measurements on a discrete number of wavelength positions characterizing an absorption feature. To accommodate this, a simple linear method is proposed to calculate the absorption feature parameters from image data. Figure 9.8 graphically explains the procedure followed.

First for the absorption feature of interest the image bands are determined that would serve as the shoulders of the absorption feature. By definition, there is a short wavelength shoulder (shoulder 2, denoted S2 in figure 9.8) and a long wavelength shoulder (shoulder 1, denoted
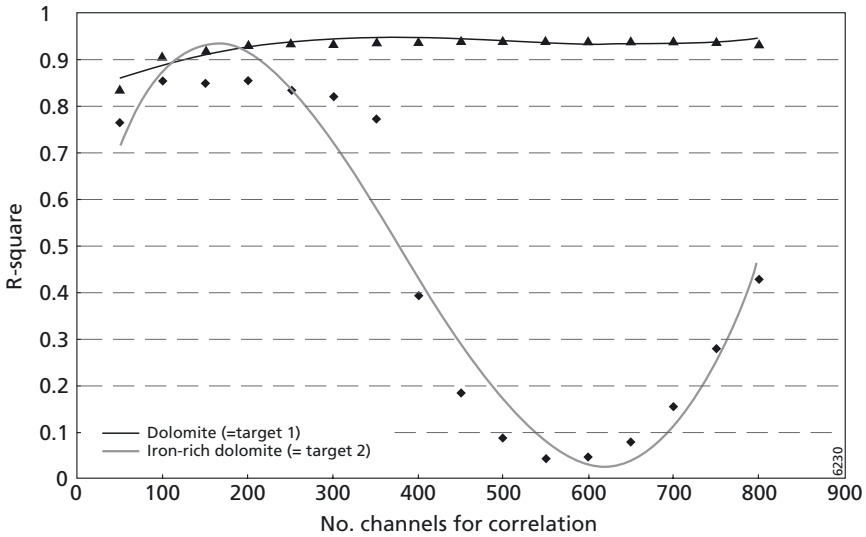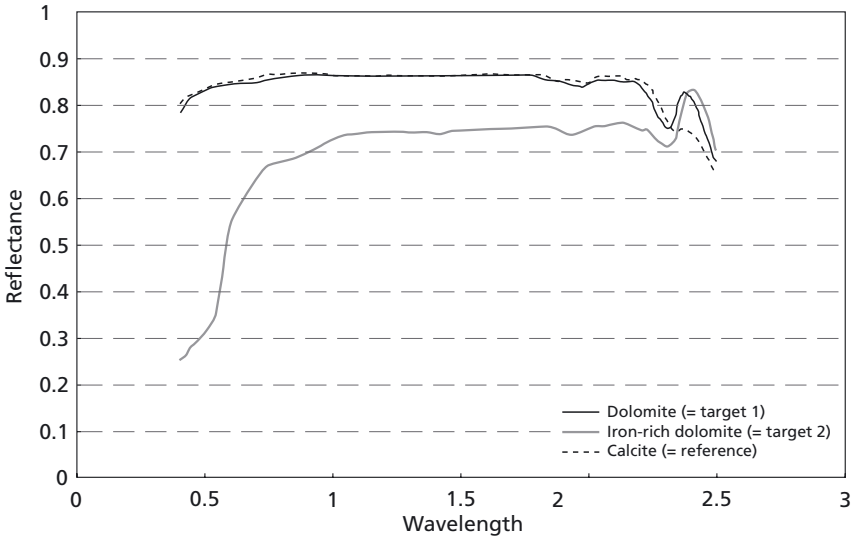
Figure 9.6 – Correlation between calcite (reference) and dolomite (target 1) and iron-rich dolomite (target 2). See text for discussion.

S1 in figure 9.8). Next, the data are continuum removed using the mentioned shoulders as starting and ending points. Subsequently, two bands are selected as the absorption points which will be used in the interpolation (points A_1 and A_2 in figure 9.8). Then, the coefficients C_1 and C_2 are calculated as

$$C_1 = \sqrt{(\text{depth}_1)^2 + (S_1 - A_1)^2} \tag{9.7}$$

Figure 9.7 – Definition of the continuum and continuum removal and subsequent definition of absorption feature characteristics.
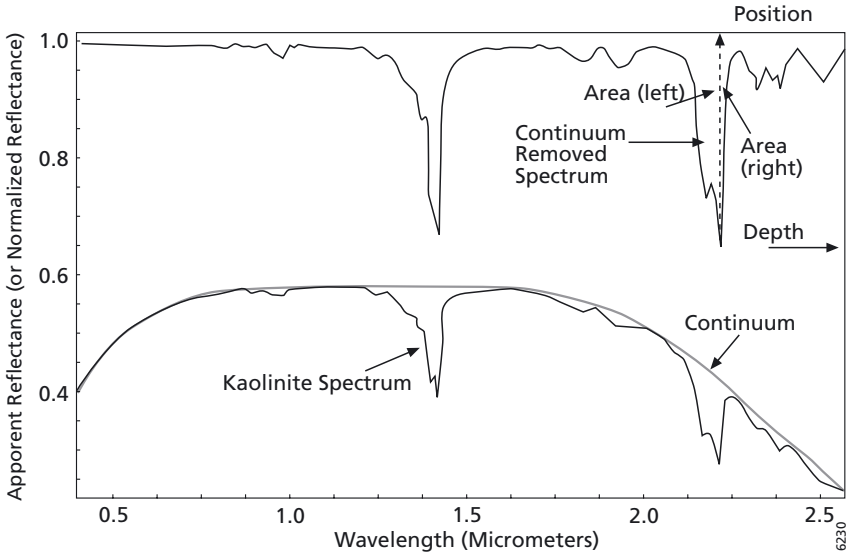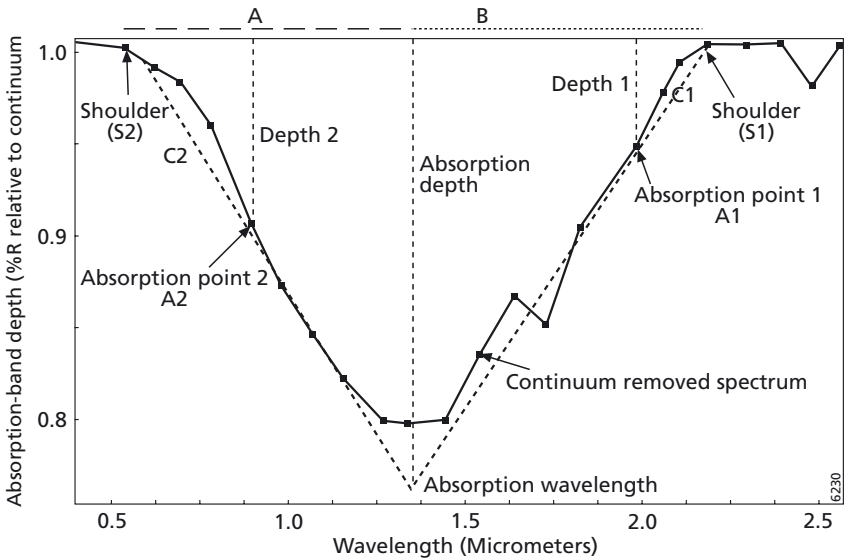

Figure 9.8 – Definition of the parameters used in the linear interpolation of absorption feature characteristics.

and

$$C_2 = \sqrt{(\text{depth}_2)^2 + (S_2 - A_2)^2} \tag{9.8}$$

From this, the interpolated wavelength position (e.g., the wavelength of maximum absorption) can be found by interpolating between the shoulders and absorption points in the spectrum as

$$\text{Absorption\_wavelength} = -\left[\frac{C_1}{C_1 + C_2} \cdot (A_1 - A_2)\right] + A_1 \tag{9.9}$$

or

$$\text{Absorption\_wavelength} = -\left[\frac{C_1}{C_1 + C_2} \cdot (A_1 - A_2)\right] + A_1 \tag{9.10}$$

The associated absorption-band depth is derived as

$$\text{Absorption\_depth} = \left[\frac{S_1 - \text{absorption\_wavelength}}{S_1 - A_1}\right] \cdot \text{depth}_1 \tag{9.11}$$

or

$$\text{Absorption\_depth} = \left[\frac{\text{absorption\_wavelength} - S_2}{A_2 - S_2}\right] \cdot \text{depth}_2 \tag{9.12}$$

The asymmetry factor of the absorption feature is calculated as

$$\text{Asymmetry} = A - B = (\text{absorption\_wavelength} - S_2) - (S_1 - \text{absorption\_wavelength}) \tag{9.13}$$

This operation returns 0 for a perfect symmetric absorption feature, a negative value for a absorption feature that is asymmetric and skewed toward the short wavelength, a positive value if the absorption feature is skewed toward the longer wavelength.

As input to the absorption-band mapping approach, continuum removed spectra were used on a selected portion of the wavelength spectrum where the absorption band of interest is found. In this first case study, focus was on clay mineral absorption features in the SWIR around 2.20 μm and carbonate absorption features in the SWIR around 2.30 μm. Two bands on the shoulders of the feature were selected to perform the continuum removal. For the Al-OH clay mineral absorption features, AVIRIS band 178 centered at 2.0509 μm (shoulder 2) and AVIRIS band 199 centered at 2.2606 μm (shoulder 1) were used. The two absorption points used for the interpolation were AVIRIS band 184 centered at 2.1110μm (absorption point 2) and AVIRIS band 196 centered at 2.2307 μm (absorption point 1) for the Al-OH feature.
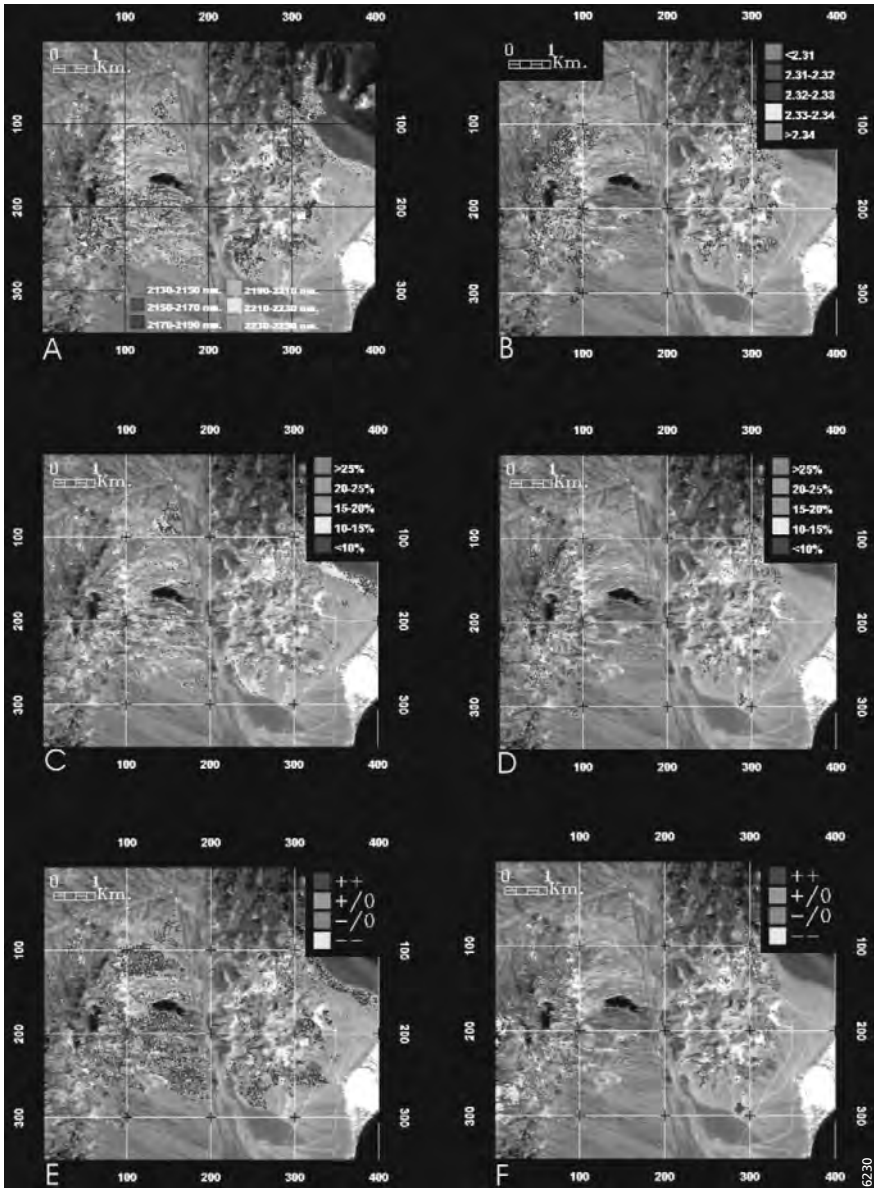
Figure 9.9 – Derived absorption feature parameters for the Al-OH and Ca absorption band: (A) position of maximum absorption wavelength for (A) AL-OH and (B) Ca, depth of the absorption feature (in % reflectance relative to the continuum) for (C) Al-OH and (D) Ca, asymmetry of the absorption feature for (E) Al-OH and (F) Ca (++ = strongly skewed to longer wavelength, +/o =weakly skewed to longer wavelength, o/–= weakly skewed to shorter wavelength, –– strongly skewed to shorter wavelength). Please consult the enclosed CDROM for a full colour version.

The resulting images are shown in figure 9.9 (Al-OH absorption feature parameters). These images can be used to (1) relate absorption feature parameters to measures of mineral chemistry and (2) to describe the hydrothermal alteration system in terms of surface composition (mineralogy) and alteration intensity. In particular the mineralogy as expressed in the AL-OH absorption parameter estimates may be of use. Table 9.1 summarizes the key mineral groups for each of the alteration phases theoretically to be found in this high sulfidation alteration system. The wavelength position of the Al-OH (figure 9.9) can be interpreted in terms of alteration phases. Short wavelength Al-OH absorption is indicative for the presence of buddingtonite and alunite indicating relative high alteration (low temperature advanced and advanced argillic alteration phases). Intermediate wavelength Al-OH absorption is confined to the argillic alteration phases (kaolinite, gypsum), whereas the potassic alteration phase (dominated by montmorillonite) and the propylitic alteration phase is dominated by chlorite thus giving relatively long wavelength Al-OH features. The absorption band depth of the Al-OH feature increases with intensity of the hydrothermal alteration both because of the increase in volume of alteration minerals as well as because of the increase in depth of mineral related absorption bands. The advanced argillic (and low temperature advanced alteration) phase, dominated by buddingtonite and alunite, show intense (deep) absorption features, whereas the argillic and the potassic and propylitic alteration phase mineral generally show less pronounced absorption features. The use of the asymmetry feature for mapping and analysis of the Cuprite data is less straightforward. In principle, by the definition of the asymmetry, the minerals with positive asymmetry values have Al-OH feature skewed to longer wavelength and those with a negative asymmetry value correspond to absorption features skewed to shorter wavelength. Typical minerals that exhibit a negative asymmetry value are montmorillonite, buddingtonite and chlorite. Alunite has a rather symmetric Al-OH absorption feature (asymmetry value of 0), whereas kaolinite, jarosite and in particular gypsum would have a positive asymmetry (because their Al-OH absorption features are skewed towards longer wavelength).

9.3   Stratified analysis of hyperspectral imagery

An alternative approach to thematic analysis of hyperspectral data is stratified analysis. The aim would be to stratify the data on known thematic data layers prior to analytical approaches being applied to the data. In many cases, field or thematic map data is available. This data can thus be used for data processing. One can imagine clustering a data set on mapping units and start analysing within these natural boundaries. Furthermore various data products from hyperspectral data sets can be integrated using statistical techniques.

As example we here look at Probe-1 (also known as HyMAP) from an area in California (Santa Barbara, figure 9.10) known for the presence of oil/gas seeps. These seeps can be detected in hyperspectral imagery either through (1) anomalous spectral behaviour of the vegetation or (2) through mineral alteration in the soil. Hence we first separated the data into a vegetation and a soil component by simply masking the data using the NDVI. Next we stratified the data on the known geological units since these not only affect the soil type and hence the vegetation type but there also is a strong link between seepage and lithology.

Figure 9.10 – Location map and flightlines for the Santa Barbara area. Please consult the enclosed CDROM for a full colour version.

The main oil reservoir rock outcrops at some areas thus allowing seepage of oil to the surface. Seeps are also more likely to appear in gas form when sitting close to the host reservoir rock.

When evaluating the imaged area in terms of vegetation properties in relation to the lithology we can clearly see the necessity for performing a stratified analysis. We calculated the following parameters:
• the NDVI
• the carter stress ratio of band 695 nm. Over band 420 nm.
• the carter stress ratio of band 695 nm. Over band 760 nm.
• and the red edge inflection point
The so-called Carter ratio's (Carter, 1994) are band ratio's that are sensitive to vegetation stress. We computed these two ratio's, 695/420 and 695/760, on a vegetation masked image (that is on pixels that have a NDVI value of greater than 0.5). Similarly we calculated the red edge inflexion point. The red edge wavelength is found by first calculating the reflectance at the inflexion point (R_{re})

$$R_{re} = (R_{670} + R_{780}) / 2 \tag{9.14}$$

And next finding the accompanying red edge wavelength (λ_{re}) by

$$\lambda_{re} = 700 + 40 \cdot ((R_{re} - R_{700}) / (R_{740} - R_{700})) \tag{9.15}$$

where R_{670}, R_{700}, R_{740} and R_{780} are the reflectance values at 670, 700, 740 and 780 nm. wavelength, respectively. In table 9.2 we summarize the results of these calculations for a number of key lithologies in the imaged area. The Monterey formation is the oil-producing
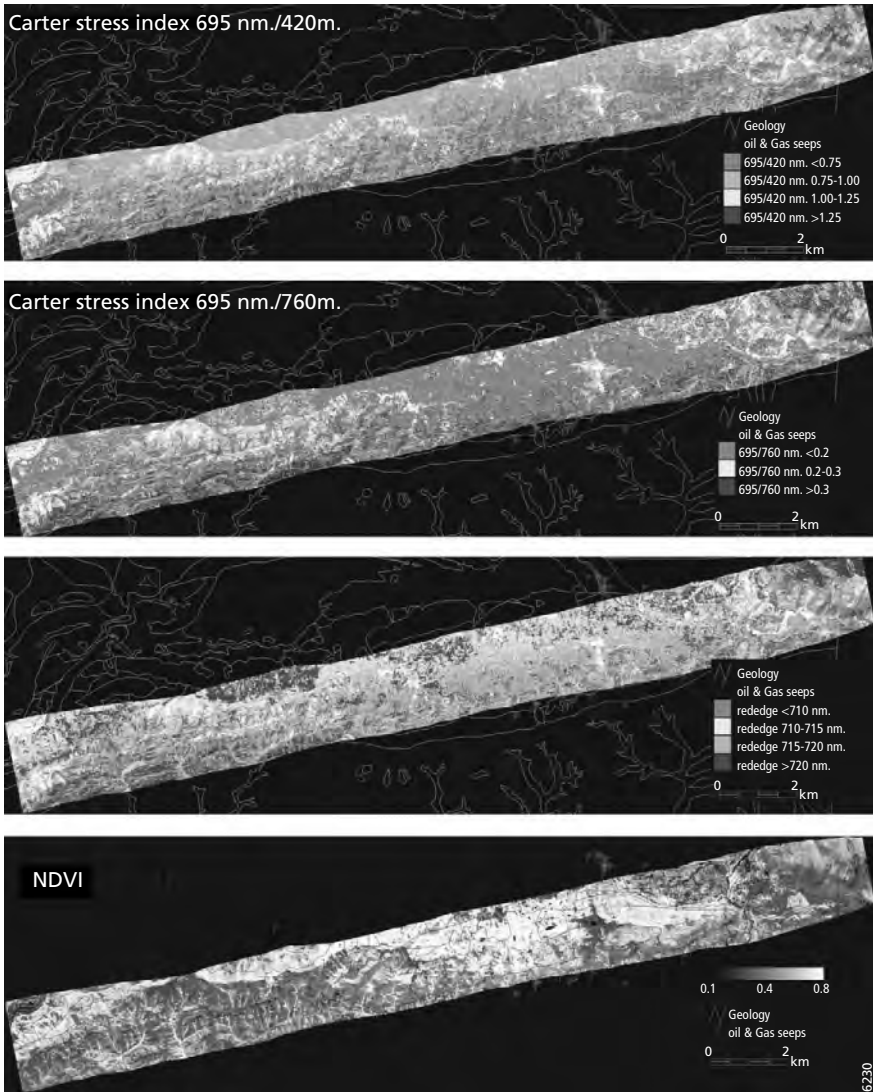

Figure 9.11 – Vegetation stress maps for the Santa Barbara area. From top to bottom the Carter 695/420 ratio, the Carter 695/760 ratio, the vegetation red edge, and the NDVI. The images are annotated with the geologic vectors and the known active oil and gas seeps. Please consult the enclosed CDROM for a full colour version.

Table 9.2 – Typical values of vegetation parameters for selected lithologies in the Santa Barbara imaged area.

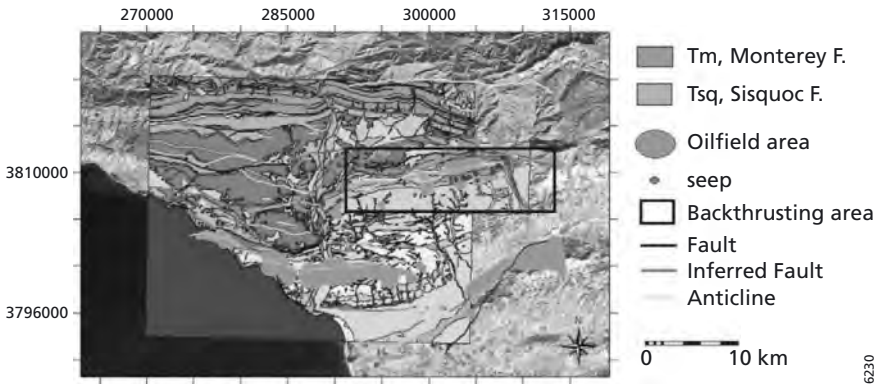| Lithology	NDVI	Red edge*	Carter 695/760	Carter 695/420
Repetto Sandstone	0.2-0.3	725 (710-736)	<0.2	0.65-1.25
Monterey Mud-siltstone	0.6-0.8	712 (700-725)	0.3-0.5	0.50-0.75
Sisquoc shale	0.5-0.8	715 (710-735)	0.2-0.3	0.99-1.2
Sespe red sandstone	0.3-0.5	721 (708-728)	0.1-0.3	1.25-1.5

* mean (min-max)

Figure 9.12 – Map showing the relationship between seeps and key stratigraphic horizons and petroleum geology of the Santa Barbara area. Please consult the enclosed CDROM for a full colour version.

unit. We summarize the results of these calculations for a number of key lithologies (figure 9.12) in the imaged area. The Monterey formation is the oil producing unit, the repetto sandstone is the reservoir unit and the Sisquoc shale and Sespe red sandstones are other key lithologies in the area. Evaluating the statistics of the four vegetation indices shows that there is a strong relationship between these parameters and the lithologies. Thus baselines for each lithology need to be established prior to analysing the scene. In fact, stratification of the image on the lithology is the key approach here.

Hence we first separated the data into a vegetation and a soil component by simply masking the data using the NDVI. Next we stratified the data on the known geological units since these not only affect the soil type and hence the vegetation type but there also is a strong link between seepage and lithology. The main oil reservoir rock at some areas outcrops thus allowing seepage of oil to the surface. Seeps are also more likely to appear in gas form when sitting close to the host reservoir rock.

The main derivative of interest for gas seepage in the vegetated areas is the red edge position, which can be regarded as an indicator of health status of the vegetation. In the soil component we singled out various mineral maps (using spectral matching techniques

described earlier) in particular iron oxides and enrichment in kaolinite and carbonate which are indicative for seepage. These data layers for each unit were integrated using statistical approaches.

The resulting spatial patterns were integrated with known oil and gas seeps using a spatial data integration approach (SDI). The basic proposition, mathematical hypotheses which we want to test, in this study is the presence or absence of an undiscovered oil/gas reservoir formulated as

$$F_p: \text{"p contains an \textbf{undiscovered} oil/gas reservoir"} \tag{9.16}$$

The probabilistic theory embedded in the favourability function allows to address this proposition. The favourability function method requires the two assumptions that: (i) past occurrences of a given type (i.e., a clearly identified type of process) can be characterized by sets of layers of supporting spatial data, and that (ii) new discoveries of the same type will occur in the future under similar circumstances. That is, the present should be able to predict the future. The mathematical framework of the Bayesian implementation of the SDI is embedded in the work of Chung & Fabbri (1993). Consider a probability at any A, $prob\{F_p\}$, for the proposition F_p. This prior probability, a pixel p will contain a future reservoir, is obtained by:

$$prob\{F_p\} = \text{size of } F / \text{size of } A \tag{9.17}$$

where F denotes the unknown areas which will be reservoirs within A and 'size of B' represent the size of the surface area covered by any subarea B in A. $Prob\{F_p\}$ has the same value for all p. The purpose of the modeling is to see how the probability at p will be changed as we observe the m pixel values at p. At pixel p, the pixel value $v_l(p)$ of the lth layer is c_r which is one of the n_l classes (map units), $\{1, 2, ..., n_l\}$. Consider a set of all pixels whose value in the first, layer is c_l. The set is the thematic class in the 1st layer whose pixel value is c_l. The set is denoted by A_{lcl} and it is one of the non-overlapping n_l sub-areas $\{A_{11}, A_{12}, ..., A_{1nl}\}$ in the 1st layer. Assume that the occurrences at each pixel p can be expressed as the joint conditional probability

$$prob\{F_p | c_1, c_2, ..., c_m\} \tag{9.18}$$

that p will be a future undiscovered oil/gas reservoir assuming that the p contains the m values, $(c_1, c_2...c_m)$. When $prob\{Fp|c_1, c_2...c_m\}$ is approximately similar to $Prob\{F_p\}$ we can state that the pixel values at the p, $(c_1, c_2...c_m)$ do not add any useful information whether the pixel is an undiscovered reservoir. However, if

$$prob\{F_p | c_1, c_2, ..., c_m\} \gg prob\{F_p\} \tag{9.19}$$

or

$$prob\{F_p | c_1, c_2, ..., c_m\} \ll prob\{F_p\} \tag{9.20}$$

then the pixel values, (c_1, c_2, ..., c_m) provide very significant information and they are highly correlated either positively or negatively with occurrences. We assume that c_l, will contain an undiscovered oil/gas reservoir and we assume that the c_l, ..., c_m are conditionally independent given the condition F_p, (p will contain an undiscovered oil/gas reservoir). Hence, under the above conditional independence assumption, the joint conditional probability becomes

$$= \frac{prob \{c_l\}...prob \{c_m\}}{prob \{c_l,...,c_m\}} prob \{F_p\} \frac{prob \{F_p|c_l\}}{prob \{F_p\}} ... \frac{prob \{F_p|c_m\}}{prob \{F_p\}} \tag{9.21}$$

Under the conditional independence assumption, this joint conditional probability can be expressed in terms of three components. The first component, the ratio of $prob\{c_l\}$... $prob\{c_m\}$ and $prob\{c_1, ..., c_m\}$ consists of the probabilities related to the input spatial data. The second component, the prior probability $prob\{F_p\}$ is the probability that a pixel p will be an undiscovered reservoir prior to having any evidence. The third component consists of m factors and each factor, the ratio of bivariate conditional probability $prob\{F_p|c_k\}$ and the prior probability $prob\{F_p\}$ indicates a contribution of each pixel value to undiscovered reservoirs.

In figure 9.13 we provide and interpretation of the patterns observed. Particularly the predicted probability map for the mineral alteration provides spectacular results. The image clearly shows an elliptical pattern of high probability values around the actual seep location forming what appears to be a halo. In the center of the halo, low values give the appearance of a clogged area similar to the resulting patterns described in edge-leakage. The vegetation stress analysis in this area did reveal less information, which is due to the fact that little pure vegetation pixels are found and that large parts over the anomalous area are relatively devoid of vegetation.
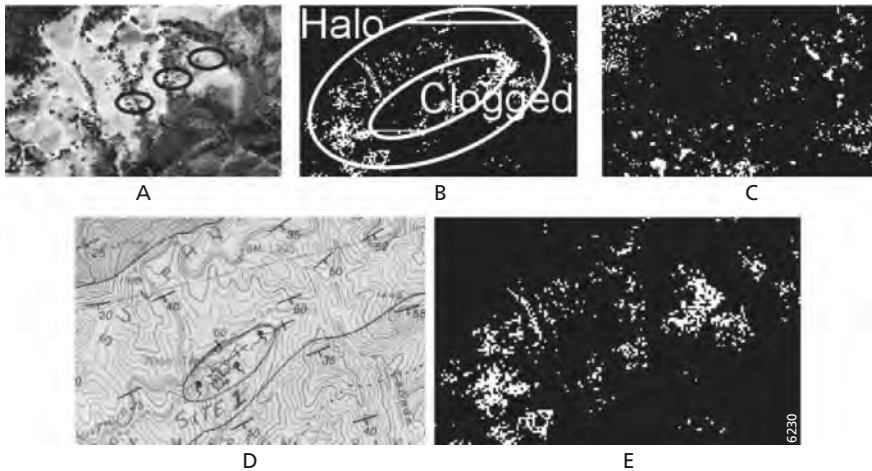

Figure 9.13 – Results and interpretation. False color image of probe bands 16, 9, 4 in RGB with seeps (A), SDI probability minerals with interpretation of the anomaly (B) SDI probability vegetation (C), geological map (D) and SDI probability minerals with annotation. All probability maps display P>0.8.

9.4   Contextual analysis of hyperspectral imagery

Stratified approaches are one step in the direction of using prior and thematic information in the analysis of hyperspectral data sets. A next step would be to include spatial and contextual information. These pixel-based methods have in common that they yield surface compositional information (e.g., in geologic applications this is often surface mineralogy) that has to be further translated into a geologic model (which involves understanding the spatial context of surface mineralogy). Furthermore, these models bypass the common notion in geology that spatial (contextual) information provides valuable information to infer the transitional nature of geologic context. In other words, field geologists working in, for example, hydrothermal alteration systems use mineral paragenesis and the mineral assemblage in their mapping. When identifying a certain suite of minerals at a location not only do they know in which part of the alteration system they spatially are, but they can also infer from this information which mineralogic transition they are about to discover when progressing through the terrain. Hence, not only do they use information on the surface mineralogy, but they also use neighborhood information to unravel the geologic history and alteration system of an area.

When applying the SAM algorithm to the hyperspectral data we often get poor results. Furthermore, we often have difficulties in selecting appropriate thresholds to classify the image. The results of the absorption feature mapping for carbonate features and OH features as shown earlier provide more direct information which allows seperation of spectral features that are partially overlapping (non distinct) such as the carbonate features. However, to include spatial and contextual information we need to develop more complex data models. In the remainder of this chapter, we look an ASTER scene from a sedimentary area in Oman. The area is dominated by limestone and dolomite and to a lesser extent by sandstones and marls. Visual and spectral investigations of the scene allow the experience geologic remote sensor to recognize these lithologies (figure 9.14). However, to include this knowledge into image processing strategies is difficult, but challenging. To allow for the inclusion of contextual information into the process of imaging spectrometry data analysis, in 2000 (Van der Meer, 2000) an inversion method was presented. This method uses a geologic-mineralogic model of the imaged area and inverts the imaging spectrometry data to that model. In an iterative way, the geologic-mineralogic model is adjusted to the observed spectral data. The inversion method theoretically showed how contextual information could be used in imaging spectrometry studies and how surface compositional information could be used as input rather than as output of a remote sensing-based model (Van der Meer, 2000).

Assuming that a set of physical measurements {$\mathbf{m}$} can be inverted to their resulting variables {$\mathbf{x}$} if the underlying physical process is known and the following relationship is assumed

$$\mathbf{m} = \Phi\,(\mathbf{x}) + \mathbf{n} \tag{9.22}$$

where $\mathbf{n}$ is the sensor noise. The direct inversion in the presence of (random) noise results in

$$\mathbf{x} = \Phi\,(\mathbf{m})^{-1} + \mathbf{n} \tag{9.23}$$

In Van der Meer (2000) a Bayesian approach has been discussed for data inversion using an artificial neural network (ANN; following Yang et al., 1999).

The input of geologic knowledge into the process will be described in the following subsections. The mismatch of the inversion model is defined as the difference between the physical measurements $\varphi(x_i)$ and the estimated geologic-physical model $\hat{\varphi}(x_i)$, hence $(\varphi(x_i)-\hat{\varphi}(x_i))$. The neural network is used to iteratively reduce this mismatch propagating the geologic model through the imaging spectrometry data.

The input layer of the neural network is comprised of one node, i, for each discriminating variable, while the one or more hidden nodes, j, each contain a user-defined number of units. The output layer contains one node, k, for each geologic class. The ANN we use (see also Yang et al., 1999) employs a classical back-propagation algorithm where a desired output is defined the on basis of training (geologic) input data (classes) and for each k class the desired output vector d_k is defined. Each training pixel is propagated through the net and the derived output vector o_k is found which in turn is used to find the error term ε which is based on the difference between the true and expected output vectors. The weights between these layers, w_{ji} and w_{kj} are adjusted after each iteration by

$$\Delta w_{kj} = LR \sum_{p=1}^{P} (d_k - o_k) \frac{d}{ds} f(S)\big|_{s_k} h_j \tag{9.24}$$

and

$$\Delta w_{ji} = LR \sum_{p=1}^{P} \left\{ \frac{d}{dS} f(S)\big|_{s_k} \sum_{k} \left[(d_k - o_k) \frac{d}{dS} f(S)\big|_{s_k} w_{kj} \right] \rho_i \right\} \tag{9.25}$$

respectively, where LR is the learning rate (used to control the speed of convergence), f is the sigmoid activation function conveniently defined as $f(S)=1/(1+e^{-s})$, p_i are the i input patterns $i=1...P$ assuming a set of p_i vector-pairs, $(x_1, y_1), (x_2, y_2), ..., (x_p, y_p)$, which are examples of a functional mapping $y=\Phi(x) : x \in R^N, y \in R^N$. We train the network so that it will approximate $o=y'=\Phi'(x)$ by finding a set of weights that fits a number of known observations. The iteration of the network is repeated until the error ε does not exceed a pre-defined threshold value.

A flexible iterative geophysical inversion can be found with the help of a neural network based on a Bayesian approach (Van der Meer, 2000). This neural network allows incorporating ground truth information and neighborhood information. We aim at finding the set of variable $\{x\}$ given the set of measurements $\{m\}$ that maximize the conditional posterior probability $f(\{x\}|\{m\})$. Bayes's basic equation states that the *joint probability* that both events A and B occur is equal to the probability that B will occur given that A has already occurred, times the probability that A will occur $f(A, B)=f(B|A)f(B)$ where $f(B|A)$ is the *conditional probability* expressing the probability that B will occur given A has already occurred.

Translating this to our specific case we can state that in case of an all-inclusive number of independent events x_i that are conditionally related to the measurement **m**, the probability that **m** will occur is simply

$$f(\mathbf{m}) = \sum_{i=1}^{n} f(\mathbf{m} \mid \mathbf{x}_i) f(\mathbf{x}_i) \tag{9.26}$$

Finding a set of parameters that maximize the observations or measurements now yield maximization of

$$\max_{\forall \mathbf{x}_i} f(\mathbf{x}_i \mid \mathbf{m}) = \frac{f(\mathbf{m} \mid \mathbf{x}_i) f(\mathbf{x}_i)}{\sum\limits_{i=1}^{n} f(\mathbf{m} \mid \mathbf{x}_i) f(\mathbf{x}_i)} \tag{9.27}$$

Note that for the time being we assume one physical measurement by the sensor (e.g., radiance or reflectance). Now let us introduce $\{\mathbf{y}\}$ as the set of parameter vectors associated with neighboring pixels. This yields the following joint probability to be maximized

$$\max_{\forall \mathbf{x}_i} f(\mathbf{x}_i \mid \mathbf{m}, \mathbf{y}) = \frac{f(\mathbf{m} \mid \mathbf{x}_i) f(\mathbf{x}_i) f(\mathbf{y} \mid (\mathbf{x}_i \mid \mathbf{m}))}{\sum\limits_{i=1}^{n} f(\mathbf{m} \mid \mathbf{x}_i) f(\mathbf{x}_i)} \tag{9.28}$$

It can be shown that this is proportional to

$$\max_{\forall \mathbf{x}_i} f(\mathbf{x}_i \mid \mathbf{m}, \mathbf{y}) = f(\mathbf{m} \mid \mathbf{x}_i) f(\mathbf{y} \mid (\mathbf{x}_i \mid \mathbf{m})) f(\mathbf{x}_i) \tag{9.29}$$

Thus maximization of the conditional probability of the set of variables $\{\mathbf{x}_i\}$ given the set of measurements $\{\mathbf{m}\}$ within a neighborhood $\mathbf{y}$ is equivalent to minimizing the mismatch between (geologic-physical) model and observation (allowing some mismatch due to sensor noise), $f(\mathbf{m}|\mathbf{x}_i)$, given a prior probability, $f(\mathbf{x}_i)$, for the variables, $\mathbf{x}_i$, and a neighborhood distribution, $f(\mathbf{y}|\mathbf{x}_i)$, which is arbitrarily inferred from a kernel of 8 surrounding pixels.

To enable the introduction of hard (outcrop) and soft (geologic interpretation) geologic data into the inversion process, a fuzzy approach has been designed to incorporate the geologic model. The algorithm implemented is based on the fuzzy C-means classification in that it employs a membership grade matrix, U, for the N (training) pixels representing the L geologic classes as

$$U = \begin{bmatrix} u_{1l} & \ldots & u_{1N} \\ \vdots & & \vdots \\ u_{L1} & \ldots & u_{LN} \end{bmatrix} \tag{9.30}$$

The fuzzy mean for each of the geologic classes, μ_l^*, calculated from the training data and the fuzzy covariance is found as

$$C_l^* = \frac{\left[\sum\limits_{n=1}^{N} u_{LN} (R_n - \mu_l^*) (R - \mu_l^*)^T \right]}{\sum\limits_{n=1}^{N} u_{LN}} \tag{9.31}$$

where R denotes reflectance in band n, and l is the cluster or class. The most important step is the definition of the fuzzy membership function on basis of a Gaussian distribution as

$$P_l^*(R, x, y) = \frac{1}{|\ C_l^*\ |^{0.5}\ (2\pi)^{k/2}}\ e^{-(R - \mu_l^*)^T\ C_l^{*-1}\ (R - \mu_l^*)\ /\ 2} \tag{9.32}$$

This function can be interpreted as a K dimensional histogram, however by introducing the factors x and y denoting the spatial domain, the distribution function is transformed to 2-K dimensions where the first and second dimension represent the image plane. The implementation uses a central pixel of known geologic class representing an actual outcrop and the $P_l^*(R, x, y)$ probability density function to describe how the probability of encountering a similar class changes in the image plane given the spectral characteristics of the classes (since for each class we retain a distribution function). The implementation of the fuzzy outcrop model into the inversion process is as described above. The mean and covariance's for the geologic classes determine the confidence of the interpreter in the geologic model. We will demonstrate in the next section how variations in these parameters affect the model output.

To demonstrate the approach, here we use ASTER data acquired over a sedimentary terrain in a desert environment in Oman. We calculated absorption band parameters for the imaged area using the absorption band interpolation method described. These clearly show the sedimentary nature of the terrain and allow deducing and subdividing the sequence in four basic members namely: limestone, dolomite, sandstone and marl. When we take a transect

Table 9.3 – Probability matrix for transitions in the selected sedimentary sequence.

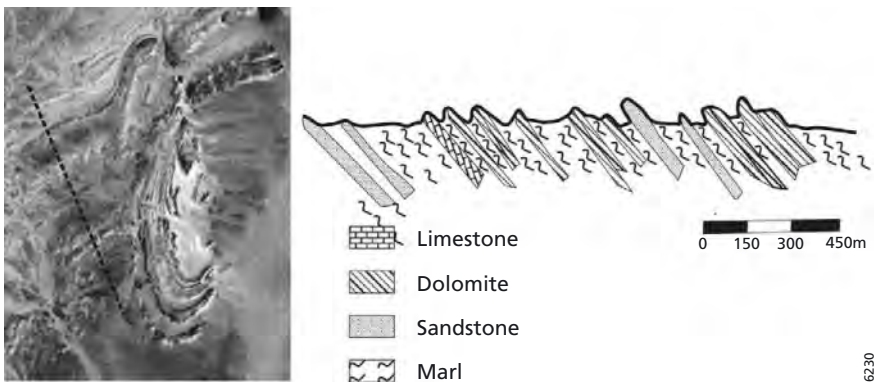|		To				Row totals
		Limestone	Sandstone	Marl	Dolomite	
	Limestone	0.69	0.01	0.21	0.09	1.0
	Sandstone	0.01	0.64	0.25	0.1	1.0
From	Marl	0.21	0.13	0.6	0.06	1.0
	Dolomite	0.05	0.08	0.1	0.72	1.0

Figure 9.14 – Cross-section (dotted line on the ASTER band 3 image) through the imaged area and interpreted lithologies.
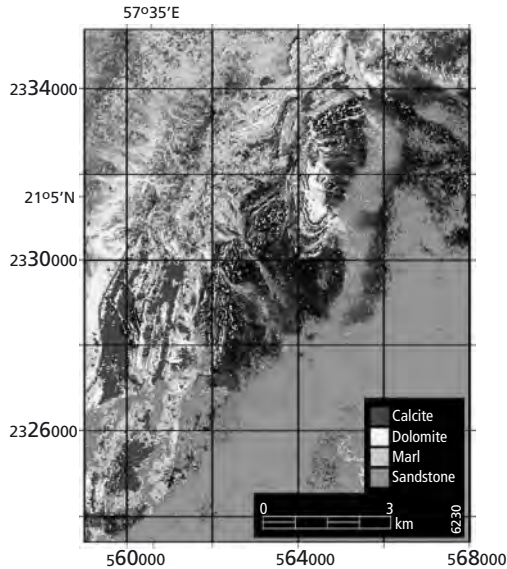
Figure 9.15 – Geoinversion of the ASTER data using 10 iterations and a rigid geologic model (results are overlain on ASTER band 3 subset). Please consult the enclosed CDROM for a full colour version.

through the stratigraphic sequence and code the pixels into the classes mentioned (limestone, dolomite, sandstone, marl) we can do a Markov analysis on the stratigraphic succession (figure 9.14).

Assuming this is an infinite repetitive cycle, we can apply the successions and mutually exclusive states and hence calculate an upward/downward transition frequency matrix. Dividing the frequencies by the total number of occurrences allows us to derive a standardized transition number which we can interpret as a probability. This probability tells us the chance that another unit follows one unit, for example 'what is the chance that we will go from limestone into dolomite'? The various transitions and associated probabilities are listed in table 9.3. Obviously, the transitions within one class are greatest, however the probability between classes can now be computed. We can also see that the upward and downward transitions can be more or less considered similar as the transition from class A to B are nearly identical to the probability of going from B to A. Hence we considered a unified probability for each of the possible transition states. So now the prior probabilities for the variables, $f(x_i)$, are simply the number of occurrences of the state in the type section studied. The joint probability in a certain neighbourhood that we wish to maximize given by:

$$\max_{\forall x_i}. \ f(x_i \mid m, y) = f(m \mid x_i) f(y \mid x_i) f(x_i) \tag{9.33}$$

is now determined by the probability of the individual states and the probability of transitions within one neighbourhood given by the probabilities of the transitions and the length of the neighbourhood.
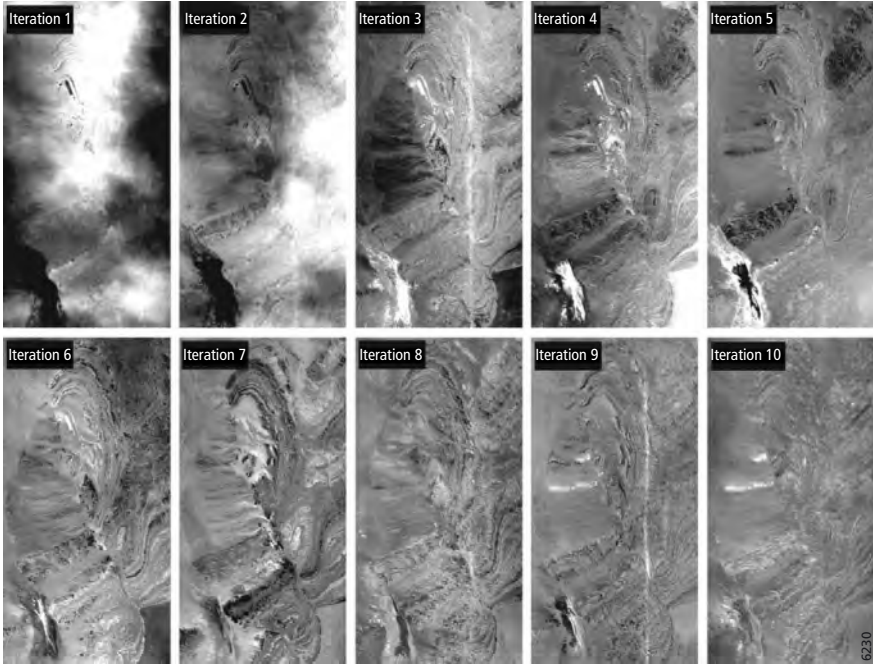
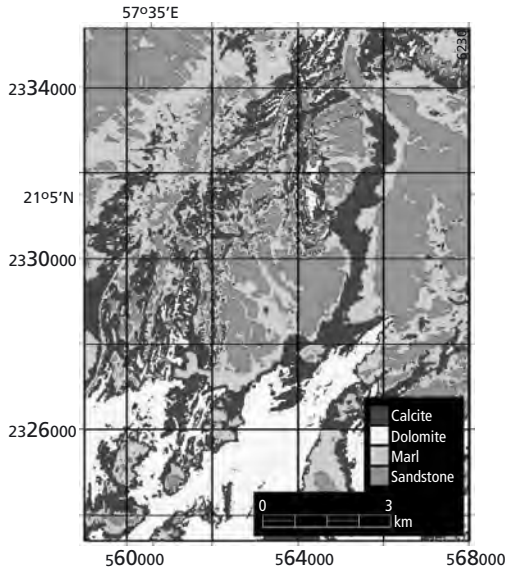*Figure 9.16 – Associated RMS images for the model run of figure 9.15.*

Figure 9.17 – Geoinversion of the ASTER data using 10 iterations and a linear directional Markov model. Please consult the enclosed CDROM for a full colour version.
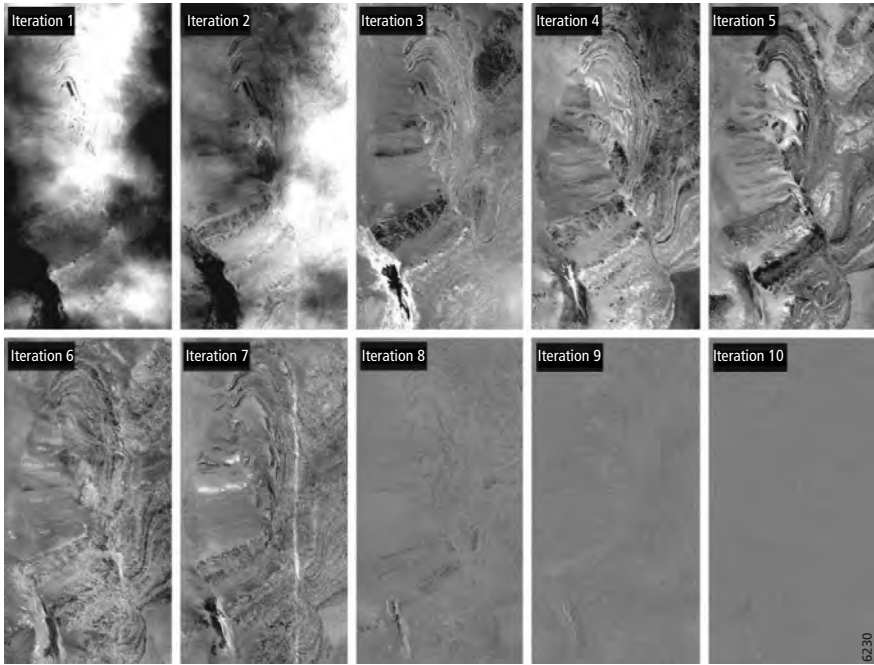
Figure 9.18 – Associated RMS images for the model run of figure 9.17.

The model inversion was run over 10 iterations using the rigid implementation of the geologic model and the fuzzy implementation (figure 9.15 and 9.17). The results are poor and the associated rms/noise images of the sequence of iterations clearly show strong spatial patterns that have been omitted in the analysis. Secondly we ran the model using the fuzzy memberships and the associated probability transitions. This resulted in a significant improvement as can be seen from the noise/rms calculated for each iteration (figure 9.16 and 9.18). A complicating factor that we are presently working on is that the sedimentary sequence is folded. Thus the transition matrix is dependent on the orientation. In our case we are working in a 9 by 9 square kernel along the diagonal directions. This implies that some correction on the probability included needs to be done relative to the orientation of the bedding.

9.5   Conclusions

Reflectance spectroscopy has been used to derive estimates of soil/rock geochemistry and foliar biochemistry using, to date, mostly field and laboratory spectroscopic techniques. These techniques most often make use of absorption feature characteristics (e.g., absorption band wavelength position, depth and asymmetry), which are combined with geochemical analysis in a multi-linear regression to find empirical relationships with chemistry of a sample. Absorption features have also been used as input to spectral feature fitting techniques that allow mapping surface composition (mainly mineralogy) from hyperspectral image data.

However, by this process, the absorption feature analysis is confined to input data in a feature fitting. A simple linear interpolation method is introduced to estimate absorption-band parameters from hyperspectral image data. By applying this hyperspectral data it has been demonstrated that absorption feature maps correspond favourably with the main alteration phases characterizing the systems studied. Thus the derived feature maps allow enhancing the analysis of airborne hyperspectral image data for surface compositional mapping. The next step is to expand in the direction of stratified analysis of hyperspectral data. This allows incorporating prior information into the analysis of hyperspectral data sets. The last example we present is using spatial information in full contextual analysis of hyperspectral data sets. In this case study we deploy Markov chain analysis to include the repetitive patterns in a sedimentary sequence for the study of hyperspectral data sets. Overall, with this paper we wish to advocate that including both prior-knowledge as well as spatial contextual information is an essential step forward in the science of hyperspectral remote sensing.

Chapter 10

Variable Multiple Endmember Spectral Mixture Analysis for Geology Applications

Klaas Scholte, Javier García-Haro & Thomas Kemper

10.1   Introduction

Variations in the earth surface composition in terms of mineralogy, vegetation, and soil patterns represent one of the main sources of systematic change on local, regional and global scale. The ability to detect these variations using multitemporal, multispectral and hyperspectral remotely sensed data is of utmost importance for both environmental research projects and management activities (Maselli, 1998). The analysis of compositional measurements on a large number of materials has to consider individual samples as mixtures of a relatively small number of endmembers (EMs), which represent the spectral characteristics of the scene cover types. Spectral Mixture Analysis (SMA) was developed in recent years to determine the sub-pixel abundance of vegetation, soils, and other spectrally distinct materials that fundamentally contribute to the spectral signal of mixed pixels (e.g. Smith et al., 1985; Adams et al., 1989). SMA aims at finding the fractions of a number of EMs that best explain the observed mixed pixel reflectance spectrum. This technique decomposes the scene in linear combinations of spectral endmembers to recover the fractional contributions of the fundamental components as abundance images (Settle & Drake, 1993). Figure 10.1 illustrates the SMA basic principal in terms of the spectral characteristics of water (endmember 1), soil (endmember 2), and vegetation (endmember 3). A scatterplot of the two bands shows the spectral variation for these three endmembers. Hence the black crosses, which can be identified as image pixels, can be considered as a mixture of these three components.

The technique, therefore, provides a means to detect and represent components that occur entirely at a subpixel level, such as soil contamination after a mining accident or minerals in mud volcano flows. When applied to multispectral satellite data or hyperspectral airborne data, the result is a series of images each depicting the proportion or abundance of a surface cover type.

Different SMA approaches have been developed in the literature. The most widely used method consists in employing the same EMs (typically between 2 and 5) on the whole image, and using all available EMs at the same time. In our case however, many contaminated soils and various mud volcano clay minerals are present in the scene, in such a way that 2-5 EMs are often insufficient to describe the scene fully, and lead to unclear results. For example,
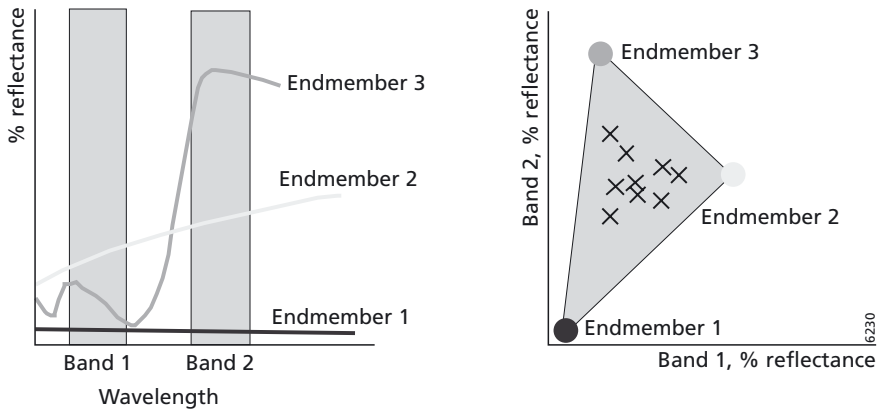
Figure 10.1 – Two dimensional spectral data, reflectance spectra of the individual endmembers (left) and the endmembers in a two-band plot (right) in which the crosses indicate the reflectance of the pixels in the image (After Adams et al., 1993).

fractions of the unmodelled EMs will be partitioned or allocated to incorrect EMs. Fractional errors result also in physically unrealistic negative or overpositive fractions. Simple unmixing is also unable to address correctly the natural variation of components in the scene. Smith et al. (1994) found that the dominant effect of EM spectral variability is expressed in changes in fractions rather than an increase of the modelling error.

In recent years, many authors have proposed a more complex model where both the number and the set of EMs vary on a per-pixel basis. The idea consists in restricting the large set of possible endmembers to a small set of appropriate endmembers, which can be different for each pixel, thereby allowing an accurate decomposition using a virtually unlimited number of endmembers. This strategy dynamically identifies the optimal EM subset for each pixel image. Several authors (García-Haro et al., 1995; Maselli, 1998; Painter et al., 1998; Roberts et al., 1998; Okin et al., 1999) have adopted this criterion and this improved SMA is known as Multiple Endmember SMA (MESMA) (e.g. Roberts et al., 1991; Lacaze et al., 1996).

However, MESMA still have problems to identify EMs that may not reflect the different surface conditions in the scene. Deviations of the linear relation as well as the limited amount of available endmembers will often produce unrealistic outcomes in terms of physically unrealistic, negative or overpositive endmember abundances. This is caused by an inappropriate set of endmembers to describe the spectral variability of the full image on a per-pixel basis. VMESMA (Variable Multiple Endmember SMA) is an extension of MESMA that attempts to overcome these problems. It relies on the use of *a priori* knowledge, which is especially necessary when different submodels tend to model the same areas equally well. An optimum strategy seems to be identifying different sub-areas and decomposing them in a separate stage. For example, for agricultural studies one possible procedure would consist of first classifying the pure pixels and then unmixing the mixed pixels (Klein-Gebbinck, 1998). VMESMA is an integrated image analysis package that incorporates appropriate tools to dynamically identify various distinct image sub-areas and uses in each specific sub-area the

most convenient set of candidate EM submodels and the most optimal criteria for submodel selection on a per-pixel basis.

10.2   Theory and methods

10.2.1   Endmember selection

The unmixing process relies on EMs that closely represent pure surface cover types that show significant spectral contrast. Therefore, the strategy to select these endmembers is one of the key issues in the successful application of SMA. Several authors have extracted the EMs from a field or laboratory spectral library (e.g. Kemper, 2003; Van der Meer, 1996). This method is somewhat limited to take into account all processes and factors influencing the data, such as instrumental drift, atmospheric effects, and illumination intensity. However this method is recommended when the object of interest is occurring only at image subpixel level and hence no pure pixel EM can be extracted. Many authors (Smith et al., 1985; Settle & Drake, 1993; Maselli, 1998; García-Haro et al., 1999; Van Der Meer & De Jong, 2000) extract EMs from the image itself subject to a set of user-defined constraints. For example, EMs are usually selected by using statistical methods, such as principal component analysis (PCA) (Richards, 1994), convex hull geometry (Boardman, 1992), or a pixel purity index (PPI) (Boardman et al., 1995). The categorisation of the scene is especially helpful to identify and estimate image EMs in user-defined areas, typically unmodelled areas or presenting unrealistic proportions. The VMESMA tools combine spatial attributes like user-selected regions of interest or segmented units, with spectral attributes (e.g. scattergram-based zonification) in order to highlight the desired features in the image. Image EMs are then extracted from these areas using different tools such as non-supervised clustering or PCA-based algorithms. These EMs are better adapted to the local variations in ground slope, elevation, soil type, etc. and reduce unmixing errors due to the uncertainty related to apparent surface reflectance retrievals.

However, image EMs may be limited to address materials not fully occupying a pixel. This weakness may be alleviated by spectrally matching the image EMs with a spectral library, which moreover provides them with a physical interpretation. With this aim, it is convenient to dispose of a comprehensive spectral library that contains spectra of plausible ground components. The library used in VMESMA is associated with a spectral attribute database, namely MedSpec, Mediterranean Spectral database (Preissler et al., 1998).

The spectral library matching tool combines the following methods: (i) spectral angle between field (f) and library (l) spectra by applying equation

$$\alpha = \cos^{-1}\left(\frac{f \cdot l}{\| f \| \, \| l \|}\right) \tag{10.1}$$

(ii) the euclidean distance between f and l, and (iii) the euclidean distance after applying a standardisation procedure, i.e. transforming the data to a set of percentage variations about the mean value. The final decision relies on the combined scores of the considered methods along with the visual examination of the matching.

In the case studies below, we have used library spectra since (1) the data are calibrated to reflectance and (2), for contamination mapping, an advanced spectral library for natural surface materials of Mediterranean ecosystem is available (Preissler et al., 1998).

10.2.2 Standardised unmixing

Shade conveys useful information regarding vegetation structure, a key to vegetation types identification and classification (Adams et al., 1995; Shimabukuro et al., 1998; Roberts et al., 1998; Peddle et al., 1999). For example, shadow patterns caused by canopy architecture may be used to infer community physiognomy (e.g. grasses, shrubs, and trees) and surface texture (Smith et al., 1990, Ustin et al., 1993). However, the utilisation of the shade EM introduces important drawbacks:

1 The difficulty to unambiguously define an average pixel signature for the shade component, since the 'obscurity' or tonality of shadow cast by vegetation varies depending on the canopy structure and the leaf transmittance.
2 The shade abundance is less directly interpretable in ecological terms than soil and vegetation maps. Moreover, shade is dependent on sun/view angles and topography, and varies with time.
3 Using a shade EM results in a more unstable solution of the SMA due to the lowering of spectral complexity between EMs since the shade EM, by definition a very dark spectrum, makes the mixing library more ill-conditioned (Boardman & Goetz, 1991; García-Haro, 1997).
4 Retrieving the absolute abundances of the EMs requires partitioning of the shade abundance between the rest components. However, renormalising the shade introduces systematic errors, since at the subpixel scale, where shadows cannot be spatially resolved, it is not possible to tell whether shade is due to shading, shadows, or to a combination of both (Smith et al., 1990).

In order to overcome many of the limitations of the shade EM, an alternative approach consists of performing a standardisation on both the EMs and the image spectra as a preliminary step before applying the SMA. This standardisation transforms the data to a set of variations about the mean value with a mean value of zero and a standard deviation of one. This allows matching of the data in a manner independent of the reflectance scale (Mackin et al., 1991):

$$\hat{\mathbf{r}} = \frac{\mathbf{r} - \mu_r}{\sigma_r} \qquad\qquad (10.2)$$

where $\hat{\mathbf{r}}$ is the standardised vector associated to the pixel vector $\mathbf{r}$, with mean μ_r and standard deviation σ_r. This procedure bypasses problems related to shadowing and brightness variations due to grain size etc., retaining and enhancing the information due to the spectral shape, such as gradient (i.e. derivative features) and absorption bands. This approach is based on the same principles and equations of the conventional SMA.

García-Haro et al. (2003) expressed the standardised SMA as follows

$$\hat{r} = \sum_{i=1}^{c} \hat{E}_i \hat{f}_i + \hat{\varepsilon} \tag{10.3}$$

where $\hat{r}$ is the standardised pixel vector, $\hat{E}_i$ represents the standardised i-th endmember spectrum of a population of c spectra, $\hat{f}_i$ is the proportion of such endmember in the standardised co-ordinates, and $\hat{\varepsilon}$ is the residual vector (expressed in standardised units). Using the definition of standardised variables, we can rewrite equation 10.3

$$\frac{r - \mu_r}{\sigma_r} = \sum_{i=1}^{c} \frac{E_i - \mu_{Ei}}{\sigma_{Ei}} \hat{f}_i + \hat{\varepsilon} \tag{10.4}$$

If we compare it with the standard SMA we find the following relationship

$$f_i = \sum_{i=1}^{c} \frac{\sigma_r}{\sigma_{Ei}} \hat{f}_i \tag{10.5}$$

This transformation ensures the 'sum-to-one' condition of the endmembers and preserves the positive fraction constraint. The standardised SMA applies the SMA using the standardised pixel vector $\hat{r}$ and the standardised endmembers $\hat{E}_i$ (i=1,... c). The solution is identical to the solution for the standard constrained SMA. The SMA solution provides estimates of the unknowns $\hat{f}_i$, and the model errors are quantified by means of a residual model $\hat{\varepsilon}$. Finally, the proportions fi constrained to sum-to-one are estimated making use of equation (10.5).

VMESMA allows applying conventional unmixing to estimate the EM proportions, based on reflectance, but it also provides an alternative solution, namely standardised unmixing, which offers new more appropriate solutions to specific problems. One advantage of applying a standardised SMA is that it is possible to use a spectral signature of a new different material, or to apply SMA with a smaller number of endmembers increasing the reliability of estimated abundances. Another practical reason for a standardised unmixing is that VMESMA does not need a fixed amount of endmember spectra such as the conventional SMA, where only a maximum of N-1 EMs can be used.

10.2.3   VMESMA features

VMESMA is conceived as an iterative feedback process, in which unmixing performance may be potentially improved in each stage until an optimum level is reached. This permits the definition of standard and repeatable pathways to incorporate information dynamically derived from the most recent unmixing outcomes with other sources of data in order to optimise the algorithms and increase the flexibility of the modelling approach. The structure of the VMESMA is summarised in figure 10.2.

After each unmixing run, the user is provided with a suite of outputs readily available to conduct the error assessment. In addition, abundances of similar EMs are usually merged to group together thematically EMs into general categories, as it provides the physical context necessary to interpret the results. As a by-product, obscuring materials – such as green/dry vegetation in geological applications or shade – may be removed from the reflectance image. One direct application would be scaling up mineral proportions in each pixel producing de-vegetated geological reflectance images for identification of rock-types (Bierwirth, 1990).
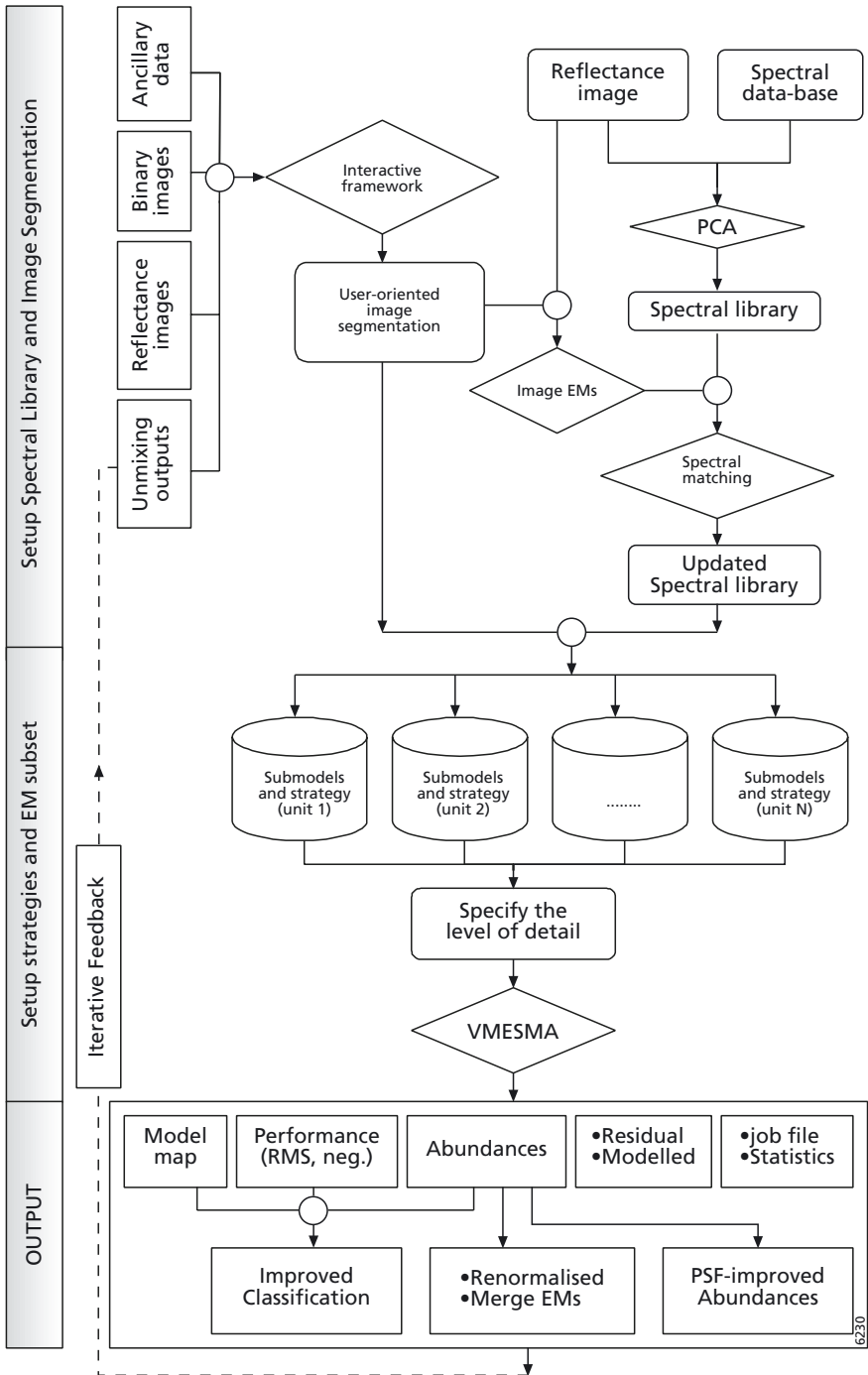
Figure 10.2 – Flow-chart of the VMESMA working scheme.

The analysis requires scientist guidance and oversight, mainly to evaluate the model performance and fractional errors. With this aim, VMESMA provides overlay capabilities that show all the specified spectral information of the chosen pixel, and real-time pan and zoom and link spectral profiling from large multiband data. Thus the analyst can seek for pixels with high root mean squared error (RMSE) or fractional errors, relating such results with the simultaneous analysis of their reflectance spectra, their best-fit modelled spectra, the residual spectra, the model chosen, the unit number and the set of abundances obtained. This information can be used to incorporate new areas to the image segmentation and modify the model lists for subsequent unmixing runs in order to improve the results.

Stratifying the images before applying more specific interpretative procedures may improve identifications of specific compounds and is the basis of the variable unmixing strategy. Multispectral information, unmixing results and any other different source of data may assist in revealing the structure of the area and allow its partition into characteristic zones with user-specified attributes. VMESMA provides tools to incorporate information from many different data sources including ancillary data (e.g. land cover, land use, soil type) and multispectral data (e.g. reflectance, modelling errors, abundances). Generally, fine-grained studies for small regions will define more EMs than coarse-grained studies of larger regions (Ustin et al., 1993). Thus, repeated analyses on spatial or spectral subunits of the image may increase the number of identified components since additional components may be identified from the residual or unmodelled spectral variance. After each unmixing run, new image subunits may be thus identified from spectral and spatial features of interest. Problematic areas are usually found from high modelling and abundances errors, i.e. typically identified from negative values or not matching the proportions derived from the field observations or other sources. Next, the analyst can extract EMs from these areas, which will be incorporated in the EMs library. The subsequent iteration will be performed on the basis of the updated image segmentation and using a modified models list extracted from the updated library. VMESMA also enables selective unmixing in which only a few image subunits are processed while leaving unaltered the abundances of the rest, as obtained in a previous iteration. This strategy may speed up considerably the computations.

One of the critical constraints of the unmixing analysis is the requirement for human intensive involvement and computational cost. VMESMA integrates speed optimisation capabilities such as an efficient expert system to select the best EM submodel, selective analysis focused on problematic areas and a compression scheme for a fast, interactive unmixing in the first stages of the iterative process. The model performance is usually assessed in the literature from the residual spectrum (e.g. RMSE, maximum residual or the quadratic chi-square of the fit. In addition, VMESMA uses a new and alternative criterion, namely colinearity factor, that has demonstrated to be very robust and faster than the residual one, since it reduces the dimensionality of the problem. Taking decisions about model creation may be useful to reduce the model set to a smaller, more appropriate one, thereby saving time of computations and improving the final results. Model subselection includes, among other methods, removal of models that account for less than a percentage of the image and/ or are spatially fragmented (Roberts et al., 1998). The first steps of the process, i.e. the EM submodels creation, hence segmentation of the area, and identification of unmodelled EMs, is usually performed using smaller images thanks to a compression scheme. Then the analyst

progressively increases the level of data quality in the successive unmixing runs with the aid of an upscaling utility that expands the segmentation image to the specified level of detail.

The Unmixing frame is an easy-to-use interface for specifying the EM submodels and the strategy to unmix each individual unit. The spatial/spectral compression scheme can be specified at each unmixing iteration. Each unmixing is executed in a sequence unit by unit, starting from the first unit. For each individual unit the scientist can specify the following parameters:

1. The expert system used to select the best EM subset. Although VMESMA is based on an adaptable selection of the number of EMs (2, 3 or 4), a 'hard' criterion (e.g. selecting always a 3-EM model) or, alternatively, a simpler mixed criterion (e.g. enabling only 2 or 3 EM solutions) are also possible. VMESMA uses an efficient expert system, which basically ties together modelling errors and fractional errors, and makes an automated decision to assign each composing material to its optimum EMs subset. The procedure is composed of three steps: (1) The colinearity factor criterion is applied to all submodels in order to preselect the most probable candidates; (2) fractional errors (ε_{neg}) and modelling errors (ε_r) are used to identify the most likely 2-, 3- and 4-EM subsets, and (3) the three best subsets are compared using an expert system in order to select a single subset.
2. The lists of candidate EM subsets. A function enables the user to create and edit the candidate EM subsets selecting them from the current library.
3. The type of unmixing algorithm, i.e. conventional or standardised unmixing.
4. The final criterion used to evaluate the modelling errors, i.e. RMSE residual, maximum residual or a new concept, namely colinearity factor (García-Haro et al., 2003).
5. Which of the following operations is performed on each individual unit: (i) mask, (ii) unmix using the updated submodels list, or (iii) keep the abundances of the last unmixing (i.e. selective unmixing).
6. The covariance matrix of the observations, e.g. to modify the relative contribution of each specific spectral band in the unmixing analysis. In general, channels that are more uncorrelated, present higher radiometric accuracy and enhance the contrast between EMs should be prevalent. A preliminary study (Brink et al., 2003) has shown that the

Table 10.1 – Summary of some relevant VMESMA features.

VMESMA Application	Relevant VMESMA feature
Use of Spatial information	Stratification driven by the targeted application EM submodel adapted to physiographic conditions Reduced EM misidentification Reduced computation time
Problem diagnosis and solution	Addressing unmodelled EMs Link with a thematic spectral library More reliable modelling of scene characteristics
Hierarchical assessment	Incorporation of prior knowledge and previous unmixing results Focused analysis of specific sub areas
Advanced unmixing methodology	Standardised unmixing Use of contextual information Speed optimisation capabilities

assessment of the carbonates and clay is increased using higher weights for channels corresponding to its absorption bands in the SWIR (e.g. the spectral interval [2200, 2450] nm), which enhanced the identification and mapping of the main soil spectral components.

In summary, the segmentation of the scene in combination with a knowledge-based expert system adds flexibility to the solution. Hence the determination of the optimum pixel submodel is not a 'black-box' but it may be effectively assisted by the unmixing outputs, the field information, the image characteristics and the targeted application (see main VMESMA features in table 10.1).

10.3 A case study from the Aznalcóllar Mine, southern Spain

10.3.1 Introduction

The Iberian Pyrite Belt (IPB) is considered one of the most important reserves of non-ferrous metals in Europe, that include the massive sulphide deposits of Rio Tinto, Aljustrel, Neves Corvo, Tharsis, Sotiel and Aznalcóllar (Almodóvar et al., 1998). Many areas in the IPB were mined since roman times. In April 1998 the dam of the tailings pond of the Aznalcóllar mine, approx. 30 km West of Seville (Spain), broke and contaminated more than four thousand hectares of flood plain and agricultural land with fine-grained pyritic sludge with high concentrations of heavy metals (figure 10.3).

The tailings were stored in the pond to prevent the pyrites from oxidation. Pyrite oxidation is a complex process that proceeds rapidly, when pyrite is exposed to air. It produces in a first step a solution of ferrous sulphate and sulphuric acid. The dissolved ferrous iron continues to oxidize and hydrolyze producing additional acidity. During the oxidation process the pyrite transforms first to copiapite, then to jarosite, schwertmannite, ferryhydrite and eventually to hematite or goethite (Nordstrom, 1982). These secondary minerals are iron-rich, hydroxyl- and/or water bearing, which makes it possible to identify them on the basis of their diagnostic spectral reflectance features (Swayze, 2000). Thus airborne hyperspectral images were acquired for mapping of the residual contamination after the first remediation campaign

Figure 10.3 – Aerial photograph of the Aznalcóllar area showing floodings right after the accident. Please consult the enclosed CDROM for a full colour version.

and for monitoring the development of the oxidation process. The airborne campaigns were accompanied by a dedicated soil sampling and spectral measurements.

10.3.2 Data set

The imaging spectrometry data were acquired with the HyMap sensor in June 1999 and July 2000. The data takes covered the entire contaminated area and were accompanied by a radiometric calibration field campaign. The HyMap system provides 128 wavebands over the range 403-2480 nm with a spectral resolution of 13-17 nm. The data were delivered atmospherically and geometrically corrected by DLR according to the methods described by Richter (1997) and Schlaepfer et al. (2001). During two extensive field campaigns in parallel to the flight campaigns seven representative sites along the affected river catchments were selected. Spectral measurements using GER S-IRIS and ASD Fieldspec II resulted in a VIS to SWIR high-resolution library hierarchically organised of rocks, soils and vegetation. Furthermore, in both years a detailed soil sampling was carried out, collecting more than 300 samples from different depths. The soil samples were geochemically analysed in the laboratory for their element composition using standard methods (XRF, AAS) and spectrally measured.

10.3.3 Detection of residual contamination and oxidation products

The selection of appropriate EM is crucial for a successful application of SMA. It has to consider the changing spectral significance of EM as a function of the variability of the present surface materials, the spatial and spectral resolution of data and the thematic purpose of the study.

For the detection of residual sludge and oxidation products, different EM had to be taken into consideration, which reflect the sludge EM and potential secondary minerals like jarosite, copiapite, ferrihydrite and goethite. However, for the images of 1999, the oxidation was limited to areas with a constant water supply and for the major part of the contaminated area no considerable oxidation took place. Thus, a single spectrum of pure sludge was sufficient
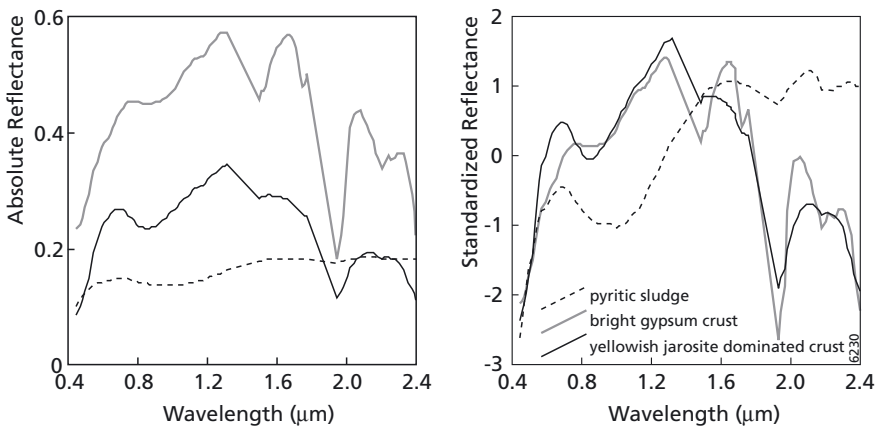

Figure 10.4 – Sludge and secondary mineral end members.

to represent the sludge fraction. In the year 2000, other sludge related spectra had to be taken into consideration, because field and image assessment confirmed that the oxidation processes had produced various crusts on the soil surface. During the second field campaign, spectral measurements of the most abundant crusts were recorded from which the EM were selected (figure 10.4). In this case study, the use of image EM derived with VMESMA from the image was not suitable due to the fact that after the clean up the sludge was worked into the soil and it was impossible to obtain a pure sludge EM from the image.

The pyritic sludge is spectrally very dark and almost featureless as shown in figure 10.4. This causes problems in conventional SMA, because the spectral contrast between sludge and other dark and spectrally flat components, like water or shade, is very small causing misidentifications. Using the standardization prior to the unmixing, which enhances strongly the weak absorption features of the sludge, solves this problem, because the shade EM can be neglected as described earlier. Moreover, also the green vegetation can be represented using as few as a single EM.

For the extraction of the residual sludge the signal had to be separated from other 'background' information. Thus, typical spectra of green and dry vegetation and two different soils were selected from the spectral database as background information (figure 10.5).

In the first unmixing step, the four background spectra were used to unmix the entire scene. The RMSE after the first unmixing clearly separated the sludge-affected areas with a high RMSE from the non-contaminated areas (figure 10.6).

The next unmixing step was performed on the segmented image. Areas outside the contaminated area were neglected, and in the affected area, a RMSE threshold was used to separate areas that were already sufficiently modelled from areas which were sludge affected. The sludge abundance map for June 1999 (figure 10.7) shows that the sludge abundances were still very high with an average abundance of 0.51 (calculated for areas with sludge abundances
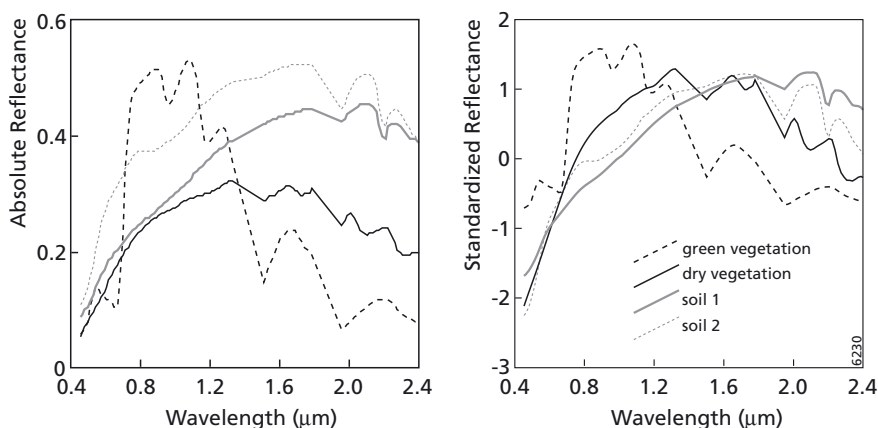

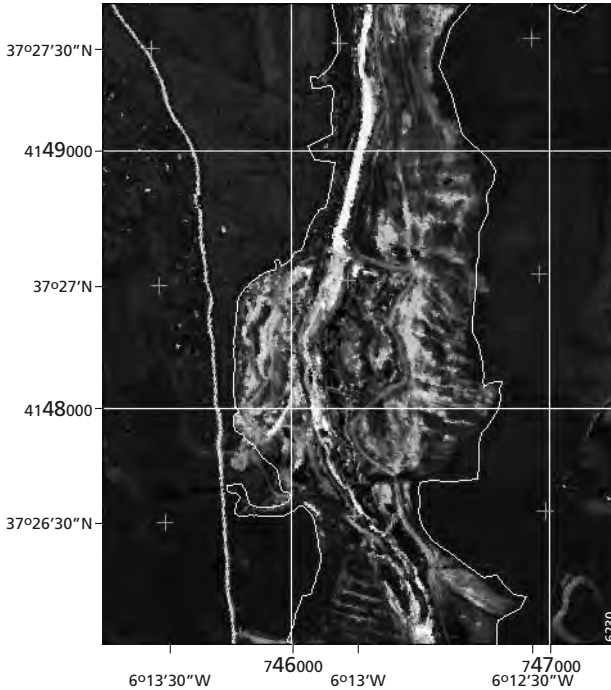*Figure 10.5 – Background end members.*

Figure 10.6 – RMSE after the first unmixing step. Most of the pixels with a high RMSE lie within the affected area indicated by the white line. Please consult the enclosed CDROM for a full colour version.

>0). The results were obtained with only one sludge EM. In fact, tests with additional sludge EMs were not successful. This is a clear indicator that at this point in time, 13 months after the accident, oxidation of pyrite did not yet reach a high intensity and consequently it was possible to map the sludge using only the pyrite sludge EM. The retrieved sludge distribution corresponds well with the field observations and the geochemical analysis and reflects the discontinuous distribution pattern caused by the mechanical clean up.

The same unmixing strategy was applied for the data collected in 2000. However, the situation had changed significantly. The remediation activities proceeded with a second cleaning phase in combination with fixation of the trace metals. This was achieved by augmentation of the pH-level of the soil through addition of lime-rich material. At the time of the second field and flight campaign the work was still ongoing. In many areas, particularly in the northern part, efflorescent crusting could be observed. According to Nordstrom (1982), these crusts are most commonly formed during dry periods when evaporation promotes the rise of subsurface water to the uppermost soil surfaces by capillary action. As the water reaches the surface it becomes progressively more concentrated and finally precipitates various salts in efflorescence. The formation of these iron sulphate salts is an intermediate step, which precedes the precipitation of more common insoluble iron minerals such as goethite and jarosite. In order to account for this change in surface composition two new
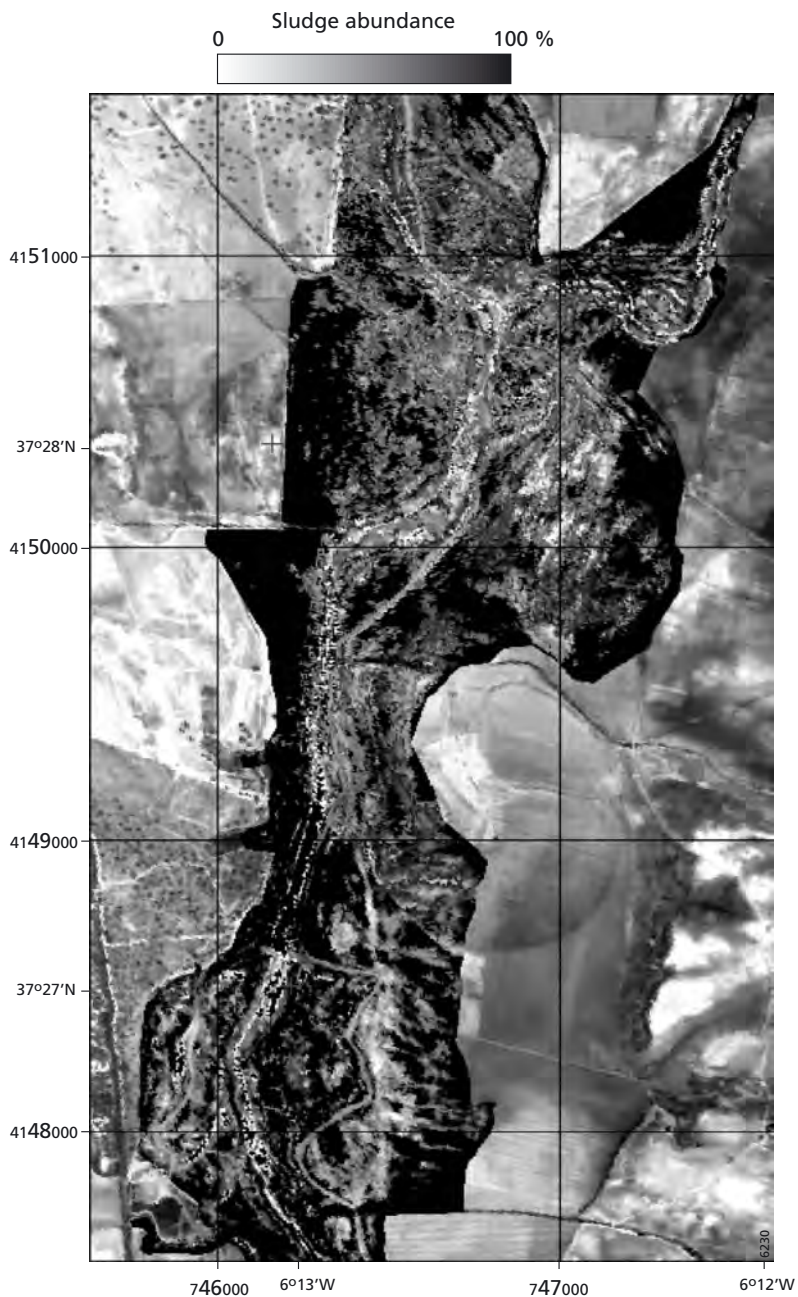
Figure 10.7 – Sludge abundance map 1999. The affected area (black) superimposed on the HyMap false colour image for better orientation. Sludge abundance within the affected area is scaled from zero (black) to one hundred percent (white). Please consult the enclosed CDROM for a full colour version.
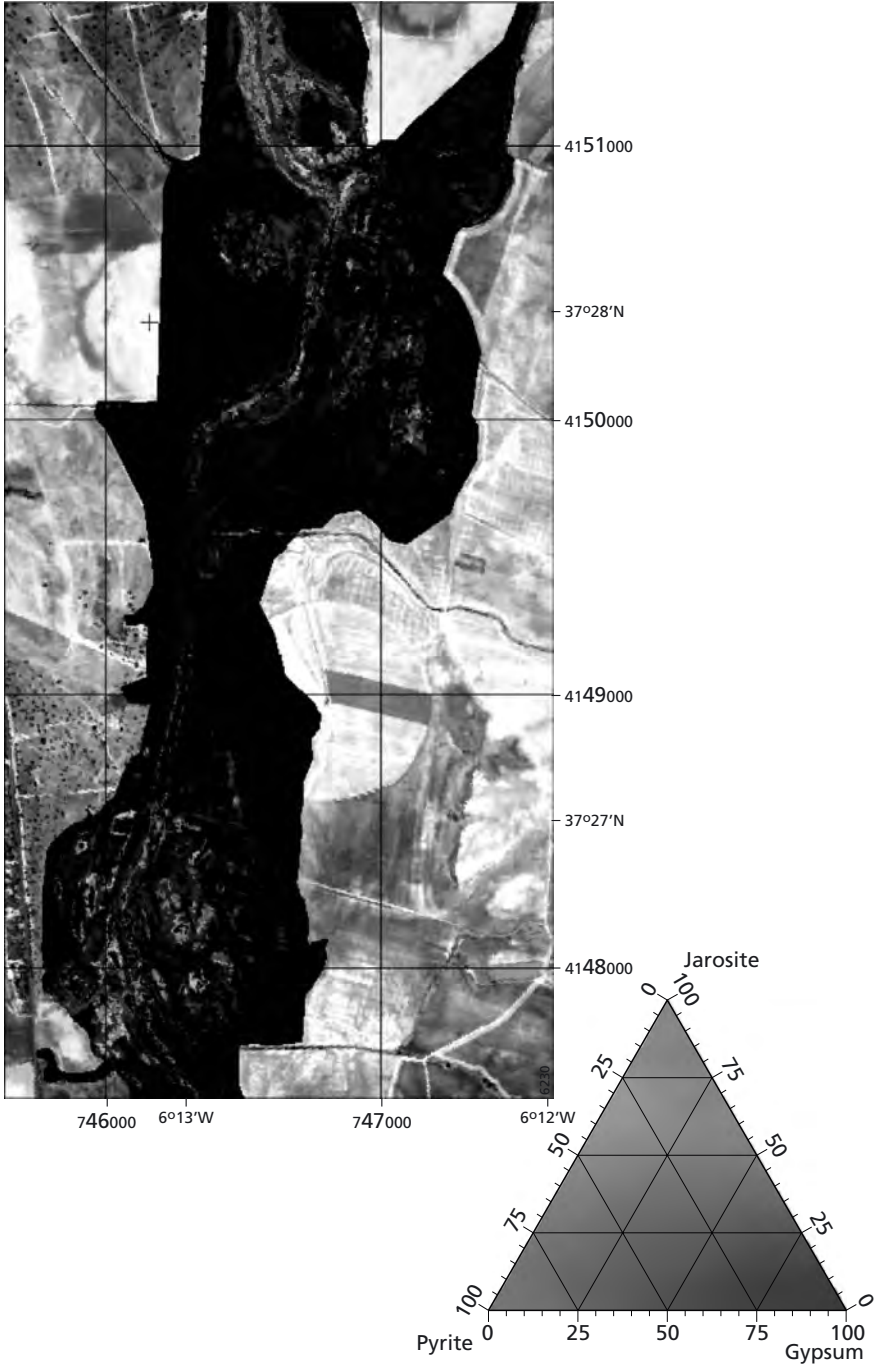
Figure 10.8 – Mineral abundance map 2000. The mixtures of the different EMs can be derived from the colour coded ternary diagram. Please consult the enclosed CDROM for a full colour version.

EMs representing these efflorescent crusts were included in the SMA modelling. The abundance map for July 2000 shows a considerable reduction of areas with sludge EM abundances compared to the abundances obtained for June 1999 (figure 10.8). This reduction was achieved by the second remediation campaign. However, in areas where the remediation was not finished, higher abundances of secondary minerals were found. In these areas, jarosite was found to be abundant. The presence of gypsum is restricted to shallow depressions, in which more water gathered after rainfalls and the humidity was sufficient for the formation of gypsum when the water evaporates. However, these few millimetres thin gypsum crusts are only on the surface, below them secondary minerals are found. Thus, the presence of gypsum is on the one hand an indicator for buffering of acidity by the distributed material Ca-rich material; on the other hand it shows that there is still residual sludge in the soil, which produces acidity.

10.4   A case study from Aktharma-Pashaly mud volcano, Azerbaijan

10.4.1   Introduction
Azerbaijan, South Caspian Basin, is one of the oldest oil producing countries in the world. Large oil and gas reserves have been proven for the country, most of which are at great depths in between 6 and 13 km, and confined to Miocene and Pliocene paleo Kura and paleo Volga deltaic sediments in the onshore part (Abrams & Narimanov, 2000; Katz et al., 2000). The Azerbaijan oil fields seem to have originated from common clastic, dark shale Source Rock (SR) with a restricted stratigraphic distribution, deposited in a transitional marine environment, referred to as the Maykop Suite (Katz et al., 2000; Inan et al., 1997). Productive Series (PS), sedimentary sequences from which the hydrocarbons can be produced, have significant mineral rock fragments (Abrams & Narimanov, 2000; Buryakovsky et al., 1995). The Great and Lesser Caucasus contain substantial Mesozoic and Cenozoic volcanogenic rocks that act as sources of montmorillonite-rich sediments. Late Pliocene PS contain less quartz, more feldspar and fragments of both sedimentary and volcanic rock fragments, reflecting a more typical paleo-Kura provenance. In general 'harder' minerals such as chlorite, illite, and kaolinite characterize Azerbaijan hydrocarbon reservoirs of argillaceous material. Beside its oils, Azerbaijan is also famous for its number of mud volcanoes. According to Abrams & Narimanov (2000), Katz et al. (2000) and Lerche & Bagirov (1998), the South Caspian Basin is characterized by very high basin sedimentation rates leading to large volumes of largely unconsolidated sediments of more than 20km. This favours the development of mud volcanism, because abnormally high pore pressures may lead to lateral rock density variations, which in turn develop mud volcanism and earthquakes (Buryakovsky et al., 1995; Kopf, 2002). Obviously in Azerbaijan, mud volcanism is intimately associated with hydrocarbon (oil and gas) seepage, which can be illustrated by a massive oil mud volcano eruption of Lokbatan mud volcano in 2001 (figure 10.9).

Mud volcanoes form on the surface as expressions of the vertical migration of oil, gas, water, clays, and bedrock, and thus reflect the geological history at a particular location. Through typical geomorphologic mud volcano vents called gryphons and salses, mud volcanoes eject argillaceous material (breccia) and build up their topography. Optical satellite images (Advanced Spaceborne Thermal Emission and Reflection – ASTER) and ASD ground

Figure 10.9 – Lokbatan oil mud volcano eruption, October 25, 2001. During this eruption hydrocarbons from the earth's interior were set on fire resulting in a flame of about 60m high; about 192,200m³ mud was expelled covering an area of about 9.61 ha. (image courtesy Neil Piggot, BP/Statoil). Please consult the enclosed CDROM for a full colour version.
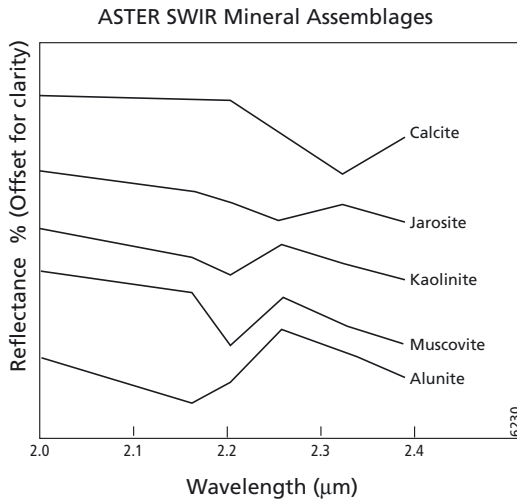

Figure 10.10 – USGS mineral spectra resampled to ASTER bandpasses in order to show the gross shape curves of typical minerals that can be identified as a group.

spectral measurements of 2001 and 2002, centred on onshore Azerbaijan, are analysed using the VMESMA tool. Basically we are interested in the surficial mineral content of the mud volcano surface since it reflects the initial products, the deep burial of rocks, and the particular assemblage of primary or secondary minerals of the subsurface. Hence we look for evidence of mineral alterations in relation to mud volcanism in terms of mineral provenance information from mud volcano flow mixtures through imaging spectroscopy in the 0.5-2.5 μm part of the electromagnetic spectrum.

10.4.2   ASTER data pre-processing

Empirical line correction for ASTER band 5 and band 9 inaccuracies
The ASTER scenes selected are of the L2 type and were obtained from the EROS Data Centre (EDC). Prior to the image analysis an empirical line correction was carried out to correct for the 'crosstalk' instrument problem. This problem is caused by the reflectance of light from ASTER band 4 (centred at 1.65 μm) optical components into ASTER band 5 (centred at 2.165 μm) and ASTER band 9 (centred at 2.39 μm) (Abrams, 2003, personal communication). Hence the sensor acquires inaccurate reflections and interpretation in terms of band absorption features is not feasible, and ASTER images from Aktharma-Pashaly mud volcano were empirical line corrected using ground truth field spectral reflectance measurements.

Time series registration
The usage of VMESMA in multi temporal ASTER imagery requires accurate co-registration of the ASTER time series. We use a statistical approach in which ground control points (GCPs) were matched and refined through cross correlation in a window of size 50 by 50, i.e. 50 points extension from the centre point, for a 12 by 12 window position (Hill & Mehl, 2003). In general the VNIR band is used for this analysis due to the high contrast between vegetation brightness response and nonvegetated surfaces, including open water, man-made features, bare soil, and dead vegetation. The advantage of this method is that it can also select GCPs in areas that do not show clearly distinguishable features such as cross-roads or other commonly used features in the manual GCP selection procedure.

10.4.3   ASTER mineral mapping
The ASTER SWIR reflective bands promise enhanced discrimination of mineral assemblages relative to Landsat TM and SPOT satellite data (table 10.2). Amongst others, Hornibrook (2002) shows that USGS spectral library measurements of muscovite with its typical 2.20 μm absorption is preserved in the ASTER gross shape curve, showing a significant spectral absorption in ASTER band 6, centred at 2.205 μm. However ASTER probably can not identify this mineral directly, but Al-OH bearing minerals (muscovite-montmorillonite-illite-Al smectite) could be identified as a group (figure 10.10). For the mapping of kaolinite using ASTER, the diagnostic doublet absorption feature near 2.175/2.210 μm shall disappear in the ASTER spectral curve, but the gross shape of the doublet will be preserved in terms of asymmetric absorption in band 6 (figure 10.10). Calcite and chlorite exhibit major absorption near ASTER band 8, centred at 2.32 μm and hence ASTER bandpasses will show this feature in terms of symmetric absorption in band 8. Other common Mg-OH bearing minerals, which are characterised by absorption features ranging from 2.32 to 2.39 μm have similar

ASTER band 8 responses. ASTER will probably have troubles in separating carbonates from Mg-OH bearing minerals, however ASTER should be able to map these as a group (figure 10.10).

10.4.4 Identification of key endmembers

As previously mentioned the EM selection procedure is a critical part of the unmixing assessment. The VMESMA tool offers Principal Component Analysis (PCA) and Cluster Analysis (CA) to evaluate the spectral variability in the image. A PCA consists in rotating the coordinate system such that most of the variation in the data is found along a limited

Table 10.2 – Possible mineral assemblages that can be detected by ASTER SWIR bandpasses.

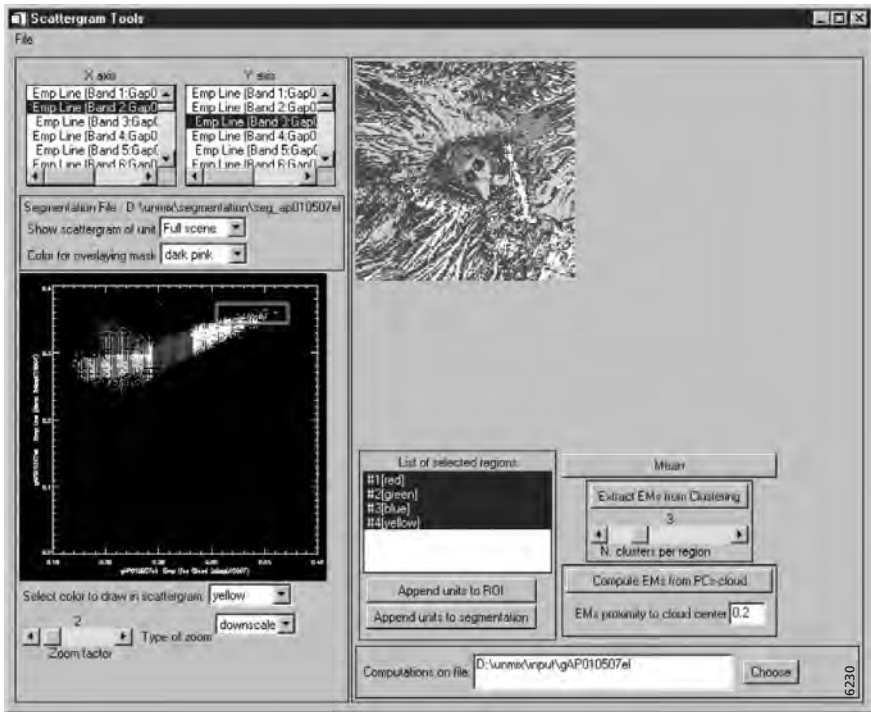| Absorption wavelength (μm)	Mineral Group
2.165	Low pH/acid environments
2.205	Al-OH bearing minerals
2.260	Jarosite
2.327	Carbonates and Mg-OH bearing minerals

Figure 10.11 – VMESMA Endmember Scattergram tool to extract spectrally different zonations in the image. Four regions are defined based on a scattergram of ASTER 2 (X-axis) and ASTER 3 (Y-axis) that matches the scattergram properties as explained by figure 10.1. Please consult the enclosed CDROM for a full colour version.

number of axis, the so-called principal components (PCs). Basically pure image endmembers are found at the extremes of each PC. However, to filter the presence of isolated points in the dataset, we take a proximity of 0.2 of the extremes of the cloud into account. In this way, the endmembers are somehow deduced form the entire data structure rather than from a few outlying pixels. Figure 10.11 plots the VMESMA Endmember scattergram tool of ASTER band 2 and ASTER band 3 in which we extract image spectral characteristics for vegetation, bare soil, and mixtures (based on figure 10.1).

10.4.5 Results

Based on figure 10.11 ASTER four image segmentations were created, each depicting typical reflectance information. Segmentation 1 (red) shows pixels which are influenced by vegetation and segmentation 2 to 4 were mainly separated in terms of reflectance intensity. Unmixing of
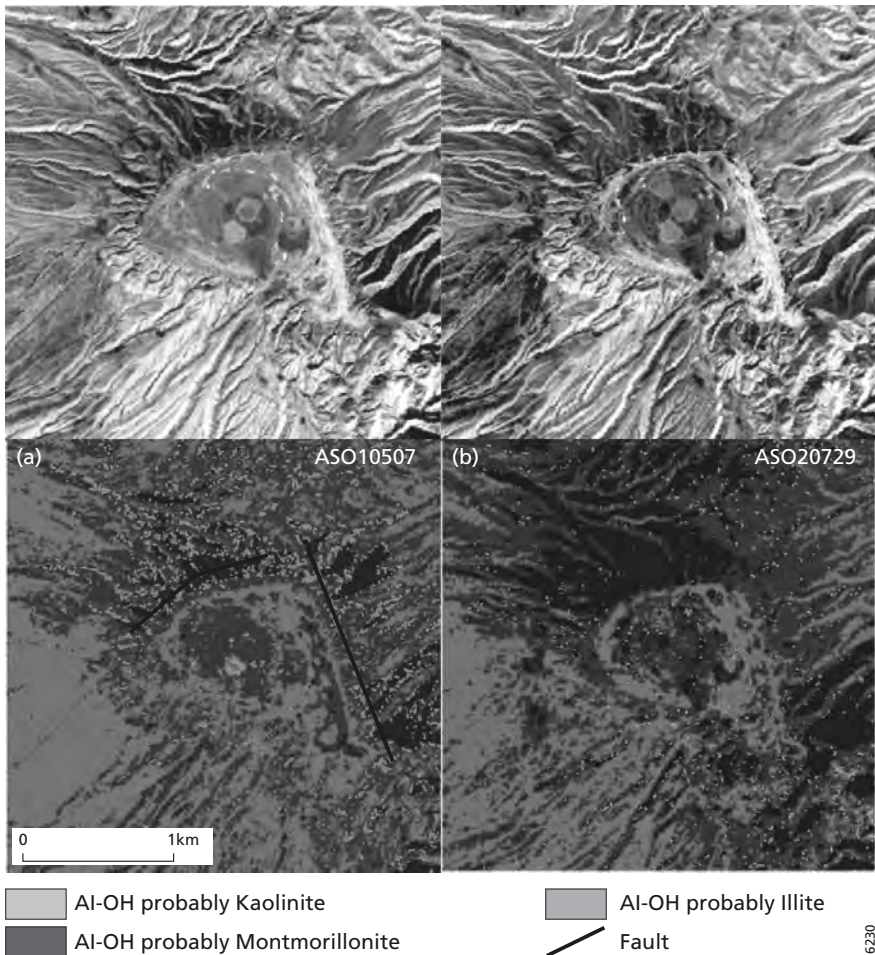

Figure 10.12 – ASTER colour composites of (a) May-7-2001 and (b) July-29-2002. Please consult the enclosed CDROM for a full colour version.

the Aktharma Pashaly ASTER scene reveals a fairly high number of negative abundance estimates (13.21% has negative violations less than 0.05), however the majority of the pixels show good abundance estimates. Figure 10.12 maps the distribution and relative abundance of Al-OH bearing minerals for Aktharma-Pashaly in a RGB plot with respectively the Al-OH kaolinite (kaolinite), the Al-OH (montmorillonite) group and the Al-OH (illite) group. It is suggested that ASTER identifies classes of aluminium hydroxyl bearing minerals, the most significant being the detection of the kaolinite group (red). The kaolinite group shows a radial pattern and they mainly appear near 2 faults in the area, indicated with a yellow line in the small ASTER RGB=321 colour composite. Probably mud migration mechanisms might be confined to faults present in the area and probably highlight argillic altered environments, hence indicating mud characteristics from the subsurface. In the ASTER image of May 2001, high illite abundances are estimated at the south-west mud volcano vent-group as well as at the northern flank of the volcano. Probably surface topography influences the signal and further image pre processing is required to take the albedo influences into account.

In terms of provenance information we focus on those sites where we expect fresh mud material from the subsurface, which we predominantly found along the circular flows and anticline faults (figure 10.12). The unmixing classification results show kaolinite or illite types of clay mineral, which we expect to find in Pliocene sequences. High montmorillonite abundances in the central part of the volcano are probably the result from secondary mineral alterations.

10.5   Conclusions

VMESMA provides abundance estimates very robust against external factors such as illumination, soil background and canopy shade. VMESMA steps the problems from the conventional spectral unmixing techniques by performing a standardization on endmember spectra to reduce the variability of undesired components, while enhancing the separability and spectral features of rocks, soils and vegetation. In fact, the separability between intra-class sub categories is significantly reduced, thereby simplifying the need of EM submodels at reducing the model sensitivity to the natural variability of EM spectra, calibration errors, topographic contamination or differences in illumination conditions. In association with sludge abundance mapping the application of VMESMA showed that after the first remediation the residual contamination was still widespread and pyrite oxidation did not yet reach a high intensity; consequently is was possible to map sludge abundances using only the pyrite sludge EM. Sludge abundance maps July 2000 showed a considerable reduction of areas with sludge EM abundances compared to June 1999. However, higher abundances of secondary minerals, in particular jarosite, were found indicating oxidation processes, which make further monitoring efforts necessary. VMESMA in association with ASTER, which is not a typical hyperspectral sensor in terms of hundreds of spectral bands, is able to detect a variety of different clay minerals, which can be used as an analogue for viable petroleum system properties.

Chapter 11

A Contextual Algorithm for Detection of Mineral Alteration Halos with Hyperspectral Remote Sensing

Harald van der Werff & Arko Lucieer

11.1   Introduction

The occurrence of hydrocarbon seeps at the Earth's surface indicates that hydrocarbon reservoirs leak. Leakage can be active or passive, visible to the human eye (macroseepage) or only chemically detectable (microseepage). In the long term, light hydrocarbons that are being oxidized by bacteria can, directly or indirectly, change the pH and Eh of the surrounding environment. Onshore, this results in formation of oxidation-reduction zones that influence mineral stability.

As many of the resulting mineral alterations can be mapped by imaging spectrometers, remote sensing could be a rapid and cost-effective means of hydrocarbon exploration when compared to geochemical surveying methods or seismic studies. This study demonstrates the development and effectiveness of an algorithm that combines spectral and spatial information in simulated hyperspectral imagery to detect alteration halos around hydrocarbon seepages.

11.2   Onshore hydrocarbon seepages

Due to pressure differences in the Earth's subsurface, hydrocarbons can migrate from subsurface reservoirs to shallower levels and eventually to the surface. Link (1952) was the first to distinguish macroseeps, which consist of seeping liquids and gases that are visible to the human eye, from microseeps, which can only be detected by geochemical means. In microseeps, trace quantities of light hydrocarbons (such as methane, ethane, propane, butane and pentane) migrate rapidly through a microfracture network, also called a chimney (Brown, 2000). Migration of heavier hydrocarbons needs more space: possible paths are reservoir rocks acting as carrier bed, unconformities, tectonic structures that breach reservoirs or seals, and surface expressions of intrusions such as mud volcanoes and salt domes (Link, 1952). As a result, migration can vary from near-vertical to lateral movements over long distances (Schumacher, 1996). A relation between geochemistry, migration paths and spatial distribution at the surface can successfully be made in areas with a simple geological setting. Understanding this relation becomes difficult when the geology is more complex.
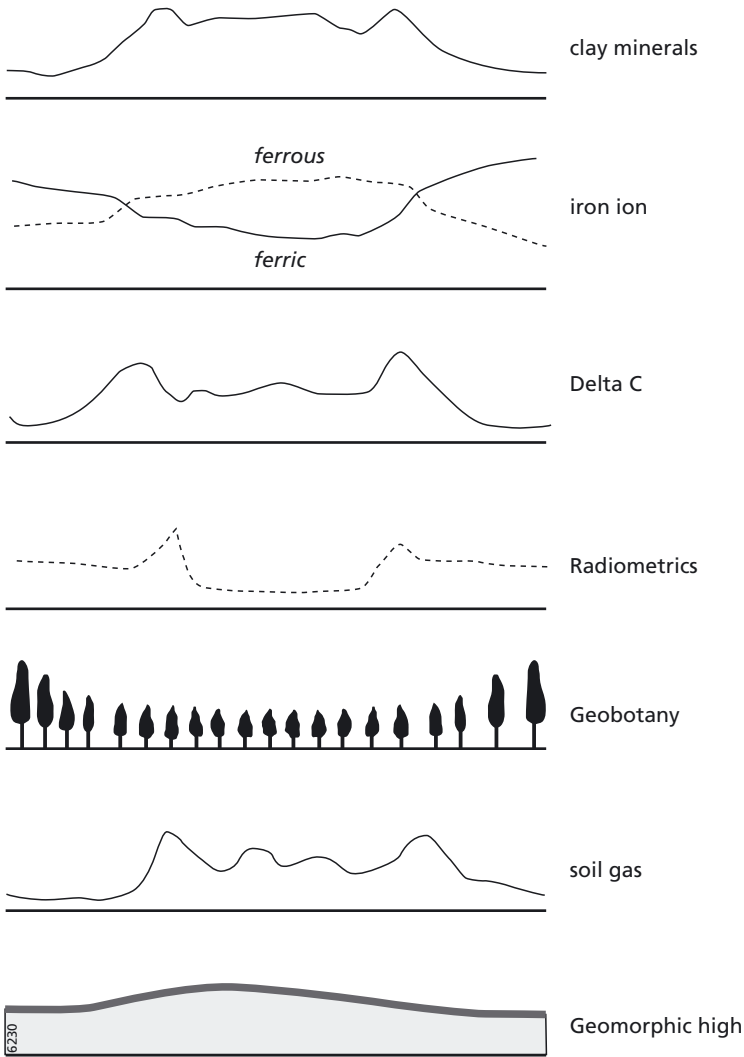
Figure 11.1 – A schematic overview of anomalies that are commonly found in onshore hydrocarbon seepages (after Yang, 1999).

Long-term leakage can lead to formation of anomalous oxidation-reduction zones. Aerobic and anaerobic bacteria that oxidize the migrating hydrocarbons are, directly or indirectly, responsible for the varied and often complex surface manifestations (figure 11.1). Observed alterations in surface mineralogy include formation of pyrite, calcite, uraninite, elemental sulfur, specific magnetic oxides and iron sulfides (Schumacher, 1996). However, the chemical processes involved in seepages and resulting surface expressions are still not fully understood. Most alterations are not unique for the redox environment of seeping hydrocarbons, which makes them difficult to distinguish from alterations caused by other soil processes.

11.3   Optical Remote Sensing of onshore hydrocarbon seepages

Heavy hydrocarbons have clear absorption features in the reflective part of the spectrum (Cloutis, 1989). Detection of macroseeps with hyperspectral imagery can successfully be made by directly mapping hydrocarbons that are present at the surface (Hörig et al, 2001).

Two gases that are commonly found in microseeps, methane and carbondioxide, also have clear absorption features in the reflective part of the spectrum. However, detection of these gases is problematic. Carbon-dioxide is already present in the atmosphere, the absorption feature of methane is too narrow to allow detection by present day airborne instruments, and hydrocarbon seepages are not the only natural source of methane and carbondioxide production. Taking into account the temporal variability in gas emissions, the subtle spatial variation of gases does not show up against a heterogeneous background (De Jong, 1998). Remote sensing of onshore gas emissions is, in contrast to offshore monitoring, disturbed by the heterogeneous surface of the Earth and by human influences on the atmosphere.

Although direct detection of gases originating from microseeps is problematic, optical remote sensing is an excellent tool for detecting microseepage-induced alterations. Almeida-Filho (1999) successfully detected bleached redbeds in an approximately 6 km² area by using band ratios of Landsat TM imagery. These results appeared to be consistent with soil gas anomalies (ethane, propane, butane and pentane) that had been measured at the same spot. On a meter scale, however, indirect detection is hampered by the same problem as direct detection of seepages: the signal of the subtle and non-unique alterations resulting from hydrocarbons is disturbed by the heterogeneous surface of the Earth. The technical question that remains is: 'how to separate a non-unique, weak signal from a variable background'.

11.4   Spectral models of hydrocarbon seepages

To improve our understanding of seepage-induced alterations and to describe their spectral signal, the number of variables found in nature should be reduced by simulating seepages in a laboratory. Botanical anomalies can be simulated, as the effects of the presence of soil gas on root systems of plants can already be seen in one growth season (Pysek & Pysek, 1989). However, it would take too much time to simulate mineralogical alterations in a laboratory; seepages in the field should be used as a 'natural laboratory' instead.

This 'chicken and egg' problem in simulation of mineralogical anomalies can be tackled by limiting the simulation to a spectral model that is based on geological models of seepages. Schumacher (1996) describes a seepage-induced alteration model in a framework of simplified basic reactions and processes. A spectral model of a hydrocarbon seep, as shown in figure 11.2, could consist of a homogeneous background spectrum (e.g. a soil), linearly mixed with spectra of iron sulphides or calcite to form a halo in the homogeneous background. This model can be made increasingly complex and realistic by decreasing the abundance of anomalous minerals, introducing a heterogeneous background, addition of e.g. vegetation masks and pixel noise. The final step towards the real world situation is to generate 'hybrid'
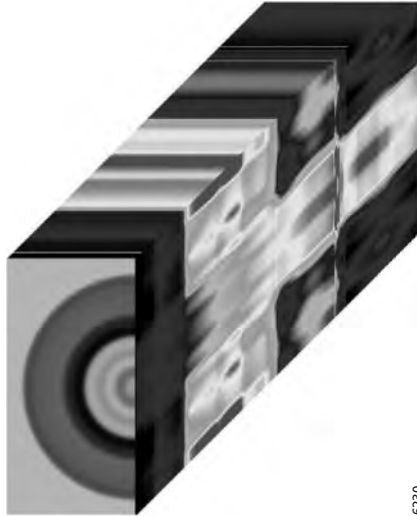
Figure 11.2 – A simulated image cube showing a spectral model of a hydrocarbon seep. This model is based on field spectra acquired at a seep in Upper Ohaj Valley, California, USA. The center of the seep consists of a bare soil, while the surrounding homogeneous background consists of a grassland. Please consult the enclosed CDROM for a full colour version.

images, made from field spectral measurements that have been acquired along transects from the central vent to areas outside of the halo.

11.5 Combining the spectral and spatial domains

A possible way to separate and identify the spectral fingerprints of seepage-induced alterations is by making use of spatial patterns that are commonly observed in seepages. At a meter scale, both macroseeps and microseeps often occur as a halo around a central vent. On a kilometer scale, the chimneys found in microseepages lead to a halo along the rim of a subsurface reservoir, while vents of macroseepages are often lined up along a fault or an outcropping carrier bed. The distribution can be described as simple, but different mathematical shapes at different scales. This contextual information allows discrimination and, therefore, detection of seepage-induced alterations.

11.5.1 An algorithm for combined spectral and spatial detection

The first step in detecting an alteration halo is to introduce the spatial pattern of seeps at the first stage of image processing. At this stage, there is not any comparison of the image spectra with reference spectra to make an identification, the purpose is only to indicate which pixels have a halo that is spectrally anomalous from the rest of the image.

We assume that alteration halos show a homogeinity of spectral fingerprints that can be found in hydrocarbon seepages. This homogeinity can be measured by calculating, for each
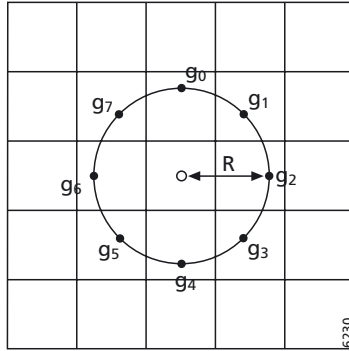
Figure 11.3 – A circular neighbourhood set with N=8 equally spaced pixels on a circle of radius R. The homogeinity of this neighbourhood set is summarized in the center pixel as one value, consisting of the variance in spectral angles calculated between all the pixels on the circlular neighbourhood.

pixel, the variance in spectral angle of the pixels in a circular neighbourhood set. The spatial information of the neighbourhood set is summarized in a single variance value assigned to the centre pixel. A relatively low value for variance indicates the presence of a spectrally homogeneous neighbourhood set.

For every pixel in the image, the algorithm calculates the spectral angles between a number of equally spaced pixels N which are on a circle with radius R from the center pixel (figure 11.3). Both R and N depend on the geological setting and on the spatial resolution of an image, and need to be set by an expert.

For any center pixel (x_c, y_c), the coordinates of the pixels belonging to the circular neighbourhood set are given by (Lucieer et al, 2003):

$$\{x_{c,i}, y_{x,i}\} = \{x_c - R \sin\left(\frac{2\pi i}{N}\right), y_c + R \cos\left(\frac{2\pi i}{N}\right)\} \tag{11.1}$$

for $i = \{0, 1, ..., N\text{-}1\}$.

The spectral information of each pixel can be described as a vector $\vec{V}$ in feature space. The spectral angle S between the vectors $\vec{V}$ of all N pixels is calculated by

$$S_{i,j} = \frac{\vec{V}_i \circ \vec{V}_j}{\|\vec{V}_i\| \cdot \|\vec{V}_j\|} \tag{11.2}$$

where i and j are pixels in the same neighbourhood set and $\circ$ denotes vector product. The number of spectral angles SA in a circular neighborhood set with N pixels is given by
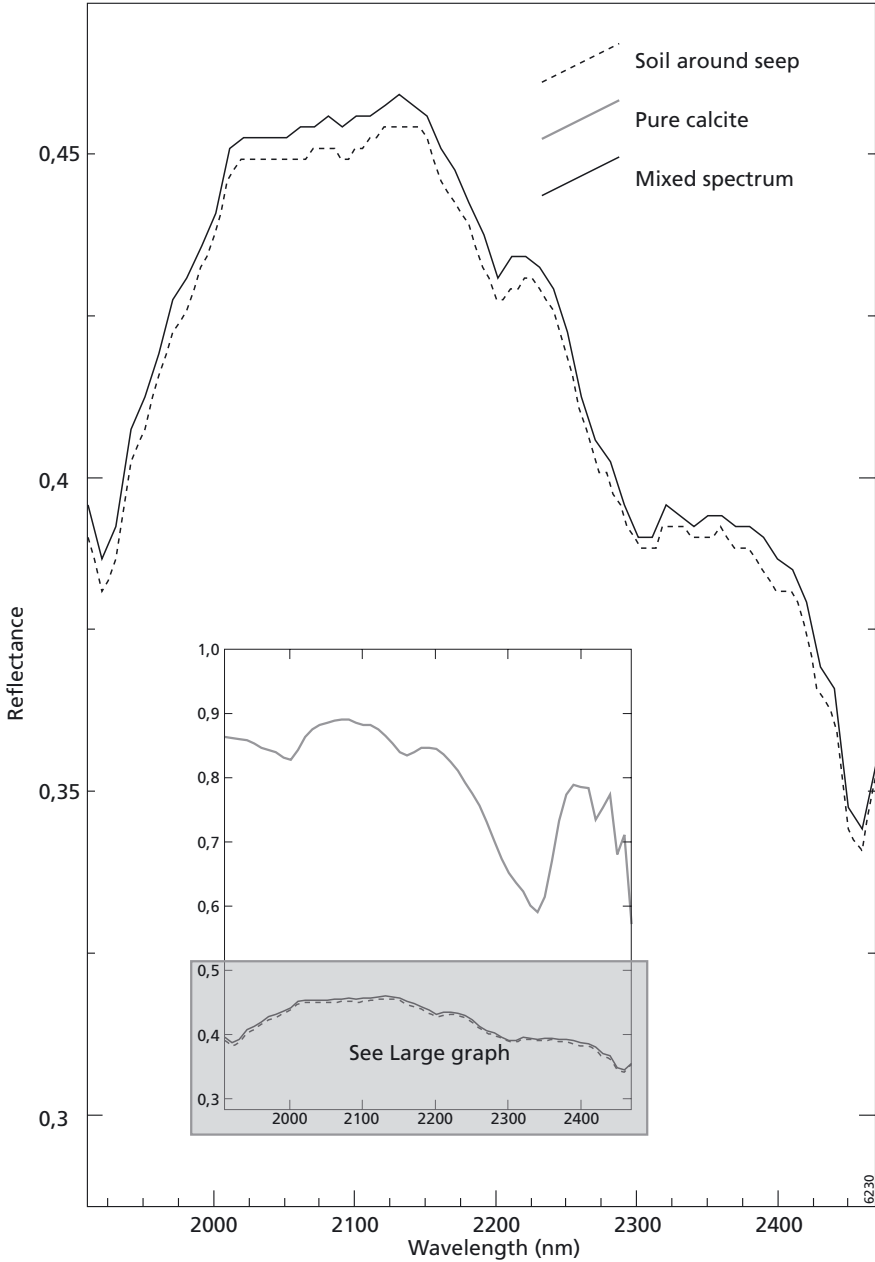
$$SA = \sum_{i=1}^{N} N - i \tag{11.3}$$

Figure 11.4 – The spectra of pure calcite, a bare soil and an anomalous soil (small graph). This anomaly consists of an addition of only 1% calcite to the original soil spectrum, resulting in a minimal difference between the soil spectrum and the anomalous spectrum (large graph).

The mean spectral angle S_{mean} of all N pixels in a neighbourhood set is given by

$$S_{mean} = \frac{\sum\limits_{i=0}^{N} \sum\limits_{j=i+1}^{N} S_{i,j}}{SA} \tag{11.4}$$

Finally, the variance S_{var} in spectral angles of this neighbourhood set is calculated by

$$S_{var} = \frac{\sum\limits_{i=0}^{N} \sum\limits_{j=i+1}^{N} \sqrt{(S_{i,j} - S_{mean})^2}}{SA} \tag{11.5}$$

11.5.2 Simulated imagery for demonstrating the algorithm
We produced two different types of simulated images to demonstrate the effectiveness of the algorithm:

1 A hybrid image that has been constructed from field spectral measurements of a natural oil seep in Upper Ojai Valley, California, USA (figure 11.2). The crisp halo that has been observed in the field has a size of approximately 20 meters in diameter, and consists of a bare soil in a grassland background.

2 Four artificial images that have been constructed from both field spectral measurements and spectra taken from the JPL spectral library (Grove et al., 1992). The background of these images is a soil spectrum that has also been acquired near the oilseep in Upper Ojai Valley. A spectrum of pure calcite has been linearly mixed with the background soil spectrum to make an anomaly of 1% calcite enrichment in the shape of a halo (figure 11.4). This halo is at 30-40 meters distance from the central vent. Both the inner and outer edges of the halo are fuzzy: the 1% calcite enrichment gradually disappears over a distance of 20 meters. To increase detection complexity, random pixel noise with a maximum of 1% of the pixel value has been added to these four images. This results in an equal signal strength of random noise with the calcite anomaly that we want to detect. Furthermore, the background soil spectrum has a heterogeneity in value, ranging in strength from 0, 10, 30 up to a maximum of 70% of the original background values. Both pixel noise and background heterogeneity have been added multiplicative, i.e. the stronger the spectral signal, the stronger the noise. Though this is different from reality, it is a desirable effect when studying the detection of weak but consistent signals in a heterogeneous environment. Another simplification is that the applied background patterns are equal in all bands, for all images. In reality, the spectral signature of the background may vary throughout different wavelengths. However, we assume it to be constant for specific wavelength regions such as VIS, NIR and SWIR.

All simulated images cover only the SWIR region of the reflective spectrum, as in this part the absorption features of calcite are most pronounced. The spectral resolution is set to match the AVIRIS imaging spectrometer. The spatial resolution is set to a pixel size of 1 by 1 meter.

11.6   Results

Figure 11.5 shows the results of applying the algorithm on the hybrid image made from field spectral measurements. The value of the dark pixels in the center of the images are about a factor 8 lower than the values of the bright neighbouring pixels. This clearly indicates the presence of a spectrally homogeneous halo for the center pixels.

The values used for the radius, R, and the number of pixels in the neighbourhood set, N, are 10, 25 and 40 meter and 8, 12 and 20, respectively. In this example, the effect of choosing different values for R mainly influences the number of center pixels that can be identified as having a halo; choosing a value higher than half the width of the halo would result in no detection at all. The effect of choosing different values for N has a strong impact on the
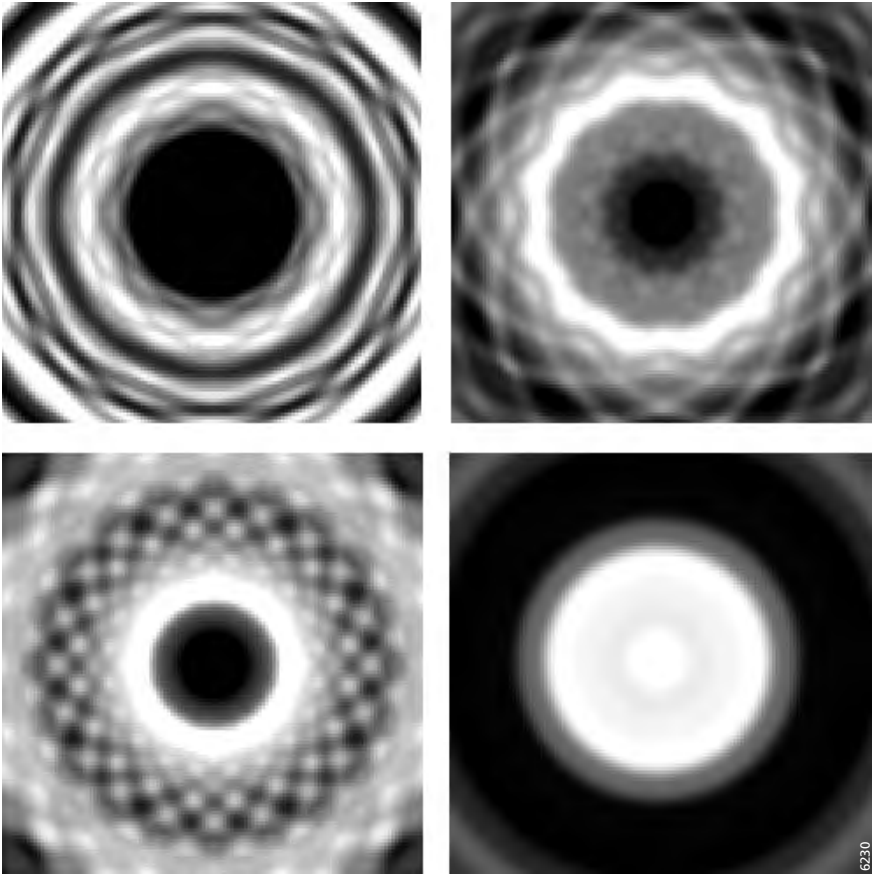
Figure 11.5 – The effect of different values for radius R and the number of pixels in the neighbourhood set N. Top-left: R=10, N=8. Top-right: R=25, N=10. Bottom-left: R=40, N=20. Bottom-right: Band 160 (1882 nm) of the simulated hybrid image.
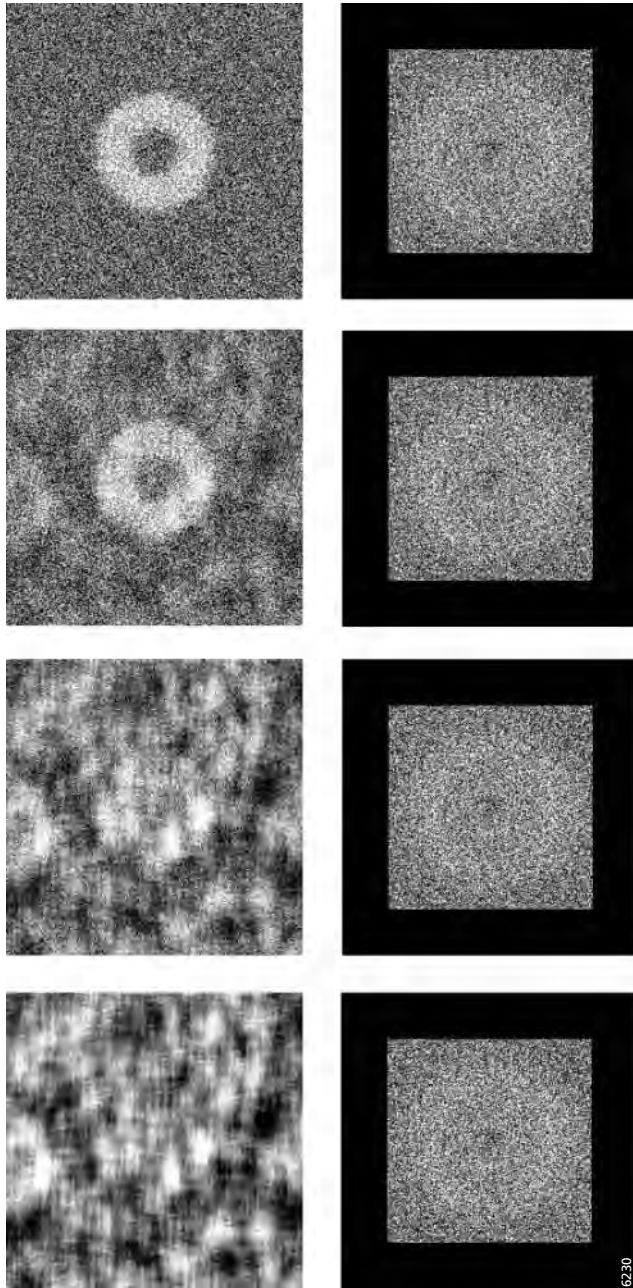
Figure 11.6 – Displayed on the left is SWIR band 160 (1882 nm) of the simulated images with different background heterogeneity, increasing from 0, 10, 30 to 70% variability from the original background value. On the right the results of the algorithm for the simulated images, which is hardly affected by the increasing heterogeinity in the images.

pattern observed in the output values. Despite the amount of computing power needed, the value for N should not be set too low in order to avoid these patterns.

Figure 11.6 shows the results of applying the algorithm to the simulated images that contain the 1% anomaly, 1% random pixel noise and different levels of background heterogeneity. The values used for R and N are the same as the values used for the hybrid image. The output appeared to be very noisy, and the values of the center pixels (which have a halo) are in the same range as the values found in the other pixels. The results for different values of R and N needed to be summed to enhance the output. However, the algorithm is able to detect the halo of 1% calcite enrichment in all simulated images.

11.7   Discussion and conclusions

Remote sensing of onshore macroseepages, which are visible to the human eye, has been succesfully carried out in the past. However, remote sensing of invisible microseeps at a small scale has not resulted in satisfactory results. The influence of oxidizing hydrocarbons on the surrounding environment is usually smaller than the influence of other soil processes in particular and natural variation in general. Moreover, the alterations that are being observed are not unique for oxidizing hydrocarbons. Problems in detecting subtle variations in a natural background are not only encountered in remote detection of microseepages, but also in many other applications of Earthobservation.

This study shows that combining spectral and spatial information in remotely sensed images is successful. Applying knowledge on hydrocarbon seepages from the field in an algorithm allows the detection of a fuzzy alteration halo consisting of only 1% enrichment in calcite.

Of course, this algorithm still has some weaknesses: the shape of the halo needs to closely resemble a circle, and the halo needs to be complete and not partial covered by e.g. vegetation. Future work will concentrate on these weaknesses: Spectrally, the number of false anomalies that would be detected in realistic images needs to be reduced by comparing the mean spectrum found at a specific radius to a reference spectrum (e.g. calcite or sulphur). Spatially, a second step is a region growing segmentation algorithm that includes spectral, spatial and shape parameters in our detection procedure.

Chapter 12

Image Segmentation Methods for Object-based Analysis and Classification

Thomas Blaschke, Charles Burnett & Anssi Pekkarinen

12.1   Introduction

The continuously improving spatial resolution of remote sensing (RS) sensors sets new demand for applications utilising this information. The need for the more efficient extraction of information from high resolution RS imagery and the seamless integration of this information into Geographic Information System (GIS) databases is driving geo-information theory and methodology into new territory. As the dimension of the ground instantaneous field of view (GIFOV), or pixel (picture element) size, decreases many more fine landscape features can be readily delineated, at least visually. The challenge has been to produce proven man-machine methods that externalize and improve on human interpretation skills. Some of the most promising results in this research programme have come from the adoption of image segmentation algorithms and the development of so-called object-based classification methodologies. In this chapter we describe different approaches to image segmentation and explore how segmentation and object-based methods improve on traditional pixel-based image analysis/classification methods.

According to Schowengerdt (1997) the traditional image processing/image classification methodology is referred to as an *image-centred approach*. Here, the primary goal is to produce a map describing the spatial relationships between phenomena of interest. A second type, the *data-centred approach*, is pursued when the user is primarily interested in estimating parameters for individual phenomena based on the data values. Due to recent developments in image processing the two approaches appear to be converging: from image and data centred views to an *information-centred* approach. For instance, for change detection and environmental monitoring tasks we must not only extract information from the spectral and temporal data dimensions. We must also integrate these estimates into a spatial framework and make *a priori* and *a posteriori* utilization of GIS databases. A decision support system must encapsulate manager knowledge, context/ecological knowledge and planning knowledge. Technically, this necessitates a closer integration of remote sensing and GIS methods. Ontologically, it demands a new methodology that can provide a flexible, demand-driven generation of information and, consequently, hierarchically structured semantic rules describing the relationships between the different levels of spatial entities.

Several of the aspects of geo-information involved cannot be obtained by pixel information as such but can only be achieved with an exploitation of neighbourhood information and context of the objects of interest. The relationship between ground objects and *image objects*

examined in remote sensing representations must be made explicit by means of spatial analysis and the construction of a semantic network. In the following sections we contrast conventional image classification/analysis methods to the new segmentation-based methods; review some current progress in image segmentation and RS/GIS integration, which adds topological and hierarchical rules to build databases of context information; and present two examples to demonstrate the utility of the segmentation-based methodology.

12.1.1   The RS/GIS image analysis continuum

Thematic mapping from digital remotely sensed images is conventionally performed by pixelwise statistical classification (Schneider & Steinwender, 1999, Blaschke & Strobl, 2001). Pixelwise analysis utilizes three of the attributes of a pixel; *Position*, *Size* and *Value* (de Kok et al., 2000). The size attribute can be usually considered as constant, except for imagery acquired in high relief areas (Burnett et al., 1999). The main drawback of pixelwise classification is that it largely neglects shape and context aspects of the image information, which are among the main clues for a human interpreter. A limited form of contextual information can be stored in the Value parameter. For example, texture or other relevant information can be analysed from the immediate neighbourhood of the pixel and result can be assigned to the central pixel. Examples of this are moving window filters which can be implemented with help of convolution masks (Jain et al., 1995). In object oriented analysis shape and context are

| a. pixelwise classification | b. pixelwise + grouping in GIS | c. per-parcel | d. segmentation as pre-classification step | e. segmentation + object relational database |
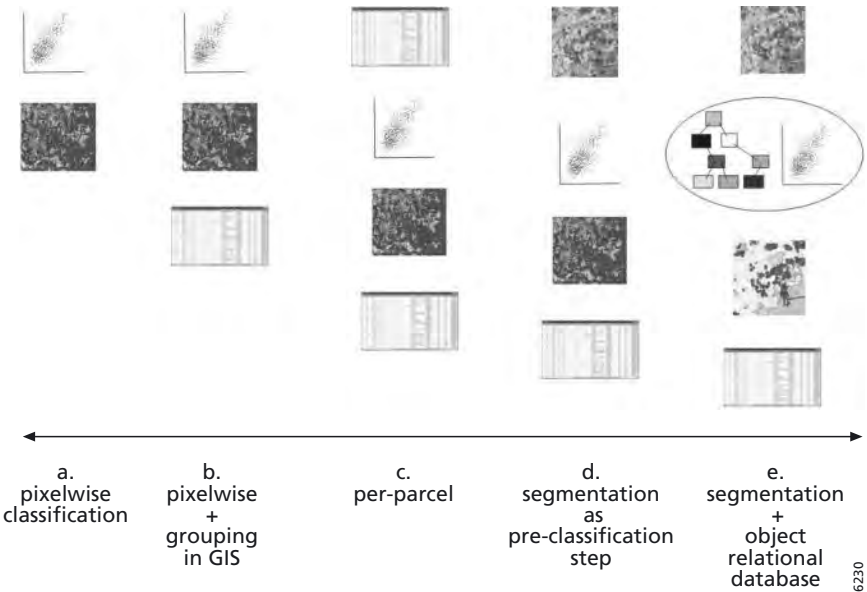
Figure 12.1 – A continuum of classification methods: (a) pixelwise classification, utilizing spectral information; (b) pixelwise with grouping of results into groups in a GIS; (c) per-parcel classification, where GIS data is used to partition the scene before a pixelwise classification; (d) single-scale segmentation prior to pixelwise classification, and; multi-scale segmentation as part of object relationship database building, with classification done by querying spectral and spatial object parameters. Please consult the enclosed CDROM for a full colour version.

clumped into a fourth attribute, that defining *Fellowship*; 'to which pixel population does this pixel belong' (de Kok et al., 2000). It has been suggested that classifying remotely sensed images in pixelwise fashion (using only the first three pixel attributes) is a special case of the super-set of object-based classification methodologies which utilise all four (Schneider & Steinwender, 1999; de Kok et al., 2000). This is not illogical and we propose the following continuum of classification methods incorporating more or less fellowship information (figure 12.1).

12.1.2 New sensors, new image/ground object relationships

Until recently, the 20m spatial resolution of SPOT was regarded as 'high spatial resolution'. Since the launch of IKONOS 2 in 1999 a new generation of very high spatial resolution (VHR) satellites was born, followed by Quick Bird late 2001. The widely used Landsat and Spot sensors are now called 'medium-resolution'. Especially the new satellite sensor generation meet the strong market demands from end-users, who are interested in image resolution that will help them observe and monitor their specific objects of interest. The increasing variety of satellites and sensors and spatial resolutions lead to a broader spectrum of applications but not automatically to better results. The enormous amounts of data created a strong need for new methods to exploit these data efficiently. In addition, the complexity of the relationship of pixel and object make it necessary to develop additional methods of classification.
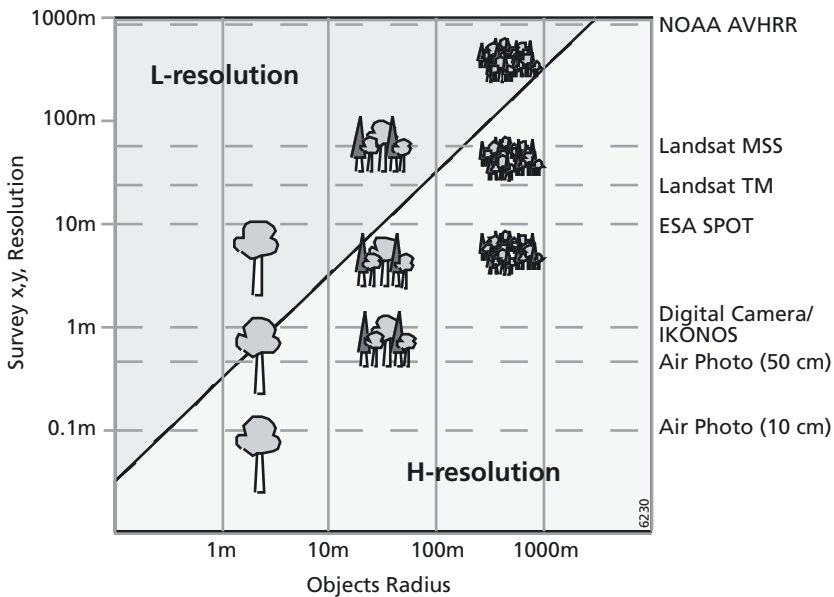
Figure 12.2 – Relationship between the remotely sensed image (survey) resolution (GIFOV) and real-world object diameter. Close to the diagonal, the diameter of the objects and the GIFOV will be nearly equal and image objects (groups of H-res pixels representing a single real-world object) may reduce to 1-pixel image-objects. For situations where the sensor GIFOV is larger than the object of interest, we are in L-res or 'mixed-pixel' territory. (Image modified from Burnett 2002.)

The number of pixels containing more than one land cover type is a function of the complexity of the scene, the spatial resolution of the sensor and the classification scheme. Therefore spatial resolution is among other factors important to the definition of classes. The relationship is based on the simple fact that higher resolution images contain a smaller percentage of pixels regarded as 'boundary pixels', falling into two or more different land cover classes (Cao & Lam, 1997, Mather, 1999). The term 'mixed pixel' does not imply that the scale of observation is inappropriate or does not match the scale of variation of the phenomenon under investigation, although a large proportion of mixed pixels are often associated with a too detailed classification system and/or an inappropriate scale for the respective application. For example, imagine a class 'buildings' consisting of sparsely distributed single houses of 10 by 10m. A Landsat 30m image will never result in 'pure pixels' but an IKONOS image would, although of course there will be many mixed pixels remaining but their percentage decreases. In natural environments we have another problem that there will always be small gaps e.g. in forest's canopy which influence the result, or their might be classes which are specifically mosaics of single entities of specific spatial arrangements of classes. It may be necessary to stress the fact that even though the relative number of mixed pixels decreases their absolute number usually increases. The mixed pixel problem can be examined with the aid of figure 12.2, which describes the relationship between pixel size and object-of-interest size. The nomenclature L-res and H-res refers to the relationship between the pixel GIFOV and the median radius of the real-world objects being imaged (figure 12.1): if the GIFOV is significantly smaller than this diameter, than we are dealing with an H-res mode – at least for that object type! The corollary is the L-res scenario (Woodcock & Strahler, 1987).

As Mather (1999) points out, where this is clearly not the case then a small proportion of pixels will be located in a 'boundary region', e.g. between adjacent fields, and may, therefore, described as 'mixed'. But Cihlar (2000) emphasises, that even in high-resolution and radiometrically well corrected data, some variation will remain which can be regarded as noise or can lead to mixed pixels falling partially into two or more classes. Sensor systems have a specific GIFOV – simply put: a certain spatial resolution. Several targets/classes of interest may be found within one unit of GIFOV. Usually, only a single category is assigned to each pixel. But in fact one pixel could represent more than one target/class.

12.1.3   From pixels to image-objects

It will be useful to clarify the terms pixel and image-object. A pixel is normally the smallest unit of analysis of RS imagery. A pixel's dimensions are determined by the sensor and scene geometry models, giving the GIFOV. The phrase 'normally the smallest' is applied because there have been attempts to decompose the spectral signature of pixels and thus do sub-pixel analysis (Aplin & Atkinson, 2001; Asner & Heidebrecht, 2002; Lucas et al., 2002; Verhoeye & de Wulf, 2002). *Image-object*s are defined by Hay et al. (2001) as... basic entities, located within an image that are perceptually generated from H-res pixel groups, where each pixel group is composed of similar digital values, and possesses an intrinsic size, shape, and geographic relationship with the real-world scene component it models.

Schneider & Steinwender (1999) suggest a simpler definition for image-objects, 'groups of pixels with a meaning in the real world'. As image GIFOV decreases we are faced with new challenges: we can resolve more and more types of real world objects. The internal or 'within-object heterogeneity' increases and the spectral separability between image objects drops. The
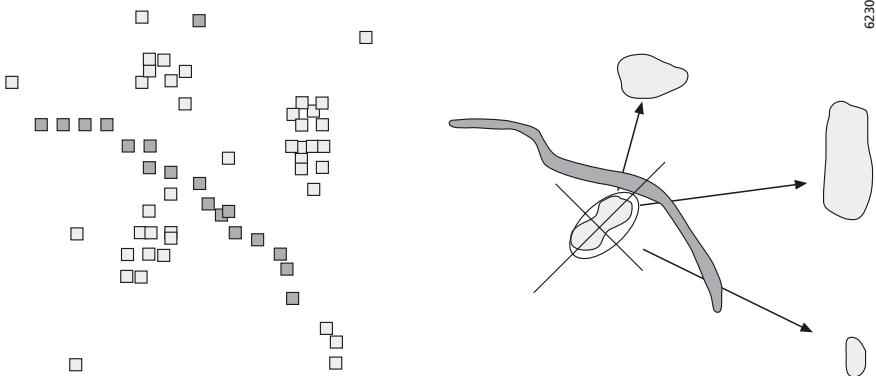
6230

Figure 12.3 – Pixels with same spectral entities vs. objects with averaged spectral properties and evolving spatial properties.

benefit of going to a segmentation approach is that you permit the incorporation of more expert knowledge – more specifically, you can incorporate more context information. This may seem at first to be counter-productive: are we not searching for methods which limit the amount of a priori information necessary to do the classification? The answer is that 'simple' methods to monitor earth processes automatically is a myth propagated in the 1980s. The fact is that our world is complex and our 'windows to the world' (RS images) are limited (Burnett & Blaschke, in press). Segmentation begets image objects, permitting the incorporation of spatial information as mutual relationships to these objects.

The incorporation of segment-level spatial information to the analysis of RS imagery introduces new dimensions to the actual analysis of the data. Instead of relying on only the Value, Location and Size attribute of single pixel, we can incorporate Fellowship (topology-related) attributes, for example image object size, shape or number of sub-object. This allows us to better utilise sophisticated GIS functions in analysing the data, e.g. to describe the spatial complexity of the objects, their spatial and spectral embeddedness in relation to neighbouring objects etc. We speak of objects if we can attach a meaning or a function to the raw information. Generally, the object is regarded to be an aggregation of the geometric, thematic and topologic properties. The topologic relations between the cells the object consists of can be examined once the user has defined his or her objectives, classification scheme and scale of analysis.

12.2 Image segmentation review

12.2.1 What is image segmentation?

One possible strategy to model the spatial relationships and dependencies present in RS imagery is image segmentation. Image segmentation is the partitioning of an array of measurements on the basis of homogeneity. To be more exact, segmentation is the division of an image into spatially continuous, disjoint and homogeneous regions. Segmentation is powerful and it has been suggested that image analysis leads to meaningful objects only

when the image is segmented in 'homogenous' areas (Gorte, 1998, Molenaar, 1998, Baatz & Schäpe, 2000) or into 'relatively homogeneous areas'. The latter term reflects better the 'near-decomposability' of natural systems as laid out by Koestler (1967) and we explicitly address a certain remaining internal heterogeneity. The key is that the internal heterogeneity of a parameter under consideration is lower than the heterogeneity compared with its neighbouring areas.

Although image segmentation techniques are well known in some areas of machine vision (see Narendra & Goldberg, 1980, Fu & Mui, 1981, Haralick & Shapiro, 1985, Cross et al., 1988), they were rarely used for the classification of earth observation (EO) data. One of the main reasons for this is that most of these algorithms were developed for the analysis of patterns, the delineation of discontinuities on materials or artificial surfaces, and quality control of products, in essence. These goals differ from our goals: the discretisation of EO remote sensing imagery aims at the generation of spectrally homogeneous segments, which show the inherent dimensions/objects of the images.

Before delving more deeply into the different algorithms that have been developed for image segmentation, and more specifically, for remotely sensed EO image segmentation, we would like to demonstrate the complexity of the process. For a 1 by 1 array, we can only partition the array only into 1 segment (figure 12.4). For a 2 by 2 array, we get a theoretical maximum of 16 combinations of segments or partitions. Note that partitions can be of any size greater than or equal to 1, and are of course, limited to the size of the array. Partitions must not overlap (they are disjoint) and the whole array must be partitioned. This means that for a typical 1:20,000 scale aerial photograph scanned to produce a 60 cm GIFOV, and which thus has 3000 rows by 3000 columns the theoretical maximum number of partitions is as large as 2 to the power 17994000! In real life, however, we would never be interested in exploring all these different
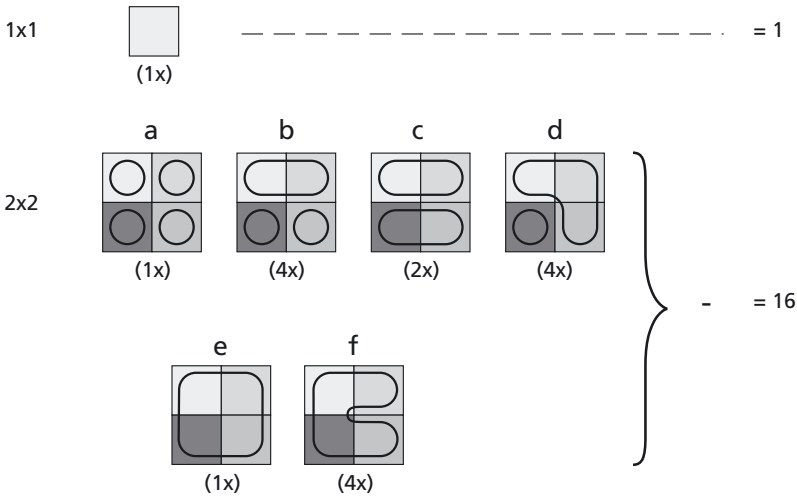

Figure 12.4 – Theoretical partitioning of 2D arrays. The grey boxes are meant to be the array, with a grey level value (GLV) shown by the 'greyness'. The coloured lines (circles, ovals, etc.) are vectors that 'partition' or 'discretize' these 2D arrays. Please consult the enclosed CDROM for a full colour version.

discretization instances, rather we want to intelligently chose an optimized partitioning. In fact, we probably want to chose 3 or more useful partitions of a single scene – but we will reserve a discussion of the use of multiple partitions (or multi-scale segmentation) until later. Still, it should be noted that we still have to use our expert knowledge to calibrate the segmentation algorithm so that the image objects that the segments delineate and the real world objects-of-interest match as closely as possible. However, let's first take a look at some of the tools that have been developed for image segmentation.

12.2.2 Types of segmentation
Traditional image segmentation methods have been commonly divided into three approaches: pixel-, edge and region based segmentation methods.

Pixel based methods include image thresholding and segmentation in the feature space. These methods do not necessarily produce a result which fulfils the requirement and definition of segmentation, and therefore the resulting output needs to be clumped. In other words, each spatially continuous unit (often referred as connected component in machine vision literature) needs to be assigned a unique label.

In edge based segmentation methods, the aim is to find edges between the regions and determine the segments as regions within these edges. From this point of view, edges are regarded as boundaries between image objects and they are located where changes in values occur. There are various ways to delineate boundaries but in general the first step of any edge-based segmentation methods is edge detection which consists of three steps (Jain et al., 1995): filtering, enhancement and detection. Filtering step is usually necessary in decreasing the noise present in the imagery. The enhancement aims to the revealing of the local changes in intensities. One possibility to implement the enhancement step is to us high-pass filtering. Finally, the actual edges are detected from the enhanced data using, for example, thresholding technique. Finally, the detected edge points have to be linked to form the region boundaries and the regions have to be labelled.

Region-based segmentation algorithms can be divided into region growing, merging and splitting techniques and their combinations. Many region growing algorithms aggregate pixels starting with a set of seed points. The neighbouring pixels are then joined to these initial 'regions' and the process in continued until a certain threshold is reached. This threshold is normally a homogeneity criterion or a combination of size and homogeneity. A region grows until no more pixels can be attributed to any of the segments and new seeds are placed and the process is repeated. This continues until the whole image is segmented. These algorithms depend on a set of given seed points, but sometimes suffering from lacking control over the break-off criterion for the growth of a region. Common to operational applications are different types of texture segmentation algorithms. They typically obey a two-stage scheme (Jain & Farrokhnia, 1991, Mao & Jain, 1992, Gorte, 1998, Molenaar, 1998, Hoffman et al., 1998).

In region merging and splitting techniques the image is divided into subregions and these regions are merged or split based on their properties. In region merging the basic idea is to merge segments starting with initial regions. These initial regions may be single pixels of objects determined with help of any segmentation technique. In region splitting methods the input usually consists of large segments and these segments are divided to smaller units if the segments are not homogeneous tough. In an extreme case region splitting starts with the

original image and proceeds by slitting it into n rectangular sub-images. The homogeneity of these rectangles is studied and each rectangle is recursively divided into smaller regions until the homogeneity requirement is fulfilled (figure 12.5). In both, region merging and splitting techniques, the process is based on a high number of pairwise merges or splits. The segmentation process can be seen as a crystallisation process with a big number of crystallization seeds. The requirement for the maintenance of a similar size/scale of all segments in a scene is to let segments grow in a simultaneous or simultaneous-like way.

Sometimes seen separately, is the group of 'split-and-merge' algorithms (Cross et al., 1988). They start by subdividing the image into squares of a fixed size, usually corresponding to the resolution of a certain level in a quad tree. These leaves are then tested for homogeneity and heterogeneous leaves are subdivided into four levels while homogeneous leaves may be combined with three neighbours into one leaf on a higher level etc.
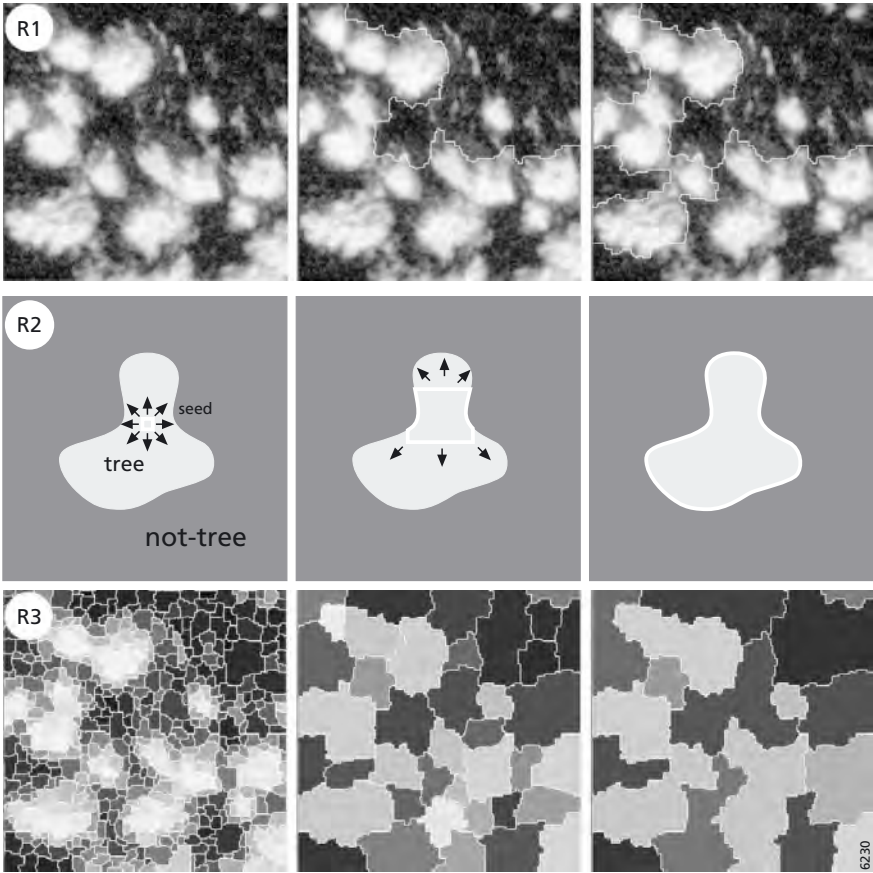

Figure 12.5 – Examples of region splitting and merging techniques.

12.2.3   Segmentation of Remotely Sensed data: state of the art

As stated above, the idea of segmentation is not new but it is becoming more widespread within the EO/RS community recently. While the foundations of the basic principles were laid out in the 80ies (see Haralick & Shapiro, 1985) and various applications demonstrated the potential in the following years for environmental applications (e.g. Véhel & Mignot, 1994, Panjwani & Healey, 1995, Lobo et al., 1996). Mainly the availability in commercial software packages catalysed a boost of applications more recently (Baatz & Schäpe, 2000, Blaschke & Strobl, 2001). Most approaches create segments which are in any sense regarded as being homogeneous by utilising geostatistical analysis (Hofmann & Böhner, 1999) and similarity approaches such as: unsupervised texture recognition by extracting local histograms and a Gabor wavelet scale-space representation with frequency (Hofmann et al., 1998); image segmentation by Markov random fields and simulated annealing; or Markov Random Fields (MRF) using a Maximum *a posteriori* (MAP) probability approach. The MRF method generally classifies a particular image into a number of regions or classes. The image is modelled as a MRF and the MAP probability is used to classify it. The problem is posed as an objective function optimisation, which in this case is the *a posteriori* probability of the classified image given the raw data which constitutes the likelihood term, and the prior probability term, which due to the MRF assumption is given by the Gibb's distribution. MRF was already exploited for an unsupervised classification by Manjunath & Chellappa (1991).

Hoffman & Böhner (1999) proposed an edge based method in which they calculate a representativeness of each pixel for its neighbours. The image segmentation is based on the representativeness values of each pixel. At first these values are calculated by a harmonic analysis of the values for each spectral channel. The minima in the matrix of representativeness – typically arranged in pixel-lineaments – represent spatial unsteadiness in the digital numbers. For the image segmentation, the vectorised minima of the representativeness delimit areas consisting of pixels with similar spectral properties (spatial segments). A convergence index is combined with a single-flow algorithm for the vectorisation of the representativeness minima. A standardisation is performed through the calculation of a convergence index for every pixel in a 3 by 3 window.

Dubuisson-Jolly & Gupta (2000) developed an algorithm for combining colour and texture information for the segmentation of colour images. The algorithm uses maximum likelihood classification combined with a certainty based fusion criterion. One of the most promising approaches is developed by Hofmann et al. (1998) and based on a Gabor wavelet scale-space representation with frequency-tuned filters as a natural image representation. Locally extracted histograms provide a good representation of the local feature distribution, which captures substantially more information than the more commonly used mean feature values. Homogeneity between pairs of texture patches or similarity between textured images in general can be measured by a non-parametric statistical test applied to the empirical feature distribution functions of locally sampled Gabor coefficients. Due to the nature of the pairwise proximity data, this algorithm systematically derives a family of pairwise clustering objective functions based on sparse data to formalize the segmentation problem. The objective functions are designed to possess important invariance properties. A clustering algorithm has been developed, that is directly applicable to the locally extracted histograms. It applies an optimisation technique known as multi-scale annealing to derive heuristic algorithms to

efficiently minimize the clustering objective functions. This algorithm has not been tested comprehensively and never been implemented within an operational/commercial software environment.

From most research following a segmentation approach it is argued that image segmentation is intuitively appealing. Human vision generally tends to divide images into homogeneous areas first, and characterises those areas more carefully later (Gorte, 1998). Following this hypothesis, it can be argued that by successfully dividing an image into meaningful objects of the land surface, more intuitive features will result. The problem is to define the term 'meaningful objects'. Nature hardly consists of hard boundaries but it is also not a true continuum. There are clear, but sometimes soft, transitions in land cover. These transitions are also subject to specific definitions and subsequently dependant on scale. Therefore, segments in an image will never represent meaningful objects at all scales, for any phenomena.

In the modelling stage characteristic features are extracted from the textured input image which include spatial frequencies (Jain & Farrokhnia, 1991, Hoffman et al., 1998), Markov Random Field models (Mao & Jain, 1992, Panjwani & Healey, 1995), co-occurrence matrices (Haralick et al., 1973), wavelet coefficients (Salari & Zing, 1995), wave packets (Laine & Fan, 1996) and fractal indices (Chaudhuri & Sarkar, 1995). In the optimisation stage features are grouped into homogeneous segments by minimising an appropriate quality measure. This is most often achieved by a few types of clustering cost functions (Jain & Farrokhnia, 1991, Mao & Jain, 1992, Hoffman et al., 1998). A further possibility is the watershed transformation. Bendjebbour et al. (2001) defined a general evidential Markovian model and demonstrated that it is usable in practice [to do what?]. Different simulation results show the interest of evidential Markovian field model-based segmentation algorithms. Furthermore, they described a variant of generalized mixture estimation, making possible the unsupervised evidential fusion in a Markovian context. It has been applied to the unsupervised segmentation of real radar and SPOT images showing the relevance of these models and corresponding segmentation methods. These approaches are just examples of what's available in scientific computing but most of these approaches are far from being operational.

12.2.4   Operational image segmentation frameworks

Per-field classification approaches have shown good results in studies (e.g. Lobo et al., 1996). Their results are often easier to interpret than those of a per-pixel classification. The results of the latter often appear speckled even if post-classification smoothing is applied. 'Field' or 'parcel' refers to homogenous patches of land (agricultural fields, gardens, urban structures or roads) which already exist and are superimposed on the image. Some studies (e.g. Janssen, 1993, Aplin et al., 1999) indicate that the methodology is positively contributing to the classification of remote sensing imagery of high to medium geometric resolution. This classification technique is especially applicable for agricultural fields (Janssen, 1993, Abkar & Mulder, 1998). Distinct boundaries between adjacent agricultural fields help to improve the classification due to the fact that boundaries in an agricultural landscape are relatively stable while the cropping pattern (also within the lots) changes often.

An alternative to approaches based on the idea of finding homogeneous areas in an image is the multi-fractal image analysis. The only operational approach widely available is implemented in a software called FracLab. FracLab is a Matlab toolbox for the multi-

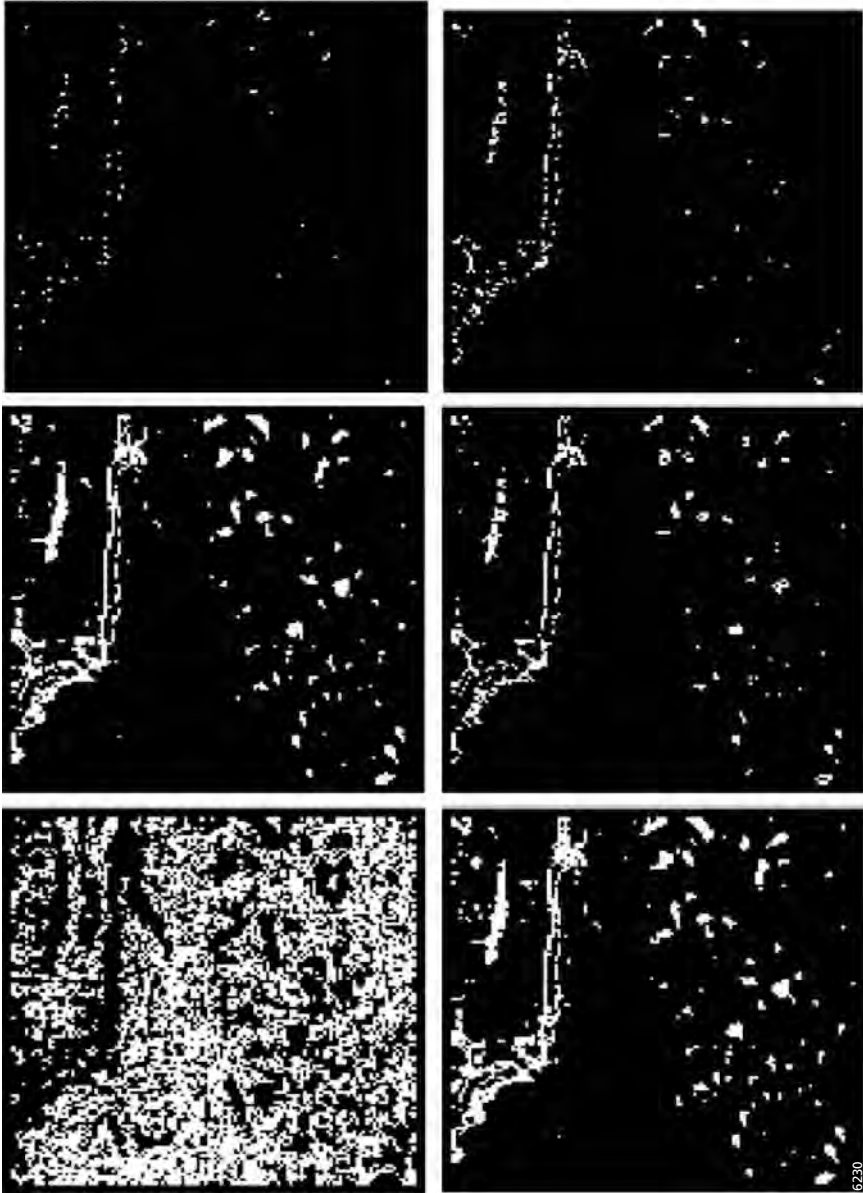*Figure 12.6 – Images a – f represent MAX Hoelder exponent of multifractal segmentation images of different parameters set-up for Band 4 (segment I).*

fractal analysis of sets. It is produced by the *Groupe Fractales* of INRIA, Paris, France. The descriptions here are based closely on the works of Jacques Vehel. In the Multi-fractal approach the image is modelled not by a function but by a measure μ. This allows the role of

resolution in image interpretation to be emphasised. The basic assumptions of the approach are the:

- Relevant information for image analysis can be extracted from the Hölder regularity of the measure μ
- Analysis is at three levels
- The pointwise Hölder regularity of μ at each point
- Variation of the Hölder regularity of μ in local neighbourhoods
- The global distribution of regularity of a whole scene
- The analysis is independent of translation and scale

Compared to other approaches to image segmentation or filtering, information about whole images is used to analyse each point instead of local comparison. The main difference between classic and multi-fractal methods is in the way they deal with regularity. The former try to obtain smoother versions of images, possibly at different scales, but multi-fractal analysis tries to obtain information directly from singular measures. Edges, for instance, are not considered as points where large variations of a signal still exist after smoothing, but as regions whose regularity is different from the background regularity in the raw data. This approach has merit for analysis of complex images.
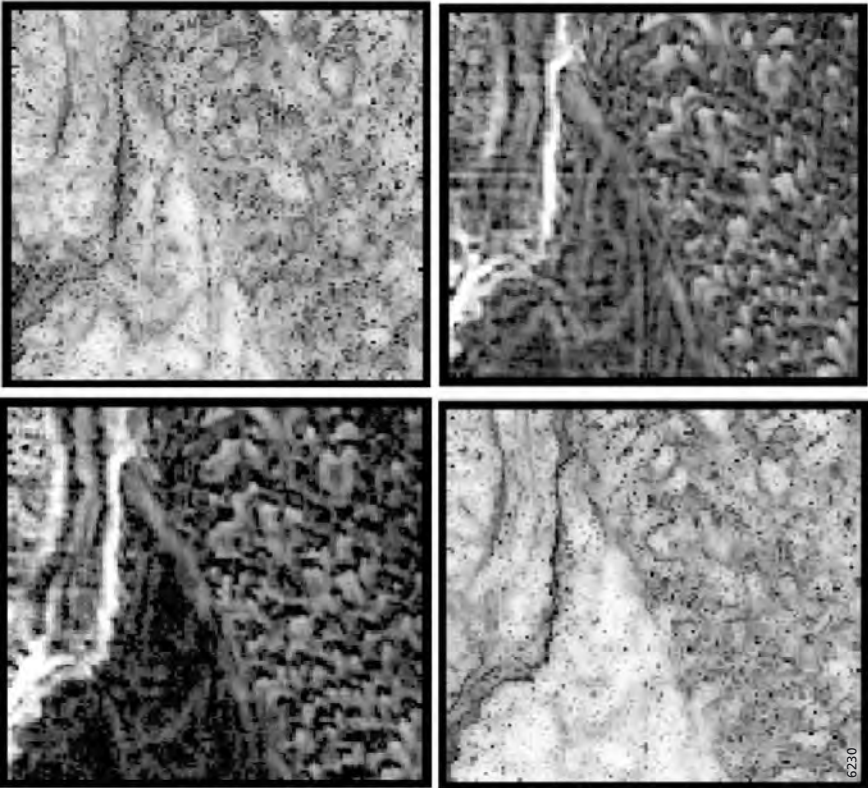

Figure 12.7 – Images a–d represent different Hoelder exponent images for Band 4 and 7 of Landsat 5.

Where grey levels of images are used in classic analysis, Hölder regularity is used for multi-fractal analysis. This is justified in situations where, as is common in complex images, important information is contained in the singular structure of image elements. Multi-fractal analysis will, for instance, find boundaries between texture regions as opposed to boundaries within textures, which is normal in classic methods.

The fractal net evolution approach (FNEA) was documented by Baatz & Schäpe (2000) and successful applications already exist (de Kok et al., 1999, Blaschke et al., 2000, Blaschke et al., 2001, Schiewe & Tufte, 2002, Neubert & Meinel, 2002, Hay et al., 2003). The FNEA is a region merging technique and starts with 1-pixel image objects. Image objects are pairwise merged one by one to form bigger objects. In this conceptualisation the procedure becomes a special instance of an assignment problem, known as pairwise data clustering. In contrast to global criteria, such as threshold procedures, decisions are based on local criteria, especially on the relations of adjacent regions concerning a given homogeneity criterion. In such an optimisation procedure each decision concerning a merge is based on all previous decisions or merges at least in its local vicinity. Therefore such a procedure includes to a certain degree historicity which can cause problems for reproducibility. The solution for this problem is the optimisation procedures and the homogeneity criteria which are maximizing the constraints in the optimisation process (Baatz & Schäpe, 2000).

12.3 Extending segmentation to an object-based analysis and classification

For many applications, a segmentation procedure is only a first, mechanistic step. Exceptions are approaches where the segmentation is performed on classification data and their respective class uncertainty values (e.g. Abkar & Mulder 1998, Klein et al., 1998). But, generally, the research interest is much deeper and image processing goes much further. Most research projects aim to map 1 to 1 the delineated (segmented) image objects to real-world entities within the geographic extent of the scene being assessed. The term image objects refers to the individually resolvable entities located within a digital image which are perceptually generated from images (Hay et al., 2001). In high resolution images a single real-world object is modelled by many individual pixels whereas low resolution implies that a single pixel represents the integrated signal of many (smaller) real world objects (Hay et al., 2003). In a remote sensing image, both situations occur simultaneously. For example, a 1 m resolution image of a forest canopy, where each tree crown exhibits a 10 m diameter, each crown image object will be composed of many pixels. The 1m pixel is high resolution in relation to the crown object it models. However, each 1 m pixel will also be composed of the integrated reflectance from many needles/leaves and branches. Thus, it will be low resolution in relation these individual crown components. As a result, image and objects tend to be composed of spatially clustered pixels that exhibit high spatial autocorrelation because they are all part of the same object. Because an 'ideal' object scale does not exist (Marceau, 1999), objects from different levels of segmentation have to be utilised for many applications.

In remote sensing, a single sensor correlates with range of scales rather than a single scale. The detectability of an object can be treated relative to the sensor's resolution. A coarse rule
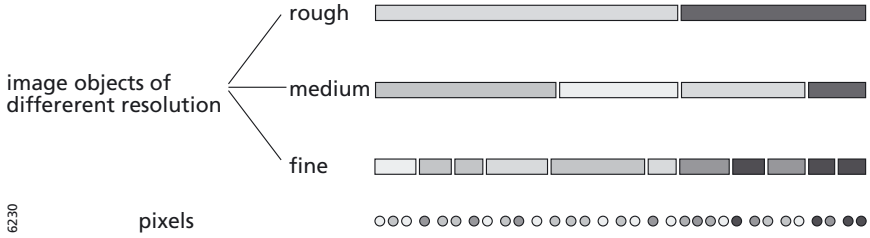
Figure 12.8 – A multi-resolution image segmentation approach.

of thumb is that the scale of image objects to be interpreted must be significantly bigger than the scale of image noise relative to texture (Haralick & Shapiro, 1985). This ensures that subsequent object oriented (OO) image processing is based on meaningful image objects. Among the most important characteristics of any segmentation procedure is the homogeneity of the objects. Only if contrasts are treated consistently, good results are expected (Baatz & Schäpe, 2000). Furthermore, the resulting segmentation should be reproducible and universal which allows the application to a large variety of data. Baatz & Schäpe argue that multi-resolution image processing based on texture and utilising fractal algorithms can fulfil all the main requirements at once.

Existing approaches show advantages but also some potential pitfalls of segmentation approaches for extracting geoinformation and useful landscape elements on 'real' (earth) surfaces (Blaschke et al., 2000, Blaschke & Strobl, 2001). The 'representativeness approach' (Hofmann & Böhner, 1999) mentioned earlier provides a good representation of the local feature distribution, which captures substantially more information than the usually used mean feature values. This one and other boundary-forming techniques (Schneider et al., 1997) and segmentation approaches (Gorte, 1998, Molenaar, 1998, Cheng, 1999, Dubuisson-Jolly & Gupta, 2000) provide good results for test areas but are not necessarily using all context information beyond the spectral information of neighbouring pixels such as texture, shape, directionality, spatial distribution within the study area, connectivity etc. But we strongly believe that this contextual information is the key to advanced classifications.

Although practically all segmentation procedures result in crisp objects, there are several ways to treat continuous transitions and fuzziness of objects. One strategy is to partition an image at several levels as discussed before and to utilize information at the finest, in most cases mechanistic level to express graininess at the higher level. The smallest spatial unit is still crisp except in the approach of Gorte (1998) but the entities at the superior level can be built up in a fuzzy decision process.

An important family of methods that strive to improve accuracy of classification are those using fuzzy sets. With this concept each pixel may have fuzzy membership with more than one class expressed as degree of its membership to each class (values range between 0 and 1). Training data for fuzzy classification need not be homogeneous as is desirable for conventional hard classifiers. Throughout the classification procedure one needs to assign known portions of mixing categories. Popular fuzzy set based approaches are the fuzzy c-means clustering (FCM) or the possibilistic c-means clustering (PCM). The fuzzy classifiers

produce images showing the degree of membership of pixels to stated categories. One caveat of the fuzzy set based methods is that he accuracy of fuzzy classification depends to a high degree on the complete definition of training data sets. Foody (2000) remarks that untrained classes will only display membership to trained classes, which can introduce a significant bias to classification accuracy.

An advanced method is the use of (artificial) neural network classifiers (ANN) borrowed from artificial intelligence research. Training data together with a known land-cover class (the input layer) are fed into the neural network system (the hidden layer). The algorithms inside the network try to match training data with the known class spectra patterns and produce an output layer together with errors of non-matching neural nodes. The procedure restarts trying to minimize errors. The process can be repeated several times. For the classification of specific objects neural networks have proven to be more accurate than conventional methods (Civco, 1993; Foschi & Smith, 1997; Skidmore et al., 1997). Main points of critique include:

- Accurate meaningful results require good training data sets; otherwise outputs will not be very reliable.
- The classification procedure needs the adjustment of various parameters which highly increases complexity of the whole system and seems to limit its usefulness.

In the following chapter, we demonstrate two applications and go into the classification stage whereby we use explicit rules and a semantic network for classification aiming to overcome these shortcomings of ANN by making the rules transparent.

12.4   Examples of applications

12.4.1   Segmentation in multi-source forest inventory

One, and increasingly popular, application field of remote sensing is multi-source forest inventory (MSFI). Since the introduction of first MSFI applications in the late 1960's (Kuusela & Poso, 1970) the rapid development of sensors and image analysis methods have resulted in many, although few operative, MSFI applications. The first operative multi-source national forest inventory began in Finland in 1990. The method employs field plot data, satellite (mostly Landsat TM) images, digital map data and k-nearest neighbour (k-NN) estimator and produces georeferenced thematic maps and detailed forest statistics for any given area (Tomppo, 1996). Similar MSFI methods have been tested in many different conditions (e.g. Franco-Lopez et al., 2000; Nilsson, 2002; Tomppo et al., 1999; Tomppo et al., 2001). In a typical MSFI application, the field data consists of sparse field sample and the interesting forest attributes are estimated for the rest of the area with help of measured field data and image information. In addition, the field data is usually gathered using relatively small field sample plots and training data is often built in a straightforward way: each field sample plot is assigned spectral information from the pixel it is located on. Methods based on this kind of approach and use of medium resolution satellite imagery have proven to produce reliable forest resource information for large and medium sized areas (Tomppo, 1996; Katila et al., 2000). However, estimation errors have been high at the plot- and stand-levels (Tokola et al., 1996, Mäkelä & Pekkarinen, 2001, Katila & Tomppo, 2001). This is due to many reasons, among which are the poor spatial resolution of the image material and the difficulty to assure

Figure 12.9 – An example of generalised AISA data. NIR channel.
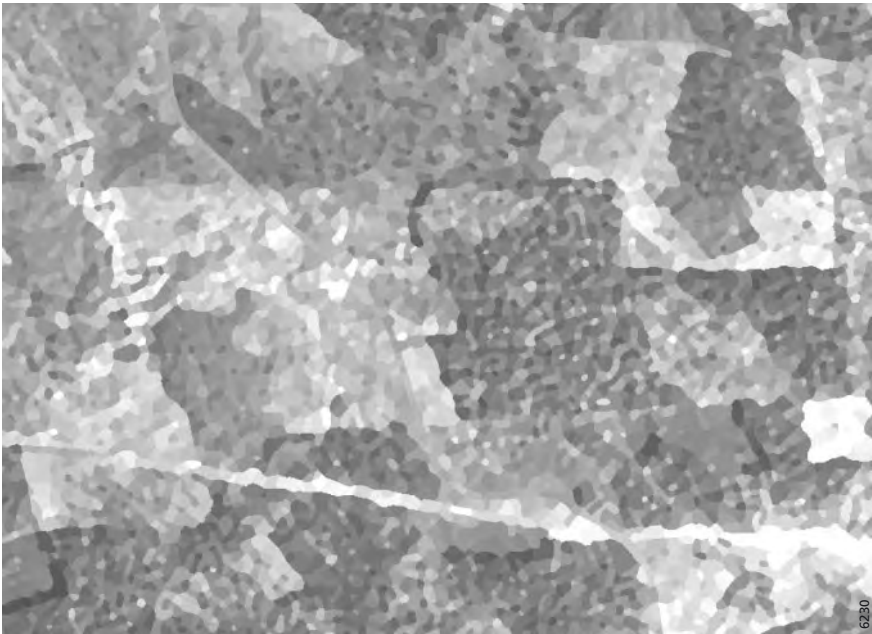

Figure 12.10 – An example of the resulting segmentation. Segment level averages of NIR channel.

exact geo-referencing in both image and field data. These problems can be avoided, at least to some extent, if the MSFI application is based on VHR data.

The increasing spatial resolution in image data results in increasing number of pixels per area unit. This is obvious if one considers the number of pixels falling into the area of a single field plot. Therefore, when comparing VHR and medium resolution data, locational errors of similar magnitude should result in smaller discrepancies between spectral and informational classes of the field plots. The problem is that the pixel-based approach to feature extraction and image analysis does not apply to VHR imagery. From a forest inventory point of view a sub-meter resolution VHR pixel is too small a unit for image analysis. It represents spectral characteristics of only a small portion of the target: a stand, a plot or a tree. In order to be able to fully utilise the improving spatial resolution, need a way to aggregate pixels into appropriate spatial units for the image analysis. One way to accomplish this is image segmentation.

Our MSFI example demonstrates the effect of segment-level feature extraction and image analysis to the resulting MSFI estimates at plot and region level. The material employed in the example has been gathered from a study area that was originally established for MSFI research employing imaging spectrometer data (Mäkisara et al., 1997). The area has been imagined with Airborne Imaging Spectrometer for Applications (AISA). The instrument has been developed in Finland and it has bee employed in several studies since the development of the first prototype AISA in early 1990's (e.g., Mäkisara et al., 1993). Currently the AISA family consists of three different systems: AISA+, AISA Eagle and AISA Birdie (http: //www.specim.fi/). The image data were pre-processed in Finnish Forest Research Institute and a mosaic of the seven original flight lines was composed. The radiometric differences between adjacent flight lines were normalised using the overlap area and histogram matching technique. The GIFOV of the resulting mosaic was 1.6 metres. Finally, the number of spectral channels of the original AISA images was reduced from 30 to 4 by means of spectral averaging. The averaging was accomplished in such a way that the resulting output would correspond as well as possible to the spectral characteristics of new generation VHR satellite images. An example of the generalised image data is presented in figure 12.9.

The averaged AISA image was segmented using a two-phase approach. In the first phase, a large number of initial segments were derived using a modified implementation of the 'Image segmentation with directed trees'-algorithm (Narendra & Goldberg, 1980; Pekkarinen, 2002). In the second phase, the minimum size of the segments was set to 10 pixels and all segment smaller than that were merged to their spectrally nearest adjacent segment. An example of the resulting segmentation is presented in figure 12.10.

The field data of our example consists of systematic grid of 262 Bitterlich (relascope) field sample plots (Mäkisara et al., 1997; Pekkarinen, 2002). Each field sample plot was assigned spectral information from A) the pixel the plot centre was located on and B) from the segment the plot was located on.
The performance of pixel- and segment-level features was compared in the estimation of volume of growing stock at plot. The plot level estimation tests were carried out using cross-validation (leave one out) technique. In other words, the total volume was estimated for each

plot with help of the rest of the plots. The actual estimate was derived using a weighted *k*-nearest neighbour estimator (*k*-NN). In weighted *k*-NN, the estimate is computed as a weighted average of *k* spectrally nearest neighbouring observations in the feature space (e.g. Tomppo, 1991, Pekkarinen, 2002). Three different values for *k* were tested, namely 1, 3 and 5. The accuracy of the estimates was judged using root mean square error (RMSE, equation 12.1) of the estimates. In addition, the within volume class distributions of the estimates and observed values were examined.

$$RMSE = \sqrt{\frac{\sum_{i=1}^{n} (\hat{y}_i - y_i)^2}{n-1}}$$ (12.1)

Where
y_i = measured value of variable y on plot i
$\hat{y}$ = estimated value of variable y on plot i
n = number of plots

The results of our experiment show that the estimates derived using segment level features have significantly lower RMSEs that estimated derived with pixel-level features. The decrease in relative RMSE was from about 11 to 13% depending on the number of *k* (figure 12.11). The benefits of the segment-level approach are also obvious at the region-level. The distribution of the resulting wall-to-wall estimated is much closer to the distribution of the field data in the segment-level estimation approach (figure 12.12).

The example shows that the segmentation-based approach gives significantly better estimation results than the pixel-level approach. However, there is still a lot of room for improvement. One fundamental prerequisite for any image analysis is that the phenomena under investigation and the unit of analysis are of similar scale. This is not the case in our example. Even though the segment level analysis gives better results it is not an optimal solution to the estimation problem: the spectral characteristics of a segment do not
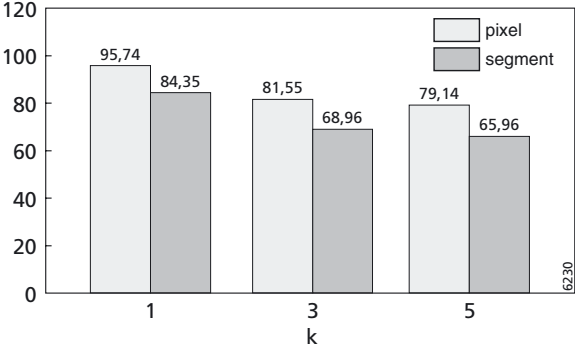

Figure 12.11 – Relative RMS errors of total volume estimates with different numbers of k. Pixel- and segment–level approaches.
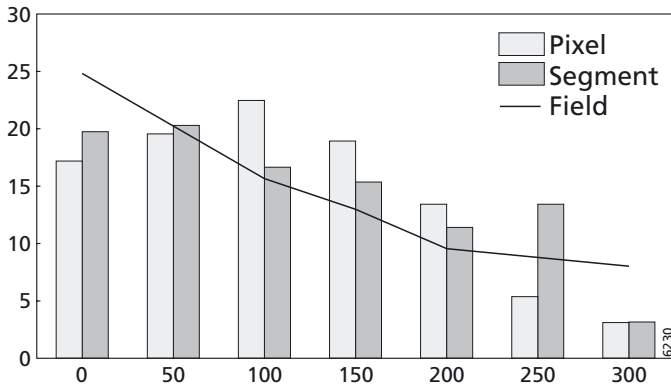
Figure 12.12 – Volume class distribution of the pixel and segment based estimates and the field data.

necessarily represent the spectral characteristics of the area from which the field information was gathered.

In an optimal case one would know the exact location of the plot, and its dimensions and could use this information in construction of the training data. In such a case the extracted spectral information would represent the plot but the problem of determining the spatial units for image analysis in unsampled areas would remain the same. Image segmentation provides a visually appealing solution to this problem but does not necessarily give significantly better plot-level estimation results than a straightforward spectral averaging in local neighbourhood (Pekkarinen, 2002).

12.4.2   Object-based forest stands mapping in an urban forest

In this second example, we demonstrate the use of segmentation as part of a two step multiscale segmentation/object relationship modelling MSS/ORM approach (Burnett & Blaschke, in press) to in a study delineating habitat patches in a mixed hardwood/deciduous urban forest. Just as in the above example, we utilise VHR remotely sensed imagery. And also in this example, 'meaningful' image objects are also deleniated, although using a different segmentation algorithm. At this point the two example diverge. Instead of using a spectral (plus textural) feature space (i.e. the *kNN*) estimator, the image is further segmented so that we have a minimum of 2 levels (scales) of image objects. Following this multiscale segmentation, the ORM step then begins, wherein expert knowledge is integrated into the classification and heuristics using both spectral as well as 'fellowship' (object inter-relationships) information. The software eCognition by Definiens AG of Munich was used for both the segmentation step and the object-relationship modelling.

The study site is located on the 11 km long island of Ruissalo (figure 12.13), west of the city of Turku in SW Finland. The forest patches in the site differ in tree species, stem density, age and stand species homogeneity; ranging from sparsely treed rocky meadows with medium sized Scots pine (*Pinus sylvestris*) to mature mixed stands of lime (*Tilia cordata*), Scots pine, Norway Spruce (*Picea abies*) and oak (*Quercus robar*) exhibiting early patch-phase dynamics. Topographic variation is slight but because of the recent emergence of the island during the
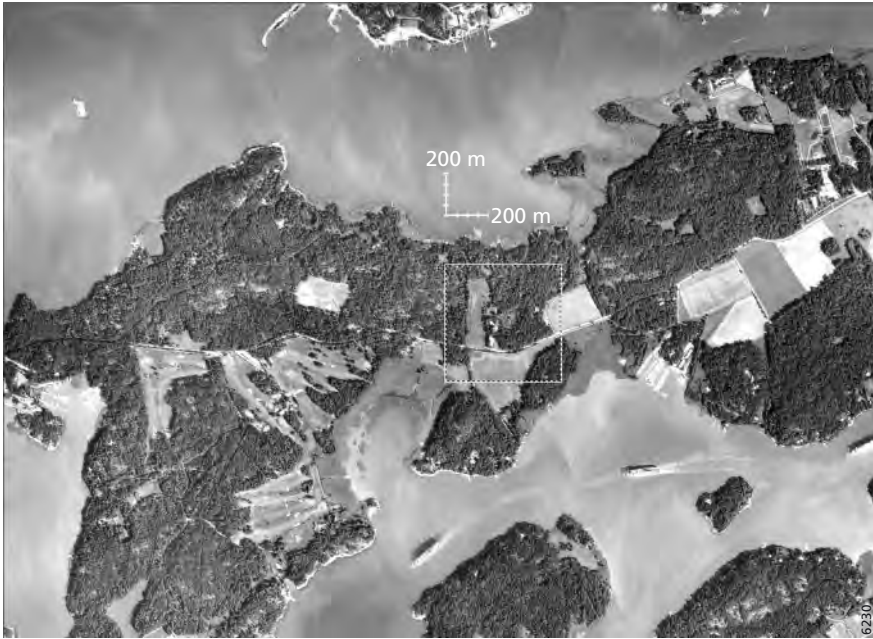
Figure 12.13 – Ruissalo Island study site marked with white box, centred on 60 25 42N & 22 08 53E. Please consult the enclosed CDROM for a full colour version.

Quaternary, organic soil layers are often very thin on upland areas. In addition to the varied microclimatic and soil types, long term human management (eg. introduced species), the island is home to one of the richest species communities in Finland (Vuorela, 2000). The island is now managed as a recreation area with a large proportion of the land area in nature reserves.

The goal of the MSS/ORM analysis was to differentiate between and map upland dry pine sites and mature mixed forests. In addition, the compositional break-down of deciduous and coniferous species in the mixed stands would be useful. The data used was 1m GIFOV digital still camera mosaic acquired with a professional Minolta digital camera, and rectified and mosaiced using software developed by the Enso Forest Company and Technical Research Centre of Finland (VTT). We also had access to the City of Turku's cadastre and road mapping data in vector format.

Multiscale segmentation

The goal of the MSS step is to find three levels (scales) of image objects: level -1 are the sub-units which are mostly characterised by their spectral features; level 0 is the main mapping units which are classified using inter-object relationships; and level +1 which is an aggregate or reporting level. The segmentation of the image was carried out so that in the forest, the smallest segmentation level comprised image objects such as tree crowns, small groups of crowns, shadow and sunlit bare rock (figure 12.14). It was found that for this image resolution/ image object combination, suitable segmentation levels could be generated in eCognition using scale parameters of 10, 50 and 100 (always with colour and shape parameters of 0.8 and

a

b

c

6230
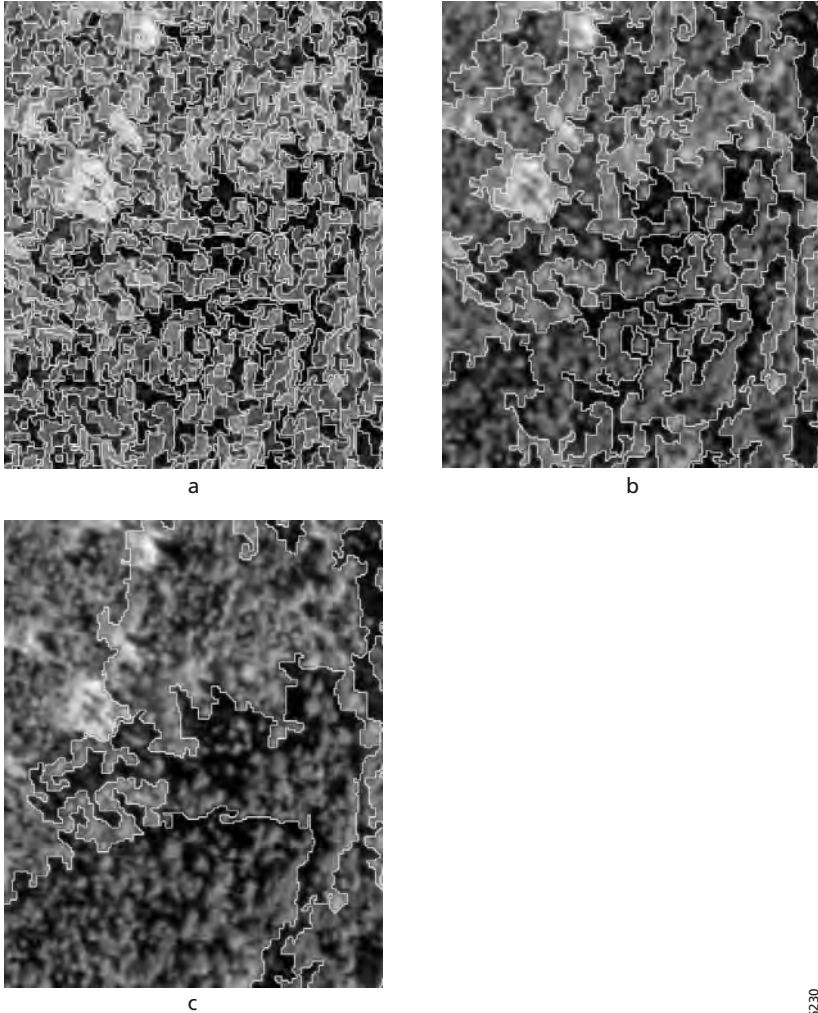
Figure 12.14 – Examples of segmented image objects created in the forested area in the SW of the study area. This is an area that transitions from the mature mixed habitat to the dry upland pine. The images show the forest canopy at the three segmentation levels -1, 0 and +1 (eCognition segmentation scale parameters of 10, 50 & 100).

0.2). We then took samples of the different tree crowns. We had field survey plots to guide us in this step. We also took samples from agricultural fields, pasture, houses and roads. Finally we classified the level -1 objects using a nearest neighbour classification routine.

Object relationship modelling

In the second step, we began to incorporate rules in order to guide the software to properly classify each of the level 0 objects. We use the term modelling, because we are in effect building rules that model (abstract) the functional relationship that exists in the real world

Figure 12.15 – Sub-object relationship mapping guide (see table 12.1).
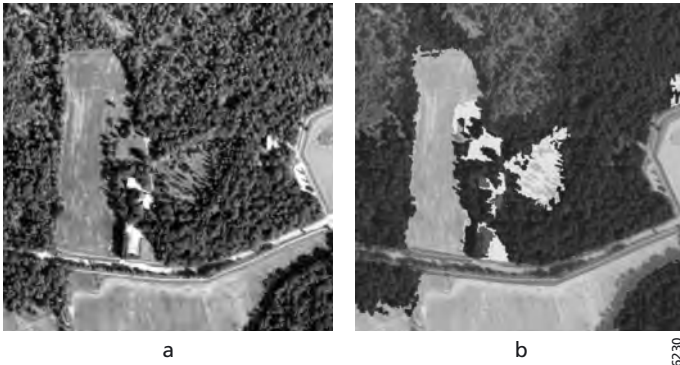
Figure 12.16 – Original image and completed classification at the Level +1 (super-object) level.

between the objects, sub-objects and super-objects. Please see figure 12.15 and table 12.1 for a concise description of these rules. We started by ruling that any object under the main road mask that came from the City of Turku cadastre should be classed 'road' (rule 1). The rules that govern agricultural areas (rule 2) involved both spectral means of the level -1 objects and their standard deviation. These objects are generally larger and smoother then those found in the forest areas. Houses (rule 3) were perhaps the simplest level 0 class: the spectral differences made only a mean of level -1 (sub-object) rule necessary.

There were large areas of shadowed fields that required special consideration (rule 4). We didn't want to confuse shadow in the forest. Here we had to examine level 0 objects to the northwest. If there were level 0 agriculture objects in this direction, we classified them as shadowed field. We could have also used a textural value such as the number of sub-objects or the standard deviation of the spectral values in the sub-objects, since these are smoother then their forest shadow cousins, but this was not needed. Pasture (rule 5) perhaps the most difficult to model. Here, there are relatively small expanses of fields but with large single trees with elongated shadows in the centre. The field sub-objects (level -1) had different spectral signatures than the bare rock found in the upland pine sites, so there was no confusion there. In the end, a heuristic that said any groups of agriculture level 0 objects with greater than 30% are covered by tree and shadow level -1 objects was arrived at after several iterations of testing. Finally, we were able to concentrate on separating the to focal forest units. We had fairly good separability of the coniferous and deciduous level -1 objects. We also used the amount of bare rock/soil level -1 objects. And we knew that the upland sites rarely touched agricultural areas. Using a combination of these rules, we came up with heuristics that modelled this 'behaviour'.

In the final step, we aggregated all neighbouring level 0 objects of the same class into single polygons (figure 12.16). These were the polygons upon which the reporting statistics and spatial indices were calculated. Values for average amount of level -1 sub-objects (i.e. tree crowns) were also reported.

The result of the multiscale analysis using the MSS/ORM methodology is a flexible mapping of these semi-natural forests, but with the added benefit of having a record of sub-object characteristics. Thus we could go further in our analysis and further classify the upland pine into areas with more or less bare rock. Or we may want to identify zones in the mature mixed forest that are within a fixed radius of an oak crown of a certain dimension. With

Table 12.1 – Object-relationship modelling rules

Diagram label	Class	Heuristic
1	Roads	Road vector layer used as mask
2	Agriculture	Classified from spectral characteristics at Level 0
3	Houses	Classified from spectral characteristics at Level 0
4	Shadowed fields	Level -1 segments classified relative to segments to NW.
5	Pasture	Agricultural level 0 segments having >30% 'single tree + shadow' sub-objects
6a	Mature mixed	Classified by spectral, textural and sub-object rules
6b	Upland dry pine	Classified by spectral, textural and sub-object rules

the increasing availability of scanning LIDAR data, this ORM modelling will be even more powerful.

12.5   Discussion and conclusions

We began the chapter with a comparison of different image processing strategies. The image analysis presented here provides methodology and examples of dealing with image semantics rather than pixel statistics. In most cases, information important for the understanding of an image is not represented in single pixels but in meaningful image objects and their mutual relations. Prerequisite for the successful automation of image interpretation are therefore procedures for image object extraction which are able to dissect images into sets of useful image objects. As stated above, segmentation is not new, but only a few of the existing approaches lead to qualitatively convincing results while being robust and operational. One reason is that the segmentation of an image into a given number of regions is a problem with a huge number of possible solutions. The high degrees of freedom must be reduced to a few which are satisfying the given requirements.

The multiscale consideration of landscape pattern gains much attraction recently but the realisation in practise becomes difficult and data-intensive. Only for some small areas, field surveys and mapping at different scale is possible. Not a solution but one step forward to support this approach is a nested multi-scale image processing of the same data sources. The resulting different object scales have to be logically connected. This is achieved through an OO approach where each object 'knows' its intrinsic relation to its superobject (*is within*) and its subobjects as well as the relations to the neighbouring objects at the same scale.
So far, it is concluded, that context based, object-oriented image classification is a promising development within integrated GIS/RS image analysis. Comprehensive studies using multi-sensor data sets which explore the 'behaviour' (stability and consistency of the image objects and their respective classification results due to different data situations) are still urgently required. However, several studies indicate that current description schemata for landscape objects are dependent on scale, resolution and class definition (Hargis et al., 1998, Herzog & Lausch, 2001). Very few studies already illustrated the potential of context-based approaches to improve classification results in real-world studies, e.g. Lobo et al. (1996). Although the literature mentions the possibilities of object-based image analysis since two decades (Kettig & Landgrebe, 1976, Haralick & Shapiro, 1985), only latest-technology hardware, intelligent software and high resolution images can advance this concept.

While using image segmentation, a somewhat implicit hypothesis is that results from objects or regions based on segmentation are often easier to interpret and more meaningful than those of per-pixel classification. Only recently, some studies compare the accuracy of both approaches. A main finding is, that the results of the latter often appear speckled even if post-classification smoothing is applied (Blaschke & Strobl, 2001, Ivits et al., 2002). The second strategy originates in conceptual ideas of landscape ecology and information structuring and puts forward a conceptionalisation of landscape in a hierarchical way utilising remote sensing and GIS data at different scales resulting in an object-oriented modelling approach and the construction of semantic networks.

This chapter took up the challenge to the technology which lies in an ontology inherent to modern landscape consideration: landscapes are composed of a mosaic of patches (Forman, 1995). But patches comprising the landscape are not self-evident; patches must be defined relative to the given situation. From an ecological perspective, patches represent relatively discrete areas (spatial domain) or periods (temporal domain) of relatively homogeneous environmental conditions, where the patch boundaries are distinguished by discontinuities in environmental character states from their surroundings of magnitudes that are perceived by or relevant to the organism or ecological phenomenon under consideration. The technical potential of oo-based image processing will be applied to the delineation of landscape objects. The involves issues of up- and downscaling and the need for an ontology and methodology of a flexible 'on-demand' delineation of landscape objects hypothesising that there are no 'right' and 'wrong' solutions but only 'useful' and 'meaningful' heuristic approximations of partition of space. The GIS development shall be the medium for the transfer of the indicators and techniques developed into operational use.

The object-oriented approach is also a philosophy of improved image understanding. Human vision is very capable of detecting objects and object classes within an image. To pursue this type of analysis, it is important to stay close to the 'intuitive' image understanding. Object-based classification starts with the crucial initial step of grouping neighbouring pixels into meaningful areas, especially for the end-user. The segmentation and object (topology) generation must be set according to the resolution and the scale of the expected objects. The spatial context plays a modest role in pixel based analysis. Filter operations, which are an important part of the pixel based spatial analysis, have the limitation of their window size. In object analysis, this limitation does not exist. The spatial context can be described in terms of topologic relations of neighbouring objects. But how to define the image objects? What should be the rule of thumb for a segmentation or a pre-segmentation of image primitives which can build up the corresponding objects? Only very recently, several approaches in image analysis and pattern recognition are exploited to generate hypothesis for the segmentation rules as an alternative to knowledge-based segmentation (Blaschke & Hay, 2001, Lang, 2002, Hay et al., 2003).

The new data available necessitate improved techniques to fully utilise the potential resulting from the combination of high-resolution imagery and the variety of medium-resolution multi-spectral imagery widely available. High-resolution panchromatic images now show variety within a so far 'homogeneous' area (a pixel in the medium-resolution image). The understanding of local heterogeneity in a panchromatic image has a strong effect on the standard deviation value in the same 'window' area of the image. Nevertheless, they can be simultaneously used to classify areas, where spectral values in multispectral bands are less important compared to local texture.

The Earth Observation data are not sufficient to characterise completely the natural environment. They need so to be associated to other data. We have to further investigate synergy effects between satellite images and GIS-derived vector data, such as a digital topographic database. The use of such topographic databases, which are built up in most countries can support the satellite image analysis. This digital database offers a geometric as well as a semantic prediction for objects in the satellite image.

Current average geometric resolution of common satellite sensors allows to develop main area-based land use classes like 'settlement', 'forest', 'water' or 'agriculture'. In combination with high-resolution imagery described above, expected results of this feature extraction allow a symbolic description of more complex image content such as 'urban forest' or 'traditional, small-sized, complex land use'. Both, the symbolic description and the digital database, are transferred in a semantic network, a compact formalism for structuring the entire knowledge. None of the various pixel-based classification methods seems to really satisfy all the needs for the production of reliable, robust and accurate information similar to objects identified by a human interpreter.

Important next research steps if image segmentation is used as a core methodology in an image analysis include:
- To develop a methodological framework of object-based analysis which offers an option to improve (semi)automatic information derivation from a rapidly increasing amount of data from different sensors;
- To achieve meaningful representations of spatial physical parameters derived from original reflectance values
- To develop new methods for accuracy assessment based on objects rather than pixels;
- To develop data analysis tools for environmental management based on multi-scale object representation in order to support decision making.

Chapter 13

Multiscale Feature Extraction from Images Using Wavelets

Luis M.T. de Carvalho, Fausto W. Acerbi Jr, Jan G.P.W. Clevers, Leila M.G. Fonseca &
Steven M. de Jong

13.1 Introduction

In the last decades, much attention has been paid to the multiresolution characteristic of processes and patterns in general. Good examples are remotely sensed images, which provide different information and noise at various spatial scales. Analysts have become aware that image processing could be considerably improved if the scenes are viewed at multiple resolutions. This is particularly important when the information of interest is characteristic of just a few scale levels. In this context, the capacity of perceiving scales might be the key for a better understanding of our landscapes and an aid to the automatic analysis of remotely sensed images.

The meaning of scale varies so much between and within disciplines that care should be taken to avoid terminological confusion. The ratio between a segment on a map and the corresponding segment on the Earth's surface is probably the oldest and the most popular notion of scale. Scale is also used to indicate the spatial extent of a study area. Comparing the two connotations above, a 'large scale map' provides more detailed and, consequently, voluminous information, which is usually limited to small geographical areas. On the other hand, a 'large scale study' covers a large geographical area and usually omits detailed information. Besides the two described concepts of cartographic scale (map scale) and geographic scale (extent or domain), other important notions of scale include the resolution (grain or sampling interval) and the operational scale. The term resolution is used to refer, for instance, to the size of the smallest observable object or to the pixel size, which defines, together with the geographic scale, the limitations to represent a given scene. Finally, the operational scale refers to the interval at which a phenomenon operates (Lam & Quattrochi, 1992). In this chapter, the meaning of scale will always be clear from the context and used mostly in the sense of resolution or geographic scale, where small scales present detailed information and large scales represent coarser views of the scenes or signals.

These important aspects of scale are useful and obvious when we make observations as a function of space (i.e., position), but the same principles apply to the temporal, spectral or other dimensions of the world and are fundamental to their proper characterisation. Even so, the vast majority of techniques for geographical information processing have been driven by the 'fixed scale paradigm'. Regarding remote sensing and GIS, resolution-invariant

methods have proliferated mainly because of simpler data structures and analysis (Csillag & Kabos, 1997). In this framework, the information contained in the multiple scales of the data cannot be analysed or used separately yielding results that also combine the influence of variables that might be characteristic of just a few scale levels. Environmental processes operate at multiple scales generating patterns that have a multiscale nature as well. Like the real world they portray, remotely sensed data 'show' different or complementary information at different scale levels. This fact has important implications for analyses, representations and interpretations of data and accuracy.

The almost infinite resolutions of our world in all of its dimensions have raised an increasing interest in scale issues, which are now recognised as fundamental to any research area. Nevertheless, only a few recent tools exist, which are appropriate to derive and study the information contained in multiple scales of the data.

13.2　Multiresolution decomposition with wavelets

Most of the data used in scientific research are generated by measuring devices that record a physical quantity of interest. In application fields ranging from chemometrics to astronomy, the device is a remote sensor and the physical quantity is the reflected or emitted electromagnetic energy, which is recorded in digital or analogue format usually as a function of space $f(x, y)$, e.g. an image. Lets pick, as an example, one line of the digital image shown in figure 13.1 and plot it as a function of just one variable $f(t)$ to simplify presentation.

One common way to extract information from this function is to compare it with a set of test functions. Basically, a high coefficient results from this comparison where the function under evaluation is more similar to the test functions. Well-known sets of test functions are the dilations by a factor ω of a single periodic function e^{it} in Fourier transformations (Fourier, 1988).

The Fourier transform accurately reflects in a_ω *which* frequencies occur in the input signal:

$$a_\omega = \langle f(t), e^{i\omega t} \rangle \tag{13.1a}$$

where, i is the imaginary unit ($i^2 = -1$) and $\langle \ , \ \rangle$ stands for the inner (or scalar) product in the space L^2 of square integrable functions. If $h(t)$ and $g(t)$ are two functions in L^2, their inner product in the interval [a,b] is a measure of similarity between the two functions, which is defined by:

$$\langle h(t), g(t) \rangle = \int_a^b h(t) \cdot \overline{g(t)} \ dt \tag{13.2}$$

where '——' stands for complex conjugate, such that the conjugate of $a + ib$ is $a - ib$, with i being the imaginary part of the complex number ib. For example, using the complex conjugate of $e^{i\omega t}$, the inner product of Equation 13.1 becomes:

$$\langle f(t), e^{i\omega t} \rangle = \int_{-\infty}^{+\infty} f(t) \cdot e^{i\omega t} \ dt \tag{13.1b}$$
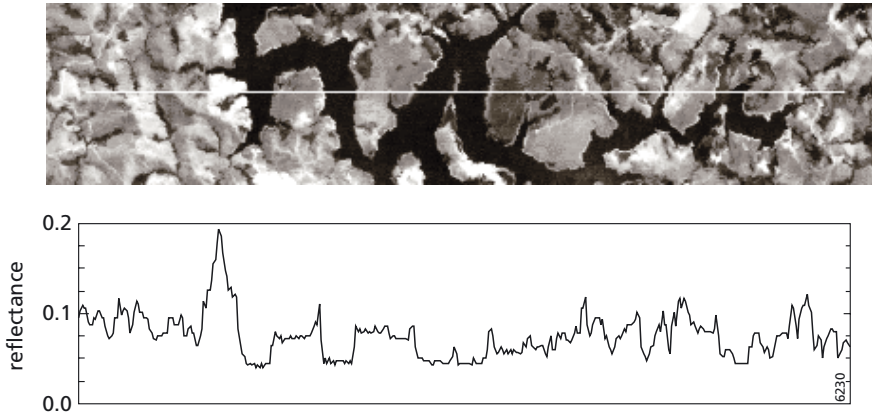
Figure 13.1 – Plot of reflectance values referent to the white line of the image on top.

Besides the frequency localisation property mentioned above, practical applications require good time (or space) localisation as well. This requirement was partially achieved by the windowed Fourier transform (Gabor, 1946), which uses pieces of periodic functions instead of infinite waves as test functions. However, sudden breaks between pieces might generate artefacts, especially in 2D signals. Moreover, a choice has to be made concerning the size of the analysing pieces, generating a compromise towards local or, otherwise, global characterisation. The new set of test functions $\psi_{jk}(t)$ in the wavelet transform goes a step further and tells us *when* (or *where*) each frequency component occurs more effectively than the windowed Fourier transform. One of its aims is to provide an easily interpretable visual representation of signals. While Fourier coefficients in Equation 13.1 have an index ω related to the frequency, the wavelet coefficients are characterised by a parameter j, referring to a scale of octaves (doubling the frequency when $\Delta j=1$), and a positional parameter k:

$$a_{jk} = \langle f(t), \psi_{jk}(t) \rangle \tag{13.3}$$

This comparison might operate in continuous time (on functions) or in discrete time (on vectors). The raster data structure of remotely sensed images is strictly discrete and consequently, the wavelet transforms presented here will also be discrete. Fortunately, multiresolution analysis and wavelet transforms have a strong connection with the discrete filters of signal processing, which will serve as the basis for the following presentation.

The remainder of this section provides a textual overview of wavelet transforms and multiresolution analysis with emphasis on aspects used in further sections. For a complete mathematical characterisation of wavelets, a few recent references will be recommended here. Strang & Nguyen (1997) bring a comprehensive introduction to the theory of wavelets and filter banks, whereas Prasad & Iyengar (1997) provide a basic mathematical background and some practical applications to image processing. Daubechies (1992) and Mallat (1998) present in-depth developments, whereas Starck et al., (1998) present application-oriented material with numerous examples in various fields, including geoinformation sciences.
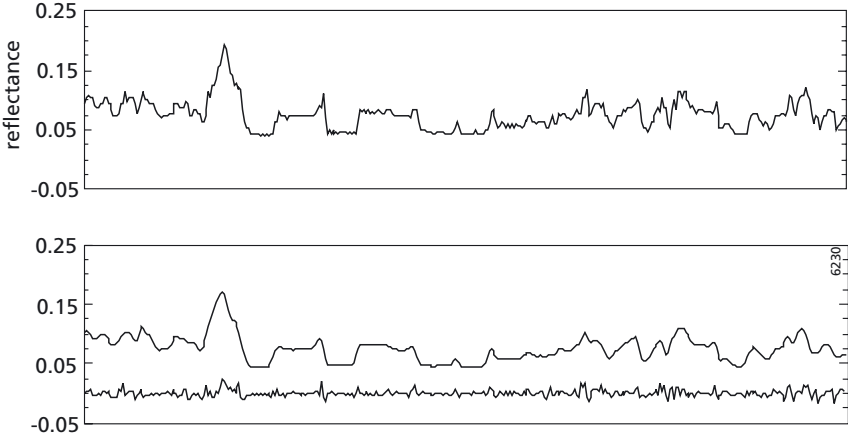
Figure 13.2 – (a) Line-profile of Figure 13.1 with (b) respective low frequency (top) and high frequency (bottom) components.
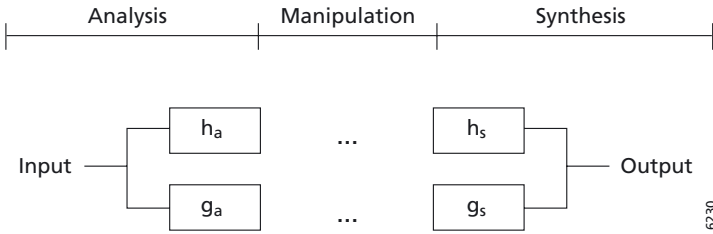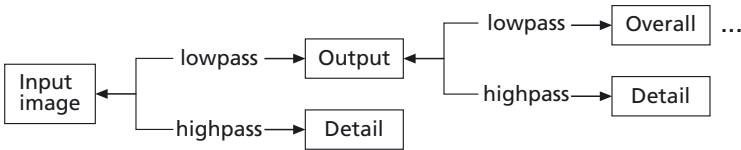

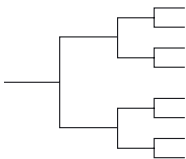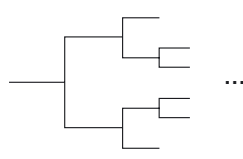*Figure 13.3 – Schematic representation of a filter bank.*

Figure 13.4 – Schematic representation of three possible structures for recursive implementation of filter banks.

13.2.1   Digital filters and filter banks

In signal processing, a digital filter is a time-invariant operator, which acts on an input vector (i.e., digital signal), producing a transformed vector by means of mathematical convolution. Let the operator be $h=[½, ½]$ acting on an input vector x, with N elements. Then, the nth element of the transformed output vector y is computed from two consecutive elements of x:

$$y(n) = \sum_l h(l)\, x(n{-}l) \tag{13.4}$$

where, $h(l)$ is the lth element in the operator.

This is the so-called moving average, because the output averages the current element $x(n)$ with the previous one as the operator moves forward over x. The moving average smoothes out the bumps in the signal. It is also called lowpass filter because it reduces the high frequency components (i.e., the bumps) keeping only the low frequency components of the signal. Now, let the operator be $g=[½, -½]$ acting on the same input vector x to produce another output vector. This operator computes 'moving differences'. It picks out the bumps or high frequencies in the signal and thus, is called highpass filter. Figure 13.2 illustrates the convolution of the example signal with a lowpass and a highpass filter.

These kinds of filtering operations are well known in geoinformation sciences and for long have been used to smooth images and enhance objects' edges (Burrough & McDonnell, 1998), but they can do a lot more. The lowpass and highpass filters alone lack the desirable property of invertibility because one cannot recover x from y. Together, they separate the input x into complementary frequency bands that can be combined to recover the original signal. This combination is termed filter bank or quadrature mirror filters (QMF) (Esteban & Galand, 1977), which only recently have gained attention from the geoinformation community and turned out to be extremely useful. The advantages are that the subband signals can be efficiently filtered, compressed, enhanced, transmitted, and then reassembled if so desired. Figure 13.3 illustrates a complete two-channel filter bank with analysis (decomposition), sub-band manipulation (e.g., filtering), and synthesis (reconstruction).

Perfect reconstruction (i.e., output=input) is achieved if no manipulation is carried out and if the synthesis bank (h_s and g_s) is the inverse of the analysis bank (h_a and g_a). In this sense, the filter banks might be orthogonal, biorthogonal (h orthogonal to g, h and g independently orthogonal), semiorthogonal (h and g independently orthogonal, but spaces associated with h and g are not individually orthogonal) or even nonorthogonal (Starck et al., 1998).

The novelty about wavelets and the key concept of 'scale' come from a procedure of *recursive* implementation of the filter bank: signals are represented with variable resolutions when we apply the same transform (lowpass and highpass filtering) on the outputs of the analysis bank. If this process iterates, we move to coarser scales as far as desired, depending on the length of the input signal and on the objectives of the analysis. Usually, we consider only the outputs of the lowpass filter for iteration, but other possibilities exist: the complete tree (lowpass and highpass are iterated) and the wavelet packets (lowpass and/or highpass are iterated) as shown in figure 13.4.

13.2.2 Wavelets and multiresolution

In continuous-time, there exist a scaling function $\phi(t)$, also known as the father wavelet, corresponding to the lowpass filter and a wavelet function $w(t)$, also known as the mother wavelet, corresponding to the highpass filter. They both involve the sets of filter coefficients $h(l)$ and $g(l)$ from discrete time. The scaling function is produced by the so-called dilation equation, whereas the wavelet function is produced by the wavelet equation:

$$\phi(t) = 2 \sum_l h(l) \phi(2t-l) \tag{13.5}$$

and

$$w(t) = 2 \sum_l g(l) \phi(2t-l) \tag{13.6}$$

Considering the filter coefficients of our example (½, ½ and ½, -½), we have the dilation equation and the wavelet equation from h and g:

$$\phi(t) = \phi(2t) + \phi(2t - 1) \ \text{ and } \ w(t) = \phi(2t) - \phi(2t - 1) \,.$$

In this case the dilation equation produces the box function and the wavelet equation produces the Haar function (figure 13.5).
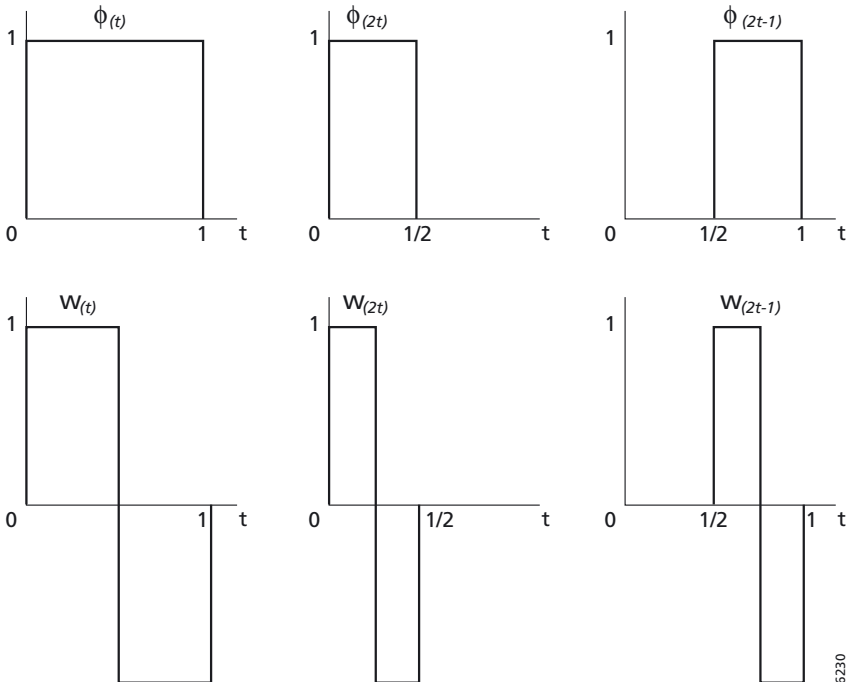

Figure 13.5 – The box function (top) and the Haar wavelets (bottom).

Wavelet stands for 'small wave' (a pulse). In the case of the Haar wavelet (figure 13.5) it is a 'square' wave. It is one of the simplest wavelets and a standard example, which is used to demonstrate the principles in most textbooks because the idea is fundamental to all others. Alfred Haar introduced it (Haar, 1910) almost 70 years before the concept of '*ondelette*' (wavelet) was born in France. Again, the novelty concerns the recursive implementation and not the functions; wavelets might be piecewise constant functions, continuous piecewise linear functions, splines etc.

The simultaneous appearance of t and $2t$ in the dilation and wavelet equations characterises its multiscale nature. Meyer (1989) introduces multiresolution using a metaphor: *'From a subtle and complicated image, one may extract... a schematic version... being a sketchy approximation resembling the pictures one can find in cartoons.'* Then, a set of better and better sketchy approximations of the original image resembles a multiresolution representation.

The goal in multiresolution analysis is the decomposition of the whole space of functions into subspaces V_j. Functions are projected at each step of the analysis onto finer subspaces such that each V_j is contained in the previous subspace V_{j-1}:

$$...\subset V_4 \subset V_3 \subset V_2 \subset V_1 \subset V_0 \subset ...$$

The function $f(t)$ in the whole space has a projection in each subspace. These projections represent the information contained in $f(t)$ in an increasing fashion, such that $f_j(t)$ (i.e., the projection of $f(t)$ in V_j) approaches $f(t)$ for decreasing j. Besides the hierarchic and complete scale of (sub-)spaces other requirements are crucial to the notion of multiresolution. The dilation requirement states that if a function $\phi(t)$ is in V_j, then $\phi(2t)$ is in V_{j-1}. The translation requirement states that if $\phi(t)$ is in V_0, then so are all its translates $\phi(t-k)$. The final requirement states that the function $\phi(t)$ with translates $\phi(t-1)$ must form a stable basis for V_0, i.e. a Riesz basis: a complete set of linearly independent testing functions, say $\phi_i(t)$, that represents in a unique way every function in V_0 as $\Sigma a_i \phi_i(t)$, with $\Sigma |a_i|^2$ being finite. Then, considering dilations by j and translations by k, the basis is generated by $\phi jk(t) = 2^{j/2}\phi(2^j t-k)$ and we have:

$$f_j(t) = \sum_k a_{jk}\, \phi_{jk}(t) \tag{13.7}$$

representing the projection of $f(t)$ in V_j.

The associated error space when moving from V_j to V_{j+1} is the wavelet space W_{j+1}. The wavelet space, which is also generated by dilations and translations of a single function, contains the 'difference in information' $\Delta f_{j+1}(t)=f_j(t)-f_{j+1}(t)$ (i.e., the 'detail' at level $j+1$). Each function in V_j is then the sum of two parts, $f_{j+1}(t)$ in V_{j+1} and $\Delta f_{j+1}(t)$ in W_{j+1}. Considering the subspaces they lie in, we have:

$$V_{j+1} + W_{j+1} = V_j \tag{13.8}$$

Then,

$V_2 + W_2 = V_1$ and $V_1 + W_1 = V_0$

hence,

$V_2 + W_2 + W_1 = V_0$

If $w_{jk}(t) = 2^{j/2}w(2^j t-k)$ is a stable basis for W_j and calling the set of associated coefficients by d_{jk} we have the complete information of $f(t)$:

$$f(t) = \sum_k a_{Jk}\,\phi_{Jk}(t) + \sum_{j=1}^{J}\sum_k d_{jk}w_{jk}(t) \tag{13.9}$$

Then, the coefficients a_{jk}, representing the projection $f_j(t)$ on V_j are obtained with the inner product $\langle f(t), \phi_{jk}(t)\rangle$, whereas the coefficients d_{jk}, representing the projections $\Delta f_j(t)$ on W_j are obtained with the inner product $\langle f(t), w_{jk}(t)\rangle$.

Concluding, wavelets come from the iteration of a filter bank (Daubechies, 1989) and because of the repeated rescaling, they decompose a signal into details at different resolutions. If the signals under consideration are remotely sensed images, the scale parameter corresponds to the size of objects on the Earth surface, which are effectively modelled with this new multiresolution representation revealing patterns that are not so clear in 'subtle and complicated' remotely sensed images.

13.2.3 Algorithms for implementation

Part of the success of the wavelet transform is due to the existence of fast algorithms. They rarely compute inner products with wavelet templates directly. Rather, implementation is normally achieved via simple discrete convolutions, where the filters and filter banks play a major role. Two basic and very popular algorithms will be presented here. Variations of these two as well as other algorithms exist. Some of them will be only cited here and the interested reader should refer to the following references. The previously mentioned 'Wavelet Packet' is described in Coifman et al. (1992). Starck et al. (1999) proposed a fusion of the wavelet transform (WT) and the pyramidal median transform (PMT), called 'PMWT', which combines the advantages of both methods in one algorithm. The 'Laplacian Pyramid' by Burt & Adelson (1983) was one of the first schemes for multiresolution decomposition and afterwards related to the wavelet transform. Bijaoui et al. (1992) proposed a scheme similar to the Laplacian pyramid called 'Half Pyramidal Wavelet Transform' in order to reduce some drawbacks of the former. Finally, the so-called 'Lifting Scheme' (Sweldens, 1996) is probably the most famous and innovative algorithm proposed recently for implementation of the wavelet transform. Because of simplified notation, the following algorithms will be described considering that our input signal is a function of one variable $f(t)$. Extensions to $f(T)$, with $T=(t_1, \dots t_n)$, are straightforward.

The 'algorithme à trous' (Holschneider et al., 1989)
Let $f(t)=a_0$, and l be symmetric around zero, i.e. $l=(\dots, -1, 0, 1, \dots)$.
Then, the projections onto V_j are:

$$a_{j,k} = \sum_l h(l)\,a_{j-1,\,k+2^{j-l}}, \text{ for all } j > 0, k \tag{13.10}$$

whereas, the projections onto W_j are:

$$d_{j,k} = a_{j-1,k} - a_{j-1}, \text{ for all } j > 0, k \qquad (13.11)$$

The reconstruction formula is:

$$a_{0,k} = a_{J,k} + \sum_{j=1}^{J} d_{j,k}, \text{ for all } k \qquad (13.12)$$

The 'algorithm à trous' is stepwise illustrated in figure 13.6.

As an example, let the operator be $h(-1)=\frac{1}{4}$, $h(0)=\frac{1}{2}$, $h(1)=\frac{1}{4}$, then the 0th element of a_1 is:

$$a_{1,0} = \frac{1}{4} a_{0,-1} + \frac{1}{2} a_{0,0} + \frac{1}{4} a_{0,1}.$$

Then, for the next resolution level, the 0th element of a_2 is:

$$a_{2,0} = \frac{1}{4} a_{0,-2} + \frac{1}{2} a_{1,0} + \frac{1}{4} a_{1,2}.$$

The 0th elements of d_1 and d_2 are:

$$d_{1,0} = a_{0,0} - a_{1,0} \text{ and } d_{2,0} = a_{1,0} - a_{2,0}.$$

With reconstruction:

$$a_{0,0} = a_{2,0} + d_{2,0} + d_{1,0}.$$

Remarks:
- The operator forgets all signal samples but every $k+2^{j-1}l$. This is achieved by inserting zeros between samples of the operator when moving from j to $j+1$. That is the reason why the algorithm bears its name, '*à trous*' means 'with holes'.
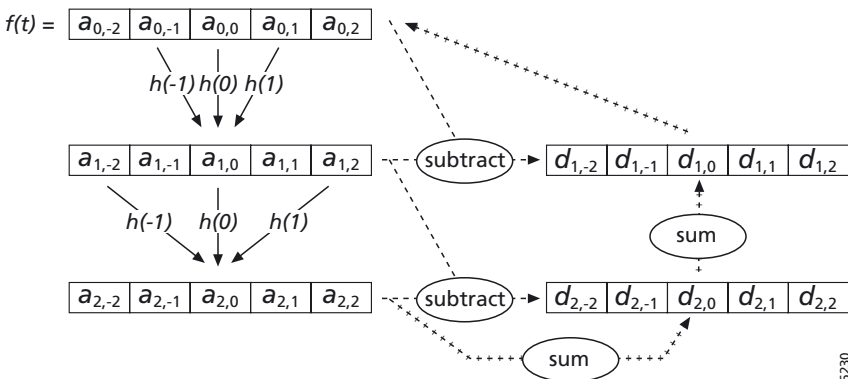
Figure 13.6 – Schematic representation of the 'à trous' algorithm with decomposition and reconstruction paths.
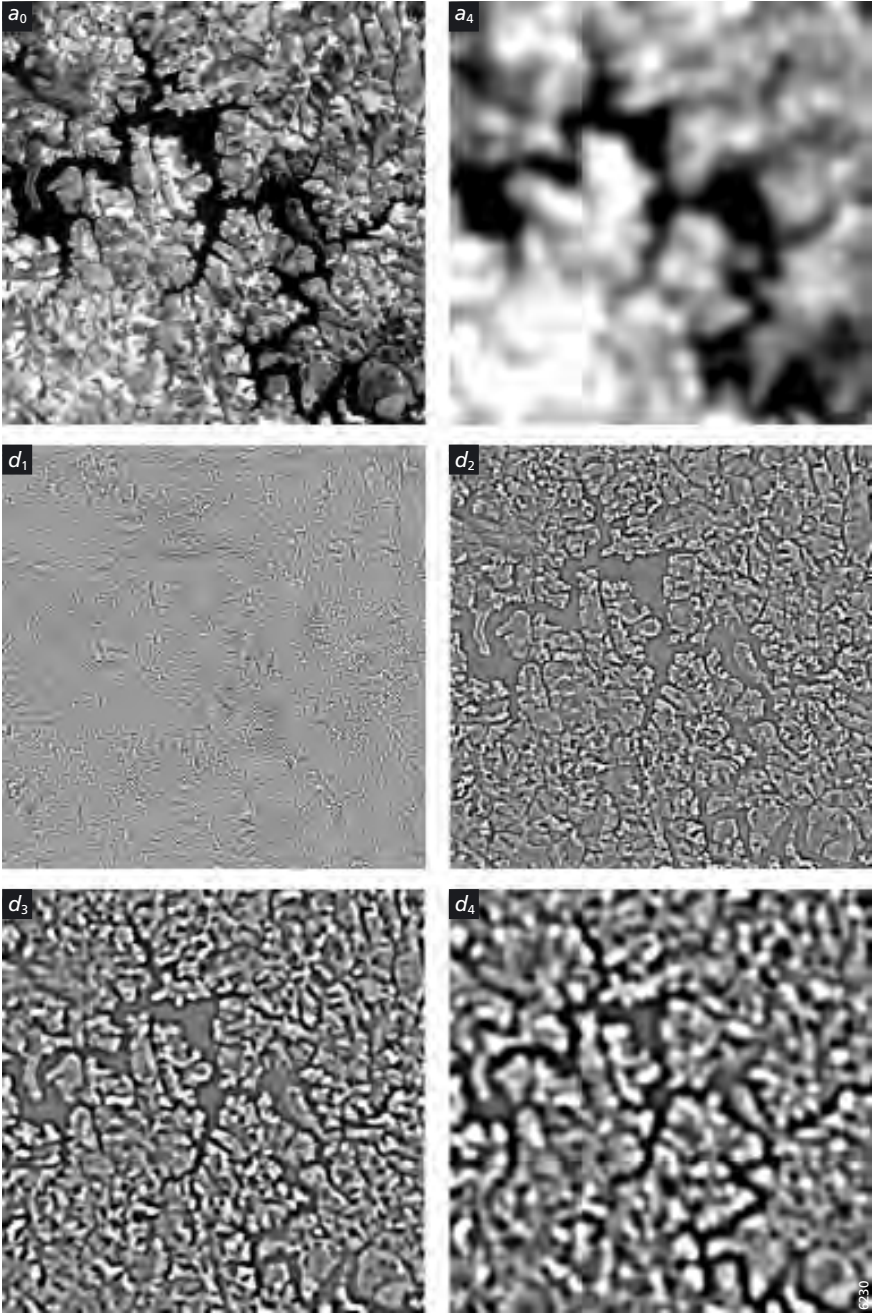
Figure 13.7 – Example of a 2D decomposition using the 'à trous' algorithm.

- 2D signals (e.g., figure 13.7) require 2D operators: $(¼ \ ½ \ ¼) = \begin{pmatrix} ¼ \\ ½ \\ ¼ \end{pmatrix} = \begin{pmatrix} 1/16 & ⅛ & 1/16 \\ ⅛ & ¼ & ⅛ \\ 1/16 & ⅛ & 1/16 \end{pmatrix}$

- Values at the boundaries of the signal are normally obtained by reflection, periodicity or continuity.
- Operators must have an odd number of elements.

Stéphane Mallat's algorithm (Mallat, 1989)
The projections onto V_j are given by:

$$a_{j,k} = \sum_l h \ (l - 2k) \ a_{j-1,l}, \text{ for all } j > 0, k. \tag{13.13}$$

whereas, the projections onto W_j are given by:

$$d_{j,k} = \sum_l [g \ (l - k) \ d_{j-1,l}, \text{ for all } j > 0, k. \tag{13.14}$$

The reconstruction formula is:

$$a_{j,k} = \sum_l [h \ (k - 2l) \ d_{j+1,l} + g(k - 2l)] \ d_{j-1,l}, \text{ for all } j, k. \tag{13.15}$$

Figure 13.8 provides a flow diagram showing stepwise the Mallat's algorithm with decomposition and reconstruction steps.

As an example, let the operators be $h = (½, ½)$ and $g = (½, -½)$, then the 0th element of a_1 and d_1 are:

$$a_{1,0} = ½ \ a_{0,0} + ½ \ a_{0,1} \text{ and } d_{1,0} = ½ \ a_{0,0} - ½ \ a_{0,1}.$$

Then, after undersampling a_1 and d_1, the 0th element of a_2 and d_2 are:

$$a_{2,0} = ½ \ a_{1,0} + ½ \ a_{1,1} \text{ and } d_{2,0} = ½ \ a_{1,0} - ½ \ a_{1,1}.$$

With reconstruction (after upsampling):

$$a_{0,0} = ½ \ a_{1,0} + ½ \ d_{1,0}.$$

Remarks:
- Mallat's algorithm requires the length of the input signal to be power of 2.
- Extension to 2D signals is implemented by applying the same 1D scheme first to the rows and then to the columns of the 2D signal. In this way, Mallat's algorithm might generate three sets of detail coefficients at each scale j, depicting high frequencies according to their orientation in the raster, i.e. vertical, diagonal and horizontal (figure 13.9).
- Values at the boundaries are also obtained by reflection, periodicity or continuity.

13.2.4   Other multiresolution decompositions
Starck et al. (1998) developed a robust multiresolution decomposition based on the median transform. The median transform is non-linear, and offers advantages for dealing with outliers
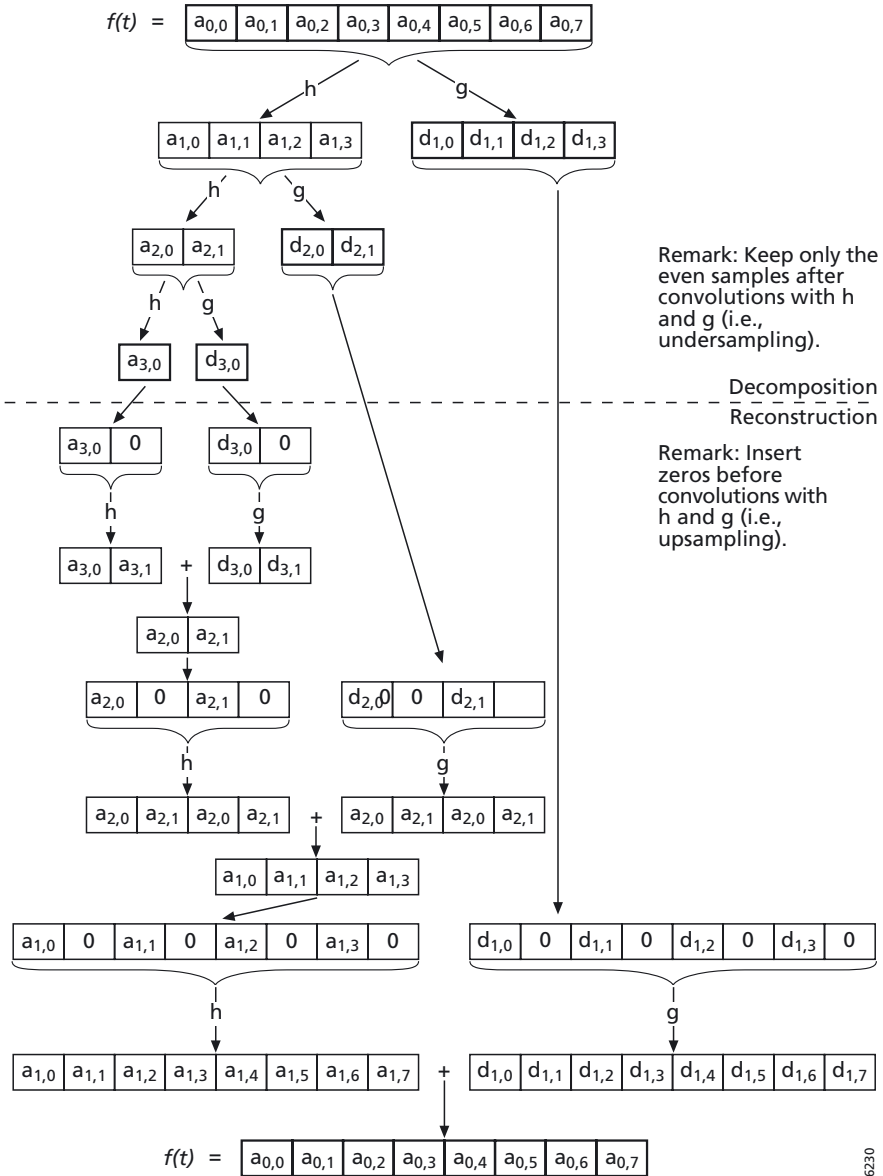
Figure 13.8 – Schematic representation of Mallat's algorithm with decomposition and reconstruction stages.

in the data. Basically, the result from a convolution with a median filter is subtracted from the original signal and followed by iteration, which leads to multiresolution representations. Similarly, multiresolution decomposition based on mathematical morphology (Serra, 1984) can be realised by taking the difference between the original image and its opening. In both
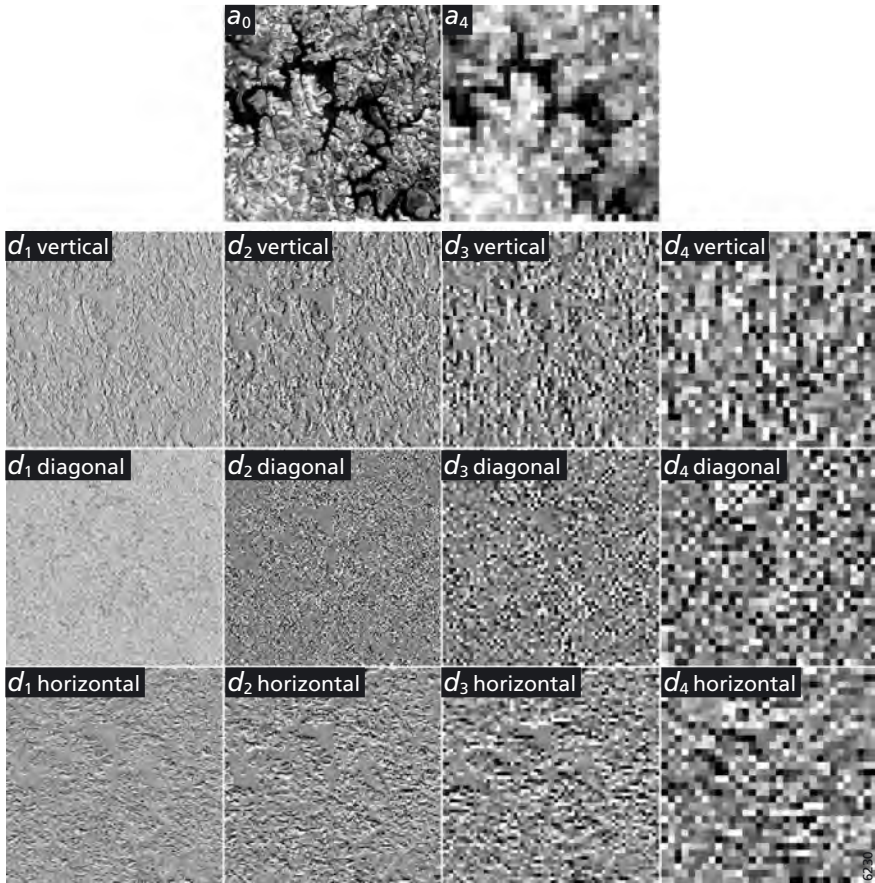
Figure 13.9 – Example of a 2D decomposition using Mallat's directional analysis.

alternative transforms, undersampling can be introduced (Starck et al., 1998), which leads to pyramidal structures like in Mallat's algorithm.

13.3 Recent applications in Remote Sensing image processing

The interest in wavelet transforms has grown rapidly in the remote sensing community. Other areas of application in image processing are being explored. The principles discussed so far also apply to the temporal and spectral domains of remotely sensed data to aid tasks such as hyperspectral data analysis, time series processing, image segmentation, image compression, detection of linear features etc. Next, we refer to recent studies tackling some of these issues. Wavelets have been used to model remotely sensed spectra for noise reduction as well as for detection and extraction of characteristic features from the spectral signatures. Bruce & Li (2001a) and Shimidt & Skidmore (2003) showed how wavelet transforms can be used to smooth spectra before further analysis. Their approach provides an effective way of selecting

appropriate width for the smoothing filters. Bruce & Li (2001) have also pointed out the significant gain in computation time achieved by the method. In another study (Koger et al., 2003), the authors demonstrated that features extracted from wavelet transforms were superior to the original spectral bands and to features extracted with principle component analysis for discriminating between weed-free soybean crops and soybean intermixed with pitted morningglory. Automated detection of hyperspectral targets was also tackled by Bruce et al. (2001) and Bruce et al. (2002a). The approach turned out to be a powerful tool for the detection of constituent's absorption bands within hyperspectral signatures. Kaewpijit et al. (2003) and Bruce et al. (2002b) applied wavelet transforms for dimensionality reduction of hyperspectral data. The former study compared the wavelet-based approach to the standard principle component analysis and showed that wavelets provided better or comparable results, but with superior computational efficiency.

Extraction of linear features like objects edges from remotely sensed images can be performed with wavelet transforms. In fact, edge detection was one of the first applications of wavelet transforms in image processing (Mallat & Zhong, 1992). The first scales of decomposition and the respective modulus maxima curves provide an efficient framework for the detection of linear features such as agricultural field boundaries, streets and roads (Ji, 1996; Dong et al., 1997; Couloigner & Ranchin, 2000). Due to the wavelet transform sparse representation (i.e., most coefficients are zero), another obvious application is data compression. Lossless as well as lossy compression can be considered. Work on remote sensing image compression has been carried out by Marçal et al. (2000), Dragotti et al. (2000), Kiema (2000), and Kiema & Bähr (2001).

Noise modelling techniques based on multiresolution wavelet transforms have been used mostly for radar image processing. Speckle suppression, feature detection, feature extraction, and texture classification are some of the studied applications (Yamaguchi et al., 1995; Aiazzi et al., 1998; Simard et al., 1998; Horgan, 1998; Fukuda & Hirosawa, 1999; Liu et al., 2000; Belhadj & Jebara, 2002; Nyoungui et al., 2002; Wu & Liu, 2003).
Digital elevation model (DEM) processing is another potential area of application for wavelet transforms. Dactu et al. (1997) compared the performance of roughness estimators and concluded that the wavelet-base estimator outperformed estimators based on the computation of the power spectrum of an image. McArthur et al. (2000) used wavelet transforms to produce a series of approximations of a DEM to constitute a hierarchical terrain database and generate triangulation models that retain the dominant terrain features at each scale level. InSAR DEM reconstruction was considered in the study of Ferretti et al. (1999), where as DEM simplification was studied by Zhu et al. (2002).

Finally, wavelets can be used to model temporal profiles as suggested by Carvalho (2001). The wavelet-based approach was considered to be promising as a preprocessing step for effective time series analysis. It can be used to remove outliers like clouds, shadows and misregistrations (Carvalho, 2003), as well as to reduce radiometric discrepancies among images in the series, resulting in biophysically sound temporal profiles. In the reminder of this chapter, we describe three case studies on the application of wavelet transforms in remote sensing that were not mentioned above, but represent promising approaches. Section 4 presents how wavelet-based feature extraction can aid the automation of image registration,

which is normally an important and time consuming pre-processing step. Next, we show in section 5 that the inherent multiresolution nature of wavelet transforms improves the fusion of images with different pixel sizes. Finally, section 6 presents the extraction of features from difference images to facilitate change detection over large geographic areas.

13.4   Case study I – feature extraction for image registration

13.4.1   Introduction

Agencies from all over the world have launched or are preparing for launching many earth observation systems of high resolution, multi-bands and multi-sensors including SPOT-5, Landsat-7, ENVISAT-1, TRMM (Tropical Rainfall Measuring Mission), EOS-AM (Earth Observing System) and CBERS (China-Brazil Earth Resources Satellite). The analysis of multi-temporal/multi-sensor remote sensing datasets acquired by these systems can be efficiently done if the data refer to the same geometry. The processing of images such that their corresponding pixels have the same geometry comprises image registration or geocoding processes. Geometrical correction and registration of high spatial resolution images must be done with more precision, whereas the increased data volume being collected demands automatic or quasi-automatic registration systems. The development of such accurate quasi-automatic systems is an important and wide field of research because the existing and upcoming data sets can vary a lot in content, radiometry and geometry.

Let us call the image to be registered the *warp* image and the image to which the *warp* image will be macthed the *reference* image. The general approach to image registration consists of the following four steps:

1   Feature identification: identifies a set of relevant features in the two images, such as edges, intersections of lines, region contours, regions, etc.
2   Feature matching: establishes correspondence between the identified features. Each feature in the *warp image* must be matched to its corresponding feature in the *reference image*. Each feature is identified with a pixel location in the image, and these corresponding points are usually referred to as *control points*.
3   Spatial transformation: determines the *mapping functions* that can match the rest of the points in the image using information about the *control points* obtained in the previous step.
4   Interpolation: resamples the sensed image using the mapping functions to bring it into alignment with the *reference image*.

In general, the registration methods are different from each other in the sense that they can combine different techniques for feature identification, feature matching and mapping functions. The most difficult step in image registration is obtaining the correspondence between the two sets of features. This task is crucial to the accuracy of image registration and much effort has been spent in the development of efficient feature matching techniques. Given the matches, the task of computing the mapping functions does not involve much difficulty and the interpolation process is quite standard.

Generally, there are two methods that can be used to register images: area based and feature based matching. Area based methods can be applied to spectrally similar images whilst

feature based matching can be used to register any pair of images. Although feature based methods are more adequate for registering multi-sensor images they fail in case of registering multi-temporal images that present reasonable changes over the time. In these cases there are not enough corresponding features in both images. The area-based method is very robust in many situations. However, if the orientation difference between the images is large the correspondences between feature points cannot be correctly found. De Castro & Morandi (1987), Zheng & Chellapa (1993) and Hsieh et al., (1997) have proposed methods to overcome this problem.

Taking into account the large amount of data, two requirements are important in the image registration methods: speed of such methods and their ability to handle multi-sensor/multi-temporal images. The multi-resolution approach presents some characteristics that facilitate these tasks. Taking advantage of the multi-resolution strategy various image registration techniques have been proposed in the literature (Bajscy & Kovacic, 1989; Zheng & Chellapa, 1993; Djamdji et al., 1993; Le Moigne, 1994; Corvi & Nicchiotti, 1995; Li & Zhou, 1996; Hsieh et al., 1997; Fonseca & Costa, 1997; Deubler & Olivo, 1997; Le Moigne, 2002). In order to illustrate how the multiresolution analysis can be applied to the problem of image registration, the next session presents a registration method based on multiresolution decomposition proposed by Fonseca (Fonseca, 1999; Fonseca & Costa, 1997; Fonseca et al., 1998).

13.4.2 Image registration based on multiresolution decomposition

The registration method presented here uses the wavelet transform to extract feature points in the images and to estimate the parameters of the transformation in an iterative way over the different scale levels in the transform domain. The algorithm is performed at progressively higher resolution, which allows for faster implementation and higher registration precision. The steps of the registration method are illustrated in figure 13.10.

Initially, the images can be processed to reduce noise, resample, generate new bands, enhance histogram etc. Subsequently, the discrete multiresolution wavelet transforms (in J scale levels) of the two images are computed. The next phase aims to identify features that are present in both images in each level of the decomposition. For this process one uses the modulus maxima of the wavelet transform to detect sharp variation points, which tend to correspond to edge points in the images.

Four steps are involved in the feature point selection process carried out at each level of decomposition:
1 Edge points extraction using the modulus maxima of the wavelet transform;
2 Selection of strong edge points;
3 Selection of edge points localized in high contrast regions;
4 Suppression of non-maxima local edge points.

The feature point extraction algorithm is applied to a Landsat-TM image taken from an urban area of Brasilia (Brazil). Figure 13.11 shows the feature points (denoted with '+' marks) superimposed on the bands of the decomposition for two scale levels. Given the feature points, the next step is to find their correspondences between the images. A correlation-

based criterion is used in the matching process. The use of the correlation coefficient as a similarity measure is motivated by results that show its good performance compared with others measures (Barnea & Silverman, 1972; Brunelli & Messelodi, 1995; Khosravi & Schafer, 1996). The initial matching is performed on the lowest resolution images and is determined by the best pairwise fitting between the feature points in the two images. At this point, some false matches inevitably occur. This first part of the matching process is a crucial phase of the registration process. If the initial registration parameters are invalid the search for a registration transformation goes off in a wrong direction, and the correct trend may not be

```
Input images
    |
    v
+-----------+              +---------------+
| Filtering |     +------->| J-1 iterations|<------+
+-----------+     |        +---------------+       |
    |             |              |                 |
    v             |              v                 |
+-----------+     |      +-----------------+       |
| Wavelet   |     |      | Strong Edges    |       |
|Decompositi|     |      | Detection       |       |
+-----------+     |      +-----------------+       |
    |             |              |                 |
    v             |              v                 |
+-----------+     |      +-----------------+       |
| Strong    |     |      | Feature         |       |
| Edges     |     |      | Matching        |       |
| Detection |     |      +-----------------+       |
+-----------+     |              |                 |
    |             |              v                 |
    v             |      +-----------------+       |
| Feature   |     |      | Parameters      |-------+
| Matching  |     |      | Refinement      |
+-----------+     |      +-----------------+
    |             |              |
    v             |              v
| Consistency|    |      +-----------------+
| Checking   |    |      | Transformation  |
+-----------+     |      +-----------------+
    |             |              |
    v             |              v
| Initial    |----+      +-----------------+
|Transformati|           | Interpolation   | 6230
+-----------+            +-----------------+
                                |
                                v
                         Registered images
```
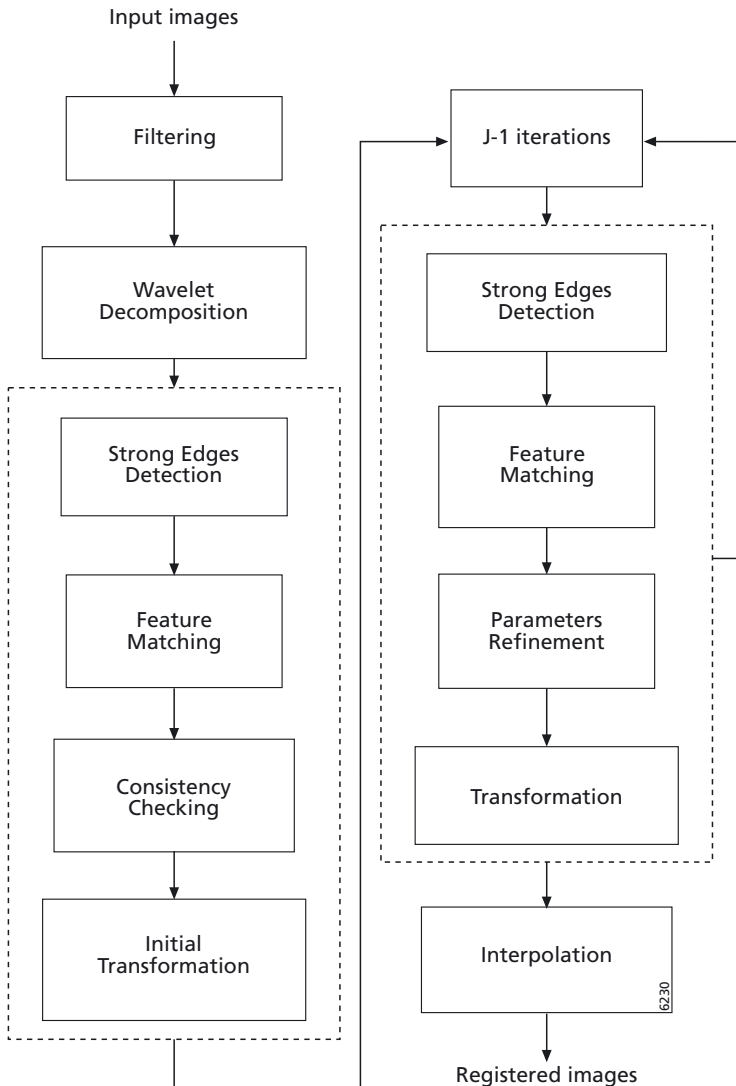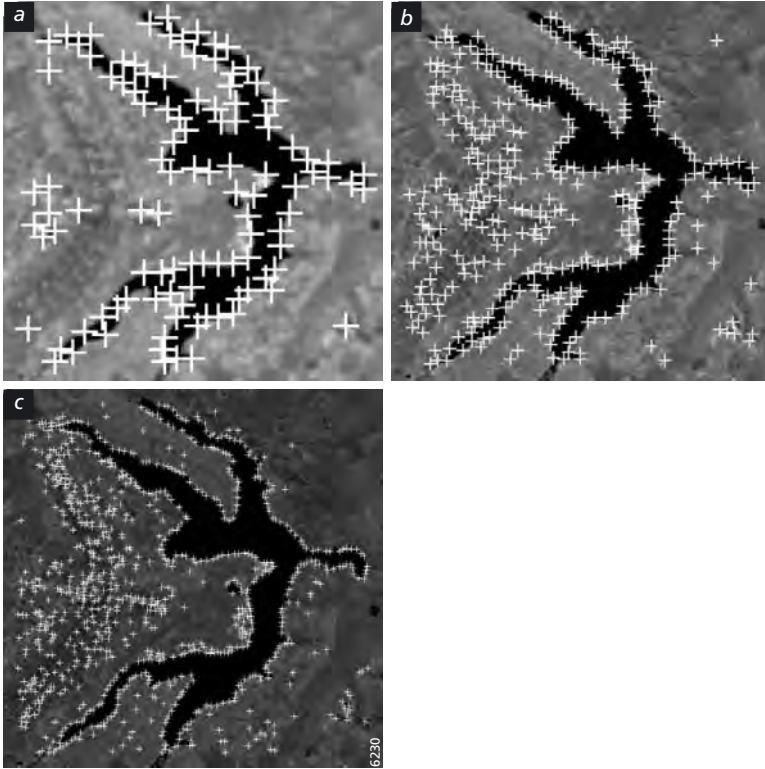
Figure 13.10 – Block diagram of registration algorithm.

Figure 13.11 – Feature points superimposed on the bands of the decomposition for two scale levels (J=2): (a) scale 2²; (b) scale 2¹ and (c) scale 2⁰.

recovered in later steps. Therefore, a consistency-checking procedure is performed in order to eliminate incorrect matches and improve initial transformation precision.

The above procedure provides a set of reliable matches, which are used to determine a warping function that gives the best registration (with respect to minimum root mean square registration error) to the precision available at level J of the wavelet transform. A 2D affine transformation is used to model the deformation between the images. In most remote sensing applications the images are preprocessed for geometrical correction that justifies the use of this class of transformation.

The point matching and image warping steps can be performed at progressively higher resolutions in a similar fashion. Finally, we obtain the registration transformation that should be used to correct the warp image. Basically, the algorithm needs one parameter that controls the number of control points.

13.4.3 Results and discussion

In order to demonstrate its feasibility the algorithm was used to register images acquired by different types of systems such as SPOT, Landsat, and JERS-1. Table 13.1 provides

information about the images used in the various experiments. Wavelet decompositions were carried out up to the second scale level, except for experiments T9, T10 and T11, where the images were decomposed up to six scale levels. The images presented good internal geometry and were warped using bilinear interpolation. Experiments T1, T2 and T3 used three pairs of Landsat-TM images of the Amazon region, cropped from the scenes used in the Amazon deforestation assessment (Batista et al., 1994). Usually, image registration in this case is a difficulty task due to the characteristic texture information of forested areas, as well as to the land use differences caused by deforestation activities in the region. Figure 13.12 shows the registration of Landsat TM images acquired in different dates over the Amazon region (experiment T1). TM945F was taken as the reference image and TM925F as the warp one. Figures 13.12(c) and (d) show the initial control points (denoted with '+' marks) superimposed on images in the lowest level of decomposition.

Images of agricultural regions were also tested (experiments T4, T5 and T6). Although these regions contain well-defined objects (fields), marked seasonal changes make difficult the localization of control points. Figure 13.13 shows the registration of Landsat TM images acquired in different dates (experiment T5). They correspond to an agricultural region near
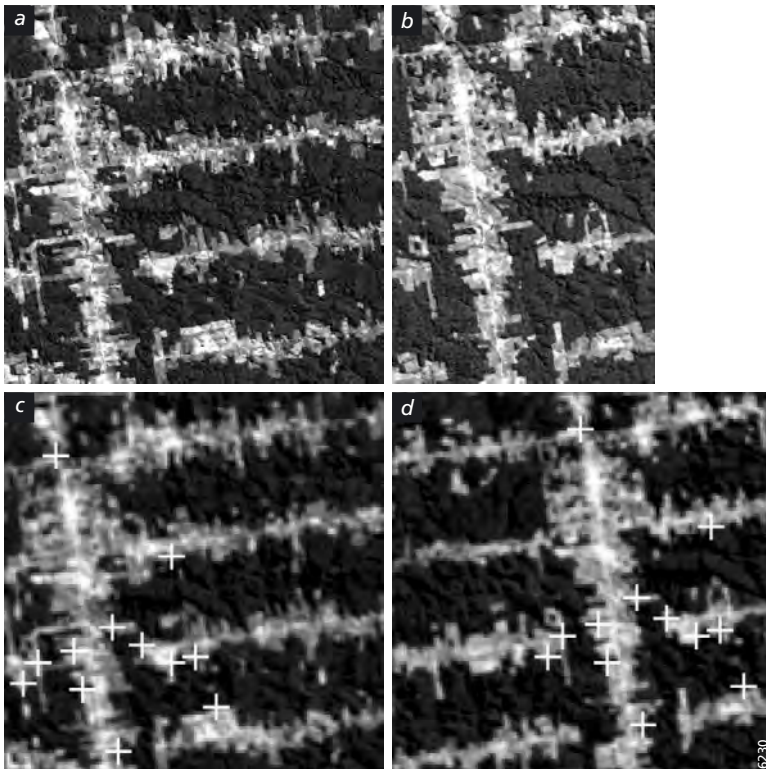

Figure 13.12 – Registering Amazon region: (a) reference image (TM945AM); (b) registered image (TM925AM); (c) and (d) show the initial control points superimposed on reference and warp images in the lowest level of resolution.

Table 13.1 – Information of the images used in the experimental results.

Experiment	Images	Region	Satellite	Band	Size (pixels)	Date	Application
T1	TM925F TM945F	Amazon	Landsat-TM5	5	512 by 512	06/07/92 07/15/94	forest
T2	TM975F TM955F	Amazon	Landsat-TM5	5	512 by 512	07/07/97 08/03/95	forest
T3	TM965F TM945F	Amazon	Landsat-TM5	5	512 by 512	07/20/96 07/15/94	forest
T4	TM905A TM945A	Itapeva	Landsat-TM5	5	512 by 512	09/09/90 07/18/94	agriculture
T5	TM905A TM945RA	Itapeva	Landsat-TM5	5	512 by 512	09/09/90 07/18/94	agriculture (georef.)
T6	TM945AG TM925AG	Agudos	Landsat-TM5	5	512 by 512	07/09/94 09/21/92	agriculture
T7	SP953SP TM944SP	São Paulo	SPOT Landsat-TM5	3 4	512 by 512	08/08/95 06/07/94	urban
T8	SP953DF TM944DF	Brasília	SPOT Landsat-TM5	3 4	512 by 512	08/08/95 06/07/94	urban
T9	JERS93 JERS96	Amazon	JERS-1	X	4000 by 5920	06/26/93 08/08/96	forest
T10	JERS93 JERS95	Amazon	JERS-1	X	4000 by 5920	06/26/93 10/10/95	forest
T11	JERS95B JERS96B	Amazon	JERS-1	X	4000 by 5920	10/10/95 08/13/96	forest

Itapeva, São Paulo, Brazil. TM945RA was taken as the reference image and TM905A as the warp one. Figures 13.13(c) and (d) show the initial control points superimposed on images in the lowest level of the decomposition.

Images of urban areas taken from SPOT (band 3) and TM (band 4) sensors, in different dates, were used in experiments T7 and T8. Figure 13.14 shows the registration of two images from an urban area in São Paulo, Brazil (experiment T7). The SPOT image (SP953SP) was reduced to a 30 m pixel size and taken as the warp image. TM944SP was taken as the reference image. Figures 13.14(c) and (d) show the initial control points superimposed on images in the lowest level of the decomposition.

The algorithm was also tested on JERS-1 images taken in different dates. JERS93 was taken as the reference image and JERS95 as the warp one (experiment T10). Before registration, these sub-images were filtered (gamma filter with 10 iterations) to reduce speckle noise (Oliver & Quegan, 1998). Figures 13.15 (a) and (b) show the reference and registered images. Figures 13.15 (c) and (d) show the initial control points superimposed on images in the lowest level of the decomposition.

Control points were manually acquired to measure registration accuracy. In some cases, such in radar images, this task was very difficult because there were just a few good features. Table 13.2 shows the number of control points (# CPs), registration error (RMSE) and computation time (in seconds) obtained for each pair of test images. The images were processed in a Sun-Ultra 30, 300 MHz. One can observe that the registration error is less than one pixel for all
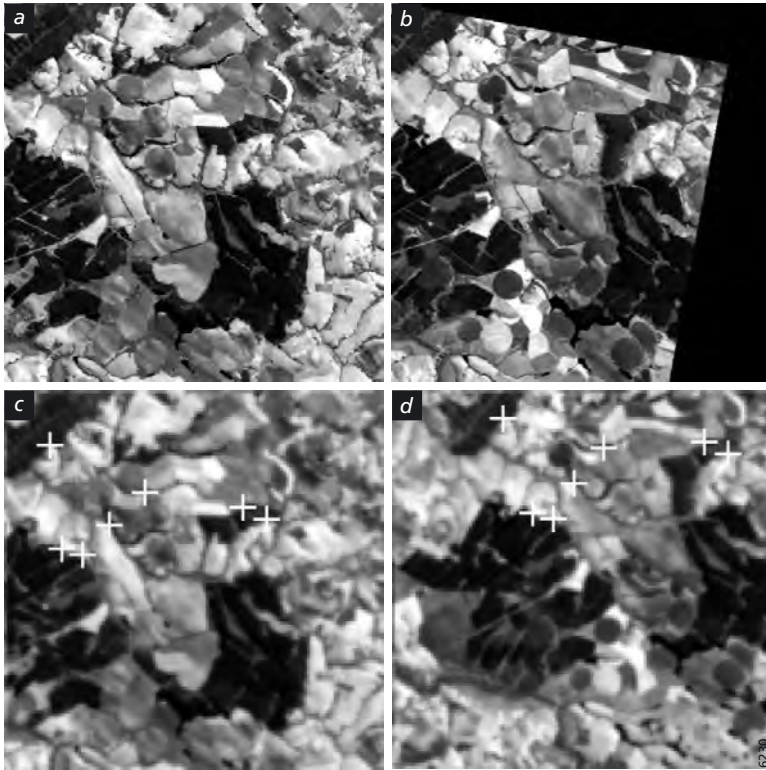
Figure 13.13 – Registering agriculture images: (a) reference image (TM945RI); (b) registered image (TM905I); (c) and (d) show the initial control points superimposed on reference and warp images in the lowest level of resolution.

Table 13.2 – Number of control points (# CPs), registration error (RMSE) and computation time obtained for each pair of test images.

Test	#CPs	RMSE (Pixel)	Time (s)
T1	169	0.787	29
T2	485	0.655	31
T3	326	0.828	29
T4	184	0.989	27
T5	287	0.828	42
T6	294	0.344	28
T7	267	0.434	29
T8	110	0.915	29
T9	153	1.101	30
T10	79	0.669	26
T11	587	0.866	10800

cases except for experiment T9. Broadly speaking, the processing has taken less than 1 minute for a 512 by 512 pixel image. The algorithm is reasonably efficient in terms of computational complexity. However, the processing time depends on the images to be registered. Besides, the algorithm has obtained a large number of control pixels that allows registering images with good precision.

13.4.4 Conclusions

The multiresolution approach has been successfully applied to two steps of the image registration process: features extraction and matching strategy that involves the transformation parameters calculation. The registration algorithm presented here is very simple and easy to apply since it needs basically one parameter. A significant amount of computation is saved in comparison to traditional pixel-by-pixel searching methods because the matching is carried out only on the selected feature points and in a coarse-to-fine manner. Due to the fact that the registration procedure uses the grey level information content of the images in the matching process, it is more adequate to register images of the same sensor or with similar spectral bands. Nevertheless, it has demonstrated technical feasibility for many images of forest, urban and agricultural areas from Landsat-TM and SPOT sensors taken in
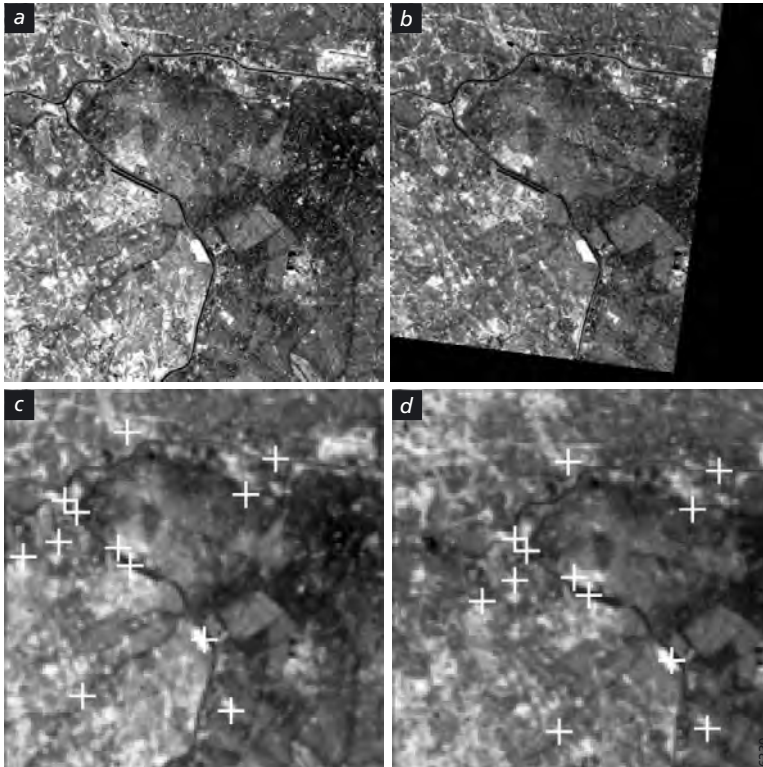

Figure 13.14 – Urban region: (a) reference image (TM944SP); (b) warp image (SP953SP) registered; (c) and (d) show the initial control points superimposed on reference and warp images in the lowest level of resolution.

different times. The registration technique described here has been implemented in a system for automatic registration and mosaic of remote sensing images under development at the Division of Image Processing (National Institute for Space Research, Brazil) and the Vision Lab (Electrical & Engineering Computer Department, UCSB). Information about this system is found in Fedorov et al. (2002) and on the internet (http://www.regima.dpi.inpe.br).

13.5 Case study II – feature extraction for data fusion

13.5.1 Introduction

With the development of remote sensing technology an increasing number of different sensors, imaging at a variety of ground scales and spectral bands, have become available. Each of these images has its own characteristics with different levels of spatial or spectral detail. High spatial resolution images are required for an accurate description of shapes, features and structures whereas different objects and land surfaces are better identified if high spectral resolution images are available. Hence, one important aspect considered in data fusion techniques is to combine the high spatial and the high spectral resolutions in
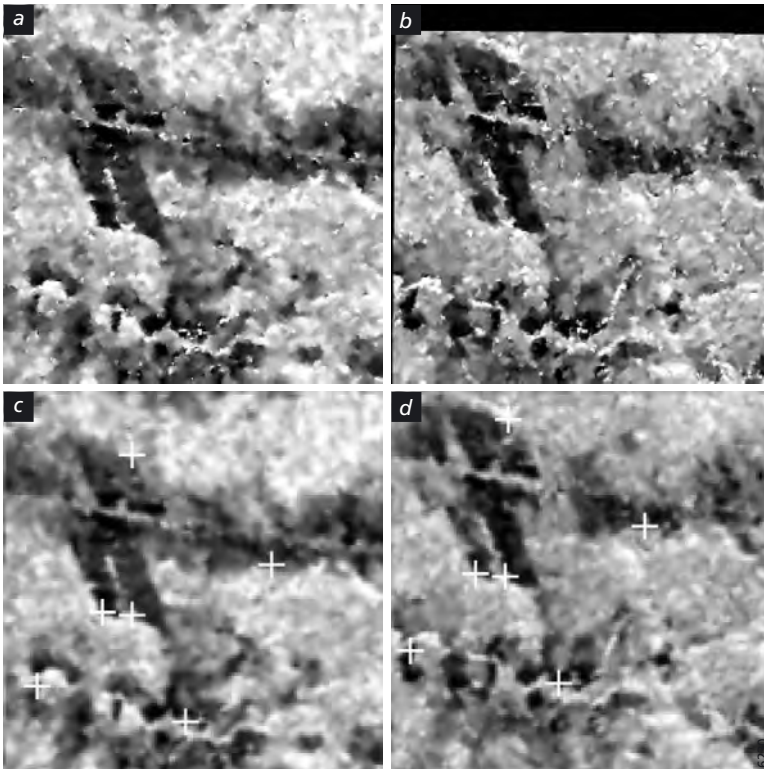

Figure 13.15 – Registering radar images: (a) reference image (JERS93); (b) warp image (JERS96) registered; (c) and (d) show the initial control points superimposed on reference and warp images in the lowest level of resolution.

order to produce synthesised images, which retain the spectral values while improving the spatial characteristics of the original multispectral image. These synthesised images should be as close as possible to reality and should simulate what a sensor having the same spectral bands but the highest spatial resolution would observe. There are several methods that allow the improvement of the spatial resolution of images however most of them do not respect the spectral content of the original multispectral images. The problem with those methods is that very often they introduce strong distortions on the pixel spectra. As classification processes are often based on spectral characteristics (spectral signatures) of objects, any error in the synthesis of the spectral signatures at the highest spatial resolution induces an error in the decision rule and the results of the classifiers are strongly compromised.

Several synthesis methods by fusion have been published or are available in commercial software packages (Ranchin et al., 2003). The most common are those based on colour transformations and on statistical and numerical approaches. The former group comprises colour compositions in Red, Green and Blue (RGB) and Intensity, Hue and Saturation (IHS) space whilst the latter deals with techniques such as Principal Component Analysis (PCA), Gram-Schmidt transform, band combinations using arithmetic operators and others (Pohl, 1998; Research Systems Inc., 2003). IHS method consists of converting the colour space RGB in the IHS space nearest to human perception. In this new space, the intensity is replaced by the high resolution band, before carrying out the inverse transformation of the IHS space to the RGB space. The PCA method transforms a multivariate data set of intercorrelated variables into a set of new un-correlated linear combinations of the original variables. It consists of the computation of the correlation matrix or covariance matrix, eigenvalues and eigenvectors and the principal components themselves.

The HPF (high pass filter) method, proposed by Chavez et al. (1991) is a technique based on injecting high frequency components into resampled versions of the multispectral data. It consists of an addition of spatial details, taken from a high-resolution image, into a bicubically-resampled version of the low-resolution image. Studies conducted by Chavez et al. (1991), Wald et al. (1997) and Terrettaz (1998) have demonstrated the superior performance of HPF results in preserving the spectral features of the enhanced bands. The main drawback of the HPF method is that the filter has a fixed kernel size and resolution; it is difficult or even impossible to find one optimal filter for various ground cover types of different sizes (Zhou et al., 1998).

Recently, several authors have used the multiresolution analysis and wavelet transforms to introduce the spatial information into the spectral bands (Guarguet-Duport, 1996; Yocky, 1996; Alparone et al., 1998; Ranchin & Wald, 1998; Zhou et al., 1998; Ventura et al., 2002; Aiazzi et al., 2002; Teggi et al., 2003; Shi et al., 2003 and Ranchin et al., 2003). All these studies are unanimous in suggesting that fusion techniques based on multiresolution decomposition of images (using wavelets transforms) preserve the spectral content better than classical techniques and thus the possibility for automatic classification of the resulting images is not compromised.

13.5.2 Multiscale analysis for image fusion

Image fusion methods are usually a trade-off between the spectral information from high spectral – low spatial resolution images and the spatial content from high spatial – low spectral resolution images. Ranchin et al. (1994, 1996) and Ranchin & Wald (1996, 1998) introduced and applied the ARSIS concept (from its French acronym *'Amelioration de la Resolution Spatial par Injection de Structures'*, which means 'spatial resolution enhancement by injection of structures') to combine from SPOT multispectral (20 m spatial resolution) and SPOT panchromatic (10 m) images to SPOT multispectral and images from the Russian panchromatic sensor KVR-1000 (2 m). The results ensured the effectiveness of the ARSIS method in preserving the spectral content of the original images when improving their spatial resolution. Ranchin et al., (2003) applied the ARSIS concept through two different multiscale models – the generalised Laplacian pyramid and the *'à trous'* wavelet algorithms – in order to combine multiscale (4 m) and panchromatic (1 m) IKONOS images. Zhou et al., (1998) applied a pyramidal wavelet transform algorithm to merge a Landsat TM and a SPOT panchromatic images of an urban area in San Diego, California. The results were compared with three other standard fusion approaches – IHS, PCA and Brovery – and simultaneous best spectral and spatial quality were only achieved with wavelet transform methods. Ventura et al., (2002) also found that wavelet methods outperform when compared with the IHS method on merged multispectral and panchromatic Landsat ETM+ images of an urban area around the city of Brasilia, Brazil.

The multiscale transform algorithm used in this study was the pyramidal linear wavelet transform, which means that the computation of the approximation was done applying a one level pyramidal wavelet transform using linear spline functions as scaling functions. First, the multispectral images (MS) were geometrically registered onto the panchromatic image (P). Then the P image was decomposed into a wavelet representation at the same resolution of the MS images. Next, the MS images, band by band, were combined with the components of the multiscale representation of the P image. As a result, the approximation images of the merged wavelet representation were the MS images whereas the detail were those images derived from the P image. Then the inverse wavelet transform was performed to obtain the final merged image, which has multispectral bands like the original MS image but with an improved spatial resolution from the P image. In order to assess the performance of multiscale analysis, its results were visually compared with four traditional methods for remotely sensed image fusion: IHS, Brovery, Principal Components and Gram-Schmidt.

13.5.3 Test site and data

The site chosen to perform the multiscale approach for image fusion was a recently formed reservoir located at the outskirts of the city of Lavras, Brazil. The multiscale fusion technique was applied in an attempt to improve the spatial resolution of the original MS image in order to allow a better characterization of the protection zone along the edges of the lake. The images used were a subset of the 218/75 scene with three reflective bands 4, 5, 3 (RGB; 30 m) and the 15 m resolution panchromatic band of the Landsat 7 ETM+ (figure 13.15). The images were acquired on February 2003.

13.5.4   Results and discussion

The output images of the five different fusion methods applied in this study are presented in figure 13.16. Pyramidal Wavelet Transform (WT), IHS Transform, Brovey Transform, Principal Components Transform and Gram-Schmidt Transform were visually assessed according the spectral and spatial quality of the synthesised images. Good quality stands for the image that better preserve both the spectral information from the multispectral images and the spatial information from the panchromatic image. The preservation of spectral characteristics is important for calibration purposes and for ensuring that targets that are spectrally separable in the original data are still separable in the fused data set (Chavez et al., 1991).

Visual inspection of the synthesised images showed that images fused using the Brovey transform preserved the least of the spectral information of the multispectral image. Distortions of pixel values were very clear in agricultural and natural vegetated areas. As the spatial resolution was improved it might be concluded that with the Brovey method more emphasis is placed on the spatial information from the panchromatic image than on the spectral content from the multispectral image. Zhou et al., (1998) found similar results for fusion of SPOT PAN and multispectral Landsat TM images. The IHS method presented less distortion of spectral values than the Brovey method. However, modification of spectral values was also visible on the IHS transform fused image, especially for water and bare soils but also for vegetation. The explanation for such distortion of spectral values is that the IHS method is based on the assumption that a close correlation between the panchromatic image (0.520-0.900 µm) and the intensity component exists. This assumption is well satisfied for ETM+ bands 3 (0.630-0.690 µm) and 4 (0.750-0.900 µm) but it is not the case for band 5 (1.55-1.75 µm).

The pyramidal wavelet transform algorithm produced a better preservation of the spectral content and also a better spatial resolution than the classical IHS, the Brovey method,
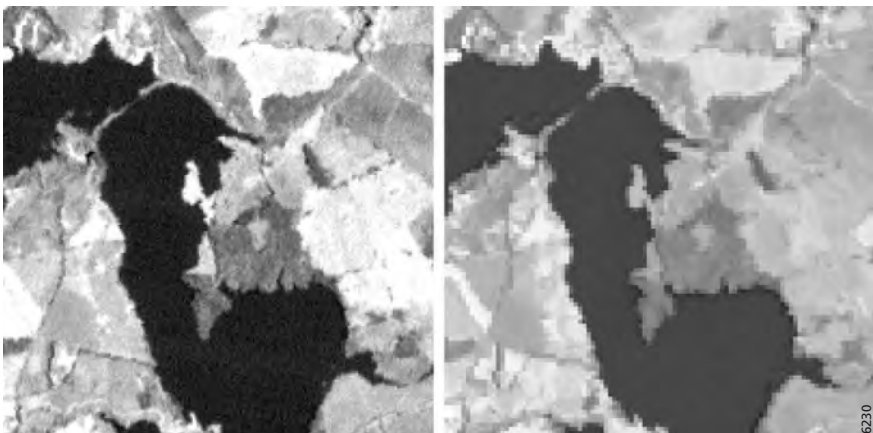

Figure 13.16 – Panchromatic (left) and multispectral (right) images used in this study. Please consult the enclosed CDROM for a full colour version.
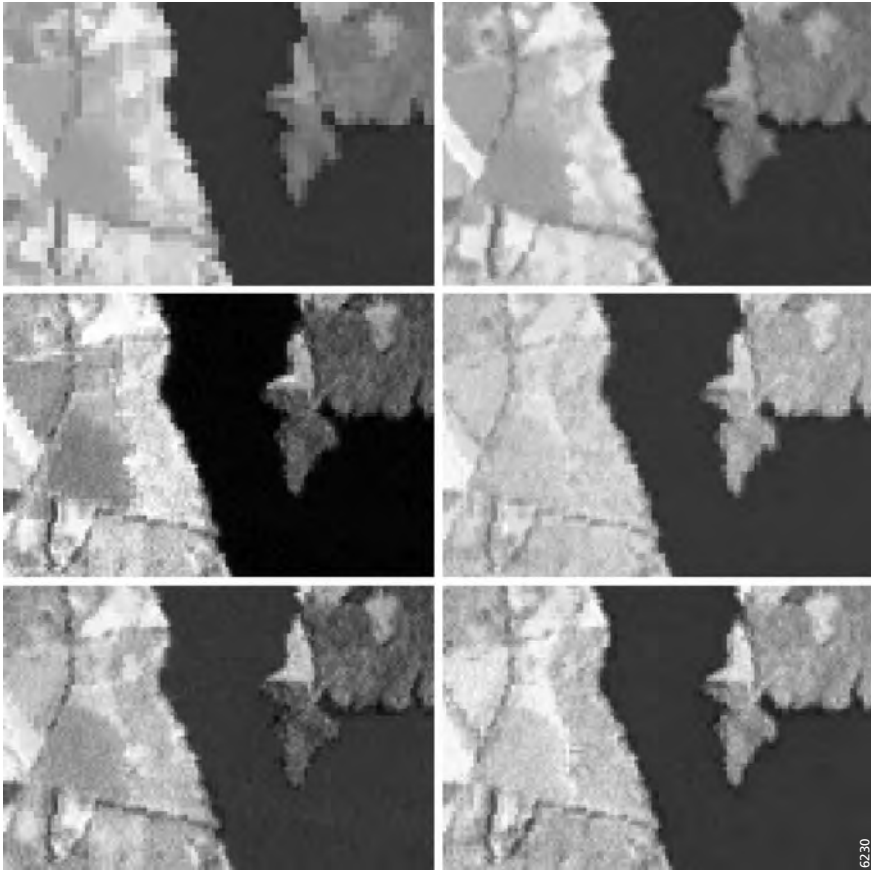
Figure 13.17 – Original multispectral image (top left) and the results from five different fusion methods: Pyramidal Wavelet Transform (top right), IHS Transform (middle left), Brovey Transform (middle right), Principal Components Transform (bottom left) and Gram-Schmidt Transform (bottom right). Please consult the enclosed CDROM for a full colour version.

Principal Components and the Gram-Schmidt transform. The wavelet coefficients provided by the multiscale analysis of the high spatial panchromatic image (P), between the scale of the P image and the scale of the multispectral image (MS), describe properly the missing information for the synthesis of the MS image at the same spatial resolution as the one of the P image. Hence, the fused image contains both the structural details of the higher spatial resolution P image and the rich spectral information from the MS image.

13.5.5 Conclusions

Visual analysis of the fused images has shown that all tested methods produced a significant improvement over the original image since the structures of the panchromatic image have been injected in the multispectral image in all fusion methods. However, besides the improvement on spatial resolution a good quality fused image should also preserve the spectral information from the multispectral image. In this context, the multiscale

analysis with wavelet transform outperformed the classical IHS and Brovey methods since the spectral content was better preserved on the synthesised image from the pyramidal wavelet transform method. The high-quality preservation of the spectral information and the improvement of the spatial content on synthesised image from the pyramidal wavelet transform method may improve the efficiency of further processing techniques such as the application of a classifier, whether it would be automatic or not.

13.6   Case study III – feature extraction for change detection

13.6.1   Introduction
Digital change detection as commonly applied to temporal remotely sensed images produces another digital image, where pixel values represent the degree of difference between the temporal scenes under investigation. In the ideal case, areas of land cover change would show high positive or negative values, whereas non-changed areas would be zero-valued. Nevertheless, additional sources of noise and the spatial multiscale nature of the input images are propagated to the outputs of digital change detection, demanding the use of tools that take these characteristics into consideration. This section presents a new approach to deal with noise and multiple spatial scales during change detection. The methodology is based on noise modelling in wavelet space for efficient and automatic thresholding. The objective of this new method was to reduce the sensitivity of digital change detection to the effects of radiometric and geometric misregistration by extracting changes according to size classes using a multiscale approach.

Current methods used to compare two or more remotely sensed images and to detect differences among them are dependent on accurate radiometric normalisation and geometric rectification (Dai & Khorram, 1998; Schott et al., 1988). These prerequisites are generally hard to achieve in many situations due to the lack of (radiometric) calibration data and difficulties in locating (geometric) control points. In addition, a threshold value to separate change from no-change areas must be defined. In the absence of noise, thresholding a difference image would be an easy procedure leading to reasonable results. Unfortunately, discrepancies in sensor characteristics, atmospheric transparency, vegetation phenology and errors in geometric registration are a few examples of noise sources present in every multitemporal and/or multisensor data set derived from optical remote sensing.

In the operational context, digital change detection has been normally performed with a category-based approach that compares land cover maps produced at different points in time. The choice for this approach is motivated by the straightforward information about old and new land cover classes represented by each image pixel that has undergone land cover change. However, uncertainty propagation reduces considerably the confidence level of change detection results obtained with map comparisons (Shi & Ehlers, 1996; Bruin & Grote, 2000). For example, two highly accurate classification results, say 80%, would produce a mere 64% accurate change detection result (Stow et al., 1980). In the research context, radiometric-based change detection techniques are more popular than category-based ones because of their ability to overcome the above-mentioned drawback, but as pointed out before, they are more sensitive to errors in geometric and radiometric registration. This becomes even

more important when different sensors with different spatial and radiometric resolutions are used for change detection. Moreover, the amount of change is dependent on the empirically defined thresholds, for which there is no theoretical guidance.

Consequently, a need for automatic analysis tools able to minimise these requirements has been recognised (Singh, 1989). The dilemma relies on how to differentiate real changes from misregistration (geometric and radiometric) noise.

13.6.2   Multiscale products for feature extraction

A change image, produced by any of the standard radiometric change detection methods (e.g., image differencing), was decomposed into several high frequency bands with variable resolutions plus a low frequency band at the coarsest resolution. The decomposition was obtained by applying the 2D extension of the algorithm '*à trous*' (Holschneider et al., 1989) with a cubic spline as the scaling function: After decomposition, the differences between the images were separated into five detail levels ranging from fine to coarse, as well as a smoothed representation of the original difference image (figure 13.17). At this stage, changed sites were discriminated according to size classes. Small area changes and geometric misregistration are captured in the fine details representation whereas overall changes, like variations due to phenology, were captured at the coarse details levels and at the smoothed representation of the original difference image. Thus, by solely using information provided by intermediate
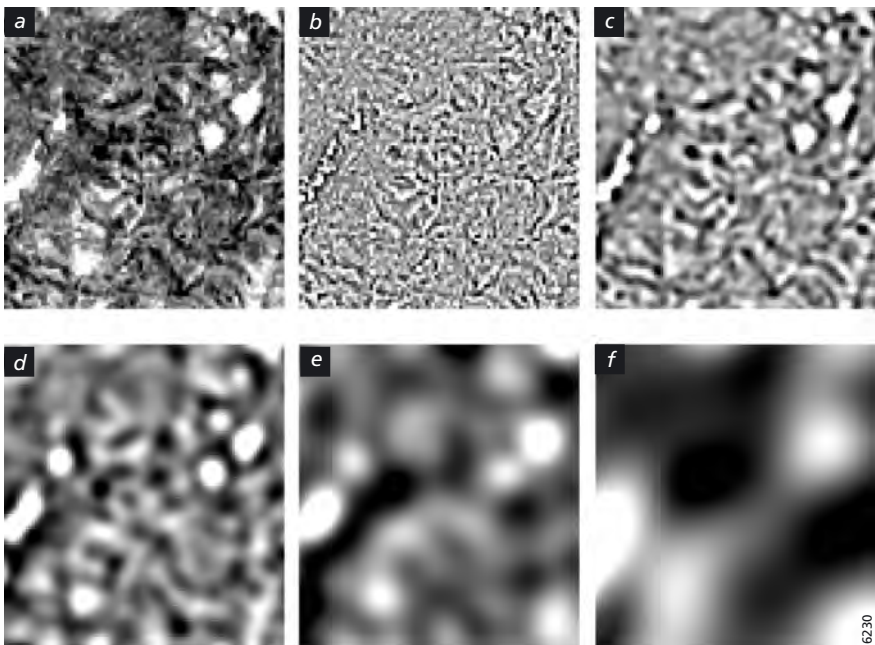

Figure 13.18 – (a) Result of image differencing (TM band 3 from 1998 and MSS band 2 from 1981. (b, c, d and e) Detail images ranging from fine to coarse and (f) smoothed version of (a) decomposed with the 'à trous' algorithm.

Composite 3 2 1 MSS, July 1981. Pixel size 60 m   Composite 4 3 2 TM, Aug 1998. Pixel size 60 m

Composite 4 5 3 TM, Nov 1985. Pixel size 30 m   Composite 4 5 3 TM, Aug 1998. Pixel size 30 m

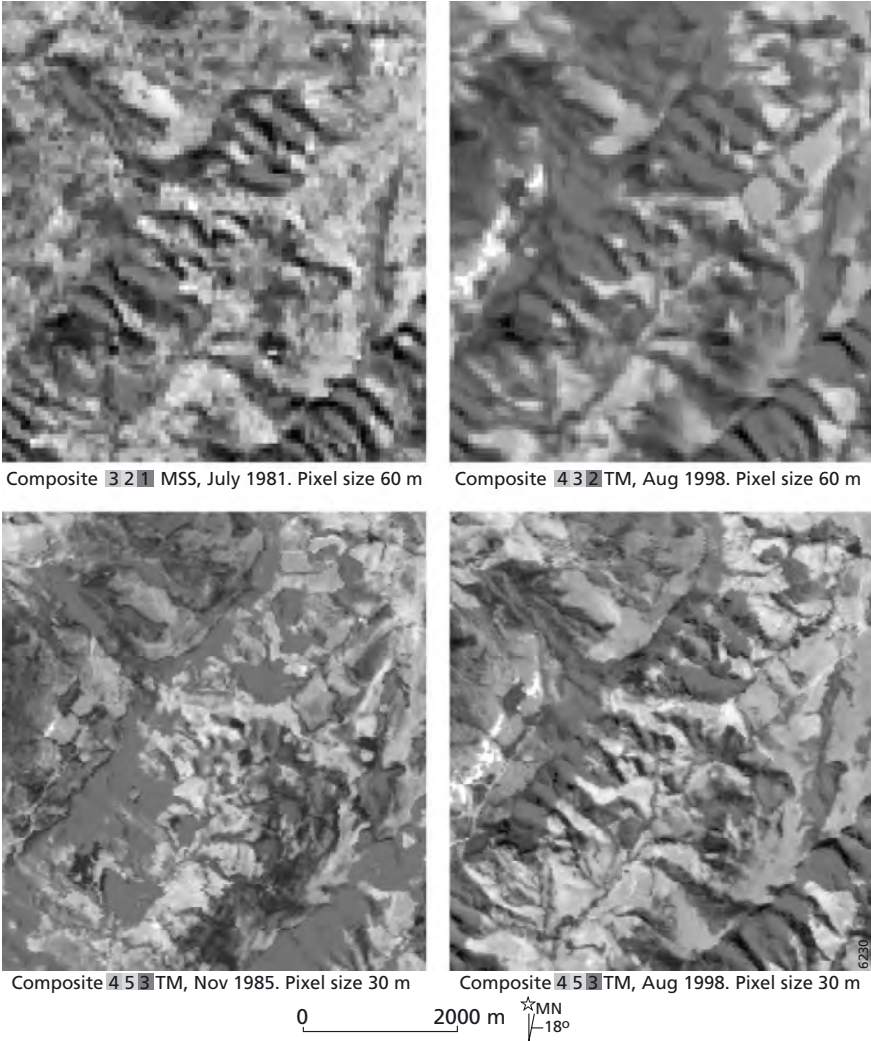0 ——————— 2000 m   ☆MN
                       ⊢18º

Figure 13.19 – Data set used in this study. Using these color combinations, forest areas appear in red tones while mining sites appear in white. Please consult the enclosed CDROM for a full colour version.

scale levels, spurious effects of misregistration were filtered out and the search space was considerably reduced.

Meaningful signal components were further separated from noise by multiplying wavelet scales. The so-called multiscale product integrates in one image the information contents of each scale level involved in the multiplication. Sadler & Swami (1999) characterised the method statistically and evaluated its performance for detection and estimation of edges. Xu et al. (1994) applied the multiscale product for filtering of magnetic resonance images,
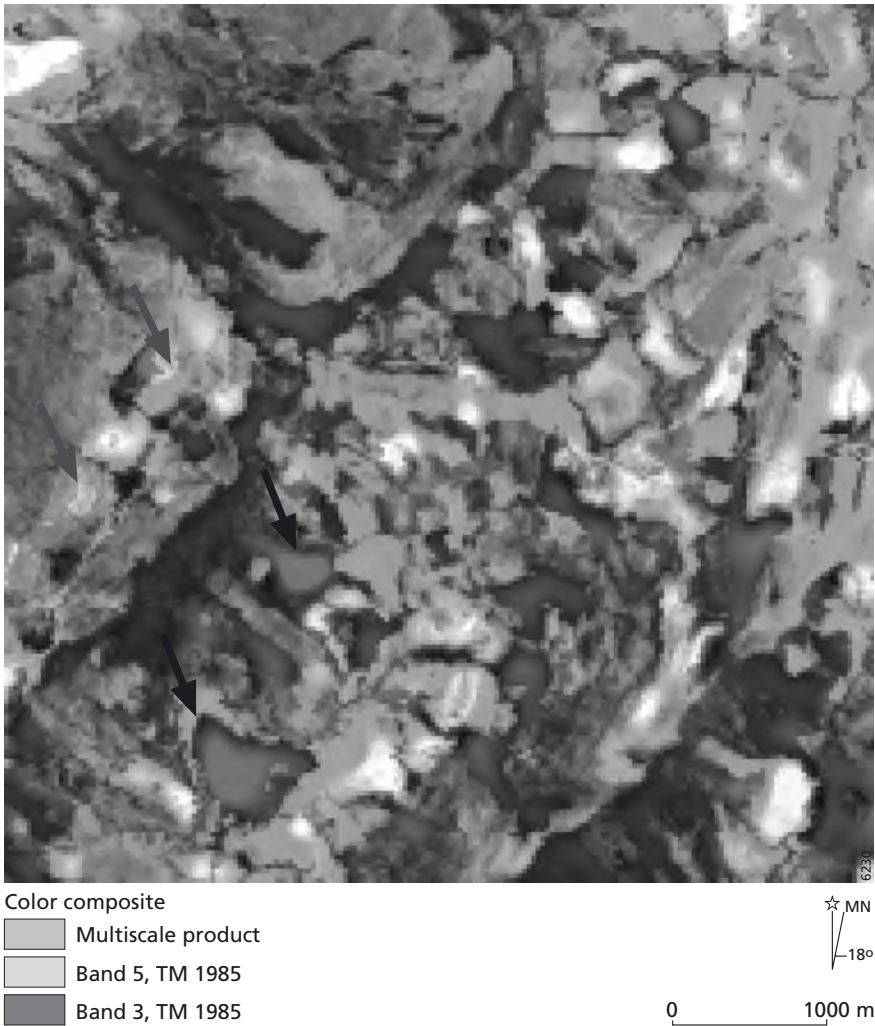
Figure 13.20 – Straightforward visualisation of changed sites. Arrows indicate areas where (yellow) deforestation and (blue) mining activities increased. Please consult the enclosed CDROM for a full colour version.

Sadler et al. (1998) for shock wave detection in acoustics and Carvalho (2003) for automatic detection of corrupted values in remotely sensed time series. The choice of scales to include in the multiscale product has an effect on the sensitivity of the approach to the size of objects in the scene.

The multiscale product is considered locally constant. This is the classical significance testing, which detects only the coefficients that are greater than their local standard deviation multiplied by a constant C. In this study, C was set to 2 and multiscale product coefficients

that do not pass the test are set to zero. The purpose of significance testing is to further remove noise by excluding unimportant multiscale product coefficients.

13.6.3   Test site and data

The site chosen to evaluate the approach is located near the city of São Tomé das Letras and is used mainly for agriculture, rock exploitation and for the protection of remnants of Cerrado (Brazilian savanna), rocky fields and semideciduous Atlantic forest. In the last 20 years there has been an increase of mining activities and losses of forest cover among periodic changes due to agricultural activities. One Landsat MSS image from July 1981 and two Landsat TM images from November 1985 and August 1998 were used in this study (figure 13.18). Each pixel of the Landsat TM and MSS images covers a ground area of about 900 m² and 3600 m² respectively.

Landsat TM bands 2 (520-600 nm), 3 (630-690 nm), 4 (760-900 nm) and Landsat MSS bands 1 (500-590 nm), 2 (610-680 nm), 3 (790-890 nm) were chosen to perform this experiment because they cover relatively comparable portions of the electromagnetic spectrum (Buiten & Clevers 1996). Note that spatial resolution, sensor characteristics and phenological conditions are very heterogeneous among these images (figure 13.19). The images were reduced to the same pixel size by applying a one level pyramidal wavelet transform using a cubic spline as scaling function. Due to decimation, the pixel size for the Landsat TM images became 60 by 60 m after the transformation. The Landsat MSS image, preprocessed by the U.S. Geological Survey and purchased with a pixel size of 57 by 57 m, was resampled to 60 by 60 m with a nearest neighbour algorithm. No radiometric rectification was applied to the input images and spatial misregistration (RMS error <1 pixel) ranged from one to three pixels when evaluated visually. Ground data were recorded during field visits in 1999 when sites of deforestation, new rock exploitation, annual crops, and forest regrowth were located in the field and over orthophotos (scale 1:10,000) acquired in 1984.

13.6.4   Results and discussion

Using the multiscale product in a simple colour composite, visualisation of changed sites can be readily done. To visualise changes from dark to light (e.g. deforestation in TM band 3), one must use the oldest image to make the composite (figure 13.20). Changes from light to dark (e.g. reforestation in TM band 3) are better visualised when using the most recent image. This
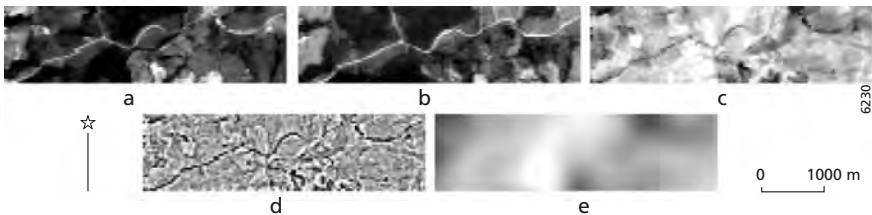

Figure 13.21 – Landsat TM from (a) 1998, (b) 1985 and (c) respective difference image. (d) Details of the difference image at the first scale level. (e) Smoothed version of the difference image at the fourth scale level. Note the misregistered road depicted in (d), while overall differences like phenological condition of vegetation patches are depicted in (e).
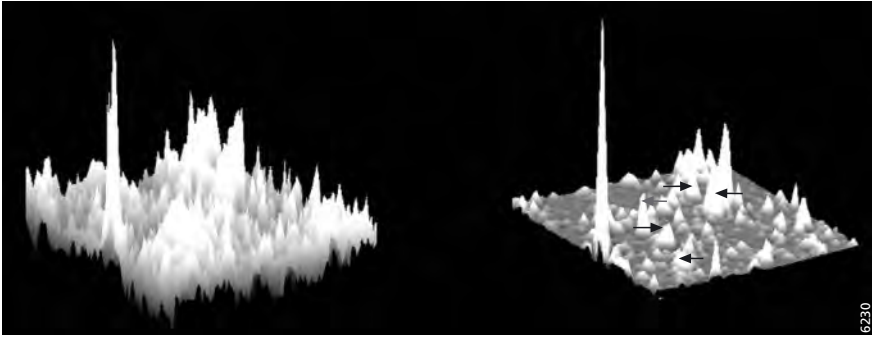
Figure 13.22 – 3D view of the difference image between band 3 of Landsat TM from 1998 and band 2 of Landsat MSS from 1981 (left). 3D view of the product of differences at second and third scales (right).

is because the background at sites where changes are to be visualised must be dark so that the changes of interest are emphasised. All changes detected by this visualisation procedure did occur although their quantification was not possible. Note that, in figure 13.6 (3), the whole triangular forest fragment at the bottom right disappeared between 1985 and 1998 although only its centre is being enhanced. This straightforward visualisation might be of much use when large areas are to be evaluated. Misregistration effects and small area changes were isolated as fine details (figure 13.20d), while differences in phenological characteristics and atmospheric conditions were captured in the smoothed representation as overall differences between the images (figure 13.20e).

Irrelevant information that could be considered noise in the difference image (figure 13.21a) does not appear in the change image built with the product of wavelet scales (figure 13.21b). This 'cleaning' effect facilitates the analysis and understanding of remotely sensed images. In figure 13.21, vegetation removal (black arrows), reforested areas (grey arrows) as well as new rock exploitation sites (white arrows) were pinpointed successfully without previous radiometric rectification or threshold definition while differences not related to land cover changes were bypassed.

13.6.5   Conclusions
The behaviour of changes at different scale levels as resulting from the new method presented here enables their discrimination according to size classes. Hence, using information from intermediate scale levels one can minimise the problems mentioned above. The method was found to be less sensitive to spatial and radiometric misregistration, although fine details are lost as well. It can be applied to the outputs of any change detection technique such as image rationing, principal components, change vector analysis etc. As for the selection of significant wavelet coefficients, the selection of scale levels to be considered for further analysis can be driven by statistical tests, which are useful when no knowledge exists on the size of features of interest. Changes in the study area were well discriminated but their quantification was not possible when using information from limited scale levels. Further research on the combination with other techniques, like region growing algorithms, could be a solution

to determine the spatial extent of changed sites. Applications of the proposed method include, for instance, the automatic selection of changed sites for GIS updating and the fast identification of priority areas for field check when large data sets are to be evaluated. Finally, the visualisation of changed sites is straightforward with a simple colour composite avoiding any threshold definition, radiometric rectification or accurate geometric registration.

Chapter 14

Contextual Analyses of Remotely Sensed Images for the Operational Classification of Land Cover in United Kingdom

Robin M. Fuller, Geoff M. Smith & Andy G. Thomson

14.1   Introduction

The use of remote sensing and image analysis for operational mapping at national scales requires a range of tools to help achieve the necessary accuracy and consistency despite variations in image quality, image acquisition dates, seasonal changes in vegetation, and a range of other confounding factors which distort or alter spectral signatures of the target classes. Contextual analyses can help to generate a coherent map structure, correct errors and extend the thematic scope of classifications. This is especially important when producers are asked to meet the wide-ranging needs of multiple end-users.

Many papers describe procedures of contextual classification where measures of context are used directly in the classification process (e.g. Cihlar et al., 1998; Stuckens et al., 2000; Debeir et al., 2002; Melgani & Serpico, 2002; Steel & Redmond, 2002). Whether intentional or coincidental, the effect of such classifiers is often to mimic the true structure of many landscapes which are divided into discrete parcels of uniform cover and use. Whilst such approaches may be very powerful, operationally it can be difficult to exert adequate control over the outcomes – for example, where the procedures attempt to balance contextual and spectral probabilities. Other papers use post-classification filtering to remove the 'noise' of mis-classified pixels in the classified data (e.g. Kim, 1996; Zukowskyj et al., 2001). However, such approaches rely more on the filter's geometric properties than the true landscape structure. Relatively few papers (e.g. Harris & Ventura, 1995; Groom et al., 1996; Barnsley & Barr, 1996) describe the use of contextual data in post-classification processes to correct and refine the basic outputs of spectral classification. However, such procedures can usefully exploit existing knowledge of landscape structure and habitat distributions. The methods can be very powerful in addressing specific problems which arise with individual classifications. There is greater scope to use a variety of data from independent, validated sources. There is considerable flexibility in the way such data can be used. Moreover, the application may use fully objective criteria. The procedures, while complex in concept and subtle in effect, may be relatively simple in definition, operation and consequence. Thus, the results obtained can be easily understood by users of the resulting data. Finally, contextually derived products can be

readily be documented, with the processes and results remaining completely transparent to the user.

This chapter draws, first, upon experience gained in making the remotely sensed Land Cover Map of Great Britain (LCMGB), nominally of 1990 (Fuller et al., 1994a). It contrasts the very simple post-classification corrections applied then with the use of geographical information systems (GIS) and GIS-based procedures (Smith et al., 2001) developed in the production of the UK Land Cover Map 2000 (LCM2000 – Fuller et al., 2002). In LCM2000, contextual analyses operated throughout. Context was used to generate a map structure which mimicked the landscape structure; image spectral data were analysed within the context of the map structure; errors in spectral classifications were corrected using contextual analyses; and cover-classes were refined and thematically extended using contextual data. These processes all helped LCM2000 to meet the many and varied needs of end-users.

14.2   The land cover map of Great Britain

LCMGB was initially developed as a 'demonstrator' project, though subsequently there have been more than 500 licensed users of the data. The map was a conventional raster-based classification of satellite images (Fuller et al., 1994a) recorded mostly in 1988-1989. Landsat Thematic Mapper (TM) red, near infrared (NIR) and middle infrared (MIR) reflectances were used for the classifications (Fuller & Parsell, 1990). Summer and winter images were used in conjunction, where available (Fuller et al., 1994b), co-registered to the British National Grid (BNG), with 25 m output pixels, giving 6 bands of composite data. A maximum likelihood classification gave a map with 25 cover-classes. Simple contextual rules were used to refine class-distinctions. An image filter removed isolated pixels and thereby reduced 'noise' in the data.

14.2.1   The scope for contextual correction in LCMGB
At the time of LCMGB production, most image analysis systems were extremely limited in their potential. They offered little scope for genuine GIS-integration and for elaborate spatial-contextual analyses. Data storage problems hindered complex analyses and limited the detailed recording of intermediate products and final data outputs – the project had access to a 1 gigabyte disk, about the maximum generally available at the time, with disk storage then costing 1000 times what it does today. It is in this context that the LCMGB and its contextual analyses should be viewed.

It is important to understand fully the characteristics of the LCMGB to recognise the limited scope for contextual correction. The 1990 map was simply a single layer, raster grid, with each cell recording the maximum likelihood class as a digital number (DN). The DNs ranged from 0 to 25, with 0 representing unclassified pixels and values between 1 and 25 recording the final output classes numbered 1 to 25. There was no information on the spatial coherence of pixel-groups, other than intuitively, through their x-, y-locations in the raster. In the output map, there was no information on the probability of the maximum likelihood class-allocations, nor of the alternative classes and their probabilities. To record this information, along with where and what contextual corrections were applied, would have increased the size of the output

dataset by an order of magnitude. And for reasons of limited disk space, there was not even the scope to identify straightforwardly, at full spatial resolution, which image-combinations contributed which pixels to the overall mosaic of cover.

14.2.2 LCMGB contextual analyses

LCMGB contextual analyses were mostly applied to correct errors in the classified map data, rather than to refine or extend the classifications (Groom et al., 1996). The procedures involved the development of zonal masks, within which certain classes were disallowed. In practice, the application of the mask was an arithmetic process, with masked areas given DN values of 100. When the mask was added to a map of classified spectral classes (usually around 80 in number before merging to the final 25 classes (Kershaw & Fuller, 1992)), DN values within a mask area became >100 and those outside the mask-zone retained the original values <100. It was thus possible to single out subclasses within or outside of masked areas and to correct erroneous elements, renumbering them to an alternative class while simply reverting allowable subclasses to their original value.

Any external data which might have been available for contextual applications were deemed either too costly or having an inappropriate format or with insufficiently high resolution for operational use – and often a combination of all three problems. Thus, all LCMGB rules relied essentially upon internal context to define masks, perhaps with limited checking against paper maps.

Terrestrial/maritime corrections

A coastal mask was used to identify maritime cover types out of context in terrestrial locations (e.g. examples of 'beaches' recorded inland); the mask was also used to correct terrestrial habitats in a maritime context (e.g. erroneous 'urban' areas found in inter-tidal zones). Semi-automated methods were developed to make masks. A spatially subsampled image, at one-third the original size, was constructed with three zones:

1 pixels classified as a maritime class;
2 'inland water';
3 'urban', 'suburban' and 'bare ground'.

A modal filter with a 3 by 3 kernel simplified the mask. A line was then defined interactively to enable removal from the mask of mis-classified maritime elements (i.e. those found inland). This line only had to be very accurately defined where exclusively maritime habitats met exclusively terrestrial ones (e.g. coastal towns, arable cliff-tops or freshwater coastal lagoons); the definition was less critical where semi-natural vegetation fringed the shore, as such habitats might be found in either zone and there had been no intention of changing the classes, whichever side of the line they occurred. The mask was then returned to its original size (i.e. zoomed x 3 and resampled by nearest neighbour). A 3 by 3 modal filter was used to remove the angularity of the coastline arising from the x 3 zoom. The mask was then simplified to a single coastal class with DNs of 100. Operation of the mask used the straightforward addition and renumbering procedure, as described earlier. Inland 'beaches' thus became inland 'bare ground'; inland 'salt marshes' were changed to 'arable land'; inter-tidal 'arable' land became 'saltmarsh'; 'suburban' and 'urban' areas on the shore were re-numbered to become 'beaches'.

Urban/arable corrections
Mixed pixels of suburban land, essentially recording mixed vegetated and non-vegetated surfaces, were frequently mis-classified as 'arable' cover. Urban masks were constructed by selecting the 'urban', 'suburban' and 'bare ground' subclasses and aggregating them thematically into a mask with DNs of 100 in the urban zones. The resultant mask was generalised by operating a 5 by 5 modal filter, running the data through the filter twice. A 3 by 3 maximum filter removed small holes in the mask. The mask was then overlaid onto the map and the mis-classified 'arable' pixels in urban zones were identified by arithmetic addition. These were relabelled to the 'suburban' class.

Upland corrections
Upland masks allowed corrections of upland mis-classifications (e.g. 'arable' and 'urban' land in uplands); they also allowed a distinction between 'lowland heaths' and 'upland heather moors'. A one-third size output was created by subsampling. Upland habitats – 'moorland grass', 'open shrub moor', 'dense shrub moor', 'herbaceous bogs' and 'bracken' – were all re-numbered to DN values of 100. A 9 by 9 modal filter was used to remove 'noise' from the initial mask. The resulting map still had larger remnant areas of incorrect 'upland'. Interactive editing (assisted by reference to topographic map in paper form) removed erroneous 'upland' areas (re-numbering them to 0). The mask was then returned to the original resolution and 3 by 3 modal filter was used to remove the angularity of the upland edges. The arithmetic mask-addition was applied to identify habitats in erroneous context for re-numbering to the most appropriate classes.

Manual re-coding
Locally, there was a very small amount of general manual re-coding. Where substantial and very obviously incorrect classifications were found, it was possible to target the mis-classified elements by thematic selection – in reality, a numerical selection made within the image analysis system, combined with a manually defined 'region of interest' to isolate the errors and rectify the problems. The image analysis system only offered fairly awkward 'graphics overlay' procedures for areal definition and spatial selection, making this a tedious and time-consuming task; consequently, this approach was very rarely used.

Contextual filtering
The final stage was to use an isolated pixel filter. A 3 by 3 window was scanned across the resultant map. Where a pixel was the only member of its class in the 3 by 3 neighbourhood, the dominant class of the other 8 pixels was substituted. This had the effect of removing some of the apparent 'noise' in the classified map.

14.2.3   Concluding comments on LCMGB contextual analyses
It is interesting to note that it was very difficult, with the data storage available at the time, to track and record quantitatively the impacts of the various correction and filtering procedures described above, especially once individual scenes were trimmed and fitted into the general mosaic of classified images which later became LCMGB. The account by Groom et al. (1996) used test areas to assess the proportional impact; these may be representative of the LCMGB as a whole, though this is not verifiable. Contextual procedures increased agreement by 4.5% in a sample of 18 one-kilometre validation squares. The isolated filter contributed <1%

change with the remaining improvements coming from mask-based corrections. Thus, while contextual corrections made an important contribution to the LCMGB, their influence was relatively small in areal terms.

14.3   Land cover map 2000

14.3.1   Background

LCM2000 was designed both as an update and an upgrade (Smith & Fuller, 2001) of the original LCMGB. A programme of research and development had produced a methodology based on image segmentation, vector-conversion of segments into parcels, and object-based classification of the parcels (Smith et al., 1998). In effect, the segmentation put every pixel into context when it grouped it with similar neighbours in the land parcels. The classification of each parcel then drew upon the member-pixels to derive mean reflectances and, comparing these with a training set, applied a label for the entire parcel. The procedure is a form of contextual classification for the pixels concerned. Post-classification stages also used contextual analyses, to correct errors of mis-classification and to extend the classification thematically, in order to meet user needs.

14.3.2   Broad habitats and LCM2000 classes

It was a logical consequence of LCMGB's widespread use that LCM2000 was funded by a consortium of users. These users comprised Government Departments with responsibilities for environmental policy, and Government agencies with executive roles in environmental protection and conservation (see the Acknowledgements section).

Key members of the consortium specified a requirement to map 'Broad Habitats'. These had been identified for implementation of, and reporting under, the UK Biodiversity Action Plan (Department of the Environment, 1994). The classification was designed to encompass the entire range of UK habitats (UK Biodiversity Steering Group, 1995); it was described by the Joint Nature Conservation Committee (Jackson, 2000). The Habitats include a number of more narrowly defined 'Priority Habitats' which the Government is required to protect under the European Union Habitats Directive (Council Directive 97/62/EC of 27 October 1997). Monitoring of the Broad and Priority Habitats is also a requirement of the 1992 UN Convention on Biological Diversity. It is clear why the funding consortium would want LCM2000 to contribute to this monitoring process.

The inclusion of the Broad Habitats in the LCM2000 classification presented a major challenge in production. Nonetheless, the team aimed to map, as far as it was possible, the widespread examples of terrestrial, freshwater and coastal Broad Habitats (table 14.1). This demanded the use of far more than just spectral image data, as some classes were characterised by soils, others by plant indicator species, while some implied elements of land use in their definitions. Contextual information was therefore crucial to the definition of such classes and to their distinction as thematic map entities. In addition, LCM2000 subdivided some Broad Habitats to meet the wider needs of other users. These additional classes also benefitted from contextual analyses.

Table 14.1 – Widespread examples of Biodiversity Action Plan 'Broad Habitats' and their relation to Land Cover Map 2000 'Target classes' and 'Subclasses'.

Widespread Broad Habitats	LCM2000 Target classes	LCM2000 Subclasses
Inshore sublittoral	Sea/Estuary	Sea/Estuary
Standing water/canals	Water (inland)	Water (inland)
Littoral rock	Littoral rock and sediment	Littoral rock
Littoral sediment		Littoral sediment
		Saltmarsh
Supra-littoral rock	Supra-littoral rock and sediment	Supra-littoral rock
Supra-littoral sediment		Supra-littoral sediment
Bogs	Bogs (deep peat)	Bogs (deep peat)
	Dwarf shrub heath (wet/dry)	Open and Dense dwarf shrub heaths
Dwarf shrub heath		
Montane habitats	Montane habitats	Montane habitats
Broad-leaved woodland	Broad-leaved wood	Broad-leaved/mixed woodland
Coniferous woodland	Coniferous woodland	Coniferous woodland
Arable & horticultural	Arable and horticultural	Arable cereals
		Arable horticulture
		Non-rotational horticulture
Improved grassland	Improved grassland	Improved grassland
	Neutral/calcareous semi-natural/rough grasslands	Setaside grass
Neutral grassland		Neutral grass
Calcareous grassland		Calcareous grass
Acid grassland	Acid grass and bracken	Acid grass
Bracken		Bracken
Fen, marsh and swamp	Fen, marsh and swamp	Fen, marsh, swamp
Built up areas, gardens	Suburban and urban	Suburban/rural developed
		Continuous Urban
Inland rock	Inland Bare Ground	Inland Bare Ground
20 relevant BHs	16 target classes	26 target/subclasses

In practice, LCM2000 is really a thematic classification of spectral data recorded in satellite images. Spectral classes (Kershaw & Fuller, 1992) were defined in the classification process and later combined thematically. The thematic classes in turn were aggregated to build various classification schemes. In practice, 'Target classes' (table 14.1, column 2) were considered the nearest match to Broad Habitats which could be achieved consistently and with a high level of accuracy. Subclasses (table 14.1, column 3) were then defined to give, as far as possible, the full complement of widespread Broad Habitats, together with a few other important cover types beyond the needs of the Broad Habitat classification. Subclasses were mapped

consistently throughout the UK, but sometimes with compromises on accuracy. Subclasses were subdivided where this was considered valuable for even wider use of data. Thus 72 class Variants (Fuller et al., 2002) are the thematic components of the Target classes and Subclasses (and they are in effect the logical thematic aggregations of the spectral subclasses). These class Variants were recognised where possible but not necessarily consistently (e.g. individual arable crops were recorded, where possible, but could not be distinguished once harvested).

In distinguishing Broad Habitats, some contextual analyses were based upon internal context within LCM2000, others drew upon external datasets. A key challenge lay in using contextual data which were not designed for such purposes and where, variously, limited thematic details, inadequate measurement accuracy, and poor spatial resolution forced compromises in operations and outputs. Because some Broad Habitats were defined using characteristics which could not be drawn either from images or tailored exactly from any other appropriate spatial data, LCM2000 distinctions had sometimes to differ a little from those published (Jackson, 2000). Table 14.1 shows the mis-match in the 'read-across' between some Broad Habitat and Target class/Subclass distinctions. Differences in nomenclature (table 14.1) aim further to draw attention to differences of definition. Also, in table 14.1, a hard line between Target classes or Subclasses shows a distinction which is generally reliable; however, a dotted line identifies situations where the distinction is more difficult. Users should be aware of these issues: details are given later.

14.3.3 Image segmentation

The LCM2000 image segmentation is a form of a priori contextual analysis which examines pixels in the context of their neighbours to identify 'relatively uniform' areas in spectral terms. It builds the spectrally similar groups into segments which tend broadly to relate to objects in the landscape: for example, fields, woodlands, water bodies and settlements. In operation, the procedures comprised two separate stages: first, edge-detection to identify boundary features; and, second, region growing from seed points selected to avoid the edges. These are described in the following sections.

Images and band selection for segmentation
Landsat TM and Enhanced TM sensors were the first choice for data supply. Indian Research Satellites LISS data offered second-choice coverage. Summer and winter images were co-registered to BNG, giving 6-band composite images, with 25 m output pixels (as in 1990). It was only possible to use three bands for the edge-detection and segmentation algorithms. Various combinations of 3 out of the 6 individual bands were considered; so too the use of vegetation indices, principal components and other mathematical combinations of bands (Lillesand & Keiffer, 1994; Mather, 1987; Schowengerdt, 1997). Experimentation finally showed that straightforward image bands would generally be best in both stages. Summer images contributed two bands, and winter images one band. A TM/ETM summer image contributed red and MIR data, a LISS summer image contributed red and NIR bands (due to coarse MIR pixel size from this sensor); the winter band was NIR, which was generally the brightest.

Edge–detection and segmentation
A Sobel edge-detection algorithm was used to ensure that the seedpoints for segments were selected away from boundary features. The algorithm gave a value for each pixel related to the strength of any apparent edges at that point. These values could then be used to identify
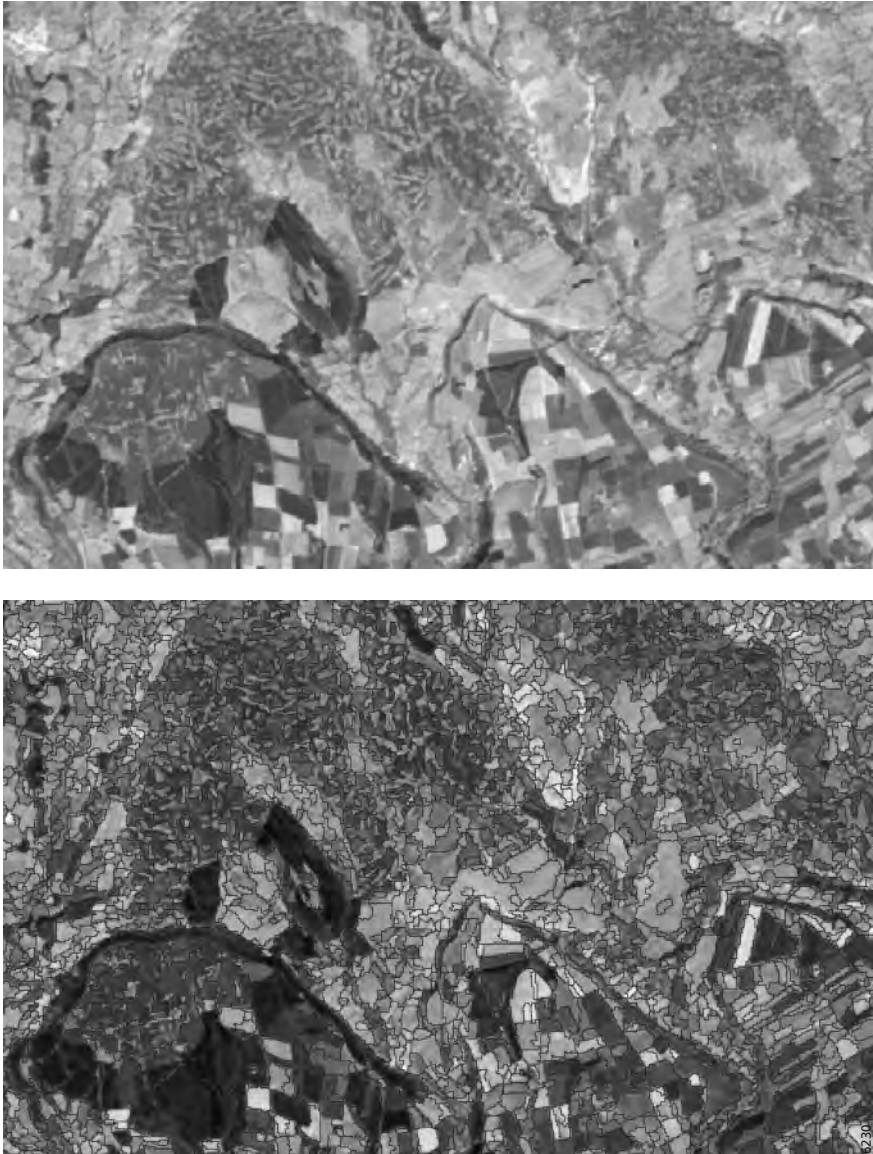

Figure 14.1 – Top: a subscene of combined summer–winter satellite images; bottom: the same scene segmented using the spectral data to build vector polygons (linework overlaid). Please consult the enclosed CDROM for a full colour version.

regions with low scores, suitable for seedpoints. The growth of segments around seedpoints, and thus the level of segmentation, was controlled by the operator. There was the potential to dictate the degree of region-growing and subsequent merging by setting thresholds for each spectral band and establishing the number of standard deviations expected to contain the majority of the pixels of a segment. The aim was to ensure a field-by-field segmentation, also separating urban and suburban zones, and subdividing heterogeneous semi-natural zones into meaningful segments, with minimal over-segmentation of land parcels. Trials showed that a threshold equal to 80% of the reflectance standard deviation range was appropriate for segmenting each band. These thresholds allocated about 95% of all pixels to segments; they gave field-by-field separations, though sub-segmenting some fields – a little over-segmentation was necessary to prevent the growth of mixed chains of edge pixels and to subdivide urban/suburban areas to match Subclass requirements.

Post-segmentation generalisation and boundary rejection
Simplification of unnecessary sub-segmentations was achieved using 'intelligent' generalisation methods. Procedures tested in a series of experiments showed that:

- non-segment edge pixels should be dissolved into adjoining parcels;
- single-pixel islands should be dissolved into their surroundings;
- the pixels of small segments <9 pixels (≤0.5 ha) should be attached to their nearest appropriate segments using a spectral minimum distance rule;
- small, spectrally similar, segments should be merged.

Once a generalised segmentation was achieved, it was necessary to create vector versions in the GIS database. This was simply a procedure of raster-to-vector conversion, where the boundaries between the segments were represented by vector lines. This created 'land parcels' (figure 14.1), to which attributes could then be attached.

14.3.4   Contextual classification – maximum likelihood classification of parcels
The per-parcel classification used a maximum likelihood algorithm (Lillesand, 1994; Mather, 1987; Schowengerdt, 1997) to determine class membership in the same way as a per-pixel classifications would have done. Training for parcel-based analyses essentially operated in the same way as that used in conventional per-pixel classification. However, training areas were identified individually by pointing to the land parcels, with no need to draw their outlines; the delineation was thus objectively based. The mean reflectances per band for each image segment were calculated from a shrunken, core area, excluding edge-pixels as far as possible. The shrinkage was made a dynamic process whereby 25 m of shrinkage was applied and, if insufficient raster data were collected (<4 pixels), the amount of shrinkage was reduced by 2.5 m and the raster extraction repeated. This process was iterated until adequate data were extracted or the amount of shrinkage reached zero. Data on the number of pixels extracted and the amount of shrinkage used were stored as land parcel attributes for future reference.

The per-parcel classification procedure compared each parcel's mean reflectances with the training set and recorded the most likely spectral subclass in statistical terms: it actually stored probabilities and subclass-labels for the top five spectral subclasses, usually covering

>90% of the probability distribution. Because each pixel of a parcel takes the class of the parcel, the analysis can be thought of as a form of contextual classification.

By way of contrast, a raster classification of the images, mimicking the 1990 product in structure, was also made. Per-pixel details were also added to the land parcels: the proportional cover per-pixel was recorded, giving scores for the top five subclasses and thereby giving an estimate of within-parcel heterogeneity. The 1990 cover per-pixel was also summarised per-parcel.

In some inter-tidal zones, it was necessary to use per-pixel classifications to contribute to LCM2000. This was because a pre-processing stage of haze-correction, developed for terrestrial areas (Liang et al., 1997), had caused a distortion in the spectral signatures of some inter-tidal areas, preventing accurate segmentation. The per-pixel thematic results for the inter-tidal areas were converted to land parcels for inclusion in the dataset.

14.3.5   Parcel selection for post-classification contextual alterations

Contextual alterations comprised two distinct elements: first, it was necessary to select the candidate parcels for a particular alteration; then, for each candidate parcel, the class code in the database had to replaced and the alteration recorded as a parcel attribute, as part of its processing history. Sometimes, these elements were kept separate: parcels were selected by interactive database queries and saved as a set for later re-coding. Other times, where changes were few, both stages were applied interactively, albeit using software which automatically altered the class-codes for the interactively selected parcels. Mostly, the parcel-selection and code-changes were made together in a fully automated process. Here, the selection rules were pre-defined in code, applied automatically, the selected parcels were renamed accordingly and their processing history updated. Whether the queries were applied interactively or prescribed and applied in background processing, a sequence of queries could be combined into a series of inter-dependent selection procedures, before operation of contextual analyses.

The definitions and operations of selection rules were much more subtle in their use than those of LCMGB 1990. Some rules were scene-specific and tailored to particular problems associated with a scene or a geographic region. Others were applied universally, though with the scope to vary the stringency of their operation in different regions or with different satellite scenes. Some selection rules were aspatial, for example, using a low probability of class-membership as a reason for a change. However, most rules also had spatial elements. Some relied purely upon internal context within the map product: for example, a parcel of erroneous 'arable land' surrounded completely by an urban context. Other selection rules drew upon independent external data, for example the use of the DEM to define an altitude limit for 'urban' land.

When external datasets were interrogated for contextual use, the results were attached as parcel-attributes in the database. Mean height, slope and aspect of parcels were calculated by reference to a digital elevation model (DEM). An acid-sensitivity map (Hornung et al., 1995) was used to define 'acid', 'neutral' and 'calcareous' contexts for each parcel. Peat drift on a geological map identified parcels with dominant peat soils >0.5 m depth. The European Union 'CORINE Land Cover' map (Brown & Fuller, 1996) provided certain land use

attributes needed to refine some of the Broad Habitats. With all these data recorded as parcel attributes, they could readily be used as criteria in the selection process.

Most external data used were in raster form. The cell-size sometimes matched that of LCM2000: for example, the coastal mask adapted from LCMGB. In other circumstances, the raster data were a little coarser: for example, the DEM was based on a 50 m grid. Acid sensitivity was recorded in very much coarser 1 km cells, but still provided indispensable contextual information. If such coarse data had been used to the correct a finer raster map, the underlying pattern of the coarse raster would have been clearly evident in the corrected product. However, when this coarse raster map was applied to the vector LCM2000, the vector structure obscured and generally rendered insignificant the artificial raster generalisation. The resolution of the vector data used as context also differed from that of LCM2000. The CORINE Land Cover map had a 25 ha minimum unit compared with LCM2000's at >0.5 ha. Again, the coarseness of the contextual dataset was hidden when LCM2000 was labelled according to its intersection with the coarser CORINE vectors. When using coarse vector or raster datasets, there was the option to select a parcel for contextual alteration if it touched a particular context, or if it were dominated by that context, or only when that context filled the parcel entirely – all such options were applied in various circumstances in LCM2000, depending on the need for the amendments to be minor or major.

Some rules were applied just to one or a few classified scenes, for example, where the seasonality of crops and semi-natural vegetation caused particular confusions at certain times of year and needed scene-specific corrections. Because each image-combination and each landscape-zone exhibited its own specific problems, the subtlety of this approach was exploited independently for each image-pair; and different rules were evolved for different circumstances. Operation of the rules, whilst seemingly complex, could be coded into an automated operation that involved very little interactive time. Evolution of the rules sometimes needed little more than minor editing of existing computer code.

By building rules into a complex sequence of queries, parcels could be selected based upon a large range of criteria: these might draw, for example, upon size, probabilities, second-choice class, neighbouring cover, past cover and regional context. As an example, 'suburban' land mis-classified as 'arable barley' could have undergone the following steps: parcels would have been selected from the 'arable' Broad Habitat with 'barley' as the class Variant; the problematic spectral subclasses of 'barley' (i.e. just those parcels with image colours similar to 'suburban' land) would have been chosen from this set; it would then be possible to retain only the larger examples, likely to be fields, for example, those >1 ha; the next stage might retain just those parcels classified with a low probability, say <30%; further refinements might select just those parcels with a 'suburban' subclass in the top-five probability list; spatial analysis might further restrict this subset to those parcels touching other parcels of 'urban' or 'suburban' land; or perhaps those with dominant urban cover in 1990; the selection procedure might specify that the set should only include examples below 250 m altitude; the final set of parcels would then be changed from 'arable barley' to 'suburban' cover.

Simple or unambiguous rules were generally applied automatically and without inspection of the candidate parcels: for, example, the maritime/terrestrial rules were applied without previewing the parcels to be affected. The more complex selection rules were more likely to use interactive selection to assess the choice of parcels going forward to contextual alterations. When contextual procedures used queries that were built interactively and sequentially, the operator could assess the effectiveness of each stage of selection: each database query resulted in a selection of parcels which would be potential candidates for correction. The set of parcels was saved, before the next stage of query and selection. If the next query proved over-rigorous in its rejection of parcels, then it was possible to go back, modify the criteria for selection or rejection, re-run the query, and retain or discard the new set. The outcomes of this iterative procedure were evaluated by inspection – a subjective approach, but one which was quickly applied and remarkably effective in operation. In practice, the iterative procedures of query, selection and inspection are no more subjective than the iterative steps of training and classification. Once created, the set was saved for later contextual alterations.

14.3.6   Contextual correction versus thematic class extension

The rules applied in the contextual analyses of LCM2000 can each be thought of as offering one of two fundamentally different roles. Some rules simply corrected errors – for example, a rule which identified inland examples of 'littoral sediments' and corrected them to 'inland bare ground'. These were similar in aim, if more subtle in operation, to those applied in LCMGB. Other rules, however, extended our knowledge about a class, adding context to help subdivide its component parcels into two or more thematic groups: for example, the acid sensitivity mask defined 'acid', 'neutral' and 'calcareous' examples of 'semi-natural grasslands'.

It was necessary to think carefully about the order of operation of contextual rules, as the outcome of each could have a significant bearing on any subsequent contextual selection process. Scene-specific corrections were operated during the final stages of the classification process, as needed. Broadly speaking, the greatest source of errors would have the highest priority in this process. A second stage of contextual analysis involved those correction rules which were applied universally. These were applied after the basic classification was completed. Some such rules had such fundamental impacts that they needed application at the earliest possible of post-classification stages (see particularly the following discussions on maximum likelihood probabilities). Other corrections, also applied universally, also had potentially wide-ranging implications and needed early application, for example, corrections made through coastal masking. It clearly is important that all corrections were completed before the final stages involving the thematic extension of the classification. These final rules were applied universally to affect the entire UK map and came after scenes had been mosaicked into larger sections of map (generally 100 km squares).

In the following sections, contextual corrections are discussed first, and contextual refinements and thematic extensions are covered subsequently.

14.3.7   Contextual corrections

Aggregation of probabilities for MLC
The 'maximum likelihood' class was not always the most appropriate label for a parcel. As an example, if a 'suburban' spectral subclass was allocated with 33% probability, but 'arable' subclasses took second to fifth place with 'wheat', 'barley', 'oats' and 'linseed' taking respectively 30%, 20%, 10% and 5% probabilities, it seemed logical to conclude that the 'arable and horticultural' Broad Habitat was much more likely to apply, with 'wheat' as the most likely class Variant.

The first step in correction was to re-examine the probabilities with which the maximum likelihood classes were allocated. Where any maximum likelihood class was allocated with a probability <50%, the other spectral subclass probabilities were summed at Broad Habitat level to see if another Broad Habitat was more appropriate (i.e. if its spectral subclasses cumulatively took a dominant percentage of the overall probability). If so, the lead Subclass/ Variant of the Broad Habitat (usually the second choice subclass) took precedence. It is recognised that this was a pragmatic solution which does not take full account of the true statistical requirements, but it was one which was easily applied and achieved the desired effect.

The probability rule was the first of all the contextual rules to operate as clearly its results had a bearing on every other contextual step beyond. In effect, it is just an extension or refinement of the maximum likelihood method.

Terrestrial/maritime corrections
LCM2000 used the coastline defined in construction of LCMGB. In the vast majority of the cases, the coastline was effectively unchanged in the decade since the first recording; manual intervention corrected minor areas of apparent erosion and accretion. Application of the mask was similar in concept to that of 1990. However, the operation was very different. There was, first, the potential to examine GIS-intersections rather than using the indirect arithmetic process of 1990. The parcel-based application gave the scope to identify whether a parcel simply touched the 'shoreline', or was predominantly maritime or entirely maritime before applying the rule-base in corrections. It seemed logical to let a 'predominantly maritime' location define the context in most cases.

NDVI correction
In a few instances, the normalised difference vegetation index (NDVI) was calculated for the parcel and used with the maritime mask to indicate the presence/absence of vegetation. This allowed extension of maritime corrections to distinguish bare 'littoral sediment' or vegetated 'saltmarsh' subclasses. The NDVI was also used to refine the classification of unknown 'arable and horticultural' crops to distinguish winter-sown Variants from those which were spring-sown – an important consideration, for example, to users modelling groundwater-quality or bird distributions.

Elevation correction

Elevation was a valuable determinant of correct and incorrect labelling. It was used to identify urban areas above the normal altitude for settlements (e.g. in reality bare hill tops or upland quarries). It defined the zone within which semi-natural vegetation would be re-coded to the montane class: an altitude of >600 m (see Ratcliffe & Thompson, 1988) was set for the 'montane habitats' and applied to any parcels of vegetation above this threshold. Low elevation levels helped to define floodplain vegetation which might in some areas be labelled as 'fen, marsh and swamp'. 'Supra-littoral rocks' and 'supra-littoral sediments' were those bare areas with a maritime context and an elevation which exceeded the normal shore levels.

Slope and aspect

Slope and aspect measures were used to select other areas of potential confusion, especially those associated with shading on northwest-facing slopes or unusually bright illumination on southeast-facing slopes. Differential illumination due to aspect had largely been removed before classification, by modelling slope and aspect and compensating to give values corrected to simulate a theoretical horizontal surface illuminated from directly overhead. However, residual differences gave distorted reflectance estimates which caused mis-classifications. Selection by spectral subclass, slope and aspect identified problem areas. A good example was the high incidence of dark 'coniferous woodlands' on northwest-facing slopes, seemingly with little or no reflectance, which were often mis-classified as 'water'. The steepness of the slopes clearly distinguished the worst such problems and allowed their correction.

Neighbourhood-based corrections

In LCM2000, suburban parcels could be mis-classified as arable land, just as was the case with mixed pixels of bare and vegetated cover in LCMGB. Neighbourhood searches identified erroneous 'arable and horticultural' parcels within 'suburban' and 'urban' contexts, and changes were made to these. It was possible to vary the measure of 'urban' context: for example, sometimes it might be sufficient for a parcel to be dominated by 'suburban and urban' neighbours; else, it was possible to define that they should be entirely surrounded by 'suburban and urban' parcels. The rule was constructed according to whether the impacts of the corrections were to be stringent or relatively mild.

Interactive inputs

'Arable' fields were often mis-classified as 'urban' or 'suburban' subclasses. Because small settlements occur in the farmland context, 'urban' areas surrounded by 'arable' land could not, without question, be changed to the 'arable' class. As a result no correction had been made for these problems in 1990. The GIS allowed greater subtlety in LCM2000 operations. The selection process first targeted just those parcels classified as particular problematic 'suburban' spectral subclasses; for these parcels the probability list was checked for 'arable' subclasses lower in the list. Further sub-selection according to low probability levels was often used to refine the selection of predominantly erroneous parcels. Further sifting often drew upon zonal location (e.g. defining just a part of the scene with a confusing soil colour background). Finally, manual intervention eliminated the few remaining real 'urban'/'suburban' areas from the selection before re-coding the erroneous 'suburban' parcels to the relevant 'arable' subclass (usually the highest scoring in the probability list).

14.3.8   Contextual refinements and thematic extensions

Consistent class coding
An evolution of the classification (with class-definitions published after the commencement of mapping in late 1998 (Jackson, 2000)), meant that some subclass-aggregations evolved and the nomenclature altered over time. A rule-base was established to ensure that any outdated nomenclature or alphanumeric coding on earlier production runs was updated to give consistency of output.

Peat masking
The 'dwarf shrub heath' and 'bogs' Broad Habitats could both comprise cover dominated by 'heathers' and similar 'ericaceous' species. 'Bogs' are characterised in the field by the presence of peatland indicator plant species, which occur in low proportions and consequently have little influence on spectral signatures. Even the waterlogged character of the 'bog' is obscured
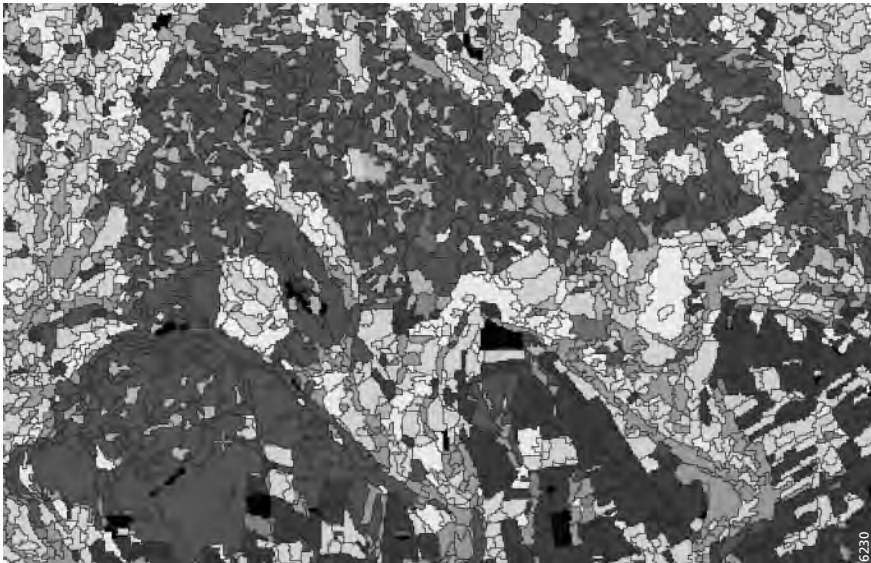
Seas / estuary		Coniferous woodland	
Inland Water		Arable land	
Supralittoral rock / sediment		Agricultural grass	
Saltmarsh		Semi-improved grass	
Grass heath / moor		Semi-natural grass	
Bog		Fen / marsh swamp	
Closed dwarf shrub heath		Suburban	
Open dwarf shrub heath		Urban	
Montane habitats		Inland bare ground	
Broad-leaf woodland			

Figure 14.2 – Classified land parcels of the satellite subscene given in figure 14.1. Please consult the enclosed CDROM for a full colour version.

by the dense vegetation cover. Class definitions (Jackson, 2000) state that a 'peat depth… greater than 0.5 m … is classified as bog for the purposes of the Broad Habitat Classification.' With this in mind, a British Geological Survey map showing peat drift >0.5 m deep was used to determine the context of 'dwarf shrub heath' and 'bog' subclasses. Any 'heath' on deep peat was re-coded to 'bog' and any 'bog' which did not coincide with peatland was re-coded to 'heath' (or 'grass moor', depending on the key cover-component).

Soil sensitivity masking
Conservation-users wished to distinguish the 'acid', 'calcareous' and 'neutral' components of the 'semi-natural grasslands'. While distinctive spectral characteristics might be associated with some grasslands, it was considered impossible to use these universally for accurate mapping. An acid-sensitivity map (Hornung et al., 1995) was used to extend labelling of semi-natural grasslands. This map defined acid sensitivity classes based on soils as: highly sensitive – pH<4.5 (i.e. truly acid); moderately sensitive – pH>4.5 and <5.5. (treated for these purposes as neutral but really slightly acid); and low sensitivity – pH>5.5 (actually with neutral and calcareous components).

CORINE
The 'arable and horticulture' Broad Habitat includes perennial crops such as 'berries and orchards'. These are difficult if not impossible to distinguish spectrally; hence the class relies upon knowledge-based corrections using interpretations made for the CORINE Land Cover map (Brown & Fuller, 1996). The CORINE vector product had an 25 ha minimum, substantially larger than that of LCM2000. Nonetheless, the map helped to identify and label the larger examples of orchards.

14.3.9 LCM2000 attribute data
Figure 14.2 shows a section of final output map, with the parcel structure overlaid. This level of detail is available for all the United Kingdom, with some 6.6 million land parcels in all. Behind this vector data structure lies a detailed GIS database. The attribute database records all the information described above: the images used for the generation and classification of each parcel; the probabilities for the top-five classes; the parcel-size and the number of core pixels. Externally derived contextual attributes, used in corrections and thematic extensions, remain with the main database (though licensing arrangements restrict dissemination of these data). All contextual analyses were also recorded as parcel attributes, so that each parcel's exact processing history can be traced. As it is possible for a parcel to undergo a series of contextual alterations, each step in the sequence of alterations is recorded in the attribute database. This gives any user the scope to reverse or refine contextual alterations, should they wish to do so.

14.3.10 Impacts in quantitative terms
There was no part of LCM2000 which did not draw upon contextual methods in production. All land areas were mapped through image segmentation prior to per-parcel classification. Per-pixel classifications of the inter-tidal zone were made in context of the pre-defined maritime zone. Both stages impose contextual constraints on the resulting classification. As a consequence, the entire United Kingdom was mapped using spatial-contextual procedures. The consequent GIS data structure relates closely to the true structure of the landscape. This

is important for all ongoing analyses, including those contextual procedures applied in post-classification stages.

The post-classification procedures played a substantial part in the derivation of accurate parcel labels. Knowledge-based corrections were highly significant elements of the LCM2000 classification; and thematic extensions of the classifications using contextual data were essential to meet user needs. To quantify the impacts of these post-classifications stages, a sample of parcels was examined to assess the role played by the different contextual elements. First, five 100 km BNG squares were chosen on a stratified random basis, out of forty-six such squares dominated by land in the United Kingdom. Then a sub-sample of parcels from each square was taken at random. This gave 327675 parcels in all or approximately an 5% sample of United Kingdom land area. The sample represents the full variety of landscapes including: the Highlands of Scotland; marginal and upland areas of North Wales; mixed pastural and arable landscapes of North East England and the Scottish borders; pastural, moorland and coastal landscapes of South West England; and lowland arable landscapes of East Anglia.

The probability rule, which re-examined maximum likelihood allocations, affected 5.4% of all parcels. The use of spectral subclasses in training the classifier had simply been an attempt to provide training data with a statistically normal distribution (Groom et al., 1996). It has been an unfortunate consequence that the procedure split the probabilities for any Broad Habitat which had many spectral subclasses. It is likely to be a weakness of maximum likelihood classification in general that this sort of problem can arise. The strength of LCM2000 is the depth of its database (Smith & Fuller, 2001) allowing the problem to be examined and rectified after classification.

Contextual corrections affect 11.9% of all parcels. This is a very substantial proportion. It emphasises the fact that achievement of the Broad Habitat classification – even the Target classification – was only possible with a very substantial element of post-classification correction to parcels which had been erroneously labelled by spectrally based classification.

The analyses which extend rather than correcting the classifications alter 14.8% of class labels. This substantial impact is not surprising as there had been little or no attempt in training and classification to make the distinctions which later would be made by universally applied contextual analyses. The relatively high proportion of contextually based class-extensions is thus a direct measure of how far user-needs outstripped the scope of straightforward spectral classifications.

In all, 25.7% of parcels were either altered or had their classifications extended using post-classification contextual analyses (or both). In areal terms, 23.7% of the land area under examination was affected – a value close to, but slightly smaller than, the proportional number of parcels. This suggests that larger parcels might have needed slightly less contextual alteration – not surprising as very small parcels have a limited number of pixels and may give poorer estimates of true reflectances for accurate cover classification.

The greatest impact of the alterations was in upland and semi-natural areas – 38.0% of parcels were affected in the central Highlands of Scotland, compared with just 12.0% in lowland

arable farmland East Anglia. This is because the peatland and acid sensitivity rules, both with extensive impacts, applied most commonly in marginal and upland areas.

While it has not been possible, yet, to quantify exactly what proportion of reallocations has been beneficial, experience and logic suggest that the majority of changes were correctly applied. Inspection alone showed that the corrections were extremely important in improving the appearance of the map, removing glaring errors and generally giving a 'cleaner' appearance to the product. The thematic extensions of the map have been more mixed in their impacts. Most peatland masking correctly identified peatland Habitats, but not all peatland Habitats were identified – the peat drift map was very conservative in its estimates of deep peat distributions. In contrast, the acid sensitivity rules substantially over-estimated 'neutral' and 'calcareous' components of grasslands, though 'acid' components were mostly correct. It is a consequence of using external data that the accuracy of the resulting map is dependent upon the accuracy of the best available contextual data – and that, sometimes, while such data may improve one's knowledge of a class, the inputs may be far from perfect.

It is testimony to the importance of contextual analysis that around a quarter of all parcels needed post-classification contextual treatment. It is a clear endorsement of the value of the technique in correcting, refining and extending image classification procedures. It is perhaps, too, a warning as to the limitations of standalone spectral classifications. Had contextual corrections not been applied, then, without the corrective element, the accuracy of LCM2000, thought to be approximately 85% at Target class level (Fuller et al., 2002), would have dipped to about 70% – well below levels that most users would have found acceptable. Also, had the post-classification extension of classes using contextual data been omitted, then the Broad Habitat classification would have been unachievable.

The final question which potential users of contextual techniques might ask concerns the time taken to apply these procedures, some of them highly interactive. Segmentation and per-parcel classification undoubtedly takes much longer than per-pixel classifications. However, the improvements in accuracy and, more importantly, in the data structure and attribute depth, give the product an unquestionable advantage over pixel-based outputs. And, because the data structure improves post-segmentation manipulations of the data – from training though classification to post-classification corrections – some of the time-penalties incurred in construction are counteracted by easier analyses in later stages. Realistically, it would have to be said that the procedure adds about 50% extra to the time for map-construction. However, the extra detail provided over and above that of LCMGB makes this investment very worthwhile. It is highly unlikely that any future update of LCM2000 would go back to a per-pixel classification. In fact, there is considerable scope for using the parcel-structure of LCM2000 to interrogate new images in future updates, potentially saving large amounts of time in the process. Indeed, the parcel-based structure may also streamline a wide variety of operational applications of the data, resulting in further time-savings in the long run. The post-classification contextual analyses are less time consuming than the segmentation stages. It is estimated that, in the entire sequence of processes, post-classification contextual analysis occupies only about 10-15% of the time. Once a reasonably satisfactory map had been produced by the iterative processes of training and classification, it was almost always quicker to deal with specific and relatively minor problems though contextual selection

and correction, rather than attempting subtle changes to the training set and making new classifications. This is because, once maps were nearing an acceptable appearance, re-training and re-classification appeared always to correct some problems but to introduce new ones, and iterations seemed potentially to be never-ending. This is simply a reflection of the fact that spectral classification alone was not good enough to serve the needs of the wide ranging classification of LCM2000. Contextual procedures thus had an indispensable role to play and justified their use.

14.4   Conclusions

Contextually based analyses, through segmentation and parcel-based classification, provided a vector data structure which relates far more closely to the real World than one based upon the gridded raster structure of the original input images. It therefore helped to analyse pixels in the context of their parent land parcel and helped to improve the accuracy and usefulness of the data. The consequences however were further reaching than just this, as the results allowed much more subtle and powerful contextual analyses to be applied after classification, further increasing accuracy and extending the thematic details offered by LCM2000. However, thematic extension to include the full range of Broad Habitats was not entirely successful. Many of the external datasets were inadequate in defining what mostly should have been clear-cut contexts for the Broad Habitats. It was found for example that the peat drift gave a very conservative picture of the true extent of deep peat soils. The acid sensitivity mask was biased towards over-recording 'neutral' and 'calcareous' components. Moreover, the 1 km grid-based product was very much coarser than the LCM2000, with its minimum mappable unit of >0.5 ha. However, there was no affordable alternative dataset with better class intervals or a finer resolution. Therefore, these data had to be used if any such distinction was to be made. Users must judge for themselves whether the class-intervals provide meaningful data for their purposes or whether they are better using the data at the Target class level, 'semi-natural grasslands', perhaps with their own soils map or other contextual data to qualify the grassland types. There are soil maps which could have improved both distinctions, but these were only available at a much higher price than the customers felt they could justify. This begs questions, then, as to whether extensions to a full Broad Habitat listing, using inadequate external data, can be justified. This is a question more easily answered by those who demanded the distinctions. If, with hindsight, the investment in more expensive external data is justified, users can of course selectively re-work the data, owing to the depth of the LCM2000 attribute database. For other users, the Target classification, established in concept before mapping started, represents a realistic assessment of what was achievable without extension using questionable external data.

It is an important finding, with much wider relevance, that 'the maximum likelihood class' is not necessarily the 'most likely' cover type when spectral subclasses are aggregated to match a narrower target classification. This observation would probably apply equally elsewhere; but for most practitioners, this fact would be obscured by the paucity of probability data held on their classified outputs. This problem would be especially true of per-pixel classifications where, at best, it may be possible to record the probability of the top-scoring class and generally no more. Producers need to think about such problems and to question whether

they can make post-classification corrections similar to those used in LCM2000. Perhaps, in fact, there should be refinements which take account of the statistical issues of class aggregation; and improvements in image analysis software might consider class-similarities and maximum likelihood aggregations during processing.

In summary, contextual analysis was an essential component of the LCM2000 production process, providing a data structure which relates to the real World and is much more amenable to further analyses during production and to operational use of the data after production. Post-classification procedures were also of relevance for about a quarter of the map area. They were crucial in achieving reasonable levels of accuracies. They were essential to extend the classifications to meet wider user needs.

Chapter 15

A Contextual Approach to Classify Mediterranean Heterogeneous Vegetation using the Spatial Reclassification Kernel (SPARK) and DAIS7915 Imagery

Raymond Sluiter, Steven M. de Jong, Hans van der Kwast & Jan Walstra

15.1 Introduction

Conventional methods for spectral classification of remote sensing images are per-pixel based. As long as the spectral response of the objects is spatially homogeneous, these methods yield mapping units of suitable size and uniformity. However, if the spectral response of the objects is spatially heterogeneous, these per-pixel classifiers are inappropriate and result in salt and pepper patterns. Especially in vegetation studies such classification results with scatter are difficult to use for survey or as input to ecological models. For example open heterogeneous vegetation patterns as commonly found in Mediterranean and in semi-arid regions cannot be characterised by per-pixel classifiers in a satisfying way.

Important progress has been made in contextual image classification methods that include the spatial domain to analyse imagery (Atkinson & Quattrochi, 2000). These methods consider not only the per-pixel spectral information but also the spectral information of neighbouring pixels during the classification process. Methods in literature can be divided in three broad categories.

1 Methods based on spectral information captured by the image like the Spatial Co-occurrence method (Franklin & Peddle, 1990), variogram methods (Curran, 1988; Woodcock et al., 1998) and fractal methods (De Jong & Burrough, 1995).
2 Methods that apply segmentation algorithms on images to identify objects to be classified, for example e-Cognition (Definiens-Imaging, 2003; Blaschke et al., 2004).
3 Methods refining previously classified images; these methods are referred to as contextual re-classifiers. Examples are the local frequency distribution method (Wharton, 1982), the Spatial Reclassification Kernel method (Barnsley & Barr, 1996) and the Spatial and Spectral Classification method (De Jong et al., 2001).

The method used in this study, the Spatial Reclassification Kernel (SPARK) was originally developed by Barnsley & Barr (1996). SPARK accounts for the spatial pattern of previously spectrally classified pixels and applies a re-classification on the basis of pre-defined reference

kernels. SPARK is based on the assumption that each land use type can be identified by its composition of neighbouring, spectrally classified pixels within a user-defined kernel. SPARK has been tested so far on urban areas in London, UK (Barnsley & Barr, 1996), in Ouagadougou, Burkina Faso (De Jong et al., 2000) and in The Netherlands (Harts et al. 2002).

In this chapter we present and test the use of SPARK in a non-urban environment: semi-natural Mediterranean heterogeneous vegetation. The main objective of this study is to create a detailed vegetation map of a Mediterranean area in southern France on the basis of airborne spectroscopical DAIS7915 images using the SPARK approach. We describe the different stages of the SPARK reclassification process in detail and evaluate the results by comparing them to vegetation maps produced by conventional per-pixel classifications and to data collected during field campaigns.

15.2   The concept of SPARK

The Spatial Reclassification Kernel (SPARK) is a contextual re-classification method. The conceptual idea behind SPARK is that the land use types of interest can be characterised by the spatial arrangement and size of objects. An example for natural areas is the spatial arrangement of objects like trees, shrubs, grass, bare soil patches and shade. An example for urban areas is the spatial arrangement of objects like streets, buildings, bare areas, shade, trees and grass. SPARK examines the local, spatial patterns of objects in a square kernel. Based on the arrangement of adjacent pixels in the kernel SPARK assigns a new class to the centre pixel. Consequently, the SPARK-method consists of three phases (Barnsley & Barr, 1996):

1   Produce a land cover map using any type of spectral classifier from a remotely sensed image, further referred to as the 'initial land cover map'.
2   Define SPARK decision rules based on local, spatial patterns of objects in typical heterogeneous and homogeneous land use types.
3   Reclassify the initial land cover map into heterogeneous and homogeneous land use types, based on the decision rules of step 2.

For the first phase, the production of the initial land cover map, several methods can be used, for example segmentation and split and merge techniques (Gorte, 1998), unsupervised clustering techniques and supervised classification techniques. Until now migrating mean clustering (Harts et al., 2002) and maximum likelihood classification (Barnsley & Barr, 1996; De Jong et al., 2000) have been used in SPARK studies.

During the second phase reference kernels for known land use types are defined. These kernels are referred to as characteristic template matrices (T_k-matrices) and are based on training datasets in the initial land cover map. Each land use type is identified by one or more T_k-matrices. Examples of characteristic template matrices for natural vegetation can be found in figure 15.1. Within each T_k-matrix the frequency and the spatial arrangement of land cover classes positioned next to each other as well as diagonally (respectively edge and vertex) are counted. Each pair of neighbouring pixels is called an adjacency event. The results

of counting the adjacency events are expressed by an adjacency event matrix (figure 15.1). As shown in figure 15.1, the dimension of the matrix depends on the number of land cover classes, while the sum of the frequencies depends on the kernel size (Barnsley & Barr, 1996).

The third phase of the SPARK process involves the counting of the frequency and the spatial arrangement of land cover classes in the initial land cover map. For each pixel, an adjacency event matrix is produced by means of a moving window. The adjacency event matrices of the initial land cover map are called M-matrices.

The M-matrices of the initial land cover map are compared with all T_k-matrices using the following equation (Barnsley & Barr, 1996):

$$\Delta k = 1 - \sqrt{0.5 \cdot N^2 \cdot \sum_{i=1}^{c} \sum_{j=1}^{c} (M_{ij} - T_{k_{ij}})^2} \tag{15.1}$$

Where:
M = adjacency event in ij matrix
T_k = template matrix for land use class K
N = total number of adjacency events in the kernel
c = number of land cover classes in the per-pixel classified image

The resulting term Δk is an index of similarity between the M-matrix and the T_k-matrix. The values can range from 0 to 1. If Δk equals 0, they are different, while a value of 1 means that they are identical.
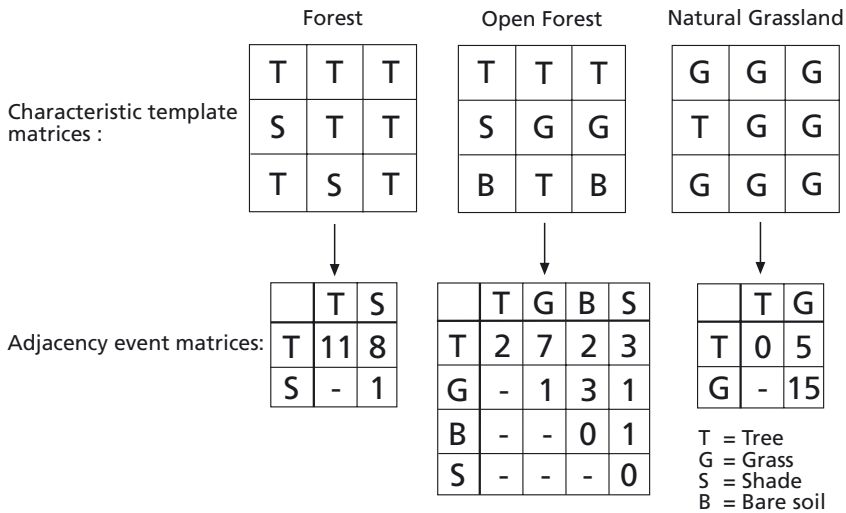

Figure 15.1 – Simulated 3 by 3 kernels of different natural vegetation types with corresponding adjacency event matrix. Only the upper triangular is considered because $M_{ij} \equiv M_{ji}$. (Barnsley & Barr, 1996).

Finally, the central pixel in the kernel is assigned to the land use class of the corresponding T_k-matrix with the highest Δk. More template kernels can be defined for each output class. The use of multiple template matrixes has the advantage that subtle differences in spatial arrangement of the pixels in the initial land cover map can be accounted for, resulting in a more accurate classification of a particular pixel (Barnsley & Barr, 1996).

We will describe two points in more detail that determine the successful application of SPARK: the selection of representative T_k-matrices and the determination of the optimal kernel size:

1   The selection of representative T_k-matrices for the SPARK algorithm is an iterative process alike to the selection of training areas in conventional image-classification procedures. The evaluation of Δk plays an important role in this stage. With the current version of SPARK the Δk of the selected T_k-matrices can be evaluated in a Δk image and a Δk cross table. The Δk image is a helpful evaluation tool to assess the performance of the SPARK algorithm. The Δk image presents the maximum Δk of all T_k-matrices for a pixel and gives the user insight in which land use types are not accurately presented by the T_k-matrices and where these land use types are located in the image. A low Δk indicates a poor match with the assigned land use type. The Δk cross table can be used to investigate the uniqueness of a T_k-matrix. A T_k-matrix may have a high Δk with other T_k-matrices associated with the same class, but should have a low Δk with T_k-matrices associated with other classes.

A T_k-matrix should be as representative or unique as possible. However, in practice most land cover classes do not have a totally unique response and more T_k-matrices are needed. Theoretically, more complex patterns, with more input classes in the T_k-matrix, are less likely to have a unique T_k-matrix. This is because the dimension of the adjacency event matrix increases and the adjacency event matrix is more variable when more classes are involved. This is shown by the open forest class in figure 15.1. Moreover, the chance that a particular M-matrix is similar to one of the T_k-matrices decreases when there are more thematic input classes in the input image. As a result the number of thematic classes in the input image should not be too large.

2   The optimal kernel size depends on the resolution of the images and the range of the spatial variation in the initial land cover map (Barnsley & Barr, 1996). Kernels that are too large in respect to the land use objects will increase the effects of edges, while too small kernels possibly do not include all spatial variation. Van der Kwast & Walstra (2001) studied the use of the range distance of semivariograms for estimating the optimal kernel size, for both DAIS7915 imagery and Mediterranean vegetation data. Their conclusions were that variogram analyses do not give unambiguous answers to the question about the optimal kernel size. Because in most studies the range of usable kernels is rather limited (typically between 3 by 3 and 15 by 15 pixels), kernel size can also be considered like a tuning parameter, which can be iteratively obtained by classifying the initial land cover map with different kernel sizes and evaluating the accuracy of the results.

Theoretically, the optimal kernel size may differ for different land cover types. Based on the SPARK algorithm we can expect the following two results:

1   Complex patterns will benefit less from larger kernel sizes because the chance that a particular M-matrix is similar to one of the T_k-matrices decreases, since the variability in the adjacency event matrix increases with increasing kernel size.

2   Pure homogeneous classes will not benefit from larger kernel sizes because edges will influence the classification. However, this is inherent for each kernel approach and hence the SPARK algorithm, which is exclusively developed to classify heterogeneous classes but in practice will be used for both heterogeneous and homogeneous classes.

The implications of the choice of number of thematic classes in the initial land cover map, the selection of the T_k-matrices and the effect of kernel size on the final result will be discussed in more detail in the next paragraphs, illustrated by a case study.

15.3   Case study

15.3.1   Introduction

We tested the suitability of SPARK for mapping Mediterranean heterogeneous vegetation in the Peyne study area, southern France. During 4 field campaigns in the summer of 1998, 2000, 2001 and 2002 we collected detailed information on vegetation. We performed the SPARK classification on high resolution airborne DAIS7915 imagery which was collected in the summer of 1998. We asked the following research questions:

- What is the best production method for the initial land cover map?
- How is the performance of SPARK compared to conventional methods?
- What is the effect of kernel size on the overall accuracy of the classification?
- Is it useful to use different kernel sizes for different classes in one SPARK classification run?

15.3.2   Study area

The Peyne study area is located in the Languedoc in southern France approximately 60 km west of Montpellier, central coordinates are 43 33 N, 3 18 E (figure 15.2). The Languedoc area is characterised by a sub-humid Mediterranean climate with hot, dry summers and cool winters. The area has known a rural depopulation over the last 50 years and farmlands are reverting to shrublands and woodlands. Because of these disturbances, various stages of re-growth and dispersion of forest and shrub communities are found in the Languedoc area (Caraux-Garson et al., 1999).

The area is located at the fringe of the 'Massif Central' and is characterised by various geological substrates ranging from sandstone formations, limestone plateaus, dolomite formations, volcanic tuffs and volcanic basalt outflows. On these geological substrates various lithological substrates are found like regosols, lithosols, brown soils and calcareous soils (Bonfils, 1993). The large variation at short distances in these substrates, of elevation, climatic factors and human disturbance is responsible for a wide range of growing conditions and hence, a large variety of vegetation types.

The central part of the area is covered by a Mediterranean oak forest dominated by Quercus ilex (holm oak) and by lower 'garrigue' shrublands. The oak forest is believed to represent
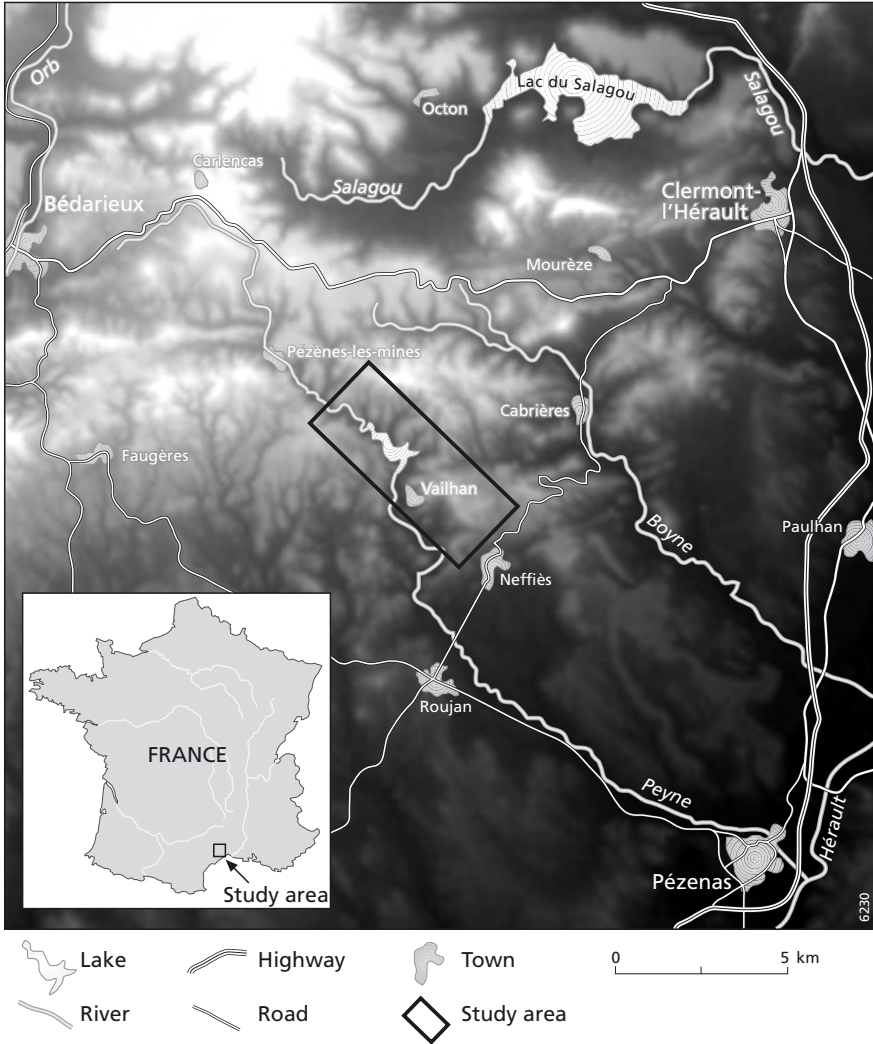
Figure 15.2 – Location of the study area in southern France.

the regional Mediterranean climax. Human and natural disturbance of the ecosystem occur scattered over the test area due to forest fires, open mining and ongoing extensive agricultural activities. The southern part of the area is used for agricultural purposes, mainly for vineyards and orchards.

15.3.3 Vegetation
The natural vegetation in the area is a degraded stage of the evergreen forest, consisting of shrubby formations referred to as 'matorral' by Tomaselli (1981). Tomaselli's definition of matorral is: 'a formation of woody plants, whose aerial parts are not differentiated into trunk

and leaves, because they are much ramified from the base, and are of shrubby habit'. Matorral can be further discriminated by height and density.

The highest and most dense matorral type is named high matorral or maquis (Tomaselli, 1981). It consists of dense and impenetrable thickets of tall shrubs, 2-5 m high. The shrubs have densely twiggy branches and small dark green leathery leaves. This vegetation type may be considered as a regional climax. Quercus ilex (holm oak) and Arbutus unedo (strawberry tree) are the most dominant species in these dense maquis vegetations. Usually an undergrowth of herbaceous species is absent because little light penetrates through the dense shrubs.

The Middle matorral type is also named garrigue. The height ranges from 0.6 to 2 m. Garrigue consists of low scattered bushes interspersed with bare patches of rock, sand or stony ground (Le Houérou, 1981). Many of the shrubs are spiny and have small leather-like leaves often covered with woolly hairs (Polunin & Huxley, 1972). When the density of the shrubs is not too high, an undergrowth of herbaceous species may be present.

The lowest matorral type is called low matorral, landes or steppe. Besides some very low shrubs (<0.6 m), the vegetation is dominated by herbaceous species: annuals as well as some woody perennials (Polunin & Huxley, 1972). In the Peyne area landes is particularly found on calcareous soils and abandoned vineyards.

Many different matorral formations are found in the Peyne area. These formations are the result of succession towards a higher stage or degradation to a lower stage, the latter due to human activities or natural processes, such as soil erosion and fires.

A. Maquis: trees >2.0 m
 1. **Coniferous forest: with coniferous trees, cover >75%**
 2. **Dense maquis: cover >75%**
 3. **Discontinuous maquis: cover 50 – 75%**
 Open maquis: cover 25 – 50%
  4. Open maquis with herb undergrowth: herb cover >25%
  5. **Open maquis with shrub undergrowth: shrub cover >25%**
  6. **Open maquis with herb and shrub undergrowth: undergrowth >25%**
  7. Open maquis without undergrowth: undergrowth <25%

B. Garrigue: shrubs 0.5 – 2.0 m
 8. **Dense garrigue: cover >75%**
 9. **Discontinuous garrigue: cover 50 – 75%**
  Open garrigue: cover 25 – 50%
  10. **Open garrigue with herb undergrowth: herb cover >25%**
  11. Open garrigue without undergrowth: undergrowth <25%

C. Landes: herbs <0.5 m
 12. **Dense landes: cover >50%**
 13. Open landes: 10 – 50%

D. Bare areas & other
 14. **Bare soils, tarmac & build-up**
 15. **Water**
 16. **Vineyard**

Figure 15.3 – Hierarchical land cover classification scheme used for field survey and for image analysis. Classes used in the 12-class SPARK classification are shown in bold.

For these dominant vegetation types a hierarchical classification method was developed, based on the vegetation composition, coverage and structure. It consists of three levels, allowing merging of classes during the classification process. The classification scheme was used for field survey and yielded the basis for image classification. The scheme is shown in figure 15.3.

15.3.4 DAIS7915 imagery

The Peyne area was one of the research locations of the European Degradation Monitoring project (Hill 1997). In 1997 and 1998, experimental flights were carried out by DAIS7915. Flown aboard a Dornier 228, DAIS7915 collects images in 72 optical bands with a spectral resolution of approximately 25 nm. and in 7 thermal bands with a spectral resolution of 0.9 μm. (Strobl et al. 1996). The images used in this study were collected on June 28th 1998 at a nominal altitude of 3300 m. resulting in a spatial resolution of 5.8 meters for the study area. A radiometric correction of the DAIS7915 images was carried out on the 72 optical bands as described in detail in De Jong et al. (2003). The radiometric correction comprised:

1 A cross track illumination correction (Kennedy et al., 1997);
2 A minimum noise fraction (MNF) to correct for system related striping (Schowengerdt, 1997; Van der Meer & De Jong, 2000);
3 An empirical line correction to convert from radiance to reflectance using field spectra of dark and bright targets (Van der Meer & De Jong, 2001).

An accurate geometrical correction was applied for locating the field observations as precise as possible. Geometrical distortions of the images result from altitude deviations and other movements of the aircraft. The ground control points (GCP's) were acquired from GPS measurements and from topographical maps. A third order polynomial was applied and the image was resampled using nearest neighbourhood resampling with an overall RMS of 2.6 pixels. Finally the reflectance of the geocorrected image was topographically normalised using a Lambertian topographic normalisation model (Colby, 1991) in combination with a high resolution DEM produced by IGN France.

15.3.5 Field survey

Field campaigns were carried out in the study area during June 1998, June 2000, June 2001, June 2002 and September 2002 to collect the necessary data for image analysis. This field survey comprised the acquisition of ground truth data for both the initial land cover map and the SPARK classification map. Some sites were visited each year to check if the classification of sites was influenced by succession of the vegetation during the time span of the different field campaigns. No difference in vegetation class could be identified in these plots from 2000 to 2002. Moreover, some sites were visited twice in June & September 2002 to check for seasonal variation. Again no difference in vegetation class could be identified between these months in the plots. Therefore we assumed that the use of the 1998 DAIS7915 imagery in combination with the data collected in later years was a valid approach. The sites with a support of 20 by 20 meter were selected in a stratified-random way in the field. On every site we collected information of total vegetation cover, plant species cover, plant species abundance and vegetation height. Visual observations were checked by line transects and vertical photographs of the vegetation. All observations were classified according the 16 class classification scheme presented in figure 15.3. In total 820 sites were sampled. Half of

these were used as training sites, while the other half was used for validation and accuracy assessments.

15.3.6 Modified SPARK NDVI approach

The first step in the SPARK approach is the selection of the production method of the initial land cover map. In an earlier SPARK pilot study carried out by Van der Kwast & Walstra (2001) a maximum likelihood classification with nine classes was used: dense maquis, coniferous forest, dense garrigue, dense landes, bare red marls, bright bare soils, dark bare soils, water bodies and vineyards. With an overall accuracy of 86.3% this classification was quite accurate but not very useful for further SPARK reclassification because of the following points:

1 The classification method failed to identify bare soil patches necessary for further SPARK processing. Bare soil patches could not be detected in between vegetation patches because soil patches are also included in the landes and garrigue training areas. Feature space plots of the training areas also show confusion between these classes.

2 Heterogeneous vegetation types were not separated by the classification into the required pattern of bare soil, grass, shrubs and trees. Instead the image was classified in homogeneous clumps of trees, shrubs and grass on which reclassification is not useful.

We tested several alternatives to produce an initial land cover map that better represents the heterogeneity of the vegetation observed both in the field and in the DAIS7915 image. The alternative techniques were supervised approaches like maximum likelihood classification using better defined classes and training areas, minimum distance to mean classification, nearest neighbourhood classification, spectral angle mapping (Kruse et al., 1993), NDVI level slicing and unsupervised approaches like isodata and K-means (Schowengerdt 1997). In the case of maximum likelihood classification where data volume and multi-collinearity of the multiple DAIS7915 bands caused erroneous results we applied a principle component transformation and used the first four PCA-bands for classification. We obtained the best final classification results with a combination of maximum likelihood classification and NDVI level slicing. This procedure consists of two steps:

1 Perform a maximum likelihood classification with 7 classes: coniferous forest, maquis, garrigue, landes, bare soil, water and vineyard.

2 Next we use the classified classes coniferous forest, bare soil, water and vineyard as a mask for a NDVI image. We calculated a Landsat TM compatible NDVI image by averaging DAIS bands 8-12 for TM band 3 and by averaging DAIS bands 16-25 for TM band 4. This NDVI image of the unmasked natural vegetation is linear level sliced into 6 to 32 NDVI-classes. The choice of the number of NDVI-classes will be discussed in the next paragraphs. Finally the masked maximum likelihood image and the NDVI image are merged into one 'initial NDVI-land cover map'. An example of an initial NDVI-land cover map can be found in figure 15.6a.

Based on the initial NDVI-land cover map and field reference data we determined T_k-matrices for the SPARK classification. We evaluated the Δk of the selected T_k-matrices with the Δk image and a Δk cross table. T_k-matrices which had high cross table Δk values with T_k-matrices of other classes were excluded from the analysis. Based on the Δk image some extra

kernels were added to obtain an optimal number of T_k-matrices. Kernels of different sizes were created by using the same centre pixel for all different kernel sizes.

Finally, we performed the SPARK classification on the combined initial NDVI-land cover map. Only 12 classes were used in the accuracy assessment because the number of observations in the field of certain classes in the classification scheme of figure 15.3 was too low. These twelve classes are highlighted in figure 15.3. To test the effect of kernel size, the whole analysis was performed by using kernel sizes of 3 by 3, 5 by 5, 7 by 7, 9 by 9 and 11 by 11 pixels. To test the effect of the number of NDVI-classes the analysis was also performed on initial NDVI-land cover maps with 7 maximum likelihood classes merged with 6, 8, 10, 12, 16, 24, 27 and 32 NDVI-classes computed by level slicing. In combination with the 5 kernel sizes the total number of 'classification runs' equals 40. For every classification run overall accuracy, kappa, producer and user accuracy for individual classes were evaluated, based on the control set as proposed by Congalton (1991). We compared the final 12-class SPARK result with the classification result of the maximum likelihood classification for the same set of classes.

15.3.7 Results

The results of the analysis of the five different methods to produce the initial land cover map are shown in table 15.1. The maximum likelihood classification with 7 classes performs best with an overall accuracy of 81.0%. The next best result is the spectral angle mapper classification. The difference in overall accuracy between these two methods is mainly caused by the fact that the spectral angle mapper classifier cannot accurately distinguish shadows from coniferous forest. The DAIS7915 PCA image and the maximum likelihood classification are shown in figure 15.4a and 15.4b, it is clearly visible that the heterogeneous vegetation in the image is classified in homogeneous clumps of trees, shrubs and grass on which the SPARK reclassification algorithm cannot be applied successfully.

To compare the results of the SPARK reclassification with results of conventional methods we also performed the maximum likelihood classification with 7, 10, 12 and 15 thematic land cover classes (table 15.2). The overall accuracy values are shown in figure 15.5. The overall accuracy drops to 60.7% as soon as heterogeneous vegetation types are taken into account in the 10-class classification. The 12-class maximum likelihood classification with an overall accuracy of 56.2% will be the reference to compare the 12-class SPARK classification to as discussed in the previous section. The 12-class maximum likelihood classification is shown in figure 15.6b.

Table 15.1 – Classification accuracy for 7 classes (coniferous forest, maquis, garrigue, landes, bare soil, water and vineyard) using different methods.

Classification method	Overall accuracy %	Kappa	Remarks
Maximum likelihood	81.0	0.78	
Spectral angle mapper	77.3	0.73	Coniferous forest over-classified
Parrallelipiped	60.4	0.52	Many pixels unclassified
Minimum distance to mean	56.9	0.50	Coniferous forest not classified
Mahalanobis distance	51.8	0.44	Water over-classified
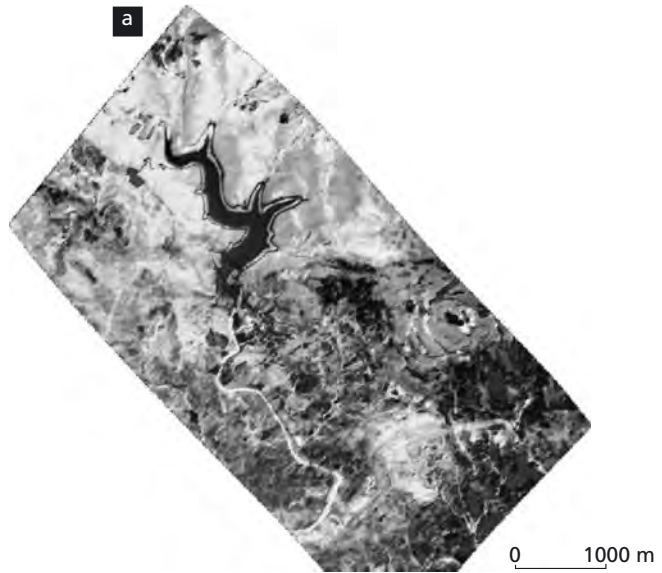
Figure 15.4a – DAIS7915 colour composite (R, G, B=PCA1,PCA2,PCA3). Green corresponds to vegetation, red to bare soil and agriculture. In the black & white image, light tones correspond to vegetation, dark tones to bare soils and low vegetation. Please consult the enclosed CDROM for a full colour version.

Coniferous forest
Dense garrigue
Dense landes
Dense maquis
Bare soil and concrete / water

Figure 15.4b – Maximum likelihood classification result with 7 classes: the heterogeneous vegetation in the image is classified in homogeneous clumps of trees, shrubs and grass. Please consult the enclosed CDROM for a full colour version.

Overall accuracy and kappa values of the result of the SPARK classification are shown in table 15.3. This table shows the results of 40 combinations of NDVI-classes and SPARK kernel sizes. The highest overall accuracy and kappa values for a certain kernel size are shown in bold. The best SPARK results, with an overall accuracy of 64.5% and kappa value of 0.61 are obtaine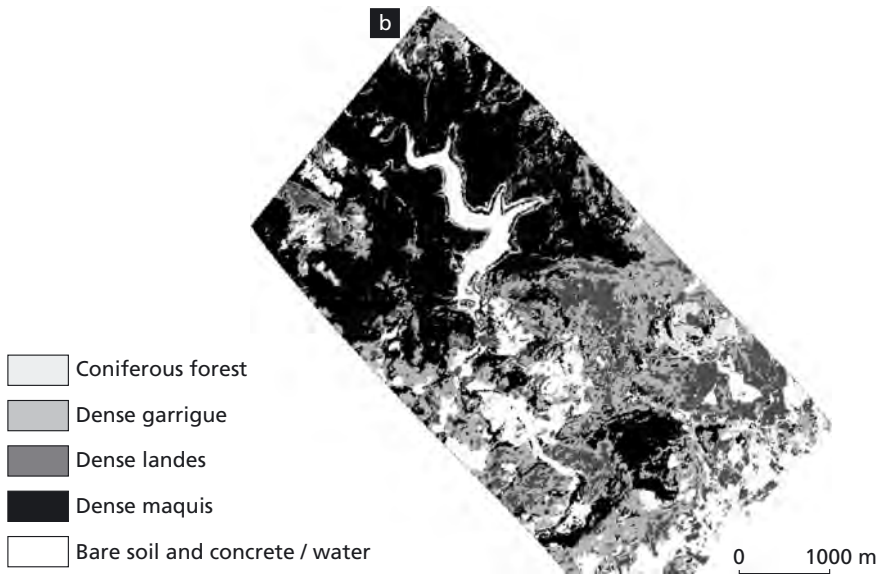d with a 3 by 3 kernel in combination with 27 NDVI-classes. Figure 15.6c shows SPARK classification results for the combination of 27 NDVI-classes and a kernel size of 3 by 3. Figure 15.6d shows SPARK classification results for the combination of 10 NDVI-

Table 15.2 – Class composition of the 7, 10, 12 and 15 class classifications.

7 classes	10 classes	12 classes	15 classes
Coniferous forest	Coniferous forest	Coniferous forest	Coniferous forest
Bare soil	Bare soil	Bare soil	Bare soil
Water	Water	Water	Water
Vineyard	Vineyard	Vineyard	Vineyard
Maquis	Dense maquis	Dense maquis	Dense maquis
Garrigue	Open maquis	Discontinuous maquis	Discontinuous maquis
Landes	Dense garrigue	Open maquis with shrubs	Open maquis with shrubs
	Open garrigue	Open maquis with shrubs & herbs	Open maquis with shrubs & herbs
	Dense landes	Dense garrigue	Open maquis without undergrowth
	Open landes	Discontinuous garrigue	Dense garrigue
		Open garrigue with herbs	Discontinuous garrigue
		Landes	Open garrigue with herbs
			Open garrigue without undergrowth
			Dense landes
			Open landes

classes and a kernel size of 11 by 11. The accuracy value of 27 NDVI-classes is relatively high compared to the results of larger kernels: when kernel size increases the best results are obtained with low NDVI class values. In general overall accuracy and kappa decrease with increasing kernel size due to aggregation and edge effects. If we consider the results of 27 NDVI-classes, the values shown in italics in table 15.3, the overall accuracy decreases from 64.5% with a 3 by 3 kernel to 55.0% with an 11 by 11 kernel. The spatial effects of a larger kernel size on the classification result are also shown in figure 15.6d. This figure shows that with larger kernels more aggregation occurs at the expense of small scale variation.
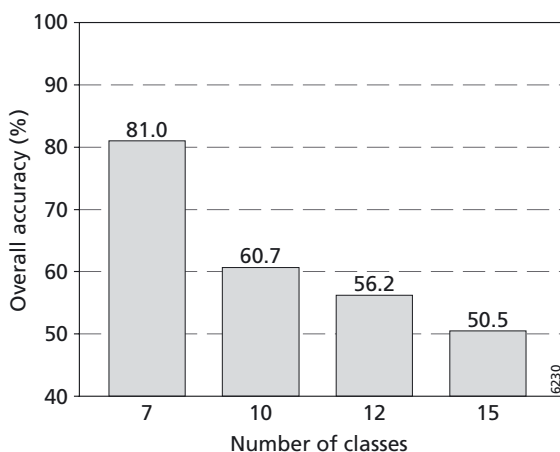

Figure 15.5 – Maximum likelihood overall accuracy values for 7, 10, 12 and 15 Classes.

Table 15.3 – Overall accuracy and kappa values of the final SPARK classification. Source files are initial NDVI-land cover maps with indicated NDVI-classes. Highest values per kernel size are shown in italics.

Overall Accuracy %	Kernel 3	Kernel 5	Kernel 7	Kernel 9	Kernel 11
6 NDVI classes	60.1	*63.1*	*62.2*	*61.0*	57.8
8 NDVI classes	60.4	61.3	61.0	58.8	56.2
10 NDVI classes	61.8	62.0	62.0	59.3	*58.0*
12 NDVI classes	62.1	61.5	60.7	58.8	57.1
16 NDVI classes	62.8	61.1	60.6	59.4	56.0
24 NDVI classes	63.4	61.0	59.9	57.9	54.2
27 NDVI classes	*64.5*	60.2	59.2	57.4	55.0
32 NDVI classes	62.9	60.1	60.5	58.1	54.9

Kappa	Kernel 3	Kernel 5	Kernel 7	Kernel 9	Kernel 11
6 NDVI classes	0.56	*0.59*	*0.58*	*0.57*	0.53
8 NDVI classes	0.56	0.57	0.56	0.54	0.52
10 NDVI classes	0.58	0.58	*0.58*	0.55	*0.55*
12 NDVI classes	0.58	0.57	0.56	0.54	0.53
16 NDVI classes	0.59	0.57	0.56	0.55	0.51
24 NDVI classes	0.59	0.57	0.55	0.54	0.50
27 NDVI classes	*0.61*	0.56	0.55	0.53	0.50
32 NDVI classes	0.59	0.56	0.56	0.53	0.50

NDVI

Bare soil and concrete / water / vineyard /
Coniferous forest

0   1000 m

Dense maquis

Discontinuous maquis

Open maquis with
shrub undergrowth

Open maquis with
herb undergrowth

Dense garrigue

Discontinuous garrigue

Open garrigue

Landes

Bare soil and concrete / water / vineyard /
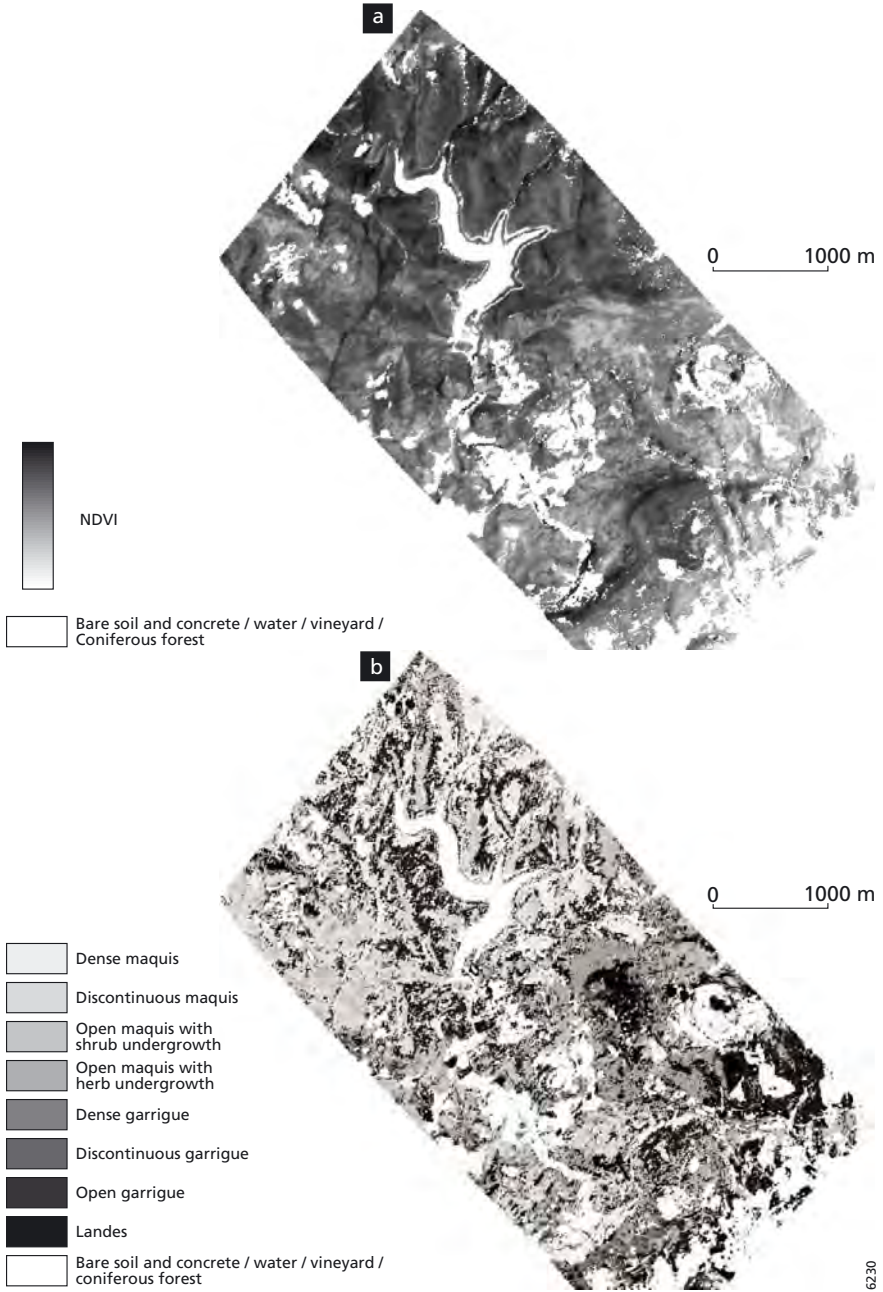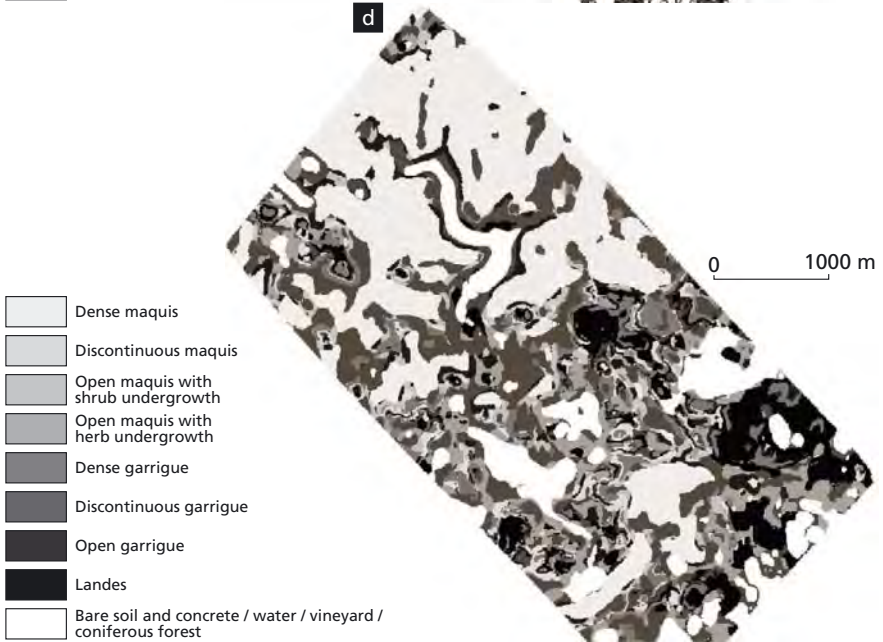coniferous forest

0   1000 m

*Figure 15.6 – a) Initial NDVI-land cover map with 27 NDVI-classes, b) 12-Class maximum
likelihood classification results, c) SPARK classification results with kernel size 3 and 27 NDVI-
classes and d) SPARK classification results with kernel size 11 and 10 NDVI-classes. Please consult
the enclosed CDROM for a full colour version.*

Legend (c):
- Dense maquis
- Discontinuous maquis
- Open maquis with shrub undergrowth
- Open maquis with herb undergrowth
- Dense garrigue
- Discontinuous garrigue
- Open garrigue
- Landes
- Bare soil and concrete / water / vineyard / coniferous forest

0 — 1000 m

Legend (d):
- Dense maquis
- Discontinuous maquis
- Open maquis with shrub undergrowth
- Open maquis with herb undergrowth
- Dense garrigue
- Discontinuous garrigue
- Open garrigue
- Landes
- Bare soil and concrete / water / vineyard / coniferous forest

0 — 1000 m

We focus on the best performing SPARK classification (kernel size 3, 27 NDVI-classes) and discuss these results in more detail here. In table 15.4, the user and producer accuracy of the individual classes are shown for the conventional maximum likelihood and SPARK classification. In addition, table 15.5 shows the confusion matrix of the SPARK classification. As expected, homogeneous classes like coniferous forest, bare soil, water and vineyard do not show large differences between the maximum likelihood classification and the SPARK classification. On average, heterogeneous vegetation classes show an increase in both producer and user accuracy. The following classes are more remarkable: dense maquis and landes show a major increase in both user and producer accuracy. Discontinuous garrigue cannot be detected at all with the maximum likelihood method, while SPARK could at least classify some pixels right. The open maquis classes show an increase in user accuracy, but controversially a decrease in producer accuracy for open maquis with herb and shrubs.

Except from analysing per pixel statistics we also evaluated the results visually to determine if the spatial arrangement of the classes makes sense. In figure 15.7 we compare a subset of the 12-class maximum likelihood classification results (figure 15.6b) to the SPARK classification results with kernel size 3 and 27 NDVI-classes (figure 15.6c). The red line in figure 15.7 roughly indicates the border between the more closed maquis dominated vegetation types in the north and the more open garrigue dominated vegetation types in the south. In the northern part, the 12-class maximum likelihood classification classifies many dense maquis as open maquis and open garrigue, the SPARK classification shows a more consistent pattern of dense maquis. In the southern part open maquis is over-classified by the 12-class maximum likelihood classification at cost of other heterogeneous vegetation types. SPARK detects for example patches of dense landes and open garrigue instead of open maquis, which matches

Table 15.4 – User and producer accuracy of the individual classes for the 12-class maximum likelihood- and 12-class SPARK classification.

Class	Maxlike: Producer accuracy	Maxlike: User accuracy	SPARK: Producer accuracy	SPARK: User accuracy	Difference Producer accuracy	Difference User accuracy
Coniferous forest	87.1	100	97.6	100	10.5	0
Dense maquis	41.6	66.3	60.6	79.1	19	12.8
Discontinuous maquis	29.6	13.3	44.4	26.7	14.8	13.4
Open maquis with shrubs	28.7	25.8	31.3	54.6	2.6	28.8
Open maquis with herbs & shrubs	57.8	13.1	35.6	34	-22.2	20.9
Dense garrigue	4.2	35.7	22.9	29	18.7	-6.7
Discontinuous garrigue	0	0	32.6	19.7	32.6	19.7
Open garrigue with herbs	22.2	8.1	36.1	17.3	13.9	9.2
Landes	22.9	32.7	53.5	42.1	30.6	9.4
Bare soils, tarmac & build up	93.7	91.1	86	99	-7.7	7.9
Water	100	100	97	100	-3	0
Vineyard	63.6	64.3	59.6	79.7	-4	15.4
				Average:	+ 8.8	+ 10.9

Table 15.5 – Confusion matrix of the 12-class SPARK classification.

Overall Accuracy (933/1447) 64.5%

Kappa Coefficient 0.62

Class	1	2	3	5	6	8	9	10	12	14	15	16	Total
1 Coniferous forest	**205**	0	0	0	0	0	0	0	0	0	0	0	205
2 Dense maquis	0	**83**	9	10	0	0	2	0	0	1	0	0	105
3 Discontinuous maquis	2	11	**24**	4	0	16	9	8	16	0	0	0	90
5 Open maquis with shrubs	0	6	0	**36**	0	7	6	8	3	0	0	0	66
6 Open maquis with herbs & shrubs	0	1	2	2	**16**	9	3	0	13	0	0	1	47
8 Dense garrigue	0	11	2	14	7	**27**	15	3	13	0	0	1	93
9 Discontinuous garrigue	3	20	9	40	2	14	**28**	1	11	2	0	12	142
10 Open garrigue with herbs	0	3	3	2	11	14	9	**13**	10	2	0	8	75
12 Landes	0	1	1	6	9	28	14	3	**77**	21	5	18	183
14 Bare soils, tarmac & build up	0	0	0	0	0	1	0	0	1	**203**	0	0	205
15 Water	0	0	0	0	0	0	0	0	0	0	**162**	0	162
16 Vineyard	0	1	4	1	0	2	0	0	0	7	0	**59**	74
Total	210	137	54	115	45	118	86	36	144	236	167	99	1447

	Dense maquis		Discontinuous garrigue
	Discontinuous maquis		Open garrigue
	Open maquis with shrub undergrowth		Landes
	Open maquis with herb undergrowth		Bare soil and concrete / water vineyard / coniferous forest
	Dense garrigue		
	Border between maquis & garrigue dominated vegetation types		0 250 m
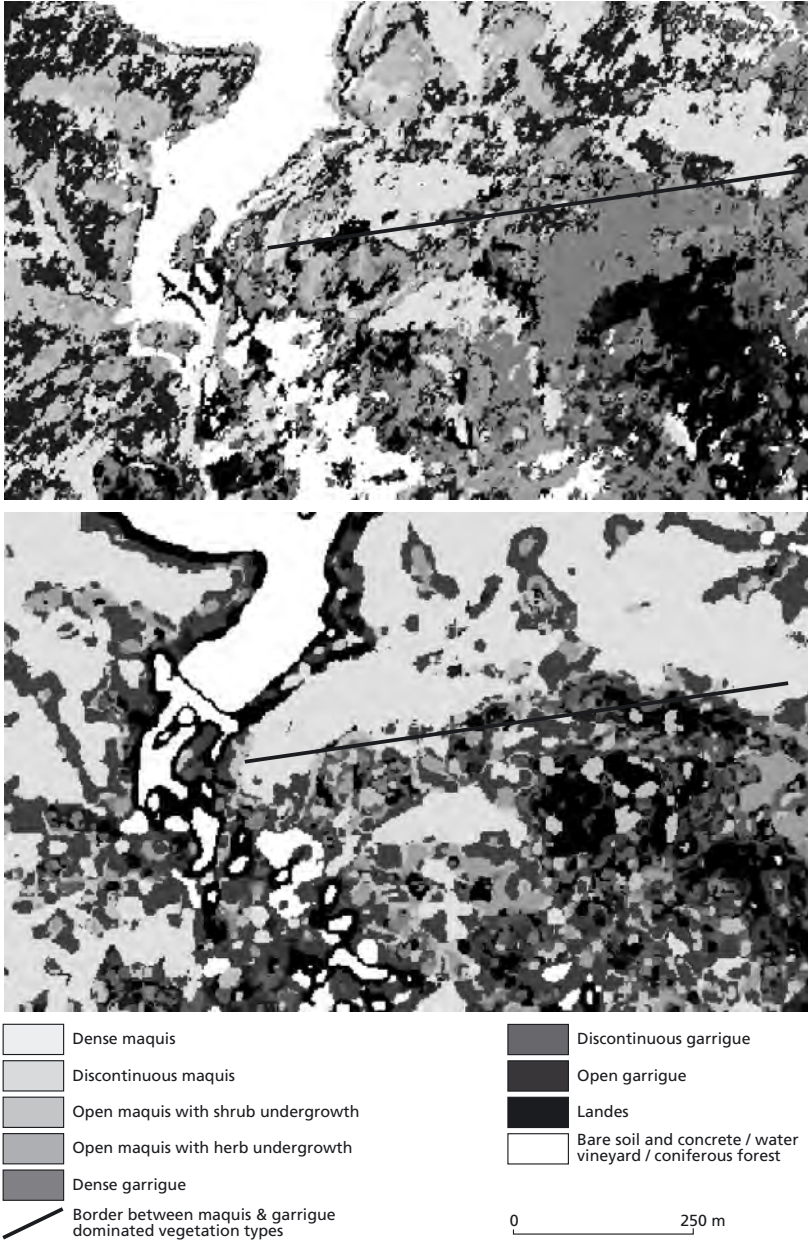
Figure 15.7 – Upper: subset of the 12-class maximum likelihood classification results (overall accuracy: 56.2%). Lower: the SPARK classification results with kernel size 3 and 27 NDVI-classes (overall accuracy 64.5%). The line roughly indicates the border between the maquis dominated vegetation types in the north and the garrigue dominated vegetation types in the south. Please consult the enclosed CDROM for a full colour version.

the field observations. In such complex areas the SPARK method is superior to the other approaches.

To investigate if it is useful to use different SPARK kernel sizes for certain classes in one SPARK classification run, we calculated table 15.6. To improve readability we consider user and producer accuracy in one table. For the best performing NDVI-class for a certain kernel size (italic items in table 15.3) we calculated the difference between the SPARK and the 12-class maximum likelihood classification for the user and producer accuracy. The value shown in the table is the average of both difference values. Hence, high positive values indicate a better performance of the SPARK approach compared to the conventional maximum likelihood method. It is clearly visible that homogeneous classes bare soil (class 14), water (class 15) and vineyard (class 16) perform worse with larger kernel sizes due to the increased effects of edges. Discontinuous maquis (class 3), open maquis (class 5) and discontinuous garrigue (class 9) perform best with a small 3 by 3 kernel. On the other hand, dense garrigue (class 8), dense landes (class 12) and dense maquis (class 2) perform better with larger kernels.

15.3.8 Discussion and conclusion

In this chapter we investigated the usefulness of a contextual image analysis method, the Spatial Reclassification Kernel referred to as SPARK, to classify complex Mediterranean vegetation types. As shown by Van der Kwast & Walstra (2001) there is a significant degree of spectral overlap between vegetation classes hampering conventional per-pixel classification. Of the conventional methods the maximum likelihood classifier performs best, but as soon as heterogeneous vegetation classes are taken into account the accuracy decreases due to spectral confusion. For 12 heterogeneous vegetation classes, the SPARK results (overall accuracy 64.5%) are better than the maximum likelihood results (overall accuracy 56.2%). It is important to note that the improvements of the SPARK results differ from vegetation class to vegetation class as might be expected. All heterogeneous classes show a significant increase of accuracy but less complex heterogeneous vegetation types (landes and dense maquis) show more improvement than more complex vegetation classes (open garrigue with herbs, dense

Table 15.6 – Average difference between producer and user accuracy of individual classes of the 12-class SPARK classification compared to the conventional 12-class maximum likelihood classification. Highest values per class are shown in italics.

Class	Kernel 3	Kernel 5	Kernel 7	Kernel 9	Kernel 11
Coniferous forest	5.3	-0.5	5.8	5.1	6.5
Dense maquis	15.9	16.1	17.7	16.7	12.3
Discontinuous maquis	14.1	5.6	10.1	10.2	8.2
Open maquis with shrubs	15.7	8.0	5.4	15.1	3.5
Open maquis with herbs & shrubs	-0.6	-8.5	7.6	9.0	-9.1
Dense garrigue	6.0	6.8	10.0	12.3	16.6
Discontinuous garrigue	*26.2*	19.7	16.2	6.7	6.1
Open garrigue with herbs	11.6	16.9	17.1	20.4	18.2
Landes	20.0	*23.2*	*28.7*	*24.4*	*26.3*
Bare soils, tarmac & build up	0.1	-0.9	-8.2	-9.2	-12.5
Water	-1.5	-3.0	-12.0	-12.0	-12.0
Vineyard	5.7	5.0	5.6	-0.3	-6.4

garrigue) as shown in table 15.4 and 15.6. This can be related to the fact that more complex patterns, with more input classes in the T_k-matrix, are less likely to have a unique T_k-matrix as described in paragraph 15.2. In general, the increase in accuracy is not spectacular but SPARK is successful in detecting vegetation classes which cannot be distinguished at all by conventional methods. This matches intuitive expectations that contextual classifiers perform better on spectrally heterogeneous objects.

An important factor is the choice of the initial land cover map. As shown in figure 15.4b a conventional classification with 7 basic classes produces an initial land cover map that is too homogeneous to be used for SPARK reclassification. In this study the best initial land cover map we produced was a hybrid map consisting of a maximum likelihood classification of homogeneous areas merged with a NDVI-level sliced map of heterogeneous areas. The choice of the number of NDVI-classes depends on kernel size. When using a small kernel the SPARK classification performs better with a relatively high number of NDVI-classes (27), while all the classifications with larger kernel sizes perform best with a low number of NDVI-classes. We could explain this behaviour by the effect that a larger number of classes in the input image can cause the number of matrices to become too large, which decreases the chance a particular M-matrix is similar to one of the T_k-matrices. The 3 by 3 kernel with 27 NDVI-classes seems to be an optimum between the number of possible M- and T_k-matrices in this study.

Visual comparison of the SPARK classification results with the maximum likelihood results shows that the vegetation classes produced by SPARK are more consistent and that the locations of the vegetation classes match the field observations.

In this study, overall accuracy decreases with increasing kernel size. However if we investigate user and producer accuracy of individual classes (table 15.6) some patterns emerge. Homogeneous classes do not benefit from larger kernel sizes because edge effects induced with larger kernels decrease the accuracy. The accuracy of heterogeneous classes differs with kernel size: complex patterns seem to be best classified with small kernels, while less complex patterns are better classified with larger kernels. This can again be related to the fact that complex patterns produce a larger amount of different M- and T_k-matrices which decreases the similarity chance. The observations in this study justify the idea to develop a version of SPARK that can use different kernel sizes for different classes in one SPARK classification run.

Note: The SPARK software used in this study is available for download at http://pcraster.geog.uu.nl

List of Contributors

Abarca-Hernández, Fransisco (fabarca@ug.es)
Remote Sensing, GIS & Geostatistics Laboratory.
Department of Geodynamics, University of Granada/CEAMA
Av. Fuentenueva S/N. 18071 Granada
Spain

Acerbi, Fausto W. (fausto.acerbi@wur.nl)
Laboratory of Geoinformation Sciences and Remote Sensing
Department of Environmental Sciences
Wageningen University
The Netherlands

Atkinson, Peter M. (p.m.atkinson@soton.ac.uk)
School of Geography University of Southampton Highfield,
Southampton SO17 1BJ
United Kingdom

Berberoglu, Süha (suha@mail.cu.edu.tr)
Department of Landscape Architecture
University of Cukurova
Adana
Turkey

Blaschke, Thomas (thomas.blaschke@sbg.ac.at)
Department of Geography & Applied Geoinformatics
University of Salzburg
Hellbrunner Str. 34
A-5020 Salzburg
Austria

Burnett, Charles (charles.burnett@sbg.ac.at)
Department of Geography & Applied Geoinformatics
University of Salzburg
Hellbrunner Str. 34
A-5020 Salzburg
Austria

Burrough, Peter A. (p.burrough@geog.uu.nl)
Faculty of Geosciences
Utrecht University
3508 TC Utrecht
The Netherlands

Carvalho, Luis M.T. de (passarinho@ufla.br)
Laboratory of Geoinformation Processing and Image Analysis
Department of Forest Sciences
Federal University of Lavras
Brazil

Chica-Olmo, Mario (mchica@ugr.es)
Remote Sensing, GIS & Geostatistics Laboratory.
Department of Geodynamics,
University of Granada/CEAMA
Av. Fuentenueva S/N. 18071 Granada.
Spain

Clevers, Jan G.P.W. (jan.clevers@wur.nl)
Laboratory of Geo-information Science and Remote Sensing
Department of Environmental Sciences
Wageningen University & Research Centre
The Netherlands

Curran, Paul J. (p.curran@soton.ac.uk)
Department of Geography
University of Southampton
Highfield
Southampton SO17 1BJ
United Kingdom

De Jong, Steven M. (s.dejong@geog.uu.nl)
Faculty of Geosciences
Utrecht University
3508 TC Utrecht
The Netherlands

Fonseca, Leila M.G. (leila@dpi.inpe.br)
Image Processing Division
National Institute for Space Research
Brazil

Foody, Giles M. (g.m.foody@soton.ac.uk)
Department of Geography
University of Southampton
Highfield
Southampton SO17 1BJ
United Kingdom

Fuller, Robin M. (rmf28@cam.ac.uk)
Unit for Landscape Modelling Sir William Hardy Building
Tennis Court Road
Cambridge CB2 3RF
United Kingdom

García-Haro, Javier (j.garcia.haro@uv.es)
Department of Thermodynamics
University of Valencia
Valencia
Spain

Gong, Peng (gong@nature.berkeley.edu)
Center for Assessment and Monitoring of Forest and Environmental Resources
University of California Berkeley
151 Hilgard Hall
Berkeley, CA 94720-3110
USA

Hay, Geoffrey J. (ghay@sympatico.ca)
Geocomputing Laboratory Departement de Géographie
Université de Montréal
C.P. 6128 Succursale Centre-Ville
Montréal Québec
Canada H3C 3J7

Kemper, Thomas (thomas.kemper@jrc.it)
Institute for Environment & Sustainability
Joint Research Centre of the European Commission
21020 Ispra
Italy

Kwast, Hans van der (h.vanderkwast@geog.uu.nl)
Faculty of Geosciences
Utrecht University
3508 TC Utrecht
The Netherlands

Lucieer, Arko (lucieer@itc.nl)
Earth Observation Science, Geo-information Processing
International Institute for Geo-Information Science and Earth Observation (ITC)
P.O. Box 6
7500 AA Enschede
The Netherlands

Marceau, Danielle J. (danielle.marceau@umontreal.ca)
Geocomputing Laboratory
Departement de Geographie
Université de Montreal
Montreal, Quebec

Pebesma, Edzer J. (e.pebesma@geog.uu.nl)
Faculty of Geosciences
Utrecht University
3508 TC Utrecht
The Netherlands

Pekkarinen, Anssi (anssi.pekkarinen@metla.fi)
METLA Finnish Forest Research Institute
Helsinki
Finland

Scholte, Klaas H. (k.h.scholte@citg.tudelft.nl)
Department of Applied Earth Sciences
Delft University of Technology, Delft
The Netherlands

Sluiter, Raymond (r.sluiter@geog.uu.nl)
Faculty of Geosciences
Utrecht University
3508 TC Utrecht
The Netherlands

Smith, Geoff M. (gesm@ceh.ac.uk)
CEH Monk Woods
Abbots Ripton Huntingdon
Cambridgeshire PE 28 2LS
United Kingdom

Thomson, Andy G. (agth@ceh.ac.uk)
CEH Monk Woods
Abbots Ripton Huntingdon
Cambridgeshire PE 28 2LS
United Kingdom

Van der Meer, Freek D. (vdmeer@itc.nl, f.d.vandermeer@citg.tudelft.nl)
Department of Earth Systems Analysis
International Institute for Geo-Information Science and Earth Observation (ITC)
P.O. Box 6
7500 AA Enschede
The Netherlands
&
Department of Technical Earth Sciences
Faculty of Civil Engineering and Geosciences
Delft University of Technology, Delft
The Netherlands

Van der Werff, Harald (vdwerff@itc.nl)
Department of Earth Systems Analysis
International Institute for Geo-Information Science and Earth Observation (ITC)
P.O. Box 6
7500 AA Enschede
The Netherlands

Walstra, Jan (j.walstra@lboro.ac.uk)
Department of Civil Engineering
Loughborough University Leicestershire LE11 3TU
United Kingdom

Xu, Bing (bingxu@nature.berkeley.edu)
Center for Assessment and Monitoring of Forest and Environmental Resources
University of California Berkeley
151 Hilgard Hall
Berkeley, CA 94720-3110
USA

Acronyms

ADEOS	Advanced Earth Observing Satellite (Japan)
A_I	Area Image
AISA	Airborne Imaging Spectrometer for Applications
ANN	Artifical Neural Network
ART	Adaptive Resonance Theory
ASAR	Advanced Synthetic Aperture Radar
ASD	Analytical Spectral Devices Inc.
ASTER	Advanced Spaceborne Thermal Emission and Reflectance Radiometer
AVHRR	Advanced Very High Resolution Radiometer
AVIRIS	Airborne Visible/Infrared Imaging Spectrometer
CASI	Compact Airborne Spectrographic Imager
CBERS	China-Brazil Earth Resources Satellite
CCD	Charge Coupled Device
CCSM	Cross Correlogram Spectral Matching
CIR	Colour Infrared photography
CM	Co-occurrence Matrix
CNSD	Conditional Negative Semi Definiteness
CV	Cross Variogram
$DAIS_{7915}$	Digital Airborne Imaging Spectrometer
DEM	Digital Elevation Model
DGPS	Differential Global Positioning System
DLR	German Aerospace Establishment
DN	Digital Number
DRU	Desertification Response Unit
EM	End Member
EO	Earth Observation
EOS	Earth Observing System
ERTS	Earth Resources Technology Satellite
ESA	European Space Agency
ETM^+	Enhanced Thematic Mapper (Landsat)
FBC	Frequency-Based Contextual Classifier
FCM	Fuzzy C-Means
FFBP	Feed Forward Back Propagation
FNEA	Fractal Net Evolution Approach
FOV	Field of View
FPCS	Feature Oriented Principal Components Selection
FWHM	Full Width Half Max
GCP	Ground Control Point
GER	Geophysical Environmental Research Inc.
G_I	Gradient Image

GIFOV	Ground Instantaneous Field of View
GIS	Geographical Information System
GLCM	Gray-Level Co-occurence Matrix
GPS	Global Positioning System
GSLIB	Geostatistical Software Library
GTI	Geostatistical Texture Image
GTO	Geostatistical Texture Operators
HNN	Hopfield Neural Network
HPDP	Hierarchical Patch Dynamics Paradigm
HPF	High Pass Filter
H-Res	High resolution
HRU	Hydrological Response Unit
HyMap	Hyperspectral Mapper
IDL	Interactive Data Language
IFOV	Instantaneous Field of View
IGN	Institut Géographique National
IHS	Intensity Hue Saturation
IPB	Iberian Pyrite Belt
IS	Imaging Spectrometry
IS_I	Image Set
JPL	Jet Propulsion Laboratory
k-NN	k-Nearest Neighbour Estimator
LAI	Leaf Area Index
LCM2000	Land Cover Map 2000 of Great Britain
LCMGB	Land Cover Map of Great Britain
L-Res	Low Resolution
MA	Madogram
MAP	Maximum a Posteriori Probability Approach
MAUP	Modifiable Areal Unit Problem
MCS	Marker-Controlled Segmentation
MedSpec	Mediterranean Spectral database
MERIS	Medium Resolution Imaging Spectrometer (Envisat)
MESMA	Multiple Endmember Spectral Mixture Analysis
M_I	Mean Image
MIR	Middle Infrared
ML	Maximum Likelihood
MLR	Multiple Linear Regression
MLP	Multi-Layer Perceptron
MNF	Maximum Noise Fraction
MODIS	Moderate Resolution Imaging Spectroradiometer
MOSA	Multiscale Object-Specific Analysis
MRF	Markov Randon Fields
MSFI	Multi-Source Forest Inventory
MSS	Multi-Scale Segmentation
MSS	Multi-Spectral Scanner
NDVI	Normalized Difference Vegetation Index

NIR	Near Infrared
NOAA	National Oceanic and Atmospheric Administration
O_I	Original Image
OK	Ordinary Kriging
ORM	Object Relationship Modelling
OSA	Object-Specific Analysis
OSU	Object-Specific Upscaling
PA	Producers Accuracy
PC	Principal Component
PCA	Principal Component Analysis
PCM	Possibilistic c-means
Pixel	Picture Element
PMT	Pyramidial Median Transform
PMWT	Pyramidial Median Wavelet Transform
PPI	Pixel Purity Index
PS	Productive Series
PSF	Point Spread Function
PV	Pseudo Cross Variogram
QMF	Quadrature Mirro Filters
RBD	Relative Absorption Band-Depth
REA	Representative Elementray Area
REP	Red Edge Position
RF	Random Function
RGB	Red Green Blue
RMS	Root Mean Square
RMSE	Root Mean Square Error
RO	Rodogram
RS	Remote Sensing
RT	Radiative Transfer Function
RV	Regionalized Variable
SAM	Spectral Angle Mapper
SAR	Synthetic Aperture Radar
SAVI	Soil Adjusted Vegetation Index
SDI	Spatial Data Integration approach
SD_n	Scale Domain
SFF	Spectral Feature Fitting
SK	Simple Kriging
SLAR	Side Looking Airborne Radar
SMA	Spectral Mixture Analysis
SNR	Signal to Noise Ratio
SPARK	Spatial Re-classification Kernel
SPOT	Système Pour l'Observation de la Terre
SR	Source Rock
SRF	Spectral Response Function
SSC	Spatial and Spectral Classifier
SV	Simple Variogram

SVM	Support Vector Machine
SWIR	Shortwave Infared
TGO	Texture Generated Operators
TIR	Thermal Infrared
TIROS	Television Infrared Observation Satellite
TM	Thematic Mapper (Landsat)
TRMM	Tropical Rainfall Measuring Mission
TS	Texture Spectrum
TU	Texture Unit
UA	Users Accuracy
USGS	United States Geological Survey
UTM	Universal Transverse Mercator map projection
VHR	Very High Spatial Resolution
V_I	Variance Image
VIS	Visible part of the electromagnetic spectrum
VMAX	Maximum Variance
VMESMA	Variable Multiple Endmember Spectral Mixture Analysis
VMIN	Minimum Variance
VNIR	Visible and Near Infrared
VTT	Technical Research Centre of Finland
W_I	Watershed Image
WT	Wavelet Transform

References

A

Abkar, A. & Mulder, N. (1998) Likelihood classification of high resolution images to generate the initial topology and geometry of land cover segments. IAPRS vol. 32(4). GIS between visions and applications, Stuttgart, pp. 1-7.

Abrams, M.A. & Narimanov, A.A. (2000) Geochemical evaluation of hydrocarbons and their potential sources in the western South Caspian depression, Republic of Azerbaijan. Marine and Petroleum Geology 14 (4): pp. 451-468.

Abrams, M.J., Ashley, R.P., Rowan, L.C., Goetz, A.F.H. & Kahle, A.B. (1977) Mapping of hydrothermal alteration in the Cuprite mining district, Nevada using aircraft scanner images for the spectral region 0.46-2.36 μm. Geology 5: pp. 713-718.

Adams, J.B. (1974) Visible and near-infrared diffuse reflectance: Spectra of pyroxenes as applied to remote sensing of solid objects in the solar system. J. Geophys. Res. 79: pp. 4829-4836.

Adams, J.B. (1975) Interpretation of visible and near-infrared diffuse reflectance spectra of pyroxenes and other rock forming minerals. In: Karr, C., (Editor), Infrared and Raman Spectroscopy of Lunar and Terrestrial Materials. Academic Press, New York, pp. 91-116.

Adams, J.B., Sabol, D.E., Kapos, V., Almeida, R. Filho, Roberts, D.A., Smith, M.O. & Gillespie, A.R. (1995) Classification of multispectral images based on fractions of endmembers: Applications to land-use change in the Brazilian Amazon, Remote Sensing of Environment 52: pp. 137-154.

Adams, J.B., Smith, M.O. & Gillespie, A.R. (1989) Simple Models for complex natural surfaces for the Hyperspectral era of Remote Sensing, in: Proceedings of the International Geoscience and Remote Sensing Symposium (IGARSS '89), Vancouver, 10-14 July 1989, pp. 16-21.

Adams, J.B., Smith, M.O. & Gillespie, A.R. (1993) Imaging Spectroscopy: Interpretation based on Spectral Mixture Analysis, in C.M. Peters and P. Englert (eds.), Remote Geochemical Analysis: Elemental and Mineralogical Composition, Topics in Remote Sensing 4. Cambridge University Press, New York, pp. 145-166.

Adams, J.B., Smith, M.O. & Johnson, P.E. (1985) Spectral mixture modelling: a new analysis of rock and soil types at the Viking Lander 1 site, Journal of Geophysical Research 91: pp. 8098-8112.

Adams, J.B., Smith, M.O. Gillespie, A.R. (1993) Imaging Spectroscopy: Interpretation Based on Spectral Mixture Analysis. In: C.M. Pieters & P.A.J. Englert (Eds.), Remote Geochemical Analysis: Elemental and Mineralogical Composition. Cambridge University Press, New York, pp. 145-166.

Adams, J.B., Smith, M.O., Johnson, P.E. (1985). Spectral Mixture Modelling: a new analysis of rock and soil types at the Viking Lander I site. Journal of Geophysical Research 91: pp. 8098-8112.

Addink, E.A., Stein, A. (1999) A comparison of conventional and geostatistical methods to replace clouded pixesl in NOAA-AVHRR images. International Journal of Remote Sensing 20: pp. 961-977.

Aiazzi, B., Alparone, L. & Baronti, S. (1998) Multiresolution local-statistics speckle filtering based on a ratio laplacian pyramid. IEEE Transactions on Geoscience and Remote Sensing 36 (5): pp. 1466-1476.

Aiazzi, B., Alparone, L. & Baronti, S. (2002) Context-driven fusion of high spatial and spectral resolution images based on oversampled multiresolution analysis. IEEE Transactions on Geoscience and Remote Sensing 40 (10): pp. 2300-2312.

Albers, J.P. & Stewart, J.H. (1972) Geology and mineral deposits of Esmeralda County, Nevada. Nevada Bureau of Mines and Geology Bulletin 78: pp. 1-80.

Allen, T.F.H. & Starr, T.B. (1982) Hierarchy Perspective for Ecological Complexity, University of Chicago Press, Chicago.

Almeida-Filho, R. (2002) Remote detection of hydrocarbon microseepage-induced soil alteration. Internation Journal of Remote Sensing, 2002, (23) 18: pp. 3523-3524.

Almodovar, G.R., Saez, R., Pons, J.M., Maestre, A., Toscano, M. & Pascual, E. (1998) Geology and Genesis of the Aznalcóllar Massive Sulphide Deposits, Iberian Pyrite Belt, Spain, Mineralium Deposita 33: pp. 111-136.

Alparone, L., Cappellini, V. & Mortelli, L. (1998) A pyramid-based approach to multisensor image data fusion with preservation of spectral signatures, in Gudmandsen (Eds.), Future Trends in Remote Sensing, Balkema, Rotterdam, pp. 419-426.

Anderson, J.R., Hardy, E.E., Roach, J.T. & Witmer, R.E. (1976) A land use and land cover classification system for use with remote sensor data. USGS Professional Paper 964, Sioux Falls, SD, USA.

Aplin, P. & Atkinson, P.M. (2001) Sub-pixel land cover mapping for per-field classification. International Journal of Remote Sensing 22: pp 2853-2858.

Aplin, P., Atkinson, P.M. & Curran, P.J. (1997) Using the spectral properties of fine spatial resolution satellite sensor imagery for national land cover and land use mapping, in G. Guyot and T. Phulpin (eds.), Physical Measurements and Signatures in Remote Sensing, Balkema, Rotterdam, pp. 661-668.

Aplin, P., Atkinson, P.M. & Curran, P.J. (1999) Per-field classification of land use using the forthcoming very fine resolution satellite sensors: problems and potential solutions. In Atkinson, P. and Tate, N. (Eds.), Advances in remote sensing and GIS analysis. Wiley & Son, Chichester, pp. 219-239.

Aplin, P., Atkinson, P.M., & Curran, P.J., (1999) Fine spatial resolution satellite sensor imagery for land cover mapping in the United Kingdom, Remote Sensing of Environment 68: pp. 206-216.

Arai, K. (1993) A classification method with a spatial-spectral variability, International Journal of Remote Sensing 14: pp. 699-709.

Argenti, F., Alparone, L. & Benelli, G. (1990) Fast algorithms for texture analysis using co-occurrence matrices, IEEE Proceedings 137: pp. 443-448.

Armstrong, M. (1998) Basic Linear Geostatistics, Springer Verlag: Berlin.

Asner G.P. & Heidebrecht, K.B. (2002) Spectral unmixing of vegetation, soil and dry carbon cover in arid regions: comparing multispectral and hyperspectral observations. International Journal of Remote Sensing 23 (19): pp. 3939-3958.

Atkinson, P. & Quattrochi, D.A. (2000) Special Issue on Geostatistics and Geospatial Techniques in Remote Sensing. Computers & Geosciences 26: pp. 359-490.

Atkinson, P.M. & Tatnall, A.R.L. (1997) Introduction: neural networks in remote sensing, International Journal of Remote Sensing 18: pp. 699-709.

Atkinson, P.M. & Curran, P.J. (1995) Defining an optimum size of support for remote sensing investigations, IEEE Transactions on Geoscience and Remote Sensing 33: pp. 768-776.

Atkinson, P.M. & Curran, P.J. (1997) Choosing an appropriate spatial resolution for remote sensing investigations, Photogrammetric Engineering & Remote Sensing, 63: pp. 1345-1351.

Atkinson, P.M. & Kelly, R.E.J. (1997) Scaling-up snow depth in the UK for comparison with SSM/I imagery, International Journal of Remote Sensing 18: pp. 437-43.

Atkinson, P.M. & Lewis, P. (2000) Geostatistical classification for remote sensing: an introduction. Computers & Geosciences 26: pp. 361-371.

Atkinson, P.M. & Martin, D. (1999) Investigating the effect of support size on population surface models, Geographical and Environmental Modelling 3: pp. 101-119.

Atkinson, P.M. & Massari, R. (1998) Mapping susceptibility to landsliding in the central Apennines, Italy, Computers and Geosciences, 24: pp. 373-385.

Atkinson, P.M. & Tate, N. (1999) Extracting information from remotely sensed and GIS data. In Atkinson, P.M. & Tate, N. (Eds.), Advances in remote sensing and GIS analysis. Wiley & Son, Chichester, pp. 263-268.

Atkinson, P.M. & Tate, N.J. (2000) Spatial scale problems and geostatistical solutions: a review, Professional Geographer, 52: pp. 607-623.

Atkinson, P.M. (1993) The effect of spatial resolution on the experimental variogram of airborne MSS imagery, International Journal of Remote Sensing 14: pp. 1005-1011.

Atkinson, P.M. (1995) A method for describing quantitatively the information, redundancy and error in digital spatial data, in Innovations in GIS II (Eds.), P. Fisher, Taylor and Francis: London, pp. 85-96.

Atkinson, P.M. (1995) Regularization of variograms of airborne MSS imagery, Canadian Journal of Remote Sensing 21: pp. 225-233.

Atkinson, P.M. (1997a) On estimating measurement error in remotely sensed images with the variogram, International Journal of Remote Sensing 18: pp. 3075-3084.

Atkinson, P.M. (1997b) Mapping sub-pixel boundaries from remotely sensed images, Innovations in GIS IV (Z. Kemp, editor), Taylor and Francis: London, pp. 166-180.

Atkinson, P.M. (2001) Geostatistical regularization in remote sensing, in Modelling Scale in Geographical Information Science (Eds.), N.J. Tate and P.M. Atkinson, Wiley: Chichester, pp. 239-262.

Atkinson, P.M. (2001) Super-resolution target mapping from soft classified remotely sensed imagery, Fifth International Conference on GeoComputation, University of Leeds: Leeds, CD-ROM.

Atkinson, P.M. (2003) Resolution Manipulation and Sub-Pixel Mapping. In: S.M. de Jong & F.D. Van der Meer (Eds), Remote Sensing Image Analysis: including the spatial domain. Kluwer Academics, Dordrecht. Chapter 4 of this volume.

Atkinson, P.M. (2004a) Super-resolution target mapping from soft classified remotely sensed imagery, Photogrammetric Engineering & Remote Sensing (submitted).

Atkinson, P.M. (2004b) Super-resolution land cover classification using geostatistical optimization, GeoENV IV: Geostatistics for Environmental Applications, (Eds.), X. Sánchez-Vila, Kluwer, Dordrecht (in press).

Atkinson, P.M., Cutler, M.E.J. & Lewis, H. (1997) Mapping sub-pixel proportional land cover with AVHRR imagery, International Journal of Remote Sensing 18 (4): pp. 917-935.

Atkinson, P.M., Cutler, M.E.J. & Lewis, H. (1997) Mapping sub-pixel proportional land cover with AVHRR imagery, International Journal of Remote Sensing 18: pp. 917-935.

Atkinson, P.M., Webster, R. & Curran, P.J. (1994) Cokriging with airborne MSS imagery, Remote Sensing of Environment 50: pp. 335-345.

Augusteijn, M.F., Clemens, L.E. & Shaw, K.A. (1995) Performance evaluation of texture measures for ground cover identification in satellite images by means of a neural network classifier, IEEE Transactions on Geoscience and Remote Sensing 33: pp. 616-625.

B

Baatz, M. & Schäpe, A. (2000) Multiresolution Segmentation – an optimization approach for high quality multi-scale image segmentation. In Strobl, J, Blaschke, T., Griesebner, G. (eds.): Angewandte Geographische Informationsverarbeitung XII, Wichmann-Verlag, Heidelberg, pp. 12-23.

Bajscy, R. & Kovacic, S. (1989) Multiresolution elastic matching. Compter Vision, Graphics and Image Processing 46: pp. 1-21.

Ball, P. (1999) The self-Made Tapestry. Pattern Formation in Nature. Oxford University Press, Oxford, 286 pp.

Barnea, D.I. & Silverman, H.F. (1972) A class of algorithms for fast digital image registration. IEEE Transactions in Computers 21 (2): pp. 179-186.

Barnsley, M.J. & Barr, S.L. (1996) Inferring Urban Land Use from Satellite Sensor Images using Kernel-based Analysis and Classification. Photogrammetric Engineering & Remote Sensing 62 (8): pp. 949-958.

Basset, O., Buquet, B., Abouelkaram, S., Delachartre, P. & Culioli, J. (2000) Application of texture image analysis for the classification of bovine meat, Food Chemistry 69: pp. 437-445.

Bastin, L. (1997) Comparison of fuzzy c-means classification, linear mixture modelling and MLC probabilities as tools for unmixing coarse pixels, International Journal of Remote Sensing 18 (17): pp. 3629-3648.

Batista, G.T., Medeiros, J.S., Mello, E.M.K., Moreira, J.C. & Bins, L.S. (1994) A new approach for deforestation assessment, in Proceedings of the International Symposium on Resource and Environmental Monitoring, Rio de Janeiro, Brazil, 26-30 September 1994, pp. 170-174.

Beale, R. & Jackson, T. (1990) Neural Computing: An Introduction, Adam Hilger, Bristol.

Belhadj, Z. & Jebara, S.B. (2002) Adaptative speckle reduction using combined multiresolution analysis and prediction technique. International Journal of Remote Sensing 23 (11): pp. 2263-2282.

Belward, A.S., Estes, J.E. & Kilne, K.D. (1999) The IGBP-DIS global 1-km land-cover data set DISCover: a project overview, Photogrammetric Engineering & Remote Sensing 65: pp. 1013-1020.

Bendjebbour, A., Delignon, Y., Fouque, L., Samson, V. & Pieczynski, W. (2001) Multisensor Image Segmentation Using Dempster-Shafer Fusion in Markov Fields Context. IEEE Transactions on Geoscience and remote sensing vol. 39 (8): pp. 1789-1798.

Ben-Dor, E., Inbar, Y. & Chen, Y. (1997) The Reflectance Spectra of Organic Matter in the Visible Near-Infrared and Short Wave Infrared Region (400-2500nm) during a Controlled Decomposition Process. Remote Sensing of Environment. 61: pp. 1-15.

Benediktsson, J.A. & Sveinsson, J.R. (1997) Feature extraction for multisource data classification with artificial neural networks, International Journal of Remote Sensing 18: pp. 727-740.

Berberoglu, S., Lloyd, C.D., Atkinson, P.M. & Curran, P.J. (2000) The integration of spectral and textural information using neural networks for land cover mapping in the Mediterranean, Computers and Geosciences, 26: pp. 385-396.

Beucher, S. & Lantuéjoul, C. (1979) Use of watersheds in contour detection, in International Workshop on Image Processing, Real-Time Edge and Motion Detection/Estimation, Rennes, France, 17-21 Sept., CCETT/IRISA Report no. 132: pp. 2.1-2.12.

Bezdek, J.C., Ehrlich, R. & Full, W. (1984) FCM: The fuzzy c-means clustering algorithm, Computers and Geosciences 10: pp. 191-203.

Bian, L. & Walsh, S.J. (1993) Scale Dependencies of Vegetation and Topography in a Mountainous Environment of Montana, The Professional Geographer 45: pp. 1-11.

Bidwell, R.G.S. (1974) Plant Physiology. MacMillan Publishing Company Inc. New York, 643 pp.

Bierkens, M.F.P., Finke, P.A., & de Willigen, P. (2000) Upscaling and Downscaling Methods for Environmental Research (Developments in Plant and Soil Sciences), Kluwer Academic Publishers, Dordrecht.

Bierwirth, P.N. (1990) Mineral mapping and vegetation removal via data-calibrated pixel unmixing, using multispectral images, International Journal of Remote Sensing 11: pp. 1999-2017.

Bijaoui, A., Rué, F. & Vandame, B. (1992) Multiscale vision and its application to astronomy, in Proceedings from the 5th Workshop in Data Analysis in Astronomy, Erice, Italy, 27 October - 3 November 1996: pp. 337-343.

Blaschke T., Burnett, C. & Pekkarinen, A. (2004) Image segmentation methods for object-based analysis and classification. In: S.M. de Jong & F.D. Van der Meer (Eds), Remote Sensing Image Analysis: including the spatial domain. Kluwer Academics, Dordrecht. Chapter 12 of this volume.

Blaschke, T. & Hay, G. (2001) Object-oriented image analysis and scale-space: Theory and methods for modeling and evaluating multi-scale landscape structure. International Archives of Photogrammetry and Remote Sensing, vol. 34: part 4/W5, pp. 22-29.

Blaschke, T. & Strobl, J. (2001) What's wrong with pixels? Some recent developments interfacing remote sensing and GIS. GIS – Zeitschrift für Geoinformationssysteme 6, pp. 12-17.

Blaschke, T. (2001) Environmental Monitoring and Management of protected areas through integrated ecological information systems – an EU perspective. In Rautenstrauch, C. (Eds.): Environmental Information Systems in Industry and Public Administration. Idea Group Publishing, Hershey, London, pp. 75-100.

Blaschke, T., Conradi, M. & Lang, S. (2001) Multi-scale image analysis for ecological monitoring of heterogeneous, small structured landscapes. Proceedings of SPIE, Toulouse, pp. 35-44.

Blaschke, T., Lang, S., Lorup, E., Strobl, J. & Zeil, P. (2000) Object-oriented image processing in an integrated GIS/remote sensing environment and perspectives for environmental applications. In Cremers, A. and Greve, K. (eds.), Environmental Information for planning, politics and the public. Metropolis Verlag, Marburg, pp. 555-570.

Blösch, G. & Silvaplan, M. (1995) Scale issues in hydrological modelling: a review. In: J.D. Kalma & M. Sivaplan (Eds.), Scale issues in hydrological modelling, Advances in Hydrological Processes, Wiley, Chichester, pp. 10-48.

Boardman, J.W. & Goetz, A.F.H. (1991) Sedimentary facies analysis using imaging spectrometry: A geophysical inverse problem, Proceedings of the Third Aviris Workshop, JPL Publication 91-28: pp. 4-13.

Boardman, J.W. (1992) Analysis, understanding, and visualization of hyperspectral data as convex sets in n space, Proceedings SPIE 2480: pp. 14-22.

Boardman, J.W., Kruse, F.A., & Green, R.O. (1995) Mapping target signatures via partial unmixing of Aviris data, Summaries, Fifth JPL Airborne Earth Science Workshop, JPL Publication 95-1(1): pp. 23-26.

Bocher, P. (2003) Investigating the Potentials of the Spatial Domain in High-Resolution Imagery for Mapping Scale-Specific Structures of Forest Vegetation. PhD Thesis, Faculty of Science, University of Aarhus, Denmark114 pp.

Bonfils, P. (1993) Carte pédologique de France à 1/100 000, feuille Lodève. Paris, INRA.

Borel, C.C. & Gerstl, S.A.W. (1994) Nonlinear spectral mixing models for vegetative and soil surfaces, Remote Sensing of Environment, 47: pp. 403-416.

Bowman, W.D. (1989) The relationships between leaf water status, gas exchange, and spectral reflectance in cotton leaves. Remote Sensing of Environment, 30: pp 249-255.

Brink, A., García-Haro, F.J. & Sommer, S (2002) Mapping soil degradation in Mediterranean ecosystems using a standardised variable unmixing strategy, International Journal of Remote Sensing, in revision.

Brown, A. (2000) Evaluation of possible gas microseepage mechanisms. The American Assiciation of Petroleum Geologists (AAPG) Bulletin 84 11: pp. 1775-1789.

Brown, D.G. (2001) A Spectral Unmixing Approach to Leaf Area Index (LAI) Estimation at the Alpine Treeline Ecotone. In: A.C. Millington, S.J. Walsh & P.E. Osborne (Eds.), GIS and Remote Sensing Applications in Biogeography and Ecology. Kluwer Academic Publishers, Norwell, Massachusetts, pp. 7-22.

Brown, M., Gunn, S.R. & Lewis, H.G. (1999) Support vector machines for optimal classification and spectral unmixing, Ecological Modelling, 120: pp. 167-179.

Brown, M., Lewis, H.G. & Gunn, S.R. (2000) Linear spectral mixture models and support vector machines for remote sensing, IEEE Transactions on Geoscience and Remote Sensing 38: pp. 2346-2360.

Bruce, L.M. & Li, J. (2001) Wavelet for computationally efficient hyperspectral derivative analysis. IEEE Transactions on Geosciences and Remote Sensing 39 (7): pp. 1540-1546.

Bruce, L.M., Koger, C.H. & Li, J. (2002b) Dimensionality reduction of hyperspectral data using discrete wavelet transform feature extraction. IEEE Transactions on Geosciences and Remote Sensing 40 (10): pp. 2331-2338.

Bruce, L.M., Li, J. & Huang, Y. (2002a) Automated detection of subpixel hyperspectral targets with adaptative multichannel discrete wavelet transform. IEEE Transactions on Geosciences and Remote Sensing 40 (4): pp. 977-980.

Bruce, L.M., Morgan, C. & Larsen, S. (2001) Automated detection of subpixel hyperspectral targets with continuous and discrete wavelet transforms. IEEE Transactions on Geosciences and Remote Sensing 39 (10): pp. 2217-2226.

Bruin, S. & Gorte, B.G.H. (2000) Probabilistic image classification using geological map units applied to land-cover change detection. International Journal of Remote Sensing 21 (12): pp. 2389-2402.

Brunelli, R. & Messelodi, S. (1995) Robust estimation of correlation with applications to computer vision. Pattern Recognition 28 (6): pp. 833-841.

Bruzzone, L., Contese, C. Maselli, F. & Foli, F. (1997) Multisource classification of complex rural areas by statistical and neural-network approaches, Photogrammetric Engineering & Remote Sensing 63: pp. 523-533.

Buiten, H.J. & Clevers, J.G.P.W. (1993) Land Observation by Remote Sensing Theory and Applications. Gordon and Breach Science Publishers, Reading, 642 pp.

Buiten, H.J. & Clevers, J.G.P.W. (1996) Land Observation by Remote Sensing: Theory and Applications. Gordon and Breach Science Publishers, Amsterdam, 642 pp.

Burnett, C. & Blaschke, T. (in press) A multi-scale segmentation/object relationship modelling methodology for landscape analysis. Ecological Modelling (accepted June 2002).

Burnett, C. (2002) Visualization and analysis of information space. PhD thesis. University of Turku, Finland, 145 pp.

Burnett, C., Leckie, D., Jay, C., Busler, J. & Aitken, J. (1999) The effect of severe topography on image resolution: implications for flight planning, post-processing and applications, In Proceedings of the 4th International Airborne Remote Sensing Conference/21st Canadian Symposium on Remote Sensing, June 21-25, Ottawa, vol. II, pp. 793-800.

Burns, R.G. (1993) Origin of Electronic Spectra of Minerals in the Visible and Near-Infrared Region. in: C.M. Pieters & P.A.J. Englert, Remote Geochemical Analysis: Elemental and Mineralogical Composition. Cambridge University Press, New York, pp. 3-30.

Burrough, P.A. & McDonnell, R.A. (1998), Principles of Geographical Information Systems. Oxford University Press, Oxford, 332 pp.

Burrough, P.A. (1981) The fractal dimensions of landscapes and other environmental data, Nature 294: pp. 85-98.

Burt, P.J. & Adelson, A.E. (1983) The laplacian pyramid as a compact image code. IEEE Transactions on Comunications, COM 31, pp. 532-540.

Buryakovsky, L.A., Djevanshir, R.Dj. & Chilingar, G.V. (1995) Abnormally-high formation pressures in Azerbaijan and the South Caspian Basin as related to smectite-illite transformations during diagenesis and catagenesis, Journal of Petroleum Science and Engineering 13: pp. 203-218.

C

Caldwell, M.M., Matson, P.A., Wessman, C. & Gamon, J. (1993) Prospects for scaling, in J.R. Ehleringer and C.B. Field (Eds.), Scaling Physiological Processes: Leaf to Globe, Academic Press, pp. 223-230.

Campbell, J.B. (2002) Introduction to Remote Sensing, Third edition (Taylor and Francis: London).

Campbell, N.A. (1984) Some aspects of allocation and discrimination, in G.N. van Vark and W.W. Howells. (Eds) Multivariate Statistical Methods in Physical Anthropology, Reidel, Dordrecht, pp. 177-192.

Cao, C. & Lam, N. (1999) Understanding the scale and resolution effects in remote sensing and GIS. In Atkinson, P. and Tate, N. (Eds.), Advances in remote sensing and GIS analysis. Wiley & Son, Chichester, pp. 57-72.

Caraux-Garson, D., Hoff, C., Lacaze, B., Sommer, S., Mehl, W. & Hill, J. (1999) Twelve years of vegetation cover monitoring from Landsat-TM data in Languedoc, southern France. Operational Remote Sensing for sustainable development. V.M. Nieuwenhuis. Rotterdam, Balkema, pp. 45-52.

Carlson, G.E. & Ebel, W.J. (1995) Co-occurrence matrices for small region texture measurement and comparison. International Journal of Remote Sensing 16: pp. 1417-1423.

Carpenter, G.A., Gopal, S., Macomber, S., Martens, S. & Woodcock, C.E. (1999) A neural network method for mixture estimation for vegetaion mapping, Remote Sensing of Environment, 70: pp. 138-152.

Carr, J.R. (1996) Spectral and textural classification of single and multiple band digital images. Computers & Geosciences 22: pp. 849-865.

Carter, G.A. (1994), Ratios of Leaf Reflectance in Narrow Wavebands as Indicators of Plant Stress. International Journal of Remote Sensing 15: pp. 697-703.

Carvalho, L.M.T. (2001) Mapping and Monitoring Forest Remnants: A Multiscale Analysis of Spatio-temporal Data. (Doctoral Thesis) Wageningen University, The Netherlands, 138 pp.

Carvalho, L.M.T. (2003) Declouding time-series of Landsat data, in Anais do XI Simpósio Brasileiro de Sensoriamento Remote. Belo Horizonte, Brasil, 05-10 April 2003, pp. 2035-2042.

Carver, S.J. (1991) Integrating multicriteria evaluation with geographical information systems, International Journal of Geographical Information Systems, 5: pp. 321-339.

Cetin, M. & Kirda, C. (2003) Spatial and temporal changes of soil salinity in a cotton field irrigated with low-quality water, Journal of Hydrology 272: pp. 238-249.

Chaudhuri, B. & Sarkar, N. (1995) Texture segmentation using fractal dimension. IEEE Transactions on Pattern Analysis and Machine Intelligence. vol. 17 (1): pp. 72-77.

Chavez, Jr., P.S., Sides, S.C. & Anderson, J.A. (1991) Comparison of three different methods to merge multiresolution and multispectral data: Landsat TM and SPOT panchromatic. Photogrammetric Engineering & Remote Sensing 57 (3): pp. 265-303.

Cheng, T. (1999) A process-oriented data model for fuzzy spatial objects. ITC publication Series no. 68: Enschede.

Chica-Olmo, M. & Abarca, F. (1998) Radiometric coregionalization of Landsat TM and Spot HRV images. International Journal of Remote Sensing 19: pp. 997-1005.

Chica-Olmo, M. & Abarca, F. (2000) Computing images texture for remotely sensed data classification, Computers & Geosciences 26: pp. 373-383.

Chilès, J.-P. & Delfiner, P. (1999) Geostatistics. Modeling Spatial Uncertainty, Wiley: New York, 695 p.

Chung, C.J. & Fabbri, A.G. (1993) The representation of geoscience information for data integration. Nonrenewable Resources 2: pp. 122-139.

Cihlar, J. (2000) Land cover mapping of large areas from satellites: status and research properties. International Journal of Remote Sensing 21 (6&7): pp. 1093-1114.

Cihlar, J., Xia, Q.H., Chen, J., Beaubien, J., Fung, K. & Latifovic, R. (1998) Classification by progressive generalization: A new automated methodology for remote sensing multichannel data. International Journal of Remote Sensing, 19: pp. 2685-2704.

Civco, D. (1993) Artificial neural networks for land-cover classification and mapping. Int. Journal of Geographical Information Systems 7: pp. 173-186.

Clark, I. (1977) Regularization of a semi-variogram, Computers and Geosciences, 3: pp. 341-346.

Clark, R.N., Gallagher, A.J. & Swayze, G.A. (1990a) Material absorption band depth mapping of imaging spectrometer data using the complete band shape least-squares algorithm simultaneously fit to multiple spectral features from multiple materials: in Proceedings of the Third Airborne Visible/Infrared Imaging Spectrometer (AVIRIS) Workshop, JPL Publication 90-54: pp. 176-186.

Clark, R.N., King, T.V.V., Kleijwa, M., Swayze, G.A. & Vergo, N. (1990b) High spectral Resolution Reflectance Spectroscopy of Minerals. J. Geophys. Res. 95: pp. 12653-12680.

Clark, R.N., Swayze, G.A., Livo, K.E., Kokaly, R.F., Sutley, S.J., Dalton, J.B., McDougal, R.R. & Gent, C.A. (2003) Imaging Spectroscopy: Earth and Planetary Remote Sensing with the USGS Tetracorder and Expert Systems. J. Geophys. Res., In Press.

Clevers, J.G.P.W. & Jongschaap, R. (2001) Imaging Spectrometry for Agricultural Applications. In: F.D Van der Meer. & S.M de Jong. (Eds.) Imaging Spectrometry. Kluwer Academic Publishers, Dordrecht, pp. 157-199.

Cloutis, E.A. (1989) Spectral Reflectance Properties of Hydrocarbons: Remote-Sensing Implications. Science 245: pp. 165-168.

Cloutis, E.A., Gaffey, M.J. Jackowski, T.L. & Reed, K.L. (1986) Calibrations of Phase Abundance, Composition, and Particle Size Distribution of Olivine-Orthopyroxene mixtures from Reflectance Spectra, J. Geophys. Res., 91: pp. 11641-11653.

Cochrane, M.A. & Souza, C.M. (1998) Linear mixture model classification of burned forests in the Eastern Amazon, International Journal of Remote Sensing 19: pp. 3433-3440.

Cohen, W.B., Maiersperger, T.K., Yang, Z., Gower, S.T., Turner, D.P., Ritts, W.D., Berterretche, M. & Running, S.W. (2003) Comparisons of land cover and LAI estimates derived from ETM+ and MODIS for four sites in North America: a quality assessment of 2000/2001 provisional MODIS products, Remote Sensing of Environment (in press).

Cohen, W.B., Spies, T.A. & Bradshaw, G.A. (1990) Semivariograms of digital imagery for analysis of conifer canopy structure, Remote Sensing of Environment 34: pp. 167-178.

Coifman, R.R., Meyer, Y. & Wickerhauser, M.V. (1992) Wavelet analysis and signal processing, in M.B. Ruskai, G. Beylkin, R.R. Coifman, I. Daubechies, S.G. Mallat, Y. Meyer and L. Raphael (eds.), Wavelets and Their Applications, Jones and Bartlett Publishers, Sudbury, pp. 153-158.

Colby, J.D. (1991) Topographic normalization in rugged terrain. Photogrammetric Engineering & Remote Sensing 57 (5): pp. 531-537.

Collins, J.B. & Woodcock, C.E. (1999) Geostatistical estimation of resolution-dependent variance in remotely sensed images, Photogrammetric Engineering & Remote Sensing 65: pp. 41-50.

Colwell, R.N. (Ed.) (1983) Manual of Remote Sensing. Second Edition. Vol I: Theory, Instruments and Techniques. American Society of Photogrammetry and Remote Sensing ASPRS, Falls Church.

Congalton, R.G. (1991) A review of assessing the accuracy of classifications of remotely sensed data, Remote Sensing of Environment, 37: pp. 35-46.

Connors, R.W., Trivedi, M.M. & Harlow, C.A. (1984) Segmentation of a high-resolution urban scene using texture operators, Computer Vision, Graphics and Image Processing 25: pp. 273-310.

Corvi, M. & Nicchiotti, G. (1995) Multiresolution image registration, in Proceedings IEEE International Conference on Image Processing. Washington DC, USA, 23-26 October 1995, pp. 224-227.

Cote, S., & Tatnall, A.R.L. (1997) The Hopfield neural network as a tool for feature tracking and recognition from satellite sensor images, International Journal of Remote Sensing, 18: pp. 871-885.

Couloigner, I. & Ranchin, T. (2000) Mapping urban areas:a multiresolution modelling approach for semi-automatic extraction of streets. Photogrammetric Engineering & Remote Sensing 66 (7): pp. 867-874.

Cracknell, A.P. (1998) Synergy in remote sensing – what's in a pixel?, International Journal of Remote Sensing 19: pp. 2025-2047.

Crapper, P.F. (1984) An estimate of the number of boundary cells in a mapped landscape coded to grid cells. Photogrammetric Engineering & Remote Sensing 50: pp. 1497-1503.

Cressie, N.A.C. (1993) Statistics for spatial data. Wiley, New York, 900 pp.

Crist, E.P. & Cicone, R.C. (1984) A Physically Based Transformation of Thematic Mapper Data: the TM Tassled Cap. IEEE Transactions on Geoscience and Remote sensing, Vol. GE-22: pp. 256-263.

Cross, A., Mason, D. & Dury, S. (1988) Segmentation of remotely-sensed images by a split-and-merge process. International Journal of Remote Sensing 9 (8): pp. 1329-1345.

Cross, A.M., Settle, J.J., Drake, N.A. & Paivinen, R.T.M. (1991) Subpixel measurement of tropical forest cover using AVHRR data, International Journal of Remote Sensing 12: pp. 1119-1129.

Crosta, A.P. & McMoore, J. (1989) Enhancement of Landsat Thematic Mapper imagery for residual soil mapping in SW Minas Gerais State, Brazil, in Proceedings 7th Thematic Conference ERIM, Calgary 2-6: pp. 1173-1187.

Crowley, J.K. & Swayze, G.A. (1995) Mapping minerals, amorphous materials, environmental materials, vegetation, water, ice, and other materials: The USGS Tricorder Algorithm. In: Summaries of the Fifth Annual JPL Airborne Earth Science Workshop, JPL Publication 95-1: pp. 39-40.

Crowley, J.K., Brickey, D.W. & Rowan, L.C. (1989) Airborne imaging spectrometer data of the Ruby mountains, Montana: mineral discrimination using relative absorption band-depth images. Remote Sensing of Environment 29: pp. 121-134.

Csillag, F. & Kabos, S. (1997) Hierarchical decomposition of variance with applications in environmental mapping based on satellite images. Mathematical Geology 28: pp. 385-405.

Curran, P.J. & Atkinson, P.M. (1998) Geostatistics and remote sensing, Progress in Physical Geography 22: pp. 61-78.

Curran, P.J. & Ojedele, B. (1988) Airborne MSS for land cover classification, Geocarto International 4: pp. 67-72.

Curran, P.J. (1985) Principles of Remote Sensing. Longman Group Limited, London, 282 pp.

Curran, P.J. (1988) The semivariogram in remote sensing: An introduction, Remote Sensing of Environment 24: pp. 493-507.

Curran, P.J. (1989) Remote sensing of foliar chemistry. Remote Sensing of Environment 30: pp. 271-278.

Curran, P.J., & Atkinson, P.M. (1999) Issues of scale and optimal pixel size, In Spatial Statistics for Remote Sensing, (ed. A. Stein, F. van der Meer and B. Gorte), Kluwer, Dordrecht, pp. 115-132.

Curran, P.J., Dungan, J.L. & Peterson, D.L. (2001) Estimating the foliar biochemical concentration of leaves with reflectance spectrometry, testing the Kokaly and Clark methodologies. Remote Sensing of Environment 76: pp. 349-359.

Curran, P.J., Dungan, J.L., Macler, B.A., Plummer, S.E. & Peterson, D.L. (1992) Reflectance spectroscopy of fresh whole leaves for the estimation of chemical concentration. Remote Sensing of Environment 39: pp. 153-166.

Curran, P.J., Foody, G.M. & Van Gardingen, P.R. (1997) Scaling up, in P.R.Van Gardingen, G.M. Foody and P.J. Curran (Eds.), Scaling up: from cell to landscape, Cambridge University Press, Cambridge, pp. 1-5.

Cushnie, J.L. (1987) The interactive effect of spatial resolution and degree of internal variability within land cover types on spatial classification accuracies, International Journal of Remote Sensing 8: pp. 15-29.

D

Dactu, M., Luca, D. & Seidel, K. (1997) Wavelet-based digital elevation model analysis, in Spiteri (ed.), Remote Sensing '96, Balkema, Rotterdam, pp. 283-290.

Dai, X. & Khorram, S. (1998) The effects of image misregistration on the accuracy of remotely sensed change detection. IEEE Transactions on Geosciences and Remote Sensing 36 (5): pp. 1566-1577.

Daubechies, I. (1988) Orthonormal bases of compactly supported wavelets, Communications On Pure and Applied Mathematics 41: pp. 906-966.

Daubechies, I. (1989) Orthonormal bases of wavelets with finite support – connection with discrete filters, in J.M. Combes, A. Grossman and P. Tchmitchian (Eds.), Wavelets: Time Frequency Methods and Phase Space, Springer-Verlag, New York, pp. 38-65.

Daubechies, I. (1992) Ten Lectures on Wavelets. CBMS Lecture Notes, SIAM, Philadelphia, 357 pp.

Dawson, B.R.P. & Parsons, A.J. (1990) Texture measures for the identification and monitoring of urban derelict land, in Proceedings of the NERC Symposium on Airborne Remote Sensing, Natural Environment Research Council, Swindon, pp. 159-175.

De Bruin, S. (2000) Querying probabilistic land cover data using fuzzy set theory, International Journal of Geographical Information Science 14: pp. 359-372.

De Castro, E. & Morandi, C. (1987) Registration of translated and rotated images using finite Fourier Transforms. IEEE Transactions in Pattern Analysis and Machine Intelligence 9 (5): pp. 700-703.

De Fries, R.S., Hansen, M.C. & Townshend, J.R.G. (2000) Global continuous fields of vegetation characteristics: a linear mixture model applied to multi-year 8 km AVHRR data, International Journal of Remote Sensing 21: pp. 1389-1414.

De Gruijter, J. (1999) Spatial Sampling Schemes for Remote Sensing (1999) In: A Stein, F. van der Meer, B. Gorte (Eds.), Spatial Statistics for Remote Sensing. Kluwer Academic Publishers, Dordrecht, pp. 211-242.

De Jong S.M., Hornstra, T. & Maas, H.G. (2001) An integrated approach to the Classification of Mediterranean Land Cover Types: the SSC Method, Journal of Applied Geosciences 3, 176-18.

De Jong, S.M. & Burrough, P.A. (1995) A fractal approach to the classification of Mediterranean vegetation types in remotely sensed images. Photogrammetric Engineering & Remote Sensing 68 (8): pp. 1041-1053.

De Jong, S.M. (1994) Derivation of vegetative variables from a Landsat TM image for erosion modelling. Earth Surface Processes and Landforms 19: pp. 165-178.

De Jong, S.M. (1998) Imaging Spectrometry for Monitoring Tree Damage Caused by Volcanic Activity in the Long Valley Caldera, California. ITC Journal, 1998 (1): pp. 1-10.

De Jong, S.M., Bagre, A., Van Teeffelen, P.B.M. & Van Deursen, W.P.A. (2000) Monitoring trends in urban growth and surveying city quarters in Ouagadougou, Burkina Faso using spot-XS. Geocarto International 15 (2): pp. 61-67.

De Jong, S.M., Hornstra, T & Maas, H.G. (2001) An Integrated Spatial and Spectral Approach to the Classification of Mediterranean Land Cover Types: the SSC Method. International Journal of Applied Geosciences Vol. 3 (2): pp. 176-183.

De Jong, S.M., Pebesma, E.J. & Lacaze, B (2003) Aboveground Biomass Assessment of Mediterranean Forests using Airborne Imaging Spectrometry: the DAIS Peyne Experiment. International Journal of Remote Sensing 24 (7): pp. 1505-1520.

De Kok, R. Schneider T. & Ammer, U. (1999) Object-base classification and applications in the alpine forest environment. In International Archives of Photogrammetry & Remote Sensing, Vol. 32, Part 7-4-3 W6, Valladolid.

De Kok, R., Schneider, T., Baatz, M. & Ammer, U. (2000) Analysis of Image Objects from VHR Imagery for Forest GIS Updating in the Bavarian Alps. ISPRS, Vol. XXXIII, Amsterdam.

De Wit, A.M.W. (2001) Runoff Controlling Factors in Various Sized Catchments in a Semi-arid Mediterranean Environment in Spain. Netherlands Geographical Studies 284, KNAG Utrecht, 229 pp.

Debeir O, Van den Steen, I., Latinne, P., Van Ham, P. & Wolff, E. (2002) Textural and contextual land-cover classification using single and multiple classifier systems. Photogrammetric Engineering & Remote Sensing 68: pp. 597-605.

Definiens-Imaging (2003) e-Cognition. WWW document, http://www.definiens-imaging.com/index.htm accessed 26-08-2003.

Dent, D. & Young, A. (1981) Soil Survey and Land Evaluation. George Allen & Uniwin Publishers, London, 278 pp.

Department of the Environment (1994). Biodiversity: The UK Action Plan. London: Department of the Environment.

Deubler, J. & Olivo, J.C. (1997) A Wavelet-Based Multiresolution Method to Automatically Register Images. Journal of Mathematical Imaging and Vision 7 (3): pp. 199-209.

Deutsch, C.V. & Journel, A.G. (1992) GSLIB. Geostatistical Software Library and User's Guide, Oxford University Press, New York, 340 pp.

Deutsch, C.V. & Journel, A.G. (1998) GSLIB: Geostatistical Software and User's Guide, Second Edition, Oxford University Press, Oxford.

Dikshit, O. (1996) Textural classification for ecological research using ATM images, International Journal of Remote Sensing 17: pp. 887-915.

Djamdji, J., Bijaoui, A. & Maniere, R. (1993) Geometrical registration of images: the multiresolution approach. Photogrammetric Engineering and Remote Sensing 59 (5): pp. 645-653.

Dong, Y, Forster, B. & Ticehurst, C. (1997) Street orientation detection and recognition in Landsat TM and SPOT HRV imagery. Pattern Recognition Letters 18: pp. 759-769.

Donoho, D.L. & Huo, X. (2000) Beamlets and multiscale image analysis, Lecture Notes in Computational Science and Engineering: Multiscale and Multiresolution Methods, Springer, pp. 149-196.

Dragotti, P.L., Poggi, G. & Ragozini, A.R.P. (2000) Compression of multispectral images by three-dimensional SPIHT algorithm. IEEE Transactions on Geosciences and Remote Sensing 38 (1): pp. 416-428.

Drake, N. & White, K. (1991) Linear mixture modelling of Landsat Thematic Mapper data for mapping the distribution and abundance of gypsum in the Tunisian Southern Atlas, Proceedings of Spatial Data 2000, Remote Sensing Society, Nottingham, pp. 168-177.

Dreyer, P. (1993) Classification of land cover using optimised neural nets on SPOT data, Photogrammetric Engineering & Remote Sensing 59: pp. 617-621.

Driscoll Jr, E.C. (1985) Spatial classification of urban land uses from land cover probabilities derived through remote sensing. PhD Dissertation, Standford University, 158 pp.

Drury, S.A. (1987) Image Interpretation in Geology, Allen & Unwin. London, 243 pp.

Dubuisson-Jolly, M.P. & Gupta, A. (2000) Color and texture fusion: application to aerial image segmentation and GIS updating. Image and Vision Computing (18): pp. 823-832.

Duggin, M.J. & Robinove, C.J. (1990) Assumptions implicit in remote sensing data acquisition and analysis, International Journal of Remote Sensing 11(10): pp. 1669-1694.

Duke, E.F. (1994) Near infrared spectra of muscovite, Tschermak substitution, and metamorphic reaction progress: implications for remote sensing, Geology, 22: pp. 621-624.

Dungan, J.L. (1995) Geostatistical approaches for spatial estimation of vegetation quantities using ground and image data, in RSS95: remote sensing in action, Remote Sensing Society, Nottingham, pp. 947-954.

Dungan, J.L., Peterson, D.L. & Curran, P.J. (1994) Alternative approaches for mapping vegetation quantities using ground and image data, in W. Michener, J. Brunt and Stafford (eds.), Environmental Information Management and Analysis: Ecosystem to Global Scales, Taylor & Francis, London, pp. 237-261.

E

Eastman, J.R. & Laney, R.M. (2002) Bayesian soft classification for sub-pixel analysis: a critical evaluation, Photogrammetric Engineering & Remote Sensing, 68: pp. 1149-1154.

Erdas Imagine (1997) Erdas Field Guide, Erdas Inc., Atlanta, 620 pp.

Esteban, D. & Galand, C. (1977) Application of quadrature mirror filters to split-band voice coding schemes, in Proccedings of the IEEE International Conference on Acoustics, Signal and Speech Processing, Hartford, USA, May 1977, pp. 191-195.

Estes, J.E. & Mooneyhan, D.W. (1994) Of maps and myths, Photogrammetric Engineering & Remote Sensing, 60: pp. 517-524.

ETM+ and field data. In: Operational Tools in Forestry using Remote Sensing Techniques. ForestSAT Symposium, August 5th-9th 2002, Edinburgh, Scotland. Proceedings (CD-ROM), 8 p.

Eyton, J.R. (1993) Urban land use classification and modeling using cover frequencies. Applied Geography, 13: pp. 111-121.

F

Fedorov, D., Fonseca, L.M.G., Kenney, C. & Manjunath, B.S. (2002) Automatic Registration and Mosaicking System for Remotely Sensed Imagery, in 9th International Symposium on Remote Sensing, Crete, Greece, 22-27 September 2002.

Ferretti, A., Prati, C. & Rocca, F. (1999) Multibaseline InSAR DEM reconstruction: the wavelet approach. IEEE Transactions on Geosciences and Remote Sensing 37 (2): pp. 705-714.

Fisher, P. (1997) The Pixel: a Snare or a Delusion. International Journal of Remote Sensing, Vol.18: pp. 679-685.

Fisher, P.F. & Pathirana, S. (1990) The evaluation of fuzzy memberships of land cover classes in the suburban zone, Remote Sensing of Environment 34: pp. 121-132.

Flack, J., Gahegan, M. & West, G. (1994) The use of sub-pixel measures to improve the classification of remotely sensed imagery of agricultural land, Proceedings of the 7th Australasian Remote Sensing Conference, Melbourne, pp. 531-541.

Fonseca de Seixas, M.J. (1998) patterns of eterogeneity derived from remote Sensing Images: Implications for the Environmental Assessment of Desertification in Southern portugal. PhD-thesis of the University of Lisboa, Portugal, 292 pp.

Fonseca, L.M.G. & Costa, M.H. (1997) Automatic registration of satellite images, in Brazilian Symposium on Graphic Computation and Image Processing, Campos de Jordão, Brasil, 13-16 October 1997, pp. 219-226.

Fonseca, L.M.G. & Manjunath, B.S. (1995) Registration techniques for multisensor remotely sensed imagery. Photogrammetric Engineering & Remote Sensing 62 (9): pp. 1049-1056.

Fonseca, L.M.G. (1999) Automatic Registration of Remote Sensing Images based on Multiresolution Decomposition. (Doctoral Thesis), INPE, São José dos Campos, Brazil, 219 pp.

Fonseca, L.M.G., Costa, M.H., Manjunath, B.S. & Kenny, C. (1998) Automatic registration of satellite imagery, in Proceedings of the Workshop on Image Registration, Greenbelt, USA, 20-21 November 1997, pp. 13-27.

Foody, G.M. (1998) Sharpening fuzzy classification output to refine the representation of sub-pixel land cover distribution, International Journal of Remote Sensing 19: pp. 2593-2599.

Foody, G.M. (2004) Sub-pixel methods in Remote Sensing. In: S.M. de Jong and F.D. van der Meer, Remote Sensing Digital Image Processing: including the spatial domain. Kluwer Academics, Dordrecht, chapter 3 this volume.

Foody, G.M. (2001) Thematic mapping from remotely sensed data with neural networks: MLP, RBF and PNN based approaches, Journal of Geographical Systems 3: pp. 217-232.

Foody, G.M. & Arora, M.K. (1997) An evaluation of some factors affecting the accuracy of classification by an artificial neural network, International Journal of Remote Sensing 18: pp. 799-810.

Foody, G.M. & Cox, D.P. (1994) Sub-pixel land cover composition estimation using a linear mixture model and fuzzy membership functions, International Journal of Remote Sensing 15: pp. 619-631.

Foody, G.M. (1996) Approaches for the production and evaluation of fuzzy land cover classifications from remotely-sensed data, International Journal of Remote Sensing, 17: pp. 1317-1340.

Foody, G.M. (1998) Sharpening fuzzy classification output to refine the representation of sub-pixel land cover distribution, International Journal of Remote Sensing 19: pp. 2593-2599.

Foody, G.M. (1999) Image classification with a Neural Network: from completely-crisp to fully-fuzzy situations. In Atkinson, P. and Tate, N. (eds.), Advances in remote sensing and GIS analysis. Wiley & Son, Chichester, pp. 17-37.

Foody, G.M. (2000a) Mapping land cover from remotely sensed data with a softened feedforward neural network classification, Journal of Intelligent and Robotic Systems 29: pp. 433-449.

Foody, G.M. (2000b) Estimation of sub-pixel land cover composition in the presence of untrained classes, Computers and Geosciences 26: pp. 469-478.

Foody, G.M. (2002a) Status of land cover classification accuracy assessment, Remote Sensing of Environment 80: pp. 185-201.

Foody, G.M. (2002b) Hard and soft classifications by a neural network with a non-exhaustively defined set of classes, International Journal of Remote Sensing 23: pp. 3853-3864.

Foody, G.M. (2002c) The role of soft classification techniques in the refinement of estimates of ground control point location, Photogrammetric Engineering & Remote Sensing 68: pp. 897-903.

Foody, G.M., Campbell, N.A., Trodd, N.M. & Wood, T.F. (1992) Derivation and applications of probabilistic measures of class membership from the maximum likelihood classification, Photogrammetric Engineering & Remote Sensing 58: pp. 1335-1341.

Foody, G.M., Lucas, R.M., Curran, P.J. & Honzak, M. (1997) Non-linear mixture modelling without end-members using an artificial neural network, International Journal of Remote Sensing 18: pp. 937-953.

Forman, R. (1995) Land mosaics. The ecology of landscapes and regions. Cambridge University Press, Cambridge.

Foschi, P. & Smith, D. (1997) Detecting Subpixel Woody Vegetation in Digital Imagery Using Two Artificial Intelligence Approaches. Photogrammetric Engineering & Remote Sensing 63: pp. 493-500.

Fotheringham, A.S. & Wong, D.W.S. (1991) The modifiable areal unit problem in multivariate statistical analysis, Environment and Planning A 23: pp. 1025-1044.

Fourier, J. (1988) Theorie Analytique de la Chaleur. Editions Jacques Gabay, Paris, 644 pp.

Fourty, Th., Baret, F., Jacquemoud, S., Schmuck, G. & Verdebout, J. (1996) Leaf optical properties with explicit description of its biochemical composition: Direct and inverse problems. Remote Sensing of Environment 56: pp. 104-117.

Franco-Lopez, H., Ek, A.R. & Bauer, M.E. (2001) Estimation and mapping of forest stand density, volume, and cover type using the k-nearest neighbours method, Remote Sensing of Environment 77 (3): pp. 251-274.

Franklin, S.E. & Peddle, D.R. (1990) Classification of SPOT HRV imagery and texture features. International Journal of Remote Sensing 11 (3): pp. 551-556.

Frizzelle, B.G. & Moody, A. (2001) Mapping continuous distributions of land cover: A comparison of maximum-likelihood estimation and artificial neural networks, Photogrammetric Engineering & Remote Sensing 67: pp. 693-705.

Fu, K. & Mui, J. (1981) A survey of image segmentation. Pattern Recognition 13 (1): pp. 3-16.

Fukuda, S. & Hirosawa, H. (1999) Smoothing effects of wavelet-based speckle filtering: the Haar basis case. IEEE Transactions on Geosciences and Remote Sensing 37 (2): pp. 1168-1172.

Fuller, R.M. & Parsell, R.J. (1990) Classification of TM imagery in the study of land use in lowland Britain: practical considerations for operational use. International Journal of Remote Sensing 11: pp. 1901-1917.

Fuller, R.M., Groom, G.B. & Jones, A.R. (1994a) The Land Cover Map of Great Britain: an automated classification of Landsat Thematic Mapper data. Photogrammetric Engineering & Remote Sensing. 60: pp. 553-562.

Fuller, R.M., Groom, G.B. & Wallis, S.M. (1994b). The availability of Landsat TM images for Great Britain. International Journal of Remote Sensing. 15: pp. 1357-1362.

Fuller, R.M., Smith, G.M., Sanderson, J.M., Hill, R.A. & Thomson, A.G. (2002). Land Cover Map 2000: a general description of the UK's new vector GIS based on classification of remotely sensed data. Cartographic Journal 39: pp. 15-25.

G

Gabor, D. (1946) Theory of communication. Journal of the IEE 93: pp. 429-457.

García-Haro, F.J. (1997) Modelización y estimación de parámetros relacionados con la cubierta vegetal en teledetección, Tesis doctoral, Univ. de Valencia.

Garcia-Haro, F.J., Gilabert, M.A. & Meliá, J. (1996) Linear spectral mixture modelling to estimate vegetation amount from optical spectral data, International Journal of Remote Sensing 17: pp. 3373-3400.

García-Haro, F.J., Gilabert, M.A. & Meliá, J. (1999) Estimation of endmembers from spectral mixtures, Remote Sensing of Environment 68: pp. 237-253.

García-Haro, F.J., Gilabert, M.A., Younis, M.T. & Meliá, J. (1995) Análisis de composición espectral (ACE) basado en un modelo de reflectividad para el estudio de la vegetación en una zona semiárida, in J.L. Casanova and J. Sanz (eds.), Teledetección, usos y aplicaciones, ISBN 84-7762-693-6: pp. 163-170.

García-Haro, F.J., Sommer, S., & Kemper, T. (2003) Variable multiple endmember spectral mixture analysis (VMESMA): a high performance computing and environment analysis tool, International Journal of Remote Sensing, (submitted).

Gibson, D. & Gaydeck, P.A. (1995) Definition and application of a fourier domain texture measure: Applications to histological image segmentation, Computers in Biology and Medicine 25: pp. 551-557.

Gillespie, A.R. (1992) Spectral mixture analysis of multi-spectral thermal infrared images, Remote Sensing of Environment 42: pp. 137-145.

Gong, P. & Howarth, P.J. (1992a) Land-use classification of SPOT HRV data using a cover-frequency method. International Journal of Remote Sensing 13 (8): pp. 1459-1471.

Gong, P. & Howarth, P.J. (1990a) The use of structural information for improving land-cover classification accuracies at the rural-urban fringe. Photogrametric Engineering & Remote Sensing 56 (1): pp. 67-73.

Gong, P. & Howarth, P.J. (1990b) Land cover to land use conversion: a knowledge-based approach, Technical Papers, Annual Conference of American Society of Photogrammetry and Remote Sensing, Denver, Colorado, Vol. 4: pp. 447-456.

Gong, P. & Howarth, P.J. (1992b) Frequency-based contextual classification and gray-level vector reduction for land-use identification. Photogrametric Engineering & Remote Sensing 58 (4): pp. 423-437.

Gong, P. & Howarth, P.J., (1989) Performance analyses of probabilistic relaxation methods for land-cover classification, Remote Sensing of Environment 30: pp. 33-42.

Gong, P. (1994) Reducing boundary effects in a kernel-based classifier. International Journal of Remote Sensing, 15 (5): pp. 1131-1139.

Gong, P. Marceau, D. & Howarth, P.J. (1992) A comparison of spatial feature extraction algorithms for land-use mapping with SPOT HRV data. Remote Sensing of Environment 40: pp. 137-151.

Gonzalez, R.C., & Wintz, P. (1987) Digital Image Processing. Addison-Wesley Publishing Com., Reading, Mass., 495 pp.

Goovaerts, P. (1997) Geostatistics for Natural Resources Evaluation. Oxford University Press, New York, 483 pp.

Gopal, S., Woodcock, C.E. & Strahler, A.H. (1999) Fuzzy neural network classification of global land cover from a 1° AVHRR data set, Remote Sensing of Environment 67: pp. 230-243.

Gorte, B. (1998) Probabilistic Segmentation of Remotely Sensed Images. In ITC Publication Series No. 63.

Gorte, B. (1998) Probabilistic segmentation of remotely sensed images, PhD Thesis Wageningen Agricultural University and ITC, 143 pp.

Green, A.A. & Graig, M.D. (1985) Analysis of aircraft spectrometer data with logarithmic residuals. In: G. Vane and A.F.H. Goetz (Editors), Proceedings of the Airborne Imaging Spectrometer Data Analysis Workshop, Pasadena, USA, NASA-JPL Publication 85-41: pp. 111-119.

Green, A.A., Berman, M., Switzer, P. &. Craig, M.D (1988) A Transformation for Ordering Multispectral Data in Terms of Image Quality with Implications for Noise Removal. IEEE Transactions on Geoscience and Remote Sensing 26: pp. 65-74.

Groom, G.B. & Fuller, R.M. (1996). Contextual correction: techniques for improving land cover mapping from remotely sensed images. International Journal of Remote Sensing. 17: pp. 69-89.

Grove, C.I., Hook, S.J. & Paylor, E.D. (1992) Laboratory reflectance spectra for 160 minerals 0.4-2.5 micrometers: JPL Publication 92-2, Jet Propulsion Laboratory, Pasadena, CA.

Guarguet-Duport, B., Girel, J., Chassery, J.M. & Pautou, G. (1996) The use of multiresolution analysis and wavelet transforms for merging SPOT panchromatic and multispectral image data. Photogrammetric Engineering & Remote Sensing 62 (9): 1057-1066.

H

Haar, A. (1910) Zur theorie der orthogonalen funktionen-systeme. Mathematische Annalen 69: pp. 331-371.

Haggett, P., Chorley, R.J &. Stoiddart, D.R. (1965) Scale standards in geographical research. A new measure of areal magnitude. Nature 205: pp. 844-847.

Hall, O. & Hay, G.J. (2003) A multiscale object-specific approach to digital change detection, International Journal of Applied Earth Observation and Geoinformation, in press.

Hall, O., Hay, G.J., Bouchard, A. & Marceau, D.J. (2003) Detecting dominant landscape objects through multiple scales: An integration of object-specific methods and watershed segmentation, Landscape Ecology, in press.

Haralick, R.M. & Shanmugham, K.S. (1974) Combined spectral and spatial processing of ERTS imagery data, Remote Sensing of Environment 3: pp. 3-13.

Haralick, R.M. & Shapiro, L. (1985) Survey: Image segmentation techniques. Computer Vision, Graphics, and Image Processing, 29 (1): pp. 100-132.

Haralick, R.M. & Shapiro, L.G. (1992) Computer and Robot Vision, Volume I, Addison-Wesley.

Haralick, R.M. (1979) Statistical and structural approaches to texture, Proceedings of the IEEE, 67 (5): pp. 786-804.

Haralick, R.M., Shanmugam, K. & Dinstein, I. (1973) Textural features for image classification, IEEE Transactions on Systems, Man and Cybernetics, 3: pp. 610-621.

Hargis, C., Bisonette, J. & David, L. (1998) The behaviour of landscape metrics commonly used in the study of habitat fragmentation. Landscape ecology 13: pp. 167-186.

Harper, D. (1983) Eye in the Skye. Introduction to Remote Sensing. Multiscience Publications Ltd. Montréal, 252 pp.

Harris, P.M. & Ventura, S.J. (1995) The integration of geographic data with remotely-sensed imagery to improve classification in an urban area. Photogrammetric Engineering & Remote Sensing 61: pp. 993-998.

Harts, J.J., Zeylmans van Emmichoven, M. & Van Dam, F. (2002) Op zoek naar plattelandsmilieus. Utrecht, Urban and Regional Research Centre Utrecht, (URU).

Hawkins, J.K. (1970) Textural properties for pattern recognition, in B.C. Lipkin and A. Rosenfeld (eds.), Picture Processing and Psychopictorics, Academic Press, New York, pp. 347-370.

Hay, G.J. & Marceau, D.J. (1998) Are image-objects the key for upscaling remotely sensed data?, in Proceedings of the Modeling Complex Systems Conference, July 12-17, New Orleans, Louisiana, pp. 88-92.

Hay, G.J. (2002) Multiscale object-specific analysis: An integrated hierarchical approach for landscape ecology. Unpublished Ph.D. Thesis, Department of Biological Sciences, University of Montreal, 184 p.

Hay, G.J., Blaschke, T., Marceau, D. & Bouchard, A. (2003) A comparison of three image-object methods for the multiscale analysis of landscape structure. International Journal of Photogrammetry and Remote Sensing (1253): pp. 1-19.

Hay, G.J., Blaschke, T., Marceau, D.J. & Bouchard, A. (2003) A comparison of three image-objet methods for the multiscale analysis of landscape structure. Photogrammetric Engineering & Remote Sensing 57: pp. 327-345.

Hay, G.J., Dubé, P., Bouchard, A & Marceau, D. (2002) A Scale-Space Primer for Exploring and Quantifying Complex Landscapes. Ecological Modelling 153 (1-2): pp. 27-49.

Hay, G.J., Marceau, D.J. & Bouchard, A. (2002b) Modelling and Visualizing Multiscale Landscape Structure within a Hierarchical Scale-Space Framework. Proceedings of the Joint International Symposium on Geospatial Theory, Processing and Applications (On CD). ISPRS Commission IV. Ottawa Congress Centre, Ottawa, Canada, 9-12 July.

Hay, G.J., Marceau, D.J., Dube, P. & Bouchard, A. (2001) A multiscale framework for landscape analysis: Object-specific analysis and upscaling. Landscape Ecology, vol. 16 (6): pp. 471-490.

Hay, G.J., Niemann, K.O. & Goodenough, D.G. (1997) Spatial thresholds, image-objects and upscaling: A multiscale evaluation, Remote Sensing of Environment 62: pp. 1-19.

Hay, G.J., Niemann, K.O. & McLean, G.F. (1995) An object-specific image-texture analysis of h-resolution forest imagery, Remote Sensing of Environment 55: pp. 108-122.

Hedger, R.D., Atkinson, P.M., Malthus, T.J. & George, D.G. (1996) Planning optimal sampling strategies for estimating the regional mean water quality in lakes, in RSS96: remote sensing science and industry, Remote Sensing Society, Nottingham, pp. 221-228.

Henderson, F.M. &. Lewis A.J (1998) Principles and Applications of Imaging Radar. Manual of Remote Sensing 3rd edition, Vol.2. American Society for Photogrammetry & Remote Sensing. Wiley & Sons, New York, 866 pp.

Hepner, G.F. Logan, T. Ritter, N. & Bryant, N. (1990) Artificial neural network classification using minimal training set. Photogrammetric Engineering & Remote Sensing 56 (4): pp. 469.

Herman, B., LaRocca, A.J. & Turner, R.E. (1993) Atmospheric Scattering. In: W.L. Wolfe & G.J. Zissis (Eds), The Infrared Handbook. Environmental Research Institute of Michigan (ERIM), Ann Arbor, Michigan, pp. 4-1 to 4-76.

Herzfeld, U.C. & Higginson, C.A. (1996) Automated geostatistical seafloor classification – principles, parameters, feature vectors and discrimination criteria, Computers and Geosciences 22: pp. 35-52.

Herzfeld, U.C. (1999) Geostatistical interpolation and classification of remote sensing data from ice surfaces, International Journal of Remote Sensing 20: pp. 307-327.

Herzog, F. & Lausch, A. (2001) Supplementing land-use statistics with landscape metrics: some methodological considerations. Environmental Monitoring and Assessment (72): pp. 37-50.

Hill, J. & Mehl, W. (2003) Geo- und radiometrische Aufbereitung multi- und hyperspektraler Daten zur Erzeugung langjähriger Zeitreihen, Photogrammetrie, Fernerkundung, Geoinformation, 1/2003: pp. 7-14.

Hill, J. (1997) Integrated Approach to Desertification Mapping and Monitoring in the Mediterranean Basin. http://www.feut.uni-trier.de:8080/forschung/demon2/ Accessed at 28/05/2003.

Hillel, D. (1992) Out of the Earth: Civilization and the Life of the Soil. University of California Press, Berkeley, 320 pp.

Hoffmann, A., Smith, G.M. & Lehmann, F. (2000) Die Klassifizierung hochauflösender Daten – ein Per-Parcel-Ansatz mit Daten des digitalen Kamerasystems HRSC-A. In Strobl, J, Blaschke, T., Griesebner, G. (eds.): Angewandte Geographische Informationsverarbeitung XII, Wichmann-Verlag, Heidelberg, pp. 228-237.

Hofmann, T. & Boehner, J. (1999) Spatial pattern recognition by means of representativeness measures. In: IEEE 6/99.

Hofmann, T., Puzicha, J. & Buhmann, J. (1998) Unsupervised texture segmentation in a deterministic annealing framework. IEEE Transactions on Pattern Analysis and Machine Intelligence. Vol. 20 (8): pp. 803-818.

Holschneider, M., Kronland-Martinet, R., Morlet, J. & Tchmitchian, P. (1989) A real time algorithm for signal analysis with the help of the wavelet transform, in J.M. Combes, A. Grossman, P. Tchmitchian (Eds.), Wavelets: Time Frequency Methods and Phase Space, Springer-Verlag, New York, pp. 286-297.

Hopfield, J.J. & Tank, D.W. (1985) Neural computation of decisions in optimization problems, Biological Cybernetics 52: pp. 141-152.

Horgan, G. (1998) Wavelets for SAR image smoothing. Photogrammetric Engineering & Remote Sensing 64 (12): pp. 1171-1177.

Hörig, B., Köhn, F., Oschötz, F. & Lehmann, F. (2001) HyMap hyperspectral remote sensing to detect hydrocarbons. International Journal of Remote Sensing, 2001 (22) 8: pp. 1413-1422.

Hornibrook, M. (2002) Spectral unmixing of ASTER data, Escondida North, Chile, Poster Presentation at Geoimage PTY ltd, Spectral Geology P/L, Eltham, Victoria, Australia.

Hornstra, T., Maas, H.G. & de Jong, S.M. (2000) Classification of Spectroscopical Imagery by Combining Spectral and Spatial Information: the SSC Method. Proceedings of the 19th ISPRS Congres, Amsterdam 16-23 July, pp. 550-558.

Hornung, M., Bull, K.R., Cresser, M., Ullyett, J., Hall, J.R., Langan, S., Loveland, P.J. & Wilson, M.J. (1995) The sensitivity of surface waters of Great Britain to acidification predicted from catchment characteristics. Environmental Pollution 87: pp. 207-214.

Hsieh, J.W., Liao, H.Y.M., Fan, K.C., Ko, M.C. & Hung, Y.P. (1997) Image Registration using a New Edge-Based Approach. Computer Vision and Image Understanding 67 (2): pp. 112-130.

Huete, A.R. &. Jackson, R.D. (1987) The Suitability of Spectral Indices for Evaluating Vegetation Characteristics on Arid Rangelands. Remote Sensing of Environment 23: pp. 213-232.

Huete, A.R. (1988) A soil adjusted vegetattion index. Remote Sensing of Environment 25: pp. 295-309.

Hunt, G.R. (1977) Spectral signatures of particulate minerals in the visible and near-infrared. Geophysics 42: pp. 501-513.

Hurcom, S.J. & Harrison, A.R. (1998) The NDVI and spectral decomposition for semi-arid vegetation abundance estimation. International Journal of Remote Sensing 19: pp. 3109-3125.

I

Imeson, A.C., Cammeraat, L.H. & Pérez-Trejo, F. (1995) Desertification response Units. In: R. Fantechi, D. Peter, P. Balabanis & J.L. Rubio (Eds.), Desertification in an European Context: Physical and Socio-economi aspects. Office for offical Publications of the European Commission, Luxembourg, pp. 263-277.

Imeson, A.C., Pérez-Trejo, F. & Cammeraat, L.H. (1996) The Response of landscape units to Desertification. In: C.J. Brandt & J.B. Thornes (Eds.), Mediterranean desertification and Land Use. Wiley, Chichester, pp. 447-469.

Inan, S, Yalçin, M.N., Guliev, I.S., Kuliev, K., & Feizullayev, A.A. (1997) Deep petroleum occurrences in the lower Kura depression, South Caspian Basin, Azerbaijan: an organic geochemical and basin modeling study, Marine and Petroleum Geology 14 (7/8): pp. 731-762.

Irons, J.R. & Petersen, G.W. (1981) Texture transforms of remote sensing data, Remote Sensing of Environment 11: pp. 359-370.

Irons, J.R., Weismiller, R.A. &. Petersen, G.W (1989) Soil Reflectance. In: G. Asrar Ed., Theory and Applications of optical Remote Sensing. Wiley, New York, pp. 66-106.

Isaaks, E.H. & Srivastava, R.M. (1989) An Introduction to Applied Geostatistics, Oxford University Press, New York.

Ivits, E., Blaschke, T. & Koch, B. (2002) Connectivity studies in eCognition from satellite images and aerial photo. Cognition User Conference, Munich, CD-ROM.

J

Jackson, D.L. (2000) JNCC Report No. 307 Guidance on the interpretation of the Biodiversity Broad Habitat Classification (terrestrial and freshwater types): definitions and the relationships with other habitat classifications. Joint Nature Conservation Committee, Peterborough.

Jain, A. & Farrokhnia, F. (1991) Unsupervised texture segmentation using Gabor filters. Pattern Recognition vol. 24, no. 12: pp. 1167-1186.

Jain, R., Kasturi, R. & Schunck, B.G. (1995) Machine Vision. McGraw-Hill, Inc. Singapore, 549 pp.

James, M. (1987) Pattern Recognition, BSP Professional Books, Oxford.

Janssen, L. (1993) Methodology for updating terrain object data from remote sensing data. The application of Landsat TM data with respect to agricultural fields. Doct. Thesis, Wageningen Agricultural Univ., Wageningen.

Janssen, L.F.F. & Huurneman, G.C. (2001) Principles of Remote Sensing. ITC Educational Textbook. International Institute for Aerospace Survey and Earth Sciences (ITC), Enschede, 180 pp.

Jarvis, P.G. (1995) Scaling processes and problems, Plant, Cell, and Environment 18: pp. 1079-1089.

Jensen, J.R. (1996) Introductory Digital Image Processing, A Remote Sensing Perspective, Prentice Hall, Upper Saddle River, New Jersey, 318 pp.

Ji, C.Y. (1996) Delineating agricultural field boundaries from TM imagery using dyadic wavelet transforms. ISPRS Journal of Photogrammetry and Remote Sensing 51: pp. 268-283.

Journel, A.G. & Huijbregts, C.J. (1978) Mining Geostatistics, Academic Press, London.

Journel, A.G. & Huijbregts, Ch.J. (1983) Mining Geostatistics. Academic Press, second edition, London.

Journel, A.G. (1996) Modelling uncertainty and spatial dependence: stochastic imaging, International Journal of Geographical Information Systems 10: pp. 517-522.

Jupp, D.L.B., Strahler, A.H. & Woodcock, C.E. (1988) Autocorrelation and regularization in digital images I. Basic theory, IEEE Transactions on Geoscience and Remote Sensing 26: pp. 463-473.

Jupp, D.L.B., Strahler, A.H. & Woodcock, C.E. (1989) Autocorrelation and regularization in digital images II. Simple image models, IEEE Transactions on Geoscience and Remote Sensing 27: pp. 247-258.

Justice, C.O. & Townshend, J.R.G. (1981) Integrating ground data with remote sensing, in Terrain Analysis and Remote Sensing (Eds. J.R.G. Townshend), Allen and Unwin, London, pp. 38-101.

K

Kaewpijit, S., Le Moigne, J. & El-Ghazawi, T. (2003) Automatic reduction of hyperspectral imagery using wavelet spectral analysis. IEEE Transactions on Geosciences and Remote Sensing 41 (4): pp. 863-871.

Kaiser, H. (1955) A quantification of textures on aerial photographs, Tech. Note No. 121, A. 69484, Boston University Research Laboratories, Boston.

Kaminsky, E.J., Barad, H. & Brown, W. (1997) Textural neural network and version space classifiers for remote sensing, International Journal of Remote Sensing 18: pp. 741-762.

Kanellopoulos, I. & Wilkinson, G.G. (1997) Strategies and best practice for neural network image classification, International Journal of Remote Sensing 18: pp. 711-725.

Kanellopoulos, I., Varfis, A., Wilkinson, G.G. & Mégier, J. (1992) Land cover discrimination in SPOT HRV imagery using an artificial neural network a 20 class experiment, International Journal of Remote Sensing 13: pp. 917-924.

Kariuki, P., Van der Meer, F. & Verhoef, P. (2003) Cation exchange capacity (CEC) determination from spectroscopy. International Journal of Remote Sensing 24: pp. 161-167.

Karpouzli, E. & Malthus, T. (2003) The empirical line method for the atmospheric correction of IKONOS imagery, International Journal of Remote Sensing 24: pp. 1143-1150.

Katila, M. & Tomppo, E. (2001) Selecting estimation parameters for the Finnish multisource National Forest Inventory. Remote Sensing of Environment 76 (1): pp. 16-32.

Katila, M., Heikkinen, J. & Tomppo, E. (2000) Calibration of small-area estimates for map errors in multisource forest inventory. Canadian Journal of Forest Research 30: pp. 1329-1339.

Katz, B., Richards, D., Long, D., & Lawrence, W. (2000) A new look at the components of the petroleum system of the South Caspian Basin, Journal of Petroleum Science and Engineering 28: pp. 161-182.

Kavzoglu, T. & Mather, P.M. (2001) Effective use of artificial neural networks for remotely sensed image classifcation, Proceedings of the First Annual Conference of the Remote Sensing and Photogrammetry Society, CD-ROM, Remote Sensing and Photogrammetry Society: Nottingham, 7 pp.

Kay, J. & Regier, H. (2000) Uncertainty, complexity, and ecological integrity: Insights from an ecosystem approach, in P. Crabbe, A. Holland, L. Ryszkowski & L. Westra (Eds.), Implementing Ecological Integrity: Restoring Regional and Global Environmental and Human Health, Kluwer, NATO Science Series, Environmental Security: pp. 121-156.

Kemper, T. (2003) Reflectance spectroscopy for mapping and monitoring of metal mining related contamination – A case study from the Aznalcóllar mining accident, Spain, Ph.D. thesis, University of Trier, 222 pp.

Kennedy, R.E., Cohen, W.B. & Takao, G. (1997) Empirical methods to compensate for a view-angle-dependent brightness gradient in AVIRIS imagery. Remote Sensing of Environment 62 (3): pp. 277-291.

Kershaw, C.D. & Fuller, R.M. (1992) Statistical problems in the discrimination of land cover from satellite images: a case study in lowland Britain. International Journal of Remote Sensing 13: pp. 3085-3104.

Ketting, R.J. & Landgrebe, D.A. (1976) Classification of multispectral image data by extraction and classification of homogeneous objects. IEEE Transactions on Geoscience and Electronics, GE-14 (1): pp. 19-26.

Key, J.R., Maslanik, J.A. & Barry, R.G. (1989) Cloud classification from satellite data using a fuzzy sets algorithm: a polar example, International Journal of Remote Sensing 10: pp. 1823-1842.

Khosravi, M. & Schafer, R.W. (1996) Template matching based on a grayscale hit-or-miss transform. IEEE Transactions on Image Processing 5 (6): pp. 1060-1066.

Kiema, J.B. & Bähr (2001) Wavelet compression and the automatic classification of urban environments using high resolution multispectral imagery and laser scanning data. Geoinformatica 5 (2): pp. 165-179.

Kiema, J.B. (2000) Wavelet compression and the automatic classification of Landsat imagery. Photogrammetric Record 16 (96): pp. 997-1006.

Kim, K.E. (1996) Adaptive majority filtering for contextual classification of remote sensing data. International Journal of Remote Sensing, 17: pp. 1083-1087.

King, T.V.V. & Ridley, W.I. (1987) Relation of the Spectroscopic Reflectance of Olivine to Mineral Chemistry and Some Remote Sensing Implications. J. Geophys. Res. 92: pp. 11457-11469.

Kittler, J. & Föglein, J. (1984) Contextual classification of multispectral pixel data. Image Vision Computing 2: pp. 13-29.

Klein, U., Sester, M. & Strunz, G. (1998) Segmentation of remotely sensed images based on the uncertainty of multispectral classification. IAPRS vol. 32(4). GIS between visions and applications, Stuttgart, pp. 299-305.

Klein-Gebbinck, M.S. (1998) Decomposition of mixed pixels in remote sensing images to improve the area estimation of agricultural fields, Ph.D. thesis, University of Nijmegen, The Netherlands, 165 pp.

Klinger, A. & Dyer, C.R. (1976) Experiments in picture representation using regular decomposition, Computer Graphics Image Processing 5: pp. 68-105.

Klinger, A. (1971) Pattern and search statistics, in J.S. Rustagi (Eds.), Optimizing Methods in Statistics, Academic Press, pp. 303-339.

Klir, G.J. & Yuan, B. (1995) Fuzzy Sets and Fuzzy Logic: Theory and Applications, Prentice-Hall: Englewood Cliffs, NJ.

Koestler, A. (1967) The ghost in the machine. Random House, New York.

Koger, C.H., Bruce, L.M., Shaw, D.R. & Reddy, K.N. (2003) Wavelet analysis of hyperspectral reflectance data for detecting pitted morningglory (Ipomoea lacunose) in soybean (Glycine max). Remote Sensing of Environment 86: pp. 108-119.

Kokaly, R.F. & Clark, R.N. (1999). Spectroscopic determination of leaf biochemistry using band-depth analysis of absorption features and stepwise multiple linear regression. Remote Sensing of Environment 67: pp. 267-287.

Kopf, A.J. (2002) Significance of mud volcanism, Reviews of Geophysics 40 (2): 2-1-2-52.

Kozlov, A.I., Ligthart, L.P. & Logvin, A.I. (2001) Mathematical and Physical Modelling of Microwave Scattering and Polarimetric Remote Sensing. Kluwer Academic Publishers, Dordrecht, 410 pp.

Krishnapuram, R. & Keller, J.M. (1993) A possibilistic approach to clustering, IEEE Transactions on Fuzzy Systems 1 (2): pp. 98-110.

Krishnapuram, R. & Keller, J.M. (1996) The possibilistic c-means algorithm: insights and recommendations, IEEE Transactions on Fuzzy Systems 4 (3): pp. 385-393.

Kruse, F.A., Lefkoff, A.B., Boardman, J.B., Heidebrecht, K.B., Shapiro, A.T., Barloon, P.J. & Goetz, A.F.H. (1993) The spectral image processing system (SIPS) – Interactive visualisation and analysis of imaging spectrometer data. Remote Sensing of Environment 44: pp. 145-163.

Kumar, L., Schmidt, K., Dury, S.& Skidmore, A. (2001) Imaging Spectrometry and Vegetation Science. In: F.D. van der Meer & S.M. de Jong (Eds.), Imaging Spectrometry. Kluwer Acdemic Publishers, Dordrecht, pp. 111-155.

Kurvonen, L., Pulliainen, J., Hallikainen, M. & Mikkela, P. (1992) Retrieval of forest parameters from multitemporal spaceborne SAR data, in Remote Sensing For A Sustainable Future, International Geoscience and Remote Sensing Symposium, IEEE, Geoscience and Remote Sensing Society, Long Beach, CA, pp. 1759-1762.

Kuusela, K. & Poso, S. (1970) Satellite pictures in the estimation of the growing stocks over extensive areas. The Photogrammetric Journal of Finland, 4.1: pp 3-9.

Kyriakidis, P.C. (2004) Geostatistical solution of the area-to-point spatial interpolation problem, Geographical Analysis, (in press).

L

Lacaze, B. & Joffre, R. (1994) Extracting Biochemical Information from Visible and Near-Infrared Reflectance Spectroscopy of Fresh and Dried Leaves. Journal of Plant Physiology 144: pp. 277-281.

Lacaze, B., Casselles, V., Coll, C., Hill, J., Hoff, C., De Jong, S.M., Mehl, W., Negendank, J.F.W., Riezebos, H., Rubio, E., Sommer, S., Texeira Filho, J. & Valor, E. (1996) Integrated approaches to desertification mapping and monitoring in the Mediterranean basin, Final Report of the DeMon-1 Project. EUR 16448, Bruxelles.

Lacaze, B., Rambal, S. & Winkel, T. (1994) Identifying spatial patterns of Mediterranean landscapes from geostatistical analysis of remotely-sensed data, International Journal of Remote Sensing 15: pp. 24372450.

Laine, A. & Fan, J. (1996) Frame representations for texture segmentation. In: IEEE Transactions on Image Processing. vol. 5, no. 5: pp. 771-779.

Lam, N. & Quattrochi, D.A. (1992) On the issues of scale, resolution, and fractal analysis in the mapping sciences. The Professional Geographer 44: pp. 88-98.

Lambers, H., Stuart, F., Chaplin, III & Pons, T.L. (1998) Plant Physiological Ecology. Springer-Verlag, New York, 540 pp.

Landgrebe, D.A. (1980) The development of spectral-spatial classifier for earth observation data. Pattern Recognition 12 (3): pp. 165-175.

Lang, S. (2002) Zur Anwendung des Holarchiekonzepts bei der Generierung regionalisierter Segmentierungsebenen in höchstauflösenden Bilddaten. In Blaschke, T. (Eds.): Fernerkundung und GIS: Neue Sensoren – Innovative Methoden. Wichmann-Verlag, Heidelberg, pp. 24-32.

Lark, R.M. (1996) Geostatistical description of texture on an aerial photograph for discriminating classes of land cover, International Journal of Remote Sensing 1: pp. 2115-2133.

LaRocca, A.J. (1993) Atmospheric Absorption. In: Wolfe W.L. & G.J. Zissis (Eds), The Infrared Handbook. Environmental Research Institute of Michigan (ERIM), Ann Arbor, Michigan, pp. 5-1 to 5-132.

Le Houérou, H.N. (1981) Impact of man and his animals on mediterranean vegetation. Ecosystems of the world 11 Mediterranean-type shrublands. F. Di Castri, D.W. Goodall and R.L. Specht, Elsevier, pp. 479-521.

Le Moigne, J. (1994) Parallell registration of multi-sensor remotely sensed imagery using wavelet coeficients, in Proceedings of the SPIE – The International Society for Optical Engineering, Orlando, USA, 14-16 February 1994, pp. 432-443.

Le Moigne, J. (2002) An automated parallel image registration technique based on the correlation of wavelet features. IEEE Transactions on Geosciences and Remote Sensing 40 (8): pp. 1849-1864.

Lee, J.H. & Philpot, W.D. (1991) Spectral texture pattern matching: A classifier for digital imagery, IEEE Transactions on Geoscience and Remote Sensing 29: pp. 545-554.

Lee, T., Richards, J.A. & Swain, P.H. (1987) Probabilistic and evidential approaches for multisource data analysis, IEEE Transactions on Geoscience and Remote Sensing 25: pp. 283-293.

Lerche, I. & Bagirov, E. (1998) Guide to gas hydrate stability in various geological settings, Marine and Petroleum Geology 15: pp. 427-437.

Levin, S.A. (1992) The problem of pattern and scale in ecology, Ecology 73: pp. 1943-1967.

Lewis, H.G., Brown, M. & Tatnall, A.R.L. (2000) Incorporating uncertainty in land cover classification from remote sensing imagery, Advances in Space Research 26: pp. 1123-1126.

Lewis, H.G., Nixon, M.S., Tatnall, A.R.L. & Brown, M. (1999) Appropriate stategies for mapping land cover from satellite imagery, Proceedings of RSS99 Earth Observation, from Data to Information, Remote Sensing Society, Nottingham, pp. 717-724.

Li, H. & Zhou, Y.T. (1996) Automatic EO/IR sensor image registration. Optical Engineering 4 (3): pp. 161-164.

Liang, S., Fallah-Adl, H., Kalluri, S., JaJa, J., Kaufman, Y.J. & Townshend, J.R.G. (1997) An operational atmospheric correction algorithm for Landsat Thematic Mapper imagery over the land. Journal of Geophysical Research 102: pp. 17173-17186.

Lichtenthaler, H.K., Gitelson, A. & Lang, M. (1996) Non-destructive determination of chlorophyll content of leaves of a green and an aurea mutant of tobacco by reflectance measurements. J. Plant Physiol. 148: pp. 483-493.

Lillesand T.M. & Kiefer, R.W. (2000) Remote Sensing and Image Interpretation. John Wiley & Sons, New York, 724 pp.

Lillesand, T.M. & Kiefer, R.W. (1994) Remote Sensing and image interpretation, John Wiley & Sons, New York, 750 pp.

Lim, J.S. (1990) Two-Dimensional Signal and Image Processing, Englewood Cliffs, NJ: Prentice Hall, pp. 469-476.

Lindeberg, T. (1994) Scale-space theory: A basic tool for analyzing structures at different scales, Journal of Applied Statistics 21 (2): pp. 225-270.

Link, W.K. (1952) Significance of oil and gas seeps in world oil exploration. The American Association of Petroleum Geologists (AAPG) Bulletin v. 36 no. 8: pp. 1505-1540

Liu, G., Xiong, H. & Huang, S. (2000) Study on segmentation and interpretation of multi-look polarimetric SAR images. International Journal of Remote Sensing 21 (8): pp. 1675-1691.

Lloyd, C.D. & Atkinson, P.M. (1998) Scale and the spatial structure of landform: optimising sampling strategies with geostatistics, in Proceedings of the 3rd International Conference on GeoComputation, GeoComputation CD-ROM, Manchester, http://divcom.otago.ac.nz/sirc/geoc98/15/gc_15.htm

Lobo, A., Chic, O. & Casterad, A. (1996) Classification of Mediterranean crops with multisensor data: per-pixel versus per-object statistics and image segmentation, International Journal of Remote Sensing 17: pp. 2385-2400.

Lucas, N.S., Shanmugam, S. & Barnsley, M. (2002) Sub-pixel habitat mapping of a coastal dune ecosystem, Applied Geography 22: pp. 253-270.

Lucieer, A., Stein, A. & Fisher, P.F. (2003) Texture-based segmentation of high-resolution remotely sensed imagery for identification of fuzzy objects. In: Proceedings of GeoComputation 2003, 8-10 September 2003, Southampton, UK. (Published on CDROM)

Luckman, A.J., Frery, A.C., Yanasse, C.C.F. & Groom, G.B. (1997) Texture in airborne SAR imagery of tropical forest and its relationship to forest regeneration stage, International Journal of Remote Sensing 18: pp. 1333-1349.

Ludwig, J.A. & Reynolds, J.F. (1988) Statistical Ecology, Wiley, New York.

M

Mackin, S, Settle, J, Drake, N. & Briggs, S. (1991) Curve shape matching, end-member selection and mixture modelling of AVIRIS and GER data for mapping surface mineralogy and vegetation communities, in Proceedings of the Airborne VISIBLE/Infrared imaging spectrometer (AVIRIS), Airborne Geoscience workshop bibliographies.

Mäkelä, H. & Pekkarinen, A. (2001) Estimation of timber volume at the sample plot level by means of image segmentation and Landsat TM imagery. Remote Sensing of Environment 77 (1): pp. 66-75.

Mäkisara, K., Heikkinen, J., Henttonen, H., Tuomainen, T. & Tomppo, E. (1997) Experiments with imaging spectrometer data in large area forest inventory context. Proceedings of the third international airborne remote sensing conference and exhibition. Copenhagen, Denmark, pp. 420-427.

Mäkisara, K., Meinander, M. & Rantasuo, M. (1993) Airborne imaging spectrometer for applicaitons (AISA). Proceedings of the '1993 International Geoscience and Remote Sensing Symposium (IGARSS'93)'. Tokyo, Japan, August 1-21, 1993: pp. 479-481.

Mallat, S. & Zhong, S. (1992) Characterization of signals from multiscale edges. IEEE Transactions on Pattern Analysis and Machine Intelligence 14 (7): pp. 710-732.

Mallat, S.G. (1989) Multiresolution approach to wavelets in computer vision, in J.M. Combes, A. Grossman, P. Tchmitchian (Eds.), Wavelets: Time Frequency Methods and Phase Space, Springer-Verlag, New York, pp. 313-327.

Mallat, S.G. (1998) A Wavelet Tour of Signal Processing. Academic Press, San Diego, 577 pp.

Mandelbrot, B.B. (1967) The Fractal geometry of nature, Science 156: pp. 636-642.

Mandelbrot, B.B. (1982) The Fractal Geometry of nature. Freeman & Co., New York.

Manjunath, B. & Chellappa, R. (1991) Unsupervised texture segmentation using Markov random field models. IEEE Transactions on Pattern Analysis and Machine Intelligence. Vol. 13: pp. 478-482.

Manslow, J.F. & Nixon, M.S. (2002) On the ambiguity induced by a remote sensor's PSF, In G.M. Foody and P.M. Atkinson (Eds), Uncertainty in Remote Sensing and GIS, Wiley, Chichester, pp. 37-57.

Mao, J. & Jain, A. (1992) Texture classification and segmentation using multiresolution simultaneous autoregressive models. Pattern Recognition, Vol. 25: pp. 173-188.

Marçal, A.R.S., Triebfürst, B., Schneider, C. & Vaughan, R.A. (2000) Compression of NOAA/AVHRR data with a wavelet transform. International Journal of Remote Sensing 21 (3): pp. 595-610.

Marceau, D.J. & Hay, G.J. (1999) Remote sensing contributions to the scale issue, Canadian Journal of Remote Sensing 25 (4): pp. 357-366.

Marceau, D.J. (1999) The scale issue in social and natural sciences, Canadian Journal of Remote Sensing 24 (5): pp. 347-156.

Marceau, D.J., Gratton, D.J., Fournier, R.A. & Fortin, J.P. (1994b) Remote sensing and the measurement of geographical entities. Part 2: The optimal spatial resolution, Remote Sensing of Environment 49 (2): pp. 105-117.

Marceau, D.J., Howarth, P., Dubois, J. & Gratton, D.J. (1990) The evaluation of the grey level co-ocurrence method for land cover classification using SPOT imagery, IEEE Transactions on Geoscience and Remote Sensing 4: pp. 513-518.

Marceau, D.J., Howarth, P.J. & Gratton, D.J. (1994a) Remote sensing and the measurement of geographical entities in a forested environment. Part 1: The scale and spatial aggregation problem, Remote Sensing of Environment 49 (2): pp. 93-104.

Marceau, D.J., Howarth, P.J., Dubois, J.M. & Gratton, D.J. (1990) Evaluation of the grey-level co-occurrence matrix method for land cover classification using SPOT imagery, IEEE Transactions on Geoscience and Remote Sensing 28: pp. 513-519.

Mas, J.F. (1999) Monitoring land-cover changes: a comparison of change detection techniques. International Journal of Remote Sensing 20 (1): pp. 139-152.

Maselli, F. (1998) Multiclass spectral decomposition of remotely sensed scenes by selective pixel unmixing, IEEE Transactions of Geoscience and Remote Sensing 36 (5): pp. 1809-1820.

Mather, P.M. (1987) Computer processing of remotely sensed images – an introduction, Wiley, Chichester.

Mather, P.M. (1999) Computer Processing of Remotely-Sensed Images, Second edition, Wiley, Chichester.

Mather, P.M. (1999) Land cover classification revised. In Atkinson, P. and Tate, N. (Eds.), Advances in remote sensing and GIS analysis. Wiley & Son, Chichester, pp. 7-16.

Matheron, G. (1965) Les variables régionalisées et leur estimation, Masson: Paris.

Matheron, G. (1971) The Theory of Regionalized Variables and its Applications, in Les Cahiers du Centre de Morphologie Mathématique de Fontainebleau, Ecole des Mines de Paris, Fascicule 5, Fontainebleau, 211 pp.

Matheron, G. (1982) La destructuration de hautes teneurs et le krigeage des indicatrices. In Internal repport of Centre de Geostatistique et Morphologie Mathematique, École des Mines de Paris, Fontainebleau, 33 pp.

McArthur, D.E., Fuentes, R.W. & Devarajan, V. (2000) Generation of hierarchical multiresolution terrain databases usingwavelet filtering. Photogrammetric Engineering & Remote Sensing 66 (3): pp. 287-295.

McBratney, A.B. & Moore, A.W. (1985) Application of fuzzy sets to climatic classification, Agricultural and Forest Meteorology 35: pp. 165-185.

McBratney, A.B. & Webster, R. (1986) Choosing functions for semi-variograms of soil properties and fitting them to sampling estimates, Journal of Soil Science 37: pp. 617-639.

McDonald, R.A. (1995) CORONA: Success for Space Reconaissance, a Look into the Cold War and a revolution for Intelligence. Photogrammetric Engineering & Remote Sensing Vol. 61: pp. 689-719.

McKay, R.J. & Campbell, N.A. (1982) Variable selection techniques in discriminant analysis II. Allocation, British Journal of Mathematical and Statistical Psychology, 35: pp. 30-41.

McKeown, D.M. (1987) The role of AI in the Integration of remotely sensed data with geographic information systems, IEEE Transactions on Geoscience and Remote Sensing, GE-25 (3): pp. 330-348.

Meentemeyer, V. (1989) Geographical perspectives of space, time, and scale, Landscape Ecology 3(3/4): pp. 163-173.

Melgani, F. & Serpico, S.B. (2002) A statistical approach to the fusion of spectral and spatio-temporal contextual information for the classification of remote-sensing images. Pattern Recognition Letters 23 (9): pp. 1053-1061.

Meyer, F. & Beucher, S. (1990) Morphological segmentation, Journal of Visual Communication and Image Representation 1 (1): pp. 21-46.

Meyer, Y. (1989) Orthonormal wavelets, in J.M. Combes, A. Grossman, P. Tchmitchian (eds.), Wavelets: Time Frequency Methods and Phase Space, Springer-Verlag, New York, pp. 21-37.

Millington, A.C., Welsh, S.J. & Osborne, P.E. (2001) GIS and Remote Sensing Applications in Biogeography and Ecology. Kluwer Academic Publishers, Dordrecht, 333 pp.

Miranda, F.P. & Carr, J.R. (1994) Application of the semivariogram textural classifier (STC) for vegetation discrimination using SIR-B data of the Guiana Shield, northwestern Brazil, Remote Sensing Reviews 10: pp. 155-168.

Miranda, F.P., Fonseca, L.E.E., Carr, J.R. & Taranik, J.V. (1996) Analysis of JERS-1 (Fuyo-1) SAR data for vegetation discrimination in northwestern Brazil using the semivariograms textural classifier (STC), International Journal of Remote Sensing 17: pp. 3523-3529.

Miranda, F.P., Fonseca, L.E.N. & Carr, J.R. (1998) Semivariogram textural classification of JERS-1 (fuyo-1) SAR data obtained over a flooded area of the Amazon rainforest, International Journal of Remote Sensing 19: pp. 549-550.

Miranda, F.P., MacDonald, J.A. & Carr, J.R. (1992) Application of the semivariogram textural classifier (STC) for vegetation discrimination using SIR-B data of Borneo, International Journal of Remote Sensing 13: pp. 2349-2354.

Mitchell, C. (1991) Terrain Evaluation. Longman Scientific & Technical Publishers, Essex, 441 pp.

Molenaar, M. (1998) An introduction to the theory of spatial object modelling for GIS. Dordrecht.

Molina, Z. & Chuvieco, E. (1996) Evaluación de índices texturales para discriminar morfología urbana: análisis de la ciudad de Maracay (Venezuela). Revista de Teledetección 7: pp. 49-57.

Moody, A., Gopal, S. & Strahler, A.H. (1996) Artificial neural network response to mixed pixels in coarse-resolution satellite data, Remote Sensing of Environment 58: pp. 329-343.

Mustard, J.F. (1992) Chemical composition of actinolite from reflectance spectra. Am. Mineral. 77: pp. 345-358.

Myers, D.E. (1989) To be or not to be stationary? That is the question, Mathematical Geology 21: pp. 347-362

Myers, D.E. (1991) Pseudo-cross variogram, positive-definiteness and cokriging, Mathematical Geology 15: pp. 633-637.

N

Narasimha Rao, P.V., Sesha Sai, M.V.R., Sreenivas, K., Krishna Rao, M.V., Rao, B.R.M., Dviwedi, R.S. & Venkataratnam, L. (2002) Textural analysis of IRS-1D panchromatic data for the land cover classification, International Journal of Remote Sensing 23: pp. 3327-3345.

Narayanan, R.M., Sankaravadivelu, T.S. & Reichenbach, S.E. (2000) Dependence of image information content on gray-scale resolution, Proceedings of IGARSS vol.1: pp. 153-155.

Narendra, P. & Goldberg, M. (1980) Image segmentation with directed trees. IEEE Transactions on Pattern Analysis and Machine Intelligency. 2(2): pp. 185-191.

Neubert, M. & Meinel, G. (2002) Segmentbasierte Auswertung von IKONOS-Daten – Anwendung der Bildanalysesoftware eCognition auf unterschiedliche Testgebiete. In T. Blaschke (Eds.), Fernerkundung und GIS: Neue Sensoren – Innovative Methoden. Wichmann-Verlag, Heidelberg, pp. 108-117.

Nilsson, M. (2002) Deriving nationwide estimates of forest variables for Sweden using Landsat

Nordstrom, D.K. (1982) Aqueous pyrite oxidation and the consequent formation of secondary iron minerals, in J.A. Kittrick, D.S. Fanning, and L.R. Hossner (eds.), Acid Sulfate Weathering, Soil Science Society of America Special Publication 10, Madison, Wisconsin, pp. 37-56.

Nyoungui, A.D., Tonye, E. & Akono, A. (2002) Evaluation of speckle filtering and texture analysis methods for land cover classification from SAR images. International Journal of Remote Sensing 23 (9): pp. 1895-1925.

O

O'Neill, R.V. & King, A.W. (1998) Homage to St. Michael: Or why are there so many books on scale?, in D.L. Peterson and V.T. Parker (eds.), Ecological Scale, Theory and Application, Columbia University Press: pp. 3-15.

O'Neill, R.V., De Angelis, D.L., Waide, J.B. & Allen, T.F.H. (1986) A Hierarchical Concept of Ecosystems, Princeton University Press, Princeton, New Jersey.

Okada, K. & Iwashita, A. (1992) Hyper-multispectral image analysis based on waveform characteristics of spectral curve. Adv. Space Res. 12: pp. 433-442.

Okin, G.S., Siegel, H., Okin, W.J. Murray, B., Collier, J., Roberts, D.A., Miller, C.D.H., Painter, T.H., & Curkendall, D.W. (1999) The supercomputing visualization workbench for the analysis and classification of imaging spectrometer data, JPL AVIRIS Conference.

Oliver, C. & Quegan, S. (1998) Understanding synthetic aperture radar images. Artech House, Norwood, 512 pp.

Oliver, M.A., (2001) Determining the spatial scale of variation in environmental properties using the variogram, in Modelling Scale in Geographical Information Science (Eds., N.J. Tate and P.M. Atkinson), Wiley, Chichester, pp. 193-219.

Openshaw, S. (1984) The modifiable areal unit problem, Concepts and Techniques in Modern Geography (CATMOG) no.38: 40 pp.

Ourcival, J.M., Joffre, R. & Rambal, S. (1999) Exploring the Relationship between Reflectance and Anatomical and Biochemical Properties in Quercus ilex leaves. New Phytologist 143: pp. 151-364.

P

Painter, T.H., Roberts, D.A., Green, R.O., & Dozier, J. (1998) The effect of grain size on spectral mixture analysis of show-covered area from AVIRIS data, Remote Sensing of Environment 65: pp. 320-332.

Palubinskas, G., Lucas, R.M., Foody, G.M. & Curran, P.J. (1995) An evaluation of fuzzy and texture-based classification approaches for mapping regenerating tropical forest classes from Landsat-TM data, International Journal of Remote Sensing 16: pp. 747-759.

Panjwani, D. & Healey, G. (1995) Markov random field models for unsupervised segmentation of textured colour images. IEEE Transactions on Pattern Analysis and Machine Intelligence. Vol. 17(10): pp. 939-954.

Paola, J.D. & Schowengerdt, R.D. (1995) Review article: A review and analysis of backpropagation neural networks for classification of remotely sensed multispectral imagery, International Journal of Remote Sensing 16: pp. 3033-3058.

Pastina, D., Lombardo, P., Farina, A. & Daddi, P. (2003) Super-solution of polarimetric SAR images of ship targets, Signal Processing 83: pp. 1737-1748.

Peddle, D.R. (1993) An empirical comparison of evidential reasoning, linear discriminant analysis and maximum likelihood algorithms for land cover classification, Canadian Journal of Remote Sensing, 19: pp. 31-44.

Peddle, D.R., Hall, F.G., & Ledrew, E.F. (1999) Spectral mixture analysis and geometric-optical reflectance modeling of boreal forest biophyscial structure, Remote sensing of Environment 67: pp. 288-297.

Pedley, M.I. & Curran, P.J. (1991) Per-field classification: an example using SPOT HRV imagery, International Journal of Remote Sensing 12: pp. 2181-2192.

Pekkarinen, A. (2002) Image segment-based spectral features in the estimation of timber volume. Remote Sensing of Environment 82 (2-3): pp. 349-359.

Picket, R.M. (1970) Visual analysis of texture in the detection and recognition of objects, in B.C. Lipkin and A. Rosenfeld (Eds.), Picture Processing and Psychopictorics, Academic Press, New York, pp. 289-308.

Platt, T. & Denman, K.L. (1975) Spectral analysis in ecology, Annals of Rev. Ecological Systems 6: pp. 189-210.

Pohl, C. (1998) Tools and methods used in data fusion, in Gudmandsen (Eds.), Future Trends in Remote Sensing, Balkema, Rotterdam, pp. 391-399.

Polunin, O. & Huxley, A. (1972) Flowers of the Mediterranean. London, Chatto and Windus, 260 pp.

Prasad, L. & Iyengar, S.S. (1997) Wavelet Analysis with Applications to Image Processing. CRC Press, New York, 279 pp.

Pratt, W.K. (1991) Digital image processing, John Wiley & Sons, New York. 758 pp.

Preissler, H., Bohbot, H., Mehl, W. & Sommer, W. (1998) MEDSPEC-A spectral database as a tool to support the use of imaging spectrometry data for environmental monitoring, 1st EARSeL Workshop on Imaging Spectrometry, Zurich, Switzerland, pp. 455-462.

Prigogine, I. (1997) The End of Certainty: Time, Chaos, and the New Laws of Nature, Free Press, New York, 240 pp.

Pysek, P. & Pysek, A. (1989) Veränderungen der Vegetation durch experimentelle Erdgasbehandlung. Weed Research 29: pp. 193-204.

Q

Quarmby, N.A., Townshend, J.R.G., Settle, J.J., Milnes, M., Hindle, T.L. & Silleos, N. (1992) Linear mixture modelling applied to AVHRR data fro crop area estimation, International Journal of Remote Sensing 13: pp. 415-425.

Quattrocchi, D.A., Lam, N.S., Qiu, H.L. & Zhao, W. (1997) Image characterization and modeling system (ICAMS): a geographic information system for the characterization and modeling of multiscale remote sensing data. In: D.A. Quatrochi & M.F. Goodchild (Eds.), Scale in Remote Sensing and GIS. Lewis Publishers, Boca Raton FA: pp. 295-308.

R

Ramstein, G., Raffy, M. (1989) Analysis of the Structure of Radiometric Remotely-Sensed Images. International Journal of Remote Sensing 10: pp. 1049-1073.

Ranchin, T. & Wald, L. (1996) Merging SPOT-P and KVR-1000 for updating urban maps, in Proceedings of the 26th International Symposium On Remote Sensing of Environment and the 18th Annual Symposium of the Canadian Remote Sensing Society, Vancouver, Canada, 25-29 March 1996, pp. 401-404.

Ranchin, T. & Wald, L. (1998) Sensor fusion to improve the spatial resolution of images: the ARSIS method, in Gudmandsen (Eds.), Future Trends in Remote Sensing, Balkema, Rotterdam, pp. 445-451.

Ranchin, T., Aiazzi, B., Alparone, L., Baronti, S. & Wald, L. (2003) Image fusion – the ARSIS concept and some successful implementation schemes. ISPRS Journal of Photogrammetry & Remote Sensing 58: pp. 4-18.

Ranchin, T., Wald, L. & Mangolini, M. (1994) Efficient data fusion using wavelet transform: the case of SPOT satellite images, in Proceedings of SPIE 1993 International Symposium on Optics, Imaging and Instrumentation. Wavelet Applications in Signals and Image Processing. San Diego, USA, 11-16 July 1994, pp. 171-178.

Ranchin, T., Wald, L. & Mangolini, M. (1996) The ARSIS method: a general solution for improving spatial resolution of images by means of sensor fusion, in Proceedings of the conference Fusion of Earth data: merging point measurements, raster maps and remotely sensed images, Cannes, France, 6-8 February 1996, pp. 81-85.

Ratcliffe, D.A. & Thompson, D.B.A. (1988) The British uplands: their ecological character and international significance. In: Ecological change in the uplands, pp 9-36, edited by M.B. Usher and D.B.A. Thompson. Blackwell Scientific Publications, Oxford.

Richard, J.A. Landgrebe D. & Swain, P.H. (1982) A means for utilizing ancillary information in multispectral classification. Remote Sensing of Environment 12: pp. 463-467.

Richards, J.A. (1994) Remote Sensing Digital Image Analysis: An Introduction, Springer-Verlag, Berlin, Germany, 340 pp.

Richter, R. (1997) Correction of atmospheric and topographic effects for high spatial resolution satellite imagery. International Journal of Remote Sensing 18: pp. 1099-1111.

Ricotta, C. & Avena, G.C. (2002) Evaluating the degree of fuzziness of thematic maps with a generalized entropy function: a methodological outlook, International Journal of Remote Sensing 20: pp. 4519-4523.

Rietkerk, M., Boerlijst, M.C. & van Langenvelde, F. et al. (2002) Self-organisation of Vegetation in Arid Ecosystems. The Amrican naturalist Vol.160: pp. 524-530.

Roberts, D.A., Gardner, M., Church, R., Ustin, S., Scheer, G., & Green, R.O. (1998) Mapping chaparral in the Santa Monica Mountains using multiple endmember spectral mixture models, Remote Sensing of Environment 65: pp. 267-279.

Roberts, D.A., Smith, M.O., Adams, J.B., & Gillespie, A.R. (1991) Leaf Spectral Types, Residuals, and Canopy Shade in an AVIRIS Image, in Proceedings of the 3rd Airborne Scientific Workshop: AVIRIS, JPL, Pasadena, CA, 20-21 May, pp. 43-50.

Roerdink, J.B.T.M. & Meijster, A. (1999) The watershed transform: definitions, algorithms and parallelization techniques, Institute for Mathematics and Computer Science, University of Groningen, Groningen, The Netherlands, IWI 99-9-06.

Rosenfeld, A., Hummel, R.A. & Zucker S.W. (1976) Scene labeling by relaxation operations. IEEE Transactions on System, Man, and Cybernetics 6 (6): pp. 420-433.

Rosin, P.L. (2001) Robust pixel unmixing, IEEE Transactions on Geoscience and Remote Sensing 39: pp. 1978-1983.

Rubin, T. (1990) Analysis of radar texture with variograms and other simplified descriptors, in Proceedings, Image Processing '89, American Society for Photogrammetry and Remote Sensing, Falls Church, VA, pp. 185-195.

Rumelhart, D.E., Hinton, G.E. & Williams, R.J. (1986) Learning internal representations by error propagation, in D.E. Rumelhart and J.L. McClelland (eds.), Parallel Distributed Processing: Explorations in the Microstructure of Cognition, volume 1: Foundations, the MIT Press, Cambridge, Massachusetts, pp. 318-362.

Running, S.W., Loveland, T.R., Pierce, L.L., Nemani, R.R. & Hunt, E.R. (1995) A remote sensing based vegetation classification logic for global land cover analysis, Remote Sensing of Environment 51: pp. 39-48.

Russ, J.C. (1999) The Image Processing Handbook, CRC Press, Boca Raton, 771 pp.

Ryherd, S. & Woodcock, C. (1996) Combining spectral and texture data in the segmentation of remotely sensed images, Photogrammetric Engineering & Remote Sensing 62: pp. 181-194.

S

Sadler, B.M. & Swami, A. (1999) Analysis of multiscale products for step detection and estimation. IEEE Transactions on Information Theory 45 (3): pp. 1043-1051.

Sadler, B.M., Pham, T. & Sadler, L.C. (1998) Optimal and wavelet-based shockwave detection and estimation. Journal of the Acoustical Society of America 104 (2): pp. 955-963.

Salari, E., & Ling, Z. (1995) Texture Segmentation using hierarchical Wavelet Decomposition. Pattern Recognition, Vol.28 (12): pp. 1819-1824.

Sali, E. & Wolfson, H. (1992) Texture classification in aerial photographs and satellite data, International Journal of Remote Sensing 13: pp. 3395-3408.

Scepan, J. (1999) Thematic validation of high-resolution global land-cover data sets, Photogrammetric Engineering & Remote Sensing 65: pp. 1051-1060.

Schiewe, J. & Tufte, L. (2002) Potential und Probleme multiskalarer Segmentierungsmethoden der Fernerkundung. In Blaschke, T. (ed.) Fernerkundung und GIS: Neue Sensoren – Innovative Methoden. Wichmann-Verlag, Heidelberg, pp. 42-51.

Schlaepfer, D., Schaepmann M. & Itten, K. (1998) PARGE: Parametric geocoding based on GCP-calibrated auxiliary data, SPIE International Symposium on Optical Science, Eng., and Instruments, San Diego (Ca), pp. 334-344.

Schneider, W. (1993) Land use mapping with subpixel accuracy from landsat TM image data, Proceedings of the 25th International Symposium on Remote Sensing and Global Environmental Change: pp. 155-161.

Schneider, W. (1999) Land cover mapping from optical satellite images employing subpixel segmentation and radiometric calibration, Machine Vision and Advanced Image Processing in Remote Sensing (Eds. I. Kanellopoulos, G. Wilkinson and T. Moons), Springer, London.

Schneider, W., Suppan, F., Steinwendner, J. & Bartl, R. (1997) Automatic Extraction of Landscape Ecology Features from Satellite Imagery by Computer Vision Techniques. In Proc. Geospatial Information Age vol. 4: pp. 630-639.

Schneider,W. & Steinwender, J. (1999) Landcover mapping by interrelated segmentation and classification of satellite images. International Archives of Photogrammetry & Remote Sensing, Vol. 32 Part 7-4-3 W6, Valladolid.

Scholte, K., García-Haro, J. & Kemper, T. (2004) Variable Multiple Endmember Spectral Mixture Analysis for Geology Applications In: S.M. de Jong and F.D. van der Meer, Remote Sensing Digital Image Processing: including the spatial domain. Kluwer Academics, Dordrecht, chapter 10 this volume.

Schott, J.R., Salvaggio, C. & Volchok, W.J. (1988) Radiometric scene normalization using pseudoinvariant features. Remote Sensing of Environment 26 (1): pp. 1-16.

Schowengerdt R.A., (1997) Remote Sensing. Models and Methods for Image Processing. Academic Press, Chestnut Hill, MA, 521 pp.

Schowengerdt, R.A. (1997) Remote Sensing: Models and Methods for Image Processing, Second edition, Academic Press, San Diego.

Schumacher, D. (1996) Hydrocarbon-induced alteration of soils and sediments. In: Hydrocarbon migration and its near-surface expression, edited by D. Schumacher and M.A. Abrams. The American Assiciation of Petroleum Geologists (AAPG) Memoir 66: pp. 71-89.

Serra, J. (1984) Image Analysis and Mathematical Morphology. Academic Press, New York, 610 pp.

Settle, J.J., & Drake, N.A. (1993) Linear mixing and the estimation of ground cover proportions, International Journal of Remote Sensing 14: pp. 1159-1177.

Shepherd, K.D. & Walsh, M.G. (2002) Development of reflectance spectral libraries for characterization of soil properties. Soil Sci. Soc. Am. J. 66: pp. 988-998

Shi, W., Zhu, C.Q., Zhu, C.Y. & Yang, X.M. (2003) Multi-band wavelet for fusion SPOT panchromatic and multispectral images. Photogrammetric Engineering & Remote Sensing 69 (5): pp. 513-520.

Shi, W.Z & Ehlers, M. (1996) Determining uncertainties and their propagation in dynamic change detection based on classified remotely-sensed images. International Journal of Remote Sensing 17 (14): pp. 2729-2741.

Shih, E.H.H. & Schowengerdt, R.A. (1983) Classification of arid geomorphic surfaces using Landsat spectral and textural features, Photogrammetric Engineering & Remote Sensing 49: pp. 337-347.

Shimabukuro, Y.E., Batista, G.T., Mello, E M.K., Moreira, J.C. & Duarte, V. (1998) Using Shade Fraction Image Segmentation To Evaluate deforestation in Landsat Thematic Mapper images of the Amazon Region, International Journal of Remote Sensing 19 (3): pp. 535-541.

Shimabukuro, Y.E., Carvalho, V.C. & Rudorff, B.F.T. (1997) NOAA-AVHRR data processing for the mapping of vegetation cover, International Journal of Remote Sensing 18: pp. 671-677.

Shimidt, K.S. & Skidmore, A.K. (2003) Spectral discrimination of vegetation types in a costal wetland. Remote Sensing of Environment 85 (1): pp. 92-108.

Simard, M., DeGrandi, G., Thomson, K.P.B. & Bénié, G.B. (1998) Analysis of speckle noise contribution on wavelet decomposition of SAR images. IEEE Transactions on Geoscience and Remote Sensing 36 (6): pp. 1953-1962.

Simon, H.A. (1962) The architecture of complexity, in Proceedings of the American Philosophical Society 106 (6): pp. 467-482.

Singh, A. (1989) Digital change detection techniques using remotely-sensed data. International Journal of Remote Sensing 10 (6): pp. 989-1003.

Skidmore, A., Turner, B., Brinkhof, W. & Knowles, E (1997) Performance of a Neural Network: Mapping Forests Using GIS and Remotely Sensed Data. Photogrammetric Engeneering & Remote Sensing 63: pp. 501-514.

Slater, P.N. (1980) Remote Sensing: Optics and Optical Systems. Addison-Wesley Publishing Company, Reading, Massachusetts, 575 pp.

Smith, G.M. & Fuller, R.M. (2000) Land Cover Map 2000: more than just an update. Society of Cartographers Bulletin 33: pp. 13-16.

Smith, G.M. & Fuller, R.M. (2001) Land Cover Map 2000 and meta data at the land parcel level. Proceedings of the RSPS meeting Uncertainty in Remote sensing and GIS, University of Southampton. 3-4 July, 2001.

Smith, G.M., Fuller, R.M., Sanderson, J.M., Hill, R.A. & Thomson, A.G. (2001) Land Cover Map 2000: a parcel-based map from satellite images. Proceedings of the Remote Sensing and Photogrammetry Society Conference, Remote Sensing Society, Nottingham.

Smith, M.O., Adams, J.B., & Sabol, D.E. (1994) Spectral mixture analysis: New strategies for the analysis of multispectral data, in J. Hill and J. Megier (eds.), Imaging Spectrometry – A tool for Environmental Observations. Euro Courses, Remote Sensing, Kluwer Academic Publishers Vol. 4: pp. 125-143.

Smith, M.O., Johnston, P.E. & Adams, J.B. (1985) Quantitative determination of mineral types and abundances from reflectance spectra using principle component analysis, Journal of Geophysical Research 90: pp. 797-804.

Smith, M.O., Ustin, S.L., Adams, B. & Gillespie, A.R. (1990) Vegetation in deserts: 1. A regional measure of abundance from multispectral images, Remote Sensing of Environment 31: pp. 1-26.

Song, C. & C.E. Woodcock (2003) Estimating Tree Crown Size from Multiresolution Remotely Sensed Imagery. Photogrammetric Engineering & Remote Sensing 69: pp. 1263-1270.

Sonka, M., Hlavac, V. & Boyle, R. (1993) Image Processing, Analysis and Machine Vision, Chapman and Hall, London.

Srinivasan, A., & Richards, J.A. (1990) Knowledge-based techniques for multi-source classification, International Journal of Remote Sensing 11: pp. 505-525.

Starck, J.L., Aussel, H., Elbaz, D., Fadda, D. & Cesarsky, C. (1999) Faint source detection in ISOCAM images. Astronomy and Astrophysics Supplement Series 138: pp. 365-379.

Starck, J.L., Murtagh, F. & Bijaoui, A. (1998) Image Processing and Data Analysis. University Press, Cambridge, 287 pp.

Stein, A., Bastiaanssen, W.G.M., De Bruin, S., Cracknell, A.P., Curran, P.J., Fabbri, A.G., Gorte, B.G.H., Van Groenigen, J.W., Van Der Meer, F.D. & Saldana, A. (1998) Integrating spatial statistics and remote sensing, International Journal of Remote Sensing 19: pp. 1793-1814.

Steinwendner, J., Schneider, W. & Suppan, F. (1998) Vector segmentation using spatial subpixel analysis for object extraction, International Archives of Photogrammetry & Remote Sensing 32: pp. 265-271.

St-Onge, B.A. & Cavayas, F. (1995) Estimation forest stand from high resolution imagery using the directional variogram, International Journal of Remote Sensing 16: pp. 1999-2021.

Stow, D.A., Tinney, L.R. & Estes, J.E. (1980) Deriving land use/land cover change statistics from Landsat: a study of prime agricultural land, in Proceedings of the 14th International Symposium on Remote Sensing of Environment, Ann Arbor, USA, April 1980, pp. 1227-1237.

Strahler, A.H., Woodcock C.C. & Smith, J.A. (1986) On the nature of models in remote sensing, Remote Sensing of Environment 20 (2): pp. 121-139.

Strang, G. & Nguyen, T. (1997) Wavelets and Filter Banks. Wellesley-Cambridge Press, Wellesley, 520 pp.

Strobl, P., Richter, R., Mueller, A., Lehmann, F., Oertel, D., Tischler, S. & Nielsen, A. (1996) DAIS system performance; first results of the 1995 evaluation campaigns. Proc. 2nd International Airborne Remote Sensing Conference and Exhibition, San Francisco, 2: pp. 325-334.

Stuckens, J., Coppin, P.R. & Bauer, M.E. (2000) Integrating contextual information with per-pixel classification for improved land cover classification. Remote Sensing of Environment 71: pp. 282-296.

Sun, W., Heidt, V., Gong, P. & Xu, G. (2003) Information fusion for land use classification from high resolution imagery, IEEE Transactions on Geoscience & Remote Sensing.

Sun, X.H. & Qin, P. (1993) Texture analysis for remotely sensed imagery, in Proceedings Ninth Thematic Conference on Geological Remote Sensing, pp. 311-322.

Swain, P.H., Vardenman, S.B. & Tilton, J.C. (1981) Contextual classification of multispectral image data, Pattern Recognition 13 (6): pp. 429-441.

Swayze, G.A. & Clark, R.N. (1990) Infrared Spectra and Crystal Chemistry of Scapolites: Implications for Martian Mineralogy. J. Geophys. Res., 95: pp. 14481-14495.

Swayze, G.A., Smith, K.S., Clark, R.N., Sutley, S.J., Pearson, R.M., Vance, J.S., Hageman, P.L., Briggs, P.H., Meier, A.L., Singleton, M.J., Roth, S. (2000) Using imaging spectroscopy to map acid mine waste. Environmental Science and Technology 34: pp. 47-54.

Sweldens, W. (1996) The lifting scheme: A custom-design construction of biorthogonal wavelets. Applied and Computational Harmonic Analysis 3: pp. 186-200.

Switzer, P. (1980) Extension of discriminant analysis for statistical classification of remotely sensed satellite imagery. Journal of the International Association for Mathematical Geology 12: pp. 367-376.

Switzer, P., Green, A.A. (1984) Min/max autocorrelation factors for multivariate spatial imagery. Technical report No. 6, Department of Statistics, Stanford University, Stanford.

T

Tate, N.J. & Atkinson, P.M. (2001) Modelling Scale in Geographical Information Science, Wiley, Chichester.

Tatem, A.J., Lewis, H.G., Atkinson, P.M. & Nixon, M.S. (2001) Super-resolution target identification from remotely sensed images using a Hopfield neural network, IEEE Transactions on Geoscience & Remote Sensing 39: pp. 781-796.

Tatem, A.J., Lewis, H.G., Atkinson, P.M. & Nixon, M.S. (2001a) Super-resolution target identification from remotely sensed images using a Hopfield neural network, IEEE Transactions on Geoscience and Remote Sensing 39: pp. 781-796.

Tatem, A.J., Lewis, H.G., Atkinson, P.M. & Nixon, M.S. (2001b) Multiple class land cover mapping at the sub-pixel scale using a Hopfield neural network, International Journal of Applied Earth Observation and Geoinformation 3: pp. 184-190.

Tatem, A.J., Lewis, H.G., Atkinson, P.M. & Nixon, M.S. (2002) Land cover simulation and estimation at the sub-pixel scale using a Hopfield neural network, Remote Sensing of Environment 79: pp. 1-14.

Tatem, A.J., Lewis, H.G., Atkinson, P.M. & Nixon, M.S. (2003) Increasing the spatial resolution of agricultural land cover maps using a Hopfield neural network, International Journal of Geographical Information Science 17: pp. 647-672.

Teggi, S., Cecchi, R. & Serafini, F. (2003) TM and IRS-1C-PAN data fusion using multiresolution decomposition methods based on the 'à trous' algorithm. International Journal of Remote Sensing, 24 (6): pp. 1287-1301.

Terretaz, P. (1998) Comparison of different methods to merge SPOT P and XS data: evaluation in an urban area, in Gudmandsen (Eds.), Future Trends in Remote Sensing, Balkema, Rotterdam, pp. 435-443.

Thomas, I., Benning, V. & Ching, N.P. (1987) Classification of Remotely Sensed Images, Adam Hilger, Bristol.

Tokola, T., Pitkänen, J., Partinen, S. & Muinonen, E. (1996) Point accuracy of a nonparametric method in estimation of forest characteristics with different satellite materials. International Journal of Remote Sensing, 17 (12): pp. 2333-2351.

Tom, C.H. & Miller, L.D. (1984) An automated land-use mapping comparison of the Bayesian maximum likelihood and linear discriminant analysis algorithms, Photogrammetric Engineering & Remote Sensing 50: pp. 193-207.

Tomaselli, R. (1981) Main physiognomic types and geographic distribution of shrub systems related to Mediterranean climates. Ecosystems of the world 11 Mediterranean-type shrublands. F. Di Castri, D.W. Goodall and R.L. Specht, Elsevier pp. 95-106.

Tomppo, E. (1996) Multi-source National Forest Inventory of Finland. New Thrusts in Forest Inventory. Proceedings of the Subject Group S4.02-00 'Forest Resource Inventory and Monitoring' and Subject Group S4.12-00 'Remote Sensing Technology'. Vol. I. IUFRO XX World Congress 6-12 August 1995, Tampere, Finland. EFI Proceedings No. 7. European Forest Institute, 15 pp.

Tomppo, E., Goulding, C. & Katila, M. (1999) Adapting Finnish multi-source forest inventory techniques to the New Zealand preharvest inventory. Scandinavian Journal of Forest Research 14: pp. 182-192.

Tomppo, E., Korhonen, K.T., Heikkinen, J. & Yli-Kojola, H. (2001) Multisource inventory of the forests of the Hebei Forestry Bureau, Heilongjiang, China. Silva Fennica 35(3): pp. 309-328.

Townshend, J.R.G. (1992) Land cover, International Journal of Remote Sensing 13: pp. 1319-1328.

Townshend, J.R.G. (1981) Terrain Analysis and Remote Sensing. George Allen & Uniwin, London, 232 pp.

Townshend, J.R.G. (1981) The Spatial Resolving Power of Earth Resources Satellites. Progress in Physical Geography 5: pp. 32-55.

Tricart, J. (1965) Principes et Méthodes de la Géomorphologie. Masson, Paris.

Tso, B. & Mather, P.M. (2001) Classification Methods for Remotely Sensed Data, Taylor and Francis, London.

Turcotte, D.L. (1992) Fractals and Chaos in geology and geophysics. Cambridge University Press, Cambridge, 220 pp.

U

UK Biodiversity Steering Group (1995) The UK Steering Group Report. Volumes 1 & 2. London: HMSO.

USDA, (1993) Soil Survey Manual. United States Department of Agriculture Handbook No. 18. United States Department of Agriculture, Washington DC, 437 pp.

Ustin, S.L., Smith, M.O. & Adams, J.B (1993) Remote sensing of ecological models using spectral mixture analysis, in J.R. Ehleringer and C.B. Field (Eds.), Scaling Physiological Processes: Leaf to Globe, Academic Press Inc. pp. 339-357.

Ustin, S.L., Smith, M.O., Jacquemoud, S., Verstraete, M. & Govaerts, Y. (1999) Geobotany: Vegetation Mapping for the Earth Sciences. In: A.N. Rencz (Eds.), Remote Sensing for the Earth Sciences. Manual of Remote Sensing Vol.3.Wiley & Sons, New York, pp. 189-248.

V

Van Collie, F.M.B., Verbeke, L.P.C., De Wulf, R.R. & Kerckhoff, E.J.H. (2001) Artificial neural network training for savannah vegetation mapping: transferring previously learned experience to new learning tasks, In A. Belward, E. Binaghi, P.A. Brivio, G.A. Lanzarone and G. Tosi (Eds.), Geo-spatial Knowledge Processing for Natural Resource Management, 28-29 June 2001, University of Insubria, pp. 357-363.

Van de Koppel, J., Rietkerk, M. & Weissing, F.J. (1997) Catastrophic Vegetation Shifts and Soil Degradation in Terrestrial Grazing Systems. trends in Ecology and Evolution 12: pp. 352-356.

Van der Kwast, J. & Walstra, J. (2001) Contextual Vegetation classification – Using the spatial reclassification kernel to classify heterogeneous vegetation from DAIS images. Utrecht, MSc Thesis Utrecht University, 60 pp.

Van der Meer, F. & Bakker, W. (1997) Cross Correlogram Spectral Matching (CCSM): application to surface mineralogical mapping using AVIRIS data from Cuprite, Nevada. Remote Sens. Environ 61: pp. 371-382.

Van der Meer, F. & Bakker, W. (1998) Validated surface mineralogy from high-spectral resolution remote sensing: a review and a novel approach applied to gold exploration using AVIRIS data. Terra Nova 10: pp. 112-118.

Van Der Meer, F. & De Jong, S.M. (2000) Improving the results of spectral unmixing of Landsat Thematic Mapper imagery by enhancing the orthogonality of end-members, International Journal of Remote Sensing 21: pp. 2781-2797.

Van der Meer, F. (1994) Extraction of mineral absorption features from high-spectral resolution data using non-parametric geostatistical techniques, International Journal of Remote Sensing 15: pp. 2193-2214.

Van der Meer, F. (1995) Spectral reflectance of carbonate mineral mixtures and bidirectional reflectance theory. Remote Sensing Rev. 13: pp. 67-94.

Van der Meer, F. (1996) Classification of remotely-sensed imagery using an indicator kriging approach: application to the problem of calcite-dolomite mineral mapping, International Journal of Remote Sensing 17: pp. 1233-1249.

Van Der Meer, F. (1996) Spectral mixture modelling and spectral stratigraphy in carbonate lithofacies mapping, ISPRS Journal of Photogrammetry and Remote Sensing 51: pp. 150-162.

Van der Meer, F. (1997) What does multisensor image fusion add in terms of information content for visual interpretation?, International Journal of Remote Sensing 18: pp. 445-452.

Van der Meer, F. (2000) Geophysical inversion of imaging spectrometer data for geologic modelling. International Journal of Remote Sensing 21: pp. 387-393.

Van der Meer, F. (1994) Sequential Indicator Conditional Simulation and Indicator Kriging Applied to Discrimination of Dolomitization in GER 63-channel Imaging spectrometer data. Nonrenewable Resources 3: pp. 146-164.

Van der Meer, F.D. & de Jong S.M. (2001) (Eds.), Imaging Spectrometry: Basic Principles and Prospective Applications. Bookseries Remote Sensing and Digital Image Processing Kluwer Academic Publishers, Dordrecht, Vol.4, 403 pp.

Van der Meer, F.D. & De Jong, S.M. (2000) Improving the results of spectral unmixing of Landsat Thematic Mapper imagery by enhancing the orthogonality of endmembers. International Journal of Remote Sensing 21: pp. 2781-2797.

Van der Meer, F.D., de Jong, S.M. & Bakker, W. (2001) Imaging Spectrometry: Basic Analytical Techniques. In: Van der Meer F.D. & S.M. de Jong (Eds.), Imaging Spectrometry, Kluwer Academics Publishers Dordrecht, pp. 17-61.

Vane, G. & Goetz, A.F.H. (1993) Terrestrial Imaging Spectrometry: Current Status, Future Trends. Remote Sensing of Environment 44: pp. 117-126.

Véhel, J.L. & Mignot, P. (1994) Multifractal Segmentation of Images, Fractals, vol.2, No.3: pp. 371-378.

Ventura, F.N., Fonseca, L.M.G. & Rosa, A.N.C.S. (2002) Remotely sensed image fusion using the wavelet transform, in Proceedings of the International Symposium of Remote Sensing of Environment, Buenos Aires, Argentina, 8-12 April 2002.

Verhoeye J. & de Wulf, R. (2002) Land cover mapping at sub-pixel scales using linear optimization techniques. Remote Sensing of Environment vol. 79 (1): pp. 96-104.

Verhoeye J., & De Wulf, R. (2002) Land cover mapping at sub-pixel scales using linear optimization techniques, Remote Sensing of Environment 79: pp. 96-104.

Verstappen, H.Th. (1977) Remote Sensing in Geomorphology. Elsevier Scientific Publishing Company, Amsterdam, 210 pp.

Verstraete, M., Pinty, M. & Myeni, R.B. (1996) Potential and limitations of information extraction on the terrestrial biosphere from satellite remote sensing, Remote Sensing of Environment 58: pp. 201-214.

Vincent, L. & Soille, P. (1991) Watersheds in digital spaces: An efficient algorithm based on immersion simulations, IEEE Transactions on Pattern Analysis and Machine Intelligence 13 (6): pp. 583-125.

Vuorella, N. (2000) Can data combinations help to explain the existance of diverse landscapes? Fennia, 178: pp. 55-80.

W

Wackernagel, H. (1995) Multivariate Geostatistics, Springer-Verlag, Berlin, 256 pp.

Wald, L., Ranchin, T. & Mangolini, M. (1997) Fusion of satellite images of different spatial resolutions: assessing the quality of resulting images. Photogrammetric Engineering & Remote Sensing 63 (6): pp. 691-699.

Waldrop, M.M. (1992) Complexity. The emerging science at the edge of order and chaos, Simon and Schuster, 380 pp.

Wang, F. (1994) The use of artificial neural networks in a geographical information system for agricultural land-suitability assessment, Environment and Planning A 26: pp. 265-284.

Wang, L. & He, D.C. (1990) A new statistical approach for texture analysis, Photogrammetric Engineering & Remote Sensing 56 (1): pp. 61-66.

Webster, R. & Oliver, M.A. (1990) Statistical Methods for Soil and Land Resources Survey, Oxford University Press, Oxford.

Webster, R., Curran, P.J. & Munden, J.W. (1989) Spatial correlation in reflected radiation from the ground and its implications for sampling and mapping by ground-based radiometry, Remote Sensing of Environment 29: pp. 67-78.

Welch, J.R. & Slater, K.G. (1971) A context algorithm for pattern recognition and image interpretation. IEEE Transactions on System, Man and Cybernetics, SMC-1 (1): pp. 24-30.

Wessman, C.A. (1989) Evaluation of Canopy Biochemistry. In: R.J. Hobbs and H.A. Mooney, Remote Sensing of Biosphere Functioning. Ecological Stduies 79. Springer-Verlag, New York, pp. 135-156.

Wessmann, C.A., Aber, J.D., Peterson, D.L. & Melillo, J. (1988) Remote sensing of canopy chemistry and nitrogen cycling in temperate forest ecosystems. Nature 335: pp. 154-156.

Wharton, S.W. (1982) A contextual classification method for recognizing land use patterns in high resolution remotely sensed data. Pattern Recognition 15 (4): pp. 317-324.

Wharton, S.W. (1983) A generalized histogram clustering scheme for multidimensional image data. Pattern Recognition, 16 (2): pp. 193-199.

Wilkinson, G.G. & Megier, J. (1990) Evidential reasoning in a pixel classification hierarchy – a potential method for integrating image classifiers and expert system rules based on geographic context, International Journal of Remote Sensing 11: pp. 1963-1968.

Wilkinson, G.G. (1997) Open questions in neurocomputing for Earth observation, in I Kanellopoulos, G.G. Wilkinson, F. Roli and J. Austin (Eds.), Neurocomputation in Remote Sensing Data Analysis, Springer, Berlin, pp. 3-13.

Williamson, H.D. (1994) Estimating sub-pixel components of a semi-arid woodland, International Journal of Remote Sensing 15: pp. 3303-3307.

Winkler, G. (2003) Image Analysis, Random Fields and Markov Chain Monte Carlo Methods. Applications of Mathematics Vol. 27. Springer-Verlag, Berlin, 388 pp.

Wolfe, W.L. &. Zissis, G.J. (1993) (Eds) The Infrared Handbook. Environmental Research Institute of Michigan (ERIM), Ann Arbor, Michigan.

Wood, J. (1996) The Geomorphological Characterisation of Digital Elevation Models, unpublished Ph.D. thesis, University of Leicester, Leicester.

Woodcock, C.E. & Harward, V.J. (1992) Nested-hierarchical scene models and image segmentation, International Journal of Remote Sensing 13: pp. 3167-3187.

Woodcock, C.E. & Strahler, A.H. (1987) The factor of scale in remote sensing, Remote Sensing of Environment 21: pp. 311-322.

Woodcock, C.E., Gopal, S. & Albert, W. (1996) Evaluation of the potential for providing secondary labels in vegetation maps, Photogrammetric Engineering & Remote Sensing 62: pp. 393-399.

Woodcock, C.E., Strahler, A.H. & Jupp, D.L.B. (1988a) The use of variograms in remote sensing – I. Scene models and simulated images, Remote Sensing of Environment 25: pp. 323-348.

Woodcock, C.E., Strahler, A.H. & Jupp, D.L.B. (1988b) The use of variograms in remote sensing – II. Real digital images, Remote Sensing of Environment 25: pp. 349-379.

Woodcock, C.E., Strahler, A.H. & Jupp, D.L.B. (1998) The use of variograms in remote sensing: II. Real digital images. Remote Sensing of Environment 25: pp. 349-379.

Wu, C. & Murray, A.T. (2003) Estimating impervious surface distribution by spectral mixture analysis, Remote Sensing of Environment (in press).

Wu, J. & Loucks, O.L. (1995) From balance of nature to hierarchical patch dynamics: A paradigm shift in ecology, The Quarterly Review of Biology 70: pp. 439-466.

Wu, J. & Marceau, D.J. (2002) Modelling complex ecological systems: An introduction, Ecological Modelling 153 (1-2): pp. 1-6.

Wu, J. (1999) Hierarchy and scaling: Extrapolating information along a scaling ladder. Canadian Journal of Remote Sensing 25 (4): pp. 367-380.

Wu, J., Jelinski, D.E., Luck, M., & Tueller, P.T. (2000) Multiscale analysis of landscape heterogeneity: Scale variance and pattern metrics, Geographic Information Sciences 6 (1): pp. 1-19.

Wu, S.Y. & Liu, A.K. (2003) Towards an automated ocean feature detection, extraction and classification scheme for SAR imagery. International Journal of Remote Sensing 24 (5): pp. 935-951.

X

Xu, B. Gong, P. Spear, R. & Seto, E. (2003) Comparison of different gray level reduction schemes for a revised texture spectrum method for land-use classification using IKONOS imagery, Photogrammetric Engineering & Remote Sensing, 69: pp. 529-536.

Xu, Y., Weaver, J., Healy, D. & Lu, J. (1994) Wavelet transform domain filters: a spatially selective noise filtration technique. IEEE Transactions on Image Processing 3 (6): pp. 747-758.

Y

Yamaguchi, Y., Nagai, T. & Yamada, H. (1995) JERS-1 SAR image analysis by wavelet transform. IEICE Transactions on Communication E78-B (12): pp. 1617-1621.

Yang, H. (1999) Imaging spectrometry for hydrocarbon microseepage. PhD Thesis. ITC, Publication No. 76, International Institute for Geoinformation Science and Earth Observation (ITC), Enschede, The Netherlands.

Yang, H., Van der Meer, F., Bakker, W. & Tan, Z.J. (1999) A back-propagation neural network for mineralogical mapping from AVIRIS data. International Journal of Remote Sensing 20: pp. 97-110.

Yoder, B.J. & Pettigrew-Crosby, R.E. (1995) Predicting nitrogen and chlorophyll content and concentrations from reflectance spectra (400-2500 nm) at leaf and canopy scales. Remote Sensing of Environment 53: pp. 199-211.

Yoky, D.A. (1996) Multiresolution wavelet decomposition image merger of Landsat thematic mapper and SPOT panchromatic data. Photogrammetric Engineering & Remote Sensing 62 (9): pp. 1067-1074.

Yuan, D., Elvidge, C.D. & Lunetta R.S. (1998) Survey of multispectral methods for land cover change analysis, in R.S. Lunetta and C.D. Elvidge (Eds.), Remote Sensing Change Detection: Environmental Monitoring and Applications, Ann Arbor Press pp. 21-40.

Z

Zhan, Q., Molenaar, M. & Lucieer, A. (2002) Pixel unmixing at the sub-pixel scale based on land cover class probabilities: application to urban areas, Uncertainty in Remote Sensing and GIS (Eds. G.M. Foody and P.M. Atkinson), Wiley, Chichester, pp. 59-76.

Zhang, R., Warrick, A.W., & Myers, D.E. (1990) Variance as a function of sample support size, Mathematical Geology 22: pp. 107-122.

Zhang, Y. (1999) Optimisation of building detection in satellite images by combining multispectral classification and texture filtering. ISPRS Journal of Photogrammetry & Remote Sensing 54: pp. 50-60.

Zhang, Z., Shimoda, H., Fukue, K. & Sakata, T. (1988) A new spatial classification algorithm for high ground resolution images. Proceedings of IGARSS'88. Edinburgh, Scotland, pp. 509-512.

Zheng, Q. & Chellappa, R.A. (1993) Computational vision approach to image registration. IEEE Transactions on Image Processing 2 (3): pp. 311-326.

Zhou, J., Civco, D.L. & Silander, J.A. (1998) A wavelet transform method to merge Landsat TM and SPOT panchromatic data. International Journal of Remote Sensing 19 (4): pp. 743-757.

Zhu, C.Q., Shi, W.Z. & Wan, G. (2002) Reducing remote sensing image and simplifying DEM data by the multi-band wavelet. International Journal of Remote Sensing, 23 (3): pp. 525-536.

Zukowskyj, P.M., Bussell, M.A., Power, C. & Teeuw, R.M. (2001) Quantitative accuracy assessment of contextually filtered classified images. International Journal of Remote Sensing 16: pp. 3203-3222.

Index